Springer Series in Materials Science 183

Andrei Benediktovitch
Ilya Feranchuk
Alexander Ulyanenkov

Theoretical Concepts of X-Ray Nanoscale Analysis

Theory and Applications

Springer

Springer Series in Materials Science

Volume 183

For further volumes:
http://www.springer.com/series/856

The Springer Series in Materials Science covers the complete spectrum of materials physics, including fundamental principles, physical properties, materials theory and design. Recognizing the increasing importance of materials science in future device technologies, the book titles in this series reflect the state-of-the-art in understanding and controlling the structure and properties of all important classes of materials.

Andrei Benediktovitch · Ilya Feranchuk
Alexander Ulyanenkov

Theoretical Concepts of X-Ray Nanoscale Analysis

Theory and Applications

Springer

Andrei Benediktovitch
Ilya Feranchuk
Physics Department
Belarusian State University
Minsk
Belarus

Alexander Ulyanenkov
Rigaku Europe SE
Ettlingen
Germany

ISSN 0933-033X
ISSN 2196-2812 (electronic)
ISBN 978-3-642-38176-8
ISBN 978-3-642-38177-5 (eBook)
DOI 10.1007/978-3-642-38177-5
Springer Heidelberg New York Dordrecht London

Library of Congress Control Number: 2013942118

Printed on acid-free paper

Springer is part of Springer Science+Business Media (www.springer.com)

Preface

X-rays have been proven to be a powerful and reliable tool in studying a large diversity of micro- and nanoscale objects. The wavelength of X-rays is a perfect fit to the typical sizes of basic structures used in all modern technologies and science: crystallographic lattice in semiconductor thin films; biological molecules in protein crystallography; nanoscale objects like quantum dots and quantum wires in optoelectronics; and many others. This fact initiated the intensive development of various measurement techniques and instrumentation to satisfy the large variety of requirements coming from scientific and industrial communities. Information on the intrinsic structure of samples is further obtained from the detailed analysis of the scattered and detected X-ray intensities, which demands robust theoretical methods for data interpretation. The experimental data obtained from modern X-ray equipment contains a large amount of information hidden in the fine structure of the measured X-ray spectra. This fine structure became measurable due to the essential progress in the development of X-ray optics, detectors, and X-ray sources. Explanation of some effects observed in conventional laboratory X-ray measurements requires fundamental investigations which are on the leading edge of a modern science. From another perspective, the application of X-ray methods in production processes requires highly automated and robust analytical tools. Thus, the growing complexity of both experiments and structure of the samples constantly stimulates the further development of the theoretical methods for data analysis.

There are multiple X-ray techniques used for sample evaluation, each of which is suitable for different kinds of the structures. For example X-ray Bragg diffraction probes samples possessing a crystallographic structure and characterizes the structure on a broad scale, from micro-crystallites in polycrystalline materials to the properties of coherent epitaxial samples averaged over large areas. For the latter case of epitaxial structures, X-ray diffraction in a high-resolution mode is used. The information obtained from X-ray diffraction patterns reconstructs the sample morphology, helps in structure determination and phase identification, and may comprise such parameters as crystallinity, mosaicity, crystallographic lattice mismatch, lattice strain status, residual stresses, lattice defects, and many others. The specular X-ray reflectivity characterizes surface and subsurface amorphous or crystalline layers in view of their electron density profiles, layer thicknesses, and interface roughness. The X-ray small-angle scattering

method exposes valuable information on the distribution and characteristics of the non-uniformities inside or on the surface of the sample. In grazing-incidence mode, this technique explores the lateral surface structure of the studied specimens. The pair-distribution function method permits us to obtain the interatomic distances for amorphous, crystalline, and quasi-crystalline materials. The important trend in recent decades is the simultaneous usage of several techniques for characterization, which deliver comprehensive and concise information on the sample structure. However, this approach requires consistent theoretical models of data interpretation for each technique used. This monograph covers the main X-ray techniques used in the material researches, including high-resolution X-ray diffraction, specular and off-specular X-ray reflectivity, grazing-incidence small-angle X-ray scattering, and residual stress analysis. This book presents the unified microscopic approach for a theoretical description of experimental data obtained by various techniques and thus can be used both as a guidance for the development of new interpretation methods in X-ray analysis and as a handbook for students studying the theory of condensed matter and interaction of radiation with the solid state matter.

In addition to the practical aspect of data analysis, the interaction of X-rays with matter plays an important and fundamental role by demonstrating the effectiveness of quantum electrodynamics and scattering theory for the investigation of macroscopic systems. The Hamiltonian describing the interaction of X-rays with atoms has a simple form and contains a small physical parameter proportional to the ratio of the amplitude of Compton scattering of photon on the free electron to the average interatomic distance. As a result, the macroscopic Maxwell's equation for transmission of X-rays in a medium can be derived from first principles after averaging the exact equations of quantum electrodynamics over the microstates of electrons, and without the use of phenomenological material equations. The deduced effective potential of the interaction of X-rays with matter is small enough to successfully use the mathematical methods of the perturbation theory for the scattering problem. This fundamental property of the X-ray optics is not sufficiently covered in the existing literature, and the aim of this book is to illuminate all the theoretical details of the interaction of X-rays with nanoscale objects. The manifestation of the mentioned property of X-ray optics is observed in high-resolution experiments, which are intensively used for the study of thin films and nano-objects possessing a complex structure.

The monograph consists of seven chapters dedicated to different application techniques and fundamental aspects of X-ray scattering from atomic systems. In the Chap. 1, the equations of X-ray optics describing the propagation of a classic wave field in a medium are derived from the Schrödinger equation for the system, which takes into account the quantum properties of both atomistic medium and electromagnetic field. Numerous approximations are discussed, which are used in analytical methods for X-ray optics including calculation of X-ray polarizability. The important aspects of the theory of X-ray scattering from macroscopic objects are considered in the Chap. 2. The relations between the temporal scattering theory of real experiments and the stationary scattering theory with boundary conditions

used in the data interpretation are established. The method of the distorted-wave Born approximation (DWBA) widely used in scattering theory is presented for different sample structures and experimental geometries. The Chap. 3 deals with the method of X-ray reflectivity (XRR) from the multilayered samples with rough interfaces. The theoretical profiles of the specularly reflected X-ray intensity are calculated on the basis of a self-consistent approach for the transition layers at the boundaries of lamellae. The original method of eigenwaves is derived, which simplifies and accelerates the calculation of XRR intensities from the periodic multilayered structures. The basic principles of the high-resolution X-ray diffraction (HRXRD) from the perfect crystalline samples are explained in the Chap. 4. The critical issues of HRXRD are discussed in the details: the transition from kinematical to dynamical theory of X-ray diffraction, the method of eigenwaves for superlattices, the grazing-incidence diffraction (GID), the diffraction from surface nanostructures, and others. The Chap. 5 is dedicated to X-ray diffuse scattering from imperfect surfaces and interfaces. The statistical approach is used to account for the fluctuations of the macroscopic parameters of the sample on the basis of DWBA method. The analysis of the accuracy delivered by different zero approximations for DWBA is performed for the geometry of XRR and grazing-incidence small-angle X-ray scattering (GISAXS) techniques, which are both intensively used for morphology characterization of modern surface nanostructures. X-ray diffraction from the crystals with defects is presented in the Chap. 6, where the attention is paid to the formation and relation between coherent diffraction intensity and diffuse scattering intensity, which is caused by scattering from the statistical ensemble of crystallographic defects. The statistical theory of X-ray diffraction in imperfect crystals is derived, which is applicable for GID case also. The analytical method for simulation of diffuse X-ray peaks caused by the defects is described. This method is applicable for an arbitrary density of the defects existing in the crystal and is comparable in accuracy to the timeconsuming Monte-Carlo calculations. Finally, the Chap. 7 is devoted to the important application of X-rays for residual stress analysis in solid bulk materials, coatings, and polycrystalline samples. The various models of grain interaction are discussed with regard to their applicability limits, and the covariant method of X-ray intensity averaging over the grain distribution is proposed.

The authors are indebted to Prof. V. G. Baryshevsky and Prof. L. I. Komarov for cooperation and innumerable scientific discussions over the years devoted to quantum theory of interaction between radiation and matter.

We also thank all our colleagues in numerous software projects, especially A. Kozlovski, A. Zhylik and M. Rusetsky, who assisted us with the numerical simulations and interpretations of experimental data. We are also thankful to Dr. T. Ulyanenkova for valuable support in the proof reading of the manuscript.

Minsk, Belarus — Andrei Benediktovitch
Minsk, Belarus — Ilya Feranchuk
Karlsruhe, Germany — Alexander Ulyanenkov

Contents

Acronyms

AFM	Atomic force microscopy
ASF	Atomic scattering factor
DDT	Dynamical diffraction theory
DWBA	Distorted-wave Born approximation
DWF	Debye–Waller factor
EAD	Extremely asymmetric diffraction
GA	Genetic algorithm
GID	Grazing-incidence diffraction
GISAXS	Grazing-incidence small-angle X-ray scattering
GIXRD	Grazing-incidence X-ray diffraction
GTR	Grating truncation rod
HRXRD	High-resolution X-ray diffraction
IR	Irreducible representation
iVW	Inverse Vook–Witt model of grain interaction
MDWBA	Modified distorted-wave Born approximation
MEW	Method of eigenwaves
ODF	Orientation distribution function
PDF	Pair-distribution function
QD	Quantum dots
QED	Quantum electrodynamics
QW	Quantum wires
RDS	Resonant diffuse scattering
RSM	Reciprocal space map
SCA	Self-consistent approach
TER	Total external reflection
VW	Vook–Witt model of grain interaction
XEC	X-ray elastic constants
XFEL	X-ray free electron laser
XRR	X-ray reflectivity
XSF	X-ray stress factors

Chapter 1
Basic Principles of the Interaction of X-Rays with Matter: Quantum Electrodynamical Analysis

Microscopic analysis of various processes arising due to the interaction of X-rays with condensed matter was considered in many papers, especially in the fundamental monograph [1], where the basic principles of X-ray optics were described. However, since that time a series of advanced techniques for X-ray structure characterization have been actively developed, such as the diffraction near the absorption edges [2], diffraction in the ferromagnetic materials [3], methods using the high-intensity radiation from the X-ray laser [4], and others.

Traditionally, the anisotropic correlative effects as well as the nonlinear processes due to the interaction of the intensive electromagnetic field with media are more essential in the optical range of wavelengths and there is a huge number of reviews in this field (for example, [5–8] and references therein). For the analysis of these processes, the microscopic equations of quantum electrodynamics have to be used, which imply the quantum properties of both the electromagnetic field and the matter are taken into account.

At the same time, in the basic books on the X-ray scattering by the inhomogeneous structures interaction of the radiation with matter is based on the simplest model where electrons are considered as classical oscillators [9, 10]. However, the progress in experimental and theoretical physics demands to consider this interaction on the basis of the first principles of quantum electrodynamics in order to analyze the limits of the conventional approximations. The main goal of this chapter is the systematic investigation of these problems.

1.1 Equations of X-Ray Optics

X-rays are the unique instrument for investigation of the structure of materials, and it is extremely important for the great number of high-technological processes. The advantages of X-ray applications are conditioned by a series of essential factors: (i) small wavelength providing the resolution compared with the characteristic size

A. Benediktovitch et al., *Theoretical Concepts of X-Ray Nanoscale Analysis*,
Springer Series in Materials Science 183, DOI: 10.1007/978-3-642-38177-5_1,

of the electron density distribution in atoms; (ii) a weak interaction of X-ray beams with the matter providing non-destructive characterization of the objects; (iii) simple and universal form of this interaction which is important for the solution of the inverse problem when the electron density distribution in the investigated medium is reconstructed on the basis of the X-ray scattering profiles; (iv) possibility to describe the evolution of X-ray wave field in a medium on the basis of the perturbation theory applied directly to the microscopic equations of quantum electrodynamics.

Let us consider the main approximations used on the way from quantum electrodynamics to the macroscopic Maxwell's equations for electromagnetic field in a medium [8, 11]. The start point is the Schrödinger equation for the total state vector $|\Phi(t)>$ that corresponds to the whole system, the non-relativistic quantum medium and the quantized electromagnetic field:

$$i\hbar\frac{\partial}{\partial t}|\Phi(t)>=\hat{H}|\Phi(t)> \tag{1.1}$$

with the Hamiltonian that has the following form in the Coulomb gauge (see, for example, [7]):

$$\begin{aligned}\hat{H}=\hat{H}_M+\sum_j^{N_e}\left\{\frac{1}{2m}\left[-2\frac{e_0}{c}\hat{\boldsymbol{p}}_j\hat{\boldsymbol{A}}(\boldsymbol{r}_j)+\frac{e_0^2}{c^2}(\hat{\boldsymbol{A}}(\boldsymbol{r}_j))^2\right]\right.\\ \left.-\frac{e_0\hbar}{2mc}\boldsymbol{\sigma}_j\hat{\boldsymbol{H}}(\boldsymbol{r}_j)\right\}+\sum_{\boldsymbol{k}s}\hbar\omega_{\boldsymbol{k}}a_{\boldsymbol{k}s}^+a_{\boldsymbol{k}s}\equiv\hat{H}_M+\hat{H}_{MR}+\hat{H}_R;\\ \hat{H}_M=\sum_j^{N_e}\frac{\hat{\boldsymbol{p}}_j{}^2}{2m}+\hat{U}(\{\boldsymbol{r}_j\});\\ \hat{\boldsymbol{A}}(\boldsymbol{r})=\sum_{\boldsymbol{k}s}\sqrt{\frac{2\pi\hbar c^2}{\omega_{\boldsymbol{k}}V}}\boldsymbol{e}_{\boldsymbol{k}s}[a_{\boldsymbol{k}s}e^{i\boldsymbol{k}\boldsymbol{r}}+a_{\boldsymbol{k}s}^+e^{-i\boldsymbol{k}\boldsymbol{r}}];\\ \hat{\boldsymbol{H}}(\boldsymbol{r})=[\nabla\times\hat{\boldsymbol{A}}];\quad(\boldsymbol{k}\boldsymbol{e}_{\boldsymbol{k}s})=0.\end{aligned} \tag{1.2}$$

Here e_0, m are the electron charge and mass, respectively; interaction between X-ray field and atomic nuclei can be neglected; $\hbar$ is the Plank constant; c is the light velocity; $a_{\boldsymbol{k}s}(a_{\boldsymbol{k}s}^+)$ is the operator of annihilation (creation) of the photon with the frequency $\omega_{\boldsymbol{k}}=ck$, wave vector $\boldsymbol{k}$ and polarization $\boldsymbol{e}_{\boldsymbol{k}s}$; $\hat{\boldsymbol{A}}(\boldsymbol{r})$ and $\hat{\boldsymbol{H}}(\boldsymbol{r})$ are the operators of the transversal vector potential and magnetic field, correspondingly; $\boldsymbol{r}_j$, $\boldsymbol{\sigma}_j/2$ are the coordinate and spin of jth electron; N_e is the total number of electrons; $\hat{H}_M$ is the Hamiltonian of the medium with the potential energy operator $\hat{U}(\{\boldsymbol{r}_j\})$ which corresponds to the Coulomb interaction between electrons and nuclei and provides the stable state of medium. Operator $\hat{H}_{MR}$ is the Hamiltonian of the electron interaction with the quantum field, the term proportional to the magnetic

field is included in order to consider the anisotropic ferromagnetic materials; $\hat{H}_R$ is the Hamiltonian of a free electromagnetic field.

Conventional approach for description of the interaction between X-rays and medium corresponds to the Maxwell's equations for the classical electromagnetic field coupled with the Schrödinger equation for the electron subsystem. Sometimes the latter one is also considered in a semiclassical way. This system of equations is the theoretical basis for so-called X-ray optics approach [1]. It is possible, however, to deduce these equations directly from the Eq. (1.1) for the state vector of the whole system if the adiabatic perturbation theory [12] is used, and that allows to define the limits of the semiclassical approximation. Figure 1.1 represents schematically the sequence of the transformation that should be done in order to pass from the quantum electrodynamics to the X-ray optics approach.

The canonical transformation of the field operator [13], being applied to the Hamiltonian (1.2), separates the time dependent classical field $\boldsymbol{A}(\boldsymbol{r}, t)$ from the radiation component $\hat{\boldsymbol{A}}_R(\boldsymbol{r})$ defined by the quantum fluctuations of the electromagnetic field relatively to the selected classical field [8]:

$$\hat{U}_R(t) = \prod_{\boldsymbol{k}s} e^{c_{\boldsymbol{k}s} a^+_{\boldsymbol{k}s} - c^*_{\boldsymbol{k}s} a_{\boldsymbol{k}s}} = \prod_{\boldsymbol{k}s} e^{c_{\boldsymbol{k}s} a^+_{\boldsymbol{k}s}} e^{-c^*_{\boldsymbol{k}s} a_{\boldsymbol{k}s}} e^{-1/2|u_{\boldsymbol{k}s}(t)|^2};$$

$$c_{\boldsymbol{k}s}(t) = u_{\boldsymbol{k}s}(t) e^{-i\omega_{\boldsymbol{k}} t}; \quad \hat{U}^+_R \hat{\boldsymbol{A}}(\boldsymbol{r}) \hat{U}_R = \boldsymbol{A}(\boldsymbol{r}, t) + \hat{\boldsymbol{A}}_R(\boldsymbol{r});$$

$$\boldsymbol{A}(\boldsymbol{r}, t) = \sum_{\boldsymbol{k}s} \sqrt{\frac{2\pi\hbar c^2}{\omega_{\boldsymbol{k}} V}} \boldsymbol{e}_{\boldsymbol{k}s} [u_{\boldsymbol{k}s} e^{i\boldsymbol{k}\boldsymbol{r} - i\omega_{\boldsymbol{k}} t} + u^*_{\boldsymbol{k}s} e^{-i\boldsymbol{k}\boldsymbol{r} + i\omega_{\boldsymbol{k}} t}];$$

$$\hat{\boldsymbol{A}}_R(\boldsymbol{r}) = \sum_{\boldsymbol{k}s} \sqrt{\frac{2\pi\hbar c^2}{\omega_{\boldsymbol{k}} V}} \boldsymbol{e}_{\boldsymbol{k}s} [a_{\boldsymbol{k}s} e^{i\boldsymbol{k}\boldsymbol{r}} + a^+_{\boldsymbol{k}s} e^{-i\boldsymbol{k}\boldsymbol{r}}]. \tag{1.3}$$

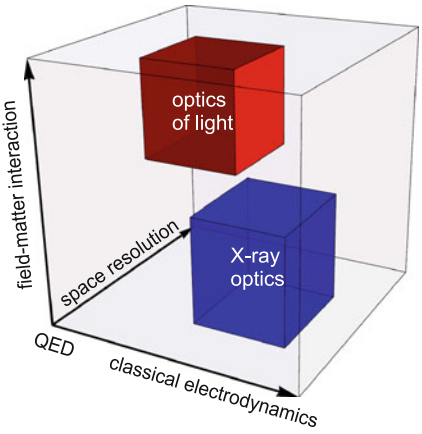

Fig. 1.1 Schematic representation of importance of different approximations for light and X-ray optics

and canonical transformation of other operators in the Eq. (1.1) leads to the following equations:

$$\begin{aligned}
\hat{H}_R(t) &= \hat{U}_R^+(t)\hat{H}_R\hat{U}_R(t) \\
&= \hat{H}_R + \sum_{\boldsymbol{ks}} \hbar\omega_{\boldsymbol{k}}[a_{\boldsymbol{ks}}^+ c_{\boldsymbol{ks}}(t) + a_{\boldsymbol{ks}} c_{\boldsymbol{ks}}^*(t) + |u_{\boldsymbol{ks}}(t)|^2]; \\
i\hbar\hat{U}_R^+\frac{\partial}{\partial t}\hat{U}_R &= i\hbar\frac{\partial}{\partial t} + i\hbar\sum_{\boldsymbol{ks}}[(\dot{u}_{\boldsymbol{ks}}(t)a_{\boldsymbol{ks}}^+ e^{-i\omega_{\boldsymbol{k}}t} - \dot{u}_{\boldsymbol{ks}}^*(t)a_{\boldsymbol{ks}}e^{i\omega_{\boldsymbol{k}}t}) \\
&\quad -i\omega_{\boldsymbol{k}}(u_{\boldsymbol{ks}}(t)a_{\boldsymbol{ks}}^+ e^{-i\omega_{\boldsymbol{k}}t} + u_{\boldsymbol{ks}}^*(t)a_{\boldsymbol{ks}}e^{i\omega_{\boldsymbol{k}}t}) - i\omega_{\boldsymbol{k}}|u_{\boldsymbol{ks}}(t)|^2 \\
&\quad +\frac{1}{2}(\dot{u}_{\boldsymbol{ks}}(t)u_{\boldsymbol{ks}}^*(t) - \dot{u}_{\boldsymbol{ks}}^*(t)u_{\boldsymbol{ks}}(t))]; \quad \dot{u}_{\boldsymbol{ks}} \equiv \frac{\partial}{\partial t}u_{\boldsymbol{ks}}.
\end{aligned} \tag{1.4}$$

The Schrödinger Eq. (1.1) is then transformed to:

$$\begin{aligned}
i\hbar\frac{\partial}{\partial t}|\Psi(t)> &= \hat{H}(t)|\Psi(t)>; \\
|\Phi(t)> &= e^{i\phi(t)}\hat{U}_R^+|\Psi(t)>; \\
\phi(t) &= \frac{1}{2}\sum_{\boldsymbol{ks}} i\hbar\omega_{\boldsymbol{k}}[\dot{u}_{\boldsymbol{ks}}(t)u_{\boldsymbol{ks}}^*(t) - \dot{u}_{\boldsymbol{ks}}^*(t)u_{\boldsymbol{ks}}(t)].
\end{aligned} \tag{1.5}$$

Here the time-dependent Hamiltonian $\hat{H}(t)$ is a functional of the undefined components $u_{\boldsymbol{ks}}(t)$ of the classical field in the medium and it has the following form:

$$\begin{aligned}
\hat{H}(t) &= \hat{H}_M + \hat{H}_{MR}(t) + \hat{H}_R; \\
\hat{H}_{MR}(t) &= \sum_j^{N_e}\left\{\frac{1}{2m}\Big[-2\frac{e_0}{c}\hat{\boldsymbol{p}}_{\boldsymbol{j}}(\boldsymbol{A}(\boldsymbol{r}_j,t) + \hat{\boldsymbol{A}}_R(\boldsymbol{r}_j)) \right. \\
&\quad \left. +\frac{e_0^2}{c^2}(\boldsymbol{A}(\boldsymbol{r}_j,t) + \hat{\boldsymbol{A}}_R(\boldsymbol{r}_j))^2\Big] - \frac{e_0\hbar}{2mc}\boldsymbol{\sigma}_j(\boldsymbol{H}(\boldsymbol{r}_j,t) + \hat{\boldsymbol{H}}_R(\boldsymbol{r}_j))\right\} \\
&\quad -i\hbar\sum_{\boldsymbol{ks}}(\dot{u}_{\boldsymbol{ks}}(t)a_{\boldsymbol{ks}}^+ e^{-i\omega_{\boldsymbol{k}s}t} - \dot{u}_{\boldsymbol{ks}}^*(t)a_{\boldsymbol{ks}}e^{i\omega_{\boldsymbol{k}}t}).
\end{aligned} \tag{1.6}$$

In the Hamiltonian of interaction $\hat{H}_{MR}(t)$, the part $\hat{H}_{MR}^c(t)$ defines the adiabatic evolution of the quantum medium under the influence of the classical electromagnetic field with the Fourier components $u_{\boldsymbol{ks}}(t)$. Actually, these values define the displaced equilibrium positions for the quantum oscillators corresponding to the quantized field modes. Semiclassical approximation is defined by the wave function of the system with the radiation field being in the ground (vacuum) state relatively to the new equilibrium positions:

$$\hat{H}^{(0)}(t) = \hat{H}_M + \hat{H}_{MR}^c(t) + \hat{H}_R;$$

$$|\Psi^{(0)}(t)>\equiv|\Psi_c(t)>=|\Psi_M(t)>|0>;\quad \hat{H}_R|0>=0;$$
$$i\hbar\frac{\partial}{\partial t}|\Psi_M(t)>=[\hat{H}_M+\hat{H}^c_{MR}(t)]|\Psi_M(t)>;$$
$$\hat{H}^c_{MR}(t)=\sum_j^{N_e}\left\{\frac{1}{2m}[-2\frac{e_0}{c}\hat{\boldsymbol{p}}_j\boldsymbol{A}(\boldsymbol{r}_j,t)\right.$$
$$\left.+\frac{e_0^2}{c^2}\boldsymbol{A}^2(\boldsymbol{r}_j,t)]-\frac{e_0\hbar}{2mc}\boldsymbol{\sigma}_j\boldsymbol{H}(\boldsymbol{r}_j,t)\right\}. \tag{1.7}$$

To investigate the stability of this state, the first order approximation relatively to the radiation field operators [12] has to be considered:

$$|\Psi(t)>\approx|\Psi_c(t)>+|\Psi^{(1)}(t)>;\quad <\Psi^{(1)}(t)|\Psi_c(t)>=0, \tag{1.8}$$

where the first order correction includes the excited states of the quantized electromagnetic field and it is orthogonal to the zeroth-order state vector. As the result, the state vector $|\Psi^{(1)}(t)>$ satisfies to the equation:

$$\left\{i\hbar\frac{\partial}{\partial t}-\hat{H}^{(0)}(t)\right\}|\Psi^{(1)}(t)>=\hat{H}^{(1)}(t)|\Psi^{(0)}(t)>;$$
$$\hat{H}^{(1)}(t)=\sum_j^{N_e}\left\{-\frac{e_0}{mc}\hat{\boldsymbol{p}}_j\hat{\boldsymbol{A}}_R(\boldsymbol{r}_j)\right.$$
$$\left.+\frac{e_0^2}{mc^2}\boldsymbol{A}(\boldsymbol{r}_j,t)\hat{\boldsymbol{A}}_R(\boldsymbol{r}_j)-\frac{e_0\hbar}{2mc}\boldsymbol{\sigma}_j\hat{\boldsymbol{H}}_R(\boldsymbol{r}_j)\right\}$$
$$-i\hbar\sum_{\boldsymbol{ks}}(\dot{u}_{\boldsymbol{ks}}(t)a^+_{\boldsymbol{ks}}e^{-i\omega_{\boldsymbol{k}}t}-\dot{u}^*_{\boldsymbol{ks}}(t)a_{\boldsymbol{ks}}e^{i\omega_{\boldsymbol{k}}t}). \tag{1.9}$$

The zeroth order state vector (1.7), being substituted into the Eq. (1.9), make it possible to calculate its projection onto the state vector $<\Psi_M(t)|$ defining the medium evolution in the selected classical field. The quantum radiation processes are neglected in the zeroth approximation, therefore the normalization condition for the corresponding state vector is conserved during the time $<\Psi^{(0)}(t)|\Psi^{(0)}(t)>=const$:

$$<\Psi_M(t)|\hat{H}^{(1)}(t)|\Psi_M(t)>|0>=0;$$
$$\sum_{\boldsymbol{ks}}\left\{\sqrt{\frac{2\pi\hbar}{\omega_{\boldsymbol{k}}V}}\boldsymbol{e}_{\boldsymbol{ks}}\boldsymbol{J}_{\boldsymbol{ks}}(t)+i\hbar\dot{u}_{\boldsymbol{ks}}(t)e^{-i\omega_{\boldsymbol{k}}t}\right\}a^+_{\boldsymbol{ks}}|0>=0;$$
$$\boldsymbol{J}_{\boldsymbol{ks}}(t)=<\Psi_M(t)|\sum_j^{N_e}\boldsymbol{J}_j(t)e^{-i\boldsymbol{k}\boldsymbol{r}_j}|\Psi_M(t)>;$$

$$\boldsymbol{J}_j(t) = \frac{e_0}{m}\hat{\boldsymbol{p}}_{\boldsymbol{j}} - \frac{e_0^2}{mc}\boldsymbol{A}(\boldsymbol{r}_j, t) + i\frac{e_0\hbar}{2m}[\boldsymbol{\sigma}_j \times \boldsymbol{k}]. \tag{1.10}$$

The zeroth order solution (1.7) will be stable relatively to the quantum fluctuation of the electromagnetic field if the coefficients at the first power of the creation operator are equal to zero, i.e. when the Eq. (1.10) is satisfied [12]. Thus, the Fourier components of the classical field are expressed through the microscopic current $\boldsymbol{J}_j(t)$ of the electrons in the medium:

$$\dot{u}_{\boldsymbol{k}s}(t) = \frac{i}{\hbar}\sqrt{\frac{2\pi\hbar}{\omega_{\boldsymbol{k}}V}}\boldsymbol{e}_{\boldsymbol{k}s}\boldsymbol{J}_{\boldsymbol{k}s}(t)e^{i\omega_{\boldsymbol{k}s}t}. \tag{1.11}$$

Following to the method described in [8], this approximation results in the conventional form of Maxwell's equations for the transversal classical field. The first derivative of the vector potential holds:

$$-\frac{1}{c}\frac{\partial}{\partial t}\boldsymbol{A}(\boldsymbol{r}, t) = \sum_{\boldsymbol{k}s}\sqrt{\frac{2\pi\hbar}{\omega_{\boldsymbol{k}}V}}\boldsymbol{e}_{\boldsymbol{k}s}\{[\dot{u}_{\boldsymbol{k}s}e^{i\boldsymbol{k}\boldsymbol{r}-i\omega_{\boldsymbol{k}}t} + \dot{u}^*_{\boldsymbol{k}s}e^{-i\boldsymbol{k}\boldsymbol{r}+i\omega_{\boldsymbol{k}}t}] + i\omega_{\boldsymbol{k}}[u_{\boldsymbol{k}s}e^{i\boldsymbol{k}\boldsymbol{r}-i\omega_{\boldsymbol{k}}t} - u^*_{\boldsymbol{k}s}e^{-i\boldsymbol{k}\boldsymbol{r}+i\omega_{\boldsymbol{k}}t}]\}, \tag{1.12}$$

and using the expressions (1.10) and (1.11) along with the relation

$$\sum_s e^{\mu}_{\boldsymbol{k}s}e^{\nu}_{\boldsymbol{k}s} = \delta_{\mu,\nu} - \frac{k_\mu k_\nu}{k^2} \equiv t_{\mu\nu},$$

the first term in (1.12) is transformed to:

$$< \Psi_M(t)|\sum_j^{N_e}\sum_{\boldsymbol{k}}\frac{4\pi}{\omega_{\boldsymbol{k}}V}t_{\mu\nu}\Big\{\Big[\frac{e_0}{m}\hat{\boldsymbol{p}}_{\boldsymbol{j}} - \frac{e_0^2}{mc}\boldsymbol{A}(\boldsymbol{r}_j, t)\Big]\sin(\boldsymbol{k}(\boldsymbol{r}-\boldsymbol{r}_j)) + \frac{e_0\hbar}{2m}([\boldsymbol{\sigma}_j \times \boldsymbol{k}]\cos(\boldsymbol{k}(\boldsymbol{r}-\boldsymbol{r}_j))\Big\}\Psi_M(t)>. \tag{1.13}$$

The expression (1.13) becomes a zero because of the presence of the odd function under the sum over $\boldsymbol{k}$.

The second term in the Eq. (1.12) represents the classical component of the electric field operator after the transformation (1.3). Thus, the Eq. (1.12) defines the conventional relationship between the vectors of the electric field strength and the vector potential for the classical transversal field:

$$-\frac{1}{c}\frac{\partial \boldsymbol{A}(\boldsymbol{r}, t)}{\partial t} = \boldsymbol{E}_t(\boldsymbol{r}, t). \tag{1.14}$$

The differentiation of the expression (1.14) results in the following formula for the derivative of the vector potential:

$$\frac{1}{c^2}\frac{\partial^2 \boldsymbol{A}(\boldsymbol{r},t)}{\partial t^2} = -\sum_{\boldsymbol{k}s}\sqrt{\frac{2\pi\hbar c^2}{\omega_{\boldsymbol{k}} V}}\boldsymbol{e}_{\boldsymbol{k}s}\Big\{k^2[u_{\boldsymbol{k}s}e^{i\boldsymbol{k}\boldsymbol{r}-i\omega_{\boldsymbol{k}}t} + u^*_{\boldsymbol{k}s}e^{-i\boldsymbol{k}\boldsymbol{r}+i\omega_{\boldsymbol{k}}t}] + i\frac{\omega_{\boldsymbol{k}}}{c^2}[\dot{u}_{\boldsymbol{k}s}e^{i\boldsymbol{k}\boldsymbol{r}-i\omega_{\boldsymbol{k}}t} - \dot{u}^*_{\boldsymbol{k}s}e^{-i\boldsymbol{k}\boldsymbol{r}+i\omega_{\boldsymbol{k}}t}]\Big\}. \quad (1.15)$$

Finally, the inhomogeneous equation for the vector potential of the classical electromagnetic field can be found by taking into account the definitions (1.3) and (1.11):

$$\Delta\boldsymbol{A}(\boldsymbol{r},t) - \frac{1}{c^2}\frac{\partial^2\boldsymbol{A}(\boldsymbol{r},t)}{\partial t^2} = -\frac{4\pi}{c}\boldsymbol{J}_t(\boldsymbol{r},t);$$

$$\boldsymbol{J}_t(\boldsymbol{r},t) = \frac{1}{2}[\boldsymbol{J}_1(\boldsymbol{r},t) + \boldsymbol{J}_1^+(\boldsymbol{r},t)]; \quad \nabla\boldsymbol{J}_t(\boldsymbol{r},t) = 0;$$

$$\boldsymbol{J}_1(\boldsymbol{r},t) = <\Psi_M(t)|\sum_j^{N_e}\sum_{\boldsymbol{k}}\frac{t_{\mu\nu}}{V}\Big\{\Big[\frac{e_0}{m}\hat{\boldsymbol{p}}_{\boldsymbol{j}} - \frac{e_0^2}{mc}\boldsymbol{A}(\boldsymbol{r}_j,t)\Big]\cos(\boldsymbol{k}(\boldsymbol{r}-\boldsymbol{r}_j)) + i\frac{e_0\hbar}{2m}([\boldsymbol{\sigma}_j\times\boldsymbol{k}]\sin(\boldsymbol{k}(\boldsymbol{r}-\boldsymbol{r}_j))\Big\}|\Psi_M(t)>. \quad (1.16)$$

Expression (1.16) for the current density can be symmetrized due to commutativity of the operators under the sum. Equations (1.14) and (1.16) define the propagation of the transversal classical field in the medium. In the framework of Coulomb gauge, the longitudinal part of the electrical field $\boldsymbol{E}_l(\boldsymbol{r},t)$ is defined as the gradient of the scalar potential $\varphi(\boldsymbol{r},t)$ which is the sum of Coulomb potentials $\hat{V}(\{\boldsymbol{r}_j\})$ of all charged particles averaged over the vector state $|\Psi_M(t)>$ of the medium. This results in the macroscopic equation [14]:

$$\nabla\boldsymbol{E}_l(\boldsymbol{r},t) = 4\pi\rho(\boldsymbol{r},t); \quad \triangle\varphi(\boldsymbol{r},t) = -4\pi\rho(\boldsymbol{r},t);$$

$$\boldsymbol{E}_l(\boldsymbol{r},t) = -\nabla\varphi(\boldsymbol{r},t); \ \rho(\boldsymbol{r},t) = e_0\sum_j <\Psi_M(t)|\delta(\boldsymbol{r}-\boldsymbol{r}_j)|\Psi_M(t)>. \quad (1.17)$$

In the neutral medium the charge density should be represented as a divergence of the vector that is used to denote as $(-\boldsymbol{P})$. Then the integral charge over the medium volume is reduced to the surface integral and equals to zero [14]:

$$\int\rho(\boldsymbol{r},t)dV = -\int\nabla\boldsymbol{P}dV = -\oint\boldsymbol{P}d\boldsymbol{S} = 0. \quad (1.18)$$

The physical meaning of the vector $\boldsymbol{P}$ follows from the formulas:

$$\int\boldsymbol{r}\rho(\boldsymbol{r},t)dV = -\int\boldsymbol{r}\nabla\boldsymbol{P} =$$

$$-\oint \boldsymbol{r}(\boldsymbol{P}d\boldsymbol{S}) + \int (\boldsymbol{P}\nabla)\boldsymbol{r}dV = \int \boldsymbol{P}dV. \tag{1.19}$$

Thus the dipole polarization vector $\boldsymbol{P}(\boldsymbol{r}, t)$ for the electron subsystem can be calculated microscopically as follows:

$$\boldsymbol{P}(\boldsymbol{r}, t) = e_0 \sum_j^{N_e} < \Psi_M(t)|\boldsymbol{r}_j \delta(\boldsymbol{r} - \boldsymbol{r}_j)|\Psi_M(t)>. \tag{1.20}$$

In general case the polarization vector $\boldsymbol{P}(\boldsymbol{r}, t)$ can be expressed through the average electron current by means of the following equation:

$$\begin{aligned} i\frac{\partial \boldsymbol{P}(\boldsymbol{r}, t)}{\partial t} = \frac{e_0}{2\hbar}\sum_j^{N_e}\{< \Psi_M(t)|[\boldsymbol{r}_j \hat{H}^{(0)}]\delta(\boldsymbol{r} - \boldsymbol{r}_j)|\Psi_M(t) > \\ + < \Psi_M(t)|\delta(\boldsymbol{r} - \boldsymbol{r}_j)[\boldsymbol{r}_j \hat{H}^{(0)}]|\Psi_M(t) >\}, \\ \boldsymbol{r}_j \hat{H}^{(0)} - \hat{H}^{(0)}\boldsymbol{r}_j = [\boldsymbol{r}_j \hat{H}^{(0)}], \end{aligned} \tag{1.21}$$

with the Hamiltonian $\hat{H}^{(0)}$ defined by formula (1.7). Calculating the commutator in (1.21), the vector $\boldsymbol{P}(\boldsymbol{r}, t)$ and its Fourier transformation $\boldsymbol{P}(\boldsymbol{r}, \omega)$ can be expressed in the following way:

$$\begin{aligned} \frac{\partial \boldsymbol{P}(\boldsymbol{r}, t)}{\partial t} = \boldsymbol{J}(\boldsymbol{r}, t); \quad \boldsymbol{P}(\boldsymbol{r}, \omega) = \frac{i}{\omega}\boldsymbol{J}(\boldsymbol{r}, \omega); \\ \boldsymbol{J}(\boldsymbol{r}, t) = \frac{1}{2} < \Psi_M(t)|\sum_j^{N_e}[\hat{\boldsymbol{J}}_j \delta(\boldsymbol{r} - \boldsymbol{r}_j) + \delta(\boldsymbol{r} - \boldsymbol{r}_j)\hat{\boldsymbol{J}}_j]|\Psi_M(t) >; \\ \hat{\boldsymbol{J}}_j = \frac{e_0}{m}\hat{\boldsymbol{p}}_j - \frac{e_0^2}{mc}\boldsymbol{A}(\boldsymbol{r}_j, t) + \frac{e_0\hbar}{2m}[\boldsymbol{\sigma}_j \times \nabla_{\boldsymbol{r}}], \end{aligned} \tag{1.22}$$

with $\boldsymbol{J}(\boldsymbol{r}, t)$ as the average electron current in the medium. In neutral medium the average current is equal to zero if the external field is absent. Vector potential $\boldsymbol{A}(\boldsymbol{r}, t)$ is the only characteristic of the field in the Hamiltonian $\hat{H}^{(0)}$. Therefore in the considered case of linear electrodynamics $\boldsymbol{J}(\boldsymbol{r}, \omega)$ should be proportional to $\boldsymbol{A}(\boldsymbol{r}, \omega)$ and is represented in the following form (see below Sect. 1.2):

$$\boldsymbol{J}_\mu(\boldsymbol{r}, \omega) = \frac{\omega^2}{4\pi c}\hat{\chi}(\omega)\boldsymbol{A}(\omega), \tag{1.23}$$

with the medium polarizability $\hat{\chi}(\boldsymbol{r}, \boldsymbol{r}', \omega)$, which is the integral tensor operator

$$(\hat{\chi}(\omega)\boldsymbol{A}(\omega))_\mu = \int d\boldsymbol{r}' \chi_{\mu,\nu}(\boldsymbol{r}, \boldsymbol{r}'\omega)A_\nu(\boldsymbol{r}', \omega). \tag{1.24}$$

This value can also be expressed as a sum of the operators $\hat{\chi}^t$ and $\hat{\chi}^l$ that define the transversal (1.16) and longitudinal parts of the average current, respectively. Finally, all physical fields in the medium are expressed through the vector potential:

$$\begin{aligned} \boldsymbol{E}(\boldsymbol{r},\omega) = \frac{i\omega}{c}\boldsymbol{A}(\boldsymbol{r},\omega) - \nabla\varphi(\boldsymbol{r},\omega) = \frac{i\omega}{c}[1-\hat{\chi}^l(\omega)]\boldsymbol{A}(\omega); \\ \boldsymbol{D}(\boldsymbol{r},\omega) = \boldsymbol{E}(\boldsymbol{r},\omega) + 4\pi\boldsymbol{P}(\boldsymbol{r},\omega) = \frac{i\omega}{c}[1+\hat{\chi}^t(\omega)]\boldsymbol{A}(\omega); \\ \boldsymbol{H}(\boldsymbol{r},\omega) = [\nabla\times\boldsymbol{A}(\boldsymbol{r},\omega)], \end{aligned} \tag{1.25}$$

where $\boldsymbol{D}(\boldsymbol{r},\omega)$ is the electrical displacement vector. Thus the use of the vector potential $\boldsymbol{A}(\boldsymbol{r},t)$ is sufficient for the description of X-ray scattering in condensed media. The formulas (1.7) and (1.16) construct the system of the coupled Schrödinger-Maxwell's equations which is the basis for the description of the field-medium interaction in X-ray optics.

In accordance with the analysis above, these equations are applicable when the off-diagonal matrix elements of the operator $\hat{H}^{(1)}(t)$ in (1.9) are negligible for the processes under consideration. These elements correspond to the transitions between quasi-energy levels of the medium in the classical field $\boldsymbol{A}(\boldsymbol{r},t)$ [8], which lead to the creation of new quanta of the electromagnetic field. The additional shift of the levels of the quasi-energy caused by these transitions can be evaluated by taking into account the second order of the adiabatic perturbation theory on the operator $\hat{H}^{(1)}(t)$ [12]. The diamagnetic term $\sim \boldsymbol{A}(\boldsymbol{r}_j,t)$ in the current density (1.16) is known to define the main contribution to the interaction between X-rays and medium [1]. Therefore, the relative shift of the quasi-energy level ϵ_f caused by the transitions of the quantum electromagnetic field to the excited one-photon states (quantum electrodynamics effects) is defined by the following dimensionless parameter:

$$\xi_{QED} \approx \sum_j^{N_e}\sum_{\boldsymbol{k}}\sum_{f'}\frac{2\pi\hbar}{\omega_{\boldsymbol{k}}V}\left(\frac{e_0^2\boldsymbol{A}(\boldsymbol{r}_j,t)}{mc}\right)^2\frac{M^j_{ff'}(\boldsymbol{k})}{|\epsilon_f||\hbar\omega_{\boldsymbol{k}}+\epsilon_{f'}-\epsilon_f|}; \\ M^j_{ff'}(\boldsymbol{k}) = <\Psi^{f'}_M|e^{i\boldsymbol{k}\boldsymbol{r}_j}|\Psi^{f'}_M>. \tag{1.26}$$

The characteristic energies of the electrons are essentially less than the energy of photons $|\epsilon_f| \ll \hbar\omega_{\boldsymbol{k}}$ if the wavelengths of X-ray range are considered. In this assumption, the classical field has the amplitude

$$A_0 \approx \frac{c}{\bar{\omega}}E_0,$$

with E_0 as the amplitude of the electric field strength, and $\bar{\omega}$ is the characteristic frequency of the field, and the parameter (1.26) can be estimated as

$$\xi_{QED} \approx \frac{4\pi e_0^2 n_e}{m\bar{\omega}^2}|\bar{M}|^2\frac{e_0^2E_0^2}{2m\bar{\omega}^2|\epsilon_f|}. \tag{1.27}$$

Here n_e is the electron density in the medium and the following estimation for the matrix elements $M^j_{ff'}(\boldsymbol{k})$ is used:

$$\sum_{\boldsymbol{k}}\sum_{f'}\frac{M^j_{ff'}(\boldsymbol{k})}{\omega^2_{\boldsymbol{k}}}\approx\frac{|\bar{M}|^2}{\bar{\omega}^2}.$$

The first factor in (1.27) has the same value as the X-ray susceptibility of the medium in the classical Maxwell's equations [1]. Therefore, the quantum effects for the electromagnetic field might be essential only if the classical field creates the medium ponderomotive [15] energy $U_p = e_0^2E_0^2/2m\bar{\omega}^2$, which is comparable with the electron energy $|\epsilon_f|$. This condition can be fulfilled, for instance, in the ultrashort pulses from the X-ray free-electron laser [4].

1.2 Average Current Density and X-Ray Polarizability

The fundamental principles of the quantum electrodynamic shows that the semiclassical approach based on the solution of the system of coupled Schrödinger-Maxwell's equations describes the interaction of X-rays and medium with an accuracy sufficient for the most of the applications. These equations follow from the formulas (1.7), (1.16):

$$\begin{aligned}
i\hbar\frac{\partial}{\partial t}|\Psi_M(t)>&=[\hat{H}_M+\hat{H}^c_{MR}(t)]|\Psi_M(t)>;\\
\hat{H}^c_{MR}(t)&=\sum_j^{N_e}\left\{\frac{1}{2m}\left[-2\frac{e_0}{c}\hat{\boldsymbol{p}}_j\boldsymbol{A}(\boldsymbol{r}_j,t)\right.\right.\\
&\left.\left.+\frac{e_0^2}{c^2}\boldsymbol{A}^2(\boldsymbol{r}_j,t)\right]-\frac{e_0\hbar}{2mc}\boldsymbol{\sigma}_j\boldsymbol{H}(\boldsymbol{r}_j,t)\right\}.
\end{aligned}\tag{1.28}$$

$$\Delta\boldsymbol{A}(\boldsymbol{r},t)-\frac{1}{c^2}\frac{\partial^2\boldsymbol{A}(\boldsymbol{r},t)}{\partial t^2}=-\frac{4\pi}{c}\boldsymbol{J}_t(\boldsymbol{r},t);\quad\nabla\boldsymbol{A}(\boldsymbol{r},t)=0,\tag{1.29}$$

where $\boldsymbol{J}_t$ is the transversal component of the average current

$$\begin{aligned}
\boldsymbol{J}(\boldsymbol{r},t)&=\frac{1}{2}<\Psi_M(t)|\sum_j^{N_e}[\hat{\boldsymbol{J}}_j\delta(\boldsymbol{r}-\boldsymbol{r}_j)+\delta(\boldsymbol{r}-\boldsymbol{r}_j)\hat{\boldsymbol{J}}_j]|\Psi_M(t)>\\
\hat{\boldsymbol{J}}_j&=\frac{e_0}{m}\hat{\boldsymbol{p}}_j-\frac{e_0^2}{mc}\boldsymbol{A}(\boldsymbol{r}_j,t)+\frac{e_0\hbar}{2m}[\boldsymbol{\sigma}_j\times\nabla_{\boldsymbol{r}}].
\end{aligned}\tag{1.30}$$

Further simplification of this system of nonlinear equations is possible due to the weak interaction of the X-ray wave-field with the medium, which makes possible the usage of the perturbation theory over the operator $\hat{H}^c_{MR}(t)$ for the solution of the Eq. (1.28). In general case, the medium state vector is defined by the series over the full set of the eigenfunctions $|\Psi_f>$ of the Hamiltonian $\hat{H}_M$:

$$|\Psi_M(t)>=\sum_f C_f(t)|\Psi_f> e^{-\frac{i}{\hbar}E_f t};\ \hat{H}_M|\Psi_f>=E_f|\Psi_f>;$$

$$\hat{H}_M=\sum_j^{N_e}\frac{\hat{p}_j^2}{2m}+U(\{\boldsymbol{r}_j\});\ |\Psi_f>\equiv|\Psi_f(\{\boldsymbol{r}_j\})>. \tag{1.31}$$

Here index f includes the whole set of the quantum numbers of the multi-electron system in the potential field $U(\{\boldsymbol{r}_j\}$ created by the Coulomb interactions between the electrons and the nuclei in the medium.

In the text below, the principal assumptions are briefly discussed, which are used in order to calculate the average current (1.30) on the basis of the solution of Eq. (1.31) [1]. There is no necessity to use any particular form of the potential field $U(\{\boldsymbol{r}_j\}$ and wave functions in (1.31), if the problem is considered in the framework of the linear response theory [16, 17]. The substitution of the expansion (1.31) into the Eq. (1.30) leads to the formula, which defines the evolution of the coefficients $C_f(t)$:

$$i\hbar\frac{\partial C_f(t)}{\partial t}=-\sum_{f'}M_{ff'}(t)C_{f'}(t)e^{\frac{i}{\hbar}(E_f-E_{f'})t};$$

$$M_{ff'}(t)=<\Psi_f|\hat{H}^c_{MR}(t)|\Psi_{f'}>. \tag{1.32}$$

The standard "adiabatic switch-off" condition is used here for the interactions within the limit $t\to-\infty$ [16, 17]:

$$M_{ff'}(t)\to M_{ff'}(t)e^{\nu t};\ \nu\to 0,$$

and the system is assumed to be in the ground state when the field is absent:

$$C_f^{(0)}=\delta_{f0}.$$

Using these approximations in the first order of the perturbation theory, the expression for C_f is obtained:

$$C_f(t)\approx\delta_{f0}+\frac{i}{\hbar}\int_{-\infty}^{t}M_{f0}(t')e^{\frac{i}{\hbar}(E_f-E_0-i\hbar\nu)t'}dt';$$

$$|\Psi_M(t)>\approx|\Psi_0>e^{-\frac{i}{\hbar}E_0 t}$$

$$+\frac{i}{\hbar}\sum_{f\neq 0} e^{-\frac{i}{\hbar}E_f t}\int_{-\infty}^{t} M_{f0}(t')|\Psi_f> e^{\frac{i}{\hbar}(E_f-E_0-i\hbar\nu)t'}dt'. \tag{1.33}$$

The formulas (1.33) are then used in the wave function (1.31), and the current (1.30) can be calculated with an accuracy of the first order on the electromagnetic field. The average current is supposed to be zero without field and is caused by the transitions of the system into the excited states:

$$J_{t\mu}(\boldsymbol{r},t)=\sum_{j,l}^{N_e}\int_{-\infty}^{t} <\Psi_0|\hat{T}^{jl}_{\mu\lambda}(\boldsymbol{r},\boldsymbol{r}',t-t')A_\lambda(\boldsymbol{r}',t')e^{\nu t'}dt'd\boldsymbol{r}'|\Psi_0>;$$

$$\hat{T}^{jl}_{\mu\lambda}(\boldsymbol{r},\boldsymbol{r}',t-t')=-\frac{e_0^2}{mc}\{\delta(\boldsymbol{r}-\boldsymbol{r}_j)\delta(\boldsymbol{r}'-\boldsymbol{r}_j)\delta_{jl}\delta(t-t')\delta_{\mu\lambda}$$

$$-\frac{im}{\hbar}\sum_{f\neq 0} e^{\frac{i}{\hbar}(E_f-E_0)(t'-t)}\hat{v}^j_\mu\delta(\boldsymbol{r}-\boldsymbol{r}_j)|\Psi_f><\Psi_f|\hat{v}^l_\lambda\delta(\boldsymbol{r}'-\boldsymbol{r}_l)$$

$$+\frac{im}{\hbar}e^{-\frac{i}{\hbar}(E_f-E_0)(t'-t)}\hat{v}^l_\lambda\delta(\boldsymbol{r}'-\boldsymbol{r}_l)|\Psi_f><\Psi_f|\hat{v}^j_\mu\delta(\boldsymbol{r}-\boldsymbol{r}_j)\};$$

$$\hat{v}^j_\mu=\frac{1}{m}\hat{p}^j_\mu+\frac{\hbar}{2m}([\boldsymbol{\sigma}_j\times\nabla_{\boldsymbol{r}}])_\mu. \tag{1.34}$$

The transversal part of the current is appeared because it is proportional to the transversal vector potential $A_\lambda(\boldsymbol{r}',\omega)$.

The substitution of the expression (1.34) into the Maxwell's Eq. (1.29) demonstrates that the linear response of the medium is defined by the integral operator $\hat{T}^{jl}_{\mu\lambda}(\boldsymbol{r},t-t')$ which has a cumbersome functional dependence on the multi-electron wave functions:

$$\Psi_f(\{r_j\})\equiv<\{r_j\}|\Psi_f>.$$

Hereinafter, we change to the Fourier representation over the time variable in the Eq. (1.29):

$$\Delta\boldsymbol{A}(\boldsymbol{r},\omega)+\frac{\omega^2}{c^2}\boldsymbol{A}(\boldsymbol{r},\omega)=-\frac{4\pi}{c}\boldsymbol{J}_t(\boldsymbol{r},\omega);$$

$$\boldsymbol{A}(\boldsymbol{r},t)=\int d\omega\boldsymbol{A}(\boldsymbol{r},\omega)e^{-i\omega t}. \tag{1.35}$$

The Fourier image of the current holds:

$$J_{t\mu}(r,\omega)=c\sum_{j}^{N_e}\sum_{l}^{N_e}\int d\boldsymbol{r}' <\Psi_0|\hat{T}^{jl}_{\mu\lambda}(\boldsymbol{r},\boldsymbol{r}',\omega)A_\lambda(\boldsymbol{r}',\omega)|\Psi_0>;$$

$$\hat{T}^{jl}_{\mu\lambda}(\boldsymbol{r},\boldsymbol{r}',\omega)=-r_0\{\delta(\boldsymbol{r}-\boldsymbol{r}_j)\delta(\boldsymbol{r}'-\boldsymbol{r}_l)\delta_{jl}\delta_{\mu\lambda}$$

$$-\sum_{f\neq 0}\frac{2(E_f-E_0)}{(E_f-E_0)^2-(\hbar\omega+i\nu)^2}$$
$$\times\,\hat{v}_\mu^j\delta(\boldsymbol{r}-\boldsymbol{r}_j)|\Psi_f><\Psi_f|\hat{v}_\lambda^l\delta(\boldsymbol{r}'-\boldsymbol{r}_l)\},\qquad(1.36)$$

where $r_0=e_0^2/mc^2$ is the classical electron radius. The first term in the operator $\hat{T}_{\mu\lambda}^{jl}(\boldsymbol{r},\boldsymbol{r}'\omega)$ is not related to the transitions of the atoms in the medium to the excited states, however, it corresponds to the coherent scattering of the electromagnetic field from the electrons with coordinates $\{\boldsymbol{r}_j\}$. This process is defined by the amplitude of the elastic Compton scattering $(-r_0)$ of the photon on the free electron at zero angle [18]. The second term is also defined by the coherent scattering of the electromagnetic field but this time through the virtual transitions of the electrons to the intermediate states with the energy E_f. In the optical wavelength range, this term solely defines the contribution to the system linear response. For the X-rays, it becomes essential near the resonance, when the photon energy almost coincides with the transition energy $E_f-E_0\approx\hbar\omega$ [1], which makes possible the following substitution:

$$\frac{2(E_f-E_0)}{(E_f-E_0)^2-(\hbar\omega+i\nu)^2}\approx\frac{1}{E_f-E_0-\hbar\omega-i\nu}.$$

After the solution of the Eq. (1.35), the dependence of the vector potential $A_\lambda(\boldsymbol{r}',\{\boldsymbol{r}_j\},\omega)$ on the electron coordinates averaged over the state vector $|\Psi_0>$ has to be taken into account. In order to separate the calculation of the electromagnetic field from the procedure of the averaging over the electron coordinates, the relationship below is used. This relationship has been proved in details in the theory of wave scattering from an arbitrary system with the large number of the scattering centers [19, 20]:

$$<\Psi_0|\hat{T}_{\mu\lambda}^{jl}(\boldsymbol{r},\boldsymbol{r}',\{\boldsymbol{r}_j\},\omega)A_\lambda(\boldsymbol{r}',\{\boldsymbol{r}_j\},\omega)|\Psi_0>=$$
$$=<\Psi_0|\hat{F}_{\mu\lambda}^{jl}(\boldsymbol{r},\boldsymbol{r}',\{\boldsymbol{r}_j\},\omega)|\Psi_0>A_\lambda(\boldsymbol{r}',\omega).\qquad(1.37)$$

Here the renormalized scattering operator $\hat{F}_{\mu\lambda}^{jl}(\boldsymbol{r},\boldsymbol{r}',\omega)$ includes all non-coherent and inelastic processes at a single scattering center. In particular, such renormalization of the amplitude for the scattering of the electromagnetic wave by free electron leads to the complex scattering amplitude with imaginary part defined by the total scattering cross-section accordingly to the optical theorem:

$$(-r_0)\Rightarrow f(0);\quad f'(0)=-r_0;\ f''(0)=\frac{\omega}{4\pi c}\sigma_t(\omega),\qquad(1.38)$$

where σ_t is the total cross-section of the Compton scattering of photon by free electron (Klein-Nishina formula) [21]:

$$\sigma_t(\omega) = 2\pi r_0^2 \Big\{ \frac{1+\beta}{\beta^3}\Big[\frac{2\beta(1+\beta)}{1+2\beta} - \ln(1+2\beta)\Big] + \frac{\ln(1+2\beta)}{2\beta} - \frac{1+3\beta}{(1+2\beta)^3}\Big\};\ \beta = \frac{\hbar\omega}{mc^2}. \tag{1.39}$$

The renormalization procedure for the part of the scattering operator related to the intermediate transitions to the excited states is defined by the substitution [20]:

$$\frac{1}{E_f - E_0 - \hbar\omega - i\nu} \Rightarrow \frac{1}{E_f - E_0 - \hbar\omega - i\Gamma_f/2}, \tag{1.40}$$

where Γ_f is the total width of the excited state of the system with the energy E_f. Actually, this value includes transitions from the level to all possible states and is connected with the total cross-section of the inelastic photon scattering at the bound electrons.

Hereinafter, the medium is considered as an unlimited continuum, which does not restrict the generality of the further analysis.The most interesting for the applications, the macroscopic non-homogeneities of real medium (layered structures, defects, deformed crystals and others), can be described within the framework of the conventional scattering theory [19]. In this approach, each macroscopic element of the investigated object is considered as unrestricted and variation of the medium properties at different parts are considered either as small perturbations (for example, [22–24]) or by means of the boundary conditions sewing together the solutions of the Maxwell's equations for different parts of the medium (for example, [9, 25]). In the case of the continuous medium, the Fourier representation over the space variables can be used for the Eqs. (1.35)–(1.37):

$$k^2\boldsymbol{A}(\boldsymbol{k},\omega) - \frac{\omega^2}{c^2}\boldsymbol{A}(\boldsymbol{k},\omega) = \frac{4\pi}{c}\boldsymbol{J}_t(\boldsymbol{k},\omega);$$
$$\boldsymbol{k}\boldsymbol{A}(\boldsymbol{k},\omega) = 0.\quad \boldsymbol{A}(\boldsymbol{r},t) = \int d\boldsymbol{k}d\omega\boldsymbol{A}(\boldsymbol{k},\omega)e^{i(\boldsymbol{k}\boldsymbol{r}-\omega t)}, \tag{1.41}$$

and the linear response function can be written in the form:

$$J_{t\mu}(\boldsymbol{k},\omega) = c\frac{1}{(2\pi)^3}\int d\boldsymbol{k}'\sum_j^{N_e}\sum_l^{N_e} F_{\mu\lambda}^{jl}(\boldsymbol{k},\boldsymbol{k}'\omega)A_\lambda(\boldsymbol{k}',\omega);$$
$$F_{\mu\lambda}^{jl}(\boldsymbol{k},\boldsymbol{k}'\omega) = f(0)\Big\{ < \Psi_0|e^{i(\boldsymbol{k}'-\boldsymbol{k})\boldsymbol{r}_j}|\Psi_0 > \delta_{jl}\delta_{\mu\lambda} - \sum_{f\neq 0}\frac{m}{E_f - E_0 - \hbar\omega - i\Gamma_f/2}$$
$$\times < \Psi_0|\hat{v}_\mu^j e^{-i\boldsymbol{k}\boldsymbol{r}_j}|\Psi_f >< \Psi_f|\hat{v}_\lambda^l e^{i\boldsymbol{k}'\boldsymbol{r}_l}|\Psi_0 > \Big\} \tag{1.42}$$

For further calculation of the average current (1.42), the state vectors $|\Psi_f>$ should be defined as the solutions of the Schrödinger Eq. (1.31) for multi-electron system. The adiabatic and one-electron approximations are used here, which are explained in many text books (for example, [26, 27]). The one-electron states are described by the wave functions which satisfy to the Schrödinger equation with self-consistent periodic potential and the Bloch theorem:

$$\psi_{\alpha,\boldsymbol{\kappa}}(\boldsymbol{r}+\boldsymbol{n}) = e^{i\boldsymbol{\kappa}\boldsymbol{n}}\psi_{\alpha,\boldsymbol{\kappa}}(\boldsymbol{r}), \tag{1.43}$$

where $\boldsymbol{n} = l_1\boldsymbol{a} + l_2\boldsymbol{b} + l_3\boldsymbol{c}$; $l_i = 0, \pm 1, \pm 2, \ldots$ is the vector of translation decomposed over the vectors $\boldsymbol{a}, \boldsymbol{b}, \boldsymbol{c}$ of the basic crystal cell. These wave functions correspond to the zone energy spectrum $\epsilon_\alpha(\boldsymbol{\kappa})$, where index α is the number of zone and $\boldsymbol{\kappa}$ is the quasi-momentum vector restricted by the first Brillouin zone [26]. The total number of different quasi-momentum vectors is equal to the number of the basic cells N due to boundary conditions [27]. All the formulas below can also be applied to the homogeneous medium in the limits $\boldsymbol{a}, \boldsymbol{b}, \boldsymbol{c} \to \infty$.

Due to the translational symmetry the wave functions can be normalized as follows:

$$\psi_{\alpha,\boldsymbol{\kappa}}(\boldsymbol{r}) = \frac{1}{\sqrt{N}}\tilde{\psi}_{\alpha,\boldsymbol{\kappa}}(\boldsymbol{r});$$
$$\int |\psi_{\alpha,\boldsymbol{\kappa}}(\boldsymbol{r})|^2 d\boldsymbol{r} = \int_\Omega |\tilde{\psi}_{\alpha,\boldsymbol{\kappa}}(\boldsymbol{r})|^2 d\boldsymbol{r} = 1, \tag{1.44}$$

where Ω is the volume of the basic cell ($V = N\Omega$).

In the considered representation, the sum over electron coordinates in the expression (1.42) in the ground state of a crystal is reduced to the summation over the filled zones taking into account the normalization condition on the total number of electrons. As for example, for the one-particle operators it means:

$$I(\boldsymbol{Q}) = \sum_j < \Psi_0|e^{i\boldsymbol{Q}\boldsymbol{r}_j}|\Psi_0 > \Rightarrow \sum_{\alpha,\boldsymbol{\kappa}}^{occ} g_{\alpha,\boldsymbol{\kappa}} \int \psi^*_{\alpha,\boldsymbol{\kappa}}(\boldsymbol{r}) e^{i\boldsymbol{Q}\boldsymbol{r}} \psi_{\alpha,\boldsymbol{\kappa}}(\boldsymbol{r}) d\boldsymbol{r}$$
$$= \frac{1}{N}\sum_{\boldsymbol{n}} e^{i\boldsymbol{Q}\boldsymbol{n}} \sum_{\alpha,\boldsymbol{\kappa}}^{occ} g_{\alpha,\boldsymbol{\kappa}} \int e^{i\boldsymbol{Q}\boldsymbol{r}} |\tilde{\psi}_{\alpha,\boldsymbol{\kappa}}(\boldsymbol{r})|^2 d\boldsymbol{r};$$
$$\sum_{\alpha,\boldsymbol{\kappa}}^{occ} \int g_{\alpha,\boldsymbol{\kappa}} |\psi_{\alpha,\boldsymbol{\kappa}}(\boldsymbol{r})|^2 d\boldsymbol{r} = \sum_{\alpha,\boldsymbol{\kappa}}^{occ} \int_\Omega g_{\alpha,\boldsymbol{\kappa}} |\tilde{\psi}_{\alpha,\boldsymbol{\kappa}}(\boldsymbol{r})|^2 d\boldsymbol{r} = N_e, \tag{1.45}$$

where $g_{\alpha,\boldsymbol{\kappa}}$ are the numbers of the filling up (multiplicity of degeneracy) of the energy levels in zones, $g_{\alpha,\boldsymbol{\kappa}} = 2$ in the case of the ideal non-polarized crystal and it varies within the limits $0 < g_{\alpha,\boldsymbol{\kappa}} < 2$ in solid solutions or crystals with defects, N_e is the total number of electrons in the crystal.

The integrations in the matrix elements (1.45) are based on the following relationships [26]:

$$\sum_{\boldsymbol{n}} e^{i\boldsymbol{Qn}} = N\frac{(2\pi)^3}{V}\sum_{\boldsymbol{H}}\delta(\boldsymbol{Q}-\boldsymbol{H});$$

$$I(\boldsymbol{Q}) = \frac{(2\pi)^3}{V}\sum_{\boldsymbol{H}}\delta(\boldsymbol{Q}-\boldsymbol{H})\sum_{\alpha,\boldsymbol{\kappa}}^{occ}\int_{\Omega} g_{\alpha,\boldsymbol{\kappa}}\tilde{\psi}^{*}_{\alpha,\boldsymbol{\kappa}}(\boldsymbol{r})e^{i\boldsymbol{Hr}}\tilde{\psi}_{\alpha,\boldsymbol{\kappa}}(\boldsymbol{r})d\boldsymbol{r}, \quad (1.46)$$

where $\boldsymbol{H}$ are the crystal reciprocal lattice vectors.

Let us consider in details the main contribution to the average current which is defined by the non-resonant scattering from electrons and is described by the first term in the Eq. (1.42). By taking into account the relation (1.46), the current is:

$$J^{(e)}_{t\mu}(\boldsymbol{k},\omega) = c\frac{1}{\Omega}f(0)\sum_{\boldsymbol{H}}F(\boldsymbol{H})A_{\mu}(\boldsymbol{k}+\boldsymbol{H},\omega);$$

$$F(\boldsymbol{H}) = \frac{1}{N}\sum_{\alpha,\boldsymbol{\kappa}}^{occ}\int_{\Omega} g_{\alpha,\boldsymbol{\kappa}}e^{i\boldsymbol{Hr}}|\tilde{\psi}_{\alpha,\boldsymbol{\kappa}}(\boldsymbol{r})|^2 d\boldsymbol{r}. \quad (1.47)$$

Here $F(\boldsymbol{H})$ stands for the cell scattering factor of the crystal basic cell, normalized by the total number N_c of the electrons in the elementary cell:

$$F(0) = \frac{1}{N}\sum_{\alpha,\boldsymbol{\kappa}}^{occ}\int_{\Omega} g_{\alpha,\boldsymbol{\kappa}} = \frac{N_e}{N} = N_c. \quad (1.48)$$

By the definition, the function

$$\rho_e(\boldsymbol{r}) = \frac{1}{N}\sum_{\alpha,\boldsymbol{\kappa}}^{occ}\int_{\Omega} g_{\alpha,\boldsymbol{\kappa}}|\tilde{\psi}_{\alpha,\boldsymbol{\kappa}}(\boldsymbol{r})|^2 = \sum_{\boldsymbol{H}}F(\boldsymbol{H})e^{-i\boldsymbol{Hr}} \quad (1.49)$$

describes the space distribution of the electron density in the cell. The transition to the constant electron density $N = 1, \Omega \to \infty, N_e \to \infty, N_e/\Omega \to n_e$ corresponds to the homogeneous medium:

$$J^{(e)}_{t\mu}(\boldsymbol{k},\omega) = cn_e f(0)A_{\mu}(\boldsymbol{k},\omega). \quad (1.50)$$

Substituting the average current into the Maxwell's Eq (1.41), the above equations are reduced to the commonly used form:

$$k^2\boldsymbol{A}(\boldsymbol{k},\omega) - \frac{\omega^2}{c^2}\sum_{\boldsymbol{H}}\varepsilon^{(e)}(\boldsymbol{H},\omega)\boldsymbol{A}(\boldsymbol{k}+\boldsymbol{H},\omega) = 0;$$

$$\varepsilon^{(e)}(\boldsymbol{H},\omega)=\delta_{\boldsymbol{H},0}+\chi^{(e)}(\boldsymbol{H},\omega);\ \chi^{(e)}(\boldsymbol{H},\omega)=\frac{4\pi c^2}{\omega^2\Omega}f(0)F(\boldsymbol{H}), \quad (1.51)$$

where $\varepsilon^{(e)}(\boldsymbol{H},\omega)$ and $\chi^{(e)}(\boldsymbol{H},\omega)$ are the Fourier components of the non-resonant part of the X-ray dielectric constant and susceptibility, respectively. To calculate the resonant part of the scattering operator in (1.41), the sum over the electron coordinates is separated into two parts:

$$\sum_j^{N_e}\sum_l^{N_e}e^{i(\boldsymbol{k}'\boldsymbol{r}_l-\boldsymbol{k}\boldsymbol{r}_j)}\Rightarrow\sum_{\boldsymbol{n}}e^{i(\boldsymbol{k}'-\boldsymbol{k})\boldsymbol{n}}\sum_j^{\tilde{N}_e}\sum_l^{\tilde{N}_e}e^{i(\boldsymbol{k}'\boldsymbol{r}_l-\boldsymbol{k}\boldsymbol{r}_j)}$$
$$+\sum_{\boldsymbol{n}}\sum_{\boldsymbol{n}'\neq\boldsymbol{n}}\sum_j^{\tilde{N}_e}\sum_l^{\tilde{N}_e}e^{i(\boldsymbol{k}'(\boldsymbol{r}_l+\boldsymbol{n}')-\boldsymbol{k}(\boldsymbol{r}_j+\boldsymbol{n}))}, \quad (1.52)$$

where $\tilde{N}_e$ includes summation over the electron coordinates in a single basic cell and the summation over the translation vectors $\boldsymbol{n}$, $\boldsymbol{n}'$ transfers it to the whole crystal.

In the framework of the Hartree approximation, the state vector of the system is defined by the simple product of the one-electron wave functions. In this case, the nonzero probabilities for the transitions to the excited states (f) present only for the terms with $\boldsymbol{n}=\boldsymbol{n}'$. The terms with $\boldsymbol{n}\neq\boldsymbol{n}'$ are accounted due to the correlation and exchange effects which are rather small for the non-relativistic atoms. They may play an important role, for example, in the resonant X-ray spectroscopy [2], however, in the majority of applications this contribution to the X-ray susceptibility is neglected [1].

The scattering operator is defined by the transitions to the levels of unfilled energy bands $E_0\rightarrow\epsilon_\alpha(\boldsymbol{\kappa});\ E_f\rightarrow\epsilon_{\alpha_1}(\boldsymbol{\kappa}_1)$ with the energy width $\gamma_{\alpha_1}(\boldsymbol{\kappa}_1)$ that takes into account various processes of atom decay from the excited state:

$$F^{jl(2)}_{\mu\lambda}(\boldsymbol{k},\boldsymbol{k}'\omega)\approx-\frac{1}{N^2}\sum_{\boldsymbol{n}}e^{i(\boldsymbol{k}'-\boldsymbol{k})\boldsymbol{n}}\sum_{\alpha,\boldsymbol{\kappa}}^{occ}g_{\alpha,\boldsymbol{\kappa}}$$
$$\times\sum_{\alpha_1,\boldsymbol{\kappa}_1}\frac{mf(0)M^{\alpha_1,\boldsymbol{\kappa}_1}_{\alpha,\boldsymbol{\kappa},\mu}(-\boldsymbol{k})M^{\alpha,\boldsymbol{\kappa}}_{\alpha_1,\boldsymbol{\kappa}_1,\lambda}(\boldsymbol{k}')}{\epsilon_{\alpha_1}(\boldsymbol{\kappa}_1)-\epsilon_\alpha(\boldsymbol{\kappa})-\hbar\omega-i\gamma_{\alpha_1}(\boldsymbol{\kappa}_1)}. \quad (1.53)$$

The matrix elements from the operator of the current $M^{\alpha_1,\boldsymbol{\kappa}_1}_{\alpha,\boldsymbol{\kappa},\mu}(-\boldsymbol{k})$ are also reduced to the integrals over the single basic cell:

$$M^{\alpha_1,\boldsymbol{\kappa}_1}_{\alpha,\boldsymbol{\kappa},mu}(-\boldsymbol{k})=\int_\Omega\tilde{\psi}^*_{\alpha_1,\boldsymbol{\kappa}_1}(\boldsymbol{r})\hat{v}_\mu e^{-i\boldsymbol{k}\boldsymbol{r}}\tilde{\psi}_{\alpha,\boldsymbol{\kappa}}(\boldsymbol{r})d\boldsymbol{r}. \quad (1.54)$$

Using the expression (1.46), the resonant contribution to the average current can be found:

$$J^{(2)}_{t\nu}(\boldsymbol{k},\omega) = c\frac{1}{\Omega} f(0) \sum_{\boldsymbol{H}} t_{\nu\mu} F_{\mu,\lambda}(\boldsymbol{k},\boldsymbol{H}) A_\lambda(\boldsymbol{k}+\boldsymbol{H},\omega);$$

$$F_{\mu,\lambda}(\boldsymbol{k},\boldsymbol{H}) = -\frac{1}{N^2}\sum_{\alpha,\boldsymbol{\kappa}}^{occ} g_{\alpha,\boldsymbol{\kappa}} \sum_{\alpha_1,\boldsymbol{\kappa}_1} \frac{m M^{\alpha_1,\boldsymbol{\kappa}_1}_{\alpha,\boldsymbol{\kappa},\mu}(-\boldsymbol{k}) M^{\alpha,\boldsymbol{\kappa}}_{\alpha_1,\boldsymbol{\kappa}_1,\lambda}(\boldsymbol{k}+\boldsymbol{H})}{\epsilon_{\alpha_1}(\boldsymbol{\kappa}_1) - \epsilon_\alpha(\boldsymbol{\kappa}) - \hbar\omega - i\gamma_{\alpha_1}(\boldsymbol{\kappa}_1)}, \quad (1.55)$$

which represents the anomalous contribution to the X-ray susceptibility of the crystal [28]:

$$k^2 A_\mu(\boldsymbol{k},\omega) - \frac{\omega^2}{c^2}\sum_{\boldsymbol{H}} \varepsilon^t_{\mu,\lambda}(\boldsymbol{k},\boldsymbol{H},\omega) A_\lambda(\boldsymbol{k}+\boldsymbol{H},\omega) = 0;$$

$$(\boldsymbol{k}\boldsymbol{A}(\boldsymbol{k},\omega)) = 0;$$

$$\varepsilon^t_{\mu,\lambda}(\boldsymbol{k},\boldsymbol{H},\omega) = \varepsilon^{(e)}(\boldsymbol{H},\omega)\delta_{\mu,\lambda} + \chi^{(a)}_{\mu,\lambda}(\boldsymbol{k},\boldsymbol{H},\omega);$$

$$\chi^{(a)}_{\mu,\lambda}(\boldsymbol{k},\boldsymbol{H},\omega) = \frac{4\pi c^2}{\omega^2\Omega} f(0) F_{\mu,\lambda}(\boldsymbol{k},\boldsymbol{H}). \quad (1.56)$$

1.3 Scattering Factors

The elastic scattering of X-ray radiation from the electrons of a crystal contributes mainly to the X-ray susceptibility, which is determined from the scattering amplitude in the formula (1.47):

$$F(\boldsymbol{H}) = \frac{1}{N}\sum_{\alpha,\boldsymbol{\kappa}}^{occ} \int_\Omega g_{\alpha,\boldsymbol{\kappa}} e^{i\boldsymbol{H}\boldsymbol{r}} |\tilde{\psi}_{\alpha,\boldsymbol{\kappa}}(\boldsymbol{r})|^2 d\boldsymbol{r}. \quad (1.57)$$

If the direct experimental measurement of the scattering amplitude could be possible, the expansion (1.47) would permit to unambiguously calculate the function $\rho_e(\boldsymbol{r}) = \sum_{\alpha,\boldsymbol{\kappa}}^{occ} g_{\alpha,\boldsymbol{\kappa}} |\tilde{\psi}_{\alpha,\boldsymbol{\kappa}}(\boldsymbol{r})|^2$, which is the main goal of X-ray structure analysis [29]. However, the measurement of the intensity of the scattered radiation allows to find the modulus $|F(\boldsymbol{H})|$ only. The values $F(\boldsymbol{H})$ are complex in general case, therefore the theoretical calculation of the scattering amplitude is necessary on the basis of preliminary model of the electron density which is defined more exactly by fitting the experimental data by means of iterative retrieval procedure [30].

In the considered here quantum description of the system, the electron density modeling is based on the choice of some approximation for the wave functions $\tilde{\psi}_{\alpha,\boldsymbol{\kappa}}(\boldsymbol{r})$ corresponding to the zone spectrum of the electron in a crystal. In the practical crystallography [29], the commonly used approach is based on the strong coupling approximation [31], which neglects the overlapping of the wave functions of electrons from different atoms. This approximation takes into account the fact that the main contribution to the amplitude is defined by the scattering from the electrons of the internal shells, the characteristic sizes of which are essentially less than the

distance between the atoms. Thus, the overlapping of the electron wave functions from different atoms is exponentially small and the electron density does not depend on the quasi-wave vector $\boldsymbol{\kappa}$:

$$|\tilde{\psi}_{\alpha,\boldsymbol{\kappa}}(\boldsymbol{r})|^2 \to |\tilde{\psi}_{\alpha}(\boldsymbol{r})|^2; \quad \frac{1}{N}\sum_{\boldsymbol{\kappa}} g_{\alpha,\boldsymbol{\kappa}} = g_{\alpha}, \tag{1.58}$$

where the values g_α define the populations of the electron states in the isolated atoms of the basic cell.

Introducing the variables $\boldsymbol{R}_a$ and ξ_a for the coordinates of the atom nucleus in the basic cell and the set of quantum numbers for the filled electron states in this atom, respectively, and the sum over the index α includes the summation over both $\boldsymbol{R}_a$ and ξ_a, the scattering factor can be represented as follows:

$$F(\boldsymbol{H}) = \sum_{\boldsymbol{R}_a,\xi_a}^{occ} g_{\boldsymbol{R}_a,\xi_a} \int_{\Omega} e^{i\boldsymbol{H}\boldsymbol{r}} |\varphi_{\xi_a}(\boldsymbol{r}-\boldsymbol{R}_a)|^2 d\boldsymbol{r}, \tag{1.59}$$

where $\varphi_{\xi_a}(\boldsymbol{r}-\boldsymbol{R}_a)$ are the normalized one-electron wave functions corresponding to the isolated atom. Within the considered in this chapter accuracy, the limits of integration in (1.59) can be expanded to the infinite volume. We also introduce the atomic scattering factors (ASF) $F_a(\boldsymbol{H})$:

$$F(\boldsymbol{H}) = \sum_{a} F_a(\boldsymbol{H}) e^{i\boldsymbol{H}\boldsymbol{R}_a}; \quad F_a(\boldsymbol{H}) = \int e^{i\boldsymbol{H}\boldsymbol{r}} \rho_a(\boldsymbol{r}) d\boldsymbol{r};$$
$$\rho_a(\boldsymbol{r}) = \sum_{\xi_a}^{occ} g_{\xi_a} |\varphi_{\xi_a}(\boldsymbol{r})|^2. \tag{1.60}$$

which are directly connected with the electron density $\rho_a(\boldsymbol{r})$ of the atom situated in the point $\boldsymbol{R}_a$. They are expressed through the one-electron wave functions $\varphi_{\xi_a}(\boldsymbol{r})$ of the isolated atom and normalized by number of electrons N_a in this atom:

$$F_a(0) = N_a; \quad \sum_{a} N_a = N_c. \tag{1.61}$$

The accuracy of this approximation is defined by the overlapping integrals I_{ab} for the wave functions of electrons from different atoms, and the correction to the scattering factor (1.59) is defined by the parameter:

$$\Delta F(\boldsymbol{H}) \sim |I_{ab}|; \quad I_{ab} = \int \varphi^*_{\xi_a}(\boldsymbol{r}) \varphi_{\xi_b}(\boldsymbol{r}-\boldsymbol{R}_b+\boldsymbol{R}_a) d\boldsymbol{r}, \; b \neq a, \tag{1.62}$$

which is connected with the characteristic width of the one-electron zones [31].

Another important renormalization of the coherent scattering factors is stipulated by the oscillations of the atomic nuclei:

$$\boldsymbol{R}_a = \boldsymbol{R}_a^{(0)} + \boldsymbol{\zeta}_a, \tag{1.63}$$

where the value $\boldsymbol{\zeta}_a$ describes the deviation of nucleus from the equilibrium positions $\boldsymbol{R}_a^{(0)}$. In the quantum solid state theory the parameter $\boldsymbol{\zeta}_a$ is expressed in terms of operators of the phonon creation and annihilation [32].

The observed value of the scattering factor, being the function of the crystal temperature T, is defined by the average on the phonon statistical distribution:

$$\bar{F}(\boldsymbol{H}, T) = Sp\left\{\hat{\rho}_{ph}(T, \boldsymbol{\zeta}_a)\sum_a F_a(\boldsymbol{H})e^{i\boldsymbol{H}(\boldsymbol{R}_a^{(0)}+\boldsymbol{\zeta}_a)}\right\}. \tag{1.64}$$

When the phonon spectrum $\omega_p(\boldsymbol{\kappa})$ (p stands for the various branches of the spectrum) is known, the averaging gives an additional factor, called Debye-Waller, in the scattering amplitude of each atom [31]:

$$e^{-W_a(\boldsymbol{H},T)}.$$

This factor takes into account the decrease of the elastic scattering amplitude due to the probability of the inelastic processes of the phonon excitation in a crystal. If the Boze-Einstein statistics for the phonon distribution is used, this factor can be represented in the form [32]:

$$\begin{aligned}\bar{F}(\boldsymbol{H}, T) &= \sum_a F_a(\boldsymbol{H})e^{i\boldsymbol{H}\boldsymbol{R}_a^{(0)}}e^{-W_a(\boldsymbol{H},T)};\\ W_a(\boldsymbol{H}, T) &= -\frac{\hbar}{M_a}\sum_{\mu,\nu} B_{\mu,\nu}H_\mu H_\nu,\end{aligned} \tag{1.65}$$

where M_a is the atomic mass, H_μ, ($\mu = 1, 2, 3$) are the projections of the reciprocal lattice vector on the basic vectors of the elementary cell; the tensor $B_{\mu,\nu}$ does not depend on the atom but does on the integral characteristics of the crystal:

$$B_{\mu,\nu} = \frac{\Omega}{(2\pi)^3}\sum_p \int e_\mu^p e_\nu^p \frac{\coth\beta_p(\boldsymbol{\kappa})}{\omega_p(\boldsymbol{\kappa})}d\boldsymbol{\kappa}; \quad \beta_p = \frac{\hbar\omega_p(\boldsymbol{\kappa})}{k_B T}. \tag{1.66}$$

The values $e_\mu^p(\boldsymbol{\kappa})$ are the projections of the polarization vector for the phonon branch p on the basic vectors of the elementary cell; k_B is the Boltzmann constant.

Another approximation for the scattering factors used in (1.60) is the calculation of ASF for isolated atoms [29]. In this approximation, the expansion of the plane wave [33] is used in formula (1.60):

$$e^{i\boldsymbol{Hr}} = \sum_{l'=0}^{\infty} (i)^{l'} (2l'+1)\, j_{l'}(Hr)\, P_{l'}(\cos \widehat{\boldsymbol{Hr}}). \tag{1.67}$$

The expansion is performed over the spherical Bessel functions $j_{l'}(Hr)$ and the Legendre polynomials $P_{l'}(\cos \widehat{\boldsymbol{Hr}})$ depending on the angle between the vectors $\boldsymbol{H}$ and $\boldsymbol{r}$. Using this model, the ASF is represented in the following form:

$$\begin{aligned} F_a(\boldsymbol{H}) &= F_{is}(H) + \Delta F_{an}(\boldsymbol{H}); \\ F_{is}(H) &= 4\pi \int \rho(r) \frac{\sin Hr}{H} r\, dr; \\ \Delta F_{an}(\boldsymbol{H}) &= \int \sum_{\xi_a}^{unoccupied} \sum_{l'=1}^{\infty} g_{\xi_a} |\varphi_{\xi_a}(r, \theta_a, \phi_a)|^2 \\ &\quad \times (i)^{l'} (2l'+1)\, j_{l'}(Hr)\, P_{l'}(\cos \widehat{\boldsymbol{Hr}})\, d\boldsymbol{r}. \end{aligned} \tag{1.68}$$

The completely occupied (closed) electron shells in any atom contributes only to the spherically symmetric part of the electron density $\rho(r)$, and therefore the isotropic part $F_{is}(H)$ of ASF is defined by the scattering from all atomic electrons. In general case, it exceeds essentially the anisotropic contribution ΔF_{an} to ASF which includes the summation over unfilled shells only. Overlapping of the wave functions from different atoms in a basic cell is important only for these electrons [29] and the contribution ΔF_{an} should be taken into account together with the correction $\Delta F(\boldsymbol{H})$ from the expression (1.62).

Thus, the basic part of the X-ray susceptibility consists of the scattering factor which is the sum of ASF for the individual atoms. Each ASF is the Fourier image of the spherically symmetric part of the atomic electron density. Unlike to the expression (1.68), in the standard X-ray applications, the ASF is usually considered as the function of the parameter s related to the transmitted scattering wave vector $\boldsymbol{Q}$ as:

$$\boldsymbol{Q} = \boldsymbol{k}' - \boldsymbol{k};\ \ Q = 4\pi s;\ \ s = \frac{\sin\theta}{\lambda}, \tag{1.69}$$

where λ is the radiation wavelength, and 2θ is the scattering angle. The parameter s is more useful for the practical applications because of with a rather good accuracy it has a variation range in the limited interval for any atom $0 \le s \le 6\ \dot{A}^{-1}$. Using these notations, the ASF is written as:

$$F_{is}(H) \to F_0(s) = \int_0^{\infty} \rho(r) \frac{\sin 4\pi sr}{s} r\, dr. \tag{1.70}$$

In order to calculate ASF from (1.70), it is necessary to choose the approximation for the electron density $\rho(r)$ in multi-electron atoms (ions). The most fundamental one is the Hartree-Fock approximation for the one-electron wave functions [34], when the wave functions are taken in the form of tables [35]. These tables are not very

convenient for the practical usage, and it is very difficult to use this approach for account of various corrections to ASF as well as for the atomic excited states and variation of the electron configurations for atoms or ions in the external field.

In certain applications, the Thomas-Fermi model for ASF calculation, which implements the electron density as a universal function in the whole range of the nucleus charge Z_a and number of electrons N_a [36, 37], is satisfactory [29]. However, this model does not take into account the shell oscillations of the electron density and its behavior at small and large distances, and as a result does not provide a sufficient accuracy for ASF calculation. Therefore, the analytical interpolation of the Hartree-Fock data directly for the function $F_0(s)$ is mostly used. The typical form of the interpolation is:

$$F_0(s) = \sum_{j=1}^{4} a_j e^{-b_j s^2} + c, \ 0 \le s \le 2,$$

with a set of the parameters a_j, b_j, c which are individual for every atom or ion and are chosen by numerical fitting of the Hartree-Fock data in the interval $0 \le s \le 2$ [38]. By means of several additional parameters, this interpolation was generalized in work [39] for the interval $2 \le s \le 6$. The results of interpolation are represented as the tables for the parameters corresponding to all atoms and some ions [29].

This approach is used in various software packages for calculation of the X-ray susceptibility (for example, [40, 41]). Unfortunately this interpolation does not refer to the wave functions and hence limits the ability of the physical interpretations. Moreover, this method does not allow to calculate the above mentioned corrections to ASF.

Recently a new model for ASF approximation was suggested in the works [42, 43] based on the analytical interpolation of one-electron wave functions by means of the parameter set, which is interpreted as the effective charges of the electron shells. This approach makes possible to calculate numerous characteristics of the isolated atoms (ions) by using the universal analytical formulas, in a similar way as in Thomas-Fermi model. The accuracy of this approach is comparable with the one by the Hartree-Fock approximation. Analytical wave functions of the model describe correctly the shell oscillations and the asymptotic behavior of the electron density and therefore can be used for the calculation of various corrections to ASF.

As mentioned above, the main approximation for quantitative description of multi-electron atoms is based on the Hartree-Fock model. All the electrons move in the field of the self-consistent potential, which is calculated together with the wave functions from the system of integro-differential equations [34]. There exist also other numerical approaches for calculation of the electron structure of atoms, for example, the method of effective potential [44] or suggested recently algorithm for the direct numerical solution of the Schrödinger equation [45]. However, the analytical approximations for the atomic wave functions are still of big interest for many applications [46, 47]. This approximation may be obtained by applying the interpolation for the numerical results with a number of fitting parameters for each orbital [48].

There exist effective analytical models for the atoms, which implement the wave function of each electron as the Coulomb orbital [49] with phenomenological values of effective charges or quantum defects (for example, [50]). These parameter [42] are calculated in the framework of the operator method for solution of the Schrödinger equation and an accurate analytical approximation for ASF is found. However, the parameters of this approximation are individual for each atom or ion and the additional pre-calculated tables have to be used. In the paper [43], the generalization of the shell model was suggested which allows a calculation of the effective charges for any atom or ion by means of the universal formula. This approach results in the effective analytical approximation for ASF and gives the possibility to calculate the above mentioned corrections.

Here we consider briefly the microscopic basis for this model. The one-electron Hamiltonian of the atom can be written in the following form (the Coulomb system of units with $e = \hbar = m = 1$ [49] is used in this paragraph):

$$\hat{H}_\sigma = \sum_i \left(\frac{\hat{p}_i^2}{2} - \frac{Z - \sigma_i}{r_i} \right). \tag{1.71}$$

The eigenfunctions and the eigenvalues correspond to the solutions of the Schrödinger equation for the hydrogen-like atom with different screening constants σ_i for every electron. This model was used successfully in the very first papers on the quantum mechanical description of the atom (for example, [51, 52]). The accurate Hartree-Fock functions are shown to be very close to the Coulomb functions [48], however, the model is not widely used as a Thomas-Fermi one for calculation of the atomic characteristics. The reason is the operator (1.71), which is derived not from the initial Hamiltonian of atom and thus no method exists to calculate the empiric parameters σ_i for the atoms or ions. Different solutions for these problems were suggested, for example, in the paper [53] the operator (1.71) was obtained by means of virial theorem and in the paper [42] the effective charges were calculated on the basis of the operator method. However, in both cases the parameters σ_i were calculated for each atom and shell by individual numerical algorithm.

Unlike the other approaches, the considered here model defines the values Z_{eff} for any electron and any atom (ion) by the universal analytical formula, which depends on the nucleus charge and occupations of the one-electron quantum levels. To prove this statement, we start from the Schrödinger equation for the non-relativistic atom with N-electrons and nucleus charge Z:

$$\hat{H}_A \Psi_\Lambda(X) = E_\Lambda \Psi_\Lambda(X);$$
$$\hat{H}_A = \sum_{i=1}^{N} \left(\frac{\hat{p}_i^2}{2} - \frac{Z}{r_i} \right) + \sum_{j>i}^{N} \sum_{i=1}^{N-1} \frac{Z}{|\boldsymbol{r}_j - \boldsymbol{r}_i|}. \tag{1.72}$$

Here the state vector depends on $4N$ variables, which are the electron coordinates and spins $X = (x_1, x_2, \ldots x_N); x_i = (\boldsymbol{r}_i, \boldsymbol{s}_i)$, and the quantum numbers $\Lambda = (\lambda_1, \lambda_2, \ldots \lambda_N); \lambda_i = (n_i, l_i, m_i, s_i)$.

The general scheme of the operator method [54, 55] is used for the solution of the Eq. (1.72), i.e. as a first step the orthonormalized set of the model functions $\psi_\Lambda(X, \Omega_\Lambda)$ depending on the variational parameters Ω_Λ has to be chosen. The different sets $\psi_\Lambda(X, \Omega_\Lambda)$ should be used for the different quantum numbers Λ [54, 55]. The corresponding to Λ wave function to be found is expanded over the model functions $\psi_\Lambda(X, \Omega_\Lambda)$:

$$\Psi_\Lambda(X) = \psi_\Lambda(X, \Omega_\Lambda) + \sum_{\Lambda' \neq \Lambda} C_{\Lambda',\Lambda} \psi_{\Lambda'}(X, \Omega_\Lambda). \tag{1.73}$$

The energy of this state and the coefficients of the expansion (1.73) are derived from the system of nonlinear algebraic equations including matrix elements of the initial Hamiltonian:

$$\begin{aligned} E_\Lambda &= H_{\Lambda\Lambda} + \sum_{\Lambda' \neq \Lambda} H_{\Lambda\Lambda'} C_{\Lambda',\Lambda}; \\ H_{\Lambda'\Lambda_1} &= < \psi_{\Lambda'}(X, \Omega_\Lambda) | \hat{H}_\Lambda | \psi_{\Lambda_1}(X, \Omega_\Lambda) >; \\ C_{\Lambda',\Lambda} &= -[H_{\Lambda'\Lambda'} - H_{\Lambda\Lambda}]^{-1} [H_{\Lambda'\Lambda} + \sum_{\Lambda_1 \neq \Lambda' \neq \Lambda} H_{\Lambda'\Lambda_1} C_{\Lambda_1,\Lambda}]. \end{aligned} \tag{1.74}$$

In according with the reference [54, 55], the successive iterations of the Eq. (1.74) are converged even for the arbitrary choice of the zero approximation functions $\psi_\Lambda(X)$. Therefore, these functions are chosen here in the form of a simple product of the one-particle Coulomb orbitals [48]:

$$\begin{aligned} \psi_\Lambda(X, \Omega_\Lambda) &= \prod_{\lambda_i}^{\lambda_{max}} \phi_{\lambda_i}(Z_{\lambda_i}, x_i); \\ \phi_{\lambda_i}(Z_{\lambda_i}, x_i) &= C_{n,l,m} R_{nl}(r_i, Z_{n,l}) Y_{lm}(\theta_i, \varphi_i) \chi_s; \\ \lambda_i &= (n, l, m, s); \sum_{\lambda_i}^{\lambda_{max}} 1 = N, \end{aligned} \tag{1.75}$$

where $R_{nl}(r_i, Z_{n,l})$ are the hydrogen-like radial wave functions corresponding to the charge $Z_{n,l}$; $Y_{lm}(\theta_i, \varphi_i)$ are the spherical harmonics and χ_s are the spin functions of the electron, $C_{n,l,m}$ is normalization coefficient.

Similarly to the Thomas-Fermi model, such a choice of the function means that the exchange interaction is neglected but the Pauli principle is taken into account because of the quantum numbers of all electrons are different. Parameter λ_{max} is defined by the number N of the electrons and $N \neq Z$ for ions. In accordance

with [56], this choice of the zeroth order wave functions leads to a good accuracy for calculation of the atomic characteristics and permits to take analytically into a account the correlation and exchange corrections.

We choose the quantum numbers λ_i in accordance with an order of occupations of one-electron states, and the increasing sequence of the integral numbers ($\lambda_i \to i$; $\lambda_{max} \to i_{max}$) is associated with this sequence. Then the zeroth approximation for energy depends on the set of variational parameters Ò $\{Z_i\}$ and is defined by the formula:

$$E_{\Lambda}^{(0)}(\{Z_i\}) = \sum_{i=1}^{i_{max}} < \phi_{\lambda_i}(Z_i, x)|[\frac{\hat{p}^2}{2} - \frac{Z}{r}]|\phi_{\lambda_i}(Z_i, x) > + \sum_{i=1}^{i_{max}} \sum_{j>i}^{i_{max}} < \phi_{\lambda_i}(Z_i, x_1), \phi_{\lambda_j}(Z_j, x_2)|\frac{1}{|\boldsymbol{r}_1 - \boldsymbol{r}_2|}|\phi_{\lambda_i}(Z_i, x_1), \phi_{\lambda_j}(Z_j, x_2)>. \tag{1.76}$$

This expression was used in the paper [54, 55] for the numerical calculation of the effective charges in the zeroth approximation of the operator method. It is possible to find analytically the approximate variational solution for these values, too. The problem only is a right choice of a sufficiently good approximation for the matrix elements of two-particle operator. Here, the following fact is used: for the hydrogen-like orbits their average radius is defined mainly by the principal quantum number and depends weakly on other quantum numbers, and thus the following estimation gives a very good accuracy:

$$\begin{aligned} &< \phi_{n_1,l_1,m_1,s_1}|r|\phi_{n_1,l_1,m_1,s_1} > \ll < \phi_{n_2,l_2,m_2,s_2}|r|\phi_{n_2,l_2,m_2,s_2} >, \text{ if } n_1 < n_2; \\ &< \phi_{n_1,l_1,m_1,s_1}|r|\phi_{n_1,l_1,m_1,s_1} > \approx < \phi_{n_2,l_2,m_2,s_2}|r|\phi_{n_2,l_2,m_2,s_2} >, \text{ if } n_1 = n_2. \end{aligned} \tag{1.77}$$

This estimate introduces the following one-particle approximation for the matrix elements of two-particle operator:

$$V_{\lambda_i,\lambda_j} \equiv < \phi_{\lambda_i}, \phi_{\lambda_j}|\frac{1}{|\boldsymbol{r}_1 - \boldsymbol{r}_2|}|\phi_{\lambda_i}, \phi_{\lambda_j} > \approx < \phi_{\lambda_j}|\frac{1}{r_2}|\phi_{\lambda_j} >, \text{ if } n_i < n_j; \tag{1.78}$$

$$V_{\lambda_i,\lambda_j} \approx \frac{1}{4}[< \phi_{\lambda_i}|\frac{1}{r_1}|\phi_{\lambda_i} > + < \phi_{\lambda_j}|\frac{1}{r_2}|\phi_{\lambda_j} >], \text{ if } n_i = n_j. \tag{1.79}$$

Formula (1.79) has a simple physical interpretation: for each electron in the atomic layer with the principal number n_j all the electrons from internal layers with $n_j > n_i$ give the identical (equal to unity) contributions to the nucleus charge screening that corresponds to the result of the classical electrodynamics for spherically symmetric charge distribution. At the same time, each additional electron in the same layer (with $n_i = n_j$) contributes to the screening with the value equals to 1/2. After the symmetrization on the coordinates of the electrons in the layer, the coefficient

in (1.79) becomes equal to 1/4. In this electrostatic approximation, the Hamiltonian of the zeroth order takes one-particle form. The approximation (1.78)–(1.79) for the matrix elements can be essentially improved if the dependence of the screening charge of every electron on its orbital momentum is also taken into account. This dependence is found in a general form with some undefined numerical coefficients if the symmetry of the group $SO(4,2)$ for atomic Hamiltonian is used [57]. Then the following approximation for the diagonal matrix elements of the two-particle operator can be used:

$$V^A_{\lambda_i,\lambda_j} = \left(1 - \frac{\alpha}{2(2l_i+1)} - \beta\frac{l_i(l_i+1)}{n_j^2}\right) < \phi_{\lambda_j}|\frac{1}{r_2}|\phi_{\lambda_j} >,\ n_i < n_j; \quad (1.80)$$

$$V^A_{\lambda_i,\lambda_j} = \frac{5}{16}\left[\left(1 + \frac{1}{6} + \beta\frac{l_i(l_i+1)}{n_i^2}\right) < \phi_{\lambda_i}|\frac{1}{r_1}|\phi_{\lambda_i} > \right.$$
$$\left. + \left(1 + \frac{1}{6} + \beta\frac{l_j(l_j+1)}{n_j^2}\right) < \phi_{\lambda_j}|\frac{1}{r_2}|\phi_{\lambda_j} >\right],\ n_i = n_j, \quad (1.81)$$

with still undefined parameters α and β, which will be discussed below.

Besides, a small modification of the screening coefficient $1/4 \to 5/16$ for the electrons in the same layer corresponds to well known variational solution for the effective charge in two-electron atom [49]. In the result, the following expression defines the energy of the state with the given set of the quantum numbers in zeroth approximation of the operator method:

$$E^{(0)}(Z,N)_\Lambda \approx \sum_\lambda g_{nlms} < R_{n,l}(Z_{n,l},r)|\left[\frac{\hat{p}^2}{2} - \frac{Z_{n,l}}{r}\right]|R_{n,l}(Z_{n,l},r) >=$$
$$-\sum_\lambda g_{nlms}\frac{Z^2_{n,l}}{2n^2};$$
$$Z_{n,l} = Z - \sum_{n_1=1}^{n-1}\sum_{l_1=0}^{n_1-1}\sum_{m_1=-l}^{l}\sum_{s_1=\pm1} g_{n_1l_1m_1s_1}\kappa_{n,l_1}$$
$$-\frac{5}{16}\left[\sum_{l_1=0}^{n-1}\sum_{m_1=-l}^{l}\sum_{s_1=\pm1} g_{nl_1m_1s_1}\kappa'_{n,l_1} - \kappa'_{n,l}\right];$$
$$\kappa_{n,l} = 1 - \frac{\alpha}{2(2l+1)} - \beta\frac{l(l+1)}{n^2};\ \kappa'_{n,l} = 1 + \frac{1}{6} + \beta\frac{l(l+1)}{n^2},$$
$$\sum_\lambda \equiv \sum_{n=1}^{n_{max}}\sum_{l=0}^{n-1}\sum_{m=-l}^{l}\sum_{s=\pm1} \quad (1.82)$$

where the occupation numbers $g_{nlms} = 1$ for the filled and $g_{nlms} = 0$ for empty one-electron states. These numbers are normalized by the condition:

$$\sum_{n=1}^{n_{max}} \sum_{l=0}^{l_{max}} \sum_{m=-l}^{l} \sum_{s=\pm 1} g_{nlms} = N. \tag{1.83}$$

In general case, the nonzero values g_{nlms} are defined by the occupations of one-electron states for the considered atom or ion. Parameter β is calculated uniquely by satisfying the formula (1.82) to the asymptotic expression for the energy of neutral atom in the limit $Z \to \infty$ (for example, [58, 59]):

$$E = -0,768745 Z^{7/3}. \tag{1.84}$$

In order to find this asymptotic expression, the sums over n, l in formulas (1.82) and (1.83) have to be replaced by the integrals and the terms with the maximal degree of Z have to be extracted:

$$n_{max} \approx \left(\frac{3}{2} Z\right)^{1/3}; \; E^{(0)}(Z, Z) \approx \frac{9}{28} 12^{2/3} Z^{7/3} \left(1 + \frac{1}{10}\beta + \frac{1}{50}\beta^2\right). \tag{1.85}$$

By comparing the formula (1.85) with the expression (1.84) the value $\beta \approx 0,417472$ is calculated. Thus, the only undefined parameter not depending on Z in the Hamiltonian (1.73) is the value α, which makes the correction of the screening value due to the presence of equivalent electrons. The mean squared radius of atoms $r_A = \sqrt{< r^2 >}$, being an important for many applications [34], proves to be most sensitive to the value α parameter. In the considered model the parameter α was chosen provided the function $r_A(Z)$ is the best approximation for the same function calculated on the basis of Hartree-Fock model [60]. Finally, the value found is $\alpha \approx 0,576$.

Thus, the wave functions (1.75) with the effective charges calculated from the analytical formulas (1.82) make it possible to estimate in a simple way and with a good accuracy the numerous characteristics of atoms and ions with arbitrary Z and N. Below the comparison is given for some physical values calculated using the analytical formulas with the numerical results of the Hartree-Fock [60] and Thomas-Fermi [58, 59] models.

Figure 1.2 shows the dependence of the total energy of the neutral atoms on the nucleus charge and Fig. 1.3 shows the functions $r_A(Z)$ for all mentioned above models. The relative deviation of the analytical results from the Hartree-Fock model is not exceeding 3 %.

Figures 1.4 and 1.5 show the radial distributions of the electron density for several atoms. The analytical approach interpolates well the Hartree-Fock numerical data in the entire range of the radial coordinate and shows the correct asymptotic behavior of the density at small and large distances.

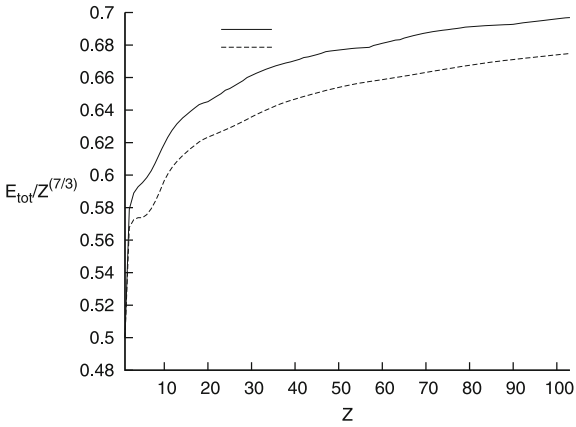

Fig. 1.2 The total energy of neutral atoms as the function of nucleus charge *solid line* corresponds to operator method and *dashed line* to Hartree-Fock results

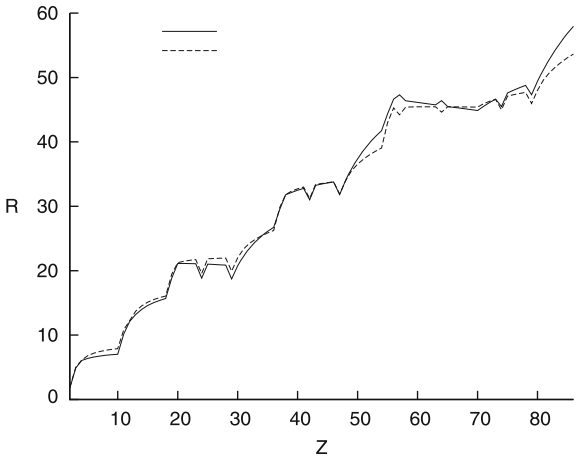

Fig. 1.3 Mean squared radius of neutral atoms as the function of nucleus charge: *solid line* correspond to operator method and *dashed line* to Hartree-Fock results

Figures 1.6 and 1.7 refer to ions of He and Li series, respectively, and demonstrate the high precision of the ionization potentials $IP(Z, N) = E_{tot}(Z, N) - E_{tot}(Z, (N-1))$ calculated in the framework of the considered model.

The considered interpolation for the wave functions delivers the analytical expressions for the isotropic part of ASF (1.70) for any ion or atom. In the one-electron approximation the isotropic electron density is defined by the population numbers g_{nl} of the atom or ion shells and the normalized radial wave functions $R_{nl}(Z_{nl}, r/a_B)$ corresponding to the Coulomb orbitals with the effective charges Z_{nl}, $a_B = 0.529177A$ is the Bohr radius:

$$\rho(r) = \frac{1}{4\pi} \sum_{nl} g_{nl} |R_{nl}(Z_{nl}, r/a_B)|^2. \tag{1.86}$$

The integral (1.70) from this equation can be calculated analytically in the following form [61]:

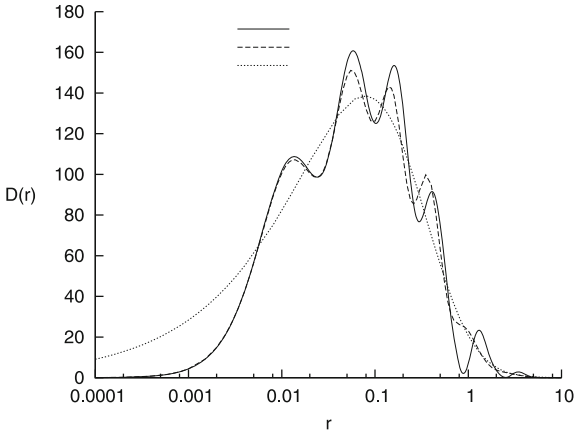

Fig. 1.4 Radial distributions of the electron densities for Bi atom: *solid line* is operator method; *dashed line* is Hartree-Fock model and *dotted line* is Thomas-Fermi model

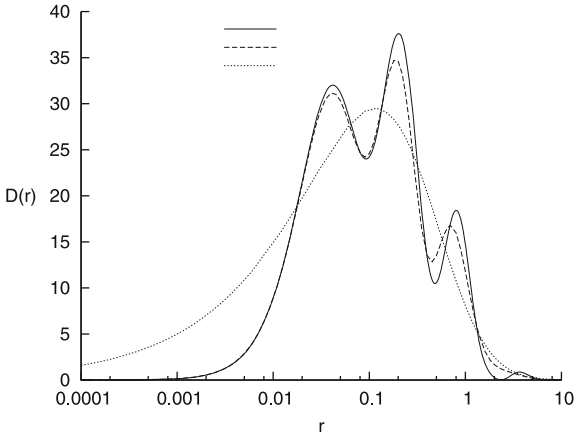

Fig. 1.5 Radial distributions of the electron densities for Fe atom: *solid line* is operator method, *dashed line* is Hartree-Fock model and *dotted line* is Thomas-Fermi model

$$F_0(s) = \sum_{nl} g_{nl} F_{nl}(\xi_{nl}, q); \quad \xi_{nl} = \frac{2Z_{nl}}{n}, \; q = 4\pi s a_B, \tag{1.87}$$

where the partial ASF values $F_{nl}(\xi_{nl}, q)$ are defined by the formula:

$$F_{nl}(\xi_{nl}, q) = -\xi_{nl}^{2l+3} \frac{(n-l-1)!(n+l)!}{2n}$$
$$\times \sum_{k=0}^{n-l-1} \sum_{k=0}^{n-l-1} \frac{\xi_{nl}^{k+m}}{(2l+k+1)!(2l+m+1)k!m!} \frac{d^{2l+1+k+m}}{d\xi^{2l+1+k+m}} \frac{1}{\xi_{nl}^2 + q^2}. \tag{1.88}$$

The explicit formulas for ASF of atoms from the periodical system is listed in the paper [42], for example, for atoms of Ne and Ca:

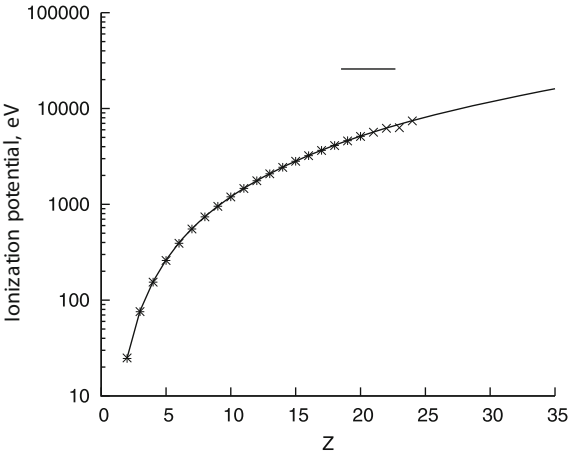

Fig. 1.6 Absolute values of the ionization potentials for He series: *solid line* is operator method; *stars* are Hartree-Fock results

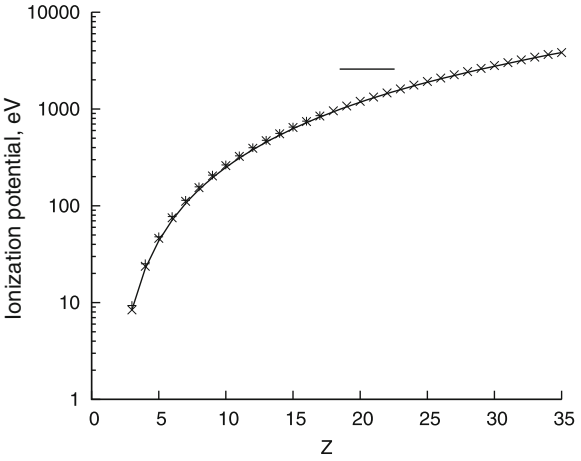

Fig. 1.7 Absolute values of the ionization potentials for Li series: *solid line* is operator method; *stars* are Hartree-Fock results

$$F_{10}(\xi_{10}, q) = \frac{16Z_{10}^4}{(4Z_{10}^2 + q^2)^2};$$
$$F_{20}(\xi_{20}, q) = \frac{Z_{20}^4(Z_{20}^4 - 3q^2Z_{20}^2 + 2q^2)}{(Z_{20}^2 + q^2)^4}. \tag{1.89}$$

The graphical dependence of ASF calculated from formula (1.87) *vs* parameter $s = \sin\theta/\lambda$ is shown in Fig. 1.8 for the atoms of Si, Ba, Cu and Mn^{3+} ion. These simulations approximate the Hartree-Fock numerical values with high accuracy [29]. The formulas above can also be applied for the ions with core in the internal shell, which is important in the case of the interaction of the femto-second pulses from X-ray free electron laser (XFEL) with the matter [4]. Figure 1.9 demonstrates a good coincidence of the analytical results with the numerical ones [62].

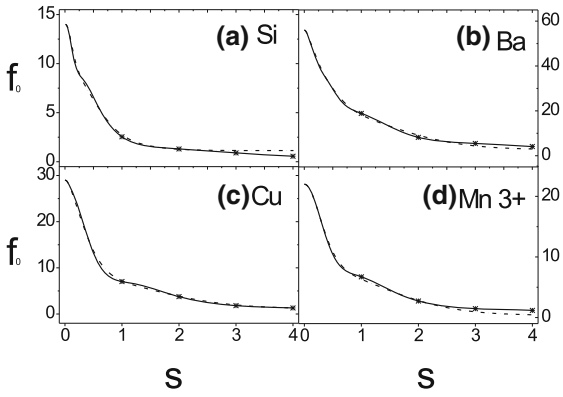

Fig. 1.8 Comparison of analytical (*lines*) and numerical (*dots*) results for ASF of Si, Ba, Cu atoms and Mn^{3+} ion

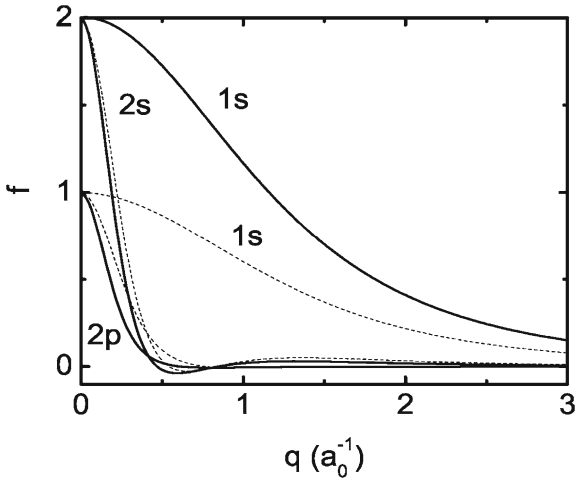

Fig. 1.9 Comparison of analytical (*solid line*) and numerical (*dotted line*) results for calculation of ASF for internal shells of ions C with core hole

The one-electron functions (1.75) accounts for the corrections (1.62) to the scattering factor of the basic cell because of the overlap of the wave functions of electrons in the external shells from the different atoms. The following procedure for the calculation of this correction in the crystals with the diamond-type basic cell (C; Si; Ge) can be considered [42]. In order to take into account the influence of the neighboring atoms, the states with the lowest energies should be found using the linear combinations of the wave functions of 4 electrons from the external shell ($n0$; $n1$) from each atom. As a result, the lowest levels are found to correspond to the collective states, where all electrons have parallel spins and are described by the following set of the functions [29]:

$$\psi_1 = \frac{1}{2}[R_{n0}Y_{00} + R_{n1}(-\sqrt{2}Y_{11} + Y_{10})];$$

$$\psi_2 = \frac{1}{2}[R_{n0}Y_{00} + Y_{11}(\sqrt{2}Y_{11} - Y_{10})];$$
$$\psi_3 = \frac{1}{2}[R_{n0}Y_{00} + R_{n1}(-\sqrt{2}Y_{11} - Y_{10})];$$
$$\psi_4 = \frac{1}{2}[R_{n0}Y_{00} + R_{n1}(\sqrt{2}Y_{11} + Y_{10})], \tag{1.90}$$

where Y_{lm} are the spherical harmonics and R_{nl} are the radial wave functions of the external electrons corresponding to the isolated atoms. Thus, the external layer gives the following contribution to the electron density:

$$\rho_n(r) = \sum_{j=1}^{4} |\psi_j|^2 = \frac{1}{4\pi}[R_{n0}^2 + 3|R_{n1}|^2],$$

that differs from the analogous value in the isolated atom:

$$\rho_n^{(0)} = \frac{1}{2\pi}[R_{n0}^2 + R_{n1}^2].$$

Figure 1.10 shows the change of ASF of each atom due to the influence of other atoms in the elementary cell:

$$\Delta F_0(s) = F_{n1}(\xi_{n1}, q) - F_{n0}(\xi_{n0}, q), \tag{1.91}$$

with $n = 2$ for C, $n = 3$ for Si, $n = 4$ for Ge. In spite of rather small correction to the absolute value of ASF, it could be essential for the analysis of the forbidden reflections [63].

The direct approximation for the wave function can also be important for the analysis of the changes in the electron density due to the effect of external or inter-crystal fields [42]. For instance, the additional Hamiltonian of the spin-orbit interaction for atoms (C; Si; Ge) in the ground state under the action of the magnetic field $\boldsymbol{\Xi}$ directed along z axis is defined as [49]:

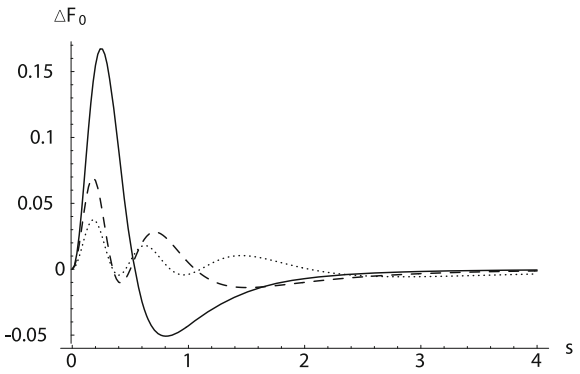

Fig. 1.10 Correction to ASF due to the influence of the neighboring atoms (C - *solid line*, Si - *dashed line*, Ge - *dotted line*)

$$\delta\hat{H} = A(\hat{\boldsymbol{L}}\hat{\boldsymbol{S}}) + \mu_B(\hat{L}_z + 2\hat{S}_z)\Xi, \tag{1.92}$$

where $A > 0$ is the constant of the spin-orbit interaction for two external p-electrons with the total orbital $\hat{\boldsymbol{L}}$ and spin $\hat{\boldsymbol{S}}$ momenta, μ_B is the Bohr magneton. This operator does not change the effective charges of the radial wave functions but effects on the angular distribution of the electron density. Eigenfunctions of the operator (1.92) are defined by its diagonalization with the eigenfunctions of the operators $\hat{\boldsymbol{L}}$, $\hat{\boldsymbol{S}}$ - $|M_L, M_S>$. Then the ground state follows from the following linear combination:

$$\begin{gathered}|\Phi_0> = c_1|1,-1> + c_2|0,0> + c_3|-1,1>; \\ c_1 = \frac{1}{\sqrt{3}}\left(1+\xi-\frac{2}{9}\xi^2\right),\ c_2 = \frac{1}{\sqrt{3}}\left(1-\frac{5}{9}\xi^2\right), \\ c_3 = -\frac{1}{\sqrt{3}}\left(1-\xi-\frac{2}{9}\xi^2\right);\quad \xi = \frac{\mu_B\Xi}{A}.\end{gathered} \tag{1.93}$$

These wave functions account for the anisotropic part in the electron density and for the anisotropic contribution (1.68) to ASF which is proportional to the second Legendre polynomial considered as the function of the angle θ between z axis and vector $\boldsymbol{H}$:

$$\begin{gathered}\Delta F_{an}(\boldsymbol{H}) = -\frac{10}{9}\xi^2 P_2(\cos\theta) f_m(s); \\ f_m(s) = \int_0^\infty r^2 R_{nl}^2(r)\left(\frac{\pi}{2qr}\right)^{1/2} J_{5/2}(qr)dr;\ q = 4\pi a_B s,\end{gathered} \tag{1.94}$$

where $J_{5/2}(qr)$ is the Bessel function.

Figure 1.11 shows the functions $f_m(s)$ for atoms Si and Ge. When the external magnetic field is strong, the anisotropic part of ASF is comparable with the anomalous dispersion corrections and may bring the important information on the inter-crystalline fields.

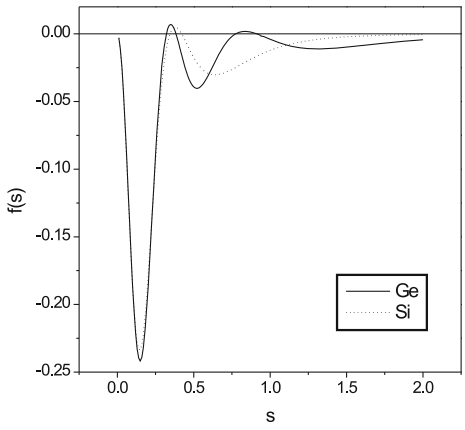

Fig. 1.11 ASF correction in the external magnetic field

1.4 Numerical Calculation of Debye-Waller Factor

Debye-Waller factor (DWF), see Eq. (1.66), gives an essential contribution to the X-ray susceptibility. Most of software packages [40, 41] calculate DWF on the basis of the Debye model for the phonon spectrum [31] and the phenomenological values of the Debye temperature Θ_D of the crystals. However, the experimental value of Θ_D is known for relatively few crystals [29]. When the experimental value of Θ_D is unknown, the average value of the Debye temperatures of the crystals for all atoms in the basic cell is used without a sufficient theoretical argumentation. Thus, the development of a method for the evaluation of Θ_D for arbitrary crystals is an actual problem. Moreover, some diffraction experiments require calculations of the DWF taking into account the anisotropy factors and different branches of the phonon spectrum. The experimental density of the phonon states [64] are known for only a few materials; the situation for most crystalline structures however is unclear. Here we consider the method for simulation of the force matrix for an arbitrary crystal, which realizes both the evaluation of Θ_D and the microscopic calculation of DWF with good accuracy [42].

In the case, when DWF is characterized by a single parameter Θ_D, the harmonic oscillations of atoms in a crystal cell result in attenuation of the elastic scattering amplitudes by the value of DWF. In the isotropic approximation, this factor for the atom with the index p in the crystallographic unit cell is defined by the formula:

$$e^{-2W_p} = e^{-B_p(T)s^2}. \tag{1.95}$$

Here $s = \frac{\sin\theta_B}{\lambda}$ and the main contribution to the temperature coefficient $B(T)$ is supposed to be introduced by the acoustic branch of the phonon spectrum, so the result can be presented in the following way [32]:

$$W_p(T) = \frac{3h^2}{2M_p\kappa_B\Theta}\int_0^1 x\coth\left(\frac{x\Theta}{2T}\right)dx, \tag{1.96}$$

where κ_B is the Boltzmann constant and the Debye temperature is defined by the expression:

$$\Theta_D = \frac{\hbar u k_D}{\kappa_B}; \qquad k_D = \left(\frac{6\pi^2}{\Omega_0}\right)^{1/3}. \tag{1.97}$$

This is a result of linear interpolation of the dispersion law for acoustic phonons $\omega(k) \simeq uk$ within the Debye sphere with the radius k_D, which depends on the volume of the unit cell of the crystal Ω_0. Thus, in the considered approximation, the value Θ_D or its related sound velocity u is the only parameter influencing DWF.

From the microscopical point of view, the parameter u should be found from the dispersion equation for the phonon frequencies defined by the harmonic force matrix of the crystal. Because the approximation of pairwise interactions is satisfactory for the real density of atoms in crystals [27], a realistic two-particle potential [65] can be

used for the construction of the force matrix. The distance between two neighboring atoms in the crystal cell is different from the equilibrium distance in the molecule consisting of the same atoms. However, according to the researches in chemical crystallography, this difference is small due to the fact that the atomic binding in the crystals is mainly defined by the same external electron shells as in the molecules [66]. Thus, since a model potential approximates the electron term of two bound atoms in some neighborhood of the equilibrium distance R_0, it can also be used for finding the force matrix elements at distances corresponding to the atomic positions within the unit cell of a real crystal. In the approximation of pairwise interaction, the element of the force matrix is defined by the following formula [27]:

$$D_{ij}^{pq} = \kappa_{pq}\left[\frac{(R_{pq} - R_{0pq})}{R_{pq}}\delta_{ij} + \frac{R_{0pq}}{R_{pq}}n_i^{pq}n_j^{pq}\right]; \qquad \boldsymbol{n}^{pq} = \frac{\boldsymbol{R}_{pq}}{R_{pq}}. \tag{1.98}$$

Here upper indices in the force matrix enumerate the different atoms in the cell and lower ones correspond to the atomic shifts from their equilibrium positions in Cartesian coordinates; κ_{pq} and R_{0pq} are the harmonic force constants and the equilibrium distance in the molecule corresponding to the atom pair with indexes (pq), respectively; vector $\boldsymbol{R}_{pq}$ is the real distance between these atoms in the crystal cell.

In this section, we use the Debye interpolation for the phonon spectrum and neglect the anisotropy effects. This means that the standard dispersion equation for the acoustical phonon branch [27] should be averaged over all directions in the space of phonon wave vectors as well as over different directions in the unit cell of the direct space. If the approximation of the nearest neighbors is used for the force matrix of the crystal, the average sound velocity can be estimated by the following simple formula:

$$u = \frac{2\pi c a_0 \bar{\nu}}{3\sqrt{2}}; \qquad a_0 = (\Omega_0)^{1/3}; \qquad \bar{\nu} = \frac{1}{\sigma}\sum_{p=1}^{\sigma}\nu_{A_pB_p}. \tag{1.99}$$

Here a_0 represents the average size of the unit cell; the summation is over all different pairs of nearest neighbor atoms in the cell, where σ is a number of such a pair; $\nu_{A_pB_p}$ is the oscillation frequency in cm^{-1} for a pair of atoms with the index p; the numerical coefficient $1/3$ in the formula (1.99) is due to averaging over all the directions. Substituting the expression (1.99) into the definition of Debye temperature (1.97), a universal correlation between Θ_D and $\bar{\nu}$ can be found:

$$\Theta_D = \frac{hc}{3\sqrt{2}\kappa_B}(6\pi^2)^{1/3}\bar{\nu}. \tag{1.100}$$

The formula (1.100) corresponds to the known interpretation of the Debye temperature of the crystal; its value is proportional to the characteristic phonon frequency. In a standard unit system the numerical coefficient in the formula (1.100) is close to unity:

$$\Theta_D[K] \simeq \bar{\nu}[\mathrm{cm}^{-1}]. \tag{1.101}$$

If a recipe for the calculation of the harmonic frequency for any given pair of atoms is known, then this formula can be used for a simple evaluation of the Debye temperature of an arbitrary crystal. The elastic constant κ_A describing the interaction between the identical atoms in two-atomic homo-nuclear molecules and the harmonic approximation for interatomic potential $V(R)$ are expressed as [67]:

$$\begin{aligned} \kappa_A &= (2\pi\nu_A c)^2 M_A, \\ V_A(R) &\simeq -E_0 + \frac{1}{2}\kappa_A (R - R_0)^2. \end{aligned} \tag{1.102}$$

Here the interatomic potential $V(R)$ corresponds to the ground electron term with the binding energy E_0 at equilibrium distance R_0; ν_A is the principal oscillation frequency of the homo-nuclear molecule in cm^{-1} composed from two identical atoms with the mass M_A; c is the velocity of light. Theoretical calculations of the constant κ_A ab initio with a spectroscopic accuracy for homo- and hetero-nuclear molecules requires some complicated quantum-mechanical calculations of electron terms [68]. However, so-called realistic potentials for atom-atom interaction like the Lennard-Jones potential, can provide a sufficient accuracy for statistically averaged macroscopic characteristics of molecular gases [65]:

$$V_A(R) = \frac{\beta_A}{R^{12}} - \frac{\alpha_A}{R^6}. \tag{1.103}$$

The parameter β_A corresponds to the repulsive part of the potential at small distances, and the constant α_A is proportional to the product of squared dipole moments of interacting atoms and simulates the Van der Waals attraction at large distances [49]. The Lennard-Jones potential does not provide the detailed description of electron terms in the entire range of the interatomic distance [68], and therefore it can not be used for precise evaluation of the dissociation energy of the molecule. Nevertheless, it describes quite well the behavior of real potentials near their minima [65], which are of special interest for us in the scope of the harmonic approximation. The above mentioned characteristics of the harmonic potential are expressed through the constants α_A and β_A as

$$R_{0A} = \left[\frac{2\beta_A}{\alpha_A}\right]^{1/6}; \qquad E_{0A} = -\frac{\alpha_A^2}{4\beta_A}; \qquad \kappa_A = 36\alpha_A \left[\frac{\alpha_A}{2\beta_A}\right]^{4/3}. \tag{1.104}$$

Actually, the temperature factor in structure amplitudes is the result of statistic averaging and therefore the fine details of the potential are not essential. With analogous accuracy the values α_A and β_A can be used for a two-atom potential in order to evaluate the Debye temperature. However, the experimental data received both from the cross-sections and from the oscillation spectra are known for a relatively small set of different atomic pairs. Therefore the general recipe for the estimation of α_{AB} and

β_{AB} for arbitrary interacting atoms A and B must be provided. Such a general recipe can be derived from the scaling dependence of the interaction potential established in the framework of statistic theory of atom [69]. A repulsive part of the potential for two different atoms (ions) has been calculated as a geometric average of interaction potentials $V_A^{(rep)}(R)$ and $V_B^{(rep)}(R)$ taken from the independent pairs AA and BB of identical atoms:

$$V_{AB}^{(rep)}(R) = \sqrt{V_A^{(rep)}(R) V_B^{(rep)}(R)}. \tag{1.105}$$

These correlations fitted well the experimental data in a large range of interatomic distances [69].

Considering the Eq. (1.105) independently for large and small interatomic distances, the values α_{AB}, β_{AB} for interactions between different atoms can be evaluated by means of the simple formulas based on the same averages:

$$\beta_{AB} \simeq \sqrt{\beta_A \beta_B}; \quad \alpha_{AB} \simeq \sqrt{\alpha_A \alpha_B}. \tag{1.106}$$

Substituting the Eqs. (1.106) into the formulas (1.103) and (1.104), we deduce the combinative rules for the evaluation of potential parameters for hetero-nuclear diatomic molecules:

$$R_{0AB} = \sqrt{R_{0A} R_{0B}}; \qquad \nu_{AB} = \left[\nu_A \nu_B \frac{M_A + M_B}{2\sqrt{M_A M_B}} \right]^{1/2};$$
$$E_{0AB} = \sqrt{E_{0A} E_{0B}}; \qquad \kappa_{AB} = (2\pi c \nu_{AB})^2 \mu_{AB}; \quad \mu_{AB} = \frac{M_A M_B}{M_A + M_B}, \tag{1.107}$$

using the experimental data for the homo-nuclear molecules. Here ν_A and ν_B are the principal oscillation frequencies of the molecules A_2 and B_2; ν_{AB} corresponds to the molecule AB and the difference in the reduced masses for homo- and hetero-nuclear molecules is taken into account.

Certainly, these combinative rules are semi-phenomenological due to the choice of the model potential and the lack of a sufficient theoretical ground for the expression (1.105). The effectiveness and accuracy of these relations can be investigated by applying them to diatomic molecules with known parameters. Table 1.1 lists all the necessary parameters for diatomic homo-nuclear molecules from the reference book [67].

The comparison of the calculated binding energy E_0 presented in the table with the energy of dissociation [67] is rather formal in our context. This is because the Lennard-Jones potential is not a good model for the electron term for all interatomic distances. In fact only the parameters ν and R_0 are important for the presented model since they exactly define the behavior of the potential in the harmonic approximation. The parameters for molecules, marked by the symbol (*), are absent in [67] and we calculated these values by means of the combinative rules (1.105) based on experimental data for materials containing these atoms along with other ones.

Table 1.1 Parameters of diatomic homo-nuclear molecules [67]

Atom	ν, cm^{-1}	E_0, eV	R_0, Å
H	4401	4.48	0.74
He	1861	2.36	1.04
Be*	1343	13.32	1.39
B	1051	3.02	1.59
C	1854	6.21	1.24
N	2358	9.76	1.10
O	1580	5.12	1.21
F	916	1.60	1.41
Ne	14	0.00	3.10
Na	159	0.72	3.08
Mg	190	0.05	3.89
Al	350	1.55	2.47
Si	510	3.21	2.25
P	780	5.03	1.89
S	726	4.37	1.89
Cl	560	2.48	1.99
Ar	26	0.01	3.76
K	92	0.51	3.90
Ca	241	0.13	4.28
Sc	42	1.65	2.40
Ti*	489	1.30	2.17
V*	552	2.48	2.09
Cr	475	1.56	2.17
Mn	110	0.23	2.59
Fe	218	1.06	2.04
Co	365	1.69	3.20
Ni	286	2.36	2.96
Cu	264	2.03	2.22
Zn*	329	1.78	3.41
Ga*	219	1.40	2.43
Ge*	336	2.82	2.16
As	429	3.96	2.10
Se	430	3.16	2.17
Br	325	1.97	2.28
Kr	24	0.02	4.03
Rb	57	0.49	3.79
Sr*	202	5.82	3.05
Y*	282	1.62	–
Zr*	423	12.05	8.41
Nb	280	11.89	2.36
Mo	370	4.89	–
Tc	–	–	–
Ru*	338	3.41	2.17
Rh*	363	2.92	2.09
Pd*	91	0.73	3.16

(continued)

Table 1.1 (continued)

Atom	ν, cm^{-1}	E_0, eV	R_0, Å
Ag	192	1.66	2.59
Cd*	164	0.08	4.28
In	142	1.01	2.86
Sn*	315	1.99	2.78
Sb	272	3.09	2.34
Te	251	2.68	2.56
I	214	1.54	2.66
Xe	30	0.02	4.36
Cs	29	0.39	4.47
Ba*	150	11.26	3.25
La*	257	2.50	2.83
Ce*	886	2.50	2.74
Pr*	240	11.59	–
Nd	–	16.02	–
Pm	–	–	–
Sm	–	7.20	–
Eu*	166	11.43	–
Gd*	216	16.84	–
Tb	248	1.32	–
Dy	–	13.13	–
Ho	251	0.82	3.11
Er	–	14.50	–
Tm	–	6.49	–
Yb	162	0.17	2.89
Lu	246	10.11	2.63
Hf	330	13.11	2.44
Ta	365	13.15	2.36
W	385	9.04	–
Re	290	–	–
Os	260	–	–
Ir	279	6.16	2.36
Pt	218	6.35	2.28
Au	191	2.30	2.47
Hg	36	0.07	3.30
Tl	102	0.90	3.07
Pb	161	0.82	3.03
Bi	156	3.09	3.07
Po	155	1.90	–
Th	249	–	–
U	207	7.61	–

Figures 1.12 and 1.13 show the comparison of experimental [67] parameters of heteronuclear molecules with their theoretical values, calculated according to the combinative rules of (1.105). X-axis at these pictures represents the experimen-

tal values and y-axis defines the theoretical values. Thus, ideal correspondence of experiment and theory should result in situation of all the points on a single straight line.

To prove the described above theory, about two hundred different molecules described in [67] have been examined. Despite the large variation in the range of absolute values for real molecule parameters, the evaluation of these values using the combinative rules is rather effective: the mean square error is 3 % when estimating R_0 and 8 % for ν. The largest deviation reaches 30 % and are related to a few molecules with the hydrogen atom, for which the statistical evaluations are not a good approximation. The formula derived can also be used for a rough estimation of the dissociation energy; the mean square error for this parameter is about 25 % because of the above mentioned reasons. The corrections to the parameters considered for interacting ions can be estimated in the framework of Thomas-Fermi model [69].

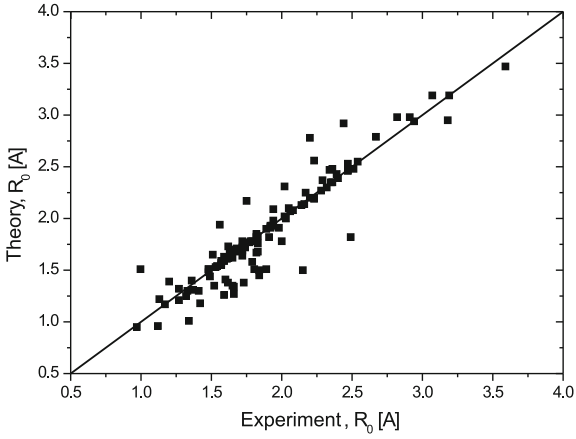

Fig. 1.12 Comparison of the calculated with (1.105) and experimental values of the equilibrium distances R_{AB} for diatomic molecules

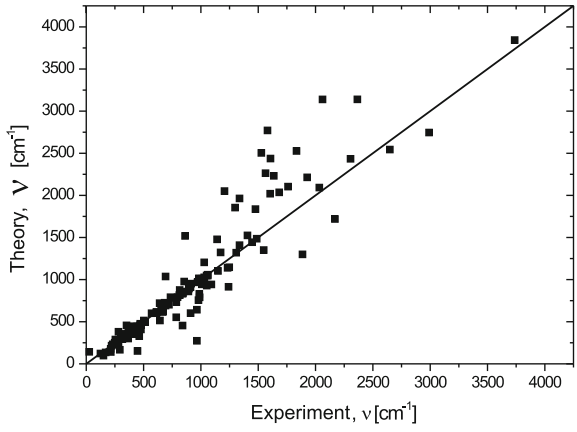

Fig. 1.13 Comparison of the calculated with (1.105) and experimental values of the principal frequencies ν_{AB} for diatomic molecules

Table 1.2 Comparison of the theoretical Θ_{th} and experimental Θ_{exp} Debye temperatures

Crystal	*Cell*	Θ_D^{exp}, *K*		Θ_D^{th}, *K*	ε
		min	*max*		
Cu	f.c.c.	304	342	264	0.101
Ag		212	220	192	0.059
Au		155	190	191	0.051
Ca		220	230	241	0.034
Sr		148	171	202	0.118
Al		375	428	350	0.069
Th		145	170	249	0.225
Pb		68	105	161	0.301
V		300	413	552	0.215
Nb		252	301	280	0.006
Ta		230	245	365	0.212
Ni		375	476	286	0.196
Rh		315	370	363	0.029
Pd		263	280	91	0.498
Ir		285	–	279	0.011
Pt		225	248	218	0.041
Li	b.c.c.	277	430	351	0.004
Na		146	180	159	0.012
K		100	163	92	0.177
Rb		58	85	57	0.113
Cs		42	54	29	0.247
Ba		115	–	150	0.132
Cr		405	485	475	0.033
Mo		360	388	370	0.005
W		270	384	385	0.081
Fe		355	467	218	0.307
C	Diamond	1800	2242	1854	0.043
Si		505	685	510	0.077
Ge		211	400	336	0.048
Sn		260	–	315	0.096
Be	h.c.p.	1000	1376	1343	0.061
Mg		290	342	190	0.249
Zn		200	305	329	0.132
Cd		120	172	164	0.058
La		132	152	257	0.288
Gd		152	–	216	0.174
Tl		96	100	102	0.020
Ti		342	430	489	0.118
Zr		250	288	423	0.223
Hf		213	–	330	0.215
Re		275	310	290	0.004
Co		385	–	365	0.027
Ru		400	426	338	0.100

(continued)

Table 1.2 (continued)

Crystal	*Cell*	Θ_D^{exp}, *K*		Θ_D^{th}, *K*	ε
		min	*max*		
Os		250	256	260	0.014
B	Tetragonal	1250	–	1051	0.086
In		78	129	142	0.157
Sn		163	258	315	0.199
Hg	Rhombohedral	37	100	36	0.311
As		224	285	429	0.255
Sb		140	200	272	0.231
Bi		62	120	156	0.263
U	Orthorhombic	200	–	207	0.017
Ga		125	240	219	0.091
Br		110	–	325	0.494
I		106	–	214	0.338
LiH	B1	815	–	1525	0.303
LiF		650	685	602	0.052
LiCl		463	–	515	0.053
LiBr		387	–	458	0.084
LiI		331	–	411	0.108
NaF		439	–	382	0.069
NaCl		270	300	301	0.027
NaBr		200	243	249	0.058
NaI		151	198	217	0.109
KF		321	333	299	0.058
KCl		218	–	227	0.020
KBr		152	–	178	0.079
KI		115	200	152	0.018
RbF		238	–	260	0.044
RbCl		176	–	187	0.030
RbBr		128	–	136	0.030
RbI		108	–	111	0.014
CsF		184	–	200	0.042
AgCl		130	143	352	0.441
PbS		230	–	414	0.286
PbSe		168	–	278	0.247
PbTe		139	–	203	0.187
MgO		750	890	553	0.194
CsCl	B2	166	–	141	0.081
CsBr		119	–	98	0.097
CsI		93.6	–	78	0.091
TlCl		125	–	283	0.387
TlBr		114	–	192	0.255
AgI	B3	120	183	203	0.145
GaAs		314	–	306	0.013
GaSb		233	–	248	0.031
ZnS		300	–	504	0.254
					$\varepsilon_{aver} = 0.135$

The Table 1.2 gives a comparison between experimental Debye temperatures Θ_D^{exp} and values calculated with the formula (1.101). Practically all calculated values of Θ_D^{th} are within $\pm 10\,\%$ of experimentally reported Debye temperatures determined by different methods [29]. Figure 1.14 is a graphical representation of the Table 1.2 in the coordinates $(\Theta_D^{exp}; \Theta_D^{th})$.

The presented method for microscopic simulation of the harmonic potential for arbitrary pair of atoms gives a recipe for an accurate calculation of DWF. The accuracy is provided by the optical branches of the phonon spectrum and anisotropy of DWF in the crystals with the polyatomic unit cell. The anharmonic effects are neglected in this case and the interaction between atoms in neighboring cells are only taken into account when calculating DWF.

In general, every force matrix element includes four components (Γ, X, Y, Z), which are described as follows:

(Γ): Contribution of the atoms situated in the same unit cell. These elements of the force matrix are denoted by $\Gamma_{i,j}^{\alpha,\beta}$. Here lower indices correspond to usual Cartesian components ($i, j = 1, 2, 3$) and upper ones enumerate s atoms in the same cell ($\alpha, \beta = 1, \ldots, s$). The unit cell is assumed to consist of s_1 atoms of one type, s_2 atoms of other type etc., where $s_1 + s_2 + \cdots = s$. The distance between some atom with number α_1 and all the atoms of the same type in the cell is expressed as:

$$R_{\alpha_1,\beta_1}^{11} = \sqrt{\sum_{i=1}^{3} (x_i^{\alpha_1} - x_i^{\beta_1})^2 a_i^2},$$

where the dimensionless atom coordinates x_i are measured in fractions of the corresponding basic vectors a_i of the crystal. In the framework of the considered approximation, the only least distances are kept and the number of them defines the coordination number for this type of atoms [27]:

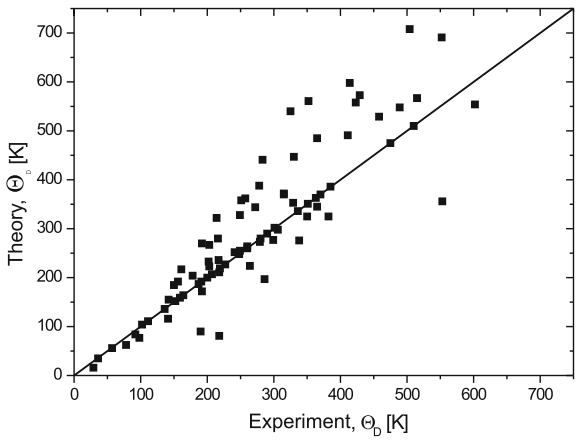

Fig. 1.14 Comparison of the experimental Θ_D^{exp} and calculated Θ_D^{th} values of the Debye temperatures for crystals

$$l_1, \quad 1 \le l_1 \le s_1; \quad 1 \le \alpha_1 \le s_1; \quad 1 \le \beta_1 \le l_1.$$

The analogous procedure delivers the distances and the coordination numbers for atoms of different types:

$$R^{pq}_{\alpha_p,\beta_q}, \quad 1 \le \alpha_p \le s_p; 1 \le \beta_q \le l_{pq},$$

where l_{pq} is the number of atoms of the type q closest to the atom of the type p. A one-cell contribution to elements of the force matrix is calculated by the Eq.(1.98):

$$\Gamma^{\alpha,\beta}_{i,j} \to \Gamma^{\alpha_p,\beta_q}_{i,j} = \kappa_{pq}(x_i^{\alpha_p} - x_i^{\alpha_q})(x_j^{\alpha_p} - x_j^{\alpha_q})a_i a_j [R^{pq}_{\alpha_p,\beta_q}]^{-2}. \tag{1.108}$$

Here κ_{pq} are the harmonic constants for the interaction between atoms of type p and q, calculated by means of the Eq. (1.107).

(X,Y,Z): 3 contributions from atoms in neighboring cells. The distance to these atoms can be found by coordinate translations by one of the basis lattice vectors:

$$(XR)^{pq}_{\alpha_p,\beta_q} = \sqrt{(x_1^{\alpha_p} - x_1^{\beta_q} - 1)^2 a_1^2 + (x_2^{\alpha_p} - x_2^{\beta_q})^2 a_2^2 + (x_3^{\alpha_p} - x_3^{\beta_q})^2 a_3^2};$$

$$(YR)^{pq}_{\alpha_p,\beta_q} = \sqrt{(x_1^{\alpha_p} - x_1^{\beta_q})^2 a_1^2 + (x_2^{\alpha_p} - x_2^{\beta_q} - 1)^2 a_2^2 + (x_3^{\alpha_p} - x_3^{\beta_q})^2 a_3^2};$$

$$(ZR)^{pq}_{\alpha_p,\beta_q} = \sqrt{(x_1^{\alpha_p} - x_1^{\beta_q})^2 a_1^2 + (x_2^{\alpha_p} - x_2^{\beta_q})^2 a_2^2 + (x_3^{\alpha_p} - x_3^{\beta_q} - 1)^2 a_3^2},$$

here the same approximation of the nearest neighbors has been used. If the pair of atoms of selected type has been already encountered in the group Γ of the initial cell, then the same pairs in the groups (XR), (YR), (ZR) are taken into account only when the inequalities $(\{S\}R)^{pq}_{\alpha_p,\beta_q} \le R^{pq}_{\alpha_p,\beta_q}$, $\{S\} = X, Y, Z$ are fulfilled. After such a selection procedure, the additional contributions to the force matrix are calculated as follows:

$$\begin{aligned}
X^{\alpha_p,\beta_q}_{i,j} &= \kappa_{pq}(x_i^{\alpha_p} - x_i^{\alpha_q} - \delta_{i1})(x_j^{\alpha_p} - x_j^{\alpha_q} - \delta_{j1})a_i a_j [(XR)^{pq}_{\alpha_p,\beta_q}]^{-2};\\
Y^{\alpha_p,\beta_q}_{i,j} &= \kappa_{pq}(x_i^{\alpha_p} - x_i^{\alpha_q} - \delta_{i2})(x_j^{\alpha_p} - x_j^{\alpha_q} - \delta_{j2})a_i a_j [(YR)^{pq}_{\alpha_p,\beta_q}]^{-2};\\
Z^{\alpha_p,\beta_q}_{i,j} &= \kappa_{pq}(x_i^{\alpha_p} - x_i^{\alpha_q} - \delta_{i3})(x_j^{\alpha_p} - x_j^{\alpha_q} - \delta_{j3})a_i a_j [(ZR)^{pq}_{\alpha_p,\beta_q}]^{-2},
\end{aligned} \tag{1.109}$$

with δ_{ij} as the Kronecker symbol.

The next step is the calculation of the phonon eigenfrequencies. Taking into account a translational symmetry of the crystal in the equations for small atomic oscillations in the conventional way [27], the equations of motion for the phonon variables $\xi_i^{\alpha_p}(\boldsymbol{k})$ and frequencies are:

$$M_p\omega^2\xi_i^{\alpha_p} = \sum_{\beta_q,j} \Gamma_{i,j}^{\alpha_p,\beta_q}(\xi_i^{\alpha_p} - \xi_j^{\beta_q}) + \frac{1}{2}\sum_{\beta_q,j} X_{i,j}^{\alpha_p,\beta_q}(\xi_i^{\alpha_p} - \xi_j^{\beta_q} e^{ik_1a_1}) + \frac{1}{2}\sum_{\alpha_q,j} X_{i,j}^{\alpha_q,\beta_p}(\xi_i^{\alpha_p} - \xi_j^{\beta_q} e^{-ik_1a_1}) + Tr\{\}. \quad (1.110)$$

here the symbol $Tr\{\}$ means that the analogous terms with matrices Y, Z should be also included, and k_i are the projections of the wave vector on the corresponding basis vectors of the unit cell. We should also note that in general the force matrices in the equations are not symmetrical on all indices. For example, the element X^{α_1,β_q} defines the interaction between atom of the type 1 in selected cell and atoms of the type q in the displaced cell. Vice versa, only that atoms of the type q from the basis cell, which are interacting with atom of the type 1 in the displaced cell, contribute to the element X^{α_q,β_1}.

The approximate solution for the Eq. (1.110) is built taking into account the fact, that the main contribution in the integrals over the phonon energy in the DWF is defined by the range of small values of k in the vicinity of the extremum of each phonon zone. The principal character of this contribution can be explained by the maximum value of the state density because of the phonon group velocity becomes zero in this range [27], and the exponentials in the Eq. (1.110) can be expanded into the series by k. Besides, the acoustic branches of the phonon spectrum can be extracted by using new variables, namely the coordinate of the center of mass of the cell:

$$R_i = \frac{1}{M}\sum_p M_p \sum_{\alpha_p} \xi_i^{\alpha_p};$$

where M is the total mass of the cell; M_p is the mass of the atom of the type p, and the relative coordinates are:

$$\rho_i^{\alpha_p} = \xi_i^{\alpha_p} - R_i; \quad \sum_p M_p \sum_{\alpha_p} \rho_i^{\alpha_p} = 0.$$

The last relation means that the number of independent equations is equal to 3(s-1) but three other components of the variable (for example, with index $\alpha_p = 1$) depend on the rest and thus can be found from the equation

$$\rho_i^1 = -\frac{1}{M_1}\sum_p M_p \sum_{\alpha_p \neq 1} \rho_i^{\alpha_p}. \quad (1.111)$$

In order to find the motion equation for the center of mass, all the Eq. (1.110) are summarized by justifying to accuracy $O(k^2)$:

$$M\omega^2 R_i = \frac{k_1^2 a_1^2}{2} \sum_p \sum_{\alpha_p} \sum_{\beta_q, j} \left[X_{i,j}^{\alpha_p, \beta_q} + X_{i,j}^{\alpha_q, \beta_p} \right] R_j$$
$$+ \frac{ik_1 a_1}{2} \sum_p \sum_{\alpha_p} \sum_{\beta_q, j} [X_{i,j}^{\alpha_p, \beta_q} - X_{i,j}^{\alpha_q, \beta_p}] \rho_j^{\beta_q} + Tr\{\}. \quad (1.112)$$

The equations for the relative variables can be solved in the approximation of the independent oscillations which is also used in the theory of small vibrations of molecules [68]. In this case, the coupling of various oscillations is taken into account only through the coordinate of the mass center. Then the average deviation of each atom from its equilibrium position is equal to zero relative to the center of mass of the unit cell. Using this fact, the equations of motion for relative coordinates are as follows:

$$M_p \omega^2 \rho_i^{\alpha_p} = -M_p \omega^2 R_i + \sum_{\beta_q, j} \left[\Gamma_{i,j}^{\alpha_p, \beta_q} + \frac{1}{2} (X_{i,j}^{\alpha_p, \beta_q} + X_{i,j}^{\alpha_q, \beta_p}) \right] \rho_j^{\alpha_p}$$
$$- \frac{ik_1 a_1}{2} \sum_{\beta_q, j} [X_{i,j}^{\alpha_p, \beta_q} - X_{i,j}^{\alpha_q, \beta_p}] R_j + Tr\{\}. \quad (1.113)$$

Physically the approximation used means that only the average force acting to selected atom from the side of all neighbors is taken into account. For the case of small k, the optical frequencies $\omega_p^{(\nu)}$; $\nu = 1, 2, 3$ can be found from the Eq. (1.113). The number of such optical branches is $3(s-1)$ and for atoms of the type p they degenerate with the multiplicity $3s_p$ (for the first one the multiplicity is $3(s_1 - 1)$). These branches of the phonon spectrum are defined by diagonalization of p matrices of dimension (3×3), which result in the following equations for the eigenfrequencies and orthonormalized polarization vectors $e_i^{\nu}(p)$:

$$\omega_p^{(\nu)} = \sqrt{\frac{\lambda_p^{\nu}}{M_p}}; \qquad \lambda_p^{\nu} e_i^{\nu} = \sum_j D_{ij}^p e_j^{\nu};$$
$$D_{ij}^p = \sum_{\beta_q, j} \left[\Gamma_{i,j}^{\alpha_p, \beta_q} + \frac{1}{2} (X_{i,j}^{\alpha_p, \beta_q} + X_{i,j}^{\alpha_q, \beta_p}) + Tr\{\} \right]. \quad (1.114)$$

The acoustic branches then can be found from the Eq. (1.110) by substitution of the relative coordinates by the center of mass. Then the spectrum of the acoustic eigenfrequencies is defined by the acoustic 4-rank tensor depending on the force matrix and the vector $\boldsymbol{k}$ [49]. As a result, there exists an anisotropy of the sound velocity in different directions of propagation even in cubic crystals. However, by the definition, the DWF depends on the constant 2-rank tensor which is determined by the symmetry of the crystal only and does not depend on the vector $\boldsymbol{k}$ [49] because of the averaging over the $\boldsymbol{k}$ during the integration on the phonon variables. This fact

allows the use of an averaging procedure over all the directions of $\boldsymbol{k}$ in the dispersion equation. Mathematically this corresponds to the following substitution:

$$\int f[\omega(\boldsymbol{k})]k^2 dk d\Omega \simeq \int f[<\omega(k)>]k^2 dk d\Omega,$$

$$<\omega(k)>=\sqrt{I}; \qquad I=\frac{1}{4\pi}\int \omega^2(\boldsymbol{k})d\Omega.$$

Then the Eq. (1.110) transform to:

$$\begin{aligned} M\omega^2 R_i = {} & \frac{k^2 a_1^2}{6}\sum_p \sum_{\alpha_p} \sum_{\beta_q, j} [X_{i,j}^{\alpha_p,\beta_q} + X_{i,j}^{\alpha_q,\beta_p}]R_j \\ & + \frac{k^2 a_1^2}{12 M_1}\sum_q M_q \sum_{\alpha_p} \sum_{\beta_q \neq 1, m} [X_{i,m}^{\alpha_p,1} - X_{i,m}^{1,\beta_p}] \\ & \times \sum_{\gamma_r, l} [D_{ml}^q]^{-1} \sum_j [X_{l,j}^{\beta_q,\gamma_r} - X_{l,j}^{\beta_r,\gamma_q}]R_j \\ & - \frac{k^2 a_1^2}{12}\sum_p \sum_{\alpha_p \neq 1} \sum_{\beta_q, m} [X_{i,m}^{\alpha_p,\beta_q} - X_{i,m}^{\alpha_q,\beta_p}] \\ & \times \sum_{\gamma_r, l} [D_{ml}^q]^{-1} \sum_j [X_{l,j}^{\beta_q,\gamma_r} - X_{l,j}^{\beta_r,\gamma_q}]R_j + Tr\{\}. \end{aligned} \tag{1.115}$$

and the problem is again reduced to the diagonalization of the symmetrical (3×3) matrix. The solution for the optical frequencies is then found in the form

$$\omega_a^\nu(k) = \frac{k a_0}{\sqrt{M}} c_\nu; \quad \nu = 1, 2, 3; a_0 = (\Omega_0)^{1/3}$$

and defines three acoustical phonon branches. In this parametrization, the normalized vectors of polarization e_{ia}^ν and eigenvalues c_ν no longer depend on k:

$$c_\nu^2 e_{ia}^\nu = \sum_j A_{ij} e_{ja}^\nu;$$

$$\begin{aligned} A_{ij} = {} & \frac{b_1^2}{6}\sum_p \sum_{\alpha_p} \sum_{\beta_q, j} [X_{i,j}^{\alpha_p,\beta_q} + X_{i,j}^{\alpha_q,\beta_p}] \\ & + \frac{b_1^2}{12}\sum_q M_q \sum_{\alpha_p} \sum_{\beta_q \neq 1, m} [X_{i,m}^{\alpha_p,1} - X_{i,m}^{1,\beta_p}] \\ & \times \sum_{\gamma_r, l} [D_{ml}^q]^{-1} \sum_j [X_{l,j}^{\beta_q,\gamma_r} - X_{l,j}^{\beta_r,\gamma_q}]R_j \end{aligned}$$

$$-\frac{k^2 b_1^2}{12}\sum_p \sum_{\alpha_p \neq 1} \sum_{\beta_q, m} [X_{i,m}^{\alpha_p,\beta_q} - X_{i,m}^{\alpha_q,\beta_p}]$$
$$\times \sum_{\gamma_r, l} [D_{ml}^q]^{-1} \sum_j [X_{l,j}^{\beta_q,\gamma_r} - X_{l,j}^{\beta_r,\gamma_q}] + Tr\{\};$$
$$b_i = \frac{a_i}{a_0}. \tag{1.116}$$

To derive a final formula for DWF, the general definition of the Debye-Waller factor is used for the atom with number t in the unit cell [29]:

$$DWF_t = e^{-\sum_{i,j} B_{ij}^t q_i q_j}; \quad B_{i,j}^t = 2\frac{\hbar^2}{M_t} W_{i,j}. \tag{1.117}$$

Here the projections of the transmitted wave vector q_i should be calculated in the coordinate system connected with unit cell

$$q_i = \frac{2\pi}{d} l_i; \qquad d = \left[\sqrt{l_1^2 g_1^2 + l_2^2 g_2^2 + l_3^2 g_3^2}\right]^{-1},$$

where d is the interplane distance for the given reflection defined by Miller indices l_i; n_i are the minimal integers for this reflection; $\boldsymbol{g}_i$ are the standard basis vectors of the reciprocal lattice. In this definition, tensor W_{ij} does not depend on the atom number and is the characteristics of the crystal as a whole [32]:

$$W_{ij} = \frac{\Omega_0}{2\hbar} \sum_{(p)} \sum_{\nu} e_i^{\nu} e_j^{\nu} \int \frac{d\boldsymbol{k}}{(2\pi)^3} f(\omega_p^{\nu}), \tag{1.118}$$

where the summation is performed on all optical and acoustic branches and f is the function of the Bose-Einstein distribution:

$$f(\omega) = \frac{1}{\omega}\left[1 + \frac{2}{\exp \hbar\omega / k_B T - 1}\right].$$

Below we split the general expression for W into two parts related to optical W^o and to acoustic W^a oscillations. The above-mentioned expansion on small k corresponds to the Einstein approximation when the optical frequencies are considered as constants in the Brillouin zone [27]. Then taking into account the multiplicity of the optical branches, W^o is calculated as:

$$W_{ij}^o = \frac{1}{2\hbar} \sum_p s_p' \sum_{\nu} e_i^{\nu p} e_j^{\nu p} f(\omega_p^{\nu}). \tag{1.119}$$

The frequencies and vectors of polarization for optical branches have been defined in the Eq. (1.114). Index s'_p means that the value $(s_1 - 1)$ should be substituted instead of s_1 for the atoms of the type 1.

The acoustic contribution to the DWF can be found in the following form

$$W^a_{ij} = \frac{1}{2\hbar} \sum_\nu e^\nu_{ia} e^\nu_{ja} \frac{\Omega_0}{2\pi^2} \int_0^{k_D} dk \frac{k\sqrt{M}}{a_0 c_\nu} \times \left[\frac{\exp\left(\hbar k a_0 c_\nu / k_B T \sqrt{M}\right)}{\exp\left(\hbar k a_0 c_\nu / k_B T \sqrt{M}\right) - 1} \right]; \quad k_D = \left(\frac{6\pi^2}{\Omega_0} \right)^{1/3}. \tag{1.120}$$

By analogy with Debye temperature, three different parameters are introduced for each polarization of the acoustic phonons:

$$\Theta_\nu = \frac{\hbar a_0 k_D c_\nu}{k_B \sqrt{M}},$$

and finally the acoustic part of DWF is:

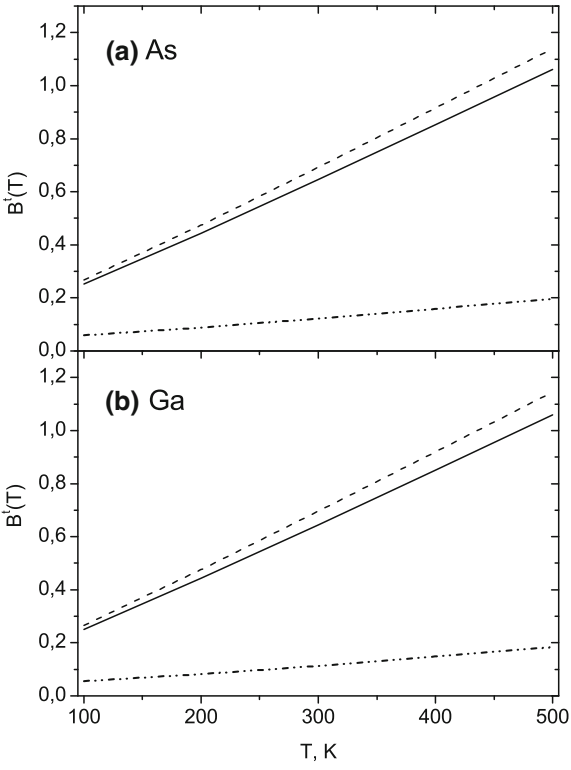

Fig. 1.15 The value $B^t(T)$ in the Debye-Waller factor for the atom of (**a**) As and (**b**) Ge in the crystal GaAs ($\Theta_D = 210K$) as a function of the temperature. The *dashed line* presents the results of [64], obtained on the basis of the experimental phonon spectrum; the *solid line* is a calculation by the present algorithm; the *dash-dotted curve* represent the optical phonon spectrum

$$W_{ij}^{a} = \frac{3}{2k_B} \sum_{\nu} e_{ia}^{\nu} e_{ja}^{\nu} \frac{1}{\Theta_\nu} \int_0^1 x \, dx \coth\left(\frac{x\Theta_\nu}{2T}\right). \tag{1.121}$$

The formulas (1.118)–(1.121) establish the algorithm for calculation of the Debye-Waller factor for X-ray susceptibilities. By this algorithm, the Fourier components of the susceptibility for crystals are calculated by using the symmetrical tensor W, which includes only 6 components in the most general case. To illustrate this result, the Debye-Wallers factors for the atoms of As and Ga in the crystal GaAs have been calculated. Figure 1.15 demonstrates a good agreement between the DWF temperature dependence calculated by proposed method and the phenomenological dependence found on the basis of the experimental density of the phonon states [64]. The optical part of the DWF, usually not taken into account in the standard program packages [40, 41], seems to be an important part of the total DWF value, as Fig. 1.15 illustrates, too.

References

1. R.W. James, *The Optical Principle of the Diffraction of X-rays* (G.Bell and Sons, London, 1962)
2. J.J. Rehr, R.C. Albers, Rev. Mod. Phys. **72**, 621 (2000)
3. S.A. Stepanov, S.K. Sinha, Phys. Rev. B **61**, 15302 (2000)
4. K.J. Gaffney, H.N. Chapman, Science **316**, 1444 (2007)
5. P. Gibbon, *Short Pulse Laser Interactions with Matter* (Imperial College Press, London, 2005)
6. S.H. Chen, M. Kotlarchyk, *Interactions of Photons and Neutrons with Matter* (World Scientific, Singapore, 2008)
7. C. Cohen-Tannoudji, J. Dupont-Roc, G. Grynberg, *Atom- Photon Interactions* (Wiley, New York, 2004)
8. M. Šindelka, Phys. Rev. A **81**, 033833 (2010)
9. A. Authier, *Dynamical Theory of X-ray Diffraction* (Oxford University Press, New York, 2001)
10. U.Pietsch, V.Holy, T.Baumbach, *High-Resolution X-ray Scattering: From Thin Films to Lateral Nanostuctures*, 2nd edn. (Springer, Berlin, 2004)
11. V.G. Baryshevsky, I.D. Feranchuk, A.P. Ulyanenkov, *Parametric X-ray Radiation from Rlativistic Electrons in a crystal: Theory Experiment and Applications* (Springer, Berlin, 2005)
12. N.N. Bogoluibov, Ukr. Matematicheskii Zh. **2**, 3 (1960) (in russian)
13. R.J. Glauber, Phys. Rev. **131**, 2766 (1963)
14. L.D. Landau, E.M. Lifshitz, *Electrodynamics of Condensed Matter*, 2nd edn. (Nauka, Moscow, 1982) (in russian)
15. V.S. Popov, Uspekhi Fiz. Nauk **174**, 921 (2004) (in russian)
16. R. Kubo, J. Phys. Soc. Japan, **12**, 570 (1957)
17. D. Chandler, *Introduction to Modern 1197 Statistical Mechanics* (Oxford University Press, Oxford, 1987)
18. V.B. Berestetsky, E.M. Lifshitz, L.P. Pitaevsky, *Relativistic Quantum Theory*, V. 1 (Nauka, Moscow, 1965) (in russian)
19. M.L. Goldberger, K.M. Watson, *Collision Theory* (Wiley, New York, 1964)
20. V.G. Baryshevsky, *Nuclear Optics of Polarized Media* (Energoatomizdat, Moscow, 1995) (in russian)
21. O. Klein, Y. Nishina, Z. für Phys. **52**, 853 (1929)

22. S. Takagi, Acta Crystallogr. **15**, 1311 (1962)
23. D. Taupin, Bull. Soc. Fr. Mineral. Cristallogr. **87**, 469 (1964)
24. M.A. Krivoglaz, *X-Ray and Neutron Diffraction in Nonideal rystals* (Springer, Berlin, 1996)
25. B.W. Batterman, Rev. Mod. Phys. **36**, 681 (1964)
26. C. Kittel, *Introduction to Solid State Physics*, 4th edn. (Wiley, New York, 1976)
27. N.W. Ashcroft, N.D. Mermin, *Solid State Physics* (Holt, Rinehart and Winston, New York, 1975)
28. B.L. Henke, E.M. Gullikson, J.C. Davis, At. Data Nucl. Data Tables **54**, 593 (1993)
29. International Tables for Crystallography. V.C., (Kluwer Academic Publishers, Dordrecht, 1992).
30. B.K. Vainshtein, *Fundamental of Crystals*, 2nd edn. (Springer, Berlin, 1996)
31. J. Ziman, *Principles of the Theory of Solids* (Campridge University Press, Campridge, 1972)
32. D. Bruesch, *Phonons: Theory and Experiments* (Springer, Berlin, 1987)
33. P.M. Mors, H. Feshbach, *Methods of Theoretical Physics*, vol. 1 (Springer, Berlin, 1987)
34. F.C. Fischcer, T. Brage, P. Jonson, *Computational atomic structure A, Multi-configuration Hartree-Fock approach* (IOP Pubishing, Bristol, 1997)
35. E. Climenti, C. Roetti, At. Nucl. Data Tables **14**, 177 (1974)
36. L.H. Thomas, Proc. Cambridge Philos. Soc. **23**, 542 (1926)
37. E. Fermi, Z. Phys. **48**, 73 (1928)
38. D.T. Cromer, J.B. Mann, Acta Cryst. A **24**, 321 (1968)
39. D. Waasmaier, A. Kirfel, Acta Cryst. A **51**, 416 (1995)
40. S. Brennan, P.I. Cowan, Rev. Sci. Instrum. **63**, 850 (1991)
41. O.M. Lugovskaya, A.S. Stepanov. Kristallografiya **36**, 856 (1991)
42. I.D. Feranchuk, L.I. Gurskii, L.I. Komarov, O.M. Lugovskaya, F. Burgaezy, A.P. Ulyanenkov, Acta Cryst. A **58**, 370 (2002)
43. V.V. Triguk, I.D. Feranchuk, J. Appl. Spectrosc. **77**, 749 (2011)
44. R.T. Sharp, G.K. Horton, Phys. Rev **90**, 317 (1953)
45. H. Nakatsuji, H. Nakashima, Y. Korokawa, A. Ishikawa, Phys. Rev. Lett **99**, 240402 (2007)
46. N.A. Cordero, N.H. March, J.A. Alonso, Phys. Rev. A **75**, 052502 (2007)
47. C. Amovilli, N.H. March, J.D.Talman. Phys. Rev. A **77**, 032503 (2008)
48. J.C. Slater, Phys. Rev. **81**, 375 (1971)
49. L.D. Landau, E.M. Lifshitz, *Quantum Mechanics*, 3rd edn. (Pergamon Press, Oxford, 1977)
50. M. Kregar, V.F. Weisskopf, Am. J. Phys. **50**, 213 (1982)
51. W. Heisenberg, Z. Phys. **39**, 429 (1927)
52. J.C. Slater, *Introduction in Theoretical Physics* (McGraw Hill, New York, 1933)
53. M. Kregar, Il Nuovo Cimento **8D**, 159 (1986)
54. I.D. Feranchuk, L.I. Komarov, I.V. Nechipor, A.P. Ulyanenkov, Ann. Phys. (NY) **A238**, 370 (1995)
55. I.D. Feranchuk, A.I. Ivanov, J. Phys. A Math. Gen. **37**, 9841 (2004)
56. I.D. Feranchuk, V.V. Triguk, Phys. Lett. A **375**, 2550 (2011)
57. L.I. Gurskii, L.I. Komarov, A.M. Solodukhin, Int. J. Quantum Chem. **72**, 499 (1999)
58. P.Gombaś, Rev. Mod. Phys. **35**, 512 (1963)
59. I.K. Dmitrieva, G.I. Plindov, *Properties of Atoms and Molecules According to Statistical Theory* (Nauka Technika, Minsk, 1991) (in russian)
60. C.F. Fischer, At. Data Nucl. Data Tables **12**, 87 (1973)
61. A. Lazar, I. Feranchuk, V. Triguk, *Proceedings Interaction of the Radiation with Solids* (Belarusian University, Minsk, 2009), p. 37
62. S.P. Hau-Riege, Phys. Rev. A **76**, 042511 (2007)
63. L.I. Datsenko, V.P. Klad'ko, Crystallogr. Rep. **45**, 705 (2000)
64. H.X. Gao, L.M. Peng, Acta Cryst. A **55**, 926 (1999)
65. R. Balescu, *Equilibrium and Nonequilibrium Statistical Mechanics*, vol. 2 (Wiley, New York, 1975)
66. G.B. Bokii, *Crystallochemie* (Nauka, Moscow, 1971)
67. K.P. Huber, G. Gerzberg, *Molecular Spectra and Molecular Structure. V. 4 . Constants of Diatomic Molecules* (Van Nostrand Reinhold, New York, 1979)
68. L.A. Gribov, S.P. Mushtakova, *Quantum Chemistry* (Gardariki, Moscow, 1999)
69. I.P. Biersack, I.F. Ziegler, Nucl. Instr. Methods **194**, 93 (1982)

Chapter 2
The Theory of X-Ray Scattering from Macroscopical Objects

Nowadays the X-rays are widely used for non-destructive quantitative and qualitative characterization of the materials used in modern electronics, optics, semiconductor industry, lasers, sensors, and many other applications on micro- and nano-level. Most of the X-ray techniques are based on the investigation of the spectra of the *elastic* scattering of X-ray radiation, when the photon frequencies ω of the incident and the scattered beams are equal, and thus the wave vectors of the incident beam ($\boldsymbol{k}_0$) and the scattered beam ($\boldsymbol{k}_1$) are connected as:

$$|\boldsymbol{k}_0| = |\boldsymbol{k}_1| = k_0 = \frac{\omega}{c} = \frac{2\pi}{\lambda},$$

where λ is a wavelength of X-ray radiation and c is the speed of light.

Thus, the information on the sample structure (electron density distribution) is contained solely in the profile of the angular distribution of the scattered X-ray radiation. The final goal of each X-ray method is the solution of the *inverse scattering problem*, i.e. determination of the sample structure from the scattered X-ray intensity profile. In the real applications, however, the intermediate stage delivering the solution of *direct scattering problem* is necessary, which includes the theoretical calculation (modeling) of the profile of the scattered X-ray intensity on the basis of microscopical model for the studied sample. In this chapter, the theoretical approaches used for the solution of the direct problem of X-ray scattering from microscopical samples, and the methods used for the solution of this problem on the basis of Maxwell's equations are considered.

2.1 The Stationary and Temporal Approaches to X-Ray Scattering Process

In Chap. 1, the physical principles of X-ray optics under the condition of elastic scattering of X-rays in continuous media have been discussed. In the reality, however, the physical samples have a certain dimension and may consist of microscopical objects

A. Benediktovitch et al., *Theoretical Concepts of X-Ray Nanoscale Analysis*,
Springer Series in Materials Science 183, DOI: 10.1007/978-3-642-38177-5_2,

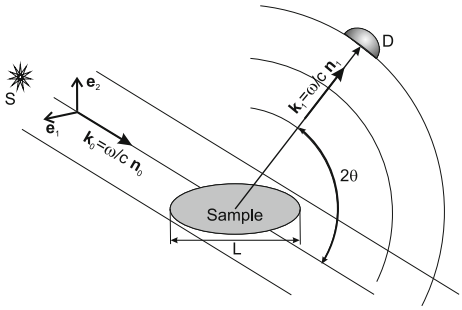

Fig. 2.1 Schematic representation of the scattering process in stationary theory

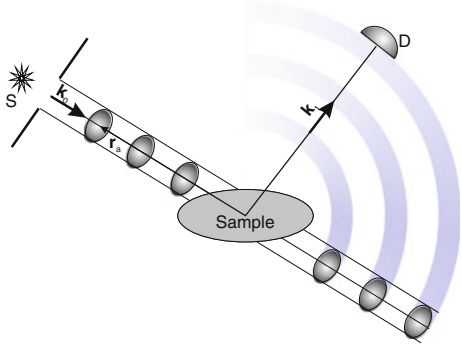

Fig. 2.2 Schematic representation of the scattering process in temporal theory

with various characteristics. To obtain the information on the investigated structure of sample, the inverse scattering problem has to be resolved: to determine the relationship between the X-ray intensity recorded by detector and the specifics of the X-ray interaction with investigated material during the transmission of radiation through the object. According to the formal scattering theory [1], there are two principal formulations of this task, which differ by the conditions for the Maxwell's equation for the wave fields. The first formulation corresponds to the *stationary scattering theory*, represented in Fig. 2.1. The incident beam is considered as monochromatic plane wave with infinite front, and the scattered wave at a large distance from the scatterer is described by the spherical wave with the amplitude depending on the scattering angle 2θ. This approach is utilized in the majority of monographs and handbooks dedicated to X-ray methods (for example, [2–6]) to establish the relation between the solutions of Maxwell's equations in continuous media and the wave field of the scattered X-ray radiation.

In real experiments, however, the quasi-monochromatic X-ray beams are used, which have limited duration and spatial distribution. These physical conditions correspond to the temporal theory of scattering [1], which is schematically shown in Fig. 2.2. The aim of this chapter is to establish a relationship between the results obtained in both approaches, and the analysis of the applicability conditions for them.

Within the stationary theory, the Maxwell's equations for the vector potential determining the scattering of the wave field from the sample are obtained from the general Eq. (1.56) for infinite medium (the formulas below assume the summation over the repeating Cartesian indices):

$$\begin{aligned}(k^2 - k_0^2)A_\mu(\boldsymbol{k},\omega) - k_0^2\sum_{\boldsymbol{H}}\chi_{\mu\nu}(\boldsymbol{k},\boldsymbol{H},\omega)A_\nu(\boldsymbol{k}+\boldsymbol{H},\omega) = 0;\\ (\boldsymbol{k}\boldsymbol{A}(\boldsymbol{k},\omega)) = 0;\\ \chi_{\mu\nu}(\boldsymbol{k},\boldsymbol{H},\omega) = \chi^{(e)}(\boldsymbol{H},\omega)\delta_{\mu\nu} + \chi^{(a)}_{\mu\nu}(\boldsymbol{k},\boldsymbol{H},\omega),\end{aligned} \tag{2.1}$$

where the contributions of Compton $\chi^{(e)}$ and resonant $\chi^{(a)}$ scattering are defined by formulas (1.51) and (1.56), respectively. Let us assume the shape of the sample as follows: $S(\boldsymbol{r}) = 1$, if the point $\boldsymbol{r}$ belongs to the sample, and $S(\boldsymbol{r}) = 0$ for the points in vacuum. If the sample under investigation consists of several elements possessing different microscopical characteristics, then each element has a specific shape function $S_b(\boldsymbol{r})$, X-ray polarizability $\chi^{(b)}_{\mu\nu}$ and the set of the reciprocal space vectors H_b. For convenience reason, Eq. (2.1) is transformed into coordinate representation:

$$\begin{aligned}A_\mu(\boldsymbol{r},\omega) = \int A_\mu(\boldsymbol{k},\omega)e^{i\boldsymbol{k}\boldsymbol{r}}d\boldsymbol{k};\ (\nabla\boldsymbol{A}(\boldsymbol{r},\omega)) = 0;\\ (\Delta + k_0^2)A_\mu(\boldsymbol{r},\omega) + \hat{V}_{\mu\nu}(\boldsymbol{r})A_\nu(\boldsymbol{r},\omega) = 0,\end{aligned} \tag{2.2}$$

with the potential $\hat{V}_{\mu,\nu}(\boldsymbol{r})$ of the interaction of the sample with radiation, which is the integral operator:

$$\begin{aligned}\hat{V}_{\mu\nu}(\boldsymbol{r},\omega)A_\nu(\boldsymbol{r},\omega)\\ \equiv k_0^2\sum_b S_b(\boldsymbol{r})\sum_{\boldsymbol{H}_b}\int\chi^{(b)}_{\mu\nu}(\boldsymbol{r}-\boldsymbol{r}_1,\boldsymbol{H}_b,\omega)A_\nu(\boldsymbol{r}_1,\omega)e^{i\boldsymbol{H}_b\boldsymbol{r}_1}d\boldsymbol{r}_1;\\ \chi_{\mu\nu}(\boldsymbol{r}-\boldsymbol{r}_1,\boldsymbol{H}_b,\omega) = \int\chi_{\mu\nu}(\boldsymbol{k},\boldsymbol{H}_b,\omega)e^{i\boldsymbol{k}(\boldsymbol{r}-\boldsymbol{r}_1)}d\boldsymbol{k}\\ = \chi^{(e)}(\boldsymbol{H}_b,\omega)\delta_{\mu\nu}\delta(\boldsymbol{r}-\boldsymbol{r}_1) + \int\chi^{(a)}_{\mu\nu}(\boldsymbol{k},\boldsymbol{H}_b,\omega)e^{i\boldsymbol{k}(\boldsymbol{r}-\boldsymbol{r}_1)}d\boldsymbol{k}.\end{aligned} \tag{2.3}$$

In the next step, the expression for the Green function $G^{(0)}_{\mu\nu}(\boldsymbol{r}-\boldsymbol{r}',k_0)$ of the Helmholtz equation [7] is used:

$$\begin{aligned}(\Delta + k_0^2)G^{(0)}_{\mu\nu}(\boldsymbol{r}-\boldsymbol{r}',k_0) = \delta_{\mu\nu}\delta(\boldsymbol{r}-\boldsymbol{r}');\\ G^{(0)}_{\mu\nu}(\boldsymbol{r}-\boldsymbol{r}',k_0) = -\delta_{\mu\nu}\frac{e^{ik_0|\boldsymbol{r}-\boldsymbol{r}'|}}{4\pi|\boldsymbol{r}-\boldsymbol{r}'|},\end{aligned} \tag{2.4}$$

and the solutions of Maxwell's equation in vacuum are defined ($\hat{V} = 0$):

$$(\Delta + k_0^2)\boldsymbol{A}^{(0)}_{\boldsymbol{k},s}(\boldsymbol{r},\omega)) = 0;\ (\nabla \boldsymbol{A}^{(0)}_{\boldsymbol{k},s}(\boldsymbol{r},\omega)) = 0;$$
$$\boldsymbol{A}^{(0)}_{\boldsymbol{k}_0,s}(\boldsymbol{r},\omega)) = \boldsymbol{e}^{(s)}e^{i\boldsymbol{k}_0\boldsymbol{r}};\ \boldsymbol{k}_0 = k_0\boldsymbol{n};\ (\boldsymbol{e}^{(s)}\boldsymbol{k}_0) = 0;\ s = 1,2. \tag{2.5}$$

Here the unity vector $\boldsymbol{n}$ defines the direction of the propagation, and the unity vectors $\boldsymbol{e}^{(s)}$, $(\boldsymbol{e}^{(1)}\boldsymbol{e}^{(2)}) = 0$ define two orthogonal polarizations of the incident wave (Fig. 2.1). Equation (2.2) is then transformed into integral form:

$$A_{\mu,s}(\boldsymbol{r},\omega,\boldsymbol{k}_0) = e^{(s)}_{\mu}e^{i\boldsymbol{k}_0\boldsymbol{r}} + \int \frac{e^{ik_0|\boldsymbol{r}-\boldsymbol{r}'|}}{4\pi|\boldsymbol{r}-\boldsymbol{r}'|}\hat{V}_{\mu\nu}(\boldsymbol{r}')A_{\nu,s}(\boldsymbol{r}',\omega)d\boldsymbol{r}'. \tag{2.6}$$

The expression (2.6) describes the distribution of the wave field for an arbitrary ratio between the distance to the observation point $|\boldsymbol{r}|$ and the linear dimension of the sample L, which is assumed to be not essentially exceeding the absorption length of X-ray radiation $|\boldsymbol{r}'| \le L_a \sim 10^{-2} \div 10^{-3}$cm (Fig. 2.1). Using the optical representation [8], there are two limiting cases in this distribution : (i) $r \le L_a$, which corresponds to the Fresnel diffraction (near-field or diffraction zone), and (ii) $r \gg L_a$, which corresponds to the Fraunhofer diffraction (far-field or wave zone). There exists also an approach, which uses the rational Fourier transformation continuously connecting these both limiting cases [9].

In the case of Fresnel diffraction, the resulting intensity of the scattered radiation depends both on the scatterer characteristics and the distance between the radiation source, the sample, and the detector. For some applications, this scheme allows to obtain the supplementary information on the shape of the sample, however, this requires a high flux X-ray radiation from synchrotron sources [10]. At the laboratory conditions, the distances between the sample and the detector are $|\boldsymbol{r}| \sim 10 \div 100$ cm, $|\boldsymbol{r}| \gg |\boldsymbol{r}'| \sim L_a$, therefore the Fraunhofer diffraction is realized, and the scattered intensity distribution is determined by the sample properties and not by the position of the X-ray source or detector. In this case, the asymptotic expansion for the Green function can be used:

$$\frac{e^{ik_0|\boldsymbol{r}-\boldsymbol{r}'|}}{|\boldsymbol{r}-\boldsymbol{r}'|} \approx \frac{e^{ik_0r}}{r}e^{-i\boldsymbol{k}_1\boldsymbol{r}'}\left[1 + O\left(\frac{k_0a^2}{r}\right)\right];\ \boldsymbol{k}_1 = k_0\frac{\boldsymbol{r}}{r}, \tag{2.7}$$

where a is a characteristic linear size of the scattered volume of the sample. As a result, the wave field (2.6) is decomposed into superposition of the plane wave and the diverging spherical wave, which is used as boundary condition for the stationary scattering theory (Fig. 2.1):

$$\boldsymbol{A}_s(\boldsymbol{r},\omega,\boldsymbol{k}_0) = \boldsymbol{e}^{(s)}e^{i\boldsymbol{k}_0\boldsymbol{r}} + \boldsymbol{T}^{(s)}(\boldsymbol{k}_0,\boldsymbol{k}_1)\frac{e^{ik_0r}}{4\pi r};$$
$$T^{(s)}_{\mu}(\boldsymbol{k}_0,\boldsymbol{k}_1) = \int e^{-i\boldsymbol{k}_1\boldsymbol{r}'}\hat{V}_{\mu\nu}(\boldsymbol{r}')A_{\nu,s}(\boldsymbol{r}',\omega)d\boldsymbol{r}', \tag{2.8}$$

where $\boldsymbol{T}^{(s)}(\boldsymbol{k}_0, \boldsymbol{k}_1)$ defines the amplitude of the vector potential of the scattered wave field. Taking into account the relation between the vector potential and the magnitude of the electric and magnetic fields [5]

$$\boldsymbol{E}_s(\boldsymbol{r}, \omega) = -i\frac{\omega}{c}\boldsymbol{A}_s(\boldsymbol{r}, \omega);\ \ \boldsymbol{H}_s(\boldsymbol{r}, \omega) = [\nabla \boldsymbol{A}_s(\boldsymbol{r}, \omega)],$$

and standard definition of the Poynting vector for the energy flux density of the electromagnetic field we obtain:

$$\boldsymbol{S} = \frac{c}{4\pi}[\boldsymbol{E}_s(\boldsymbol{r}, \omega)\boldsymbol{H}_s(\boldsymbol{r}, \omega)]. \tag{2.9}$$

Then the differential cross-section of the radiation with certain polarization into solid angle $d\Omega$ and in the vicinity of direction $\boldsymbol{k}_1$ is delivered by the ratio of the energy flux of the scattered into the detector aperture $r^2 d\Omega$ wave to the energy flux density of the incident wave:

$$\frac{d\sigma^{(s)}}{d\Omega} = r^2\frac{(\boldsymbol{k}_1\boldsymbol{S}_{sc})}{(\boldsymbol{k}_0\boldsymbol{S}_0)} = \frac{1}{(4\pi)^2}\sin^2\theta_{1s}|\boldsymbol{T}^{(s)}(\boldsymbol{k}_0, \boldsymbol{k}_1)|^2;\ \ \theta_{1s} = \widehat{\boldsymbol{k}_1\boldsymbol{T}^{(s)}}. \tag{2.10}$$

Because of the elastic scattering satisfies the condition $|\boldsymbol{k}_0| = |\boldsymbol{k}_1|$, the expression obtained depends only on the direction of incident $\boldsymbol{k}_0 = k_0\boldsymbol{n}_0$ and scattered $\boldsymbol{k}_1 = k_0\boldsymbol{n}_1$ waves. This dependence is conveniently parametrized by the scattering angle 2θ and the momentum transfer $\boldsymbol{q}$:

$$2\theta = \widehat{\boldsymbol{k}_1\boldsymbol{k}};\ \boldsymbol{q} = \boldsymbol{k}_1 - \boldsymbol{k};\ q^2 = 4k_0^2\sin^2\theta. \tag{2.11}$$

Within the framework of the stationary theory, the expression (2.10) is used for the calculation of the observed profiles of the scattered X-ray intensity (see, for example, [4]).

How this result is related to the real experiments (Fig. 2.2), when both the incident and the scattered beams are not described by plane or spherical waves and have a certain spatial and temporal dimension? The applicability condition for the stationary theory and the relation between both approaches follows from the formal scattering theory [1], based on the solution of the Eq. (1.16) for time-dependent vector potential $\boldsymbol{A}(\boldsymbol{r}, t)$. This equation is represented in the form, similar to the one of Eq. (2.2):

$$\left(\Delta - \frac{1}{c^2}\frac{\partial^2}{\partial t^2}\right)A_\mu(\boldsymbol{r}, t) + \hat{V}_{\mu\nu}(\boldsymbol{r}, t)A_\nu(\boldsymbol{r}, t) = 0;$$
$$(\nabla \boldsymbol{A}(\boldsymbol{r}, t)) = 0, \tag{2.12}$$

with operator $\hat{V}_{\mu,\nu}(\boldsymbol{r}, t)$:

$$\hat{V}_{\mu\nu}(\boldsymbol{r},t)A_\nu(\boldsymbol{r},t) \equiv -\frac{1}{c^2}\frac{\partial^2}{\partial t^2}\sum_b S_b(\boldsymbol{r}) \times \sum_{\boldsymbol{H}_b}\int \chi^{(b)}_{\mu\nu}(\boldsymbol{r}-\boldsymbol{r}_1,\boldsymbol{H}_b,t-t_1)A_\nu(\boldsymbol{r}_1,t_1)e^{i\boldsymbol{H}_b\boldsymbol{r}_1}d\boldsymbol{r}_1 dt_1;$$

$$\chi_{\mu\nu}(\boldsymbol{r},\boldsymbol{H},t) = \int \chi_{\mu\nu}(\boldsymbol{k},\boldsymbol{H},\omega)e^{i(\boldsymbol{k}\boldsymbol{r}-\omega t)}d\boldsymbol{k}d\omega. \tag{2.13}$$

Due to the linearity, the solution for Eq. (2.12) is obtained as the superposition of the solutions for the stationary Maxwell's Eq. (2.6) with the coefficients $C^{(s)}_{\lambda\mu}(\boldsymbol{k},\omega)$ to be found:

$$A_\mu(\boldsymbol{r},t) = \sum_s \int d\boldsymbol{k}d\omega C^{(s)}(\boldsymbol{k},\omega)A_{\mu,s}(\boldsymbol{r},\omega,\boldsymbol{k})e^{-i\omega t}. \tag{2.14}$$

The coefficients of the expansion in Eq. (2.14) have to be found from the initial conditions:

$$A_\lambda(\boldsymbol{r},t)|_{t=0} = A^{(0)}_\lambda(\boldsymbol{r}), \tag{2.15}$$

where $A^{(0)}_\lambda(\boldsymbol{r})$ is a vector potential, corresponding to the wave field of the beam conditioned by the monochromators and slits (collimators), see Fig. 2.2. The most prominent advantage of X-ray techniques is their non-destructive character in the majority of applications when using standard incoherent sources of X-rays. The usage of the coherent X-ray radiation from X-ray lasers [11] leads to the destruction of the investigated object, and the analysis of X-ray scattering in this case requires special methods [12], which are not considered in this book. Thus, the structure of the function $A^{(0)}_\lambda(\boldsymbol{r})$ is considered below in the assumption of the incoherent X-ray beam. Each X-ray photon corresponds to the the wave packet created by the optical beam path after the X-ray source. The vector potential of the wave field of the beam in vacuum is expressed as a product of the wave packets of the unique photons:

$$\begin{aligned} A^{(0)}_\mu(\boldsymbol{r}) &= \sum_{s=1,2}\int d\boldsymbol{k}d\omega e^{(s)}_\mu(\boldsymbol{k})G^{(s)}(\boldsymbol{k}-\boldsymbol{k}_0)\delta(k-\omega/c)e^{i\boldsymbol{k}(\boldsymbol{r}-\boldsymbol{r}_a)} \\ &= \sum_{s=1,2}\int d\boldsymbol{n}_k\frac{\omega^2 d\omega}{c^2}e^{(s)}_\mu(\boldsymbol{k})G^{(s)}((\boldsymbol{n}_k-\boldsymbol{n}_0),(\omega-\omega_0))e^{i\boldsymbol{n}_k(\boldsymbol{r}-\boldsymbol{r}_a)\omega/c} \end{aligned} \tag{2.16}$$

Here $\boldsymbol{n}_k$ is the unity vector along the direction of the wave vector $\boldsymbol{k}$, $|\boldsymbol{k}| = \omega/c$, the phase $e^{-i\boldsymbol{n}_k\boldsymbol{r}_a\omega/c}$ corresponds to the wave packet of photon with index a, the values $G^{(s)}((\boldsymbol{n}_k-\boldsymbol{n}_0),(\omega-\omega_0))$ define the probability amplitudes for the plane wave with frequency ω, wave vector $\boldsymbol{k} = \boldsymbol{n}_k\omega/c$ and polarization $e^{(s)}_\mu(\boldsymbol{k})$ in the wave packet. In the typical experiment, the function $G^{(s)}$ is distributed around the frequency ω_0 of the monochromator $\boldsymbol{n}_0$, $\boldsymbol{k}_0 = \boldsymbol{n}_0\omega/c$. The dispersions of the frequency $\Delta\omega$ and

the direction of the wave vector $\Delta \boldsymbol{n}$ are conditioned by the monochromator and slit (collimator), respectively (Fig. 2.3a). The single photon wave packet (2.16) is represented as follows:

$$A_{\mu}^{(0)}(\boldsymbol{r}) = \sum_{s=1,2} e^{i\boldsymbol{k}_0(\boldsymbol{r}-\boldsymbol{r}_a)} e_{\mu}^{(s)}(\boldsymbol{k}_0) F^{(s)}(\boldsymbol{r}-\boldsymbol{r}_a)$$

$$F^{(s)}(\boldsymbol{r}) = c \int d\boldsymbol{q}_{\perp} dq_z G^{(s)}(\boldsymbol{q}_{\perp}, q_z) e^{i\boldsymbol{q}\boldsymbol{r}};$$

$$\boldsymbol{q}_{\perp} = \frac{\omega_0}{c}(\boldsymbol{n}_k - \boldsymbol{n}_0);\ q_z = \frac{1}{c}(\omega - \omega_0);\ z \parallel \boldsymbol{k}_0. \tag{2.17}$$

The function $F^{(s)}(\boldsymbol{r})$ describes the spatially localized wave packet with the length $\Delta z \approx \frac{c}{\Delta\omega}$ in the direction of X-ray beam and with the width $\Delta r_{\perp} \approx \frac{c}{\omega_0 |\Delta \boldsymbol{n}|}$ in the perpendicular direction (Fig. 2.3b).

The energy flux of the photon beam (2.9) consisting of wave packets (2.17) is calculated by neglecting the term $\sim |\frac{\nabla F^{(s)}}{k_0 F^{(s)}}| \approx |\Delta \boldsymbol{n}|$:

$$\boldsymbol{S}_0 = \frac{\omega_0^2}{4\pi} \sum_{a,s} \sum_{b,s'} \boldsymbol{k}_0 (\boldsymbol{e}^{(s)*} \boldsymbol{e}^{(s')}) F^{(s)}(\boldsymbol{r}-\boldsymbol{r}_a) F^{(s')*}(\boldsymbol{r}-\boldsymbol{r}_b) e^{i\boldsymbol{k}_0(\boldsymbol{r}_a - \boldsymbol{r}_b)}, \tag{2.18}$$

where the summation is performed over the initial coordinates of all wave packets of single photons. By averaging over the coordinates of the particles within the beam, the expression (2.18) is transformed to:

$$\boldsymbol{S}_0 = \frac{\rho_{ph}^2 \omega_0^2}{4\pi} \sum_{s} \sum_{s'} \boldsymbol{k}_0 (\boldsymbol{e}^{(s)*} \boldsymbol{e}^{(s')}) \times \int d\boldsymbol{r}_1 d\boldsymbol{r}_1' F^{(s)}(\boldsymbol{r}-\boldsymbol{r}_1) F^{(s')*}(\boldsymbol{r}-\boldsymbol{r}_1') e^{i\boldsymbol{k}_0(\boldsymbol{r}_1 - \boldsymbol{r}_1')} g(\boldsymbol{r}_1, \boldsymbol{r}_1'), \tag{2.19}$$

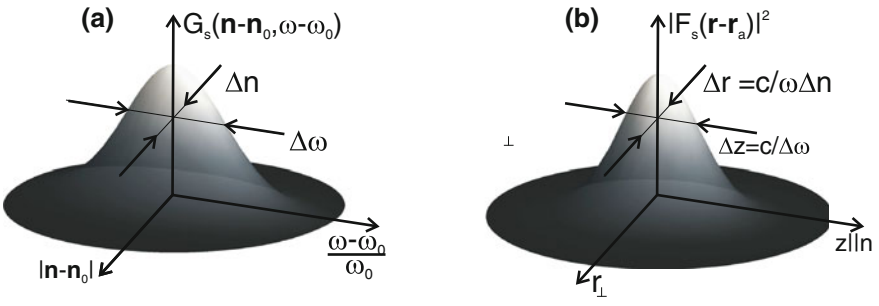

Fig. 2.3 **a** The probability density $|G^{(s)}(\boldsymbol{k}-\boldsymbol{k}_0), (\omega-\omega_0))|^2$ in the coordinates of variables of the incident beam: the frequency ω, the incidence angle α. **b** The function $|F^{(s)}(\boldsymbol{r})|^2$, describing the distribution of the wave field intensity in the coordinate space

where ρ_{ph} is the photon density within the beam; the function $g(\boldsymbol{r}_1, \boldsymbol{r}'_1)$ accounts all possible correlations in the distribution caused by the properties of X-ray source. Moreover, the beam might be partially coherent, when the wave packets corresponding to different photons are overlapped, and the averaging of the phase factor $\exp\{i\boldsymbol{k}_0\boldsymbol{r}_1\}$ over the distribution of the particles within the beam results in non-zero value. These conditions are satisfied for high flux beams, used in modern free electron X-ray lasers [11, 13]. In the laboratory experiments considered in this monograph, the correlation of photons in the beam is not essential for the description of the scattering problem. This statement is valid, if the overlapping of the wave packets is negligible in the expression (2.17), and the following inequalities are fulfilled:

$$|z_a - z_b| \geq \Delta z; \quad |(\boldsymbol{r}_a - \boldsymbol{r}_b)_\perp| \geq \Delta r_\perp, \tag{2.20}$$

restricting the photon density value inside the beam:

$$\rho_{ph} \approx |z_a - z_b|^{-1} |(\boldsymbol{r}_a - \boldsymbol{r}_b)_\perp|^{-2} \leq \frac{\omega_0^2}{c^3} \Delta\omega |\Delta\boldsymbol{n}|^2. \tag{2.21}$$

These inequalities correspond to the following condition for the brightness B [11] of X-ray source:

$$B \leq 7.2\ 10^{25} \frac{\Delta\omega}{\omega_0} \frac{\Delta\alpha_x \Delta\alpha_y}{\lambda_0^3} \left[\frac{ph}{\text{mm}^2\text{s mrad}^2\ 0.1\%\text{bandwidth}} \right], \tag{2.22}$$

where $\lambda_0 = 2\pi c/\omega_0$ is the wavelength of X-ray radiation in Å, $\Delta\alpha_x$, $\Delta\alpha_y$ are the angular width of the beam in radians in the direction perpendicular to the propagation direction. In modern laboratory X-ray instruments used for non-destructive characterization, the condition (2.22) is fulfilled, and the energy flux of the incident beam is:

$$\boldsymbol{S}_0 = \frac{\omega_0^2}{4\pi} \sum_{a,s} \boldsymbol{k}_0 |F^{(s)}(\boldsymbol{r} - \boldsymbol{r}_a)|^2 \approx \boldsymbol{k}_0 \rho_{ph} \frac{\omega_0^2}{4\pi} \sum_s \int d\boldsymbol{r}_a |F^{(s)}(\boldsymbol{r} - \boldsymbol{r}_a)|^2 \tag{2.23}$$

and corresponds to the propagation of non-overlapping wave packets of single photons. In the absence of correlations, the summation over all photons can be replaced by the integration with the photon density ρ_{ph}.

The initial condition (2.15) has to be fulfilled for each wave packet independently, which makes possible the calculation of the coefficients (2.14) by using (2.15) and the orthogonality of the solutions (2.6) for the stationary Maxwell's equations:

$$
\begin{aligned}
C^{(s)}(\boldsymbol{k},\omega) &= \int d\boldsymbol{r}\int d\boldsymbol{q}d\omega'\sum_{s'} A^{*}_{\mu,s}(\boldsymbol{r},\omega,\boldsymbol{k}) \\
&\quad\times e^{(s')}_{\mu}(\boldsymbol{q})G^{(s')}(\boldsymbol{q}-\boldsymbol{k}_0)\delta(q-\omega'/c)e^{i\boldsymbol{q}(\boldsymbol{r}-\boldsymbol{r}_a)} \\
&= G^{(s}(\boldsymbol{k}-\boldsymbol{k}_0)\delta(k-\omega/c) \\
&\quad+\int d\boldsymbol{r}\int d\boldsymbol{r}'\int d\boldsymbol{q}d\omega'\sum_{s'}\int e^{(s')}_{\mu}(\boldsymbol{q})G^{(s')}(\boldsymbol{q}-\boldsymbol{k}_0)\delta(q-\omega'/c) \\
&\quad\times e^{i\boldsymbol{q}(\boldsymbol{r}-\boldsymbol{r}_a)}\frac{e^{-ik|\boldsymbol{r}-\boldsymbol{r}'|}}{4\pi|\boldsymbol{r}-\boldsymbol{r}'|}\hat{V}^{*}_{\mu\nu}(\boldsymbol{r}')A^{*}_{\nu,s}(\boldsymbol{r}',\omega)\equiv C_1+C_2 \quad .
\end{aligned}
\tag{2.24}
$$

The second term in the expression above takes into account a possible influence of the scattering potential on the formation of the wave packet. By integrating over $\boldsymbol{r}$, this term is written as:

$$
\begin{aligned}
C_2 &= \int d\boldsymbol{r}'\int d\boldsymbol{q}d\omega'\sum_{s'}\int e^{(s')}_{\mu}(\boldsymbol{q})G^{(s')}(\boldsymbol{q}-\boldsymbol{k}_0)\delta(q-\omega'/c) \\
&\quad\times\frac{e^{i\boldsymbol{q}(\boldsymbol{r}'-\boldsymbol{r}_a)}}{q^2-k^2}\hat{V}^{*}_{\mu\nu}(\boldsymbol{r}')A^{*}_{\nu,s}(\boldsymbol{r}',\omega) \\
&\approx \int d\boldsymbol{r}'\frac{e^{i\boldsymbol{k}_0(\boldsymbol{r}'-\boldsymbol{r}_a)}}{k_0^2-k^2}e^{(s')}_{\mu}(\boldsymbol{k}_0)F^{(s)}(\boldsymbol{r}'-\boldsymbol{r}_a)\hat{V}^{*}_{\mu\nu}(\boldsymbol{r}')A^{*}_{\nu,s}(\boldsymbol{r}',\omega).
\end{aligned}
\tag{2.25}
$$

The value $\sim \hat{V}^{*}_{\mu\nu}(\boldsymbol{r}_a)$ contributes to the process in the case of long-range scattering potential [14], which has a non-zero magnitude at the position of X-ray source. For the X-ray scattering processes considered here, this contribution in (2.24) can be neglected. The coefficients found are then substituted in (2.14), that results in:

$$
\begin{aligned}
A_{\mu}(\boldsymbol{r},t) &= \sum_{s}\int d\boldsymbol{k}d\omega e^{-i\omega t}\Big\{G^{(s)}(\boldsymbol{k}-\boldsymbol{k}_0)e^{-i\boldsymbol{k}\boldsymbol{r}_a}\delta(k-\omega/c) \\
&\quad\times\Big[e^{(s)}_{\mu}(\boldsymbol{k})e^{i\boldsymbol{k}\boldsymbol{r}}+\int d\boldsymbol{r}'\frac{e^{ik|\boldsymbol{r}-\boldsymbol{r}'|}}{4\pi|\boldsymbol{r}-\boldsymbol{r}'|}\hat{V}_{\mu\nu}(\boldsymbol{r}')A_{\nu,s}(\boldsymbol{r}',\omega)\Big]\Big\} \\
&\equiv A^{(0)}_{\mu}(\boldsymbol{r},t)+A^{(1)}_{\mu}(\boldsymbol{r},t).
\end{aligned}
\tag{2.26}
$$

The first term in this expression:

$$
\begin{aligned}
A^{(0)}_{\mu}(\boldsymbol{r},t) &= \sum_{s}\int d\boldsymbol{k}d\omega e^{-i\omega t}\delta\Big(k-\frac{\omega}{c}\Big)G^{(s)}(\boldsymbol{k}-\boldsymbol{k}_0)e^{(s)}_{\mu}e^{i\boldsymbol{k}(\boldsymbol{r}-\boldsymbol{r}_a)} \\
&= \sum_{s=1,2}e^{i\boldsymbol{k}_0(\boldsymbol{r}-\boldsymbol{r}_a)-i\omega_0 t}e^{(s)}_{\mu}(\boldsymbol{k}_0)F^{(s)}(z-z_a-ct,(\boldsymbol{r}-\boldsymbol{r}_a)_{\perp}),
\end{aligned}
\tag{2.27}
$$

describes the propagation of free wave packet corresponding to the photons, which did not undergo the scattering at the time t localized near the point $\boldsymbol{r}(t) = \boldsymbol{r}_a + ct\boldsymbol{n}_0$ (Fig. 2.4).

The second term in the expression (2.26) describes the distribution of the scattered wave field in the space. In the limits of large distances from the scatterer $r \gg r'$, the asymptotic (2.8) can be used for the solution of the stationary problem, which results in the following equation:

$$A_\mu^{(1)}(\boldsymbol{r}, t) \approx \sum_s \int d\boldsymbol{k} d\omega T_\mu^{(s)}\left(\boldsymbol{k}, k\frac{\boldsymbol{r}}{r}\right)\frac{e^{ikr}}{4\pi r} \times e^{-i\omega t - i\boldsymbol{k}\boldsymbol{r}_a}\delta\left(k - \frac{\omega}{c}\right)G^{(s)}(\boldsymbol{k} - \boldsymbol{k}_0) = \sum_{s=1,2} e^{-i(\boldsymbol{k}_0\boldsymbol{r}_a - i\omega_0 t)}\hat{T}_\mu^{(s)}(\boldsymbol{k}_0, \boldsymbol{k}_1)\frac{e^{ik_0 r}}{4\pi r}F^{(s)}[(r - ct)\boldsymbol{n}_0 - \boldsymbol{r}_a]. \quad (2.28)$$

This expression describes the wave field as a spherical segment (Fig. 2.4) with the radius $r(t) = c(t - t_0)$; $t_0 = (\boldsymbol{n}_0\boldsymbol{r}_a)/c$ and thickness $\Delta r \approx c/\Delta\omega$, and centered at the position of the scatterer. The calculation of the energy flux transmitted by the scattered wave field (2.28) and the summation over the coordinates $\boldsymbol{r}_a$ is carried out similarly to Eqs. (2.9) and (2.23):

$$\boldsymbol{S}_{sc}^{(s)} \approx \frac{\boldsymbol{k}_1\rho_{ph}}{(4\pi r)^2}\sin^2\theta_{1s}|\boldsymbol{T}^{(s)}(\boldsymbol{k}_0, \boldsymbol{k}_1)|^2\int d\boldsymbol{r}_a|F^{(s)}[(r - ct)\boldsymbol{n}_0 - \boldsymbol{r}_a]|^2. \quad (2.29)$$

The differential cross-section of the scattered intensity, being calculated as the ratio of the flux density of the scattered radiation to the flux density of the incident photons, is found to be equal to:

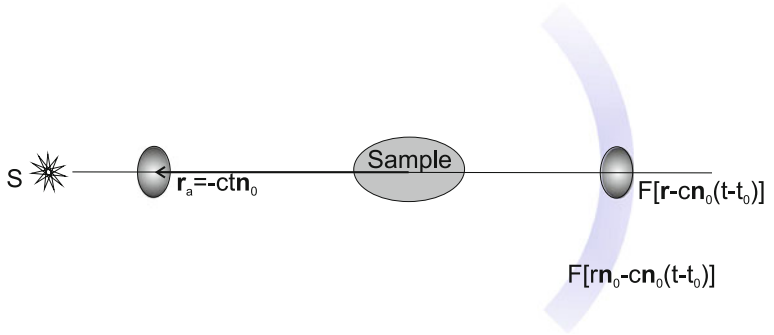

Fig. 2.4 The transformation of a single-photon wave packet during the scattering process

$$\frac{d\sigma^{(s)}}{d\Omega} = r^2 \frac{(\boldsymbol{k}_1 \boldsymbol{S}_{sc})}{(\boldsymbol{k}_0 \boldsymbol{S}_0)} = \frac{1}{(4\pi)^2} \sin^2\theta_{1s} |\boldsymbol{T}^{(s)}(\boldsymbol{k}_0, \boldsymbol{k}_1)|^2 \times \frac{\int d\boldsymbol{r}_a |F^{(s)}[(r-ct)\boldsymbol{n}_0 - \boldsymbol{r}_a]|^2}{\int d\boldsymbol{r}_a |F^{(s)}(\boldsymbol{r} - \boldsymbol{r}_a - ct\boldsymbol{n}_0)|^2}. \tag{2.30}$$

In a standard X-ray experiment with the laboratory sources, the temporal length of the photon beam is considerably larger then the duration of the single-photon wave packet, therefore the integrals in the expression (2.30) are canceled, and the formula for the cross-section in the temporal scattering theory coincides with the result (2.10) for the stationary scattering theory provided the condition (2.21) for the flux density of photons is fulfilled.

2.2 Approximate Methods for the Solution of Stationary Scattering Problem

The intensity of the scattered X-ray radiation registered by the detector, being normalized to the intensity of the incident radiation, is defined by the differential cross-section of the scattering from the sample of finite dimension, and is given by the formula (2.10):

$$\frac{d\sigma^{(s)}}{d\Omega} = \frac{1}{(4\pi)^2} \sin^2\theta_{1s} |\boldsymbol{T}^{(s)}(\boldsymbol{k}_0, \boldsymbol{k}_1)|^2; \quad \theta_{1s} = \widehat{\boldsymbol{k}_1 \boldsymbol{T}^{(s)}}, \tag{2.31}$$

with the amplitude $\boldsymbol{T}^{(s)}(\boldsymbol{k}_0, \boldsymbol{k}_1)$, which is calculated within the framework of the stationary scattering theory:

$$T_\mu^{(s)}(\boldsymbol{k}_0, \boldsymbol{k}_1) = \int e^{-i\boldsymbol{k}_1 \boldsymbol{r}'} \hat{V}_{\mu\nu}(\boldsymbol{r}') A_{\nu,s}(\boldsymbol{r}', \omega) d\boldsymbol{r}'. \tag{2.32}$$

The amplitude of the scattering depends on the vector potential $A_{\nu,s}(\boldsymbol{r}', \omega)$, which in turn is found from the integral Eq. (2.8). Provided that the scattering potential is weak, the iteration method can be used for the solution of this equation, which result in the Born series for the vector potential:

$$\begin{aligned} A_{\mu,s}(\boldsymbol{r}, \omega, \boldsymbol{k}_0) &= A_{\mu,s}^{(0)} + A_{\mu,s}^{(1)} + \ldots \\ &\equiv e_\mu^{(s)} e^{i\boldsymbol{k}_0 \boldsymbol{r}} + \int \frac{e^{ik_0|\boldsymbol{r}-\boldsymbol{r}'|}}{4\pi|\boldsymbol{r}-\boldsymbol{r}'|} \hat{V}_{\mu\nu}(\boldsymbol{r}') e_\nu^{(s)} e^{i\boldsymbol{k}_0 \boldsymbol{r}'} d\boldsymbol{r}' + \ldots. \end{aligned} \tag{2.33}$$

As a result, the scattering amplitude in the first order of Born approximation is:

$$T_{\mu,B}^{(s)}(\boldsymbol{k}_0, \boldsymbol{k}_1) = \int d\boldsymbol{r} e^{-i\boldsymbol{k}_1 \boldsymbol{r}} \hat{V}_{\mu\nu}(\boldsymbol{r}) e_\nu^{(s)} e^{i\boldsymbol{k}_0 \boldsymbol{r}}. \tag{2.34}$$

Using the definition (2.3) for the scattering potential, the expression for the cross-section of X-ray scattering in *Born approximation*, called also *kinematical scattering theory*, is written as:

$$\begin{aligned} T^{(s)}_{\mu,B}(\boldsymbol{k}_0,\boldsymbol{k}_1) &= k_0^2 \sum_b \int d\boldsymbol{r} e^{-i\boldsymbol{k}_1\boldsymbol{r}} S_b(\boldsymbol{r}) \\ &\quad \times \sum_{\boldsymbol{H}_b} \int d\boldsymbol{r}_1 \chi^{(b)}_{\mu\nu}(\boldsymbol{r}-\boldsymbol{r}_1,\boldsymbol{H}_b,\omega) e^{(s)}_\nu e^{i(\boldsymbol{k}_0+\boldsymbol{H}_b)\boldsymbol{r}_1} \\ &= k_0^2 \sum_b \sum_{\boldsymbol{H}_b} \int d\boldsymbol{r} S_b(\boldsymbol{r}) e^{-i(\boldsymbol{q}-\boldsymbol{H}_b)\boldsymbol{r}} \\ &\quad \times [e^{(s)}_\mu \chi^{(e)}_b(\boldsymbol{H}_b,\omega) + \chi^{(a)}_{\mu\nu,b}(\boldsymbol{k}_0+\boldsymbol{H}_b,\boldsymbol{H}_b,\omega) e^{(s)}_\nu]; \\ \frac{d\sigma^{(s)}}{d\Omega} &\approx \frac{1}{(4\pi)^2} \sin^2\theta_{1s} |\boldsymbol{T}^{(s)}_B(\boldsymbol{k}_0,\boldsymbol{k}_1)|^2, \end{aligned} \tag{2.35}$$

where $\boldsymbol{q} = \boldsymbol{k}_1 - \boldsymbol{k}_0$, $\chi^{(e)}_b$; $\chi^{(a)}_{\mu\nu,b}$ are the Compton and resonant contributions into the sample polarizability, defined by formulas (1.51) and (1.56), respectively. The Eq. (2.35) for the scattering cross-section is valid under the condition of the convergence of the perturbation series for the vector potential (2.33). This condition implements the restrictions for the linear dimension of microscopical elements of the investigated sample [5]:

$$L_b < L^{ext}_b \equiv \frac{c}{\omega |\chi^{(e)}_b(0,\omega)|}, \tag{2.36}$$

where the value L^{ext}_b is called *an extinction length*.

For the monochromatic radiation used in most of laboratory X-ray experiments, the observed X-ray intensity is parametrized by four angular variables. These variables define the unity vectors $\boldsymbol{n}_0 = \frac{c}{\omega}\boldsymbol{k}_0$ and $\boldsymbol{n}_1 = \frac{c}{\omega}\boldsymbol{k}_1$, which in turn define the directions of the propagation of the incident and scattered waves, respectively. Thus, in general case the scattering is described by the 4-dimensional hyper-surface in the space of these variables. The modern diffractometers (Fig. 2.5) allows to vary the mutual positions of the sample, X-ray source and detector in broad limits, and represent the X-ray measurement results as one-dimensional (profiles) or two-dimensional (maps) sections of this hyper-surface.

The different application areas of X-ray structure analysis utilize various sections of the hyper-surface (scattering geometry) and different models for investigated structures to analyze the measured data. The Born approximation is a basic one for numerous applications, and it requires the averaging of the expression (2.35) over the characteristics S_b, $\boldsymbol{H}_b$, $\chi^{(b)}$ of the microstructure of investigated object. The replacement of the averaging of the recorded X-ray intensity during the experiment, which occurs in real X-ray experiment, by the averaging over the statistical ensemble of sample microstructure parameters corresponds to the ergodic hypothesis [5].

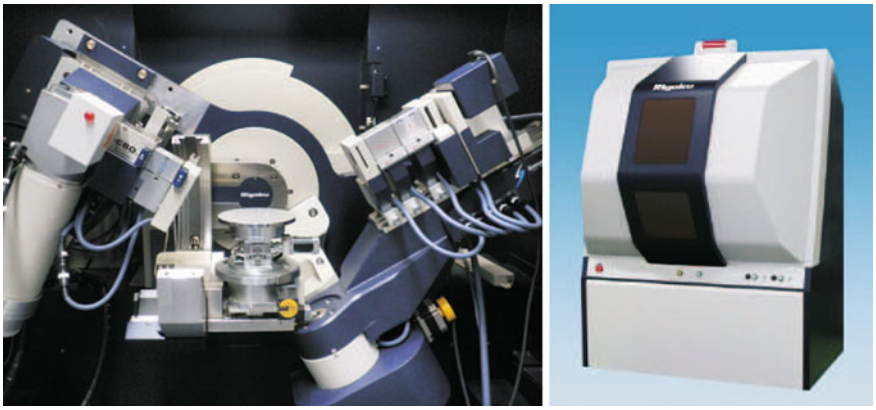

Fig. 2.5 Modern multi-purpose X-ray diffractometer SmartLab© (Rigaku Corporation) for non-destructive investigation of material structure

The mentioned averaging depends on the correlation properties of microstructure parameters and is specific for each unique application.

The most widely used applications of X-ray analysis based on the Born approximation and listed below are of their own the large domains of X-ray science with a long publication record. Therefore, the only references to the monographs and the critical reviews are given in the list, without detailed introduction in these applications (some of them are discussed in the next chapters).

- Powder X-ray diffraction: phase identification and crystal structure determination of powders and polycrystalline materials [15].
- Structure analysis and determination of organic and biological objects [16].
- X-ray residual stress and texture analysis in polycrystals [17, 18].
- Small-angle X-ray scattering: shape and distribution determination of the nano-sized objects [19].
- Pair-distribution function determination of crystalline, polycrystalline and amorphous materials [20].

The applicability limits of the kinematical scattering theory can be essentially extended by using the distorted-wave Born approximation (DWBA) [1]. The principal idea of this approach is based on the possibility to find an exact solution of the stationary Maxwell's Eq. (2.8) for some models of the scattering potential. Denoting the model potential as $\hat{V}^{(M)}_{\mu\nu}(\boldsymbol{r})$ and assuming the known solutions of the stationary Maxwell's equations, the following expressions can be used as a start point:

$$(\Delta + k_0^2 + \hat{V}^{(M)}_{\mu\nu}(\boldsymbol{r}))A^{(\pm)}_{\boldsymbol{k},\nu,s}(\boldsymbol{r},\omega) = 0;$$

$$A^{(\pm)}_{\boldsymbol{k},\mu,s}(\boldsymbol{r},\omega) = e^{(s)}_{\mu} e^{i\boldsymbol{k}\boldsymbol{r}} + \int d\boldsymbol{r}' \frac{e^{\pm ik_0|\boldsymbol{r}-\boldsymbol{r}'|}}{4\pi|\boldsymbol{r}-\boldsymbol{r}'|} \hat{V}^{(M)}_{\mu\nu}(\boldsymbol{r}') A^{(\pm)}_{\boldsymbol{k},\mu,s}(\boldsymbol{r}',\omega). \tag{2.37}$$

There exist two sets of solutions, which correspond to the ingoing and outgoing spherical waves at large distances from the scatterer. These solutions are connected by a simple relationship [7]:

$$A^{(-)}_{\boldsymbol{k},\mu,s}(\boldsymbol{r},\omega) = [A^{(+)}_{-\boldsymbol{k},\mu,s}(\boldsymbol{r},\omega)]^*, \tag{2.38}$$

and both are used for the sequential approximations of DWBA. When the complete set of the solutions for (2.37) is known, the Green function can be found [21]:

$$(\Delta + k_0^2)G^{(M)}_{\mu\nu}(\boldsymbol{r},\boldsymbol{r}') + \hat{V}^{(M)}_{\mu\lambda}(\boldsymbol{r})G^{(M)}_{\lambda\nu}(\boldsymbol{r},\boldsymbol{r}') = \delta_{\mu\nu}\delta(\boldsymbol{r}-\boldsymbol{r}'). \tag{2.39}$$

To establish the DWBA scheme for the Fraunhofer diffraction, the asymptotic for the Green function at $r \gg r'$ is enough instead of the concise expression (2.37). This asymptotic is calculated from Eq. (2.39) in the integral form using the formula (2.4) for Green function of the Helmholtz equation:

$$\begin{aligned} G^{(M)}_{\mu\nu}(\boldsymbol{r},\boldsymbol{r}') &= G^{(0)}_{\mu\nu}(\boldsymbol{r}-\boldsymbol{r}',k_0) \\ &\quad - \int d\boldsymbol{r}_1 G^{(0)}_{\mu\lambda}(\boldsymbol{r}-\boldsymbol{r}_1,k_0)\hat{V}^{(M)}_{\lambda\eta}(\boldsymbol{r}_1)G^{(M)}_{\eta\nu}(\boldsymbol{r}_1,\boldsymbol{r}'); \\ G^{(0)}_{\mu\nu}(\boldsymbol{r}-\boldsymbol{r}',k_0) &= -\delta_{\mu\nu}\frac{e^{ik_0|\boldsymbol{r}-\boldsymbol{r}'|}}{4\pi|\boldsymbol{r}-\boldsymbol{r}'|}. \end{aligned} \tag{2.40}$$

As a next step, the iteration scheme for the solution of Eq. (2.40) is constructed:

$$\begin{aligned} G^{(M)}_{\mu\nu}(\boldsymbol{r},\boldsymbol{r}') &= G^{(0)}_{\mu\nu}(\boldsymbol{r}-\boldsymbol{r}',k_0) \\ &\quad - \int d\boldsymbol{r}_1 G^{(0)}_{\mu\lambda}(\boldsymbol{r}-\boldsymbol{r}_1,k_0)\hat{V}^{(M)}_{\lambda\eta}(\boldsymbol{r}_1)G^{(0)}_{\eta\nu}(\boldsymbol{r}_1-\boldsymbol{r}',k_0) + \cdots, \end{aligned} \tag{2.41}$$

and the asymptotic expansion (2.7) for function $G^{(0)}_{\mu\nu}(\boldsymbol{r}-\boldsymbol{r}',k_0)$ is used at $r \gg r'$:

$$\begin{aligned} G^{(M)}_{\mu\nu}(\boldsymbol{r},\boldsymbol{r}') &\approx -\delta_{\mu\nu}\frac{e^{ik_0 r}}{4\pi r}e^{-i\boldsymbol{k}_1\boldsymbol{r}'} \\ &\quad - \delta_{\mu\lambda}\frac{e^{ik_0 r}}{4\pi r}\int d\boldsymbol{r}_1 e^{-i\boldsymbol{k}_1\boldsymbol{r}_1}\hat{V}^{(M)}_{\lambda\eta}(\boldsymbol{r}_1)\delta_{\eta\nu}\frac{e^{ik_0|\boldsymbol{r}_1-\boldsymbol{r}'|}}{4\pi|\boldsymbol{r}-\boldsymbol{r}'|} + \cdots; \\ \boldsymbol{k}_1 &= k_0\frac{\boldsymbol{r}}{r}. \end{aligned} \tag{2.42}$$

The fact of the preservation of the wave field in the transverse direction with the accuracy $\sim |\chi_0|^2 < 10^{-10}$ [2] is taken here into account, too. Therefore, the only transverse part is selected in (2.42), which is carried out [22] by the substitution of the Kronecker symbols by transverse tensor $t_{\mu,\nu}(\boldsymbol{k})$:

$$t_{\mu,\nu}(\boldsymbol{k}) = \delta_{\mu\nu} - \frac{k_\mu k_\nu}{k^2} = \sum_s e_\mu^{(s)}(\boldsymbol{k}) e_\nu^{(s)}(\boldsymbol{k}). \tag{2.43}$$

The function of the wave field distribution with certain polarization is represented as:

$$G_{\mu\nu}^{(M,s)}(\boldsymbol{r},\boldsymbol{r}') \approx -e_\mu^{(s)}(-\boldsymbol{k}_1)\frac{e^{ik_0 r}}{4\pi r}\left[e_\nu^{(s)}(-\boldsymbol{k}_1)e^{-i\boldsymbol{k}_1\boldsymbol{r}'} + \int d\boldsymbol{r}_1 e_\lambda^{(s)}(-\boldsymbol{k}_1)e^{-i\boldsymbol{k}_1\boldsymbol{r}_1}\hat{V}_{\lambda\nu}^{(M)}(\boldsymbol{r}_1)\frac{e^{ik_0|\boldsymbol{r}_1-\boldsymbol{r}'|}}{4\pi|\boldsymbol{r}-\boldsymbol{r}'|}\right] + \ldots. \tag{2.44}$$

The asymptotic expression for Green function follows from the formula (2.43) and definition of the function $A_{\boldsymbol{k},\mu,s}^{(-)}(\boldsymbol{r},\omega)$ in formula (2.37):

$$\begin{aligned} G_{\mu\nu}^{(M,s)}(\boldsymbol{r},\boldsymbol{r}') &\approx -e_\mu^{(s)}(\boldsymbol{k}_1)\frac{e^{ik_0 r}}{4\pi r}[A_{\boldsymbol{k},\nu,s}^{(-)}(\boldsymbol{r},\omega)]^* \\ &= -e_\mu^{(s)}(-\boldsymbol{k}_1)\frac{e^{ik_0 r}}{4\pi r}A_{-\boldsymbol{k},\nu,s}^{(+)}(\boldsymbol{r},\omega). \end{aligned} \tag{2.45}$$

The iteration scheme for the solution of the stationary Maxwell's equation is constructed as follows:

$$(\Delta + k_0^2 + \hat{V}_{\mu\nu}^{(M)}(\boldsymbol{r}) + \hat{V}_{\mu\nu}(\boldsymbol{r}))A_{\boldsymbol{k},\nu,s}(\boldsymbol{r},\omega) = 0, \tag{2.46}$$

which assumes the consideration of the additional scattering potential $\hat{V}_{\mu\nu}(\boldsymbol{r})$ within the limits of the perturbation theory. Using the definition (2.39), Eq. (2.46) in the integral form reads:

$$\begin{aligned} A_{\boldsymbol{k},\mu,s}(\boldsymbol{r},\omega) &= A_{\boldsymbol{k},\mu,s}^{(+)}(\boldsymbol{r},\omega) - \int d\boldsymbol{r}' G_{\mu\lambda}^{(M,s)}(\boldsymbol{r},\boldsymbol{r}')\hat{V}_{\lambda\nu}^{(M)}(\boldsymbol{r}')A_{\boldsymbol{k},\mu,s}(\boldsymbol{r}',\omega) \\ &\approx A_{\boldsymbol{k},\mu,s}^{(+)}(\boldsymbol{r},\omega) - \int d\boldsymbol{r}' G_{\mu\lambda}^{(M,s)}(\boldsymbol{r},\boldsymbol{r}')\hat{V}_{\lambda\rho}(\boldsymbol{r}')A_{\boldsymbol{k},\rho,s}^{(+)}(\boldsymbol{r}',\omega) + \cdots \end{aligned} \tag{2.47}$$

In the same way as in Born approximation (2.33), the plane and spherical waves are distinguished in (2.47) by using (2.8) and (2.45):

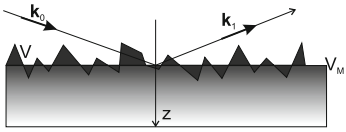

Fig. 2.6 The choice of the potential in case of DWBA for diffuse X-ray scattering from rough surfaces and interfaces

$$A_{\boldsymbol{k},\mu,s}(\boldsymbol{r},\omega) \approx e_{\mu}^{(s)}(\boldsymbol{k}_0)e^{i\boldsymbol{k}_0\boldsymbol{r}} + \frac{e^{ik_0 r}}{4\pi r} \times \left[\int d\boldsymbol{r}' e^{-i\boldsymbol{k}_1\boldsymbol{r}'} \hat{V}_{\mu\nu}^{(M)}(\boldsymbol{r}') A_{\boldsymbol{k},\nu,s}^{(+)}(\boldsymbol{r}',\omega) \right.$$
$$\left. + \int d\boldsymbol{r}' e_{\mu}^{(s)}(-\boldsymbol{k}_1) A_{-\boldsymbol{k}_1,\nu,s}^{(+)}(\boldsymbol{r}',\omega) \hat{V}_{\nu\rho}(\boldsymbol{r}') A_{\boldsymbol{k},\rho,s}^{(+)}(\boldsymbol{r}',\omega) + \cdots \right]. \tag{2.48}$$

Finally, the expression for the scattering amplitude in DWBA approximation is found, which generalize the formula (2.34):

$$T_{\mu,DWBA}^{(s)}(\boldsymbol{k}_0,\boldsymbol{k}_1) = \int d\boldsymbol{r}' e^{-i\boldsymbol{k}_1\boldsymbol{r}'} \hat{V}_{\mu\nu}^{(M)}(\boldsymbol{r}') A_{\boldsymbol{k},\nu,s}^{(+)}(\boldsymbol{r}',\omega)$$
$$+ \int d\boldsymbol{r}' e_{\mu}^{(s)}(-\boldsymbol{k}_1) A_{-\boldsymbol{k}_1,\nu,s}^{(+)}(\boldsymbol{r}',\omega) \hat{V}_{\nu\rho}(\boldsymbol{r}') A_{\boldsymbol{k},\rho,s}^{(+)}(\boldsymbol{r}',\omega), \tag{2.49}$$

and permits to calculate the scattering cross-section in correspondence with (2.31). The necessity of usage of the waves $A_{-\boldsymbol{k}_1,\nu,s}^{(+)}$ for the calculation of the matrix element with perturbation operator is known also in optics, where they are used for the description of the electromagnetic radiation from the atoms in refractive media (reciprocity theorem [8]). The scattering potential $\hat{V}^{(M)}$ and the perturbation potential $\hat{V}$ are chosen in dependence on the application, and here several examples are given for some recognized X-ray techniques:

- Diffuse X-ray scattering from the surface and interface roughness [23]. The potential $\hat{V}^{(M)}$ represents the sample with ideally plane surface/interface, and $\hat{V}$ defines the scattering potential of the roughness (Fig. 2.6).
- Grazing-incidence small-angle X-ray scattering (GISAXS) from the nano-objects located on the surface or embedded in the bulk samples [24]. The potential $\hat{V}^{(M)}$ corresponds to the ideally uniform sample, and $\hat{V}$ describes the nano-objects (Fig. 2.7).
- X-ray dynamical diffraction theory in crystals [3]. This theory utilizes the two-wave approximation, which corresponds to the selection of $\hat{V}^{(M)}$ in the form of the scattering potential of the perfect crystal (1.51) with accounting of only two Fourier components of X-ray polarizability $\chi(0,\omega)$; $\chi(\boldsymbol{H},\omega)$. The potential $\hat{V}$ defines the scattering potential of various defects inside the crystal [25] (Fig. 2.8).

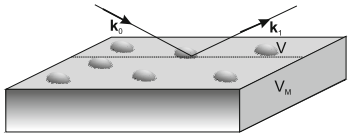

Fig. 2.7 Scattering potential of DWBA for GISAXS application

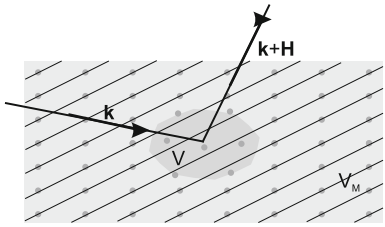

Fig. 2.8 X-ray dynamical diffraction theory as zeroth approximation of DWBA for the description of X-ray scattering from crystal defects

References

1. M.L. Goldberger, K.M. Watson, *Collision Theory* (John Wiley, New York, 1964)
2. R.W. James, *The Optical Principle of the Diffraction of X-rays* (G.Bell and Sons, London, 1962)
3. A. Authier, *Dynamical Theory of X-ray Diffraction* (Oxford University Press, New York, 2001)
4. U. Pietsch, V. Holy, T. Baumbach, *High-Resolution X-ray Scattering: From Thin Films to Lateral Nanostuctures*, 2nd edn. (Springer, Berlin, 2004)
5. L.D. Landau, E.M. Lifshitz, *Electrodynamics of Condensed Matter*, 2nd edn. (Nauka, Moscow, 1982) (in Russian)
6. B.W. Batterman, Rev. Mod. Phys. **36**, 681 (1964)
7. L.D. Landau, E.M. Lifshitz, *Quantum Mechanics*, 3rd edn. (Pergamon Press, Oxford, 1977)
8. M. Born, E. Wolf, *Principles of Optics*, 7th edn. (Cambridge University Press, Cambridge, 1999)
9. A.A. Malyutin, Quantum Electron. **34**, 960 (2004)
10. P. Cloetens, R. Barrett, J. Baruchel, J.-P. Guigay, M. Schlenker, J. Phys. D: Appl. Phys. **29**, 133 (1996)
11. K.J. Gaffney, H.N. Chapman, Science **316**, 1444 (2007)
12. S.-K. Son, L. Young, R. Santra, Phys. Rev. A **83**, 033402 (2011)
13. I.A. Vartanyants et al., Phys. Rev. Lett. **107**, 144801 (2011)
14. I.D. Feranchuk, O.D. Skoromnik, Phys. Rev. A **82**, 052803 (2010)
15. V. Pecharsky, P. Zavalij, *Fundamentals of Powder Diffraction and Structural Characterization of Materials*, 2nd edn. (Springer, Berlin, 2008)
16. M. Rossmann, E. Arnold, in *Crystallography of Biological Molecules*. International Tables for Crystallography, vol. F (Kluwer Academic Publishers, Dordrecht, 2001)
17. I.C. Noyan, J.B. Cohen, *Resudial Stress: Measurements by Diffraction and Iterpretation* (Springer, New York, 1987)
18. H.-J. Bunge, *Texture Analysis in Materials Science* (Butterworth, London, 1983)
19. L.A. Feigin, D.I. Svergun, *Structure Analysis by Small-Angle X-Ray and Neutron Scattering* (Plenum Press, New York, 1987)
20. T. Egami, S.J.L. Billinge, *Underneath the Bragg Peaks: Structural Analysis of Complex Materials* (Pergamon Press Elsevier, Oxford, 2003)
21. P.M. Morse, H. Feshbach, *Methods of Theoretical Physics* (McGraw-Hill, New York, 1953)
22. A.I. Akhiezer, V.B. Berestetsky, *Quantum Electrodynamics* (Nauka, Moscow, 1969)
23. S.K. Sinha, E.B. Sirota, S. Garoff, H.B. Stanley, Phys. Rev. B **38**, 2297 (1988)
24. G. Renaud, R. Lazzari, F. Leroy, Surf. Sci. Rep. **64**, 255 (2009)
25. M.A. Krivoglaz, *X-Ray and Neutron Diffraction in Nonideal Crystals* (Springer, Berlin, 1996)

Chapter 3
X-Ray Reflectivity

The general calculation of the scattered from the sample X-ray intensity requires the solution of the Eq. (2.1). However, the geometry of the experiment has to be also taken into account, because of the mutual arrangement of the X-ray source, the sample and the detector as well as the shape of the sample influence the observed results. Depending on the experimental geometry, X-rays can be used for probing of different properties of the investigated sample, and there are numerous experimental setups, which realize various X-ray application techniques. The special case of the experimental geometry, which is proved to be effective for investigation of the sample surface and subsurface layers is *X-ray specular reflectivity* or simply *X-ray reflectivity* (XRR) that is the main goal of this chapter.

3.1 Experiment Geometry and Basic Parameters of XRR

In this case the incident and reflected waves constitute the grazing angles with the sample surface (Fig. 3.1).

We define here the coordinate system x, y by the sample surface (horizontal plane) and by the axis z as an inward normal to this surface. By the definition, in the X-ray specular reflectivity the interaction of the incident radiation with the elements of the scattered potential $S_b(\boldsymbol{r})$ in formula (2.2) involves solely a zeroth harmonics of X-ray polarizability (1.56), which is proportional to the electron density n_e of the sample element:

$$\begin{gathered}\varepsilon_{\mu,\lambda}(\boldsymbol{k},0,\omega)=\varepsilon^{(e)}(0,\omega)\delta_{\mu,\lambda}+\chi^{(a)}_{\mu,\lambda}(\boldsymbol{k},0,\omega);\\ \varepsilon^{(e)}(0,\omega)=1+\chi^{(e)}(0,\omega);\ \chi^{(e)}(0,\omega)=\frac{4\pi c^2}{\omega^2}f(0)n_e;\\ f(0)=f'(0)+if''(0);\quad f'(0)=-r_0;\ f''(0)=\frac{\omega}{4\pi c}\sigma_t(\omega),\end{gathered}\tag{3.1}$$

where σ_t is a cross-section of the elastic Compton scattering (1.39).

A. Benediktovitch et al., *Theoretical Concepts of X-Ray Nanoscale Analysis*,
Springer Series in Materials Science 183, DOI: 10.1007/978-3-642-38177-5_3,

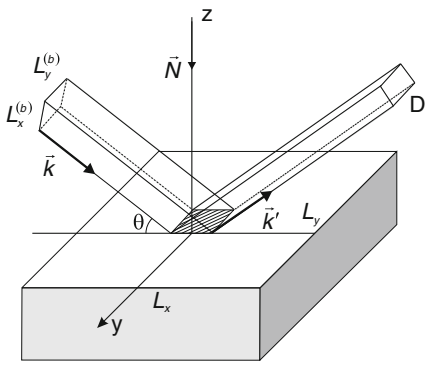

Fig. 3.1 The experimental geometry in the case of X-ray reflectivity

The anomalous contribution $\chi^{(a)}_{\mu,\lambda}(\boldsymbol{k}, 0, \omega)$ into X-ray polarizability is described by formula (1.56). In general case, it is a tensor depending both on the frequency and the direction of the vector $\boldsymbol{k}$. However, the interaction of X-ray radiation with atoms of the sample is dominated by the scattering from atom's inner shells, which have a spherically symmetric electron density distribution. Therefore, in the most of the practical applications the anisotropy of X-ray polarizability can be ignored [1] and the scalar refractive index for the description of the scattering properties of the uniform media is used.

$$n^2(\omega) = \varepsilon(\omega) = 1 + \chi(\omega); \quad n(\omega) \equiv 1 + \beta + i\delta \approx 1 + \frac{1}{2}\chi(\omega);$$
$$\beta = \frac{2\pi c^2}{\omega^2} n_e[f'(0) + \Delta f'(\omega)], \delta = \frac{2\pi c^2}{\omega^2} n_e[f''(0) + \Delta f''(\omega)]. \tag{3.2}$$

The main contribution to the real part of the refractive index is given by the value $n' = 1 + \beta < 1; \beta < 0$, and thus for X-rays the uniform media is optically less dense than vacuum, which results in a wave phase velocity $v_{ph} = c/(1 + \beta) > c$ [2]. At the same time, the group velocity of the X-ray beam in the media is less than the speed of light.

$$v_{gr} = c[\frac{d}{d\omega}(\omega n')]^{-1} \approx c(1 + \beta) < c. \tag{3.3}$$

The values $\Delta f'(\omega)$ and $\Delta f''(\omega)$ are the real and imagine parts of the correction for anomalous dispersion, respectively. These values become essential at the characteristic frequencies, which are close to the absorption edges of the atoms composing the media [1]. The characteristic frequencies are defined by the energies of electron ionization for different shells of the atom. The correction for the anomalous dispersion can be calculated by using formula (1.56) and one of the approximation for the wave function of the electrons in the atom [1], however, in practice the databases are used for this purpose, which utilize the experimentally measured cross-sections of X-ray radiation from the atoms (for example, [3]). The typical dependence of the anomalous dispersion correction on the frequency is shown in Fig. 3.2.

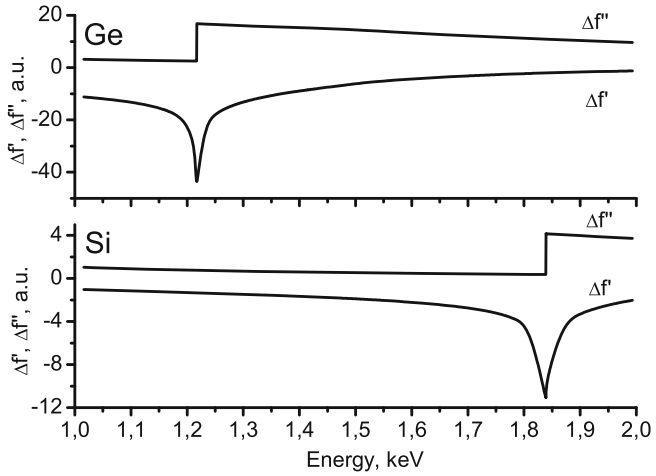

Fig. 3.2 Frequency dependence of the correction for the anomalous dispersion near the K-edge of the silicon atom and L-edge of the germanium atom

The calculation of the scattered X-ray intensity and the analysis of the experimental data for XRR has been presented in numerous monographs (see, for example, [4–7]). Therefore, we make an emphasis in this chapter to the theoretical aspects of the solution of the scattering problem in XRR geometry and some specific cases discussed in recent publications [8–16]).

The calculation of X-ray scattering from the ideally smooth surface corresponding to the plane $z = 0$ (Fig. 3.1) is a basis for the further analysis of the reflection from the imperfect samples. In most cases, this problem is reduced to the solution of the one-dimensional wave equation assuming the infinite size of the sample in the directions (x, y). However, real samples have always a finite size and therefore we present here an analysis based on the scattering theory utilizing the DWBA approach considered in the previous chapter (2.37). The results of this analysis are used in next sections for the description of X-ray scattering from imperfect surfaces. The scattering potential has the form, following from the relation (3.2) and the definition (2.3) (see Fig. 3.1):

$$V^{(M)}(\boldsymbol{r}, \omega) = k_0^2 \chi(\omega) H(z), \tag{3.4}$$

and the perturbation potential depends on the sample size in lateral plane and the X-ray beam size:

$$V(\boldsymbol{r}, \omega) = -k_0^2 \chi(\omega) S(\boldsymbol{r});$$
$$S(\boldsymbol{r}) = H(z)\left[1 - H\left(\frac{\tilde{L}_x}{2} - x\right) H\left(\frac{\tilde{L}_x}{2} + x\right) H\left(\frac{\tilde{L}_y}{2} - y\right) H\left(\frac{\tilde{L}_y}{2} + y\right)\right]. \tag{3.5}$$

The sample with the surface at $z = 0$ and the edges L_x, L_y is considered here. The shape function is defined by the Heaviside functions ($H(u) = 1,\ u > 0;\ H(u) = 0,\ u < 0$), where the value $\tilde{L}_x$ is chosen as minimal from L_x and $L_x^{(b)}/\sin\theta$, and $\tilde{L}_y = \min\{L_y, L_y^{(b)}\}$. Here $L_x^{(b)}$, $L_y^{(b)}$ are the linear dimensions of the cross-section of the incident beam, and $\tilde{L}_{x,y}$ defines the beam spot on the plane $z = 0$ (Fig. 3.1). First of all, we consider the solution with the potential (3.4), and the Maxwell's equation (2.37) is transformed to:

$$(\Delta + k_0^2[1 + \chi(\omega)H(z)])\boldsymbol{A}_{\boldsymbol{k},s}^{(+)}(\boldsymbol{r},\omega) = 0, \tag{3.6}$$

with the boundary condition for the wave impinging the sample:

$$\boldsymbol{A}_{\boldsymbol{k},s}^{(+)}(\boldsymbol{r},\omega) \approx \boldsymbol{e}^{(s)}(\boldsymbol{k})\, e^{i(k_x x + k_z z)};\quad z \to -\infty;\ s = 1, 2 \tag{3.7}$$

The coordinate system is positioned in the way that the plane $y = 0$ coincides with the plane of the beam incidence composed by the vector $\boldsymbol{k}$ and the normal $\boldsymbol{N}$ to the sample surface, i.e. $k_y = 0$, $k_x = k_0\cos\theta$, $k_z = \sqrt{k_0^2 - k_x^2} = k_0\sin\theta$. The polarization vector $\boldsymbol{e}^{(1)}(\boldsymbol{k})$ lies in the incidence plane (π-polarization), $\boldsymbol{e}^{(2)}(\boldsymbol{k})$ is perpendicular to the incidence plane (σ-polarization), see Fig. 3.3.
The variables in the Eq. (3.6) are separated and the general solution is represented as a combination of plane waves (Fig. 3.3):

$$\begin{aligned}
&\boldsymbol{A}_{1,s}^{(+)} = \boldsymbol{e}^{(s)}(\boldsymbol{k})\, e^{i(k_x x + k_z z)} + R^{(s)}\boldsymbol{e}^{(s)}(\boldsymbol{k}')\, e^{i(k'_x x + k'_z z)},\ z < 0\\
&\boldsymbol{A}_{2,s}^{(+)} = T^{(s)}\boldsymbol{e}^{(s)}(\boldsymbol{k}_m)\, e^{i(k_{xm} x + k_{zm} z)}\ z > 0;\\
&k'_x = k_0\cos\theta', k'_z = -k_0\sin\theta'; k_{xm} = k_0 n\cos\theta_1, k_{zm} = \sqrt{k_0^2 n^2 - k_{xm}^2},
\end{aligned} \tag{3.8}$$

with undefined amplitudes $R^{(s)}$, $T^{(s)}$. The coefficient at the reflected wave within media $R_m^{(s)}$ is equal to zero due to the asymptotic condition for $\boldsymbol{A}_{\boldsymbol{k},s}^{(+)}$ caused by the

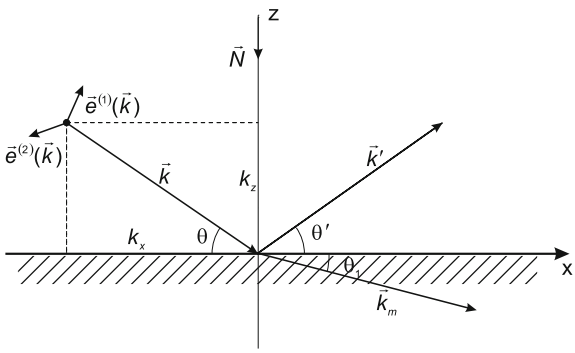

Fig. 3.3 Wave propagation sketch for the X-ray scattering process from the surface

absence of the convergent waves far from the sample. As the next step, the continuity condition for the lateral components of the electrical and magnetic fields [17] is used at the boundary of two media ($z = 0$):

$$\boldsymbol{E}_{1,\tau}|_{z=0} = \boldsymbol{E}_{2,\tau}|_{z=0};\ \boldsymbol{H}_{1,\tau}|_{z=0} = \boldsymbol{H}_{2,\tau}|_{z=0}. \tag{3.9}$$

Using the relationship (2.9) between wave fields and vector potential, the boundary conditions for functions (3.8) for σ-polarization are written as:

$$A_{1,y}|_{z=0} = A_{2,y}|_{z=0};\ \frac{\partial}{\partial z}A_{1,y}|_{z=0} = \frac{\partial}{\partial z}A_{2,y}|_{z=0}. \tag{3.10}$$

Due to the validity of the condition (3.10) in each point on the surface, the x-dependent phase coefficients are equal each to other when substituting (3.8) into (3.10), and therefore the lateral component of the wave vector is preserved:

$$\begin{aligned} &k_x = k'_x = k_{xm};\ \theta = \theta';\ \cos\theta_1 = \frac{1}{n}\cos\theta; \\ &k'_z = -k_z;\ k_{zm} = k_0\sqrt{n^2 - \cos^2\theta}. \end{aligned} \tag{3.11}$$

The Eq. (3.11) means that the scattering of X-ray from the ideal surface occurs exclusively for the angle equals to the incidence angle (specular reflection). For σ-polarization, the conditions (3.10) lead to the following equations for the amplitudes (the solutions are the Fresnel coefficients [17]):

$$\begin{aligned} &1 + R^{(2)} = T^{(2)};\ k_z(1 - R^{(2)}) = k_{zm}T^{(2)}; \\ &R^{(2)} \equiv r_F = \frac{k_z - k_{zm}}{k_z + k_{zm}} = \frac{\sin\theta - \sqrt{n^2 - \cos^2\theta}}{\sin\theta + \sqrt{n^2 - \cos^2\theta}}; \\ &T^{(2)} \equiv t_F = \frac{2k_z}{k_z + k_{zm}} = \frac{2\sin\theta}{\sin\theta + \sqrt{n^2 - \cos^2\theta}}. \end{aligned} \tag{3.12}$$

For π-polarization, the results are slightly different:

$$\begin{aligned} &A_{1,x}|_{z=0} = A_{2,x}|_{z=0}; \\ &\left(\frac{\partial}{\partial z}A_{1,x} - \frac{\partial}{\partial x}A_{1,z}\right)|_{z=0} = \left(\frac{\partial}{\partial z}A_{2,x} - \frac{\partial}{\partial x}A_{2,z}\right)\Big|_{z=0}. \end{aligned} \tag{3.13}$$

$$\begin{aligned} &(1 - R^{(1)}) = \frac{\sin\theta_1}{\sin\theta}T^{(1)};\ 1 + R^{(1)} = \left(\frac{k_{zm}}{k_0}\sin\theta_1 + \frac{\cos^2\theta}{n}\right)T^{(1)}; \\ &R^{(1)} = \frac{k_z n^2 - k_{zm}}{k_z n^2 + k_{zm}} = r_F + O(|\chi(\omega)|) \end{aligned}$$

$$T^{(1)} = \frac{2k_z n^2}{k_z n^2 + k_{zm}} = t_F + O(|\chi(\omega)|). \tag{3.14}$$

For the electromagnetic radiation of the wavelengths in X-ray region the magnitude of $|\chi(\omega)| \sim 10^{-5}$, and therefore the Fresnel coefficients of the reflection r_F and transmission t_F are independent on the polarization and defined by the formulas (3.12). This statement follows from the fact of the conservation of the transversality of X-ray wave field in media with the same accuracy (Sect. 2.2). Figure 3.4 demonstrates the behavior of the intensity of the reflected and transmitted waves (proportional to $|r_F(\sin\theta)|^2$ and $|t_F(\sin\theta)|^2$, respectively) for silicon and germanium crystals. As follows from the Eq. (3.12), the reflection coefficient is only essential within a narrow diapason of the incidence angles compared to the critical angle of the total external reflection θ_c:

$$\sin\theta \approx \theta \sim \theta_c \equiv \sqrt{2|\beta|} \sim 10^{-2} rad, \tag{3.15}$$

and the parameter β follows from Eq. (3.2).

Thus, adopting the above used approximations, the interaction of X-ray radiation with a matter in case of XRR does not depend on the polarization, and as a consequence the incident wave can be considered in the calculations as fully polarized one in the direction perpendicular to the incidence plane, for example. The scattering problem for the potential (3.4) is then reduced to the scalar case:

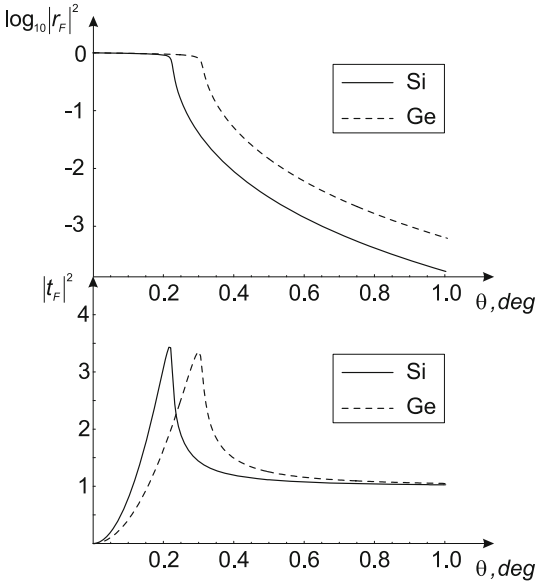

Fig. 3.4 Functions $|r_F(\sin\theta)|^2$ and $|t_F(\sin\theta)|^2$ for silicon ($\beta = -0.76\ 10^{-5}$; $\delta = 1.73\ 10^{-7}$) and germanium ($\beta = -1.45\ 10^{-5}$; $\delta = 4.32\ 10^{-7}$) crystals at X-ray wavelength $\lambda = 1.54$ nm

$$\begin{aligned} \boldsymbol{A}_{\boldsymbol{k}}^{(+)} &= \boldsymbol{e}^{(2)}(\boldsymbol{k})e^{ik_x x}E^{(+)}(z); \\ E^{(+)}(z) &= [e^{ik_z z} + r_F e^{-ik_z z}]H(-z) + t_F e^{ik_{zm} z}H(z). \end{aligned} \tag{3.16}$$

The solution of the Eq. (3.6), corresponding to the convergent wave, is found from the formula (2.38):

$$\begin{aligned} \boldsymbol{A}_{\boldsymbol{k}}^{(-)} &= \boldsymbol{A}_{-\boldsymbol{k}}^{(+)*} = \boldsymbol{e}^{(2)}(-\boldsymbol{k})e^{ik_x x}E^{(-)}(z); \\ E^{(-)}(z) &= [e^{ik^*_{zm} z} + r^*_F e^{-ik^*_{zm} z}]H(z) + t^*_F e^{ik_z z}H(-z); \\ t^*_F &= \frac{2k^*_{zm}}{k_z + k^*_{zm}};\ r^*_F = -\frac{k_z - k^*_{zm}}{k_z + k^*_{zm}}. \end{aligned} \tag{3.17}$$

The Green function of the wave Eq. (3.6) after the separation of the polarizations [8–10]:

$$\begin{aligned} (\Delta + k_0^2[1 + \chi(\omega)H(z)])G(\boldsymbol{r}, \boldsymbol{r}') &= \delta(\boldsymbol{r} - \boldsymbol{r}'); \\ G(\boldsymbol{r}, \boldsymbol{r}') &= \frac{1}{4\pi^2}\int_{\boldsymbol{p}_\perp < k_0} d\boldsymbol{p}_\perp e^{i\boldsymbol{p}_\perp(\boldsymbol{r} - \boldsymbol{r}')} g_{p_z}(z, z'). \end{aligned} \tag{3.18}$$

The Green function $g_{p_z}(z, z')$ of the one-dimensional wave equation is constructed by using the standard methods of the differential equation theory [8–10, 18]:

$$\begin{aligned} g_{k_z}(z, z') = \frac{i}{2p_{zm}t_F}[&E^{(+)}(z)E^{(-)*}(z')H(z' - z) \\ &- E^{(+)}(z')E^{(-)*}(z)H(z - z')]. \end{aligned} \tag{3.19}$$

To calculate the observed differential cross-section of X-ray scattering (2.10), the integral representation (2.6) has to be used:

$$\boldsymbol{A}_{\boldsymbol{k}}^{(+)} = \boldsymbol{e}^{(2)}[e^{i\boldsymbol{k}\boldsymbol{r}} + \int \frac{e^{ik_0|\boldsymbol{r} - \boldsymbol{r}'|}}{4\pi|\boldsymbol{r} - \boldsymbol{r}'|} V^{(M)}(z')e^{ik_x x'}E^{(+)}(z')d\boldsymbol{r}']. \tag{3.20}$$

with the potential taken from (3.4). The use of the latter formula is motivated by the transition in the formulas above to the asymptotic representation at $r \gg r'$. However, for the considered here sample model this condition is not fulfilled because of the function $E^{(+)}(z')$ is found using the boundary conditions for the potential, which are unlimited in the tangential plane. Thus, the application of the formula (2.10) for wave field (3.20) leads to the contradiction with the formal scattering theory [19]. To avoid this contradiction, the conditions have to be found at which the contribution to the wave field from the perturbation potential (3.5) becomes negligible. In this case, the calculation of the cross-section within the asymptotic scattering theory using (2.10) is equivalent to the calculation of the intensity of the reflected wave with the boundary conditions (3.16). The general equation for the wave field in the framework

of DWBA approach (2.47) and after separation of the polarizations is written as:

$$\begin{aligned} \boldsymbol{A_k}(\boldsymbol{r}) &= \boldsymbol{e}^{(2)}\Psi_{\boldsymbol{k}}(\boldsymbol{r}); \\ \Psi_{\boldsymbol{k}}(\boldsymbol{r}) &= [e^{i\boldsymbol{k}\boldsymbol{r}} + \int \frac{e^{ik_0|\boldsymbol{r}-\boldsymbol{r}'|}}{4\pi|\boldsymbol{r}-\boldsymbol{r}'|} V^{(M)}(z')e^{ik_x x'} E^{(+)}(z')d\boldsymbol{r}' \\ &\quad - \int G(\boldsymbol{r},\boldsymbol{r}')V(\boldsymbol{r}')\Psi_{\boldsymbol{k}}(\boldsymbol{r}')d\boldsymbol{r}'], \end{aligned} \tag{3.21}$$

with Green function (3.18), and the formula (3.21) can be further transformed into:

$$\begin{aligned} \Psi_{\boldsymbol{k}}(\boldsymbol{r}) &= e^{i\boldsymbol{k}\boldsymbol{r}} + \int_{\boldsymbol{r}'_\perp \subset \tilde{S}_\perp} \frac{e^{ik_0|\boldsymbol{r}-\boldsymbol{r}'|}}{4\pi|\boldsymbol{r}-\boldsymbol{r}'|} V^{(M)}(z')e^{ik_x x'} E^{(+)}(z')d\boldsymbol{r}' \\ &\quad - \frac{k_0^2\chi(\omega)}{4\pi^2} \int_{\boldsymbol{p}_\perp < k_0} d\boldsymbol{p}_\perp \int_{\boldsymbol{r}'_\perp \supset \tilde{S}_\perp} e^{i\boldsymbol{p}_\perp(\boldsymbol{r}-\boldsymbol{r}')} e^{ik_x x'} \\ &\quad \times H(z')[g^{(0)}_{p_z}(z,z')E^{(+)}(z') - g_{p_z}(z,z')e^{-ik_x x'}\Psi_{\boldsymbol{k}}(\boldsymbol{r}')]d\boldsymbol{r}', \end{aligned} \tag{3.22}$$

where $\tilde{S}_\perp = \tilde{L}_x\tilde{L}_y$ and $g^{(0)}_{p_z}(z,z')$ is a Green function for one-dimensional equation for free wave field:

$$g^{(0)}_{p_z}(z,z') = \frac{i}{2p_z} e^{ip_z|z-z'|}. \tag{3.23}$$

The first two terms in (3.22) correspond to the standard treatment of XRR as one-dimensional problem [5–12]. The last term describes the contribution of the Fresnel diffraction from the sample edges [2], which is usually neglected. The conditions at which this contribution is negligible have to be considered thoroughly using one-dimensional integral over variable x in (3.22):

$$I(k_x, L) = \int_L^\infty dx' e^{i(k_x - p_x)x'} + \int_{-\infty}^{-L} dx' e^{i(k_x - p_x)x'}. \tag{3.24}$$

This integral is a generalized function [20], which integrates a smooth function related to the averaged wave vector in our case:

$$J(L) = \frac{1}{\sqrt{2\pi}\Delta_k} \int_{-\infty}^{\infty} dk_x e^{-\frac{(k_x - k_{x0})^2}{2\Delta_k^2}} I(k_x, L). \tag{3.25}$$

Here the value k_{x0} defines the "center" of the wave package and Δ_k is the width of package (see 2.1). Changing the integration sequence in (3.25), the expression can be simplified:

$$J(L) = 2\int_L^\infty dx' \cos[(k_{x0} - p_x)x']e^{-(x'\Delta_k)^2/2}$$
$$= \frac{\sqrt{\pi}}{2\Delta_k} e^{-\frac{q^2}{2\Delta_k^2}} \left[2 - \Phi\left(\frac{L\Delta_k - iq/\Delta_k}{\sqrt{2}}\right) - \Phi\left(\frac{L\Delta_k + iq/\Delta_k}{\sqrt{2}}\right)\right], \quad (3.26)$$

where $q = k_{x0} - p_x$ and

$$\Phi(z) = \frac{2}{\sqrt{\pi}}\int_0^z e^{-t^2} dt$$

is a probability integral [18]. In real experiments, the transverse size of the sample $L \geq 0.1\ cm$, $\Delta_k \approx k_0\Delta\theta \geq 10^3\ cm^{-1}$, and as result $L\Delta_k \gg 1$; $L\Delta_k \gg |q|/\Delta_k$. That is a reason to use an asymptotic for the function $\Phi(z)$ in (3.26) [18], and the contribution of the edge effects into wave field (3.22) is found to be an exponentially small value:

$$J(L) \approx \frac{1}{\Delta_k\sqrt{\pi L\Delta_k}} e^{-\frac{q^2}{2\Delta_k^2}} e^{-(L\Delta_k)^2} \ll 1. \quad (3.27)$$

In those parts of the expression remaining after the integration of the wave field (3.22), the further integration is performed over the limited area, which makes possible to utilize the asymptotic of Green function:

$$\Psi_{\boldsymbol{k}}(\boldsymbol{r}) \approx e^{i\boldsymbol{k}\boldsymbol{r}} + \frac{e^{ik_0\boldsymbol{r}}}{4\pi\boldsymbol{r}} T(\boldsymbol{k}_1, \boldsymbol{k});\ \boldsymbol{k}_1 = k_0\frac{\boldsymbol{r}}{r};$$
$$T(\boldsymbol{k}_1, \boldsymbol{k}) = k_0^2\chi(\omega)\int_{\boldsymbol{r}'_\perp \subset \tilde{S}_\perp} d\boldsymbol{r}'_\perp \int_0^\infty dz' e^{-i\boldsymbol{k}_1\boldsymbol{r}'} e^{ik_x x'} E^{(+)}(z'), \quad (3.28)$$

and using the formula (2.10) for calculation of the differential cross-section of X-ray scattering:

$$\frac{d\sigma}{d\Omega} = \frac{1}{(4\pi)^2}|\boldsymbol{T}(\boldsymbol{k}_0, \boldsymbol{k}_1)|^2. \quad (3.29)$$

Here the fact of the independence of the cross-section on the polarization is taken into account and the condition $\sin\theta_s = 1$ is fulfilled with the accuracy $\sim |\chi|$. For XRR experiments, the radiation scattered (reflected) into angles defined by $z < 0$, corresponding to $\boldsymbol{k}_1 = (\boldsymbol{k}_{1\perp}, k_{1z} = -\sqrt{k_0^2 - \boldsymbol{k}_{1\perp}^2})$ attracts most of interest. Substituting (3.16) into (3.28), the differential cross-section is found:

$$\frac{d\sigma}{d\Omega} = \frac{k_0^4|\chi(\omega)|^2}{(4\pi)^2}\frac{|t_F|^2}{|k_{zm} - k_{1z}|^2}\frac{16\sin^2(k_x - k_{1x})\tilde{L}_x/2}{(k_x - k_{1x})^2}\frac{\sin^2 k_{1y}\tilde{L}_y/2}{k_{1y}^2}. \quad (3.30)$$

Using the asymptotic relationship from [21], which is valid with an accuracy (3.27):

$$\frac{\sin^2 Ax}{x^2} = \pi A\delta(x),\ A \gg 1, \quad (3.31)$$

and the relationships $k_0^2\chi_0 = k_{zm}^2 - k_z^2,\ k_z = -k_{1z}$, the formula (3.30) is transformed to the following form:

$$\frac{d\sigma}{d\Omega} = \frac{|k_{zm} - k_z|^2 |t_F|^2}{4} \tilde{L}_x \tilde{L}_y \delta(k_x - k_{1x}) \delta(k_y - k_{1y}). \tag{3.32}$$

Finally, from the expression (3.12) for the Fresnel coefficients [7] and the equation

$$d\Omega = \frac{dk_{1x} dk_{1y}}{k_0 k_z}$$

for the solid angle, the integral cross-section of the scattered photons registered by the detector in the plane perpendicular to the wave vector of reflected wave $\boldsymbol{k}_1$ is obtained:

$$\sigma_D = \frac{k_z}{k_0} |r_F|^2 \tilde{L}_x \tilde{L}_y. \tag{3.33}$$

By the definition [21], the scattering cross-section is normalized to the incident flux, whereas the XRR applications [7] deal with the reflectivity: the intensity of the reflected radiation normalized to the intensity of the incident beam:

$$\begin{aligned} |R(\theta)|^2 &= \frac{\sigma_D}{L_x^{(b)} L_y^{(b)}} = |r_F|^2 F_b(\theta); \\ F_b(\theta) &= \sin\theta \frac{\tilde{L}_x \tilde{L}_y}{L_x^{(b)} L_y^{(b)}}, \end{aligned} \tag{3.34}$$

where the factor $F_b(\theta)$ is independent on the characteristics of the reflecting media and defined by the geometrical dimensions of the X-ray beam and the sample. As a rule, the beams of the sizes essentially less than the sample size are used in XRR technique, thus the conditions are fulfilled:

$$\sin\theta_b \equiv \frac{L_x^{(b)}}{L_x} < \theta_c;\ L_y^{(b)} \ll L_y,$$

which implement the factor $F_b(\theta)$ to be equal:

$$F_b(\theta) = \frac{\sin\theta}{\sin\theta_b},\ \theta < \theta_b; \quad F_b(\theta) = 1,\ \theta > \theta_b.$$

Taking into account a small angle divergence $\theta_S < \theta_b$ of X-ray sources in XRR experiments, the averaging procedure results in the following modification of formula (3.34):

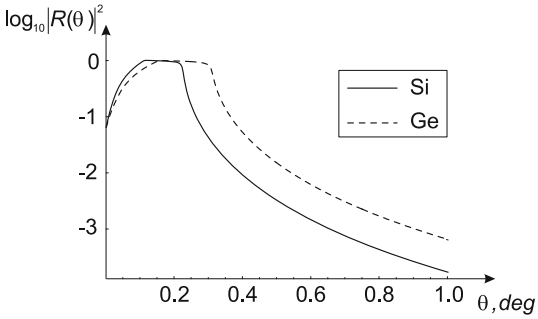

Fig. 3.5 X-ray reflectivity calculated for the same sample parameters as in Fig. 3.4, but with geometrical factor ($\theta_S = 0.5\theta_b = 0.25\theta_c$)

$$|R(\theta)|^2 = |r_F|^2 \bar{F}_b(\theta);$$

$$\bar{F}_b(\theta) \approx \frac{1}{2\theta_S\theta_b}\left(\theta + \frac{\theta_S}{2}\right)^2, \ \theta < \frac{\theta_S}{2};$$

$$\bar{F}_b(\theta) \approx \frac{\theta}{\theta_b}, \ \frac{\theta_S}{2} < \theta < \theta_b; \quad \bar{F}_b(\theta) = 1, \ \theta > \theta_b. \tag{3.35}$$

Figure 3.5 shows how the reflectivity is deviated from the Fresnel reflection after accounting of geometrical factors.

3.2 Reflection of X-Ray Radiation from Rough Surface

The modeling of the sample surface as an ideally flat plane used in previous section is a very limiting approximation for the description of real samples. This approximation is valid in the case when the linear dimension l of microscopic (atomic) heterogeneities on the surface are small comparing to the lateral wavelength of X-ray beam $\lambda_\parallel \approx \lambda/\theta_c \sim 10^2$ nm. However, the majority of the samples investigated by XRR technique possesses the mesoscopic heterogeneities $l_i \geq \lambda_\parallel$, so called roughness, which is implemented during the sample growth and treatment (Fig. 3.6). This imperfection modifies the intensity of the specularly reflected X-ray wave and yields the radiation scattered at the angles different than incidence angle and known as *diffuse X-ray scattering*.

Theoretical description of specular and off-specular (diffuse) X-ray scattering from rough surfaces and interfaces is of special importance for the analysis of modern semiconductor and other nanoscale devices. As it has been demonstrated in one of the pioneering work in this field [22], the imperfection of surfaces and interfaces is not comprehensively described by only root mean square of the roughness amplitude σ; the roughness correlation length L_c and fractal dimension $(3 - h)$, where h is a Hurst parameter, have to be considered, too.

The most effective method for calculation of X-ray scattering from rough surfaces is proved to be distorted-wave Born approximation (DWBA), which is extensively

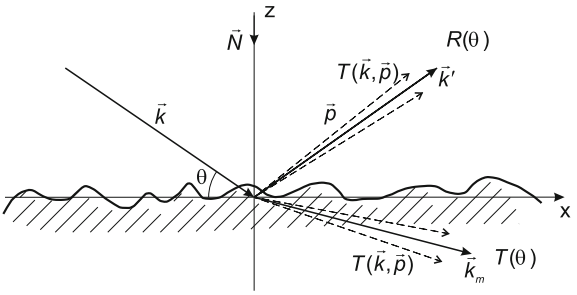

Fig. 3.6 Scattering of X-ray radiation from the surface possessing roughness. The intensity of the specularly reflected $R(\theta)$ and transmitted $T(\theta)$ waves are modified due to the scattering of radiation at different then specular angles (diffuse scattering) and are expressed through the scattering amplitude $T(\boldsymbol{k}, \boldsymbol{p})$ for various wave vectors $\boldsymbol{p}$ in a final state

described in literature (see, for example, [7]). For zeroth approximation of DWBA, either the specular reflection from perfect plane interface (Fresnel reflection) or the reflection from interface modeled by transition layer with profile delivering an exact solution [11] are usually used. The roughness correlations are taken into account in the first-order DWBA on the deviation of real scattering surface from the model one.

The diffuse X-ray scattering leads to the reduction of the intensity of specular (coherent) reflection due to the conservation of the radiation flux. To calculate this loss, typically the semi-phenomenological Debye-Waller $F_{DW} = \exp(-2k_z^2\sigma^2)$ or Nevot-Croce [23] $F_{NC} = \exp(-2k_z k_{zm}\sigma^2)$ factor is used, which, however, depends not on the roughness correlations but solely on the parameter σ. However, the reflection coefficient from rough surface, as shown in [8–10, 22], depends also on the roughness correlations. This dependence is described by second-order DWBA, and both F_{DW} and F_{NC} are derived as limiting cases for the magnitude of roughness correlation. The re-normalization of the coefficient $R_s(\theta)$ in [8–10] has been performed with the accuracy of the 2nd order DWBA on the imperfection of the surface. As a result, the specular reflection coefficient depends both on the parameter σ and on the roughness correlation. For the large scattering angles, the phenomenological "exponentiating" operation was applied to $R_s(\theta)$, which calculated the first and the second DWBA approximations by expanding the exponent into series. In real experiments, however, the exponential behavior of $R_s(\theta)$ at large angles has not been observed [24]. For example, for long correlation length L_c roughness, the X-ray scattering is close to the one from perfect surface, where $R_s(\theta)$ is decayed as $R_s(\theta) \sim \theta^{-2}$ with the increase of scattering angle. Moreover, the above assumption is not self-consistent: any re-normalization of the Fresnel reflection coefficient is equivalent to introduction of transition layer at interface [11], whereas the solutions for perfect interface are used for calculation of the corrections for reflection coefficient and diffuse scattering intensity. Another semi-phenomenological description of exponential behavior of reflection coefficient at large scattering angles θ has been done in [24].

The main goal of the present section is description of the method for calculation of specularly reflected intensity from rough surfaces and interfaces without any phenomenological assumptions. It is based on the solution of the X-ray scattering problem from transition layer with arbitrary profile $\Lambda(z)$ has been reported [13],

which delivers analytical expression for reflection and transmission coefficients from profile $\Lambda(z)$ with a high accuracy. The self-consistent approach for the specular and diffuse scattering for high order DWBA was then formulated in [16].

In accordance with the previous section the polarization effects are negligible for X-rays and thus the propagation of electromagnetic wave with arbitrary polarization is described by the solution $\phi_{\boldsymbol{k}}(\boldsymbol{r})$ of the scalar wave Eq. (2.2):

$$[\Delta + k_0^2 + V(\boldsymbol{r})]\phi_{\boldsymbol{k}}(\boldsymbol{r}) = 0, \tag{3.36}$$

with standard asymptotical boundary conditions, which correspond to the scattering on the unlimited in the direction x surface [11]:

$$\begin{aligned} \phi_{\boldsymbol{k}}(\boldsymbol{r}) &\sim e^{i\boldsymbol{kr}} + R(\boldsymbol{k}, \boldsymbol{p})\, e^{i\boldsymbol{pr}},\ p_z < 0,\ z \to -\infty, \\ \phi_{\boldsymbol{k}}(\boldsymbol{r}) &\sim T(\boldsymbol{k}, \boldsymbol{p})\, e^{i\boldsymbol{pr}},\ p_z > 0,\ z \to \infty, \end{aligned} \tag{3.37}$$

where $\boldsymbol{k}$ is the wave vector of incident and $\boldsymbol{p}$ of scattered ($p^2 = k_0^2$) waves, respectively; $R(\boldsymbol{k}, \boldsymbol{p}), T(\boldsymbol{k}, \boldsymbol{p})$ are the amplitudes of the reflected and transmitted waves; the condition $\boldsymbol{p}_\perp = \boldsymbol{k}_\perp$ defines the case of specular reflection and $\boldsymbol{p}_\perp \neq \boldsymbol{k}_\perp$ is the case of diffuse scattering [22].

The angle $\theta \sim \theta_c = \sqrt{|\chi|} \ll 1$, corresponding to effective interaction length $l \sim \lambda\theta^{-1}$, plays an essential role in the scattering from surface. Because of the value of l exceeds essentially the atomic dimension, the interaction potential between X-rays and semi-infinite media is determined from the expression [11]:

$$V(\boldsymbol{r}) = k_0^2 \chi(\omega) H[z - z_0(x, y)], \tag{3.38}$$

where $H[z - z_0(x, y)]$ is the Heaviside function with random function argument $z_0(x, y)$ defining the surface roughness (Fig. 3.6). The ideal, perfectly smooth surface corresponds to $z_0 = 0$.

The main problem in the solving of the Eq. (3.36) is that the function $\phi_{\boldsymbol{k}}(\boldsymbol{r})$ is a complex non-linear functional of random function $z_0(x, y)$. This fact does not permit to construct a closed equation for function $\langle\phi_{\boldsymbol{k}}(\boldsymbol{r})\rangle$ averaged over the distribution $z_0(x, y)$. The common solution for this problem in X-ray reflectometry is based on the proportionality of the amplitude of specular (coherent) reflection to entire sample surface $\sim S$. At the same time, the amplitude of diffuse (incoherent) scattering is proportional to $\sim \sqrt{S}$ and is small even for large roughness, that makes possible to take it into account by DWBA [11]. The potential (3.38) can be written in the form:

$$\begin{aligned} V(\boldsymbol{r}) &= V_0(z) + \xi V_1(\boldsymbol{r}) \equiv V_0(z) + \xi\{k^2 \chi H[z - z_0(x, y)] - V_0(z)\}, \\ V_0(z) &\equiv k^2 \chi(\omega) \Lambda(z), \end{aligned} \tag{3.39}$$

where $V_0(z)$ is one-dimensional coherent potential of transition layer, taking into account the influence of roughness on specular reflectivity; the dimensionless function $\Lambda(z)$ defines the profile of this layer [11], and by definition $\Lambda(z) \to 0,\ z \to$

$-\infty,\ \Lambda(z) \to 1,\ z \to \infty$. The formal parameter ξ is introduced to order the terms of the perturbation series on their smallness, and in the final expressions it will be set to $\xi = 1$. Using potential (3.39), Eq. (3.36) is transformed to the integral equation:

$$\phi_{\boldsymbol{k}}(\boldsymbol{r}) = \phi_{\boldsymbol{k}}^{(0)}(\boldsymbol{r}) - \xi \int d\boldsymbol{r}' G_k(\boldsymbol{r}, \boldsymbol{r}') V_1(\boldsymbol{r}') \phi_{\boldsymbol{k}}(\boldsymbol{r}'). \tag{3.40}$$

The zeroth approximation $\phi_{\boldsymbol{k}}^{(0)}(\boldsymbol{r})$ is derived from the equation with potential $V_0(z)$:

$$[\Delta + k_0^2 + V_0(z)]\phi_{\boldsymbol{k}}^{(0)}(\boldsymbol{r}) = 0,\ \phi_{\boldsymbol{k}}^{(0)}(\boldsymbol{r}) = e^{i\boldsymbol{k}_\perp \boldsymbol{r}} \varphi_{k_z}(z), \tag{3.41}$$

and boundary conditions for one-dimensional wave equation are:

$$\begin{aligned} \left[\frac{d^2}{dz^2} + k_z^2 + k_0^2 \chi \Lambda(z)\right] \varphi_{k_z}(z) = 0,\ k_z = \sqrt{k_0^2 - k_\perp^2}, \\ \varphi_{k_z}(z) \sim e^{ik_z z} + R^{(0)}(k_z)\, e^{-ik_z z},\ z \to -\infty, \\ \varphi_{k_z}(z) \sim T^{(0)}(k_z)\, e^{ik_{1z} z},\ k_{1z} = \sqrt{k_z^2 + k_0^2 \chi},\ z \to \infty, \end{aligned} \tag{3.42}$$

which deliver the zeroth approximation $R^{(0)}(k_z)$ for the specular reflection coefficient. The Green function $G_k(\boldsymbol{r}, \boldsymbol{r}')$ satisfies the following equation:

$$\{\Delta + k_0^2 + V_0(z)\} G_k(\boldsymbol{r}, \boldsymbol{r}') = \delta(\boldsymbol{r} - \boldsymbol{r}'), \tag{3.43}$$

and according to general theory of differential equations can be expressed [8–10] through two fundamental solutions of the Eq. (3.42):

$$\begin{aligned} G_k(\boldsymbol{r}, \boldsymbol{r}') = \int_{|\boldsymbol{k}'_\perp| < k} \frac{d\boldsymbol{k}'_\perp}{4\pi^2} e^{i\boldsymbol{k}_\perp(\boldsymbol{r} - \boldsymbol{r}')} g_{k'_z}(z, z'),\ k'_z = \sqrt{k^2 - k_\perp'^2}, \\ g_{k'_z}(z, z') = -\frac{\varphi_{k'_z}(z_1)\varphi_{-k'_z}(z_2)}{W},\ z_1 = \min(z, z'),\ z_2 = \max(z, z'), \\ W = \varphi_{-k'_z} \frac{d\varphi_{k'_z}}{dz} - \varphi_{k'_z} \frac{d\varphi_{-k'_z}}{dz}. \end{aligned} \tag{3.44}$$

Using Eqs. (3.42)–(3.44) and iteration scheme for approximate solution of the Eq. (3.40), the formal series of DWBA approximations can be obtained for the scattering amplitude $T(\boldsymbol{k}, \boldsymbol{p})$. The square of this amplitude delivers in the differential cross-section of X-ray scattering in half plane $z < 0$ [8–10]. The explicit expressions for the terms of this series up to the second order of potential $V_1(\boldsymbol{r})$, i.e. parameter ξ, are:

$$\begin{aligned} T(\boldsymbol{k}, \boldsymbol{p}) \approx T^{(0)}(\boldsymbol{k}, \boldsymbol{p}) + \xi T^{(1)}(\boldsymbol{k}, \boldsymbol{p}) + \xi^2 T^{(2)}(\boldsymbol{k}, \boldsymbol{p}) + \ldots \\ T^{(0)}(\boldsymbol{k}, \boldsymbol{p}) = R^{(0)}(k_z)(2\pi)^2 \delta(\boldsymbol{p}_\perp - \boldsymbol{k}_\perp); \end{aligned}$$

$$
\begin{aligned}
R^{(0)}(k_z) &= \int dz e^{ik_z z} V_0(z)\varphi_{k_z}, \\
T^{(1)}(\boldsymbol{k}, \boldsymbol{p}) &= \int d\boldsymbol{r} e^{i(\boldsymbol{p}_\perp - \boldsymbol{k}_\perp)\boldsymbol{r}} \varphi^*_{-k_z} V_1(\boldsymbol{r})\varphi_{p_z}, \\
T^{(2)}(\boldsymbol{k}, \boldsymbol{p}) &= \int d\boldsymbol{r} d\boldsymbol{r}' \int_{|\boldsymbol{k}'_\perp|<k} \frac{d\boldsymbol{k}'_\perp}{k'_z} e^{i(\boldsymbol{k}'_\perp - \boldsymbol{k}_\perp)\boldsymbol{r}} e^{i(\boldsymbol{p}_\perp - \boldsymbol{k}'_\perp)\boldsymbol{r}'} \\
&\quad \times \varphi^*_{-k_z}(z) V_1(\boldsymbol{r}) \varphi_{k'_z}(z) \varphi^*_{-k'_z}(z') V_1(\boldsymbol{r}') \varphi_{p_z}(z'),
\end{aligned}
\tag{3.45}
$$

where $R^{(0)}(k_z)$ is the specular reflection coefficient from the interface with profile $\Lambda(z)$. The observed differential cross-section of X-ray scattering is calculated in accordance with general formula (2.10):

$$
\frac{d\sigma}{d\Omega} = \frac{1}{16\pi^2} \langle |T(\boldsymbol{k}, \boldsymbol{p})|^2 \rangle, \tag{3.46}
$$

after averaging $\langle \ldots \rangle$ over the ensemble of random functions $z_0(x, y)$. In zeroth approximation, the only specular reflection $\sim |R^{(0)}(k_z)|^2$ is obtained from Eq. (3.45). The diffuse scattering [22] is caused by the fluctuations of the scattering square amplitude, i.e. appears in the first-order DWBA $\sim \xi^2(\langle |T^{(1)}(\boldsymbol{k}, \boldsymbol{p})|^2 \rangle - |\langle T^{(1)}(\boldsymbol{k}, \boldsymbol{p}) \rangle|^2)$. Thus, its contribution to the cross-section has the same order as the term depending on the second order DWBA $\sim \xi^2 R^{(0)}(k_z) \langle T^{(2)}(\boldsymbol{k}, \boldsymbol{p}) \rangle$, and therefore, for calculation of the scattering cross-section both contributions have to be taken into account. The validity conditions for presented approach coincide rather with the validity area of DWBA than one of perturbation theory. Concerning the validity of DWBA convergence, it might be defined by the ratio of the spectral intensity of specular reflection to diffusely scattered intensity [11]. This is small because of the cross-section of X-ray scattering from averaged potential $V_0(z)$ is proportional to the square of sample surface S, whereas scattering from fluctuations depends on the roughness *rms*, correlation length and scattering angle.

To use formulas (3.44)–(3.46), the analytical expression for the profile of zeroth approximation $\Lambda(z)$ has to be chosen, and then the explicit expression for $\varphi_{k_z}(z)$ has to be found. In meantime, definite distribution model for the ensemble of random functions $z_0(x, y)$ has to be selected. It is widely used (for example, [8–10]), the perfect plane interface is selected as zeroth approximation, which is a typical choice for DWBA applications:

$$
\begin{aligned}
\Lambda(z) &\approx \Lambda_0(z) = H(z), \\
\varphi^{(0)}_{k_z}(z) &= (e^{ik_z z} + r_F e^{-ik_z z}) H(-z) + t_F e^{ik_{1z} z} H(z),
\end{aligned}
\tag{3.47}
$$

where r_F and t_F are the Fresnel reflection and transmission coefficients for ideal surface (3.14) . For this choice of initial profile, the first- and second-order DWBA corrections for specular reflection coefficient, accounting roughness correlations, can be calculated [8–10]. For small scattering angles, the specular reflection coefficient

varies in dependence on roughness correlations within the limits:

$$r_F(k_z)(1-2\sigma^2k_z^2) < R_s(k_z) < r_F(k_z)(1-2\sigma^2k_zk_{1z}). \tag{3.48}$$

At small scattering angles $k_z\sigma \ll 1$, the calculations of [8–10] are completely microscopical. They demonstrate that reconstruction of transition layer, which influences the reflection coefficient, depends both on averaged roughness and roughness correlations. However, at larger scattering angles the formula for specular reflection (3.48) fails, and accounting of high order terms in (3.40) is necessary, which is difficult to realize in practice. Commonly accepted approach to solve this problem is an additional phenomenological assumption about terms in parentheses in (3.48), which are supposed to be the first terms in the expansion over parameter $k_z\sigma$ of Gaussian exponent ("exponentiating" operation). The latter makes a re-normalization of the reflection coefficient:

$$\begin{aligned} &r_F(k_z)e^{-W_{DW}} < R_s(k_z) < r_F(k_z)e^{-W_{NC}};\\ &e^{-W_{DW}} = e^{-2\sigma^2k_z^2}; \quad e^{-W_{NC}} = e^{-2\sigma^2k_zk_{1z}}. \end{aligned} \tag{3.49}$$

Depending on the correlations, this exponent reduces to Debye-Waller ($e^{-W_{DW}}$) or Nevot-Croce exponent ($e^{-W_{NC}}$) [8–10]. Let us note that in the same approximation the Fresnel transmission coefficient should be also re-normalized [7]:

$$t_F(k_z) \to t_F(k_z)e^{\frac{\sigma^2}{2}(k_z-k_{zm})^2} \tag{3.50}$$

This simple re-normalization describes well experimental data, when measured sample possesses a roughness of small amplitude. However, for larger σ values, the observed $R_s(k_z)$ may considerably differ from exponential one. Therefore, for large roughnesses the alternative phenomenological approximation has been proposed [24], which introduces additional parameter, a maximal roughness amplitude. This approach is proved to describe well experimental data from sample with very rough surface, as shown in [24]. Nevertheless, the solution of the following problem remains actual and demanded: is a microscopical description of the reflection from imperfect surface possible for arbitrary scattering angles by low orders DWBA and without any additional assumptions?

The physical reason for necessity of the re-normalization of specular reflection coefficient is the conservation of the photons flux. The emission of the diffuse X-ray scattering is compensated by the reduction of the intensity of specular reflection [8–10]. The calculated intensity of diffuse scattering depends on the DWBA order applied, therefore the corrections for $R^{(0)}(k_z)$ also vary in each higher DWBA approximation. These corrections, however, can not be summed up in general case, which causes the phenomenological modeling of $R^{(0)}(k_z)$ in conventional theories.

The key point of the proposed self-consistent approach is to do not fix the profile of the transition layer initially, but to consider

$$\Lambda^{(0)}(z) \Rightarrow \Lambda(k_z, z) \tag{3.51}$$

as a variational function changing with DWBA order and depending on k_z. This additional degree of freedom can be used for transformation of differential cross-section of X-ray scattering, simulated on the basis of DWBA. The physical meaning of variational profile dependence on k_z is conditioned by the dependence of averaged within the higher DWBA orders surface potential on the projection of correlation length onto the incidence beam.

Assume that differential cross-section of X-ray scattering (3.45) is calculated with the accuracy up to the second order of ξ. Then performing an averaging over ensemble of random functions $z_0(x, y)$, it is expressed as:

$$\begin{aligned}
\frac{d\sigma}{d\Omega} &= \frac{1}{16\pi^2}|T(\boldsymbol{k}, \boldsymbol{p})|^2; \\
|T(\boldsymbol{k}, \boldsymbol{p})|^2 &= \{|T^{(0)}(\{\Lambda(k_z, z)\}) + \xi\langle T^{(1)}(\{\Lambda(k_z, z))\}\rangle|^2 \\
&\quad + 2\xi^2\Re[T^{(0)*}(\{\Lambda(k_z, z)\})\langle T^{(2)}(\{\Lambda(k_z, z)\})\rangle]\} \\
&\quad + \xi^2[\langle|T^{(1)}(\boldsymbol{k}, \boldsymbol{p})|^2\rangle - |\langle T^{(1)}(\boldsymbol{k}, \boldsymbol{p})\rangle|^2].
\end{aligned} \tag{3.52}$$

All the terms in this expression are the functionals of the profile $\Lambda(k_z, z)$. This profile can be chosen in such a way that the sum of all terms in specular reflection ($\boldsymbol{p}_\perp = \boldsymbol{k}_\perp$), except first one, equals to zero:

$$\begin{aligned}
\{\xi^2\{|\langle T^{(1)}(\{\Lambda(k_z, z))\}\rangle|^2 + [\langle|T^{(1)}(\boldsymbol{k}, \boldsymbol{p})|^2\rangle - |\langle T^{(1)}(\boldsymbol{k}, \boldsymbol{p})\rangle|^2]\} \\
+ 2\Re\{T^{(0)*}(\{\Lambda(k_z, z)\})[\xi\langle T^{(1)}(\{\Lambda(k_z, z)\})\rangle \\
+ \xi^2\langle T^{(2)}(\{\Lambda(k_z, z)\})\rangle]\}\}_{(\boldsymbol{p}_\perp = \boldsymbol{k}_\perp)} = 0.
\end{aligned} \tag{3.53}$$

The solution to this functional equation delivers the function $\Lambda(k_z, z)$, which is a profile of the transition layer, and the specular reflection coefficient is:

$$R(k_z) \approx T^{(0)}(k_z, \{\Lambda(k_z, z)\}), \tag{3.54}$$

with already performed re-normalization. Thus, the scattering cross-section for all exit angles is separated into coherent specular and incoherent diffuse scattering.

In order to realize the algorithm (3.51)–(3.54) the principle problem has to be considered: the analytical solution of the zeroth-order Eq. (3.43) for arbitrary profile $\Lambda(z)$ should be found. This solution has been proposed in Refs. [13, 16] on the basis of the following analysis.

Let us consider the wave field $E(z)$ of monochromatic X-ray beam reflected from the substrate with one-dimensional transition layer on the top is defined by equation:

$$\left[\frac{d^2}{dz^2} + q^2 + V\varphi(z)\right] E(z) = 0. \tag{3.55}$$

As before the z-axis is assumed to be perpendicular to the surface of substrate; the in-plane component of the wave vector is conserved and the normal z-component is defined for the convenience as $k_z \equiv q = k_0 \sin\theta$; function $\varphi(z)$ determines the normalized potential of transition layer with amplitude $V = k_0^2\chi(\omega)$, the conditions $\varphi(-\infty) = 0$ and $\varphi(\infty) = 1$ are fulfilled.

The integral form of equation (3.55) with the Green function (3.23) is:

$$E(z) = Ae^{iqz} + Be^{-iqz} + \frac{V}{2iq}\left\{e^{iqz}\int_z^\infty dz' e^{-iqz'}\varphi(z')E(z') + e^{-iqz}\int_{-\infty}^z dz' e^{iqz'}\varphi(z')E(z')\right\}. \tag{3.56}$$

Direct iterations of this equation with constants A and B following from the boundary conditions result in Born series of perturbation theory. If one uses in the integral part of the Eq. (3.56) the wave field corresponding to the ideal interface

$$E_0(z) = [e^{iqz} + r_F e^{-iqz}]H(-z) + t_F e^{-ipz}H(z);\ \ p^2 = q^2 + V, \tag{3.57}$$

the Rayleigh approximation (re-normalized Born approximation) for the reflection coefficient $R_B(q)$ from the interface with transition layer can be calculated in the following form [25]:

$$R_B(q) = r_F\int_{-\infty}^\infty dz\frac{d\varphi}{dz}e^{2iqz}. \tag{3.58}$$

This formula is widely used for solution of the inverse problem [5] because in this case the density profile is simply connected with the Fourier transformation of the reflection coefficient. However this approximation is not available for all values of the system parameters. Especially it concerns to phase of the reflection coefficient.

Self-consistent approach [12] for solution of Eq. (3.56) assumes the use of another approximate form $E_0(z)$ for function $E(z)$ and finding of parameters for this form by Eq. (3.56). Specifically, in Ref. [12] function $E_0(z)$ has been taken as the solution of the wave equation for sharp interface with variable position z_0 of interface. This solution improves essentially the perturbation theory, but does not eliminate the ambiguity in reflection and transmission coefficients because of dependence on the self-consistency mode and it does not allow to calculate the successive corrections for zeroth approximation.

It is possible to formulate another self-consistent ansatz for $E(z)$ [13, 16]. Let us redefine the potential function and solutions in the following way (Fig. 3.7):

$$\begin{aligned}\varphi(z) &= H(z-\sigma) + \lambda(z)H(\sigma - z)H(z+\sigma)\\ E(z) &= H(-z-\sigma)[e^{iqz} + Re^{-iqz}]\\ &\quad + u(z)H(\sigma - z)H(z+\sigma) + H(z-\sigma)Te^{ipz}.\end{aligned} \tag{3.59}$$

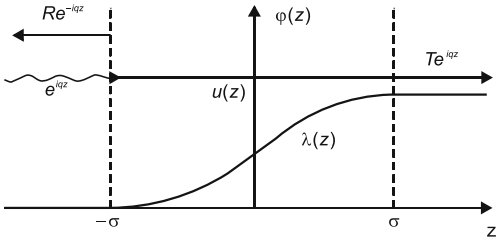

Fig. 3.7 Sketch of the scattering wave fields and potential of the transition layer

Here $H(z)$ is the Heaviside function; $\lambda(z)$ is a potential function varied from zero to unity inside the transition layer located between the planes with coordinates $\pm\sigma$ (in general case can be chosen as $\sigma \to \infty$); coefficients R and T in function $E(z)$ are the exact coefficients of reflection and transmission. By definition, function $E(z)$ describes the transmitted wave at $z = +\infty$ if the condition is satisfied:

$$p^2 = q^2 + V \equiv k_{zm}^2. \tag{3.60}$$

The function $u(z)$ is defined within the interval $|z| < \sigma$ and satisfies the boundary conditions at $z = \pm\sigma$, as follows from the discontinuity condition for the solution:

$$u(\sigma) = Te^{ip\sigma}; \qquad u(-\sigma) = Re^{iq\sigma} + e^{-iq\sigma}. \tag{3.61}$$

Substituting (3.59) into (3.56), we derive the equation:

$$Ae^{iqz} + Be^{-iqz} + \frac{V}{2iq} e^{iqz} \left\{ \int_{-\sigma}^{\sigma} d\xi e^{-iq\xi} \lambda(\xi) u(\xi) + \int_{\sigma}^{\infty} d\xi e^{-iq\xi} T e^{ip\xi} \right\} = e^{iqz} + Re^{-iqz}; \quad z < -\sigma$$

$$Ae^{iqz} + Be^{-iqz} + \frac{V}{2iq} \left\{ e^{-iqz} \left[\int_{-\sigma}^{\sigma} d\xi e^{iq\xi} \lambda(\xi) u(\xi) + \int_{\sigma}^{z} d\xi e^{iq\xi} T e^{ip\xi} \right] + e^{iqz} \int_{z}^{\infty} d\xi e^{-iq\xi} T e^{ip\xi} \right\} = Te^{ipz}; \quad z > \sigma$$

$$Ae^{iqz} + Be^{-iqz} + \frac{V}{2iq} \left\{ e^{iqz} \int_{\sigma}^{\infty} d\xi e^{-iq\xi} T e^{ip\xi} \right.$$

$$+e^{iqz}\int_{z}^{\sigma} d\xi e^{-iq\xi}\lambda(\xi)u(\xi) + e^{-iqz}\int_{-\sigma}^{z} d\xi e^{-iq\xi}\lambda(\xi)u(\xi)\Bigg\}$$
$$= u(z); \quad -\sigma < z < \sigma. \tag{3.62}$$

Equating the coefficients at fast-oscillating exponents in both parts, the constants are found to be $A = 0; \quad B = R$, whereas the reflection and transmission coefficients and the function $u(z)$ should be defined from the equations:

$$R + \frac{VT}{2q(p+q)}e^{i(p+q)\sigma} + \frac{V}{2iq}\int_{-\sigma}^{\sigma} d\xi e^{iq\xi}\lambda(\xi)u(\xi) = 0;$$
$$\frac{VT}{2q(p-q)}e^{i(p-q)\sigma} + \frac{V}{2iq}\int_{-\sigma}^{\sigma} d\xi e^{-iq\xi}\lambda(\xi)u(\xi) = 1;$$
$$u(z) = Re^{-iqz} + \frac{VT}{2q(p-q)}e^{i(p-q)\sigma}e^{iqz}$$
$$+\frac{V}{2iq}\int_{-\sigma}^{\sigma} d\xi[e^{iq(z-\xi)}H(\xi - z) + e^{-iq(z-\xi)}H(z-\xi)]\lambda(\xi)u(\xi). \tag{3.63}$$

The system of Eqs. (3.62) for function $u(z)$ along with boundary conditions (3.61) is the exact consequence of primary integral equation. However, the advantage of it is the implicit form of fast oscillating terms in equations, that permits to solve the integral equation for function $u(z)$ within the limited interval, and latter function is parametrized mainly by the potential function $\lambda(z)$. To approximately calculate the self-consistent values $R(q)$ and $T(q)$, some model form (ansatz) for function $u(z)$ has to be chosen. This model function is expected to satisfy the following conditions: (i) its variation is mainly determined by potential function, (ii) it satisfies the boundary conditions (3.61), (iii) it does not include any additional parameters. The simplest representation of $u(z)$, fulfilling the mentioned conditions, is:

$$u_0(z) = \lambda(z)Te^{ipz} + [1 - \lambda(z)](Re^{-iqz} + e^{iqz}). \tag{3.64}$$

Ansatz (3.64) is the basic expression of the self-consistent approach and it can be considered as the zeroth-order iteration for solution of integral Eq. (3.62). The substitution of this ansatz into Eq. (3.63) results in self-consistent equations for calculation of reflection and transmission coefficients through the potential function:

$$\left[1 - i\frac{VK(0)}{2q}\right]R(q) + \frac{VL(p+q)}{q(p+q)}T(q) = i\frac{VK(2q)}{2q};$$
$$-i\frac{VK(-2q)}{2q}R(q) + \frac{VL(p-q)}{q(p-q)}T(q) = 1 + i\frac{VK(0)}{2q};$$

$$K(r) = \int_{-\sigma}^{\sigma} dz e^{irz} \lambda(z)[1 - \lambda(z)]; \quad L(r) = \int_{-\sigma}^{\sigma} dz e^{irz} \lambda(z)\lambda'(z), \tag{3.65}$$

from which the result for zeroth-order approximation follows:

$$\begin{aligned} R(q) &= \frac{D_R}{\Delta}; \quad T(q) = \frac{D_T}{\Delta}; \\ D_R &= iV^2[K(2q)L(p-q)(p+q) - K(0)L(p+q)(p-q)] \\ &\quad - 2qVL(p+q)(p-q); \\ D_T &= \frac{V}{2}\{V^2[K^2(0) - K(2q)K(-2q)] + 4q^2\}; \\ \Delta &= iV^2[K(-2q)L(p+q)(p-q) - K(0)L(p-q)(p+q)] \\ &\quad + 2qVL(p-q)(p+q). \end{aligned} \tag{3.66}$$

Equation (3.66) confirms the fact, that self-consistent calculation of reflection and transmission coefficients permits to express them directly through the density profile of transition layer, though this relation is more complicated than for Born approximation. The successive approximations for coefficients can be easily found because of Eq. (3.63) is obtained from the exact integral equation for function $u(z)$. The procedure for finding $u^{(1)}(z)$ is the following: the Eq. (3.62) is iterating and new solutions are substituted into expressions for reflection and transmission coefficients. It was shown for series of potentials [13], that these iterations converged very quickly and zeroth approximation was proved to be very accurate and sufficient for experimental data interpretation.

The presented self-consistent approach (SCA) for solution of Maxwell's equations is a direct analogue of operator method for Schrödinger equation, which is proved to be effective for the solution of many problems of quantum mechanics [26]. The coincidence of the zeroth approximation with the exact solution in limiting cases, where the analytical methods can be used, is shown in Ref. [26] to be an important feature of any uniformly suitable approximation. For studied here case with arbitrary potential, such analytical results can be found in two limit cases. The first one is the region of incidence angles less than critical angle of total external reflection ($q^2 < |V|$), where the equation $p = \sqrt{q^2 + V} = i\kappa$ is fulfilled. For real potential, the integrals for SCA are represented as $K(q) = K^*(-q)$; $L(q) = L^*(-q)$, and substitution of these equations into Eq. (3.66) demonstrates the fulfillment of the SCA zeroth approximation to the exact condition in considered angular range:

$$|R^{(0)}(q)|^2 = 1, \quad q^2 < |V|. \tag{3.67}$$

In the second limit case of large incidence angles ($q^2 \gg |V|$), one can use the following estimations for integrals:

$$K(q) = -\frac{i}{q}\left[\int_{-\sigma}^{\sigma} dz e^{iqz}\lambda'(z) - L(q)\right]; \quad L(q) \simeq \frac{e^{iq\sigma}\lambda'(\sigma)}{iq} + O(q^{-2});$$

$$L(p-q) \simeq \frac{i(p-q)}{2}\left[\sigma - \int_{-\sigma}^{\sigma} dz\lambda^2(z)\right]. \quad (3.68)$$

Substituting these expressions into the Eq. (3.66), the reflectivity is written as:

$$R^{(0)}(q) \simeq \frac{V}{2q^2}\int_{-\sigma}^{\sigma} dz e^{2iqz}\lambda'(z),$$

i.e. for large value of q, SCA zeroth approximation is equivalent to Born approximation (3.58), which is asymptotically exact at large angles.

Thus, the proposed ansatz is believed to be a uniformly suitable approximation for electromagnetic wave field, scattered from one-dimensional graded interface, since it satisfies to all the limiting cases and its successive approximations converge to the exact solution.

As an example, Fig. 3.8 compares the results of various methods for the Epstein profile [27] widely used to model the transition layer in reflectometry:

$$\varphi_E(z) = \frac{1}{2}\left[1 + \tanh(z/\sigma_E)\right]. \quad (3.69)$$

An exact formulas for coefficients are well-known for this case (see, e.g., Ref.[11]):

$$R_E(q) = -\frac{q+p}{q-p}\frac{\Gamma(iq\sigma_E)}{\Gamma(-iq\sigma_E)}\frac{\Gamma^2[-i(q+p)\sigma_E/2]}{\Gamma^2[i(q-p)\sigma_E/2]};$$
$$T_E(q) = \frac{q+p}{2p}\frac{\Gamma^2[-i(q+p)\sigma_E/2]}{\Gamma(-iq\sigma_E)\Gamma(-ip\sigma_E)}, \quad (3.70)$$

and integrals from Eq. (3.65) are also expressed analytically for this potential:

$$K(r) = \frac{\pi\sigma_E^2 r}{4\sinh(\pi\sigma_E r/2)};$$
$$L(r) = \frac{\pi\sigma_E r(1 + i\sigma_E r/2)}{4\sinh(\pi\sigma_E r/2)}. \quad (3.71)$$

Let us use the ansatz (3.64) for solution of the Eq. (3.43):

$$\varphi_{k_z}(z) = \Lambda(z)T^{(0)}e^{ik_{1z}z} + [1 - \Lambda(z)](R_s^{(0)}e^{-ik_z z} + e^{ik_z z}), \quad (3.72)$$

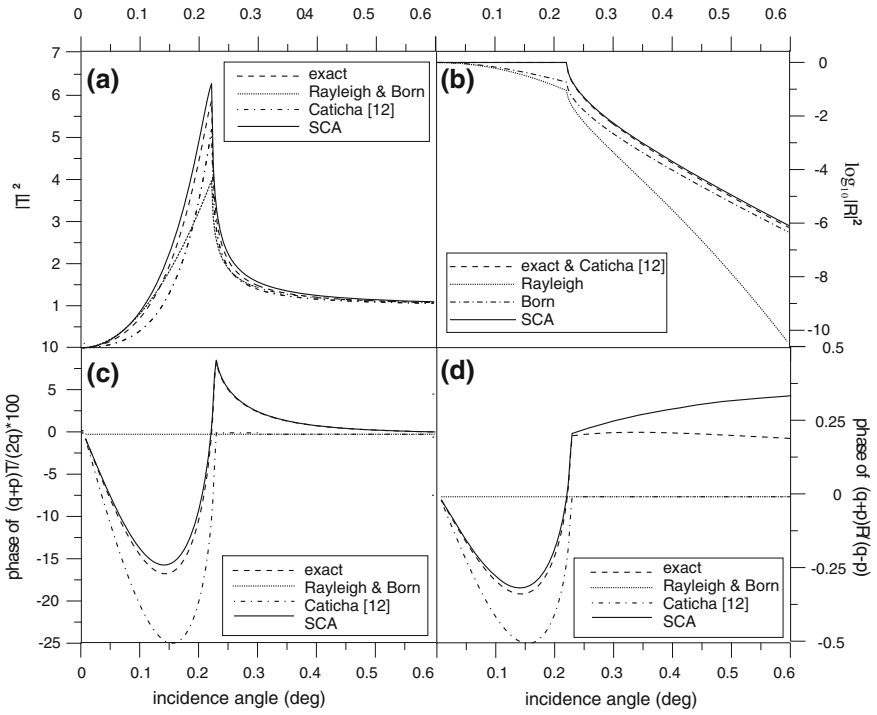

Fig. 3.8 Reflection (decimal logarithmic scale) and transmission coefficients and their phases (in radians) calculated by various methods for the Epstein profile

with the coefficients being the functionals of the profile $\Lambda(z)$ and amplitude of the potential $A = k_0^2\chi(\omega)$:

In this case the specular reflection and transmission coefficients in (3.72) are expressed through the potential amplitude A in and integrals (3.71) with function $\Lambda(z)$:

$$
\begin{aligned}
R_s^{(0)}(k_z) &= \frac{D_R(k_z)}{\Delta(k_z)}; \quad T^{(0)}(k_z) = \frac{D_T(k_z)}{\Delta(k_z)};\\
D_R(k_z) &= iA[K(2k_z)L(k_{zm}-k_z)(k_{zm}+k_z)\\
&\quad - K(0)L(k_{zm}+k_z)(k_{zm}-k_z)] - 2k_zL(k_{zm}+k_z)(k_{zm}-k_z);\\
\Delta(k_z) &= iA[K(-2k_z)L(k_{zm}+k_z)(k_{zm}-k_z)\\
&\quad - K(0)L(k_{zm}-k_z)(k_{zm}+k_z)] + 2k_zL(k_{1z}-k_z)(k_{1z}+k_z);\\
D_T(k_z) &= A^2[K^2(0) - K(2k_z)K(-2k_z)] + 4k_z^2.
\end{aligned}
\tag{3.73}
$$

Accordingly to the self-consistent algorithm described by formulas (3.52), (3.53) the profile $\Lambda^{(0)}(z)$ in the first DWBA order is defined by the following condition:

$$\langle T^{(1)}(\{\Lambda^{(0)}(z)\})\rangle =$$

$$\int d\boldsymbol{r} e^{i(\boldsymbol{p}_\perp - \boldsymbol{k}_\perp)\boldsymbol{r}} \varphi^*_{-k_z}(z)[\langle H[z - z_0(x, y)]\rangle - \Lambda^{(0)}(z)]\varphi_{k_z}(z) = 0. \quad (3.74)$$

and the solution for the profile $\Lambda^{(0)}(z)$ is:

$$\Lambda^{(0)}(z) = \langle H[z - z_0(x, y)]\rangle.$$

Thus, in the first DWBA order self-consistent approach leads to the simple result: the specular reflection from rough surface depends on the potential of transition layer, which is calculated by the averaging of real potential over the surface. In this approximation $\Lambda^{(0)}(z)$ doesn't depend on the roughness correlation:

$$\Lambda^{(0)}(z) = \frac{1}{S_\perp}\int_{S_\perp} dxdy H[z - z_0(x, y)] = \int_{-\infty}^{\infty} dz_0 f(z_0) H[z - z_0]. \quad (3.75)$$

Here $S_\perp$ is the flat area of the surface, and the ergodic hypothesis [28]

$$\frac{dxdy}{S_\perp} = dz_0 f(z_0)$$

is used in order to substitute the averaging over roughness amplitudes with the distribution function $f(z_0)$ instead of integration over the surface.

As for example, assuming the Gaussian distribution of roughness amplitudes on the surface, the profile of the transition layer is expressed through the error function [23]:

$$\Lambda^{(0)}(z) =< H[z - z_0(x, y)] >= \frac{1}{\sigma\sqrt{2\pi}}\int_{-\infty}^{z} dz_0 e^{-z_0^2/2\sigma^2} = \Phi\left(\frac{z}{\sigma\sqrt{2}}\right). \quad (3.76)$$

When the second-order DWBA is considered (3.52), the correlation of roughness [22] has to be taken into account in the averaging of Eq. (3.53). For homogeneous surface and standard definition of the correlation function can be used:

$$\langle [z_0(\boldsymbol{r}_\perp) - z_0(\boldsymbol{r}_\perp + \boldsymbol{R}_\perp)]^2\rangle = g(R_\perp). \quad (3.77)$$

In order to analyze quantitatively effect of roughness correlation one should choose some model for the function $g(R_\perp)$. There are several models for the roughness correlations that are used in reflectometry: widespread fractal model [22] or terrace model for interface [29]. Slight difference between the results on the basis of these models is appeared in the diffuse (non-coherent) scattering [29]. However, it proved not to be important for analysis of specular reflection. Therefore for definiteness the fractal model is considered here and further:

$$g(R_\perp) = 2\sigma^2\left(1 - e^{-\left(\frac{R_\perp}{L_c}\right)^{2h}}\right), \tag{3.78}$$

where two parameters: h as the fractal dimension and L_c as the correlation length are used for fitting of the specular reflection profile. Figure 3.9 illustrates the differences between the statistical properties of the surface with various values of these parameters.

The X-ray scattering cross-section from potential (3.39) with accuracy up to ξ^2 is obtained by averaging of Eq. (3.52) on Gaussian distribution of the random function $z_0(x, y)$ and with the correlation function (3.78):

$$\begin{aligned}\frac{d\sigma}{d\Omega} &= \frac{k^4|\chi|^2}{4} S_\perp |T(\boldsymbol{k}, \boldsymbol{p})|^2; \\ |T(\boldsymbol{k}, \boldsymbol{p})|^2 &= \delta(\boldsymbol{p}_\perp - \boldsymbol{k}_\perp)\{|T^{(0)}(k_z, \{\Lambda^{(1)}(z)\}) + \xi B(k_z)|^2 \\ &\quad + 2\xi^2 k^2 \Re[T^{(0)*}(k_z, \{\Lambda^{(1)}(z)\})\chi T^{(2)}(k_z)]\} + \xi^2 K(\boldsymbol{k}, \boldsymbol{p}).\end{aligned} \tag{3.79}$$

where $S_\perp$ is the surface area of the sample. All the terms in (3.79) have a clear physical interpretation and are calculated as described below. The function

$$T^{(0)}(k_z, \{\Lambda^{(1)}(z)\}) = \int_{-\infty}^{\infty} dz e^{ik_z z} \Lambda^{(1)}(z)\varphi_{k_z}(z) \tag{3.80}$$

is the amplitude of specular reflection from the profile $\Lambda^{(1)}(z)$. The additional contribution of the first order $B(k_z)$ into specular amplitude is caused by the difference

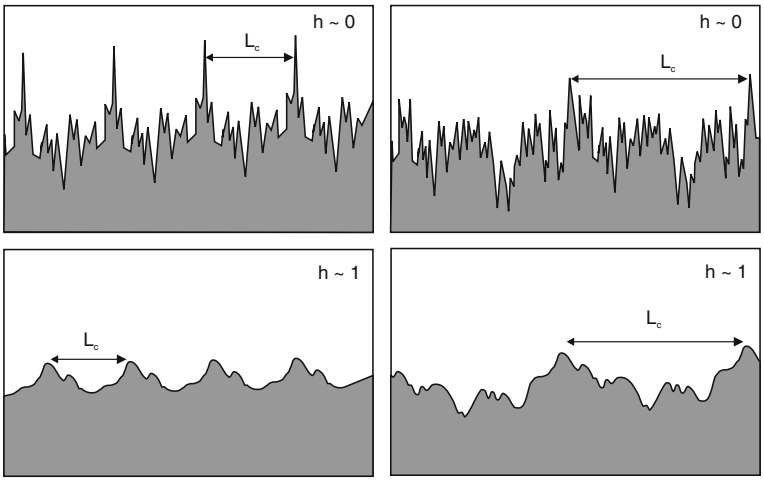

Fig. 3.9 The characteristic forms of the surface with different values of the correlation length L_c and fractal dimension h

between function $\Lambda^{(1)}(z)$ and profile (3.76), which is taken as error function $\Lambda^{(0)}(z)$. The latter does not depend, by definition, on the roughness correlation.

$$B(k_z) = \int_{-\infty}^{\infty} dz \varphi^*_{-k_z}(z)[\Lambda^{(0)}(z) - \Lambda^{(1)}(z)]\varphi_{k_z}(z). \tag{3.81}$$

The term $T^{(2)}(k_z)$ in (3.79) corresponds to double scattering of wave field within media [8–10] and is calculated as the second-order correction in the solution of Eq. (3.53). The term $K(\boldsymbol{k}, \boldsymbol{p})$ is a single incoherent scattering depending on the root-mean-square fluctuation $[\langle V^2\rangle - \langle V\rangle^2]$ of the scattering potential (3.51) after averaging over the correlated roughness distribution.

$$\begin{aligned} T^{(2)}(\boldsymbol{k}) = & \int_{|\boldsymbol{k}'_\perp|<k} \frac{d\boldsymbol{k}'_\perp}{k'_z} \int_{-\infty}^{\infty} dz \int_{-\infty}^{\infty} dz' \int d\boldsymbol{R}_\perp e^{i(\boldsymbol{k}'_\perp - \boldsymbol{k}_\perp)\boldsymbol{R}_\perp} \\ & \times \varphi^*_{-k_z}(z')\varphi_{k'_z}(z')\varphi^*_{-k'_z}(z)\varphi_{k_z}(z) \\ & \times \left\{ \int_{-\infty}^{\infty} da_1 \int_{-\infty}^{\infty} da_2 W(a_1, a_2, R_\perp) H[z' - a_1] H[z - a_2] \right. \\ & \left. + [\Lambda^{(0)}(z) - \Lambda^{(1)}(z)][\Lambda^{(0)}(z') - \Lambda^{(1)}(z')] \right\}. \end{aligned} \tag{3.82}$$

$$\begin{aligned} K(\boldsymbol{k}, \boldsymbol{p}) = & \frac{1}{4\pi^2} \int_{-\infty}^{\infty} dz \int_{-\infty}^{\infty} dz' \int d\boldsymbol{R}_\perp \int_{-\infty}^{\infty} da_1 \int_{-\infty}^{\infty} da_2 \\ & \times W(a_1, a_2, R_\perp) \times e^{i(\boldsymbol{p}_\perp - \boldsymbol{k}_\perp)\boldsymbol{R}_\perp} \\ & \times \varphi^*_{-p_z}(z') H[z' - a_1] \varphi^*_{k_z}(z') \varphi_{-p_z}(z) H[z - a_2] \varphi_{k_z}(z). \end{aligned} \tag{3.83}$$

The functions $\varphi_{k_z}(z)$ are the solutions of wave Eq. (3.42) with profile $\Lambda^{(1)}(z)$, and two-dimensional distribution of the roughness amplitudes $W(a_1, a_2, R_\perp)$ is:

$$\begin{aligned} W(a_1, a_2, R_\perp) = & \frac{1}{\pi\sigma} \left\{ \frac{1}{\sqrt{2g(R_\perp)}} e^{-(a_1+a_2)^2/4\sigma^2} e^{-(a_1-a_2)^2/2g(R_\perp)} \right. \\ & \left. - \frac{1}{2\sigma} e^{-(a_1^2+a_2^2)/2\sigma^2} \right\}, \end{aligned} \tag{3.84}$$

with correlation function $g(R_\perp)$ from (3.77).

The differential cross-section (3.79) describes both specular ($\boldsymbol{p}_\perp = \boldsymbol{k}_\perp$) and diffuse scattering $K(\boldsymbol{k}, \boldsymbol{p})$, when the transverse component of wave vector is not preserved. The term $K(\boldsymbol{k}, \boldsymbol{p})$ is a non-zero for $\boldsymbol{p}_\perp = \boldsymbol{k}_\perp$, and variational profile $\Lambda^{(1)}(z)$ has to be calculated taking in consideration this term in Eq. (3.53). To proceed with the simulations, the number of quanta $N(\boldsymbol{n})$ registered by detector in the direction of unit vector $\boldsymbol{n} = (\boldsymbol{k}_\perp/k, -k_z/k)$, which corresponds to specular reflection, is calculated. The value of $N(\boldsymbol{n})$ depends on the width of angular cone $\Delta\Omega$ covered by detector :

$$N(\boldsymbol{n}) = I_0 \int d\boldsymbol{n}' f(\boldsymbol{n}-\boldsymbol{n}') \frac{d\sigma}{d\Omega'};$$
$$f(\boldsymbol{n}-\boldsymbol{n}') = \exp\left[-\frac{\Delta_x^2}{\delta_x^2} - \frac{\Delta_y^2}{\delta_y^2}\right];\ \boldsymbol{\Delta} = (\boldsymbol{n}-\boldsymbol{n}'). \tag{3.85}$$

Here I_0 is an incident beam intensity; $f(\boldsymbol{n}-\boldsymbol{n}')$ is the detector instrumental function assumed to be a Gaussian; the unit vector $\boldsymbol{n}'$ defines the direction of the wave vector $\boldsymbol{p}$. Because of in reflectometry experiments the detectors with small angular resolution ($\delta_x \sim \delta_y \ll 1$) are used, the integration over $\boldsymbol{n}'$ in Eq. (3.85) is carried out in the plane perpendicular to $\boldsymbol{n}$. The differential cross-section (3.79) is related, however, to the sample surface [22], and therefore the variations of the wave vector and the vector $\boldsymbol{\Delta}$ are connected as:

$$q_x = k_z \Delta_x,\ q_y = k\Delta_y. \tag{3.86}$$

Substituting (3.79) into (3.85), the number of photons scattered by the incident at angle θ to the sample surface beam and detected in the direction of specular reflection is ($\xi = 1$):

$$N(\theta) = N_0 \frac{k^4|\chi|^2}{4k_z^2}\left\{|T^{(0)}(k_z, \{\Lambda^{(1)}(z)\}) + B(k_z)|^2 + \right.$$
$$\left. 2\Re[T^{(0)*}(k_z, \{\Lambda^{(1)}(z)\})T^{(2)}(k_z)] + \int d\boldsymbol{q}_\perp e^{-\frac{q_x^2}{k_z^2\delta_x^2} - \frac{q_y^2}{k^2\delta_y^2}} K(\boldsymbol{k}, \boldsymbol{p})\right\}, \tag{3.87}$$

where $N_0 = I_0 S k_z/k$ is a number of photons at the sample surface in time unit, and $\boldsymbol{p}_\perp = \boldsymbol{k}_\perp + \boldsymbol{q}_\perp;\ p_z = \sqrt{k^2 - p_\perp^2}$.

For any profile $\Lambda^{(1)}(z)$, the main contribution to (3.87) in the region of small scattering angles is given by term $\sim |T^{(0)}(k_z, \{\Lambda^{(1)}(z)\})|^2$. However, for scattering angles larger than total external reflection angle $\theta > \theta_c = \sqrt{|\chi_0|}$, the specular reflection coefficient decreases drastically, and correlation effects, being included in Eq. (3.87), become essential. The profile $\Lambda^{(1)}(z)$ has to be selected in a way that the sum of the following terms is equal to zero for all k_z:

$$2\Re\{T^{(0)*}(k_z, \{\Lambda^{(1)}(z)\})[B(k_z) + T^{(2)}(k_z)]\} + |B(k_z)|^2$$
$$+ \int d\boldsymbol{q}_\perp e^{-\frac{q_x^2}{k_z^2\delta_x^2} - \frac{q_y^2}{k^2\delta_y^2}} K(\boldsymbol{k}, \boldsymbol{p}) = 0. \tag{3.88}$$

Then the number of detected photons (3.87) is:

$$N(\alpha) = N_0 |R_s^{(0)}(k_z, \{\Lambda^{(1)}(z)\})|^2, \tag{3.89}$$

where the specular reflectivity $R_s^{(0)}$ is calculated from (3.73) and depends on the amplitude of coherent scattering (3.75):

$$\frac{k^2\chi}{2}T^{(0)}(k_z, \{\Lambda^{(1)}(z)\}) = -k_z R_s^{(0)}(k_z, \{\Lambda^{(1)}(z)\}).$$

To qualitatively consider the correlation effects in X-ray reflectivity, the measured [24] X-ray reflectivity (Fig. 3.10) from rough $Si_{0.65}Ge_{0.35}$ surface is analyzed. The X-ray polarizability of sample is $\chi_0 = -1.99 \times 10^{-5} + i5.27 \times 10^{-7}$, and X-rays with wavelength CuK_α have been used. The scanning angle θ is in degrees, and intensity is normalized to unity.

The theoretical surface profile $\Lambda^{(0)}(z)$ is chosen accordingly to (3.76) as an error function, if Gaussian roughness distribution and first order DWBA are assumed. The analytical function $\varphi_{k_z}^{(0)}(z)$ and reflection coefficient $|R_s^{(0)}(k_z, \{\Lambda^{(0)}(z)\})|^2$ have also been calculated and are shown by dash line in Fig. 3.10. The fit obtained demonstrates a good agreement for the angles $\theta_r > \theta > \theta_c$ and roughness $\sigma \approx 45.0$ Å. For qualitative analysis of reflectivity curve, an additional parameter θ_r has been introduced to distinguish different regions of scanning angles. This parameter determines the range, where the specular reflection from averaged interface profile dominates over the diffuse scattering, i.e. interval, where the intensity drops exponentially:

$$\theta_r \approx \frac{1}{2k\sigma} \tag{3.90}$$

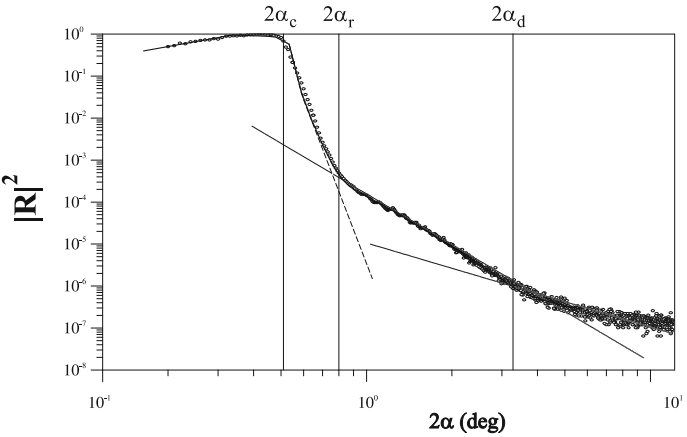

Fig. 3.10 The fitted by self consistent approach experimental reflectivity from $Si_{0.65}Ge_{0.35}$ sample with large roughness [24]. For the fitting of the entire area of scattering angle, the formula (3.87) has been used with the following parameters:$\sigma = 45$ Å, $h = 2$, $\nu = k^2\alpha_c\delta_x\delta_y L_c^2 = 0.012$. For comparison the dashed line shows the reflected intensity re-normalized by conventional Nevot-Croce factor. The vertical lines distinguish the angle areas with different behavior of X-ray reflectivity

For the angles $\theta > \theta_r$, however, the intensity decreases as power function, and therefore the re-normalization $|R_s^{(0)}(k_z, \{\Lambda^{(1)}(z)\})|^2$ due to second-order DWBA corrections is essential. To determine a profile $\Lambda^{(1)}(z)$ accounting correlations, the Eq. (3.88) has to be solved. As the solution for this equation is convenient to obtain directly a specular amplitude instead of profile $\Lambda^{(1)}(z)$:

$$T^{(0)}(k_z, \{\Lambda^{(1)}(z)\}) = \int_{-\infty}^{\infty} dz e^{ik_z z} \Lambda^{(1)}(z) \varphi_{k_z}^{(1)}(z), \tag{3.91}$$

where function $\varphi_{k_z}^{(1)}(z)$ is the solution of wave equation for considered profile of transition layer.

The solving of cumbersome integral equation is simplified due to following reasons: (i) the accuracy up to the second order of ξ is required, and (ii) the angular region $\theta > \theta_r$ is considered, where reflection coefficient is small independently on profile shape. In this angular region:

$$\varphi_{k_z}^{(1)}(z) \approx \varphi_{k_z}^{(0)}(z) \approx e^{ik_z z}, \tag{3.92}$$

and terms of Eq. (3.88) are:

$$\begin{aligned} T^{(0)}(k_z, \{\Lambda^{(1)}(z)\}) &\approx T^{(0)}(k_z, \{\Lambda^{(0)}(z)\}) - B^{(0)}(k_z), \\ B(k_z) \approx B^{(0)}(k_z) &= \int_{-\infty}^{\infty} dz e^{ik_z z} \Lambda^{(1)}(z) \varphi_{k_z}^{(0)}(z). \end{aligned} \tag{3.93}$$

Then Eq. (3.88) is resolved with respect to $B^{(0)}(k_z)$, and the expression for scattered amplitude is obtained assuming $\xi = 1$ and with mentioned above accuracy:

$$\begin{aligned} T^{(0)}(k_z, \{\Lambda^{(1)}(z)\}) = [|T^{(0)}(k_z, \{\Lambda^{(0)}(z)\})|^2 + \\ 2\Re[T^{(0)*}(k_z, \{\Lambda^{(0)}(z)\}) \tilde{R}^{(2)}(k_z)] + \int d\boldsymbol{q}_\perp e^{-\frac{q_x^2}{k_z^2 \delta_x^2} - \frac{q_y^2}{k^2 \delta_y^2}} \tilde{K}(\boldsymbol{k}, \boldsymbol{p})]^{1/2}, \end{aligned} \tag{3.94}$$

where $\tilde{R}^{(2)}$ and $\tilde{K}$ correspond to profile $\Lambda^{(0)}(z)$. The correction $\Lambda^{(1)}(z)$ for zero-order profile is calculated using Fourier transformation of (3.93), and generally it depends on both z and k_z.

Similarly to Refs. [8–10], the approximation (3.92) for function $\varphi_{k_z}^{(0)}(z)$ is used for calculation of amplitudes (3.94). Moreover, the influence of amplitude $\tilde{R}^{(2)}$ is negligible at considered angles because of exponentially decreasing $T^{(0)*}(k_z)$. Averaging $\tilde{K}(\boldsymbol{k}, \boldsymbol{p})$ over roughness distribution with function (3.78), the following expression for X-ray intensity in the direction of specular beam is:

$$N(\theta) = N_0 \left\{ |R_s^{(0)}(\theta)|^2 + \frac{k^5 |\chi|^2}{4\pi^2 k_z^3} \pi \delta_x \delta_y \int_{-\infty}^{\infty} dX \int_{-\infty}^{\infty} dY \right.$$

$$\times e^{-k_z^2\delta_x^2X^2/4-k^2\delta_y^2Y^2/4}[e^{-k_z^2\sigma^2(1-g(R_\perp))}-e^{-k_z^2\sigma^2}]\Big\}. \tag{3.95}$$

For the angles $\theta > \theta_r$, the dependence of specularly reflected intensity on the incidence angle is mostly governed by the second term in (3.45) and decreases as power function:

$$N(\theta) \sim N_0 \frac{1}{\theta^4}. \tag{3.96}$$

The tiny oscillations within the area between 1° and 2° of exit angle, may be associated with the interference with the weak waves reflected from the interface between film and Si substrate that were not considered in this section (see Sect. 3.3). The large roughness of the surface has been artificially created by large-scale gratings on the surface, which are supposed to be random. However, some ordering of this grating is probable, which causes the oscillating behavior of reflectivity curve. Another effect influencing the behavior of curve is seen in the region $\theta < \theta_c$, where the decrease of reflection coefficient occurs. As it was described by formula (3.35) this effect is due to effective reduction of sample size L_x at small scattering angles comparatively to illuminated by X-ray beam of size L_b area $L_b/\sin\theta$. This effect is taken into account by modification of (3.95) with the function $\bar{F}_b(\theta)$ defined in (3.35):

$$N_{eff}(\theta) = N(\theta)\bar{F}_b(\theta). \tag{3.97}$$

The formulas (3.96) and (3.97) has been used to fit experimental data in Fig. 3.10. For convenience reasons, the vertical lines separate the regions of qualitatively different behavior of reflectivity curve. The best fit is found for $\sigma = 4.5\,\text{nm}$, $h = 2$. The additional parameter has been introduced regulating the contribution of diffuse scattering (second term in (3.96)) into total intensity:

$$\nu = k^2\theta_c\delta_x\delta_y L_c^2 = \frac{L_c^2}{S_{coh}}. \tag{3.98}$$

The physical meaning of this parameter is the ratio of the illuminated by X-rays sample area, where the correlations are essential, to the tangential coherence area S_{coh}, which is set up by angular resolution of detector [7]. The fitting in Fig. 3.10 is obtained at $\nu_{opt} \approx 0.012$. The specular X-ray reflectivity depends on correlation length through dimensionless parameter (3.98), which also contains the detector parameters δ_x, δ_y. The draft value of L_c in considered experiment is found to be $L_c \approx 70\,\text{nm}$ which follows from $\delta_x \approx \delta_y \approx 0.1\,\theta_c$.

For X-ray reflectometry, one more characteristic parameter has to be considered: the angle θ_d, after which reflectivity depends dominantly on detector noise, background, geometrical factors, measurement dynamical range, beam size, parameters δ_x, δ_y, etc. The non-exponential behavior of the reflection coefficient due to correlation effects in the intermediate angular region $\theta_d > \theta > \theta_r$ is observable when the condition is fulfilled [24]:

$$\theta_r = \frac{1}{k_0 \sigma} < \theta_d. \tag{3.99}$$

The value θ_d depends on the dynamical range of used in experiment detector. Therefore, the roughness amplitude, at which the correlations can be observed in the reflection coefficient, depends also on experimental conditions:

$$\sigma > \frac{1}{k_0 \theta_d}. \tag{3.100}$$

For smaller roughness amplitudes, Nevot-Croce factor is satisfactory for data fitting. The upper limit for σ is defined by the applicability of DWBA, i.e. spectral density of the specular (coherent) beam is higher than one of the diffuse (incoherent) intensity [11]:

$$\sigma < \frac{1}{k_0 \theta_c}. \tag{3.101}$$

For considered here experimental data, (3.101) results in $\sigma < 7\,\text{nm}$.

Thus, the detailed analysis of the reflectivity profile allows one to measure both the electron density in the sample and a series of characteristics of its surface.

3.3 X-Ray Reflectivity from Multilayered Structures

The prominent abilities of the X-ray reflectivity technique are strongly demanded for investigation of non-uniform samples consisting of the stack of thin layers separated by the pronounced parallel interfaces and grown on the thick substrate (Fig. 3.11). The multilayers, consisting of the large number of thin layers, make up a wide class of samples in semiconductor and nanotechnology industries. X-ray methods are proved to be very advantageous for investigation of these structures (see, for example, [4–7]). However, an increasing demand for the X-ray methods from industry and science emphasizes the problem of algorithm improvements, both in acceleration and precision aspects. This task is especially important when the experimental data from complex samples have to be quickly, robustly and accurately fitted by theoretical models.

As it was shown in the previous section, provided the condition (3.27) is fulfilled, the dimensions of the sample (x, y) are treated as infinite, which ensures the conservation of the transversal component of the wave vector $\boldsymbol{k}_\perp$ through the entire depth of the sample. As a result, similarly to the case of a single surface the solution for vector potential is found from (3.21), (3.41):

$$\boldsymbol{A}_{\boldsymbol{k}}(\boldsymbol{r}) = \boldsymbol{e} e^{i\boldsymbol{k}_\perp \boldsymbol{r}} \varphi_{k_z}(z), \tag{3.102}$$

where the function $\varphi_{k_z}(z)$ satisfies the scalar wave equation:

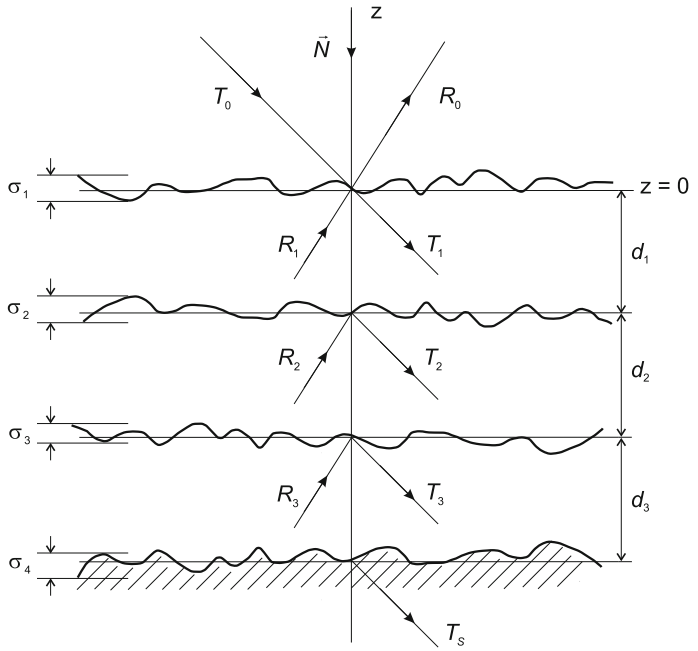

Fig. 3.11 The sketch of multilayered structure investigated by XRR method: $d_j,\ j = 1, 2 \ldots L$ are the thicknesses of layers; T_j, R_j are the amplitudes of coherently scattered waves inside each layer. The interfaces between the layers possess the roughness with root mean square $\sigma_j,\ j = 1, 2 \ldots (J + 1)$

$$\left\{ \frac{d^2}{dz^2} + k_z^2 + V(\boldsymbol{r}) \right\} \varphi_{k_z}(z) = 0; \qquad k_z = k_0 \sin\theta. \tag{3.103}$$

The coherent scattering only is taken into account when the interaction of the wave field with each interface is considered in XRR. Therefore, the imperfection (roughness) of the interfaces is accounted according to the relationships (3.51)–(3.53) for the transition layers at boundaries. The scattering potential in (3.103) is a function of sole coordinate z (Fig. 3.12):

$$V(\boldsymbol{r}) \to V(z) = k_0^2 \sum_{j=0}^{J} \{\chi_{j+1}(\omega) \Lambda_j(z) + \chi_j(\omega)[1 - \Lambda_j(z)]\}, \tag{3.104}$$

where $\chi_j(\omega)$ is a polarizability of the material composing j-th layer; $\chi_{J+1}(\omega)$ is a polarizability of the substrate material; $\chi_0(\omega) = 0$ is a polarizability of the vacuum; $\Lambda_j(z)$ is a profile of the transition layer between j and $(j + 1)$ layers, normalized according to the conditions (3.39). Evidently the XRR investigation of the multilay-

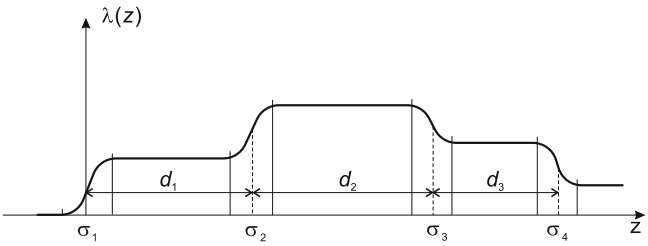

Fig. 3.12 Characteristic shape of the coherent scattering potential for X-ray reflectivity from multilayered structures with imperfect interfaces

ered structure is very effective, if the total thickness of multilayered stack is less than absorption depth of X-ray radiation:

$$D = \sum_{j=1}^{J} d_j < L_{abs} = \frac{1}{2k_0 \Im\chi(\omega)} \sim 10^5\, nm, \tag{3.105}$$

where d_j is a thickness of j-th layer. The entire structure may consist of up to thousands layers. We assume that the root mean square of the interface roughness σ_j, which defines the thickness of the transition layers $\Lambda_j(z)$ at each interface is less than the thickness of the layers themselves:

$$\sigma_j \sim \sigma_{j+1} < d_j. \tag{3.106}$$

In general case, the solution of Maxwell's Eq. (3.104) for calculation of X-ray reflectivity in multilayers was firstly reduced to the system of recurrent Parratt equations in [30]. Advanced method based on the transfer matrices [31, 32] for solution of these equations, delivered convenient formalism for theoretical interpretation of the experimental X-ray data . For periodical structures, using the powers of the transfer matrix for the interface boundary conditions, the time of calculation could be considerably reduced [33, 34]. However, this technique requires the calculation of high powers of matrices, which is also time-consuming procedure because of the number of numerical operations exponentially increases with the number of multilayer elements. It is especially important in the case of reflectivity from periodical multilayered structures (superlattices). There are several approximated methods for reduction of calculation time, for example, kinematical approach and single-reflection approximation [7], but they do not provide sufficient precision for thick multilayers and superlattices with large number of layers.

The method proposed in [14, 15] utilizes the possibility to express the Bloch eigenwaves of one-dimensional periodical infinite layer stack through the solutions of X-ray scattering problem within the single basic element composing the superlattice period. The combination of Parratt's recursive equations for basic element of

superlattice with the eigenwave approach allows one to achieve the best performance of simulation technique.

To derive Parratt's equations, the expression (3.104) for the wave field inside l-th layer and outside of transition layers associated with l-th and $(l+1)$-th interfaces is used provided the condition (3.106) is fulfilled. The solution of this equation is represented as a linear combination of the plane waves with amplitudes T_l, R_l, spreading in the positive and negative directions of axis z, respectively (Fig. 3.12):

$$\begin{aligned} \varphi_{k_{zj}}^{(j)}(z) &= T_j e^{ik_{zj}z} + R_j e^{-ik_{zj}z}; \\ k_{zj} &= k_0\sqrt{\sin^2\theta + \chi_j(\omega)}. \end{aligned} \tag{3.107}$$

The scattering of the waves at each interface is considered to be based on the boundary conditions (3.47) with respect to the phase shift conditioned by the position of the interface. Defining the coordinate of the j-th layer with respect to the entrance boundary of the interface as

$$z_j = \sum_{l=0}^{j} d_l, \tag{3.108}$$

the following relationship between the wave amplitudes in neighbor layers can be derived using formula (3.47):

$$\begin{aligned} t_{j+1,j}T_{j+1}e^{-ik_{z(j+1)}z_j} &= T_j e^{-ik_{zj}z_j} + R_j r_{j+1,j} e^{ik_{zj}z_j}; \\ t_{j+1,j}R_{j+1}e^{ik_{z(j+1)}z_j} &= T_j r_{j+1,j} e^{-ik_{zj}z_j} + R_j e^{ik_{zj}z_j}, \end{aligned} \tag{3.109}$$

which is the system of $2J$ equations for the amplitudes of waves within the layers. The reflection $r_{j+1,j}$ and transmission $t_{j+1,j}$ coefficients at interface between j-th and $(j+1)$-th layers are expressed through the Fresnel coefficients, re-normalized in accordance with the formulas (3.49) and (3.50) provided the root mean square of roughness σ_j satisfies the inequality (3.101):

$$\begin{aligned} r_{j+1,j} &= \frac{k_{zj} - k_{z(j+1)}}{k_{zj} + k_{z(j+1)}} e^{-2\sigma_j^2 k_{zj} k_{z(j+1)}}; \\ t_{j+1,j} &= \frac{2k_{zj}}{k_{zj} + k_{z(j+1)}} e^{\frac{\sigma_j^2}{2}(k_{zj} - k_{z(j+1)})^2}. \end{aligned} \tag{3.110}$$

In some applications of XRR [5], the structures with the roughness amplitude compared to the layer thickness are studied. In this case, the re-normalized reflection and transmission coefficients can be calculated from the formulas similar to the expressions (3.38), provided the corresponding projections of the wave vector and the amplitudes of the scattering potential in neighbor layers are used:

$$
\begin{aligned}
r_{j+1,j} &= \frac{D_r}{\Delta}; \quad t_{j+1,j} = \frac{D_t}{\Delta};\\
D_r &= iA_{j+1,j}[K(2k_{zj})L(k_{z(j+1)} - k_{zj})(k_{z(j+1)} + k_{zj})\\
&\quad - K(0)L(k_{z(j+1)} + k_{zj})(k_{z(j+1)} - k_{zj})]\\
&\quad - 2k_{zj}L(k_{z(j+1)} + k_{zj})(k_{z(j+1)} - k_{zj});\\
\Delta &= iA_{j+1,j}[K(-2k_{zj})L(k_{z(j+1)} + k_{zj})(k_{z(j+1)} - k_{zj})\\
&\quad - K(0)L(k_{z(j+1)} - k_{zj})(k_{z(j+1)} + k_{zj})]\\
&\quad + 2k_zL(k_{z(j+1)} - k_{zj})(k_{z(j+1)} + k_{zj});\\
D_t &= A^2_{j+1,j}[K^2(0) - K(2k_{zj})K(-2k_{zj})] + 4k_{zj})^2;\\
A_{j+1,j} &= k_0^2[\chi_{j+1} - \chi_j].
\end{aligned}
\tag{3.111}
$$

The profiles of the transition layers $\Lambda_j(z)$ at the interfaces, which are required for calculation of integrals $L(q)$, $K(q)$ in (3.38) can be either selected using various models allowing the analytical calculation of the integrals [13, 16], or found using a self-consistent approach (3.88). Parratt derived [30] a most effective way to solve the equations system (3.109) by implementing the system of the recurrent equations for new variables:

$$
X_j = \frac{R_j}{T_j}e^{2ik_{zj}z_j}; \quad X_0 = R_0; \; X_{J+1} = 0. \tag{3.112}
$$

The boundary condition $X_{J+1} = 0$ corresponds to the reflected wave inside substrate, and the reflection coefficient R_0 from the entire structure is equal to X_0 assuming the amplitude of the incident wave in vacuum equals to unity (Fig. 3.11). The Eqs. (3.109) are transformed to the simple form:

$$
X_j = \frac{r_{j,j+1} + X_{j+1}e^{-2ik_{z(j+1)}d_{j+1}}}{1 + r_{j,j+1}X_je^{2ik_{zj}d_j}}. \tag{3.113}
$$

Figure 3.13 demonstrates the measured reflection curve from the multilayered structure and the simulated curve fitted on the basis of the Eqs. (3.113). The theoretical simulations reproduce the oscillations of X-ray reflectivity accurately, and thus the following characteristics of the sample can be evaluated: the layer thicknesses, the electron density depth profiles, and roughness of the interfaces. The X-ray reflectivity can also be simulated using ansatz (3.72), (3.73) and potential (3.104) for the entire sample structure instead of separate calculations for each interface. The result of this approach (Fig. 3.13) delivers the same accuracy as Parratt's formalism does, however, requires less computing time. The use of ansatz is especially effective for the structures with imperfect interfaces, for which the condition (3.106) is not fulfilled. The application of the Eqs. (3.113) in this case requires a large number of the transition layers for modeling of the electron density variation at the interfaces, and thus increases the computation time of reflectivity curve essentially.

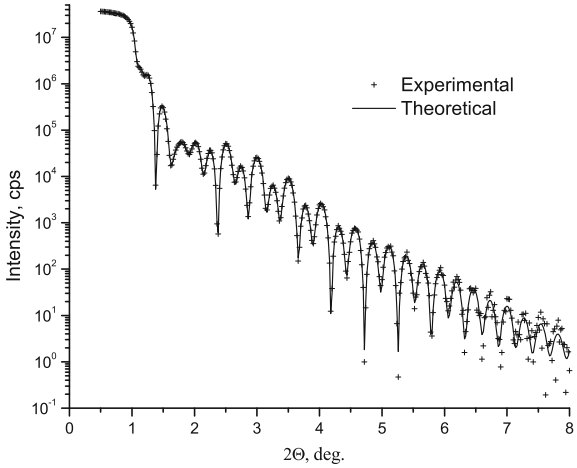

Fig. 3.13 X-ray reflectivity from multilayered structure consisting of three layers on SiO_2 substrate. The refined layer parameters are: $Ta_2O_5(d_1 = 2.77\,\text{nm}; \sigma_1 = 0.74\,\text{nm})$; $Ta(d_2 = 17.08\,\text{nm}; \sigma_2 = 0.38\,\text{nm})$; $NiFe(d_3 = 15.34\,\text{nm}; \sigma_3 = 0.59\,\text{nm})$; for substrate $\sigma_4 = 0.44\,\text{nm}$. The model of the transition layer with error function profile has been used for data fitting. The simulated curves calculated by Parratt's formalism and by ansatz (3.72) are not distinguishable on the plot

There is a special class of multilayered structures called *superlattices*, the structures consisting of the periodically repeated N times sets of L layers (Fig. 3.14), where the number N can be in the range $N \sim 100$. Such a superlattice represents an one-dimensional crystal, which yields the superlattice peaks in the reflected X-ray intensity at certain angles of observation [7]. The simulation of the reflection curve for superlattices using Parratt's equations (3.113) requires for each reflection angle $\sim (4)^{N+L}$ mathematical operations, and computation time increases exponentially with the increase of the number of superlattice periods. This fact complicates essentially the solution of the inverse problem of the structure refinement from the fitting of X-ray measured and simulated curves. The method of eigenwaves (MEW) has been developed [14, 15] to overcome this obstacle.

Within the framework of MEW, each superlattice layer (Fig. 3.14), is determined by two indices: the layer number within the basic period $j = 1, 2 \ldots L$ and the period number $l = 1, 2 \ldots N$. The thickness of the basic period is

$$d = \sum_{j=1}^{L} d_j,$$

where d_j are the thicknesses of layers composing a basic period. The general solution of Maxwell's equations for the layer with indexes j, l is

$$E_l(x, z) = e^{ikx\cos\theta}\Psi_{jl}(z);$$

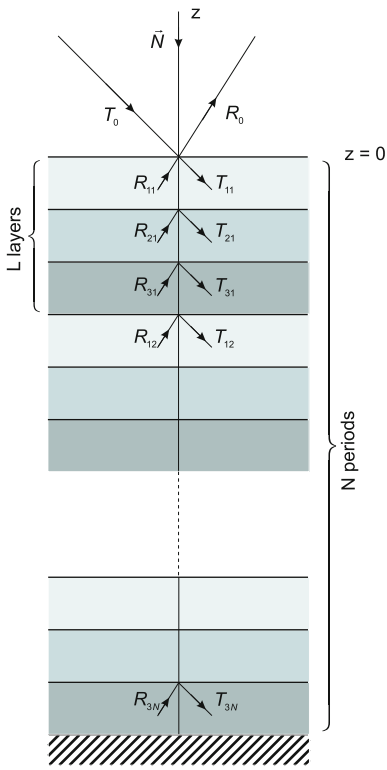

Fig. 3.14 The electromagnetic wave fields inside the superlattice consisting of N periods of repeated L layers

$$\Psi_{jl}(z) = T_{jl}e^{ik_{zj}(z-ld)} + R_{jl}e^{-ik_{zj}(z-ld)}, \tag{3.114}$$

and z-component of the wave vector k_{jz} doesn't depend on index l because of the periodicity of lattice. Transmission T_{jl} and reflection R_{jl} coefficients in the neighboring layers are connected because of the boundary conditions for the wave field at the interfaces. In the result the (2×2) transfer matrix $\hat{M}$ can be introduced, which defines the transformation of transmission and reflection coefficients for the first layers of the neighbor basic periods of superlattice:

$$T_{1(l+1)} = M_{11}T_{1l} + M_{12}R_{1l}; \quad R_{1(l+1)} = M_{21}T_{1l} + M_{22}R_{1l}. \tag{3.115}$$

If the phase of wave field is defined in accordance with the Eq. (3.114), then the transfer matrix does not depend on index l numbering the superlattice periods because of the Bloch's theorem for the wave field in the periodical medium [35]. This fact makes it possible to use the product of matrix $\hat{M}$ for calculation of full transfer matrix of superlattice. Such an approach reduces the calculation time in comparison with the direct solution of recurrent equations [33, 34]. However, methods of eigenwaves simplifies this solution even more because it expresses the total reflection coefficient

in analytical form. To derive this form, the two-component eigenvectors $\boldsymbol{A}^{(s)} = (T^{(s)}, R^{(s)})$; $s = 1, 2$ of matrix $\hat{M}$ has to be introduced:

$$\begin{aligned}
&\hat{M}\boldsymbol{A}^{(s)} = \lambda_s \boldsymbol{A}^{(s)};\\
&\lambda_{1,2} = \frac{M_{11} + M_{22}}{2} \pm \sqrt{\frac{(M_{11} - M_{22})^2}{4} + M_{12}M_{21}};\\
&R^{(s)} = \nu_s T^{(s)} = \frac{\lambda_s - M_{11}}{M_{12}} T^{(s)}.
\end{aligned} \tag{3.116}$$

The wave fields determined by coefficients (3.116) create a basis of eigenwaves in infinite periodical layer stack. It should be stressed that the eigenvalues $\lambda_{1,2}$ are complex-valued and eigenvectors $\boldsymbol{A}^{(s)}$ are non-orthogonal because of the matrix $\hat{M}$ includes the imaginary parts of the medium polarizability and therefore it is non-Hermitian. The values $T^{(s)}$ represent the amplitudes of eigenwaves if they are excited in the finite stack by the incident plane wave. To find these amplitudes $T^{(s)}$, the boundary conditions have to be used at the interfaces superlattice/vacuum and superlattice/substrate.

To find the eigenwaves of the system, the transfer matrix $\hat{M}$ has to be calculated for basic multilayer structure ($j = 1, \ldots L$) of the superlattice. By the definition, this matrix gives a relation between the coefficients $T_{1,(L+1)} = T_{2,1}$; $R_{1,(L+1)} = T_{2,1}$ and parameters T_1, R_1 for the wave fields $\Psi_{l,j}$. The solution of this problem can be found on the basis of the recurrent Eq. (3.109) for this structure. However to use these equations for calculation of matrix $\hat{M}$, the boundary conditions (3.112) for X_j : $X_L = 0$; $R_L = 0$; $T_0 = 1$ have to be changed. In the considered here case the initial transmission and reflection coefficients are not directly related. The most convenient way to calculate the transition matrix $\hat{M}$ seems to be matrix method [31, 32].

The recurrent Eq. (3.109) being resulted from the transformation of vectors $(T_{1j}; R_{1j})$ are represented then by matrices:

$$\begin{aligned}
\hat{A}_j &= \frac{1}{t_{j+1,j}} \begin{pmatrix} e^{i(k_{zj} - k_{z(j+1)})z_j} & r_{j+1,j} e^{-i(k_{zj} + k_{z(j+1)})z_j} \\ r_{j+1,j} e^{i(k_{zj} + k_{z(j+1)})z_j} & e^{-i(k_{zj} - k_{z(j+1)})z_j} \end{pmatrix};\\
\hat{B}_j &= \frac{1}{t_{j+1,j}} \begin{pmatrix} e^{ik_{zj}z_j} & r_{j+1,j} e^{-ik_{zj}z_j} \\ r_{j+1,j} e^{ik_{zj}z_j} & e^{-ik_{zj}z_j} \end{pmatrix}.
\end{aligned} \tag{3.117}$$

The matrices $\hat{B}_j$ have to be used at both interfaces of basic period to eliminate the phase in the matrix $\hat{M}$ at the interface between the neighboring basic periods. Then the total transformation of the vector $(T_{11}; R_{11})$ results to the transition matrix:

$$\hat{M} = \hat{B}_L \hat{A}_{L-1} \hat{A}_{L-2} \ldots \hat{A}_2 \hat{B}_1. \tag{3.118}$$

Then the eigenvalues $\lambda_{1,2}$ and their eigenvectors follow from the Eq. (3.116), if the elements of the matrix $\hat{M}$ in Eq. (3.118) are used. The equations for amplitudes resulting from the boundary conditions for wave fields at the surface of superlattice

and at the interface between superlattice and substrate are then written as

$$\begin{aligned} 1 + R_0(\theta) &= T_{1,1} + R_{1,1} = T^{(1)}(1+\nu_1) + T^{(2)}(1+\nu_2); \\ k_{z0}[1 - R_0(\theta)] &= k_{z1}[T_{1,1} - R_{1,1}] \\ &= k_{z1}[T^{(1)}(1-\nu_1) + T^{(2)}(1-\nu_2)], \qquad (3.119) \\ T_{sub}e^{ik_{zs}Nd} &= T_{N,L}e^{ik_{zL}d} + R_{N,L}e^{-ik_{zL}d}; \\ k_{zm}T_{sub}e^{ik_{zs}Nd} &= k_{zL}[T_{N,L}e^{ik_{zL}d} - R_{N,L}e^{-ik_{zL}d}], \qquad (3.120) \end{aligned}$$

where the value $k_{zs} = k_0\sqrt{\sin^2\theta + \chi_s(\omega)}$ corresponds to the substrate.

To satisfy the continuity conditions (3.120) for wave fields at the interface between bottommost basic layer and substrate, the amplitudes $T_{N,L}$ and $R_{N,L}$ have to be expressed through the amplitudes $T_{N,1}$ and $R_{N,1}$ by means of the matrix:

$$\hat{M}_{L-1} = \hat{A}_{L-1}\hat{A}_{L-2}\ldots\hat{A}_2\hat{B}_1. \qquad (3.121)$$

The amplitudes within the arbitrary l-period of the superlattice are expressed through the amplitudes inside the first period by the following analytical formulas:

$$\begin{aligned} T_{l,1} &= \lambda_1^{(l-1)}T^{(1)} + \lambda_2^{(l-1)}T^{2)}; \\ R_{l,1} &= \nu_1\lambda_1^{(l-1)}T^{(1)} + \nu_2\lambda_2^{(l-1)}T^{(2)}; \\ R_{l,L} &= (\hat{M}_{L-1})_{21}T_{l,1} + \nu_{(1,2)}(\hat{M}_{L-1})_{22}R_{l,1}; \\ T_{l,L} &= (\hat{M}_{L-1})_{11}T_{l,1} + \nu_{(1,2)}(\hat{M}_{L-1})_{12}R_{l,1}, \qquad (3.122) \end{aligned}$$

where l is assumed to be equal N when the amplitudes are substituted in Eq. (3.120).

Then the analytic formula for reflection coefficient $R_0(\theta)$ from the superlattice can be found:

$$\begin{aligned} R_0(\theta) &= -\frac{k_{z1}[1-\nu_1+P_N(1-\nu_2)] - k_{z0}[1+\nu_1+P_N(1+\nu_2)]}{k_{z1}[1-\nu_1+P_N(1-\nu_2)] + k_{z0}[1+\nu_1+P_N(1+\nu_2)]}; \\ P_N &= -\left(\frac{\lambda_1}{\lambda_2}\right)^N \frac{(k_{zs}-k_{zL})(T_L^{(1)}e^{ik_{zL}d} + (k_{zs}+k_{zL})R_L^{(1)}e^{-ik_{zL}d}}{(k_{zs}-k_{zL})T_L^{(2)}e^{ik_{zL}d} + (k_{zs}+k_{zL})R_L^{(2)}e^{-ik_{zL}d}}; \\ R_L^{(1,2)} &= (\hat{M}_{L-1})_{21} + \nu_{(1,2)}(\hat{M}_{L-1})_{22}; \\ T_L^{(1,2)} &= (\hat{M}_{L-1})_{11} + \nu_{(1,2)}(\hat{M}_{L-1})_{12}. \qquad (3.123) \end{aligned}$$

Figure 3.15 demonstrates the simulated X-ray reflectivity curves from the multicomponent superlattice $(AlAs/GaAs/InAs/GaSb)_{40}$ on the GaAs substrate, where the layer thicknesses are equal to $(10/20/5/10)_{40}$ nm, respectively. The comparison of required computer time for both straightforward Parratt's approach (t_P) and the eigenwaves technique (t_M) as the function of repetition period is presented on the

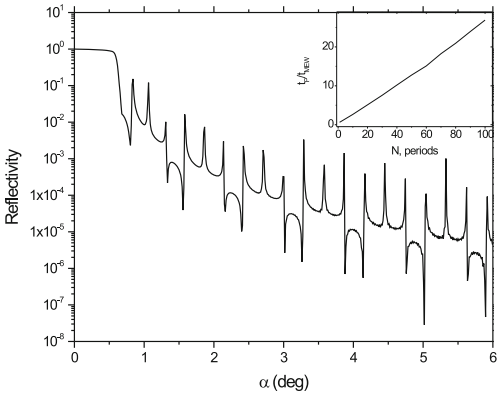

Fig. 3.15 Simulated X-ray reflectivity from $(AlAs/GaAs/InAs/GaSb)_{40}$ superlattice on the GaAs substrate. Insert shows the ratio of the computer times required for simulation by Parratt's equations (t_P) and method of eigenwaves (t_{MEW}) as the function of superlattice periods number

inset in this figure. In some cases the calculation time for single simulation is reduced from several seconds (t_P) to the fraction of seconds (t_M).

At first sight, this reduction seems to be not principal for real applications because of absolute computation time is relatively short. However, in most cases, the treatment of X-ray experimental data from real superlattices requires the fitting of many parameters (thickness, roughness, electron density, lattice mismatches, etc), which often are very approximately known from growth conditions. Moreover, possible aperiodicity of superlattice structure and large number of layers in the stack even aggravate the situation. The effective fitting procedures minimizing the cost function, e.g. genetic algorithms or simulating annealing, also require tens of thousands single simulations to find a non-ambiguous solution. In this case, the speeding up of calculations by using method of eigenwaves plays essential role in software performance.

Calculation time is also important for simulation of diffuse X-ray scattering caused by rough interfaces in superlattices. Distorted-wave Born approximation used for calculation of diffuse scatter, expresses the diffuse intensity $I(\theta, \theta_f)$ through the matrix elements of potential $\hat{V}$, describing the rough interfaces, and incident Ψ_{in} at angle θ and reflected Ψ_{out} at angle $\theta_f \neq \theta$ wave fields calculated for ideal superlattice (see, for example, [7]):

$$I(\theta, \theta_f) \simeq | < \Psi_{in}(\theta) | \hat{V} | \Psi_{out}(\theta_f) > |^2.$$

Each wave field contains the set of $2NL$ amplitudes $T_i(\theta)$, $R_i(\theta)$ or $T_i(\theta_f)$, $R_i(\theta_f)$, and the application of analytical formulas (3.123) instead of numerical solution of Parratt's equations reduces considerably the simulation time for calculation of diffusely scattered intensity in dependence on angles θ and θ_f.

It seems for the first sight that Eqs. (3.122) for amplitudes are valid for the case of ideal superlattice periodicity only. At the same time the superlattices with regularly (due to strain, for example) or irregularly (due to non-stability of growth conditions) fluctuating basic periods are quite a typical samples in nano-coating and semiconductor science and industry. The deformation of superlattice period can be taken

into account directly by Parratt's equations, however the averaging over the period fluctuations is complicated task [36].

In the framework of eigenwave method, this effect can be taken into account by renormalization of the transfer matrix of basic period as, for example, the averaging of atomic vibrations in dynamical diffraction theory results in the Debye-Waller factor for X-ray susceptibility. In the case of the fluctuating period the transfer matrix $\hat{M}^{(l)}$ and two-component vector $\boldsymbol{A}_l = (T_l, R_l)$ both depend on the period number l, therefore the recurrent formula containing these vectors in two successive superlattice periods can be introduced instead of Eq. (3.116) for eigenvalues.

$$\hat{M}^{(l)}\boldsymbol{A}_l = \boldsymbol{A}_{(l+1)}. \tag{3.124}$$

To introduce a parameter for description of above-mentioned fluctuations, the transfer matrix $\hat{M}^{(l)}$ has to be re-interpreted on the basis of formal scattering theory [37]. From this point of view, the matrix elements can be considered as elements of scattering operator $\hat{S}^{(l)}(z)$ defined with the functions of initial i and final f states:

$$(\hat{M}^{(l)})_{if} = (\hat{S})_{if} = \int_{z_l}^{z_{l+1}} dz e^{-ik_f(z-ld)}\hat{S}_L(z-ld)e^{ik_i(z-ld)}. \tag{3.125}$$

The matrix elements (3.125) are shown above to be independent on indices l, in the case of ideal superlattice. In real superlattices, the period thickness has a statistical fluctuations δ_l, and thus $z_l = ld + \delta_l, \quad \delta_l \ll 1$. As a result, the transfer matrix obtains an additional random phase coefficient

$$(\hat{M}^{(l)})_{if} = (\hat{M})_{if}e^{i(k_i-k_f)\delta_l}, \tag{3.126}$$

which is absent in matrix $\hat{M}$, corresponding to ideal periodicity. The coherent part of the transfer matrix can be derived by averaging over the statistical distribution of random phases, in the same way as for coherent polarizability of crystal [38]:

$$\begin{aligned}(\hat{M}^{(l)})_{if} &= < (\hat{M})_{if}e^{i(k_i-k_f)\delta_l} > + (\hat{V}^{(l)})_{if};\\ (\hat{V}^{(l)})_{if} &\equiv (\hat{M}^{(l)})_{if} - < (\hat{M}_L)_{if}e^{i(k_i-k_f)\delta_l} >,\end{aligned} \tag{3.127}$$

with $\hat{V}^{(l)}$ as the incoherent scattering potential. In particular case of negligible vertical correlation of interfacial roughness (which sometimes can be essential for interpretation of diffuse X-ray scattering [39]), the coherent part of matrix elements in (3.127) obtains an additional factor, which does not depend on l. Assuming the Gaussian distribution of period fluctuations with root-mean-square σ_d, and averaging the Eq. (3.127) over the fluctuations, we arrive at:

$$< (\hat{M}^{(l)}_{if} >= e^{-1/2\sigma_d^2(k_f-k_i)^2}(\hat{M})_{if}. \tag{3.128}$$

The exponential factor reduces the amplitude of elastic scattering of the wave field by superlattice basic period analogously to Debye-Waller factor for crystallographic unit cell derived for X-ray polarizability of the crystal [38]. This result causes the re-normalization of matrix elements (3.116):

$$< M_{11} >= M_{11}; \qquad < M_{12} >= M_{12} e^{-1/2\sigma_d^2 (k_{zL}+k_{z1})^2};$$
$$< M_{22} >= M_{22}; \qquad < M_{21} >= M_{21} e^{-1/2\sigma_d^2 (k_{zL}+k_{z1})^2}, \tag{3.129}$$

Then the analytical solution of Eq. (3.124) for the coherent eigenwaves is

$$\boldsymbol{A}_l = (\lambda_s)^l \boldsymbol{A}^{(s)}$$

with eigenvalues λ_s, determined from the similar to (3.116) equation:

$$< \hat{M} > \boldsymbol{A}^{(s)} = \lambda_s \boldsymbol{A}^{(s)}. \tag{3.130}$$

Figure 3.16 shows how the parameter σ_d, taking into account the fluctuation of superlattice period, influences the formation of the coherent superlattice peaks. The experimental measurements (dots) from superlattice $(W/Al_2O_3)_{64}$ on the Si substrate with the nominal layer thicknesses $(1.2/1.9)_{64}$ nm have been taken in conventional $\theta - 2\theta$ geometry using knife edge collimator and anti-scattering detector slit at CuK_α radiation. The first simulation (dashed) is carried out on the eigenwave basis for superlattice with constant periodicity and taking into account interface roughness by Nevot-Croce exponent (this curve is equivalent to Parratt's simulations):

$$\bar{r}_{j+1,j} = r_{j+1,j} e^{-2k_j k_{j+1} \sigma_r^2},$$

where the parameter σ_r is the root-mean-square (rms) of interface roughness.

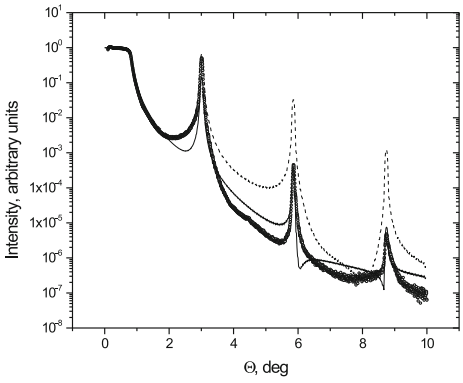

Fig. 3.16 Measured (*dots*) and simulated by MEW with Nevot-Croce exponent (*dashed line*) and by MEW with averaged fluctuations (*solid line*) X-ray reflectivity from $(W/Al_2O_3)_{64}$ superlattice on the Si substrate

The value σ_r has been roughly fitted as 0.25 nm and equal for all interfaces, and the reflectivity has been convoluted with resolution function describing the limited angular resolution of detector. The second simulation (solid line) is done by using eigenwave method with integral period fluctuations (Eq. (3.128)) with the same $\sigma_d = 0.25$ nm. In both cases, the same roughness rms σ_r and σ_d influences the amplitude of superlattice peaks in different way, however, the latter approach explains the experiment better. It should be noted, that Fig. 3.16 represents only the qualitative fit; the influence of incoherent matrix $(\hat{V}^{(l)})_{if}$ in recurrent Eq. (3.124) on the phase of the transfer matrix can be taken into account to reach better fit on the wings of superlattice peaks.

3.4 Characterization of Samples Using Experimental XRR Data

The information about bulk properties and interface morphology of multilayered nanostructures and thin solid films can be extracted from XRR data refinement. The typical refinement procedure consists of iterative sample modeling with respect to the fitness of experimental data to the theoretical curves simulated in the framework of certain physical processes. The sample model for XRR simulations depends usually on the following physical parameters: electron density and thickness of film or layer in multilayers and roughness of interfaces between layers.

The important part of iteration process is the fitting algorithm, which minimizes the discrepancy between theory and experiment. Commonly used classical optimization procedures as calculus-based search and gradient (hill-climbing) methods like simplex and others show acceptable performance but remain unreliable due to, for example, a tendency to be trapped in local extrema or the necessity to know the explicit form of derivatives of minimized function to reach high efficiency of convergence. The random search methods assume the stochastic search of extremum in parameter space and do not have any aimed strategy of solution finding. The recently invented simulated annealing technique is successful in many applications but has some disadvantages in search strategy, e.g. systematical loss of information obtained in previous iterations.In contrast, the genetic algorithms (GA) developed during the recent decade combine the advantages of stochastic search with intelligent strategy of solution finding. These algorithms mimic the main features of the Darwinian theory of evolution operating on the basis of "struggle for life" and "survival of fittest" principles. The successful applications of GA in science and engineering [40–42] have demonstrated this technique to be robust and effective.

Figure 3.17a shows measured (open dots) and simulated (solid lines) X-ray reflectivity at wavelength $\lambda = 0.154056$ nm from gold and magnetite thin solid films on MgO substrate. The sample model consisting of the sequence Au/Fe_3O_4/MgO with the nominal thicknesses 55 nm/120 nm/substrate and some roughness at the interfaces between the layers has been used for fitting of simulated by the described above formalism X-ray reflectivity to the measured curves. The fitted parameters were the thicknesses of the layers t_{Au} and $t_{Fe_3O_4}$ and the roughnesses of the sam-

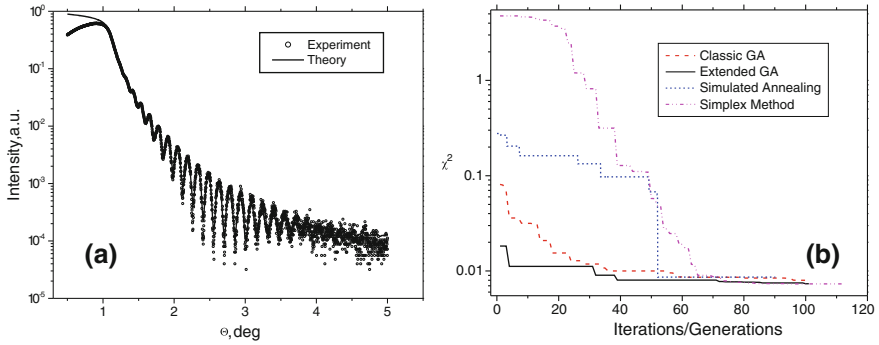

Fig. 3.17 **a** Measured (*open dots*) and fitted (*solid line*) X-ray reflectivity from Au/Fe_3O_4/MgO sample; **b** Convergence of χ^2 function for various optimization techniques recorded during the fitting of X-ray reflectivity data in panel (**a**). The iteration scale of simulated annealing and simplex techniques is reduced to genetic algorithm generations scale by adjustment of computation time

ple surface and the interfaces. Different optimization methods used to fit [42] this data (classic genetic algorithm, simulated annealing, simplex, and extended genetic algorithm) resulted in acceptable fitness of curves with slight difference in refined parameters which, however, is within the precision of experimental data. The values of thicknesses and roughnesses are found to be $t_{Au} \simeq 53.8\,\text{nm}$, $t_{Fe_3O_4} \simeq 146.3\,\text{nm}$, $\sigma_{surf} \simeq 0.78\,\text{nm}$, $\sigma_{Au/Fe_3O_4} \simeq 0.1\,\text{nm}$, $\sigma_{Fe_3O_4/MgO} \simeq 0.3\,\text{nm}$. However, the effectiveness of methods is evidently different, as follows from the Fig. 3.17b showing the cost function χ^2 convergence diagrams for each used technique. To adjust the time scales of algorithms, the iteration scales of simulated annealing and simplex methods are brought into correspondence to genetic algorithms generations scale by multiplying them by ratios of computation times t_{GA}/t_{SA} and t_{GA}/t_{SM}. Diagrams show that extended genetic algorithm finds the best available solution faster than other methods.

Another example of how XRR data fitting helps to recognize the difference in depth structure between two similar samples grown by different technologies is given in Ref. [43] for ZnSe thin layer on GaAs substrate. Two samples grown by molecular beam epitaxy differed in initial growing conditions; the first was prepared by Se-treatment of a GaAs substrate, and the second one was exposed to Zn before growth of the ZnSe film. The structure and morphology of the interface between the ZnSe film and GaAs substrate were investigated by XRR technique. Fitting the experimental data indicated the presence of a Ga_2Se_3 transition layer between the ZnSe film and GaAs substrate for the Se-treated sample, confirming that Zn-treatment during the growing process improves the interface quality. Furthermore, the simulations indicated that the concentration of the Ga_2Se_3 was less than unity. From this, we propose that the transition layer is discontinuous e.g. possesses an island like morphology.

The X-ray reflectivity was measured at beamline 17C of the Photon Factory of KEK (Tsukuba, Japan). To enhance the electron density contrast between the epitaxial layer, the transition layer and the substrate, the reflectivity measurements were carried

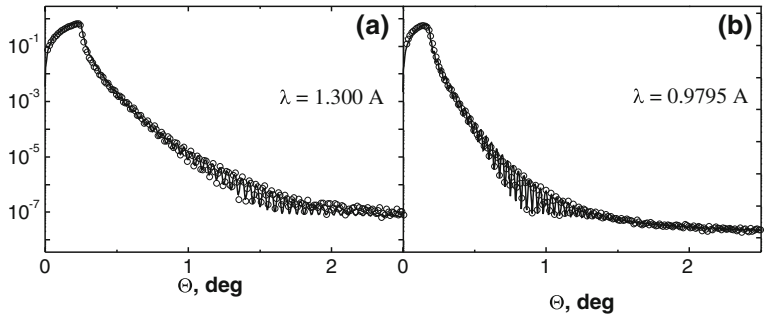

Fig. 3.18 Experimental (*dots*) and simulated (*solid lines*) X-ray reflectivity profiles from Se-treated ZnSe/GaAs sample at different wavelengths, λ = 1.300 Å (**a**), and 0.9795 Å (**b**)

out using synchrotron radiation both near and far from the Se K absorption edge. The experiment was carried out in air using a grazing incidence X-ray diffractometer. X-ray wavelengths of 1.3000 Å, 1.1800 Å, and 0.9795 Å were selected by a Si(111) double-crystal monochromator. These three wavelengths were below the absorption edges of all the structural atoms, between Ga and As absorption edges, and above the Se K absorption edge (the Se K-edge : 0.97977 Å), respectively. The size of the incident beam was 0.1 mm (vertical) × 8 mm (horizontal). The reflected beam was collimated by a vertical 0.2 mm (vertical) slit and a 0.6 degree (horizontal) Soller slit in front of a NaI scintillation counter.

The solid lines in Fig. 3.18 show the best fit to the experimental data using the theory presented in previous sections. The values for film thickness and surface roughness were found by fitting as follows, $t_{ZnSe} = 700 \pm 7$ Å, $\sigma_s = 10 \pm 1$ Å for the Se-treated sample (we don't show here the results for the Zn-treated sample, the reader is referred to [43]). The fitted values for the oxide layer thickness and top density are $t_{ox} = 17.3$ Å, $\rho_{top} = 0.74$. We identified, with some certainty, the presence of Ga_2Se_3 within the Se-treated sample, for which the fitting procedure gives the values for concentration of Ga_2Se_3 within the transition layer $C_{Ga_2Se_3} = (84.4 \pm 5)$ % and thickness $t_{Ga_2Se_3} = 6 \pm 1$ Å.

The application of XRR technique to the wide class of thin film structures called superlattices is demonstrated in [44]. Specular X-ray scattering has been used to probe the mesoscopic structure of interfaces within two, thirty-period Mo/Si superlattices, grown on a silicon (sample 1) and glass (sample 2) substrates by ion beam sputtering. The data are evaluated qualitatively and quantitatively on the basis of a distorted-wave Born approximation, which includes a correlating behavior of interface roughness in both the lateral and vertical directions (see Chap. 5 for more details). Different initial conditions of the substrate's surface result in distinguishable characters of roughness replications in the direction of growth. The average value, lateral correlation and fractal dimension of roughness are found to be different in both samples, which leads to differences in the reflective properties of multilayer mirrors. The X-ray reflectivity intensities were measured using a high-resolution X-ray diffractometer (Advanced

Thin Film X-ray System ATX-G, Rigaku Corporation). X-rays with wavelength λ = 0.15405 nm (CuK_{α_1}) are generated from a Cu rotating anode (50 kV, 300 mA), collimated by a parabolic multilayer mirror and monochromated by a channel cut Ge(111) asymmetric monochromator. A divergent (0.1 × 10 mm) slit was used to control the exposure area on the sample surface, while a parallel pair of slits (0.2 × 15 mm) was used to limit the output signal. Quantitative estimations of the sample parameters were determined from the iterative sample modeling with respect to fitting of the experimental X-ray data to the theoretical curves. The detailed numerical analysis has been performed with specular reflectivity ($\theta - 2\theta$ scan).

A large number of superlattice peaks in the reflectivity curve measured from sample 1, shown in Fig. 3.19a by open dots, is indicative of abrupt interfaces within this specimen. The theoretical simulations (same figure, solid lines) confirm this fact, giving the best agreement with experiment for relatively small roughness with root-mean-square value of $\sigma_{Si} \sim 0.5$ nm for silicon layers and $\sigma_{Mo} \sim 0.2$ nm for molybdenum layers. The inter-diffusion layers within this sample are found to be of the thickness $t_{Mo-on-Si} \sim 1.2$ nm and $t_{Si-on-Mo} \sim 0.8$ nm, and the basic Mo and Si layers are of thickness $t_{Mo} \sim 3.5$ nm and $t_{Si} \sim 3.7$ nm, respectively. These findings confirm the nominal values expected from the growth conditions. The presence of asymmetry in the inter-diffusion layer's thickness is in agreement with other studies on Mo/Si multilayers and can be explained by a difference in the ease of imbedding a heavy Mo adatoms into amorphous silicon rather than light Si atoms into polycrystalline Mo structure. The reflectivity data from sample 2 are shown in Fig. 3.19b. The imperfect layer boundaries of this sample cause the preferential attenuation of high orders of superlattice reflections. The values of interfacial roughness obtained by data fitting in this case, $\sigma_{Si} \sim 0.9$ nm and $\sigma_{Mo} \sim 0.6$ nm, are twice as large as those obtained for sample 1. This is consistent with the general characteristics of the reflectivity curve. The thickness of basic and inter-diffusion layers are found to be nearly the same as for the sample on a crystalline substrate.

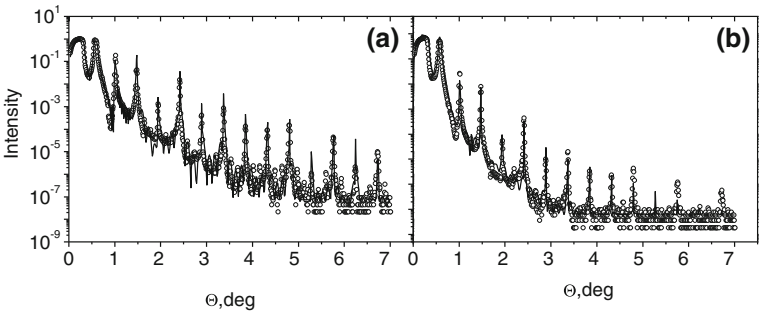

Fig. 3.19 Specular X-ray reflectivity curves measured in $\theta - 2\theta$ scans for samples 1 (**a**) and 2 (**b**). The measurements are depicted by *open dots* and the simulations are shown by *solid lines*. The attenuation of superlattice peaks in sample 2 indicates poor quality of interfaces

The X-ray characterization of thin solid films and multilayers is even more effective when performed in the combination of two X-ray techniques, the X-ray reflectivity and diffuse scattering measurements (Chap. 5). This combination delivers a synergy, which allows to characterize the interface (surface) morphology and bulk structure of samples and interfaces. The simultaneous fitting of specular and off-specular data gives precise information on surface and buried interface smoothness. The X-ray reflectivity measurements being simulated taking into account the diffuse component and simultaneously with diffuse scans, give proper values of film thickness, interface and surface roughness, layer density. Whereas the analysis of the diffuse scans reproduces the lateral structure of surface and interface.

References

1. E. Prince (ed.), *International Tables for Crystallography* vol. C (Kluwer Academic Publishers, Dordrecht/Boston/Lomdon, 2004)
2. M. Born, E. Wolf, *Principles of Optics*, 7th edn. (Cambridge University Press, UK, 1999)
3. B.L. Henke, E.M. Gullikson, J.C. Davis, At. Data Nucl. Data Tables **54**, 181 (1993)
4. J. Daillant, A. Gibaud, *X-Ray and Neutron Reflectivity: Principles and Applications* (Springer-Verlag, Berlin Heidelberg, 1999)
5. M. Tolan, *X-Ray Scattering from Soft-Matter Thin Films* (Springer-Verlag, Berlin Heidelberg, 1999)
6. J. Als-Nielsen, D. McMorrow, *Elements of Modern X-Ray Physics* (Wiley, New York, 2001)
7. U. Pietsch, V. Holy, T. Baumbach, *High-Resolution X-Ray Scattering: from Thin Films to Lateral Nanostuctures*, 2nd edn. (Springer-Verlag, Berlin Heidelberg, 2004)
8. D.K.G. de Boer, Phys. Rev. B **49**, 5817 (1994)
9. D.K.G. de Boer, Phys. Rev. B **51**, 5297 (1995)
10. D.K.G. de Boer, Phys. Rev. B **53**, 6048 (1996)
11. S. Dietrich, A. Haase, Phys. Rep. **260**, 1 (1995)
12. A. Caticha, Phys. Rev. B **52**, 9214 (1995)
13. I.D. Feranchuk, S.I. Feranchuk, L.I. Komarov, A. Ulyanenkov, Phys. Rev. B **67**, 235417 (2003)
14. I.D. Feranchuk, S.I. Feranchuk, A.A. Minkevich, A.P. Ulyanenkov, Phys. Rev. B. **68**, 235307 (2003)
15. I. Feranchuk, A. Ulyanenkov, European Patent EP1469302 **A 1**, (2004)
16. I.D. Feranchuk, S.I. Feranchuk, A.P. Ulyanenkov, Phys. Rev. B. **75**, 085414 (2007)
17. L.D. Landau, E.M. Lifshitz, *Electrodynamics of Condensed Matter*, 2nd edn. (Nauka, Moscow, 1982) (in russian)
18. P.M. Mors, H. Feshbach, *Methods of Theoretical Physics*, vol. 1 (Springer-Verlag, Berlin, 1987)
19. V.K. Ignatovich, *Neutron Optics* (Fizmatlit, Moscow, 2006) (in russian)
20. L. Hörmander, *The Analysis of Linear Partial Differential Operators* (Springer-Verlag, Berlin Heidelberg, 1983)
21. L.D. Landau, E.M. Lifshitz *Quantum Mechanics*, 3rd edn. (Pergamon Press, Oxford, 1977)
22. S.K. Sinha, E.B. Sirota, S. Garoff, H.B. Stanley, Phys. Rev. B **38**, 2297 (1988)
23. L. Nevot, P. Croce, Rev. Phys. Appl. **15**, 761 (1980)
24. I.D. Feranchuk, A.A. Minkevich, A.P. Ulyanenkov, Eur. Phys. J. Appl. Phys. **24**, 21 (2003)
25. J. Als-Nielsen, D. Jacquemann, K. Kjaer, F. Leveiller, M. Lahav, L. Leseirowitz, Phys. Rep. **246**, 251 (1994)
26. I.D. Feranchuk, L.I. Komarov, I.V. Nichipor, A.P. Ulyanenkov, Ann. Phys. NY **238**, 370 (1995)
27. P.S. Epstein, Proc. Natl. Acad. Sci. USA **16**, 67 (1930)
28. P. Walters, *An Introduction to Ergodic Theory* (Springer, New York, 1982)

29. V. Holý, C. Giannini, L. Tapfer, T. Marschner, W. Stolz, Phys. Rev. B **55**, 9960 (1997)
30. L.G. Parratt, Phys. Rev. **95**, 359 (1954)
31. L. Abeles, Ann. Phys (Paris) **3**, 504 (1948)
32. L. Abeles, Ann. Phys (Paris) **5**, 596 (1950)
33. D.W. Berremen, Phys. Rev. B **14**, 4313 (1976)
34. S.A. Stepanov, R.Köhler, J. Phys. D **27**, 1923 (1994)
35. J.M. Ziman, *Principles of The Theory of Solids* (Oxford Univ. Press, New York, 2001)
36. A.P. Payne, B.M. Clemens, Phys. Rev. B **47**, 2289 (1993)
37. T.-Y. Wu, T. Omura, *Quantum Theory of Scattering* (Prentice-Hall Inc., New York, 1962)
38. R.W. James, *The Optical Principle of the Diffraction of X-rays* (G.Bell and Sons, London, 1962)
39. V. Holy, T. Baumbach, Phys. Rev. B **49**, 10668 (1994)
40. D.E. Goldberg, E. David, *Genetic Algorithms in Search Optimization and Machine Learning* (Addison-Wesley Reading, MA, 1989)
41. A. Ulyanenkov, K. Omote, J. Harada, Physica B **283**, 237 (2000)
42. A. Ulyanenkov, S. Sobolewski, J. Phys.D: Appl. Phys. **38**, A235 (2005)
43. A. Ulyanenkov, A. Takase, M. Kuribayashi, K. Ishida, A. Ohtake, K. Arai, T. Hanada, T. Yasuda, H. Tomita, S. Komiya, J. Appl. Phys. **85**, 1520 (1999)
44. A. Ulyanenkov, R. Matsuo, K. Omote, K. Inaba, J. Harada, M. Ishino, M. Nishii, O. Yoda, J. Appl. Phys. **87**, 7255 (2000)

Chapter 4
X-Ray Diffraction in Ideal Crystals

The reflection phenomena, discussed in the previous chapter, are inherent for radiation of arbitrary wavelength. The microscopic physical parameter controlling the reflection process is the homogeneous part of the susceptibility, in the case of X-rays it is the zeroth harmonics of values (2.3) and (1.56). The part of the susceptibility which has a variation on the atomic length scale is specific for the radiation of wavelengths of magnitude Ångstroms: X-rays, neutrons and electrons. This part of susceptibility represents the atomic arrangement inside a sample and, as described in the Eq. (2.1), causes the certain distribution of the diffracted electromagnetic field, containing an information about the spatial atomic ordering. The diffraction experiments, aiming for the reconstruction of the atomic spatial structure, are most easily performed using X-rays: comparing to neutrons there are widely available high-intensity sources of X-rays, and comparing to electrons X-rays interact weakly with the matter that simplifies drastically the sample preparation procedure and evaluation of the diffraction results.

The information about the atomic arrangement, however, is incapsulated in the diffracted intensity distribution in an indirect way. In order to obtain this information, the specific treatment based on the trial and error fitting algorithms is required. This task can be simplified essentially when the Born approximation (2.34) is valid, and the simulation of the diffraction process under this assumption is called kinematical diffraction theory. In the cases when the anomalous scattering can be neglected, according to (1.49) and (1.51), the intensity distribution as a function of $\boldsymbol{q}$ is just a square modulus of the Fourier transformation of the electron density. Due to the wide validity range of the kinematical approximation, the analysis of X-ray diffraction data is much easier than e.g. the analysis of the electron diffraction patterns for which the whole series (2.33) is usually required.

The Born approximation implies that the scattering process happens for the primary wave only, and the secondary scattering of the scattered wave can be neglected. This is true provided the diffracted wave amplitude is small compared to the primary one, that occurs when the dimension of the coherently scattering crystal is smaller than the extinction length. For the large crystalline objects, the solution of (2.1) is

A. Benediktovitch et al., *Theoretical Concepts of X-Ray Nanoscale Analysis*,
Springer Series in Materials Science 183, DOI: 10.1007/978-3-642-38177-5_4,

obtained on the basis of Bloch waves, and generally small values of X-ray susceptibility enable to restrict this basis to two waves only in most cases. Such an approach is called dynamical diffraction theory, and it enables a detailed description of the finest effects of X-ray diffraction from thick crystals.

There is a vast amount of journal articles [1] and monographs [2–4] devoted to both kinematical and dynamical diffractions. This chapter is intended (i) to present the basic equations of two-beam dynamical diffraction theory, that assists to better understanding of the dedicated monographs [2, 4], (ii) to discuss the crossover between kinematical and dynamical diffraction, (iii) to formulate an application of the dynamical diffraction method for investigation of the multilayered structures and (iv) to consider specific geometrical configurations, where the length scale at which the dynamical effects are formed is significantly reduced (grazing incidence diffraction, or GID).

4.1 Kinematical X-Ray Diffraction Theory

The distribution of the diffracted radiation can be described by means of the differential cross-section, the general expression for which is given by Eq. (2.10), where the quantity $\boldsymbol{T}^{(s)}(\boldsymbol{k}_0, \boldsymbol{k}_1)$ can be found from the integral equation (2.8). This integral equation is expressed in the form of the infinite series (2.33). If the scattered wave is significantly weaker than the primary wave (a quantitative criterion will be deduced below), only the first term in the series (2.33) can be considered. This assumption is known as first Born approximation, and in the domain of X-ray diffraction it is usually called a *kinematical approximation*. The resulting expression for the differential cross-section is given by (2.35).

Let us consider the Compton contribution to susceptibility in the sum (2.35), and restrict ourselves to a single reciprocal lattice vector $\boldsymbol{H}$ and a single object with shape $S(\boldsymbol{r})$:

$$\frac{d\sigma^{(s)}}{d\Omega} = \frac{1}{(4\pi)^2} \sin^2\theta_{1s} k_0^4 |\chi(\boldsymbol{H}, \omega)|^2 \left| \int d\boldsymbol{r}\, S(\boldsymbol{r}) e^{-i(\boldsymbol{q}-\boldsymbol{H})\boldsymbol{r}} \right|^2 . \tag{4.1}$$

The commonly used X-ray detectors do not make a difference between the polarization states, hence the detected cross-section is a sum of cross-sections corresponding to each polarization:

$$\frac{d\sigma}{d\Omega} = P_1 \frac{d\sigma^{(1)}}{d\Omega} + P_2 \frac{d\sigma^{(2)}}{d\Omega},$$

where $P_{1,2}$ are the probabilities of the corresponding polarizations in the incident X-ray beam.

The polarization of incident wave is characterized with the respect to the diffraction plane, a plane which contains the wave vector of incident wave $\boldsymbol{k}_0$ and the diffracted wave $\boldsymbol{k}_1$. The polarization state for which the polarization vector is perpendicular to the diffraction plane is called σ polarization (from German *senkrecht*, or

sagittal to the diffraction plane); polarization state for which polarization vector is parallel to the diffraction plane is called π polarization (from *parallel*). In the framework of kinematical diffraction, the expressions for cross-sections for both polarizations are equivalent except for a factor $\sin^2\theta_{1s}$. Using the definitions $\theta_{1s} = \boldsymbol{k}_1\widehat{\boldsymbol{T}}^{(s)} = \boldsymbol{k}_1\widehat{\boldsymbol{e}}^{(s)}$ we obtain $\sin\theta_{1\sigma} = 1$ and $\sin\theta_{1\pi} = \cos 2\theta$, here 2θ is angle between $\boldsymbol{k}_0$ and $\boldsymbol{k}_1$. In a case of a linearly polarized wave with polarization vector making an angle ψ to the diffraction plane, the expression $\sin^2\psi + \cos^2\psi\cos^2 2\theta$ is obtained for the polarization factor $\sum_{s=\sigma,\pi}\sin^2\theta_{1s}$. For the unpolarized X-rays $\langle\sin^2\psi\rangle = \langle\cos^2\psi\rangle = 1/2$ and the result is:

$$\frac{d\sigma}{d\Omega} = \frac{1}{(4\pi)^2}\frac{1+\cos^2 2\theta}{2}k_0^4|\chi(\boldsymbol{H},\omega)|^2\left|\int d\boldsymbol{r}\,S(\boldsymbol{r})e^{-i(\boldsymbol{q}-\boldsymbol{H})\boldsymbol{r}}\right|^2. \tag{4.2}$$

The maximum magnitude of the cross-sections of X-ray scattering is reached when the condition $\boldsymbol{q} - \boldsymbol{H}$ is satisfied, or

$$\boldsymbol{k}_1 - \boldsymbol{k}_0 = \boldsymbol{H}, \tag{4.3}$$

and this vector equation (or 3 scalar equations) are called *Laue equations*. Rewriting the Eq. (4.3) as $\boldsymbol{k}_1 = \boldsymbol{H} + \boldsymbol{k}_0$ and taking square from the left and from the right sides and taking into account $\boldsymbol{k}_1^2 = \boldsymbol{k}_0^2 = k_0^2$, the Bragg condition is obtained:

$$2\boldsymbol{k}_0\boldsymbol{H} + \boldsymbol{H}^2 = 0, \tag{4.4}$$

or, in terms of angle 2θ:

$$2k_0\sin\frac{2\theta_B}{2} = H;\ d\sin\theta_B = n\frac{\lambda}{2}. \tag{4.5}$$

Here $2\theta_B$ is the angle satisfying the Bragg condition; $k_0 = 2\pi/\lambda$; $H = 2\pi n/d$; λ is the X-ray wavelength; d is the distance between the crystallographic planes, defined by the vector $\boldsymbol{H}$ (Fig. 4.1).

The simplicity of the basic equations for the kinematical theory (4.2) and (4.3) makes it possible to develop fast and reliable methods for determination of the

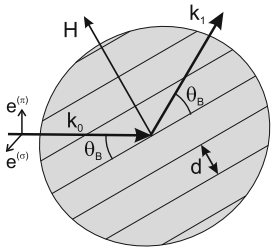

Fig. 4.1 Basic vectors and parameters used for characterization of the X-ray diffraction

crystalline shape and structure parameters, and most of them rely on the specific properties of Fourier transformation [5, 6]. To define the range of the applicability of kinematical theory, two examples are considered here. Assuming a crystal has a shape of a ball of radius R_0, the reflectivity $|R|^2$, or the ratio of total diffracted intensity to the total intensity impinging on the sample, according to (2.10) is found to be:

$$|R|^2 = \frac{\int d\Omega \frac{d\sigma}{d\Omega}}{\pi R_0^2}, \tag{4.6}$$

where πR_0^2 is the illuminated by the beam area of the sample. Since the diffracted intensity can not be larger than intensity impinging the sample, the criterion $|R|^2 < 1$ gives a limitation for the sample size for applicability of the above presented formulas. Assuming the ball size is large enough, the cross-section $\frac{d\sigma}{d\Omega}$ as a function of $\boldsymbol{k}_1$ at a fixed $\boldsymbol{k}_0$ drops-off quickly, and thus the main contribution to (4.6) comes from the exit beam angle regions where the deviations of $\boldsymbol{k}_1$ from (4.3) are small. The value $\boldsymbol{k}_1$ can be represented as $\boldsymbol{k}_1 = \boldsymbol{H} + \boldsymbol{k}_0 + \boldsymbol{\kappa}$, where it is assumed that $\boldsymbol{k}_0$ satisfies the condition (4.4), and the vector $\boldsymbol{\kappa}$ describes the deviation of $\boldsymbol{k}_1$ from the exact condition (4.3). Due to the condition $\boldsymbol{k}_1^2 = k_0^2$, the end of vector $\boldsymbol{k}_1$ must lie on a sphere, however, for small deviations we can approximate it by a tangential plane and describe by vector $\boldsymbol{\kappa}$ satisfying $\boldsymbol{\kappa} \cdot (\boldsymbol{H} + \boldsymbol{k}_0) = 0$. This approach is called a *tangential plane approximation*. By selecting a coordinate system with z axis along $\boldsymbol{H} + \boldsymbol{k}_0$, the vector $\boldsymbol{\kappa}$ has two components only. Within the same approximation, the solid angle where X-ray intensity is diffracted is expressed as:

$$d\Omega = \frac{d\kappa_x d\kappa_y}{k_0^2}, \tag{4.7}$$

and for the total cross-section of X-ray scattering, the following result is obtained:

$$\int d\Omega \frac{d\sigma}{d\Omega} = \frac{1}{(4\pi)^2} \frac{1 + \cos^2 2\theta_B}{2} k_0^2 |\chi(\boldsymbol{H}, \omega)|^2 \times \int d\kappa_x d\kappa_y \left| \int dx dy dz S(\boldsymbol{r}) e^{-i(\kappa_x x + \kappa_y y)} \right|^2. \tag{4.8}$$

Since $\boldsymbol{\kappa}$ has no z component, the integration of $S(\boldsymbol{r})$ over z results in the length of the ball in the direction of z equals to $2\sqrt{(R_0^2 - x^2 - y^2)}$. Using the identities from the theory of Fourier integrals [7]:

$$\int dk_x dk_y |f_{k_x,k_y}|^2 = (2\pi)^2 \int dx dy |f(x, y)|^2,$$
$$f_{k_x,k_y} = \int dx dy f(x, y) e^{-i(k_x x + k_y y)}, \tag{4.9}$$

the following expression is derived:

$$\int d\Omega \frac{d\sigma}{d\Omega} = \frac{1}{(4\pi)^2} \frac{1+\cos^2 2\theta_B}{2} k_0^2 |\chi(\boldsymbol{H},\omega)|^2 \times 4(2\pi)^2 \int_{x^2+y^2<R_0^2} dxdy(R_0^2 - x^2 - y^2). \tag{4.10}$$

By calculating the integral (e.g. in polar coordinates), the value for reflectivity is:

$$|R|^2 = \frac{1+\cos^2 2\theta_B}{4} k_0^2 |\chi(\boldsymbol{H},\omega)|^2 R_0^2, \tag{4.11}$$

and the condition $|R|^2 < 1$ leads to:

$$R_0 << \frac{1}{k_0|\chi(\boldsymbol{H})|}. \tag{4.12}$$

The size of the crystal at which X-ray reflectivity exceeds a unity and hence kinematical theory breaks down depends significantly on the object shape and the orientation of the vectors $\boldsymbol{k}_0$, $\boldsymbol{k}_1$, $\boldsymbol{H}$ with respect to the crystal, i.e. the geometry of the diffraction experiment. In order to demonstrate this fact, a crystal of a rectangular parallelepiped shape is considered here with the dimensions L_x, L_y, L_z. Assuming the axes of the coordinate system are parallel to the parallelepiped edges, and the origin is located in the center of the upper facet, and the z axis being parallel to the facet normal, the Eq. (4.2) is modified to:

$$\frac{d\sigma}{d\Omega} = \frac{1}{(4\pi)^2} \frac{1+\cos^2 2\theta}{2} k_0^4 |\chi(\boldsymbol{H},\omega)|^2 \times \frac{\sin^2(q_x - H_x)L_x/2}{((q_x - H_x)/2)^2} \frac{\sin^2(q_y - H_y)L_y/2}{((q_y - H_y)/2)^2} \frac{\sin^2(q_z - H_z)L_z/2}{((q_z - H_z)/2)^2}. \tag{4.13}$$

The assumption $L_x, L_y >> 1/k_0$ generally contradicts to the conditions used for deriving (4.1), however, applying the same reasoning as in Sect. 3.1 used for derivation of Eq. (3.27), and utilizing the Eq. (3.31), the X-ray scattering cross-section is:

$$\frac{d\sigma}{d\Omega} = \frac{1}{(4\pi)^2} \frac{1+\cos^2 2\theta}{2} k_0^4 |\chi(\boldsymbol{H},\omega)|^2 \times (2\pi)^2 L_x L_y \delta(q_x - H_x)\delta(q_y - H_y) \frac{\sin^2(q_z - H_z)L_z/2}{((q_z - H_z)/2)^2}. \tag{4.14}$$

In order to calculate the X-ray reflectivity, the Eq. (4.14) has to be integrated over the directions of $\boldsymbol{k}_1$. Due to the delta-functions present in (4.14), the integration is performed without tangential plane approximation. The direction of $\boldsymbol{k}_1$ is parametrized

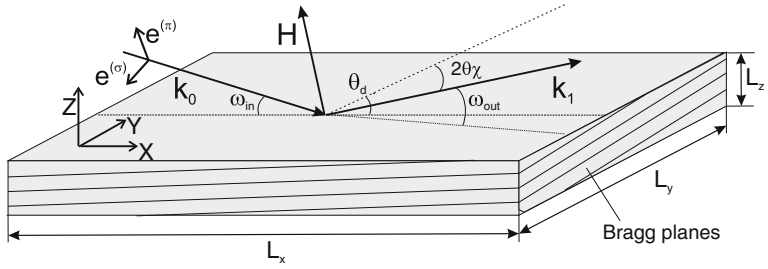

Fig. 4.2 The definitions of the angles and the axes used for the analysis of the X-ray diffraction at the rectangular sample

in terms of the angles $\theta_d, 2\theta\chi$ associated with the detector position: the detector arm is first rotated for the angle θ_d toward the $-y$ direction and then rotated within the plane constructed by the current detector arm and the y axis by the angle $2\theta\chi$ (Fig. 4.2). In this parametrization, the vector $\boldsymbol{k}_1$ has following form:

$$\boldsymbol{k}_1(\theta_d, 2\theta\chi) = k_0(\cos 2\theta\chi \cos\theta_d, -\sin 2\theta\chi, \cos 2\theta\chi \sin\theta_d). \tag{4.15}$$

The value of the solid angle corresponding to $\boldsymbol{k}_1$ is expressed through $d\theta_d, d2\theta\chi$ as

$$d\Omega = \frac{d\theta_d d2\theta\chi}{k_0^2}\left|\frac{\partial \boldsymbol{k}_1(\theta_d, 2\theta\chi)}{\partial\theta_d} \times \frac{\partial \boldsymbol{k}_1(\theta_d, 2\theta\chi)}{\partial 2\theta\chi}\right|^2 = \cos 2\theta\chi d\theta_d d2\theta\chi \tag{4.16}$$

Finally, the expression for the total cross-section of X-ray scattering is:

$$\begin{aligned}\int d\Omega \frac{d\sigma}{d\Omega} &= \frac{1}{(4\pi)^2}\frac{1+\cos^2 2\theta}{2}k_0^4|\chi(\boldsymbol{H},\omega)|^2(2\pi)^2 L_x L_y \\ &\times \int \cos 2\theta\chi d\theta_d d2\theta\chi \delta(k_0 \cos 2\theta\chi \cos\theta_d - k_{0x} - H_x) \\ &\times \delta(-k_0 \sin 2\theta\chi - k_{0y} - H_y)\frac{\sin^2(q_z - H_z)L_z/2}{((q_z - H_z)/2)^2} \\ &= \frac{1}{(4\pi)^2}\frac{1+\cos^2 2\theta}{2}k_0^2|\chi(\boldsymbol{H},\omega)|^2 \\ &\times (2\pi)^2 L_x L_y \frac{1}{\cos 2\theta\chi \sin\theta_d}\frac{\sin^2(q_z - H_z)L_z/2}{((q_z - H_z)/2)^2},\end{aligned} \tag{4.17}$$

where the property of delta-function $\delta(f(x)) = \frac{\delta(x-x_0)}{|f'(x_0)|}$ (here x_0 is the root of equation $f(x_0) = 0$) have been used, and in the last line it is implied that $q_z = \sqrt{k_0^2 - (k_{0x} + H_x)^2 + (k_{0y} + H_y)^2} - k_{0z}$ and the values of angles $d\theta_d, d2\theta\chi$ satisfy the Laue Eq. (4.3) for lateral components: $k_0 \cos 2\theta\chi \cos\theta_d - k_{0x} - H_x = 0$ and $-k_0 \sin 2\theta\chi - k_{0y} - H_y = 0$. For calculation of X-ray reflectivity, the Eq. (4.17) has

to be normalized to the beam illumination area on the sample, with the normalization coefficient $L_x L_y \sin\omega_{\text{in}}$, where ω_{in} is the angle between k_0 and XY planes. Using $\cos 2\theta\chi \sin\theta_d = \sin\omega_{\text{out}}$, the X-ray reflectivity is:

$$|R|^2 = \frac{1}{(4\pi)^2}\frac{1+\cos^2 2\theta}{2}k_0^2|\chi(\boldsymbol{H},\omega)|^2 \times (2\pi)^2\frac{1}{\sin\omega_{\text{in}}\sin\omega_{\text{out}}}\frac{\sin^2(q_z - H_z)L_z/2}{((q_z - H_z)/2)^2}. \tag{4.18}$$

When the exact Bragg condition is satisfied, the last term of (4.17) yields L_z^2 and from the condition $|R|^2 < 1$ the inequality follows:

$$L_z << \frac{\sqrt{|\sin\omega_{\text{in}}\sin\omega_{\text{out}}|}}{k_0|\chi(\boldsymbol{H})|}. \tag{4.19}$$

By comparing the Eqs. (4.19) and (4.12), there two peculiarities are observed: (i) the limitation for L_z value only is derived, the values L_x and L_y are assumed to be infinite. Hence, the lateral dimensions of the parallelepiped can be infinitely large, however, if the parallelepiped is thin enough the kinematical theory can be applied. This observation delivers the recipe for the construction of the dynamical theory [8]: the object can be divided into thin lamellas, and the scattering in each lamella is calculated kinematically, and the calculations are reduced to one dimensional problem of the re-scattering of radiation between lamellas. This was the basic idea of Darwin's extinction theory [9] and a similar approach is used for the description of electron diffraction [10], where dynamical effects are strong. (ii) In comparison with the Eq. (4.12), there is a factor $\sqrt{|\sin\omega_{\text{in}}\sin\omega_{\text{out}}|}$ which depends on the geometry of the diffraction experiment. When the Bragg condition is satisfied for either $\boldsymbol{k}_0$ or $\boldsymbol{k}_1$ making the shallow angles with the sample surface (extremely asymmetric diffraction), the enhancement of the dynamical effects occurs. The highest contribution of the dynamical effects is expected when both angles ω_{in} and ω_{out} are shallow. This case is referred to as grazing-incidence diffraction (GID), and the diffraction at these conditions demonstrates additional dynamical effects [11].

4.2 Basics of Two-Wave Dynamical Diffraction

The limitations on the sample thickness (4.19) for application of kinematical diffraction theory follows from the fact that in the kinematical theory the diffracted wave neither reduces the amplitude of the primary wave nor undergoes diffraction itself. In order to overcome this limitation, both the primary and the diffracted waves should be treated on an equal basis. In the dynamical diffraction theory (DDT) such a nonperturbative solution of equation (1.56) is constructed as a linear combination of the incoming and the diffracted waves [2]. This simple approach proves to be

correct in the most of the experiments. The validity of this solution of the nonperturbative problem follows from the small value of X-ray susceptibility that makes the secondary waves effects negligible. The DDT is suitable for X-rays, however, for the similar scattering in photonic crystals or in case of electron diffraction it can not be applied directly [10]. To illustrate this fact, we consider the example of a semi-infinite crystal. The equation to be solved is (1.56):

$$\left(k^2 - \frac{\omega^2}{c^2}(1+\chi_0)\right) A_\mu(\boldsymbol{k},\omega)$$
$$-\frac{\omega^2}{c^2} t_{\mu,\nu}(\boldsymbol{k}) \sum_{\boldsymbol{H}} \chi(\boldsymbol{k},-\boldsymbol{H},\omega) A_\nu(\boldsymbol{k}+\boldsymbol{H},\omega) = 0;$$
$$(\boldsymbol{k}\boldsymbol{A}(\boldsymbol{k},\omega)) = 0; \;\; t_{\mu,\nu} = \delta_{\mu,\nu} - \frac{k_\mu k_\nu}{k^2}$$
$$\chi_{\mu,\lambda}(\boldsymbol{k},\boldsymbol{H},\omega) \equiv \chi(\boldsymbol{k},\boldsymbol{H},\omega)\delta_{\mu,\lambda};$$
$$\chi(\boldsymbol{k},\boldsymbol{H},\omega) = \chi^{(e)}(\boldsymbol{H},\omega) + \frac{1}{3}\chi^{(a)}_{\mu,\mu}(\boldsymbol{k},\boldsymbol{H},\omega), \tag{4.20}$$

where the anisotropic part of susceptibility (1.55) is assumed to be negligible. The background of this assumption is the summation in (1.55), which is performed over all electron states. Because of the electron wave functions of the filled electron shells are spherically symmetric, the contribution from the filled shells results in isotropic susceptibility. The only anisotropic contribution can be expected from the upper unfilled shells, however, for all but light atoms the relative fraction of these electrons is low and, in addition, their contributions are attenuated due to the large spread of wave function and the integration with the oscillating exponents in (1.54) results in lower values compared to the internal shells. The isotropic properties of the atoms in X-ray scattering process are implied in the most of the calculations, e.g. in the determination of the symmetry of forbidden reflections. In some cases, the anisotropy of the atomic form-factors breaks the symmetry and is exposed in weak quasi-forbidden reflections [12, 13]. These situations are usually analyzed in the framework of the kinematical theory.

Let us consider the wave field which is excited by the incoming wave with the wave vector $\boldsymbol{k}_0$. Since the diffraction effects are strong for the wave vectors close to the Bragg condition (4.4), the vector $\boldsymbol{k}_0$ is assumed to be near the Bragg condition for the reciprocal lattice vector $\boldsymbol{H}$. We consider here only the part of susceptibility corresponding to $\boldsymbol{H}$: $\chi(\boldsymbol{k},-\boldsymbol{H},ck_0)$, $\chi(\boldsymbol{k},\boldsymbol{H},ck_0)$, i.e. so called two-wave approximation is used. The analysis is restricted to the vicinity of the Bragg peak, thus the susceptibilities are implied to be independent on $\boldsymbol{k}$: $\chi_{-\boldsymbol{H}} \equiv \chi(\boldsymbol{k}_0,-\boldsymbol{H},ck_0)$, $\chi_{\boldsymbol{H}} \equiv \chi(\boldsymbol{k}_0,\boldsymbol{H},ck_0)$. Equation (4.20) shows the coupling between wave fields $\boldsymbol{A}(\boldsymbol{k})$, $\boldsymbol{A}(\boldsymbol{k}+\boldsymbol{H})$, $\boldsymbol{A}(\boldsymbol{k}-\boldsymbol{H})$, $\boldsymbol{A}(\boldsymbol{k}+2\boldsymbol{H})$, $\boldsymbol{A}(\boldsymbol{k}-2\boldsymbol{H})$..., and the frequency $\omega = ck_0$ is omitted in arguments of the functions below:

$$
\begin{aligned}
&\left(k^2-\frac{\omega^2}{c^2}\epsilon_0\right)A_\mu(\boldsymbol{k})-\frac{\omega^2}{c^2}\chi_{-\boldsymbol{H}}t_{\mu,\nu}(\boldsymbol{k})A_\nu(\boldsymbol{k}+\boldsymbol{H})\\
&\quad-\frac{\omega^2}{c^2}\chi_{\boldsymbol{H}}t_{\mu,\nu}(\boldsymbol{k})A_\nu(\boldsymbol{k}-\boldsymbol{H})=0;\\
&\left((\boldsymbol{k}+\boldsymbol{H})^2-\frac{\omega^2}{c^2}\epsilon_0\right)A_\mu(\boldsymbol{k}+\boldsymbol{H})-\frac{\omega^2}{c^2}\chi_{-\boldsymbol{H}}t_{\mu,\nu}(\boldsymbol{k}+\boldsymbol{H})A_\nu(\boldsymbol{k}+2\boldsymbol{H})\\
&\quad-\frac{\omega^2}{c^2}\chi_{\boldsymbol{H}}t_{\mu,\nu}(\boldsymbol{k}+\boldsymbol{H})A_\nu(\boldsymbol{k})=0;\\
&\left((\boldsymbol{k}-\boldsymbol{H})^2-\frac{\omega^2}{c^2}\epsilon_0\right)A_\mu(\boldsymbol{k}-\boldsymbol{H})-\frac{\omega^2}{c^2}\chi_{-\boldsymbol{H}}t_{\mu,\nu}(\boldsymbol{k}-\boldsymbol{H})A_\nu(\boldsymbol{k})\\
&\quad-\frac{\omega^2}{c^2}\chi_{\boldsymbol{H}}t_{\mu,\nu}(\boldsymbol{k}-\boldsymbol{H})A_\nu(\boldsymbol{k}-2\boldsymbol{H})=0;\\
&\left((\boldsymbol{k}+2\boldsymbol{H})^2-\frac{\omega^2}{c^2}\epsilon_0\right)A_\mu(\boldsymbol{k}+2\boldsymbol{H})-\frac{\omega^2}{c^2}\chi_{-\boldsymbol{H}}t_{\mu,\nu}(\boldsymbol{k}+2\boldsymbol{H})A_\nu(\boldsymbol{k}+3\boldsymbol{H})\\
&\quad-\frac{\omega^2}{c^2}\chi_{\boldsymbol{H}}t_{\mu,\nu}(\boldsymbol{k}+2\boldsymbol{H})A_\nu(\boldsymbol{k}+\boldsymbol{H})=0;\\
&\left((\boldsymbol{k}-2\boldsymbol{H})^2-\frac{\omega^2}{c^2}\epsilon_0\right)A_\mu(\boldsymbol{k}-2\boldsymbol{H})-\frac{\omega^2}{c^2}\chi_{-\boldsymbol{H}}t_{\mu,\nu}(\boldsymbol{k}-2\boldsymbol{H})A_\nu(\boldsymbol{k}-\boldsymbol{H})\\
&\quad-\frac{\omega^2}{c^2}\chi_{\boldsymbol{H}}t_{\mu,\nu}(\boldsymbol{k}-2\boldsymbol{H})A_\nu(\boldsymbol{k}-3\boldsymbol{H})=0;\\
&\cdots,
\end{aligned}
\tag{4.21}
$$

with $\epsilon_0=1+\chi_0$ as a dielectric constant of the medium.

By omitting the special case of the simultaneous excitation of multiple Bragg reflections [4], the vector $\boldsymbol{k}_0$ being in Bragg condition with vector $\boldsymbol{H}$ is far from the Bragg conditions for the vectors $-\boldsymbol{H}$, $2\boldsymbol{H}$, $-2\boldsymbol{H}$, ..., and thus the contributions $\boldsymbol{A}(\boldsymbol{k}-\boldsymbol{H})$, $\boldsymbol{A}(\boldsymbol{k}+2\boldsymbol{H})$, $\boldsymbol{A}(\boldsymbol{k}-2\boldsymbol{H})$... can be neglected and the system of two matrix equations describes the problem:

$$
\begin{aligned}
\left(k^2-\frac{\omega^2}{c^2}(1+\chi_0)\right)A_\mu(\boldsymbol{k})-\frac{\omega^2}{c^2}\chi_{-\boldsymbol{H}}t_{\mu,\nu}(\boldsymbol{k})A_\nu(\boldsymbol{k}+\boldsymbol{H})=0;\\
\left((\boldsymbol{k}+\boldsymbol{H})^2-\frac{\omega^2}{c^2}(1+\chi_0)\right)A_\mu(\boldsymbol{k}+\boldsymbol{H})-\frac{\omega^2}{c^2}\chi_{\boldsymbol{H}}t_{\mu,\nu}(\boldsymbol{k}+\boldsymbol{H})A_\nu(\boldsymbol{k})=0.
\end{aligned}
\tag{4.22}
$$

Using the notations:

$$
\begin{aligned}
X(\boldsymbol{k})&\equiv\left(k^2-\frac{\omega^2}{c^2}(1+\chi_0)\right),\\
X(\boldsymbol{k}+\boldsymbol{H})&\equiv\left((\boldsymbol{k}+\boldsymbol{H})^2-\frac{\omega^2}{c^2}(1+\chi_0)\right),
\end{aligned}
\tag{4.23}
$$

and evaluating $A_\mu(\boldsymbol{k}+\boldsymbol{H})$ from the second line of (4.22) and substituting it in the first line:

$$\left(X(\boldsymbol{k})t_{\mu,\nu}(\boldsymbol{k}) - \frac{\omega^4}{c^4}\frac{\chi_{\boldsymbol{H}}\chi_{-\boldsymbol{H}}}{X(\boldsymbol{k}+\boldsymbol{H})}t_{\mu,\sigma}(\boldsymbol{k})t_{\sigma,\tau}(\boldsymbol{k}+\boldsymbol{H})t_{\tau,\nu}(\boldsymbol{k})\right)A_\mu(\boldsymbol{k}) = 0, \quad (4.24)$$

where an additional projector $t_{\mu,\nu}(\boldsymbol{k})$ is implemented before $A_\mu(\boldsymbol{k})$ in order to get more symmetrical expression (this insertion is justified by the fact that $A_\mu(\boldsymbol{k})$ is transversal). The matrix on the left hand side of (4.24) preserves the transversality of the vector $A_\mu(\boldsymbol{k})$, and thus can be considered as a 2×2 matrix acting on the vectors transversal to $\boldsymbol{k}$. Then the Eq. (4.22) is formulated in the coordinate-free form as:

$$\begin{aligned}
&\hat{\beta}\cdot\boldsymbol{A} = 0,\\
&\hat{\beta} = \left(X(\boldsymbol{k}) - \frac{\omega^4}{c^4}\frac{\chi_{\boldsymbol{H}}\chi_{-\boldsymbol{H}}}{X(\boldsymbol{k}+\boldsymbol{H})}\right)\hat{I}_2\\
&\quad + \frac{\omega^4}{c^4}\frac{\chi_{\boldsymbol{H}}\chi_{-\boldsymbol{H}}}{X(\boldsymbol{k}+\boldsymbol{H})(\boldsymbol{k}+\boldsymbol{H})^2}(\boldsymbol{k}+\boldsymbol{H})_\perp\otimes(\boldsymbol{k}+\boldsymbol{H})_\perp = 0,
\end{aligned} \quad (4.25)$$

where $\hat{I}_2$ is a two dimensional unitary operator acting in the space of the vectors transversal to $\boldsymbol{k}$, $\otimes$ denotes diad (outer) product, and the equalities $\hat{t}(\boldsymbol{a}) = \hat{I} - \frac{\boldsymbol{a}\otimes\boldsymbol{a}}{a^2}$ with $\hat{I}$ as the two-dimensional unit operator and $(\boldsymbol{k}+\boldsymbol{H})_\perp = \hat{t}(\boldsymbol{k})\cdot(\boldsymbol{k}+\boldsymbol{H})$ are used. The expression $\hat{\beta}\cdot\boldsymbol{A} = 0$ is fulfilled only in the case when $\det\beta = 0$, which gives an equation for possible values of $\boldsymbol{k}$: the dispersion equation. For the two-dimensional matrices, in according to Cayley-Hamilton theorem, the determinant is expressed through the matrix traces as:

$$\det\beta = \frac{(\mathrm{Tr}\beta)^2 - \mathrm{Tr}\beta^2}{2}. \quad (4.26)$$

The matrix β has a structure of kind $C_1\hat{I}_2 + C_2\boldsymbol{v}\otimes\boldsymbol{v}$, and the direct calculation of the traces results in $\det\beta = 2C_1(C_1 + C_2v^2)$. Finally, an application of these results to (4.25) yields the following dispersion equation:

$$\left\{X(\boldsymbol{k}) - \frac{\omega^4}{c^4}\frac{\chi_{\boldsymbol{H}}\chi_{-\boldsymbol{H}}}{X(\boldsymbol{k}+\boldsymbol{H})}\right\}\left\{X(\boldsymbol{k}) - \frac{\omega^4}{c^4}\frac{\chi_{\boldsymbol{H}}\chi_{-\boldsymbol{H}}}{X(\boldsymbol{k}+\boldsymbol{H})}\frac{(\boldsymbol{k}\cdot(\boldsymbol{k}+\boldsymbol{H}))^2}{k^2(\boldsymbol{k}+\boldsymbol{H})^2}\right\} = 0. \quad (4.27)$$

The dispersion Eq. (4.27) is factorized into product of two equations. Each of them corresponds to independent polarization states, which can be treated separately reducing the order of the dispersion equation. Indeed, the starting Eq. (4.22) is a system of 4 equations (2 equations corresponding to 2 polarization states for each of the waves $\boldsymbol{A}(\boldsymbol{K})$, $\boldsymbol{A}(\boldsymbol{k}+\boldsymbol{H})$) and each equation contains the unknown value $\boldsymbol{k}^2$, thus a 8th order equation has to be solved. However, due to the approximation of the isotropic susceptibility (4.20), it is factorized into two 4th order Eq. (4.27). Otherwise, the

polarizations are not separated in (4.27) and a 8th order dispersion equation describing both polarization states simultaneously has to be considered.

Both polarizations (or in mathematical terms, the eigenvectors of $\hat{\beta}$ corresponding to zero eigenvalue) can be found directly from the Eqs. (4.27) and (4.23). Assuming the first multiplier in (4.27) to be equal zero, the corresponding polarization vector $\boldsymbol{e}_1$, as follows from (4.25) is equal to:

$$(\boldsymbol{k}+\boldsymbol{H})_\perp \otimes (\boldsymbol{k}+\boldsymbol{H})_\perp \cdot \boldsymbol{e}_1 = 0.$$

This condition is fulfilled for the vector $\frac{[\boldsymbol{k},\boldsymbol{k}+\boldsymbol{H}]}{|[\boldsymbol{k},\boldsymbol{k}+\boldsymbol{H}]|}$ since it is orthogonal to both $\boldsymbol{k}$ and $(\boldsymbol{k}+\boldsymbol{H})_\perp$. Note, that assuming $\boldsymbol{k}$ to be close to $\boldsymbol{k}_0$ and $\boldsymbol{k}+\boldsymbol{H}$ to be close to $\boldsymbol{k}_1$, we come to the definition of σ polarization given above, and notation $\boldsymbol{e}_1 \equiv \boldsymbol{e}_\sigma$ can be used. The second polarization vector, named $\boldsymbol{e}_\pi$, should be orthogonal to the vectors $\boldsymbol{k}$ and $\boldsymbol{e}_\sigma$ and can be constructed as a vector product of them:

$$\boldsymbol{e}_\sigma = \frac{\boldsymbol{k}\times(\boldsymbol{k}+\boldsymbol{H})}{|\boldsymbol{k}\times(\boldsymbol{k}+\boldsymbol{H})|}, \quad \boldsymbol{e}_\pi = \frac{\boldsymbol{k}\times\boldsymbol{e}_\sigma}{|\boldsymbol{k}\times\boldsymbol{e}_\sigma|}. \tag{4.28}$$

Dispersion equation (4.27) for both polarizations can be written down in a similar way:

$$X(\boldsymbol{k})X(\boldsymbol{k}+\boldsymbol{H}) - Q_s = 0,\ s = \sigma,\pi$$

$$Q_s = \frac{\omega^4}{c^4}\chi_{\boldsymbol{H}}\chi_{-\boldsymbol{H}}C_s^2, \tag{4.29}$$

$$C_s^2 = \begin{cases} 1 & \text{for } \sigma \\ \frac{(\boldsymbol{k}\cdot(\boldsymbol{k}+\boldsymbol{H}))^2}{k^2(\boldsymbol{k}+\boldsymbol{H})^2} \approx \cos^2 2\Theta_B & \text{for } \pi \end{cases} \text{ polarization.} \tag{4.30}$$

Here $\boldsymbol{k}$ is assumed to be close to the Bragg condition for π polarization. Since the dynamical theory is advantageous near the Bragg condition, the quantity C_π is treated below as a constant equals to $\cos^2 2\Theta_B$.

Let us discuss the solutions of the dispersion Eq. (4.29). The unknown quantity is a wave vector $\boldsymbol{k}$ inside the crystal. In the most problems of DDT one deals with the diffraction from the plane-parallel layered crystal structures [3]. In this case it is convenient to represent the vector in the following form:

$$\boldsymbol{k} = -\boldsymbol{N}u + \boldsymbol{k}_{0||},\ \ \boldsymbol{k}_{0||} = \hat{t}(\boldsymbol{N})\cdot\boldsymbol{k}_0, \tag{4.31}$$

where $\boldsymbol{N}$ is a crystal surface normal. The reason for the equality of the lateral components of the wave vector in a vacuum and in the media is the same as for the specular reflection law (3.11): in order to fulfill the boundary conditions at the crystal surface, the exponential pre-factors have to be equal for the waves in a vacuum and in the medium. Hence the dispersion equation is a 4th order equation in term of u:

$$\left[u^2 + k_{0||}^2 - \frac{\omega^2}{c^2}\epsilon_0\right]\left[(u + H_z)^2 + (\boldsymbol{k}_{0||} + \boldsymbol{H}_{||})^2 - \frac{\omega^2}{c^2}\epsilon_0\right] - Q_s = 0, \quad (4.32)$$

where the z axis is chosen inwards the sample and opposite to the outward surface normal, $\boldsymbol{H}_{||} = \hat{\imath}(\boldsymbol{N}) \cdot \boldsymbol{H}$. In general case, the solution of the quaternary Eq. (4.32) can be found using Ferrari-Cardano formulas. However, these formulas are cumbersome, require multiple checking of appropriate roots, and do not provide an insight in the physics of the process. In two special cases, the Eq. (4.32) is reduced to the biquadratic one and is solved exactly. Assuming $H_z = 0$, the solution is:

$$u_{i,s} = \pm\sqrt{\frac{\omega^2}{c^2}\epsilon_0 - \frac{1}{2}\left(k_{0||}^2 + k_{1||}^2\right) \pm \sqrt{\frac{1}{4}\left(k_{0||}^2 - k_{1||}^2\right)^2 + Q_s}},$$
$$\boldsymbol{k}_{1||} = \boldsymbol{k}_{0||} + \boldsymbol{H}_{||};\ i = 1 \ldots 4. \quad (4.33)$$

This case corresponds to the grazing-incidence diffraction and will be considered in this chapter separately. Another biquadratic case is $\boldsymbol{H}_{||} = 0$, where using the re-definition $u = u_c - H_z/2$, the biquadratic equation for variable u_c provides the solutions:

$$u_{i,s} = \pm\sqrt{\frac{H_z^2}{4} + \frac{\omega^2}{c^2}\epsilon_0 - k_{0||}^2 \pm \sqrt{H_z^2\left(\frac{\omega^2}{c^2}\epsilon_0 - k_{0||}^2\right) + Q_s}} - \frac{H_z}{2},$$
$$i = 1 \ldots 4. \quad (4.34)$$

This case corresponds to the symmetric diffraction, when the crystallographic planes corresponding to the reciprocal lattice vector $\boldsymbol{H}$ are parallel to the crystal surface. In fact, the X-ray diffraction in this case can be also considered as refraction from a periodic stack of the atomic layers in a way similar to the Sect. 3.3. The problem reduces to a one-dimensional second order linear differential equation with the periodic potential similar to the Kronig-Penney model, which is exactly solvable provided the reflection and transition coefficients of a single layer are known [14]. Thus, the symmetric diffraction case can be solved analytically beyond the two-wave approximation.

In other cases, when $H_z \neq 0$ and $\boldsymbol{H}_{||} \neq 0$, to avoid the use of bulky Ferrari-Cardano formulas for the solution of (4.32), the approximation utilizing the neglect of the quantities containing some small parameter has to be used. The natural small parameter in X-ray scattering process is X-ray susceptibility, and further results are accurate up to the first non-vanishing order in X-ray susceptibility.

By considering the Eq. (4.32) in the case when the diffraction is "switched-off" $\chi_{\boldsymbol{H}} = \chi_{-\boldsymbol{H}} = 0$, this expression factorizes into two equations describing the propagation of two plane waves which do not interact with each other. The first multiplier in (4.32) corresponds to the refracted incident wave, and the obvious solution of the uncoupled dispersion equation is:

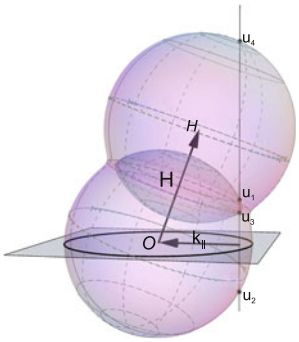

Fig. 4.3 The dispersion surface for two-wave diffraction. The actual value of the wave vector in the media is determined by in-plane component of the incidence wave vector. The roots u_1, u_2, u_3, and u_4 correspond to the incident, the specularly reflected incident, the diffracted, and the specularly reflected diffracted waves, respectively

$$u_{\text{direct, uncoupled}} = \pm\gamma_0, \;\; \gamma_0 = \sqrt{\frac{\omega^2}{c^2}(1+\chi_0) - k_{0||}^2}. \tag{4.35}$$

By "switching-on" the diffraction, the solution is found in the form of the dispersion surface for the refracted incident wave with addition of a small correction δ [15]:

$$u_{1,s} = \gamma_0 + \delta_{1,s}, \tag{4.36}$$

then the dispersion equation is modified to:

$$\left[\delta_{1,s}^2 + 2\delta_{1,s}\gamma_0\right]\left[\delta_{1,s}^2 + 2\delta_{1,s}(\gamma_0 + H_z) + \alpha\right] - Q_s = 0. \tag{4.37}$$

Here the parameter α is introduced describing the deviation from the Bragg condition as

$$\alpha = 2\gamma_0 H_z + 2\boldsymbol{k}_{0||} \cdot \boldsymbol{H}_{||} + \boldsymbol{H}^2. \tag{4.38}$$

This formula differs from the Eq. (4.4) by the refraction correction in variable γ_0. In the region far from the Bragg condition $|\alpha|/k_0^2 \sim 1$ and this value is much greater than $\delta_{1,s}$, which corresponds to the considered diffracted wave. Assuming $\delta_{1,s}k_0 \ll \alpha$, $\delta_{1,s} \ll k_0$, the Eq. (4.37) is modified to:

$$\delta_{1,s\text{ far from Bragg}} \approx \frac{Q_s}{2\gamma_0\alpha} \sim |\chi_H|^2 k_0, \tag{4.39}$$

and thus the correction to γ_0 is proved to be negligible. Satisfying the exact Bragg condition $\alpha = 0$ and assuming $\delta \ll k_0$ we get:

$$\delta_{1,s\text{ exact at Bragg}} \approx \sqrt{\frac{Q_s}{4\gamma_0(\gamma_0 + H_z)}} \sim |\chi_H| k_0, \tag{4.40}$$

and thus $\delta_{1,s}$ corresponding to the incoming wave is always a small quantity, and the assumption $\delta_{1,s} \ll k_0$ in each of multiplier in (4.37) can be used, which simplifies the dispersion equation to the quadratic one with the roots:

$$\begin{aligned} \delta_{1,s} &= \frac{-\alpha\gamma_0 + \mathrm{Sign}(\Re(\alpha\gamma_0))\sqrt{\alpha^2\gamma_0^2 + Q_s(\alpha + 4\gamma_0(\gamma_0 + H_z))}}{\alpha + 4\gamma_0(\gamma_0 + H_z)} \\ u_{1,s} &= \gamma_0 + \delta_{1,s}. \end{aligned} \tag{4.41}$$

Both limiting cases (4.39) and (4.40) follow from the Eq. (4.41). The root of (4.32) which tends to $u_0 = -\gamma_0$ in (4.35) describes the specularly reflected incident wave, see Fig. 4.3. This wave is far from the Bragg condition, and according to (4.39) it can be written with the accuracy $\sim |\chi_H|^2 k_0$ as:

$$u_{2,s} = -\gamma_0. \tag{4.42}$$

A similar analysis can be performed with the second multiplier in (4.32) which describes a free propagation of the diffracted wave. The solution corresponding to the "switched-off" diffraction is:

$$u_{\text{diffracted, uncoupled}} = \pm\gamma_H - H_z, \;\; \gamma_H = \sqrt{\frac{\omega^2}{c^2}(1 + \chi_0) - (\boldsymbol{k}_{0||} + \boldsymbol{H})^2}, \tag{4.43}$$

and looking for the solution in the form

$$u_{3,s} = \gamma_H - H_z + \delta_{3,s} \tag{4.44}$$

and introducing the deviation parameter α_H:

$$\alpha_H = -2\gamma_H H_z - 2\boldsymbol{k}_{0||} \cdot \boldsymbol{H}_{||} - \boldsymbol{H}_{||} + H_z^2, \tag{4.45}$$

which is close to $-\alpha$ near the Bragg condition, the Eq. (4.32) is modified to:

$$\left[\delta_{3,s}^2 + 2\delta_{3,s}(\gamma_H - H_z) + \alpha_H\right]\left[\delta_{3,s}^2 + 2\delta_{3,s}\gamma_H\right] - Q_s = 0, \tag{4.46}$$

and finally results in:

$$\begin{aligned} \delta_{3,s} &= \frac{-\alpha_H\gamma_H + \mathrm{Sign}(\Re(\alpha_H\gamma_H))\sqrt{\alpha_H^2\gamma_H^2 + Q_s(\alpha_H + 4\gamma_H(\gamma_H - H_z))}}{\alpha_H + 4\gamma_H(\gamma_H - H_z)} \\ u_{3,s} &= \gamma_H - H_z + \delta_{3,s}, \\ u_{4,s} &= -\gamma_H - H_z. \end{aligned} \tag{4.47}$$

The wave fields existing in the crystal under diffraction process are the sum of coupled waves $\boldsymbol{A}_{i,s}(\boldsymbol{k})$ and $\boldsymbol{A}_{i,s}(\boldsymbol{k}+\boldsymbol{H})$ corresponding to all dispersion equation solutions i for polarization states $s = \sigma, \pi$. The relationship between them follows from (4.22):

$$\begin{aligned} \boldsymbol{A}_{i,s}(\boldsymbol{k}_{i,s}+\boldsymbol{H}) &= \hat{V_{i,s}} \cdot \boldsymbol{A}_{i,s}(\boldsymbol{k}_{i,s}), \\ \hat{V_{i,s}} &= V_{i,s}\hat{t}(\boldsymbol{k}_{i,s}+\boldsymbol{H}), \\ V_{i,s} = \frac{\omega^2}{c^2}\chi_{\boldsymbol{H}}\frac{1}{X(\boldsymbol{k}_{i,s}+\boldsymbol{H})} &= \frac{\omega^2}{c^2}\chi_{\boldsymbol{H}}\frac{X(\boldsymbol{k}_{i,s})}{Q_s}, \end{aligned} \tag{4.48}$$

where the expression (4.29) has been taken into account. The amplitudes $A_{i,s}(\boldsymbol{k}_{i,s})$ are determined by the boundary conditions, and in general case the wave field in the crystal is:

$$\boldsymbol{A}(\boldsymbol{r},t) = \sum_{i,s} A_{i,s} e^{i(\boldsymbol{k}_{||}\boldsymbol{r}_{||}+u_{i,s}z-\omega t)}\left(1+e^{i\boldsymbol{H}\boldsymbol{r}}\hat{V}_{i,s}\right)\cdot\boldsymbol{e}_s. \tag{4.49}$$

Here the solution for the dispersion equation $u_{i,s}$ is taken from the formulas (4.41), (4.42), and (4.47); the expressions for the amplitude ratios $\hat{V}_{i,s}$ (4.48) and the polarization vectors (4.28) are substituted, accordingly.

The dispersion equation and the amplitude ratio is usually analyzed in different ways for various diffraction geometries, which depends on the mutual disposition of the main vectors: the incident wave vector $\boldsymbol{k}_0$, the surface normal $\boldsymbol{N}$, the reciprocal lattice vector $\boldsymbol{H}$ for the considered crystallographic planes and the diffracted wave vector $\boldsymbol{k}_1 = \boldsymbol{k} + \boldsymbol{H}$ (Fig. 4.4). For practical applications (except grazing incidence diffraction) the coplanar geometry is mainly used when all these vectors are in the same plane. In this case the in-plane wave vector has only one component connected directly with the angles ω_{in} and ω_{out} between sample surface, incident and diffracted beams respectively (Fig. 4.4):

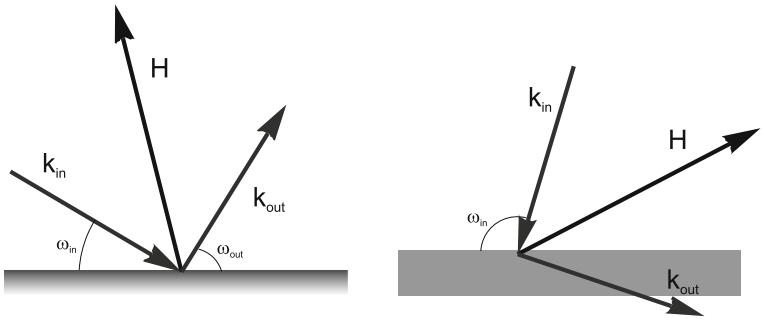

Fig. 4.4 Various coplanar geometries that are used in the dynamical diffraction theory: Bragg case (*left*) and Laue case (*right*)

$$\boldsymbol{k}_{||} \to k_x = k_0 \cos\omega_{in}, \quad k_x + H_x = k_0 \cos\omega_{out}. \tag{4.50}$$

Let us discuss below some properties of the wave field (4.49) focusing on the structure of transmitted and diffracted wave close to the Bragg conditions.

4.2.1 Amplitude Ratio

The ratio of the amplitudes of the diffracted and incident waves shows directly how strong the diffracted wave is. For example, the root $u_{1,s}$ (4.41) in the absence of diffraction corresponds to the incident wave (4.35). The diffraction process implements a correction (4.36) and according to (4.49) the incident wave $\boldsymbol{A}_{\text{inc}}(\boldsymbol{r}, t) = A_{1,s} e^{i(\boldsymbol{k}_{||}\boldsymbol{r}_{||} + u_{1,s} z - \omega t)} \boldsymbol{e}_s$ is accompanied by the diffracted wave $\boldsymbol{A}_{\text{diffr}}(\boldsymbol{r}, t) = e^{i\boldsymbol{H}\boldsymbol{r}} \hat{V}_{i,s} \cdot \boldsymbol{A}_{\text{inc}}(\boldsymbol{r}, t)$. Thus, the value $\hat{V}_{i,s}$ can be used as a measure of the diffraction effects. For the root $u_{1,s}$, the quantity $X(\boldsymbol{k}) = 2\gamma_0\delta_{1,s} + \delta_{1,s}^2$, and with the above-mentioned accuracy in terms of $|\chi_H|$, the following expression for the amplitude ratio is derived:

$$\hat{V}_{1,s} = \frac{\omega^2}{c^2} \chi_{\boldsymbol{H}} \frac{2\gamma_0\delta_{1,s}}{Q_s} \hat{t}(\boldsymbol{k} + \boldsymbol{H}). \tag{4.51}$$

The amplitude of the diffracted wave is proportional to the deviation $\delta_{1,s}$ of the dispersion surface from the non-disturbed position due to the diffraction phenomenon. Here several limiting cases are considered.

i. Large deviations from the Bragg condition, from (4.41) and (4.39) it follows:

$$V_{1s,\text{far from Bragg}} \approx \frac{\omega^2}{c^2} \frac{\chi_{\boldsymbol{H}}}{\alpha} \sim |\chi_H|, \tag{4.52}$$

and the diffracted wave is $|\chi_H|$ times weaker than the incident wave.

ii. Exact Bragg condition, from (4.41), (4.40), and (4.29) it follows:

$$V_{1s,\text{at Bragg}} \approx \sqrt{\frac{\chi_{\boldsymbol{H}}}{C_s \chi_{-\boldsymbol{H}}}} \sqrt{\frac{\gamma_0}{\gamma_0 + H_z}} \sim 1. \tag{4.53}$$

Hence, at exact Bragg condition the diffracted wave has the same order of magnitude as the incident one. As follows also from (4.53), at the Bragg condition the diffracted wave amplitude is independent on the magnitude of $\chi_{\boldsymbol{H}}$. This situation is typical for perturbations theory in the presence of degenerate states [16]: even infinitesimally small perturbation leads to the rearrangement of the eigenstates of the system into correct linear combinations of the degenerate states. In the case of diffraction, two degenerate states are the waves satisfying the dispersion equations $X(\boldsymbol{k}) = 0$ and $X(\boldsymbol{k} + \boldsymbol{H}) = 0$ at the same value of the wave vector $\boldsymbol{k}$, and the perturbation is caused by the spacial periodic susceptibility $\chi_{\boldsymbol{H}}$.

The maximal peak value (4.53) is independent on the magnitude $\chi_{\boldsymbol{H}}$, however, the peak width is proportional to it. Let us consider a simplified case which enables to get an analytical representation of $\hat{V}_{1,s}$. Under the following conditions:

- $\alpha \ll \gamma_0(\gamma_0 + H_z)$, which is true close to the Bragg condition;
- $\gamma_0 > 0$, $\gamma_0 + H_z < 0$, that corresponds to the case of the reflection (Bragg) geometry when the diffracted wave moves in vertical direction opposite to the incident wave;
- $\chi_{\boldsymbol{H}} = (\chi_{-\boldsymbol{H}})^*$, Q_s is real and $\Im(\chi_0) = 0$, that corresponds to the case of no absorption,
- σ polarization, than $\hat{t}(\boldsymbol{k} + \boldsymbol{H}) = 1$,

Equation (4.53) converts into:

$$V_{1,\sigma} = \frac{\omega^2}{c^2}\chi_{\boldsymbol{H}}\frac{\gamma_0}{2Q(\gamma_0 + H_z)}\left(\mathrm{Sign}(\Re(\alpha))\sqrt{\alpha^2 - \left|\frac{4Q(\gamma_0 + H_z)}{\gamma_0}\right|} - \alpha\right). \quad (4.54)$$

$$V_{1,\pi} = \frac{\omega^2}{c^2}\chi_{\boldsymbol{H}}\frac{C_\pi\gamma_0}{2Q(\gamma_0 + H_z)}\left(\mathrm{Sign}(\Re(\alpha))\sqrt{\alpha^2 - \left|\frac{4Q(\gamma_0 + H_z)}{\gamma_0}\right|} - \alpha\right). \quad (4.55)$$

If the value of α is smaller than

$$\alpha_{\mathrm{edge}} = \sqrt{\left|\frac{4Q(\gamma_0 + H_z)}{\gamma_0}\right|} \sim |\chi_{\boldsymbol{H}}|, \quad (4.56)$$

the quantity in brackets equals to $i\sqrt{\alpha_{\mathrm{edge}}^2 - \alpha^2} - \alpha$ and its modulus square is α_{edge}^2.

The deviation parameter α is a function of wave vector $\boldsymbol{k}_0$ of incoming wave (4.38), which is described by means of the angle ω_{in} between the wave vector of the primary beam and the crystal surface, see Figs. 4.2 and 4.4. In this parametrization, the variable α becomes a function of ω_{in}, the explicit form is obtained by substitution $k_{||} = \frac{\omega}{c}\cos\omega_{\mathrm{in}}$ into Eqs. (4.35) and (4.38). In the range of $-\alpha_{\mathrm{edge}} < \alpha < \alpha_{\mathrm{edge}}$ the modulus square of the diffracted to the incident amplitudes ratio does not depend on the incident angle ω_{in} . It means that the intensity of the diffracted beam remains equal to its peak value. This phenomena is known as *Darwin's table*, as shown in Fig. 4.5. The width of the "table" is $2\alpha_{\mathrm{edge}}$ and is proportional to $|\chi_{\boldsymbol{H}}|$. The weaker the diffraction effect quantified by $|\chi_{\boldsymbol{H}}|$, the more narrow is the region wherein total radiation is diffracted.

On the top of the Darwin table, the X-ray reflectivity $|R|^2$ equals 1, which is explained by the presence of the imaginary part in the variable $u_{1,s}$ in this region, which means that waves can not propagate inside the crystal and total incident radiation comes out into diffracted wave. The imaginary part of $u_{1,s}$ denotes the band gap for X-ray photons, and the situation is similar to that for the conductive electrons in the solids [17]. The band gap for weakly bound conductive electrons takes place

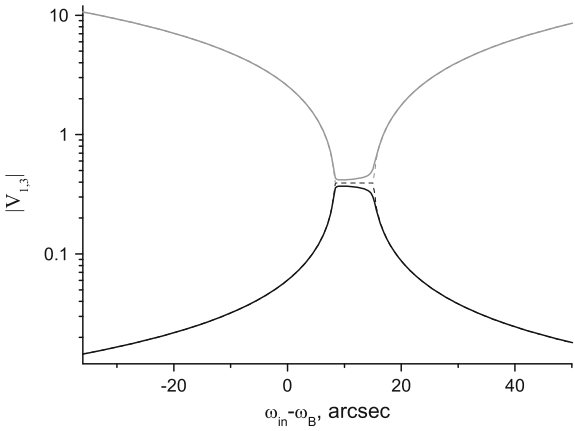

Fig. 4.5 The values $|V_{1,\sigma}|$ (*black line*) and $|V_{3,\sigma}|$ (*gray line*) near the Bragg condition for Si (224), CuK-α radiation as the functions of the incidence angle ω_{in}; ω_{B} corresponds to the kinematical Bragg condition (4.4). *Dashed curves* correspond to $|V_{1,3,\sigma}|$ calculated with neglected X-ray absorption

at the edge of Brillouin zone, the Bragg condition (4.4) is nothing but equation in terms of $\boldsymbol{k}$ describing the plane, which separates two Brillouin zones.

At the edge of Darwin table the variable $|V_{1,\sigma}|^2$ has a kink as a function of α, and its first derivative is discontinued. This behavior is of the same nature as Van Hove singularities near the edge of the band gap [17]. When the X-ray absorption is taken into account, the kinks at the edges of Darwin table become smoothed and the table becomes asymmetric, see Fig. 4.5.

The function $V_{3,\sigma}$ corresponds to root (4.43) and refers to the propagation of the diffracted wave. From (4.46) and (4.48), the expression for this function is derived:

$$\hat{V}_{3,s} = \frac{\omega^2}{c^2}\chi_{\boldsymbol{H}}\frac{1}{2\gamma_0\delta_{3,s}}\hat{t}(\boldsymbol{k}+\boldsymbol{H}). \tag{4.57}$$

Here the deviation parameter appears in the denominator, and the behavior of the function is inverse to that of (4.51). The function $V_{3,\sigma}$ possesses a Darwin's table, like behavior at Bragg condition, and in the region far from the Bragg condition it grows according to:

$$V_{3,s,\text{far from Bragg}} \approx \frac{c^2}{\omega^2}\frac{\alpha_H}{\chi_{-\boldsymbol{H}}} \sim \frac{1}{|\chi_H|}. \tag{4.58}$$

This inverse behavior (see upper curve at Fig. 4.5) can be explained as follows: for the root $u_{3,s}$ the wave with the wave vector, which is close to $\boldsymbol{k}+\boldsymbol{H}$, is considered as a primary wave (4.43) and the wave with the wave vector, which is close to $\boldsymbol{k}$, can be interpreted as a wave emerged due to the diffraction, corresponding to the reciprocal lattice vector $-\boldsymbol{H}$ of the primary one. The amplitude ratio of the waves close to $\boldsymbol{k}$ and to $\boldsymbol{k}+\boldsymbol{H}$ is $\frac{1}{V_{3,s}}$, and this ratio describing the diffraction of the wave $\boldsymbol{k}+\boldsymbol{H}$ behaves as predicted by the Eq. (4.51).

4.2.2 Anomalous Absorption and Extinction

The imaginary part of the wave vector describes the attenuation of the wave in medium. Under the no absorption condition $\chi_{\boldsymbol{H}} = (\chi_{-\boldsymbol{H}})^*$ and in the exact Bragg condition, the quantity $\delta_{1,s}$ being an addition to k_z due to the diffraction, is purely imaginary, see (4.40):

$$\delta_{1,s\,\text{exact at Bragg}} = i\frac{\omega^2}{c^2}\frac{|\chi_{\boldsymbol{H}}|}{2\sqrt{\gamma_0(\gamma_0 + H_z)}}. \tag{4.59}$$

The depth $L_{\text{Bragg},\,e}$ at which the wave is attenuated e times is $1/\Im\delta_{1,s}$. To compare this length parameter with the length L_z characterizing the validity limitation of the kinematical theory (4.19), the following values are set $\gamma_0 = k_0 \sin\omega_{in}$, $H_z - \gamma_0 = k_0 \sin\omega_{out}$ (here $k_0 = \omega/c$) assuming the absence of the refraction effects:

$$L_{\text{Bragg},\,e} = 2\frac{\sqrt{|\sin\omega_{\text{in}} \sin\omega_{\text{out}}|}}{k_0|\chi(\boldsymbol{H})|} = 2L_z. \tag{4.60}$$

In the kinematical theory, the parameter L_z emerges as a thickness of a slab at which the reflectivity $|R|^2$ exceeds unity, i.e. the diffracted wave becomes more intense than the incident one. In the dynamical theory, the maximal amplitude of the diffracted wave normalized to the primary wave is given by (4.53) and results in $|R|^2 = 1$. The attenuation (4.59) in non-absorbing crystal means that the primary wave is transformed into the diffracted wave. Thus, the wave attenuation occurs not due to the absorption but due to the transformation into the diffracted wave, and the characteristic length scale at which this transfer takes place is $L_{\text{Bragg,e}}$. Not surprisingly, this length scale equals to the thickness of a slab L_z, for which the diffracted wave amplitude becomes comparable with the primary wave amplitude, as given by the kinematical theory. This phenomenon of the coherent attenuation is called extinction, and when the crystal is absorbing, both attenuation mechanisms act together, Fig. 4.6.

As a next step, the situation $\gamma_0 + H_z > 0$ at Bragg condition is considered. In this case, the diffracted wave propagates in the same direction as a primary wave and exits the crystal plate at the opposite side of the entry plane (*transmission* or Laue geometry). Under this condition, the parameter (4.40) is real, and the corresponding length scale, equal to (4.60) has the meaning of the length at which the primary wave is transferred back and forth into diffracted wave. This effect is called *Pendellosung* taking its origin from a mechanical analogy: primary and diffracted waves in Laue geometry have the same behavior versus z as two weakly coupled pendulums behave in time, the energy flows back and forth from one to another (Fig. 4.7).

In the Laue case, the diffraction phenomenon influences the absorption property of the material. The physical background for this effect is the change of the structure of the wave field interacting with the crystal comparing to the plane wave used in the calculation of the absorption. The absorption of the wave field (4.49), which

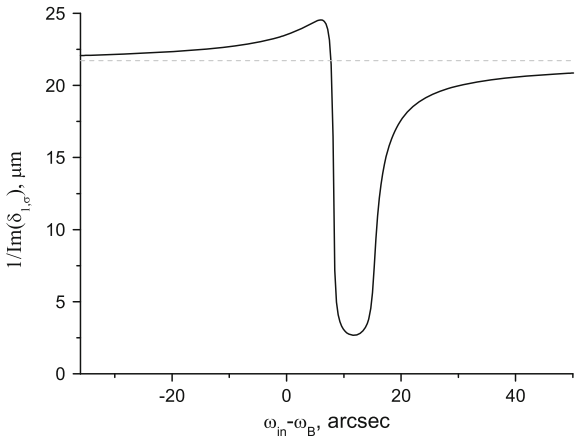

Fig. 4.6 The function $1/\Im\delta_{1,s}$ at the same conditions as in Fig. 4.5. The *dashed line* corresponds to the absorption in the absence of diffraction

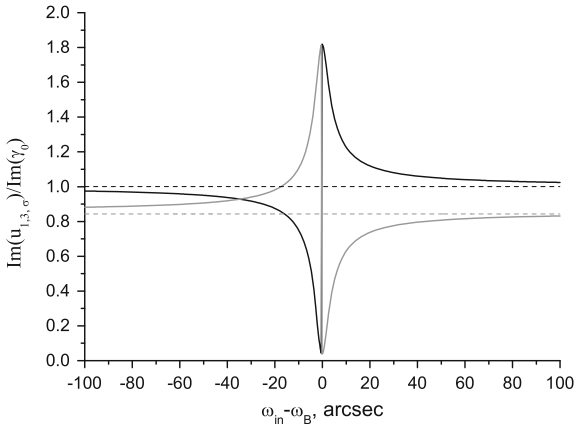

Fig. 4.7 The functions $\Im u_{1,\sigma}/\Im\gamma_0$ (*black line*) and $\Im u_{3,\sigma}/\Im\gamma_0$ (*gray line*) for the Laue diffraction from Si (220) crystal with 10° miscut of crystallographic planes

is a superposition of two waves alternating in space with the period of the order of the interatomic distance, can be higher or lower than one for the plane wave field. The situation is similar to the phenomenon of the electromagnetically induced transparency [18], where the absorption of the media is changed due to the creating the atomic quantum mechanical wave functions in the superposition state.

The absorption coefficient is calculated straightforwardly from the imaginary part of the wave vector component parallel to the sample surface normal, by taking the imaginary part of $u_{i,s}$ from (4.41), (4.42), and (4.47). The final imaginary component is composed of the parts caused by the following contributions:

- γ_0, γ_H have imaginary part since their definitions (4.35) and (4.43) contain complex value χ_0, the imaginary part of which describes the absorption in the region far from the Bragg condition;
- α, α_H depend on γ_0, γ_H as follows from (4.38) and (4.45);
- Q_s in (4.29) due to $\chi_{\boldsymbol{H}} \neq (\chi_{-\boldsymbol{H}})^*$.

The susceptibility $\chi_{\boldsymbol{H}}$ is a complex value due to two reasons:

i. summation in (1.60); even if all $F_a(\boldsymbol{H})$ are real, the total $F(\boldsymbol{H})$ will be in general a complex value. However, for the real $F_a(\boldsymbol{H})$, the value $\chi_{\boldsymbol{H}}\chi^*_{-\boldsymbol{H}}$ is real, too;

ii. absorption, which is contained in the anomalous dispersion correction (1.55); the single atom form factor $F_a(\boldsymbol{H})$ is complex itself, and $F(\boldsymbol{H})$ is complex in general, too.

The part of the susceptibility $\chi_{\boldsymbol{H}}$ which is contributed by the summation (1.60) of the real parts $F_a(\boldsymbol{H})$ is traditionally denoted as $\chi^{\mathrm{R}}_{\boldsymbol{H}}$ and by summation of the imaginary parts as $i\chi^{\mathrm{I}}_{\boldsymbol{H}}$. In general, both are complex values and

$$\begin{aligned}\chi_{\boldsymbol{H}} &= \chi^{\mathrm{R}}_{\boldsymbol{H}} + i\chi^{\mathrm{I}}_{\boldsymbol{H}} \\ \chi_{-\boldsymbol{H}} &= \chi^{\mathrm{R}\,*}_{\boldsymbol{H}} + i\chi^{\mathrm{I}\,*}_{\boldsymbol{H}} \neq (\chi_{\boldsymbol{H}})^*.\end{aligned} \tag{4.61}$$

When a single Bragg reflection is considered, the relative phase difference $\phi = \phi_I - \phi_R$ between $\chi^{\mathrm{R}}_{\boldsymbol{H}} = |\chi^{\mathrm{R}}_{\boldsymbol{H}}|e^{i\phi_R}$ and $\chi^{\mathrm{I}}_{\boldsymbol{H}} = |\chi^{\mathrm{I}}_{\boldsymbol{H}}|e^{i\phi_I}$ enters in the final expressions, so the phase $e^{i\phi_R}$ is often set to 0 by means of shifting the origin in (1.66). This origin choice is different for various reciprocal lattice vectors, and the attention must be paid when using tabulated susceptibilities in the case if a wide scan containing several Bragg reflections is simulated [19]. To a get a simple analytical estimations for the mentioned above values, the following assumptions for the imaginary part of $u_{i,s}$ are considered:

- $H_z = 0$: a symmetric Laue geometry, this assumption makes α to be a real value,
- $\phi_R = 0$: appropriate origin minimizing ϕ_R is used, $\phi = \pi$, which is the case for centrosymmetric crystals,
- $\alpha = 0$: exact Bragg condition,
- $\chi^{\mathrm{I}}_0 \ll \chi^{\mathrm{R}}_0$, $\chi^{\mathrm{I}}_{\boldsymbol{H}} \ll \chi^{\mathrm{R}}_{\boldsymbol{H}}$: absorption is assumed to be weak,

in the first order of χ^{I}_0 from roots $u_{1,s}$, $u_{3,s}$ (4.47), (4.41):

$$\Im u_s = \frac{\omega^2}{2c^2\Re\gamma_0}(\chi^{\mathrm{I}}_0 \pm C_s\chi^{\mathrm{I}}_{\boldsymbol{H}}) = \Im\gamma_0\left(1 \pm \frac{C_s\chi^{\mathrm{I}}_{\boldsymbol{H}}}{\chi^{\mathrm{I}}_0}\right). \tag{4.62}$$

Thus, under the Bragg diffraction condition the absorption for one wave is increased and for other is decreased. The values for χ^{I}_0 and $\chi^{\mathrm{I}}_{\boldsymbol{H}}$ are obtained from the same expression (1.60), the difference between them is due to the phase and the Debye-Waller factor. For the reflections with even indices of f.c.c. materials [2], the phase factor is equal to unity, and anomalously low absorption takes place. This is called *Borrmann effect*, which being observed experimentally was one of the first convincing experiments confirming dynamical diffraction theory.

4.2.3 Group Velocity

The presented above analysis is dedicated to the stationary state of X-ray wave field in the crystal. In recent decade, an essential progress has been achieved in the construction of X-ray sources of femtosecond pulse duration and in the pulse-probe experiments with the same timescale resolution [20]. These developments demand the theory for X-ray pulse propagation in the crystals at the diffraction condition.

Considering the interaction of X-ray radiation with atom in the framework of perturbation theory, the equations describing the propagation of X-ray radiation in the crystal are linear (1.56) and resulting time structure of the diffracted pulse $\boldsymbol{A}_{\text{diffr}}(\boldsymbol{r}, t)$ is obtained using the Fourier representation:

$$\boldsymbol{A}_{\text{diffr}}(\boldsymbol{r}, t) = \int d^3\boldsymbol{k}_1 d\omega \hat{R}(\boldsymbol{k}_0, \boldsymbol{k}_1, \omega)\boldsymbol{A}_{\text{in}}(\boldsymbol{k}_0, \omega)e^{i(\boldsymbol{kr}-\omega t)}, \tag{4.63}$$

where $\hat{R}(\boldsymbol{k}_0, \boldsymbol{k}_1, \omega)$ is a matrix which connects the primary and the diffracted plane waves treated on the basis of the plane wave dynamical diffraction theory, $\boldsymbol{A}_{\text{in}}(\boldsymbol{k}_0, \omega)$ is a Fourier decomposition of the incident pulse. The calculations based on this approach show the change of the space-time pulse shape and other effects [21–23]. Below the influence of the Bragg diffraction condition on X-ray pulse propagation is discussed. The parameter characterizing the rate of the pulse propagation in dispersive media is a group velocity:

$$\boldsymbol{v}_{gr}(\boldsymbol{k}, \omega) \equiv \frac{\partial\omega}{\partial\boldsymbol{k}}, \tag{4.64}$$

where the variables ω and $\boldsymbol{k}$ are connected via the dispersion equation (4.29):

$$\begin{aligned} D(\boldsymbol{k}, \omega) &= X(\boldsymbol{k}, \omega)X(\boldsymbol{k}+\boldsymbol{H}, \omega) - Q_s \\ &= \left(k^2 - \frac{\omega^2}{c^2}(1+\chi_0)\right)\left((\boldsymbol{k}+\boldsymbol{H})^2 - \frac{\omega^2}{c^2}(1+\chi_0)\right) - Q_s = 0. \end{aligned} \tag{4.65}$$

In the Eq. (4.65), the frequency is taken as $\omega = \omega(\boldsymbol{k})$ and by differentiating (4.65) over $\boldsymbol{k}$:

$$\boldsymbol{v}_{gr}(\boldsymbol{k}, \omega) = \frac{\partial\omega}{\partial\boldsymbol{k}} = -\frac{\frac{\partial D(\boldsymbol{k},\omega)}{\partial\boldsymbol{k}}}{\frac{\partial D(\boldsymbol{k},\omega)}{\partial\omega}}. \tag{4.66}$$

For calculation of the derivatives in (4.66), only a non resonant part of susceptibility (1.51) is taken into account and approximation $\chi \sim 1/\omega^2$ is used.

The value $\boldsymbol{v}_{gr}$, being a function of $\boldsymbol{k}_{||}$, at a fixed ω is:

$$\boldsymbol{v}_{gr}(\boldsymbol{k}) = c\frac{\boldsymbol{k}X(\boldsymbol{k}+\boldsymbol{H}) + (\boldsymbol{k}+\boldsymbol{H})X(\boldsymbol{k})}{\frac{\omega}{c}(X(\boldsymbol{k}+\boldsymbol{H}) + X(\boldsymbol{k}))}. \tag{4.67}$$

In the region far from the Bragg condition, the function v_{gr} tends to the value of the speed of light, however under the Bragg condition one can expect a significant deviation of this behavior. For the calculation of (4.67), the solutions of the dispersion equation are used. At the Bragg condition, both terms $X(\boldsymbol{k}+\boldsymbol{H})$ and $X(\boldsymbol{k})$ are small, and the expression (4.67) has a structure like $0/0$ and expansions over small parameters like α, Q must be treated with caution. We use here the exact solution (4.34), which is valid for the symmetric case, and the results obtained will be general in the sense that the reference system is chosen in such a way that $z||\boldsymbol{H}$ and thus the Eq. (4.34) is utilized. The group velocity is decomposed into two components: one parallel to the plane for which $\boldsymbol{e}_z$ is normal, and one along $\boldsymbol{e}_z$:

$$\boldsymbol{v}_{gr}(\boldsymbol{k}) = c\frac{\boldsymbol{k}_{||}}{\omega/c} + \boldsymbol{e}_z c\frac{u_i X(\boldsymbol{k}+\boldsymbol{H}) + (u_i + H)X(\boldsymbol{k})}{\frac{\omega}{c}(X(\boldsymbol{k}+\boldsymbol{H}) + X(\boldsymbol{k}))}. \tag{4.68}$$

The magnitude of $v_{gr,z}$, being calculated on the basis of the equation (4.34), decreases when approaching the Bragg condition. At the value of the parameter α_{0z} equal to

$$\alpha_{0z} = \pm\left(H^2 - \sqrt{H^4 - 4H^2\sqrt{Q_s}}\right) \approx \pm 2\sqrt{Q_s} \approx \alpha_{\text{edge}}, \tag{4.69}$$

the z component of the group velocity equals to zero in the absence of the absorption. Because of at the selected choice of the coordinate system and by satisfying the Bragg condition $\gamma_0 = H/2$, the considered region coincides with the Darwin table as follows from Eq. (4.56). Thus, under the Bragg condition, the pulse propagation in the direction of the reciprocal lattice vector decelerates down to zero, i.e. the pulse gets "entangled" within the crystal. This is also a manifestation of the fact that Bragg diffraction is essentially a multi scattering effect; to be formed, the stationary state (4.49) needs a large number of the re-scattering processes. The simulations of the formation process of Bragg curve from a time-limited pulse [24] show clearly: while the smooth tails appears in time of the order of L_{ext}/c, the curved part near the Darwin table needs much longer time, and the kink at the edge of the Darwin table appears only in asymptotic.

4.3 Dynamical Diffraction in Multilayers and Superlattices

The analysis presented in the previous sections deals with the structure of the wave field in the crystal, and in two wave approximation it has the structure presented by formula (4.49). The parameters, required in (4.49) for the comprehensive wave field determination are: the amplitudes $A_{i,s}$ and the in-plane component of the wave vector $\boldsymbol{k}_{||}$. All other values are calculated based on the vector $\boldsymbol{k}_{||}$, as shown in the Eqs. (4.41), (4.42), and (4.47) for $u_{i,s}$ and in the Eq. (4.48) for the amplitude ratios $\hat{V}_{i,s}$, and in the Eq. (4.28) for the polarization vectors. The unknown values $A_{i,s}$, $\boldsymbol{k}_{||}$ are defined by the wave which enters the crystal. This wave satisfies to the Maxwell's

equations within the localized media volume on the border of the crystal. To make the Maxwell's equations be valid in the entire space, the wave fields have to fulfill the boundary conditions.

To apply Maxwell's equations at the boundary S between two media, (1) and (2), the lateral τ and the normal n to the boundary field components have to be preserved continuous (3.9):

$$\begin{aligned} \boldsymbol{E}_{1,\tau}|_S = \boldsymbol{E}_{2,\tau}|_S;\ \boldsymbol{D}_{1,n}|_S = \boldsymbol{D}_{2,n}|_S; \\ \mathbf{H}_{1,\tau}|_S = \mathbf{H}_{2,\tau}|_S;\ \boldsymbol{B}_{1,n}|_S = \boldsymbol{B}_{2,n}|_S. \end{aligned} \tag{4.70}$$

The vector potential $\boldsymbol{A}$ in the Coulomb gauge has been used in previous sections as a fundamentals of theoretical models. The potential is a key variable in the quantum mechanical Hamiltonian (1.2) as well as this parameter serves to describe the electromagnetic field in the framework of gauge theory, which is the basis of standard model of fundamental interactions. The connection between $\boldsymbol{A}$ and directly observable fields in (4.70) in vacuum is straightforward:

$$\begin{aligned} \boldsymbol{E}_{\text{vac}} = \boldsymbol{D}_{\text{vac}} = -\frac{1}{c}\frac{\partial \boldsymbol{A}}{\partial t} - \nabla\phi \\ \boldsymbol{B}_{\text{vac}} = \mathbf{H}_{\text{vac}} = \nabla \times \boldsymbol{A}. \end{aligned} \tag{4.71}$$

However, the situation is changed if the medium is involved into consideration, see the derivation of Eq. (1.15). Using expressions (1.15), the boundary conditions (4.70) can be formulated for the vector potential $\boldsymbol{A}$, and to derive them in a compact matrix form, the following projectors have to be introduced:

$$\begin{aligned} \hat{t}(\boldsymbol{k}) = \hat{I} - \frac{\boldsymbol{k} \otimes \boldsymbol{k}}{k^2}, \quad \hat{l}(\boldsymbol{k}) = \frac{\boldsymbol{k} \otimes \boldsymbol{k}}{k^2} \\ \hat{P}_\tau = \hat{I} - \boldsymbol{N} \otimes \boldsymbol{N}, \quad \hat{P}_n = \boldsymbol{N} \otimes \boldsymbol{N}. \end{aligned} \tag{4.72}$$

As a next step, two vector relations are constructed by means of summing up the equations for $\boldsymbol{E}_\tau \equiv \hat{P}_\tau \cdot \boldsymbol{E}$, $\boldsymbol{D}_n \equiv \hat{P}_n \cdot \boldsymbol{D}$ and $\mathbf{H}_\tau \equiv \hat{P}_\tau \cdot \mathbf{H}$, $\boldsymbol{B}_n \equiv \hat{P}_n \cdot \boldsymbol{B}$ in (4.70):

$$\begin{aligned} \boldsymbol{A} + \hat{P}(\boldsymbol{k}, \boldsymbol{N}) \cdot \hat{\chi} \cdot \boldsymbol{A} = \text{const} \\ \boldsymbol{k} \times \boldsymbol{A} = \text{const}, \end{aligned} \tag{4.73}$$

here the product $\hat{\chi} \cdot \boldsymbol{A}$ should be understood as (1.24), and a combined projector is introduced:

$$\hat{P}(\boldsymbol{k}, \boldsymbol{N}) \equiv \hat{P}_n \cdot \hat{t}(\boldsymbol{k}) - \hat{P}_\tau \cdot \hat{l}(\boldsymbol{k}). \tag{4.74}$$

The typical case of the boundary condition problem is the application of (4.73) to the plane interface between two crystal slabs, which is a basic model for X-ray diffraction from the multilayered crystalline structures. Within the framework of a two-beam case, the wave field in each medium is written as in Eq. (4.49). To formulate

the relation between amplitudes $A_{i,s}^{(1,2)}$ in the crystals 1 and 2, the following matrix form is used:

$$S_{i,s;i',s'}^{(1)} A_{i',s'}^{(1)} = S_{i,s;i'',s''}^{(2)} A_{i'',s''}^{(2)}, \tag{4.75}$$

where the repeated indices i, s mean the summation $i, i', i'' = 1...4$; $s, s', s'' = \sigma, \pi$. The boundary conditions (4.73) have to be fulfilled at each point of the plane interface, which is possible only in the case when the exponential factors $e^{i\boldsymbol{k}_{||}^{(1,2)}\boldsymbol{r}_{||}}$ and $e^{i(\boldsymbol{k}_{||}^{(1,2)}+\boldsymbol{H}_{||}^{(1,2)})\boldsymbol{r}_{||}}$ are equal at both sides of the interface. Thus, the conditions for the lateral components of wave vectors are:

$$\begin{aligned} \boldsymbol{k}_{||}^{(1)} &= \boldsymbol{k}_{||}^{(2)} = \boldsymbol{k}_{||} \\ \boldsymbol{H}_{||}^{(1)} &= \boldsymbol{H}_{||}^{(2)} = \boldsymbol{H}_{||}. \end{aligned} \tag{4.76}$$

The first condition results in the same conclusions as for X-ray reflectivity (3.11). The second condition in the case of crystalline media means that only in the materials with the same in-plane reciprocal lattice vectors the diffracted waves are coupled through the boundary conditions, i.e. in-plane lattice parameters are the same, or in other words, the interface is pseudomorphic. If this is not the case, the diffracted wave with the in-plane wave vector $\boldsymbol{k}_{||}^{(1)} + \boldsymbol{H}_{||}^{(1)}$ excites a new wave with the wave vector $\boldsymbol{k}_{||}^{(2)} = \boldsymbol{k}_{||}^{(1)} + \boldsymbol{H}_{||}^{(1)}$ which undergos a diffraction at the reciprocal lattice vector $-\boldsymbol{H}^{(2)}$, in turn resulting in a wave with the in-plane vector $\boldsymbol{k}_{||}^{(1)} + \boldsymbol{H}_{||}^{(1)} - \boldsymbol{H}_{||}^{(2)}$, etc. Each successive wave moves away from the Bragg condition, and the theory for this case is considered in details in [25, 26].

As follows from the similar logics as above, the boundary conditions (4.73) for the waves with different in-plane wave vectors have to be considered separately. Using Eq. (4.49) and the first equation in (4.73), which is a consequence of electric field boundary conditions (4.70), and considering the factors with the same $e^{i\boldsymbol{k}_{||}\boldsymbol{r}_{||}}$, the formula is derived:

$$\begin{aligned} &\sum_{i,s} \left(\hat{I} + \hat{P}(\boldsymbol{k}_{i,s}^{(1)}, \boldsymbol{N}) \cdot (\chi_0^{(1)} \hat{I} + \chi_{-\boldsymbol{H}}^{(1)} \hat{V}_{i,s}^{(1)}) \right) \cdot \boldsymbol{e}_{i,s}^{(1)} A_{i,s}^{(1)} \\ &= \sum_{i',s'} \left(\hat{I} + \hat{P}(\boldsymbol{k}_{i',s'}^{(2)}, \boldsymbol{N}) \cdot (\chi_0^{(2)} \hat{I} + \chi_{-\boldsymbol{H}}^{(2)} \hat{V}_{i',s'}^{(2)}) \right) \cdot \boldsymbol{e}_{i',s'}^{(2)} A_{i',s'}^{(2)}, \end{aligned} \tag{4.77}$$

and the same for $\boldsymbol{k}_{||} + \boldsymbol{H}_{||}$:

$$\begin{aligned} &\sum_{i,s} \left(\hat{V}_{i,s}^{(1)} + \hat{P}(\boldsymbol{k}_{i,s}^{(1)} + \boldsymbol{H}^{(1)}, \boldsymbol{N}) \cdot (\chi_0^{(1)} \hat{V}_{i,s}^{(1)} + \chi_{-\boldsymbol{H}}^{(1)} \hat{I}) \right) \cdot \boldsymbol{e}_{i,s}^{(1)} A_{i,s}^{(1)} \\ &= \sum_{i',s'} \left(\hat{V}_{i',s'}^{(2)} + \hat{P}(\boldsymbol{k}_{i',s'}^{(2)} + \boldsymbol{H}^{(2)}, \boldsymbol{N}) \cdot (\chi_0^{(2)} \hat{V}_{i',s'}^{(2)} + \chi_{-\boldsymbol{H}}^{(2)} \hat{I}) \right) \cdot \boldsymbol{e}_{i',s'}^{(2)} A_{i',s'}^{(2)}. \end{aligned} \tag{4.78}$$

From the second equation in (4.73), which is a consequence of magnetic field boundary conditions (4.70), and considering the factors with the same $e^{i\boldsymbol{k}_{||}\boldsymbol{r}_{||}}$, the following formula is obtained:

$$\sum_{i,s} \boldsymbol{k}_{i,s}^{(1)} \times \boldsymbol{e}_{i,s}^{(1)} A_{i,s}^{(1)} = \sum_{i',s'} \boldsymbol{k}_{i',s'}^{(2)} \times \boldsymbol{e}_{i',s'}^{(2)} A_{i',s'}^{(2)}, \tag{4.79}$$

and analogous one for $\boldsymbol{k}_{||} + \boldsymbol{H}_{||}$:

$$\begin{aligned} &\sum_{i,s} \left(\boldsymbol{k}_{i,s}^{(1)} + \boldsymbol{H}^{(1)}\right) \times (\hat{V}_{i,s}^{(1)} \cdot \boldsymbol{e}_{i,s}^{(1)}) A_{i,s}^{(1)} \\ &= \sum_{i',s'} \left(\boldsymbol{k}_{i',s'}^{(2)} + \boldsymbol{H}^{(2)}\right) \times (\hat{V}_{i',s'}^{(2)} \cdot \boldsymbol{e}_{i',s'}^{(2)}) A_{i',s'}^{(2)}. \end{aligned} \tag{4.80}$$

The equations above are assumed to describe a pseudomorphic case, and the boundary plane was assumed to be at $z_b = 0$. If $z_b \neq 0$, each amplitude $A_{i,s}^{(1,2)}$ in Eqs. (4.77) and (4.79) has to be multiplied with the exponent $e^{iu_{i,s}^{(1,2)} z_b}$ and in Eqs. (4.78) and (4.80) by the exponent $e^{i(u_{i,s}^{(1,2)} + H_z^{(1,2)}) z_b}$. The boundary conditions in the form of (4.75) are obtained from Eqs. (4.77)–(4.80) in the following way: by introducing a combined index $\nu = \{(1,\sigma); (2,\sigma); (3,\sigma); (4,\sigma); (1,\pi); (2,\pi); (3,\pi); (4,\pi)\}$, the formula (4.75) is written as:

$$S_{\mu,\nu}^{(1)} A_{\nu}^{(1)} = S_{\mu,\rho}^{(2)} A_{\rho}^{(2)}. \tag{4.81}$$

Now let us consider a scalar product of each equation with the corresponding two non-collinear vectors $\boldsymbol{e}_a^{(i)}$, $\boldsymbol{e}_b^{(i)}$, the definitions of which will be specified later. Using the following notations:

$$\begin{aligned} \boldsymbol{W}_{\nu}^{(\mathrm{El.},\boldsymbol{k},(1,2))} &= \left(\hat{I} + \hat{P}(\boldsymbol{k}_{\nu}^{(1,2)}, \boldsymbol{N}) \cdot (\chi_0^{(1,2)} \hat{I} + \chi_{-\boldsymbol{H}}^{(1,2)} \hat{V}_{\nu}^{(1,2)})\right) \cdot \boldsymbol{e}_{\nu}^{(1,2)} \\ \boldsymbol{W}_{\nu}^{(\mathrm{El.},\boldsymbol{k}+\boldsymbol{H},(1,2))} &= \left(\hat{V}_{\nu}^{(1,2)} + \hat{P}(\boldsymbol{k}_{\nu}^{(1,2)} + \boldsymbol{H}^{(1,2)}, \boldsymbol{N}) \cdot (\chi_0^{(1,2)} \hat{V}_{\nu}^{(1,2)} + \chi_{-\boldsymbol{H}}^{(1,2)} \hat{I})\right) \cdot \boldsymbol{e}_{\nu}^{(1,2)} \\ \boldsymbol{W}_{\nu}^{(\mathrm{M.},\boldsymbol{k},(1,2))} &= \boldsymbol{k}_{\nu}^{(1,2)} \times \boldsymbol{e}_{\nu}^{(1,2)} \\ \boldsymbol{W}_{\nu}^{(\mathrm{M.},\boldsymbol{k}+\boldsymbol{H},(1,2))} &= \left(\boldsymbol{k}_{\nu}^{(1,2)} + \boldsymbol{H}^{(1,2)}\right) \times (\hat{V}_{\nu}^{(1,2)} \cdot \boldsymbol{e}_{\nu}^{(1,2)}), \end{aligned} \tag{4.82}$$

the 8×8 matrix $S_{\mu,\nu}^{(1,2)}$ is constructed from following rows:

$$S_{\mu,\nu}^{(1,2)} = \begin{pmatrix} \boldsymbol{W}_{\nu}^{(\text{El.},\,\boldsymbol{k},(1,2))} \cdot \boldsymbol{e}_a^{(1)} \\ \boldsymbol{W}_{\nu}^{(\text{El.},\,\boldsymbol{k}+\boldsymbol{H},(1,2))} \cdot \boldsymbol{e}_a^{(2)} \\ \boldsymbol{W}_{\nu}^{(\text{M.},\,\boldsymbol{k},(1,2))} \cdot \boldsymbol{e}_a^{(3)} \\ \boldsymbol{W}_{\nu}^{(\text{M.},\,\boldsymbol{k}+\boldsymbol{H},(1,2))} \cdot \boldsymbol{e}_a^{(4)} \\ \boldsymbol{W}_{\nu}^{(\text{El.},\,\boldsymbol{k},(1,2))} \cdot \boldsymbol{e}_b^{(1)} \\ \boldsymbol{W}_{\nu}^{(\text{El.},\,\boldsymbol{k}+\boldsymbol{H},(1,2))} \cdot \boldsymbol{e}_b^{(2)} \\ \boldsymbol{W}_{\nu}^{(\text{M.},\,\boldsymbol{k},(1,2))} \cdot \boldsymbol{e}_b^{(3)} \\ \boldsymbol{W}_{\nu}^{(\text{M.},\,\boldsymbol{k}+\boldsymbol{H},(1,2))} \cdot \boldsymbol{e}_b^{(4)}. \end{pmatrix} \tag{4.83}$$

The boundary conditions in the form (4.81)–(4.83) can be applied for an arbitrary diffraction geometry in two-wave case, including the non-coplanar diffraction geometry [27] (the wave vector of incoming wave $\boldsymbol{k}_0$, vectors $\boldsymbol{H}$ and $\boldsymbol{N}$ are non-coplanar) and arbitrary deviations from the Bragg condition [28]. However, for most of the practical cases, the simplifications based on the coplanar geometry and/or vicinity to the Bragg peak can be made for the formulas derived above.

For the vector $\boldsymbol{W}_{\nu}^{(\text{El.},\,\boldsymbol{k},(1,2))}$, the magnitude of the summand $\hat{P}(\boldsymbol{k}_{\nu}^{(1,2)}, \boldsymbol{N}) \cdot (\chi_0^{(1,2)} \hat{I} + \chi_{-\boldsymbol{H}}^{(1,2)} \hat{V}_{\nu}^{(1,2)})$ compared to value $\hat{I}$ is estimated below. The quantities $\chi_0, \chi_{\boldsymbol{H}}$ are small values, hence the term with $\chi_0^{(1,2)}$ can be safely neglected. As it was shown in the previous section, the order of magnitude of $\hat{V}_{\nu}$ is about 1 at the Bragg angle (4.53), therefore the whole summand with the projector $\hat{P}$ can be neglected at the Bragg condition. In the region far from the Bragg angle, the terms for which ν corresponds to the roots describing in asymptotic the incoming wave (4.41) and (4.42), the quantity $\hat{V}_{\nu}$ is of order $|\chi_{\boldsymbol{H}}|$ (4.52), therefore for this roots the part with the projector $\hat{P}$ is negligible.

In the case of the roots, corresponding to the diffracted wave (4.47) in the region far from Bragg angle, the value $\hat{V}_{\nu}$ is of order $1/|\chi_{\boldsymbol{H}}|$ (4.58), therefore the summands with $\hat{I}$ and $\hat{P}$ become of equal importance. Summarizing, at the Bragg condition the summand with $\hat{P}$ is about $|\chi|$ times smaller than $\hat{I}$, but far from the Bragg angle the part $\hat{P} \cdot \chi_{-\boldsymbol{H}} \hat{V}_{\nu}$ has to be preserved. This contribution has been analyzed in [28], that demonstrated the essential discrepancy between dynamical and kinematical theories in the region far from the Bragg condition in the case if this term is abandoned. Keeping further the focus on the angular range near the Bragg condition, the summand with $\hat{P}$ is neglected, which simplifies $\boldsymbol{W}_{\nu}^{(\text{El.},\,\boldsymbol{k},(1,2))}$ significantly:

$$\boldsymbol{W}_{\nu}^{(\text{El.,Bragg};\,\boldsymbol{k},(1,2))} = \boldsymbol{e}_{\nu}^{(1,2)}. \tag{4.84}$$

Considering the vector $\boldsymbol{W}_{\nu}^{(\text{El.},\,\boldsymbol{k}+\boldsymbol{H},(1,2))}$, the same analysis shows that in the Bragg condition the summand with $\hat{P}$ can be neglected. Far from the Bragg condition, the terms with ν corresponding to the roots which describe in asymptotic the incoming wave terms $\hat{V}_{\nu}$ and $\hat{P}\chi_{-\boldsymbol{H}}$, are of equal importance. In the vicinity of Bragg range, the simplification results in:

$$\boldsymbol{W}_{\nu}^{(\text{El.,Bragg; }\boldsymbol{k}+\boldsymbol{H},(1,2))} = \hat{V}_{\nu}^{(1,2)} \cdot \boldsymbol{e}_{\nu}^{(1,2)}. \tag{4.85}$$

For the vector $\boldsymbol{W}_{\nu}^{(\text{M.},\,\boldsymbol{k},(1,2))}$ corresponding to boundary conditions for the magnetic field, by representing the wave vector in the form of (4.31) and using the condition (4.76), this vector is split into two parts:

$$\begin{aligned}\boldsymbol{W}_{\nu}^{(\text{M.},\,\boldsymbol{k},(1,2))} &= \boldsymbol{W}_{\nu,\,||}^{(\text{M.},\,\boldsymbol{k},(1,2))} + \boldsymbol{W}_{\nu,\,N}^{(\text{M.},\,\boldsymbol{k},(1,2))} \\ &= \boldsymbol{k}_{||} \times \boldsymbol{e}_{\nu}^{(1,2)} - u_{\nu}^{(1,2)} \boldsymbol{N} \times \boldsymbol{e}_{\nu}^{(1,2)}.\end{aligned} \tag{4.86}$$

Here the term $\boldsymbol{W}_{\nu,\,||}^{(\text{M.},\,\boldsymbol{k},(1,2))}$ is a vector product of $\boldsymbol{k}_{||}$ and $\boldsymbol{W}_{\nu}^{(\text{El.,Bragg; }\boldsymbol{k},(1,2))}$ from the Eq. (4.84). Because of this term is a linear combination of the boundary conditions for the electric field, it does not contain new information and can be omitted. So far as expression (4.84) is valid, a reduced vector can be used instead of $\boldsymbol{W}_{\nu,\,||}^{(\text{M.},\,\boldsymbol{k},(1,2))}$:

$$\boldsymbol{W}_{\nu}^{(\text{M., Bragg; }\boldsymbol{k},(1,2))} = u_{\nu}^{(1,2)} \boldsymbol{N} \times \boldsymbol{e}_{\nu}^{(1,2)}. \tag{4.87}$$

The same logics, being applied to $\boldsymbol{W}_{\nu}^{(\text{M.},\,\boldsymbol{k}+\boldsymbol{H},(1,2))}$ and (4.85), results in:

$$\boldsymbol{W}_{\nu}^{(\text{M., Bragg; }\boldsymbol{k}+\boldsymbol{H},(1,2))} = (u_{\nu}^{(1,2)} + H_z^{(1,2)}) \boldsymbol{N} \times (\hat{V}_{\nu}^{(1,2)} \cdot \boldsymbol{e}_{\nu}^{(1,2)}). \tag{4.88}$$

To further simplify the matrix $S_{\mu,\nu}^{(1,2)}$ (4.83), the choice of $\boldsymbol{e}_a^{(i)}$, $\boldsymbol{e}_b^{(i)}$ and the conditions under which $S_{\mu,\nu}$ can be composed of 4 matrixes of size 4×4 are discussed below. The expression

$$S_{\mu,\nu}^{(1,2)} = \begin{pmatrix} S^{(\sigma,\sigma)} & S^{(\sigma,\pi)} \\ S^{(\pi,\sigma)} & S^{(\pi,\pi)} \end{pmatrix}^{(1,2)}, \tag{4.89}$$

can be simplified in such a way that $S^{(\sigma,\pi)}$ and $S^{(\pi,\sigma)}$ would be a zero 4×4 matrices. In this case, the polarizations σ and π are treated separately. For the vectors $\boldsymbol{e}_a^{(1)} = \boldsymbol{e}_{1,\sigma}$ and $\boldsymbol{e}_b^{(1)} = \boldsymbol{e}_{1,\pi}$, the scalar product is calculated based on the formula (4.28):

$$\boldsymbol{e}_{i,\pi} \cdot \boldsymbol{e}_{1,\sigma} = \frac{(\boldsymbol{k}_{i,\pi} \cdot \boldsymbol{H})(\boldsymbol{k}_{i,\pi}, \boldsymbol{H}, \boldsymbol{k}_{1,\sigma})}{|\boldsymbol{k}_{i,\pi}|^2 |\boldsymbol{H}|^2 |\boldsymbol{k}_{1,\sigma}|}, \tag{4.90}$$

where $(\boldsymbol{a}, \boldsymbol{b}, \boldsymbol{c})$ is the scalar triple product. This value is equal to zero in the case of a coplanar geometry and for $i = 1$. The Eq. (4.90) is proportional to $u_{i,\pi} - u_{1,\sigma}$, which is close to zero with the accuracy $|\chi_{\boldsymbol{H}}|$ for the roots in the vicinity of the Bragg condition. This choice of $\boldsymbol{e}_a^{(1)}$ makes the first rows of matrices $S^{(\sigma,\pi)}$ and $S^{(\pi,\sigma)}$ to be equal to zero in two important cases: (i) coplanar geometry (exact zero value), and (ii) non-coplanar geometry but all roots $u_{i,s}$ are close to each other, that occurs under the GID condition. In this chapter, the focus is kept on these two cases only.

Other scalar products have the following properties:

- $\boldsymbol{e}_{i,\sigma} \cdot \boldsymbol{e}_{j,\sigma}$ equals unity for coplanar geometry, close to unity in GID case
- $\boldsymbol{e}_{i,\pi} \cdot \boldsymbol{e}_{j,\pi}$ is $\frac{k_{||}^2 + u_{i,\pi} u_{j,\pi}}{\sqrt{k_{||}^2 + u_{i,\pi}^2}\sqrt{k_{||}^2 + u_{j,\pi}^2}}$ for coplanar geometry; and close to unity in GID case.
  For coplanar geometry this product is close (up to $|\chi_{\boldsymbol{H}}|$) to unity for $i, j = 1, 3$ at Bragg condition (4.41), (4.47).

Summarizing, under the approximations made above
i. in coplanar geometry, and close to the Bragg condition:

$$S_{1,i}^{(\sigma,\sigma)} = (1, 1, 1, 1) \qquad (4.91)$$
$$S_{1,i}^{(\pi,\pi)} = (1, \boldsymbol{e}_{1,\pi} \cdot \boldsymbol{e}_{2,\pi}, 1, \boldsymbol{e}_{1,\pi} \cdot \boldsymbol{e}_{4,\pi}).$$

ii. in GID condition:

$$S_{1,i}^{(\sigma,\sigma)} = S_{1,i}^{(\pi,\pi)} = (1, 1, 1, 1), \qquad (4.92)$$

and $S_{1,i}^{(\pi,\sigma)} = S_{1,i}^{(\sigma,\pi)} = (0, 0, 0, 0)$. In a similar way, the choice $\boldsymbol{e}_a^{(2)} = \hat{t}(\boldsymbol{k}_{1,\sigma} + \boldsymbol{H}) \cdot \boldsymbol{e}_{1,\sigma}$ and $\boldsymbol{e}_b^{(2)} = \hat{t}(\boldsymbol{k}_{1,\pi} + \boldsymbol{H}) \cdot \boldsymbol{e}_{1,\pi}$ results in:
i. coplanar geometry, and close to the Bragg condition:

$$S_{2,i}^{(\sigma,\sigma)} = (V_{1,\sigma}, V_{2,\sigma}, V_{3,\sigma}, V_{4,\sigma}) \qquad (4.93)$$
$$S_{2,i}^{(\pi,\pi)} = (V_{1,\pi}, V_{2,\pi}\tilde{p}_{2,1}, V_{3,\pi}, V_{4,\pi}\tilde{p}_{4,1}),$$

where

$$\tilde{p}_{j,1} = \frac{(\hat{t}(\boldsymbol{k}_{j,\pi} + \boldsymbol{H}) \cdot \boldsymbol{e}_{j,\pi}) \cdot (\hat{t}(\boldsymbol{k}_{1,\pi} + \boldsymbol{H}) \cdot \boldsymbol{e}_{1,\pi})}{|\hat{t}(\boldsymbol{k}_{1,\pi} + \boldsymbol{H}) \cdot \boldsymbol{e}_{1,\pi}|^2} \qquad (4.94)$$

is the geometrical factor;
ii. GID condition:

$$S_{2,i}^{(s,s)} = (V_{1,s}, V_{2,s}, V_{3,s}, V_{4,s}), \;\; s = \sigma, \pi,$$

and $S_{2,i}^{(\pi,\sigma)} = S_{2,i}^{(\sigma,\pi)} = (0, 0, 0, 0)$. In order to nullify two remaining rows of the matrices $S^{(\pi,\sigma)}$ and $S^{(\sigma,\pi)}$, the choice of the vectors $\boldsymbol{e}_{a,b}^{(3,4)}$ is reverse to that above, namely $\boldsymbol{e}_a^{(3)} = \boldsymbol{e}_{1,\pi}$ and $\boldsymbol{e}_b^{(3)} = \boldsymbol{e}_{1,\sigma}$. The product $(\boldsymbol{N} \times \boldsymbol{e}_{i,\sigma}) \cdot \boldsymbol{e}_{1,\pi}$ is equal to zero for coplanar geometry and is proportional to $u_{i,\sigma} - u_{1,\pi}$ in general case. By selecting $\boldsymbol{e}_a^{(4)} = \hat{t}(\boldsymbol{k}_{1,\pi} + \boldsymbol{H}) \cdot \boldsymbol{e}_{1,\pi}$ and $\boldsymbol{e}_b^{(4)} = \hat{t}(\boldsymbol{k}_{1,\sigma} + \boldsymbol{H}) \cdot \boldsymbol{e}_{1,\sigma}$, the matrix under GID condition is:

$$S_{ij}^{(s,s)(1,2)} = \begin{pmatrix} 1 & 1 & 1 & 1 \\ V_{1,s} & V_{2,s} & V_{3,s} & V_{4,s} \\ u_{1,s} & u_{2,s} & u_{3,s} & u_{4,s} \\ (u_{1,s}+H_z)V_{1,s} & (u_{2,s}+H_z)V_{2,s} & (u_{3,s}+H_z)V_{3,s} & (u_{4,s}+H_z)V_{4,s} \end{pmatrix}^{(1,2)}, \tag{4.95}$$

and in coplanar geometry close to the Bragg condition:

$$S_{ij}^{(\sigma,\sigma)(1,2)} = \begin{pmatrix} 1 & 1 & 1 & 1 \\ V_{1,\sigma} & V_{2,\sigma} & V_{3,\sigma} & V_{4,\sigma} \\ u_{1,\sigma} & u_{2,\sigma}q_{2,1} & u_{3,\sigma} & u_{4,\sigma}q_{4,1} \\ (u_{1,\sigma}+H_z)V_{1,\sigma} & (u_{2,\sigma}+H_z)V_{2,\sigma}r_{2,1} & (u_{3,\sigma}+H_z)V_{3,\sigma} & (u_{4,\sigma}+H_z)V_{4,\sigma}r_{4,1} \end{pmatrix}^{(1,2)}, \tag{4.96}$$

$$S_{ij}^{(\pi,\pi)(1,2)} = \begin{pmatrix} 1 & \boldsymbol{e}_{1,\pi}\cdot\boldsymbol{e}_{2,\pi} & 1 & \boldsymbol{e}_{1,\pi}\cdot\boldsymbol{e}_{4,\pi} \\ V_{1,\pi} & V_{2,\pi}\tilde{p}_{2,1} & V_{3,\pi} & V_{4,\pi}\tilde{p}_{4,1} \\ u_{1,\pi} & u_{2,\pi}\tilde{q}_{2,1} & u_{3,\pi} & u_{4,\pi}\tilde{q}_{4,1} \\ (u_{1,\pi}+H_z)V_{1,\pi} & (u_{2,\pi}+H_z)V_{2,\pi}\tilde{r}_{2,1} & (u_{3,\pi}+H_z)V_{3,\pi} & (u_{4,\pi}+H_z)V_{4,\pi}\tilde{r}_{4,1} \end{pmatrix}^{(1,2)}, \tag{4.97}$$

where $p_{i,j}$; $\tilde{p}_{i,j}, q_{i,j}$; $\tilde{q}_{i,j}, r_{i,j}$; $\tilde{r}_{i,j}$ are the geometrical factors of order of unity that are made of various scalar products of the polarization vectors and are not essential for further analysis; this quantities become closer to unity as roots approach each other. The matrices $S^{(\pi,\sigma)}$ and $S^{(\sigma,\pi)}$ are equal to zero.

In the case of GID, all the values in (4.95) are of the same order and equally important. However, in the coplanar case close to the Bragg angle, the Eqs. (4.96) and (4.97) can be further simplified. The roots u_2 and u_4 correspond to the specularly reflected waves and are far from the Bragg condition. The waves corresponding to these roots are weak, about $|\chi_{\boldsymbol{H}}|$ in magnitude, and the same is about V_2, V_4. The amplitudes A_2, A_4 in the boundary conditions can be neglected keeping the same accuracy. Neglecting 2nd and 4th columns in (4.96) and (4.97), the transformations result in 4 equations for 2 unknowns, and by taking into account the approximations $u_1 \approx u_3 \approx \gamma_0$ in the vicinity of Bragg angle, the first row of (4.96) and (4.97) is found to be proportional to the third one, whereas the second row is proportional to the forth one. Finally:

$$S_{ij}^{(s,s)(1,2)} = \begin{pmatrix} 1 & 1 \\ V_{1,s} & V_{3,s} \end{pmatrix}^{(1,2)}. \tag{4.98}$$

In the calculations below, the boundary conditions are assumed to be applicable separately for π and σ polarizations, i.e. $S^{(\pi,\sigma)}$ and $S^{(\sigma,\pi)}$ are approximated as zeros. The GID case is considered as a most general one, and the coplanar case is automatically obtained by omitting the reflected waves, which means the elimination of the 3rd and 4th rows and 2nd and 4th column in the matrices S (see (4.95)–(4.98)). The boundary conditions written in the form of (4.81) enable to find the wave field inside the multilayered crystalline structure. The difference in the crystallographic

structures of the layers composing the whole multilayered structure can be caused either by different elemental composition of the layers or by the gradient lattice deformation of a single layer due to the external forces. In order to determine the wave field, the Eq. (4.81) has to be applied to each inter-layer interface, including the interface between vacuum and the first layer and the interface between the last layer and the substrate [29]. The wave field in vacuum is:

$$\boldsymbol{A}_{\mathrm{vac},\,s}(\boldsymbol{r}) = \left(e^{i\boldsymbol{k}^{(0)}\boldsymbol{r}} + A_{\mathrm{R}}e^{i\boldsymbol{k}^{(R)}\boldsymbol{r}} + A_{\mathrm{H}}e^{i\boldsymbol{k}^{(H)}\boldsymbol{r}}\right)\boldsymbol{e}_s, \tag{4.99}$$

$$\boldsymbol{k}^{(0)} = \boldsymbol{k}_{||} + u_0\boldsymbol{e}_z,\ \boldsymbol{k}^{(R)} = \boldsymbol{k}_{||} - u_0\boldsymbol{e}_z,\ \boldsymbol{k}^{(D)} = \boldsymbol{k}_{||} + \boldsymbol{H}_{||} - u_H\boldsymbol{e}_z,$$

$$u_0 = \sqrt{\frac{\omega^2}{c^2} - k_{||}^2},\ u_H = \sqrt{\frac{\omega^2}{c^2} - (\boldsymbol{k}_{||} + \boldsymbol{H}_{||})^2},$$

where (0), (R), (H) stand for the incident, the reflected and the diffracted waves, respectively. To keep the boundary conditions for the interface between vacuum and the first layer in the form of (4.81), the amplitude of the incident wave (equal to unity), and the amplitudes A_{R} and A_{H} are combined into a vector $A^{(v)} = (1, 0, A_{\mathrm{R}}, A_{\mathrm{H}})$. The matrix $S^{(v)}$, corresponding to the same sequence of boundary conditions as was used for (4.95)–(4.97), has the form:

$$S^{(v)} = \begin{pmatrix} 1 & 0 & 1 & 0 \\ 0 & 1 & 0 & 1 \\ u_0 & 0 & -u_0 & 0 \\ 0 & u_H & 0 & -u_H \end{pmatrix}, \tag{4.100}$$

and the boundary condition at the interface between vacuum and the first layer takes the following form:

$$S^{(v)} \cdot A^{(v)} = S^{(1)} \cdot A^{(1)}. \tag{4.101}$$

For the wave fields inside the layers lying in the depth of the crystal, the initial phase depends on the choice of the origin of the coordinates. Using the convention from [30], the wave field for nth layer with X-ray susceptibility taken in two-wave approximation, is written in the following form:

$$\boldsymbol{A}^{(n)}(\boldsymbol{r}) = \sum_{i,s} A_{i,s}^{(n)} e^{i\boldsymbol{k}_{i,s}^{(n)}\boldsymbol{r}} \left(1 + e^{i\boldsymbol{H}^{(n)}(\boldsymbol{r}-\boldsymbol{r}_n)+i\phi_n}\hat{V}_{i,s}^{(n)}\right)\cdot\boldsymbol{e}_s, \tag{4.102}$$

$$\chi^{(n)}(\boldsymbol{r}) = \chi_0^{(n)} + \chi_H^{(n)} e^{i\boldsymbol{H}(\boldsymbol{r}-\boldsymbol{r}_n)+i\phi_n} + \chi_{-H}^{(n)} e^{-i\boldsymbol{H}(\boldsymbol{r}-\boldsymbol{r}_n)-i\phi_n}.$$

The phase ϕ_n is then chosen as a phase of the diffracted wave and the susceptibility is supposed to be continuous:

$$\phi_n = \sum_{l=1}^{n-1} H_z^{(l)} d^{(l)}, \tag{4.103}$$

where $d^{(l)}$ is the thickness of the lth layer. Using these conventions, the boundary conditions for the interface between nth and $n+1$th layer take the following form:

$$S^{(n)} \cdot F^{(n)}(z_n) \cdot A^{(n)} = S^{(n+1)} \cdot F^{(n+1)}(z_n) \cdot A^{(n+1)}, \tag{4.104}$$
$$F_{ij}^{(n)}(z_n) = \mathrm{diag}(e^{iu_i^{(n)} z_n}).$$

For the interface between the last layer (Nth) and the substrate, the fact should be taken into account that in the substrate the wave field corresponding to the root with the negative imaginary part (leading to the growing amplitudes) does not exist. The roots of the dispersion equation can be combined in pairs corresponding to the direct and the reflected waves, which results in the number of roots with positive imaginary part to be equal to that with the negative imaginary part [30]. Thus, the vector of the amplitudes in the substrate has the form $A^{(\mathrm{sub})} = (A_1^{(\mathrm{sub})}, A_2^{(\mathrm{sub})}, 0, 0)$ and the boundary conditions are:

$$S^{(N)} \cdot F^{(N)}(z_N) \cdot A^{(N)} = S^{(\mathrm{sub})} \cdot A^{(\mathrm{sub})}, \tag{4.105}$$

where the vector of amplitudes for the substrate has been modified to include the phase factors: $A^{(\mathrm{sub})} = (e^{iu_1^{(sub)} z_{sub}} A_1^{(\mathrm{sub})}, e^{iu_2^{(sub)} z_{sub}} A_2^{(\mathrm{sub})}, 0, 0)$. By applying the expressions (4.101) and (4.104) to each inner interface, and using the formula (4.105), we arrive at:

$$A^{(\mathrm{sub})} = X_N \cdot X_{N-1} \cdot \ldots \cdot X_1 \cdot (S^{(1)})^{-1} \cdot S^{(v)} \cdot A^{(v)}, \tag{4.106}$$
$$X_n = (S^{(n+1)})^{-1} \cdot S^{(n)} \cdot F^{(n)}, \; X_N = (S^{\mathrm{sub}})^{-1} \cdot S^{(N)} \cdot F^{(N)}.$$
$$F^{(n)} = \mathrm{diag}(e^{iu_i^{(n)} d_n}).$$

Thus, four equations (4.106) for four unknown variables A_{R}, A_{H}, $A_1^{(\mathrm{sub})}$, $A_2^{(\mathrm{sub})}$ determine comprehensively the electromagnetic wave field.

A wide class of the multilayered systems are the superlattices, which were already considered in Chap. 3. The method of transfer matrix, used in the reflectivity case for the solution of the boundary conditions can be applied to diffraction case, too. However, this calculation involves more bulky expressions due to the higher order of the matrices. The theory presented below assumes that the superlattice consists of the repeating N times basic period, each composed of L crystalline layers. The propagation of the wave field inside the basic period of the superlattice is described precisely by the matrix $\hat{M}_L$, which structure follows straightforward from the Eq. (4.106):

$$M_L = X_L \cdot X_{L-1} \ldots \cdot X_1; \quad X_k = (S^{(k+1)})^{-1} \cdot S^{(k)} \cdot F_k. \tag{4.107}$$

Let us now introduce the normalized four-components eigenvectors $\bar{\Psi}^s$ and eigenvalues λ_s, enumerated in a natural order of the solutions for the equation:

$$\hat{M}_L \bar{\Psi}^s = \lambda_s \bar{\Psi}^s; \quad s = 1, \ldots, 4; \quad \sum_{i=1}^{4} (\Psi_i^s)^* (\Psi_i^s) = 1;$$
$$|\lambda_1| < |\lambda_2| < |\lambda_3| < |\lambda_4|. \tag{4.108}$$

The matrix $\hat{M}_L$ is not self-conjugated due to the absorption in the crystals, and therefore its eigenvectors do not satisfy the conditions of completeness and orthogonality, making the eigenvalues complex-valued. The method of eigenwaves (MEW) technique using these eigenwaves is realized in the same way as in the reflectivity case. Firstly, the wave field in the topmost layer of the basic period has to be represented as a linear superposition of the eigenvectors with coefficients defined by continuity of the vacuum wave field vector at the sample surface:

$$A_1^{(1)} = \sum_{w=1}^{4} A_w \bar{\Psi}^w; \quad S^{(v)} \cdot A^{(v)} = S^{(1)} \cdot A_1^{(1)} = S^{(1)} \cdot \sum_{w=1}^{4} A_w \bar{\Psi}^w. \tag{4.109}$$

The evolution of wave field through N periods of the superlattice is calculated algebraically:

$$F^{(1)}(z_{L,N}) \cdot A_1^{(N+1)} = (M)^N \cdot A_1^{(1)} = \sum_{w=1}^{4} (\lambda_w)^N A_w \bar{\Psi}^w. \tag{4.110}$$

The condition of the continuity at the interface between the superlattice and the substrate has to be applied to the 4-vector $A_L^{(N)}$, determining the wave filed amplitude in the bottommost layer of the stack (4.8):

$$S_L \cdot F^{(L)}(z_{L,N}) \cdot A_L^{(N)} = S_1 \cdot F^{(1)}(z_{L,N}) \cdot A_1^{(N+1)};$$
$$S_{sub} \cdot A^{(\mathrm{sub})} = S_L \cdot F^{(L)}(z_{L,N}) \cdot A_L^{(N)}. \tag{4.111}$$

As a result, the system of equations for 8 unknown values (A_R, A_H, A_s, $A_{1,2}^{sub}$) is written as:

$$(\hat{S}_1^{-1} \hat{S}_{sub})_{ij} A_j^{(sub)} = \sum_{s=1}^{4} (\lambda_s)^N A_s \Psi_i^s;$$
$$(\hat{S}_1^{-1} \hat{S}_0)_{ij} A_j^{(vac)} = \sum_{s=1}^{4} A_s \Psi_i^s. \tag{4.112}$$

The orthogonality condition for eigenvectors (4.108) can not be used for the solution of these equations (see discussion after Eq. (4.108)). However, this system can be solved in a general form, if four components of four eigenvectors are considered as (4×4) matrix:

$$\Psi_i^s \rightarrow (\hat{\Psi})_i^s.$$

Then the values A_s can be excluded from the Eq. (4.112) using the reverse matrix $\hat{\Psi}^{-1}$:

$$(\hat{S}_1^{-1}\hat{S}_0)_{ij}A_j^{(vac)} = \sum_{s=1}^{4}(\lambda_s)^{-N}(\hat{\Psi})_i^s(\hat{\Psi}^{-1})_j^s(\hat{S}_1^{-1}\hat{S}_{sub})_{jk}A_k^{sub}. \tag{4.113}$$

In order to avoid the exponentially increasing terms, the normalized matrix can be defined:

$$(\hat{Q})_{ij} = \sum_{s=1}^{4}(\frac{\lambda_1}{\lambda_s})^N(\hat{\Psi})_i^s(\hat{\Psi}^{-1})_j^s, \tag{4.114}$$

and Eq. (4.113) is written then in the following form:

$$A^{(vac)} = \frac{1}{\lambda_1^N}\hat{Z}A^{sub}; \quad \hat{Z} = \hat{S}_0^{-1}\hat{S}_1\hat{Q}\hat{S}_1^{-1}\hat{S}_{sub}, \tag{4.115}$$

and the exponentially increasing value $(\lambda_1)^{-N}$ is canceled in the expression for amplitude A_H:

$$A_H = \frac{Z_{22}Z_{41} - Z_{42}Z_{21}}{Z_{11}Z_{22} - Z_{12}Z_{21}}. \tag{4.116}$$

Thus, the following problems of X-ray diffraction simulation are solved on the basis of MEW: (i) the time of calculation depends no longer on repetition period N, (ii) numerical algorithm operates with only finite values (Fig. 4.8).

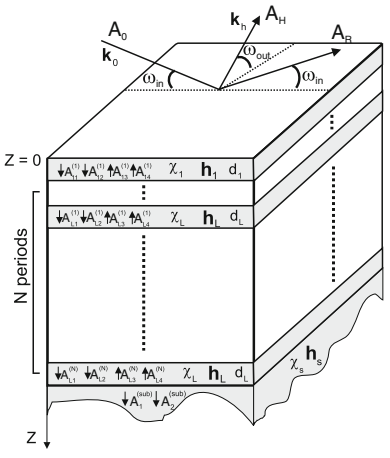

Fig. 4.8 Sketch of the wave fields for crystalline superlattice

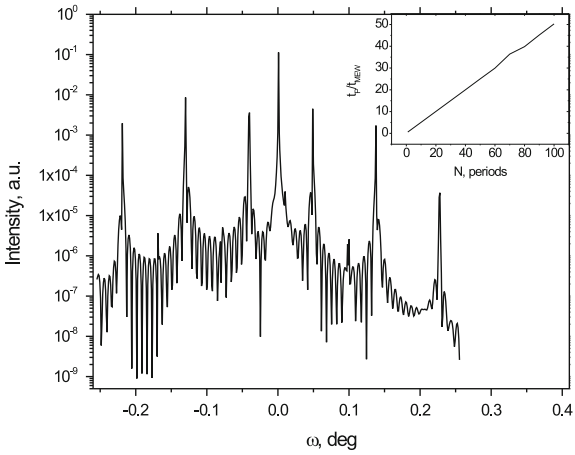

Fig. 4.9 X-ray diffraction from $(Ge/Si/Si_{0.8}Ge_{0.2})_{100}$ superlattice on the Si substrate simulated both by recursive method and MEW. Inset shows the ratio of the computer times required for simulation by recursive method (t_R) and MEW (t_{MEW}) as the function of superlattice periods number

Figure 4.9 shows the spectrum for the superlattice with crystalline layers $(Ge/Si/Si_{0.8}Ge_{0.2})_{100}$ with the thicknesses (30/20/10) nm, respectively, on the Si substrate. The curve has been simulated both by the recursive method [30] and MEW. Evidently, the results are undistinguishable because both methods are exact. However, MEW decreases drastically the calculation time t_M in comparison with time t_R, required for the recursive method, especially for the multi-periodic superlattices (insert on Fig. 4.9). Method of eigenwaves permits to naturally introduce an important integral characteristics of superlattices, viz. root-mean-square fluctuation σ_L of basic period. The fluctuations are usually caused by imperfections of the interfaces or/and by the statistical fluctuations of sample growth conditions (temperature, etc). Similarly to reflectivity case (3.129), MEW takes into account the period fluctuations by Debye-Waller factor in non-diagonal elements of the averaged transition matrix $\langle \hat{M}_L \rangle$:

$$\langle \hat{(}M_L)_{ij} \rangle = \hat{(}M_L)_{ij} e^{-1/2\sigma_L^2 k^2 (u_1^i - u_L^j)^2}. \tag{4.117}$$

The period fluctuations result in the damping effect for SL-peaks in the same way as it was described in Chap. 3 for reflectometry. Moreover, the intensity damping factor of SL-peaks depends considerably on the harmonic order of peaks. The introduction of this parameter improves the fitting accuracy of experimental data by theory. The alternative methods for calculation of X-ray diffraction are not adapted for such a parametrization [30]. The SL-peaks are formed due to the interference of waves, scattered from one-dimensional periodical SL structure, and therefore the intensity in peak maxima is proportional to the periods number N and does not depend on the fluctuation period [7]. However, the spectral width of the peaks decreases proportionally to the non-diagonal matrix elements (4.117), and the integral photon number decreases, too. Therefore, the success of the fitting of experimental measurements from the superlattice with fluctuating period essentially depends on convolution of theoretical intensity with the instrumental function of the detector.

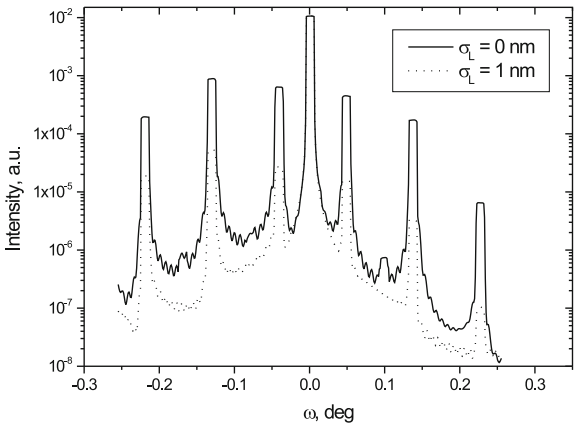

Fig. 4.10 Convolution of the simulated X-ray diffraction from $(Ge/Si/Si_{0.8}Ge_{0.2})_{100}$ superlattice with detector apparatus function for various fluctuations of the basic superlattice period, $\sigma_L = 0$ (*solid line*), $\sigma_L = 1\,\text{nm}$ (*dots*)

Figure 4.10 illustrates the effect of SL period fluctuations on the convoluted theoretical intensity simulated for the superlattice used in Fig. 4.9. The solid line and dots correspond to the values $\sigma_L = 0$ and $\sigma_L = 1\,\text{nm}$, respectively. When the value A_H is found, the reflectivity (in case of diffraction called diffractivity) (4.6) can be found. The diffracted intensity is calculated based on (2.10) and (4.99), taking into account that the sectional area of incidence beam is $L_x L_y \sin\omega_{\text{in}} = L_x L_y |u_0|/k_0$ and of diffracted beam $L_x L_y \sin\omega_{\text{out}} = L_x L_y |u_H|/k_0$, we obtain for reflectivity:

$$|R|^2 = |A_H|^2 \left|\frac{u_H}{u_0}\right|. \tag{4.118}$$

4.4 Grazing Incidence and Extremely Asymmetric Diffraction

In Sect. 4.2, the expressions for the extinction length (4.60) and the region of the Darwin table $2\alpha_{\text{edge}}$ have been derived:

$$L_{\text{Bragg},\,e} = 2\frac{\sqrt{|\sin\omega_{\text{in}}\sin\omega_{\text{out}}|}}{k_0|\chi(\boldsymbol{H})|}, \quad 2\alpha_{\text{edge}} = 2\sqrt{\left|\frac{4Q\sin\omega_{\text{out}}}{\sin\omega_{\text{in}}}\right|}.$$

The following approximation is assumed to be valid at Bragg condition: $\gamma_0 = k_0 \sin\omega_{\text{in}}$, $\gamma_0 + H_z = k_0 \sin\omega_{\text{out}}$. At the grazing incidence or exit angles of X-ray beam, the extinction length tends to approach zero, which means that X-ray wave field in the crystal is confined into a thin under surface region. This fact enables to perform a sensitive depth-resolved study of the sample surface properties [31], demanded by technology in recent decades. The extinction length, however, does not reach an exact zero value as well as the Darwin width is not equal to infinity. The reason preventing this behavior is a natural parameter called the angle of the total

external reflection (TER) (3.15). The extinction length takes the extreme value when the specular reflection and the Bragg diffraction condition occur simultaneously. At these conditions, the approximate solutions (4.41), (4.42), and (4.47) of the dispersion equation are no longer valid, since the diffraction corrections $\delta_{i,s}$ are of the same order of magnitude as the values $\gamma_0(\gamma_H)$ and the higher orders of $\delta_{i,s}$ in (4.37) and (4.46) can not be neglected. Thus, the dispersion equation of a higher order has to be solved, and physically that means a larger number of the waves are interacting with each other.

There are several widely used geometries which combine the effects of X-ray specular reflection and Bragg diffraction. Here we consider two of them used often in the practice: extremely asymmetric diffraction (EAD) and grazing incidence diffraction (GID). The former uses a coplanar geometry at which the incidence (or exit) angle is close to the angle of total external reflection [11], Fig. 4.11. The latter uses a non-coplanar geometry, at which the diffraction vector lies close to the surface plane (the diffracting crystallographic planes are almost perpendicular to the crystal surface), the incident angle and the exit angle of the diffracted wave are close to the angle of total external reflection [32], Fig. (4.12).

The dispersion equation in the case of EAD has a specific feature [33], which is discussed below. The transformations resulted in (4.37) are valid in this case, and the correction δ satisfies the equation:

$$\left[\delta_{1,s}^2 + 2\delta_{1,s}\gamma_0\right]\left[\delta_{1,s}^2 + 2\delta_{1,s}(\gamma_0 + H_z) + \alpha\right] - Q_s \qquad (4.119)$$
$$= \delta_{1,s}^4 + \delta_{1,s}^3 2H_z + \delta_{1,s}^2(\alpha + 4H_z\gamma_0) + 2\delta_{1,s}\gamma_0\alpha - Q_s = 0.$$

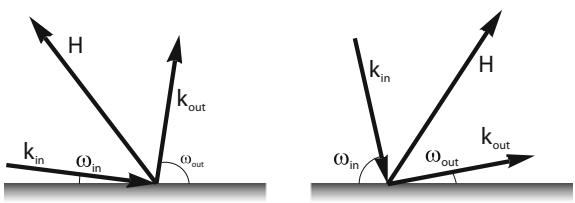

Fig. 4.11 EAD geometries: grazing incidence (*left*) and grazing exit (*right*)

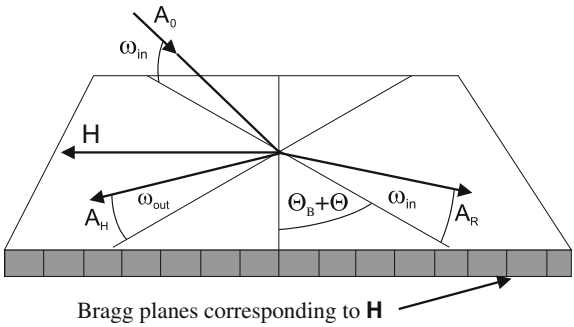

Fig. 4.12 The sketch of GID geometry

However, the estimation (4.40) and the solution (4.41) are no longer valid for EAD. Indeed, in case of grazing incidence angle and large outgoing vector the value of γ_0 is close to zero. As a result, in the first term the parameter $\delta_{1,s}^2$ can not be neglected as done with the term $2\delta_{1,s}\gamma_0$. The correction δ is a small quantity comparing to H_z, thus the value $\delta_{1,s}^4$ can be omitted because of its smaller order than $\delta_{1,s}^3 2H_z$, however, all other terms are of the same order as the latter term. In the limiting case, when the deviation from the Bragg condition α and γ_0 are equal zero, the estimate for the correction δ is written as:

$$\delta_{\text{EAD, exact at Bragg}} \approx \sqrt[3]{\frac{Q_s}{2H_z}} \sim |\chi_H|^{\frac{2}{3}} k_0. \tag{4.120}$$

The correction δ, being a small quantity, is $|\chi_H|^{-\frac{1}{3}}$ times larger in EAD case than in the ordinary Bragg case (4.40). The simultaneous effects of specular reflection and X-ray diffraction results in a stronger alternation of the dispersion surface comparing to the alternation caused by both phenomena acting independently. There is a common rule, which is applicable in this case: the higher the degree of the degeneracy of the states under perturbation, the larger the effect of the perturbation is.

Under the grazing incidence EAD condition, there are 3 waves which are close to the Bragg condition: the incident wave, the reflected wave and the diffracted wave. In the solution (4.32) for dispersion equation, there are 3 roots to be selected, two of them are close to the values $\pm\gamma_0$ (4.35) and one corresponds to $\gamma_H - H_z$ (4.43). The fourth root corresponding to the specularly reflected diffracted wave can be taken as $-\gamma_H - H_z$ (see (4.47)), and this wave can be excluded from the consideration. Another way to solve the dispersion equation is to formulate it with the notations γ_0, γ_H from the Eqs. (4.35) and (4.43) in the form:

$$\left[u^2 - \gamma_0^2\right]\left[(u + H_z)^2 - \gamma_H^2\right] - Q_s \approx \tag{4.121}$$

$$\left[u^2 - \gamma_0^2\right]\left[(u + H_z) - \gamma_H\right] 2\gamma_H - Q_s = 0, \tag{4.122}$$

where the approximations of u as a small quantity and $(u+H_z)+\gamma_H$ as $2\gamma_H$ are used, which results in a 3rd order equation providing 3 roots in the vicinity of the Bragg condition. The boundary conditions have to be written for all 3 waves described above [29]. The specularly reflected diffracted wave is weak, about $|\chi_{\boldsymbol{H}}|$ in magnitude, and the same is true for V_4. The amplitude A_4 in the boundary conditions can be omitted with the same accuracy, too. By neglecting the 4th column in the expressions (4.96) and (4.97), there are 4 equations for 3 unknowns variables. In the vicinity of the Bragg condition, the roots u_1, u_2, u_3 are much smaller than H_z due to the grazing condition, and the 4th row in expressions (4.96) and (4.97) is proportional to the 2nd one, and thus the 4th row can be discarded from the calculations. The geometrical factors $p_{i,j}; \tilde{p}_{i,j}, q_{i,j}; \tilde{q}_{i,j}, r_{i,j}; \tilde{r}_{i,j}$ in the Eqs. (4.96) and (4.97) are close to unity provided the roots are close to each other, and the result is:

$$S_{ij}^{(s,s)} = \begin{pmatrix} 1 & 1 & 1 \\ V_{1,s} & V_{2,s} & V_{3,s} \\ u_{1,s} & u_{2,s} & u_{3,s} \end{pmatrix}. \tag{4.123}$$

Using the expression for the wave in the vacuum as in (4.99) and combining the amplitudes into a vector $A^{(v)} = (1, A_{\mathrm{R}}, A_{\mathrm{H}})$, the matrix $S^{(v)}$ is written in the form of:

$$S^{(v)} = \begin{pmatrix} 1 & 1 & 0 \\ 0 & 0 & 1 \\ u_0 & -u_0 & 0 \end{pmatrix}. \tag{4.124}$$

We use here the physically reasonable assumption of damping wave in the substrate, which correspond to the incoming wave with the dispersion equation root possessing the positive imaginary part, the vector of the amplitudes inside the substrate has a form $A^{(sub)} = (A_{1,s}, 0, 0)$. Applying the boundary conditions (4.106), we arrive at 3 equations for 3 unknown variables A_{R}, A_{H}, $A_{1,s}$. At the grazing incidence EAD condition, the wave vector corresponding to the specularly reflected wave is changing due to the diffraction process, which results in a small zigzag feature in the reflectivity curve shown in Fig. 4.13. Due to the refraction phenomena, a spike in the diffracted intensity appears at the angle of the total external reflection, which is similar to the Yoneda wing discussed in Chap. 5.

The grazing exit EAD case can be treated in a similar way as grazing incidence EAD case. The dispersion equation is simplified to:

$$2\gamma_0 \left[u - \gamma_0\right] \left[(u + H_z)^2 - \gamma_H^2\right] - Q_s = 0, \tag{4.125}$$

providing 3 roots corresponding to the incident, the diffracted and the specularly reflected diffracted waves, all of which are close to the Bragg condition. In the boundary conditions, the specularly reflected wave, being far from the Bragg condition, is

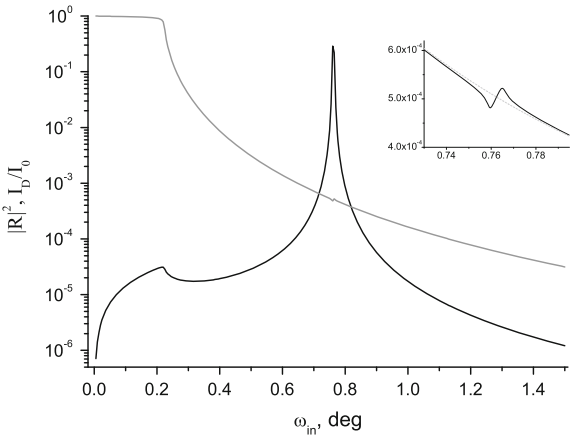

Fig. 4.13 Diffracted intensity (*black line*) and reflected intensity (*gray line*) at EAD condition. The inset shows the variation of the reflected intensity at the region corresponding to the Bragg peak. The *curves* are simulated for Si (224) crystal with 8° miscut of crystallographic planes with respect to the sample surface, CuK-α radiation, and σ polarization

omitted and thus the second column in the expressions (4.96) and (4.97) is discarded. In the vicinity of the Bragg angle, the values $u_{i,s} + H_z$ are small, and the values $u_{i,s}$ are close to $-H_z$, therefore the 1st and the 3rd rows are almost proportional to each other. Discarding the 3rd row:

$$S_{ij}^{(s,s)} = \begin{pmatrix} 1 & 1 & 1 \\ V_{1,s} & V_{3,s} & V_{4,s} \\ (u_{1,s} + H_z)V_{1,s} & (u_{3,s} + H_z)V_{3,s} & (u_{4,s} + H_z)V_{4,s}. \end{pmatrix}. \tag{4.126}$$

By neglecting the reflected wave in a vacuum and combining the amplitudes into a vector $A^{(v)} = (1, A_{\mathrm{H}}, 0)$, the matrix $S^{(v)}$ is written as:

$$S^{(v)} = \begin{pmatrix} 1 & 0 & 0 \\ 0 & 1 & 1 \\ 0 & -u_H & u_H \end{pmatrix}. \tag{4.127}$$

In the substrate, there are two damping wave fields corresponding to the incident and specularly reflected diffracted waves, and the vector of the amplitudes has the form $A^{(sub)} = (A_{1,s}, 0, A_{4,s})$. Applying the boundary conditions (4.106) formulated with the matrices (4.126), (4.127), there 3 equations for 3 unknown variables $A_{\mathrm{H}}, A_{1,s}, A_{4,s}$ are finally obtained.

After all the amplitudes are found, the reflectivity (4.118) can be calculated, which approaches the unity at the Bragg condition. The amplitude of the diffracted wave A_H, however, can be larger than the amplitude of the incident wave, which assumed to be equal unity, due to the factor $|u_H/u_0|$. This factor describes the ratio of the incident and the diffracted beam sectional areas. In the case of grazing exit EAD the sectional area of the diffracted beam is $L_x L_y |u_H|/k_0$, which is essentially smaller than that of the incident beam $L_x L_y |u_0|/k_0$. Thus, the intensity of the diffracted beam is amplified in $|u_0/u_H|$ times, and this effect of the geometrical magnification is used in the applications of EAD geometry for X-ray optical elements [2].

In the case of GID, all 4 waves, incident, reflected, diffracted and specularly reflected diffracted, are close to the Bragg condition. In the dispersion Eq. (4.121), the values γ_0, γ_H, H_z are small, and the 4th order equation has to be solved [32]. An analytical solution (4.33) is available for important case $H_z = 0$:

$$u_{i,s} = \pm\sqrt{\frac{\gamma_0^2 + \gamma_H^2}{2} \pm \sqrt{\frac{1}{4}\left(\gamma_0^2 - \gamma_H^2\right)^2 + Q_s}}, \quad i = 1 \ldots 4. \tag{4.128}$$

By considering the case of $\gamma_0 = \gamma_H$, and in terms of the small angle ω_{in}:

$$u = \pm k_0 \sqrt{\omega_{\mathrm{in}}^2 + \chi_0 \pm \sqrt{Q_s}}. \tag{4.129}$$

Comparing (4.129) to (3.11) and (3.15), two critical angles [32] can be introduced:

$$\theta_{c;1,2} = \sqrt{\chi_0 \pm \sqrt{C_s^2 \chi_H \chi_{-H}}}, \tag{4.130}$$

which clearly indicates the synergy effect of reflection and diffraction phenomena at GID condition.

As shown above, the correction to the dispersion surface at Bragg condition for non-grazing geometry is of the order of $|\chi_H| k_0$ (4.40), and at EAD condition (4.120) the correction is $|\chi_H|^{\frac{2}{3}} k_0$, whereas at the GID condition, using (4.128) and (4.129), the correction can be estimated as $|\chi_H|^{\frac{1}{2}} k_0$. The boundary conditions for GID case have to be formulated for full 4×4 matrix as in (4.95) and (4.100), according to the general scheme described in Sect. 4.3. However, the application of the matrix method for the multilayered systems under the GID condition in the form of (4.106) faces certain numerical difficulties when the incidence angle of X-ray beam lies in between $\theta_{c,1}$ and $\theta_{c,2}$. In this region, the matrices $F^{(n)}$ contain the growing and decaying exponents, which leads to large and small addenda in the matrix elements and the calculations require a high numerical accuracy. The required precision is different for different angle regions and grows exponentially with the layer thickness. A recursive algorithm has been proposed in [30], which overcomes this precision problem. In this method, the waves are divided into groups, one with increasing and one with decreasing exponents, the boundary conditions are formulated separately for each group, and the recurrence relations establishing the coupling between the groups of waves in adjacent layers are set up. The proper simulation of GID intensities from multilayered samples possessing rough interfaces requires the accounting of X-ray diffuse scattering accompanying the coherent signal diffracted from the structure [34]. In this case, the matrix formalism becomes more sophisticated and needs a prove of convergence of the algorithm as described in [34].

The grazing incidence diffraction is a non-coplanar technique, and there are several ways to perform the measurements. The incident wave vector is uniquely defined by two angles, e.g. the angle ω_{in} between the wave vector $\boldsymbol{k}_0$ and the sample surface and the angle θ between the projection of $\boldsymbol{k}_0$ on sample surface and the vector $\boldsymbol{H}$ [35]. In Fig. 4.14, the dependence of the diffracted intensity I_D on this two angles is demonstrated, where θ_B is an angle corresponding to the exact Bragg condition. The direction of the diffracted wave is determined by the expressions (4.99). The parametrization of vector $\boldsymbol{k}_0$ by angles $\omega_{\text{in}}, \theta - \theta_B$ shows that u_H becomes negative when:

$$\theta - \theta_B < \frac{\omega_{\text{in}}^2}{2 \sin 2\theta_B}, \tag{4.131}$$

where the assumption of small angles $\omega_{\text{in}}, \theta - \theta_B$ has been used. Figure 4.14 demonstrates the behavior of the diffracted X-ray intensity described above, whereas Fig. 4.15 shows the section of Fig. 4.14 at $\theta = \theta_B$. At the GID condition, the reflected wave is modified due to simultaneous diffraction, as shown in Fig. 4.16, where two gaps correspond to two critical angles (4.129).

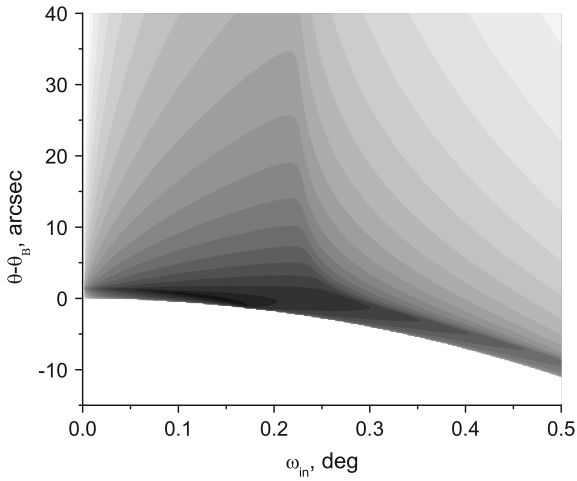

Fig. 4.14 Diffracted intensity I_D/I_0 at GID condition from Si (220), CuK-α radiation, σ polarization

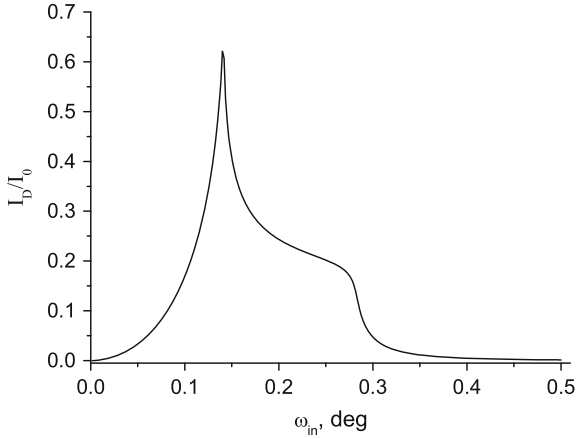

Fig. 4.15 Diffracted intensity I_D/I_0 corresponding to the section of Fig. 4.14 at $\theta = \theta_B$. The simulation conditions are the same as for Fig. 4.14

4.5 X-Ray Diffraction from Lateral Nanostructures

In recent years the technological progress has opened up possibilities for fabrication of high quality semiconductor lateral nanostructures. This fact has stimulated considerable experimental and theoretical activity in the field of mesoscopic systems. Quantum wires (QW) and quantum dots (QD) exhibit novel optoelectronic properties which can be realized in modern semiconductor lasers and modulators, x-ray optical elements and fiber communication devices. Significantly lower threshold current densities of semiconductor quantum wire lasers in comparison with the same characteristics of a respective quantum well structure improve the performance of devices considerably. Besides the up-to-date fabrication technologies for defining the vertical stacking, such as molecular beam epitaxy and metal organic chemical

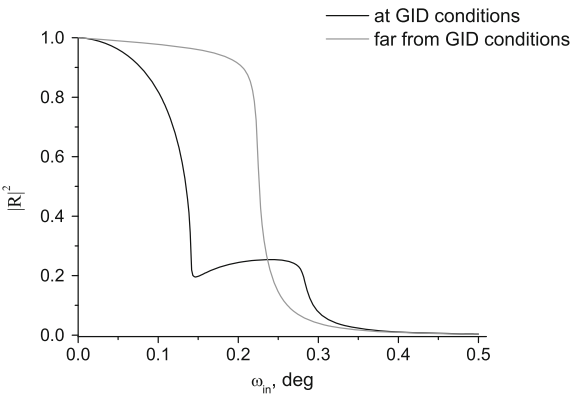

Fig. 4.16 Reflectivity at GID condition, $\theta = \theta_B$, and far from GID condition. Two critical angles $\theta_{c;1,2}$ in case of GID are clearly observed. The simulation conditions are the same as for Fig. 4.14

vapor deposition, nanolithography and wet-chemical and electron beam etching procedures have been developed to define the lateral confinement of low-dimensional surface nanostructures. However, no one of them can produce a perfect structure. The real structure imperfections, as strains in crystallographic lattice and fluctuations of the wire shape, influence the device-relevant physical properties crucially. Therefore, the developing of methods for the structural characterization of samples play an important role in modeling of real nanostructures.

X-ray techniques take a special place among other methods due to their non-destructive nature and their sensitivity to lattice strains induced during the preparation process [36–39]. Lateral surface gratings, such as quantum wires, give rise to structured X-ray diffraction pattern. Both for coplanar and grazing incidence geometries, equidistant diffraction maxima appear due to the lateral periodicity of the wires. These maxima have a fine structure which reflects the detailed geometrical shape of the wires and the strain status of the crystallographic lattice. In principle, the diffraction curves of GID from nanostructures contain direct information on the shape and strain distribution within the QW, providing the possibility of a complete study of a sample by a single method.

We use the distorted-wave Born approximation [37] for a theoretical description of the diffraction process on the multilayered surface and buried gratings. To take into account the double-diffraction effects, the perturbation theory was extended up to second order, by analogy with [40]. This approach was already used for the calculation of conventional X-ray reflectometry pattern in the Chap. 3.

The lattice and wire imperfections cause diffuse scattering accompanying the coherent component of the output intensity. The incoherent component contains certain information about QW shape fluctuations, and interface [41, 42] and lattice imperfections [43]. Although this component is clearly visible in some of the experiments presented here, we simulate the theoretical intensities in the coherent approximation to distinguish the principal features of the applied method.

The scattering of X-rays from lateral nanopatterns is described by the wave equation (we consider here σ-polarization of X-rays)

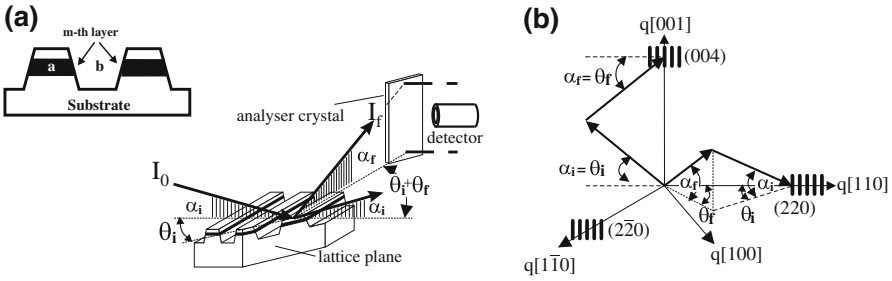

Fig. 4.17 **a** Sample model of free-standing lateral nanopattern and detailed GID experimental setup with all relevant angles depicted, **b** sketch of the reciprocal space showing the measured reciprocal space points and the corresponding geometry

$$(\Delta + K^2)\psi(\boldsymbol{r}) = V(\boldsymbol{r})\psi(\boldsymbol{r}). \tag{4.132}$$

The incident wave Φ with vacuum wave vector K being scattered by an optical potential V originates the wave $\psi(\boldsymbol{r})$ which can be written in general as

$$\psi(\boldsymbol{r}) = \Phi(\boldsymbol{r}) + \int d\boldsymbol{r}' \;\; G_0(\boldsymbol{r}, \boldsymbol{r}')V(\boldsymbol{r}')\psi(\boldsymbol{r}') \tag{4.133}$$

with $G_0(\boldsymbol{r}, \boldsymbol{r}')$ as the Green function of the free particle. By using the Heisenberg representation of quantum mechanics we express the solution of Eq. (4.132) in the complete orthogonal basis of solutions for the wave equation

$$(\Delta + K^2)\psi^{(0)}(\boldsymbol{r}) = V_1(\boldsymbol{r})\psi^{(0)}(\boldsymbol{r}), \tag{4.134}$$

where $\psi^{(0)}(\boldsymbol{r})$ is the distorted wave scattered by the potential V_1. This wave is considered further as the initial state for the scattering by the perturbation potential $V_2 = V - V_1$. Following perturbation theory, the eigenfunction $\psi(\boldsymbol{r})$ can be expanded as the series

$$\psi(\boldsymbol{r}) = \psi^{(0)}(\boldsymbol{r}) + \psi^{(1)}(\boldsymbol{r}) + \psi^{(2)}(\boldsymbol{r}) + \ldots \tag{4.135}$$

where high-order approximations to $\psi(\boldsymbol{r})$ are calculated by means of the recursion formula

$$\psi^{(n)}(\boldsymbol{r}) = \int d\boldsymbol{r}' G_1(\boldsymbol{r}, \boldsymbol{r}')V_2(\boldsymbol{r}')\psi^{(n-1)}(\boldsymbol{r}') \tag{4.136}$$

with $G_1(\boldsymbol{r}, \boldsymbol{r}')$ as the Green function of a particle interacting with the potential V_1.

Let us now consider the multilayered gratings (Fig. 4.17a) which can be buried within the structure, in general case. The non-perturbed potential within layer m $V_1^{(m)}$ is chosen to be proportional to the mean electric susceptibility of this layer

$$V_1^{(m)} = -K^2\langle\chi_0^{(m)}\rangle = \chi_{0a}^{(m)}\Omega_a^{(m)}(\boldsymbol{r}) + \chi_{0b}^{(m)}\Omega_b^{(m)}(\boldsymbol{r}). \tag{4.137}$$

Here the susceptibilities $\chi_{0a}^{(m)}$ and $\chi_{0b}^{(m)}$ correspond to regions a and b (Fig. 4.17a), respectively, which can be filled by materials with different refractive properties. The Heaviside functions $\Omega_a^{(m)}(\boldsymbol{r})$ and $\Omega_b^{(m)}(\boldsymbol{r})$ describe the geometrical configuration of layer segments and are expressed by the Heaviside function of grating shape $\Omega_{SG}(\boldsymbol{r}_\parallel, z)$ and the function $\Omega_{ML}^{(m)}(z)$ defining a vertical multilayered structure.

$$\begin{aligned}\Omega_a^{(m)}(\boldsymbol{r}) &= \Omega_{SG}^{(m)}(\boldsymbol{r}_\parallel, z)\Omega_{ML}^{(m)}(z);\\ \Omega_b^{(m)}(\boldsymbol{r}) &= (1-\Omega_{SG}^{(m)}(\boldsymbol{r}_\parallel, z))\Omega_{ML}^{(m)}(z).\end{aligned} \tag{4.138}$$

We have chosen the perturbation potential V_2 in the form:

$$V_2^{(m)} = -K^2 e^{i\boldsymbol{h}(\boldsymbol{r}-\boldsymbol{u}^{(m)}(\boldsymbol{r}))}\left[\chi_{ha}^{(m)}\Omega_a^{(m)} + \chi_{hb}^{(m)}\Omega_b^{(m)}\right] \equiv -K^2\chi_{GID}^{(m)} \tag{4.139}$$

Here we introduced the susceptibilities of regions a and b of layer m for grazing incidence diffraction on reciprocal lattice vector $\boldsymbol{h}$. The vector functions $\boldsymbol{u}^{(m)}(\boldsymbol{r}) = \boldsymbol{u}_0^{(m)}(\boldsymbol{r}) + \Delta\boldsymbol{u}^{(m)}(\boldsymbol{r})$ are the atom displacement functions describing the elastic deformation of the lattice structure and consisting of an undisturbed part $\boldsymbol{u}_0^{(m)}(\boldsymbol{r})$ originated during the epitaxial growth and displacements $\Delta\boldsymbol{u}^{(m)}(\boldsymbol{r})$ caused by grating-induced periodic distortions during the etching process.

Due to the periodicity, the susceptibility $\chi_{GID}^{(m)}$ of layer m can be expanded into the series

$$\chi_{GID}^{(m)}(\boldsymbol{r}) = e^{i\boldsymbol{h}(\boldsymbol{r}-\boldsymbol{u}_0^{(m)}(\boldsymbol{r}))}\sum_H \tilde{\chi}_{h,H}^{(m)}(z)e^{i\boldsymbol{H}\boldsymbol{r}_\parallel} \tag{4.140}$$

with Fourier components

$$\begin{aligned}\tilde{\chi}_{h,H}^{(m)}(z) = \frac{\chi_{ha}^{(m)}}{D}\int_{-D/2}^{D/2} dx\; e^{-i\boldsymbol{H}\boldsymbol{r}_\parallel}e^{-i\boldsymbol{h}\Delta\boldsymbol{u}^{(m)}(\boldsymbol{r})}\Omega_a^{(m)}(\boldsymbol{r})\\ + \frac{\chi_{hb}^{(m)}}{D}\int_{-D/2}^{D/2} dx\; e^{-i\boldsymbol{H}\boldsymbol{r}_\parallel}e^{-i\boldsymbol{h}\Delta\boldsymbol{u}^{(m)}(\boldsymbol{r})}\Omega_b^{(m)}(\boldsymbol{r}),\end{aligned} \tag{4.141}$$

where the vector $\boldsymbol{H} = \frac{2\pi}{D}\boldsymbol{e}_x$ is the reciprocal grating vector and $\boldsymbol{e}_x$ is the unit vector in the x-direction. The reciprocal grating vector describes the grating truncation rods (GTR), the two-dimensional diffraction pattern formed by the scattering process on the periodic grating mesostructure. The position of GTRs in reciprocal space is defined by the condition for the scattering vector $\boldsymbol{Q}_\parallel = \boldsymbol{K}_{h\parallel} - \boldsymbol{K}_{0\parallel} = \boldsymbol{h}_\parallel + \boldsymbol{H}$ ($\boldsymbol{K}_0$ and $\boldsymbol{K}_h$ are wave vectors of incident and diffracted waves, respectively).

Here we drop the cumbersome explicit expressions for the diffracted wave amplitudes and refer the reader to the monograph [3]. For a simulation of the wave ampli-

tudes, perturbation theory has been developed up to second order (4.135) giving a DWBA of second order. In this way the mutual interaction between the diffracted and reflected wave fields as well as the *Umweganregung* between the diffraction processes forming different GTRs are taken into consideration. The grating structure acts as transmission media both for incoming and outgoing (diffracted) waves. The changes in the intensity profile caused by such a two-fold diffraction may be considerable in comparing with the theoretical treatment based on the first order distorted-wave Born approximation. The structure amplitude of layer m corresponding to the reciprocal lattice vector $\boldsymbol{h}$ is composed of the scattering amplitudes of different GTRs:

$$S_h^{(m)}(\boldsymbol{Q}) = 4\pi^2 \sum_H \delta(\boldsymbol{Q}_\parallel - \boldsymbol{h}_\parallel - \boldsymbol{H}) S_{h,H}^{(m)}(Q_z), \tag{4.142}$$

where the amplitudes $S_{h,H}^{(m)}(Q_z)$ are defined by

$$S_{h,H}^{(m)}(Q_z) = e^{ih_z(z_m - u_{0z}^{(m)}(z_m))} \int_{z_m}^{z_{m+1}} dz\ \tilde{\chi}_{h,H}^{(m)}(z) e^{i(Q_z - h_z)(z - z_m)} \tag{4.143}$$

The values $\tilde{\chi}_{h,H}^{(m)}(z)$ for the freestanding wires (Fig. 4.17a) are calculated by Eq. (4.141), neglecting the second term. Formula (4.143) represents the contribution of one layer to the scattering amplitude of one grating truncation vector $\boldsymbol{H}$. To evaluate the total layer scattering amplitude, we replace the periodic grating shape function $\Omega_a^{(m)}(\boldsymbol{r})$ and grating-induced displacement function $U^{(m)}(\boldsymbol{r}) \equiv \exp(-i\boldsymbol{h}\Delta\boldsymbol{u}^{(m)}(\boldsymbol{r}))$ by their Fourier transforms:

$$U^{(m)}(\boldsymbol{r}) = \sum_H U_H^{(m)}(z) e^{i\boldsymbol{H}\boldsymbol{r}_\parallel}, \qquad \Omega_a^{(m)}(\boldsymbol{r}) = \sum_H \Omega_{aH}^{(m)}(z) e^{i\boldsymbol{H}\boldsymbol{r}_\parallel}. \tag{4.144}$$

Upon substituting the expression (4.144) into Eq. (4.141), the layer scattering amplitude for freestanding wires is derived from (4.143):

$$\tilde{S}_H^{(m)}(Q_z) = \chi_{ha}^{(m)} \sum_{H'} \int dz\ e^{-iQ_z(z - z_m)} U_{H'}^{(m)}(z) \Omega_{aH-H'}^{(m)}(z). \tag{4.145}$$

In the case of buried gratings (overgrown by other plane layers), this function is modified to

$$\begin{aligned} \tilde{S}_H^{(m)}(Q_z) = (\chi_{ha}^{(m)} - \chi_{hb}^{(m)}) \sum_{H' \neq H} \int dz e^{-iQ_z(z - z_m)} U_{H'}^{(m)}(z) \Omega_{aH-H'}^{(m)}(z) \\ + \int dz\ e^{-iQ_z(z - z_m)} U_H^{(m)}(z) \langle \chi_h^{(m)} \rangle(z). \end{aligned} \tag{4.146}$$

The first term in Eq. (4.146) is proportional to the compositional contrast $\chi_{ha}^{(m)} - \chi_{hb}^{(m)}$ between the segments of the (a) real and (b) "inverted" wires. The second term describes the scattering on the mean virtual layer with the susceptibility $\langle \chi_h^{(m)} \rangle$ averaged over the grating period.

In the quantum wires, the lattice displacements are expected mainly in the vertical z-direction and lateral x-direction, neglecting the strain fields along the wires (y-direction). Thus choosing the reciprocal lattice vector $\boldsymbol{h}$ to be perpendicular to displacement vectors $\boldsymbol{u}^{(m)}$ (i.e. parallel to y-axis), the diffraction process is insensitive to the strain distribution within sample because all the vectors $U_{H' \neq 0}^{(m)}$ vanish. In our case this situation corresponds to diffraction on ($\bar{2}20$) reflection (transverse scans, see Fig. 4.17b), and from GTRs we obtain information about the shape and composition of wires. Conversely, longitudinal scans from the strong (220) reflection include information on both the shape and the strain. According to the theory developed above, the combination of longitudinal and transverse scans gives a complete knowledge about the strain profile, shape and composition of free-standing and buried quantum wires. Moreover, the separation of the information in different types of scans simplifies the analysis of diffraction curves and eliminates ambiguity during the fitting of experimental data.

The coherent intensity of diffracted waves scattered by layer m to the position of the GTR in reciprocal space is proportional to

$$W_h^{(m)}(Q_z) = -K^2 \Big[T_0^{(m)} S_h^{(m)}(q_{z0}^{(m)}) T_h^{(m)} + R_0^{(m)} S_h^{(m)}(q_{z1}^{(m)}) T_h^{(m)} + T_0^{(m)} S_h^{(m)}(-q_{z1}^{(m)}) R_h^{(m)} + R_0^{(m)} S_h^{(m)}(-q_{z0}^{(m)}) R_h^{(m)} \Big]. \tag{4.147}$$

Here the transmitted and reflected wave amplitudes $T_{0,h}^{(m)}$ and $R_{0,h}^{(m)}$ of incident and diffracted waves are calculated on the basis of the Fresnel formalism for an undisturbed potential V_1. The values $q_{z0}^{(m)}$ and $q_{z1}^{(m)}$ are determined from

$$q_{z0}^{(m)} \equiv K_{zh}^{(m)} - K_{z0}^{(m)}; \qquad q_{z1}^{(m)} \equiv K_{zh}^{(m)} + K_{z0}^{(m)}, \tag{4.148}$$

where the z-components of the wave vectors of incident and diffracted waves in layer m are related to the mean layer susceptibility (scattering by potential V_1) by

$$K_{hz}^{(m)} = \sqrt{K^2 \langle \chi_h^{(m)} \rangle - K_{h\|}^2}; \qquad K_{0z}^{(m)} = \sqrt{K^2 \langle \chi_h^{(m)} \rangle - K_{0\|}^2}. \tag{4.149}$$

As mentioned above, the diffuse component of X-ray scattering was not taken into account in our simulations. Some contribution of diffuse intensity is evident in the measured diffraction curves [37] as a broadening of the peak bottoms and side wings that causes a slight discrepancy between theory and experiment. Certainly, the incoherent scattering brings valuable information on structure imperfections, and this topic is discussed in the Chaps. 5 and 6.

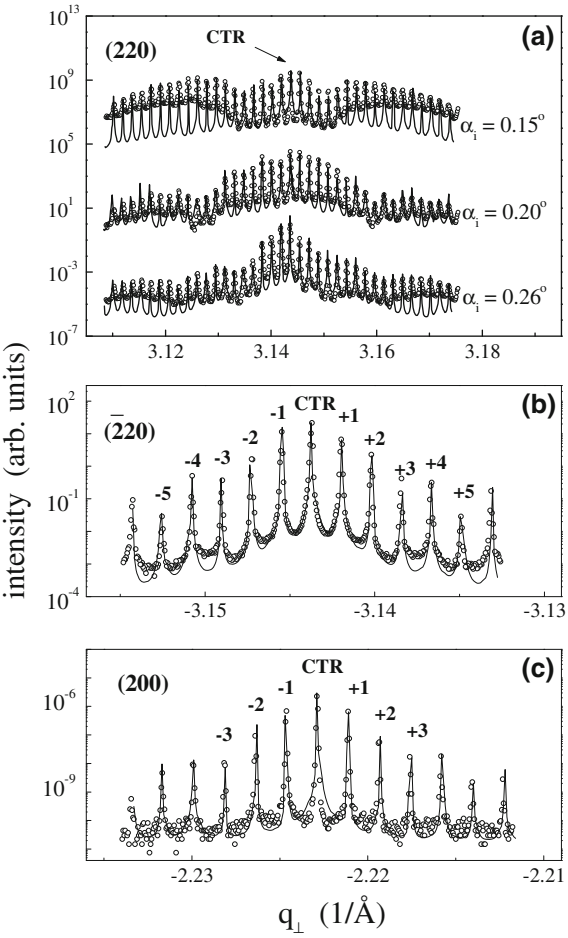

Fig. 4.18 In-plane scans for sample from Fig. 4.17 recorded with GID from the both symmetry equivalent strong in-plane reflections, **a** longitudinal (220) and **b** transverse ($\bar{2}20$) and **c** from the weak (200) Bragg reflections. The Crystal Truncation Rod and satellite reflections caused by the presence of nanopattern contain valuable information on the topography and the strain status of quantum wires

Figure 4.18 demonstrates the GID experimental and simulated results [37] for the sample, schematically shown in Fig. 4.17a. The 5 nm thick $Ga_{0.97}In_{0.03}As$ single quantum well has been grown on the GaAs (001) substrate, and capped by a GaAs layer with a nominal thickness of 20 nm. The pattern, a one dimensional grating along the $[1\bar{1}0]$ direction with a periodicity $D = 250$ nm and a nominal wire width of $t_{top} = 95$ nm, was created by lithography process.

The diffracted intensities have been measured from (220), ($\bar{2}20$) and (200) Bragg reflections, performing both $q_\perp$- and q_z-scans. Figure 4.18a, b and c show the longitudinal (220), transverse ($\bar{2}20$) and (200) $q_\perp$-scans, the experimental (dots) and theoretical (lines) curves. Here we show the diffracted intensities recorded for only one exit angle α_f corresponding to the value $q_z = 0.044$ Å^{-1}. The (220) diffraction curves at different incidence angles α_i (Fig. 4.18a) show a visible contribution of diffusely scattered intensity appearing as wide wings at both sides of the crystal

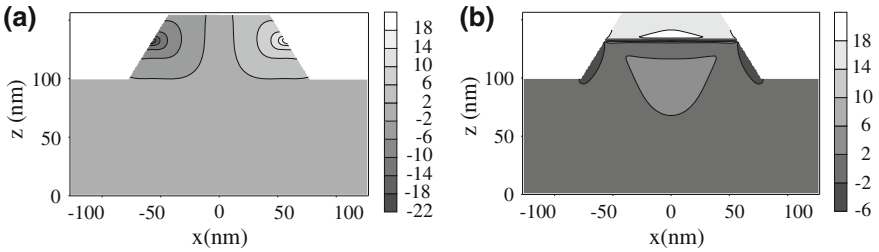

Fig. 4.19 Finite Elements Method calculation of the displacements δx (**a**) and δz (**b**) of the free-standing nanopattern (quantum wires). The limits of the contour bands are given in units of 10^{-3} nm

truncation rod. Their appearance is a consequence of the trapezoid shape of the wires but their intensity is caused mainly by the defects located at the wire side walls. The transverse scan across the $\bar{2}20$ reciprocal lattice point shown in Fig. 4.18b provides a unique possibility to investigate the geometrical parameters of the quantum wires because of the insensitivity to the strain profile of the sample. Finally, the GTRs of the weak (200) Bragg reflection (Fig. 4.18c) give a measure of the scattering contrast between the base compound of the wire (GaAs) and the single quantum well ($Ga_{0.97}In_{0.03}As$) embedded into the wire. The diffraction pattern from this reflection is also sensitive to the strain profile. The phase shift induced by the single quantum well and the interference between surface and quantum well scattered waves produce an anharmonic modulation of GTRs, typical for (200) reflection.

Thus, by measuring and evaluating X-ray diffraction curves in various geometries including GID, we are able to comprehensively characterize the complex semiconductor nanopatterns possessing both vertical and lateral structures (quantum wires and quantum dots). Whereas the transverse scans make it possible to study separately the shape of the QW, the longitudinal scans across the (220) Bragg reflection, being sensitive to the strains, allows a check of the validity of the displacement profile simulated by a finite elements method (Fig. 4.19). From the whole set of X-ray measurements, the shape and dimensions of nanopattern elements can be deducted as well as the crystallographic lattice strain status of embedded quantum wells is evaluated, too.

References

1. H. Cole, B.W. Batterman. Dynamical diffraction of X rays by perfect crystals. Rev. Mod. Phys. **36**(3), 681–717 (1964)
2. A. Authier, *Dynamical Theory of X-ray Diffraction* (Oxford University Press, New York, 2001)
3. U. Pietsch, V. Holy, T. Baumbach. High-resolution X-ray scattering: from thin films to lateral nanostructures. 2nd edn. (Springer, Heidelberg, 2004)
4. S.-L. Chang, *Multiple Diffraction of X-rays in Crystals* (Springer, Heidelberg, 1984)

5. S. Marchesini, A. Noy Stefan, P. Hau-Riege, C. Cui, M.R. Howells, R. Rosen, H. He, J.C.H. Spence, U. Weierstall, T. Beetz, C.J. David Shapiro, H.N. Chapman, A. Barty. High-resolution ab initio three-dimensional X-ray diffraction microscopy. J. Opt. Soc. Am. A **23**, 1179–1200 (2006)
6. I.K. Robinson, I.A. Vartanyants, G.J. Williams, M.A. Pfeifer, J.A. Pitney, Reconstruction of the shapes of gold nanocrystals using coherent X-ray diffraction. Phys. Rev. Lett. **87**, 195505 (2001)
7. L.D. Landau, E.M. Lifshitz, *Electrodynamics of Condensed Matter*, 2nd edn. (Nauka, Moscow, 1982) (in Russian)
8. V.K. Ignatovich, M. Utsura, *Handbook of Neutron Optics* (Wiley-VCH, Weinheim, 2010)
9. C.G. Darwin. Xcii. the reflexion of X-rays from imperfect crystals. *Phil. Mag. Ser. 6*, *43*(257), 800–829 (1922)
10. J.M. Cowley, *Diffraction Physics*. (Elsevier Science B.V., New York, 1995)
11. A.M. Afanasev, O.G. Melikyan, A modified dynamical theory (mdt) of X-ray diffraction in extremely asymmetric schemes. Phys. Status Solidi (a), **122**(2), 459–468 (1990)
12. V.E. Dmitrienko, K. Ishida, A. Kirfel, E.N. Ovchinnikova, Polarization anisotropy of X-ray atomic factors and 'forbidden' resonant reflections. Acta Crystallogr. A **61**(5), 481–493 (2005)
13. D.H. Templeton, L.K. Templeton, X-ray birefringence, forbidden reflections, and direct observation of structure-factor phases. Acta Crystallogr. A **43**(4), 573–574 (1987)
14. A. Caticha, Diffraction of X rays at the far tails of the Bragg peaks. ii. Darwin dynamical theory. Phys. Rev. B **49**, 33–38 (1994)
15. T.A. Alexeeva, A.I. Benediktovich, I.D. Feranchuk, T. Baumbach, A. Ulyanenkov, Long-range scans and many-beam effects for high-resolution X-ray diffraction from multilayered structures: experiment and theory. Phys. Rev. B **77**, 174114 (2008)
16. E.M. Lifshitz, L.D. Landau, *Quantum Mechanics: Non-Relativistic Theory*, 3rd edn. (Pergamon Press, New York , 1977)
17. J.M. Ziman, *Principles of the Theory of Solids*. (Cambridge University Press, Cambridge 1972)
18. M. Fleischhauer, A. Imamoglu, J.P. Marangos, Electromagnetically induced transparency: optics in coherent media. Rev. Mod. Phys. **77**, 633–673 (2005)
19. V.M. Kaganer, Crystal truncation rods in kinematical and dynamical X-ray diffraction theories. Phys. Rev. B **75**, 245425 (2007)
20. T. Pfeifer, C. Spielmann, G. Gerber, Femtosecond X-ray science. Rep. Prog. Phys. **69**(2), 443 (2006)
21. V.A. Bushuev, Diffraction of X-ray free-electron laser femtosecond pulses on single crystals in the Bragg and Laue geometry. J. Synchrotron Radiat. **15**(5), 495–505 (2008)
22. W. Graeff, Tailoring the time response of a Bragg reflection to short X-ray pulses. J. Synchrotron Radiat. **11**(3), 261–265 (2004)
23. D. Ksenzov, S. Grigorian, U. Pietsch, Time-space transformation of femtosecond free-electron laser pulses by periodical multilayers. J. Synchrotron Radiat. **15**(1), 19–25 (2008)
24. J.S. Wark, R.W. Lee, Simulations of femtosecond X-ray diffraction from unperturbed and rapidly heated single crystals. J. Appl. Crystallogr. **32**(4), 692–703 (1999)
25. A.P. Ulyanenkov, S.A. Stepanov, U. Pietsch, R. Kohler, A dynamical diffraction approach to grazing-incidence X-ray diffraction by multilayers with lateral lattice misfits. J. Phys. D Appl. Phys. **28**(12), 2522 (1995)
26. A.I. Benediktovich, I.D. Feranchuk, A. Ulyanenkov, X-ray dynamical diffraction from partly relaxed epitaxial structures. Phys. Rev. B **80**, 235315 (2009)
27. D.W. Berreman, A.T. Macrander, Asymmetric X-ray diffraction by strained crystal wafers: 8x8-matrix dynamical theory. Phys. Rev. B **37**, 6030–6040 (1988)
28. A. Caticha, Diffraction of X rays at the far tails of the bragg peaks. Phys. Rev. B **47**, 76–83 (1993)
29. S. Stepanov, R. Kohler, A dynamical theory of extremely asymmetric X-ray diffraction taking account of normal lattice strain. J. Phys. D Appl. Phys. **27**(9), 1922 (1994)

30. S.A. Stepanov, E.A. Kondrashkina, R. Köhler, D.V. Novikov, G. Materlik, S.M. Durbin, Dynamical X-ray diffraction of multilayers and superlattices: recursion matrix extension to grazing angles. Phys. Rev. B **57**, 4829–4841 (1998)
31. I.K. Robinson, D.J. Tweet, Surface X-ray diffraction. Rep. Progr. Phys. **55**(5), 599 (1992)
32. P.A. Aleksandrov, A.M. Afanasiev, S.A. Stepanov. Bragg-Laue diffraction in inclined geometry. Phys. Status Solidi (a), **86**(1), 143–154 (1984)
33. V.M. Kaganer, V.L. Indenbom, M. Vrana, B. Chalupa, Laue-to-Bragg transition in extremely asymmetric dynamic neutron diffraction. Phys. Status Solidi (a) **71**(2), 371–380 (1982)
34. A. Ulyanenkov, Grazing-incidence X-ray diffraction from multilayers, taking into account diffuse scattering from rough interfaces. Appl. Phys. A **66**, 193–199 (1998)
35. X. Huang, M. Dudley, A universal computation method for two-beam dynamical X-ray diffraction. Acta Crystallogr. A **59**(2), 163–167 (2003)
36. A. Ulyanenkov, T. Baumbach, N. Darowski, U. Pietsch, K.H. Wang, A. Forchel, T. Wiebach, J. Appl. Phys. **85**(3), 1524 (1999)
37. A. Ulyanenkov, N. Darowski, J. Grenzer, U. Pietsch, K.H. Wang, A. Forchel, Phys. Rev. B **60**, 16701 (1999)
38. U. Pietsch, N. Darowski, A. Ulyanenkov, J. Grenzer, K.H. Wang, A. Forchel, Phys. B **283**, 92–96 (2000)
39. A. Ulyanenkov, K. Inaba, P. Mikulik, N. Darowski, K. Omote, U. Pietsch, J. Grenzer, A. Forchel, J. Phys. D Appl. Phys. **34**, A179–A18296 (2001)
40. Q. Shen, Acta Cryst. A **42**, 525 (1986)
41. S.A. Stepanov, E.A. Kondrashkina, M. Schmidbauer, R. Köhler, J.U. Pfeiffer, T. Jach, A. Yu. Souvorov, Phys. Rev. B **54**, 8150 (1996)
42. V. Holý, T. Baumbach, Phys. Rev. B **49**, 10668 (1994)
43. V.M. Kaganer, R. Köhler, M. Schmidbauer, R. Opitz, B. Jenichen, Phys. Rev. B **55**, 1793 (1997)

Chapter 5
Diffuse X-Ray Scattering from Imperfect Surfaces and Interfaces

In the Chap. 2, the description of the interaction of X-ray radiation with media (X-ray optics) has been shown to be based on the solution of wave Eq. (2.2)

$$(\Delta + k_0^2)A_\mu(\boldsymbol{r}, \omega) + \hat{V}_{\mu\nu}[\rho(\boldsymbol{r}), S_b(\boldsymbol{r})]A_\nu(\boldsymbol{r}, \omega) = 0. \tag{5.1}$$

The scattering potential is obtained by the averaging of the Hamiltonian over the microscopic condition of the media. The potential is defined by the formula (2.3) and linearly depends on the distribution of the electron density $\rho(\boldsymbol{r})$ inside the sample and on the shape of macroscopic elements $S_b(\boldsymbol{r})$ (containing the number of macroscopic scatterers) inside the investigated sample. In the previous chapters, these values were defined by simple functions depending on few parameters, which are modeling the structure of the sample (atomic concentrations, relaxation degree of the crystallographic layers, etc) and the boundaries between the sample elements (interfaces, layer thicknesses). This approach, however, describes the real samples not accurately enough for some applications. Having the same microstructure, different samples may have various macroscopic fluctuations from real model, e.g. the randomly located atomic and electron density fluctuations, the defects of the crystallographic structure, the irregular shape of the boundaries between the sample elements caused by the growth conditions. All these distortions of structure have to be taken into account in the analysis of scattered X-ray intensity profiles.

The various aspects of X-ray scattering from imperfect media possessing uniform and crystallographic structures have been considered in numerous monographs and reviews (for example, [1, 2]) In present chapter, the general statistical approach based on the distorted-wave Born approximation is used for accounting of structure fluctuations. This approach is further applied for calculation of diffuse X-ray scattering under the reflection condition from the boundaries between different media (layers) possessing the roughness, and for simulation of X-ray scattered intensity under grazing-incidence small-angle condition (GISAXS) from the samples with macroscopic non-uniformity.

A. Benediktovitch et al., *Theoretical Concepts of X-Ray Nanoscale Analysis*,
Springer Series in Materials Science 183, DOI: 10.1007/978-3-642-38177-5_5,

5.1 Statistical Approach for X-Ray Scattering from Imperfect Structures

To evaluate the physical structure of the investigated sample by using experimental X-ray scattering data, the direct problem must be effectively resolved, i.e. the X-ray scattering intensity has to be accurately calculated based on the sample model parametrized by physical parameters. The very detailed modeling of the imperfections of structure requires a large number of parameters, which practically cannot be identified due to the limited resolution of X-ray detector and optics, which averages the scattering from the fluctuations. Therefore, the statistical approach is proved to be most effective in description of X-ray scattering from imperfect structures.

Here we remind the basic principles of the statistical description of the scattering problem. Despite of any sample has a deterministic structure, the irregular character of fluctuations $\rho(\boldsymbol{r})$ $S_b(\boldsymbol{r})$ makes it possible to consider the sample as a statistical ensemble, each element of which differs from others by the distribution of fluctuations over the sample volume. The whole ensemble can be characterized by the set of stochastic functions $\{\tilde{\rho}(\boldsymbol{r})\}$ and $\{\tilde{S}_b(\boldsymbol{r})\}$ and then the statistic distributions $\Phi(\tilde{\rho}, \tilde{S}_b)$ are modeled instead these functions.

All further calculations are based on the ergodic hypothesis (see, for example, [3]): for the physical value $M[\rho(\boldsymbol{r}), S_b(\boldsymbol{r})]$ depending on $\rho(\boldsymbol{r})$ and $S_b(\boldsymbol{r})$, the averaging over the random fluctuations of these functions can be substituted by averaging over the ensemble of stochastic functions $\tilde{\rho}$, $\tilde{S}_b$:

$$\overline{M[\rho(\boldsymbol{r}), S_b(\boldsymbol{r})]} = \int d\tilde{\rho} d\tilde{S}_b M(\tilde{\rho}, \tilde{S}_b) \Phi(\tilde{\rho}, \tilde{S}_b). \tag{5.2}$$

The essential advantage of the statistical approach is a small number of parameters modeling the principal qualitative features of the fluctuations in real samples (see Fig. 3.9). Another advantage of this approach is a natural estimate valid for all macroscopic systems consisting of N elements: the relative fluctuations $\xi = \sigma_M / < M >$ for the observed physical value are of order $\sim 1/\sqrt{N}$ [4]. This fact makes it possible to derive an approximate solution of the Eq. (5.1) and any observable characteristic of the system as a series on parameter ξ by using the DWBA (Sect. 2.2).

The general scheme of the expansion of the Eq. (5.1) assumes the scattering potential and wave field to be the functional of the stochastic functions:

$$\{\Delta + k_0^2 + \hat{V}_{\mu\nu}(\{\tilde{\rho}, \tilde{S}_b\})\} A_\nu(\boldsymbol{r}, \omega, \{\tilde{\rho}, \tilde{S}_b\}) = 0. \tag{5.3}$$

The part of this equation which is determined by the average values of the functions over statistic ensemble due to linearity of the scattering potential is:

$$\begin{aligned} \hat{V}_{\mu\nu}[\rho(\boldsymbol{r}), S_b(\boldsymbol{r})] = \overline{\hat{V}_{\mu\nu}(\{\tilde{\rho}, \tilde{S}_b\})} = \hat{V}_{\mu\nu}(\overline{\{\tilde{\rho}\}}, \overline{\{\tilde{S}_b\}}); \\ \rho(\boldsymbol{r}) = \overline{\{\tilde{\rho}\}}, \quad S_b(\boldsymbol{r}) = \overline{\{\tilde{S}_b\}}. \end{aligned} \tag{5.4}$$

In the scattering theory, this component of potential is called "coherent" [5] because of its amplitude is proportional to the whole number of the scattering centers N. The wave equation with this potential:

$$\{\Delta + k_0^2 + \hat{V}_{\mu\nu}[\rho(\boldsymbol{r}), S_b(\boldsymbol{r})]\} A_\nu(\boldsymbol{r}, \omega) = 0;$$
$$A_\nu(\boldsymbol{r}, \omega) = \overline{A_\nu(\boldsymbol{r}, \omega, \{\tilde{\rho}, \tilde{S}_b\})}, \tag{5.5}$$

determines the propagation of the coherent wave [6] with non-zero amplitude after averaging over the statistical fluctuations of sample parameters. This equation has been considered in Sects. 3.2, and 3.3 for the description of X-ray optical reflectivity and diffraction. Despite of the small magnitude of the amplitude of the coherent potential, which depends on the X-ray polarizability $|\chi| \sim 10^{-5}$, the influence of this amplitude on the wave scattering in the media depends on the relationship between sample size L and extinction length $L_{ext} = (k|\chi|)^{-1}$, or finally on the parameter $k_0 L|\chi|$. For majority of real samples, this parameter becomes a unity and therefore the propagation of the coherent wave in media should be considered beyond the perturbation theory, for example as X-ray reflectivity and dynamical diffraction processes are treated. The incoherent component of the wave field:

$$A_\nu^{NC}(\boldsymbol{r}, \omega) = A_\nu(\boldsymbol{r}, \omega, \{\tilde{\rho}, \tilde{S}_b\}) - A_\nu(\boldsymbol{r}, \omega), \tag{5.6}$$

after the averaging over the fluctuations appears in the quadratic terms of wave parameters which are proportional to the density matrix of the scattered radiation [7]:

$$M_{\nu,\mu}(\boldsymbol{r}, \boldsymbol{r}') = \overline{A_\nu(\boldsymbol{r}, \{\tilde{\rho}, \tilde{S}_b\}) A_\mu(\boldsymbol{r}', \{\tilde{\rho}, \tilde{S}_b\})}. \tag{5.7}$$

Therefore, after the averaging of expression (5.1) over the statistical parameters of media, the wave equation for coherent wave (5.5) is bound to the equation for the density matrix of wave field, which depends both on the averaged value (5.4) and on the correlations of the fluctuations of the scattered potential. The theory describing the evolution of wave field in fluctuating media has been developed in work [8] and the statistical approach for X-ray dynamical diffraction theory in imperfect crystals was derived based on this theory (see, for example, [9] and citation therein). Within the framework of this approach, the Eq. (4.1) describing the diffraction of coherent wave in ideal crystal are connected to the equations defining the variation of the radiation intensity caused by the scattering from the defects of crystallographic structure. Thus, the final equations describe the redistribution dynamics of the coherent intensity into incoherently scattered waves during the propagation of the radiation inside crystal.

However, the information derived by such approach is oversampled because of the X-ray scattered intensity is recorded by detector placed outside the studied crystal. Therefore, an alternative approach is used for accounting of incoherent scattering in the detected intensity. In this approach, the averaging over the fluctuations of media is performed not in the Eq. (5.1) but directly for the cross-section of the observed X-ray intensity (2.31) at the detector position placed at far distance from

the investigated sample. For the wavelengths region corresponding to X-rays, the use of non-perturbative theory for the solution of (5.1) is only necessary for coherent wave due to small amplitude of the scattering potential. All the incoherent channels of the scattering can be taken into account by DWBA approach. The accuracy of the approximation in each order of DWBA is defined by the contribution of the sequential approximation. The algorithm utilizing this fact was proposed in [10] for the case of X-ray reflectivity (see also Sect. 2.2), where the influence of incoherent processes on the formation of coherent wave was accounted by self-consistent choice of the coherent potential of the scattering.

The method proposed in [10] can be formulated in a general form for scattering problem described by Eq. (5.1) for arbitrary scattering potential. To construct the zeroth approximation of DWBA, the coherent non-stochastic potential $\hat{V}_c$ is introduced and the Eq. (5.3) is written in the following form:

$$\{\hat{L} + \xi\hat{V}_1\}|A_\lambda >= 0; \quad \hat{L} = \Delta + k_0^2 + \hat{V}_c; \quad \hat{V}_1 = \hat{V} - \hat{V}_c, \tag{5.8}$$

where $\hat{V}_c$ can be an integral operator in general case.

Here, the symbol $|A_\lambda >$ is introduced for the state of electromagnetic field described by the solution of wave Eq. (5.3). This equation corresponds to the state $|\lambda >= \boldsymbol{e}_s \exp(i\boldsymbol{kr})$ in vacuum for the incident wave with wave vector $\boldsymbol{k}$ and polarization $\boldsymbol{e}_s$, thus the state index is defined by parameter $\lambda = (\boldsymbol{k}, \boldsymbol{e}_s)$ (Fig. 5.1). The formal parameter ξ is introduced for ordering the terms of the series on the fluctuation component of the scattering potential $\sim 1/\sqrt{N}$ and the value $\xi = 1$ is assumed in final expressions.

For the solution of wave equation in zeroth approximation of DWBA, the method is used which delivers the vector of wave field $|A_{c,\lambda} >$ not using the kinematical theory and with accuracy $\sim |\chi|^2$ for arbitrary sample size. The following notations are used for this solution (Fig. 5.1):

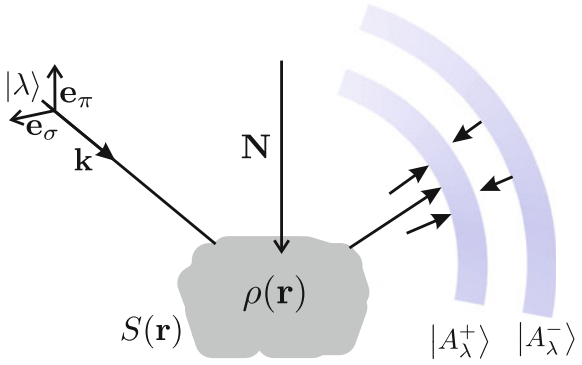

Fig. 5.1 The states of the electromagnetic field in the statistical approach to the scattering problem

$$\{\Delta + k_0^2 + \hat{V}_c\}|A^{\pm}_{c,\lambda} >= 0;$$
$$|A^{+}_{c,\lambda} >= |\lambda > -\hat{G}_0\hat{V}_c|A^{+}_{c,\lambda} >;\ |A^{-}_{c,\lambda} >= |\lambda > -\hat{G}^*_0\hat{V}_c|A^{-}_{c,\lambda} >;$$
$$\hat{L}_0\hat{G}_0 \equiv \{\Delta + k_0^2\}\hat{G}_0 = 1;\quad \hat{L}\hat{G} \equiv \{\Delta + k_0^2 + \hat{V}_c\}\hat{G} = 1;$$
$$\hat{G}_0 = \sum_{\lambda} \frac{|\lambda >< \lambda|}{k_0^2 - k^2 - i0};\ \hat{G} = \sum_{\lambda} \frac{|A^{+}_{c,\lambda} >< A^{+}_{c,\lambda}|}{k_0^2 - k^2 - i0}. \tag{5.9}$$

The solutions $|A^{\pm}_{c,\lambda} >$ correspond to divergent (convergent) spherical waves at large distance from the scatterer (see Sect. 2.2), the Green functions $\hat{G}_0$ and $\hat{G}$ correspond to the wave equations in vacuum and in media with coherent potential, respectively.

The DWBA series for the solution of Eq. (5.8) with asymptotic of the divergent wave and with the accuracy up to the terms of the second order of ξ is written as:

$$|A_\lambda >= |\lambda > -[\hat{G}_0\hat{V}_c + \xi\hat{G}\hat{V}_1 - \xi^2\hat{G}\hat{V}_1\hat{G}\hat{V}_1 + \ldots]|A^{+}_{c,\lambda} >. \tag{5.10}$$

Using the asymptotic of Green function (2.45) at large distances from the scatterer:

$$\hat{G}_0 = -\frac{e^{ik_0 r}}{4\pi r} < \lambda|;\quad \hat{G} = -\frac{e^{ik_0 r}}{4\pi r} < A^{-}_{c,\lambda}|, \tag{5.11}$$

the radiation flux can be found, which is scattered without change of the frequency, and the differential cross-section (2.31) can be derived, which has to be averaged over the ensemble of stochastic functions (5.3). Substituting the vectors (5.10) into (2.31), the expression for the differential cross-section of scattering with required accuracy is found, which corresponds to the transition of electromagnetic wave between the states $|\lambda > \rightarrow |\lambda' >$:

$$\frac{d\overline{\sigma(\lambda', \lambda)}}{d\lambda'} = \frac{1}{(4\pi)^2}\sin^2\theta_{1s}\overline{|T(\lambda', \lambda)|^2},$$
$$\overline{|T(\lambda', \lambda)|^2} = |T_0(\lambda', \lambda)|^2 + 2\xi\Re\{T_0^*(\lambda', \lambda)\overline{T_1(\lambda', \lambda)}\}$$
$$+ \xi^2\{\overline{|T_1(\lambda', \lambda)|^2} - 2\Re\{T_0^*(\lambda', \lambda)\overline{T_2(\lambda', \lambda)}\};$$
$$T_0(\lambda', \lambda) =< \lambda'|\hat{V}_c|A^{+}_{c,\lambda} >;\ \overline{T_1(\lambda', \lambda)} =< A^{-}_{c,\lambda'}|(\overline{\hat{V}} - \hat{V}_c)|A^{+}_{c,\lambda} >;$$
$$\overline{|T_1(\lambda', \lambda)|^2} = \overline{|< A^{-}_{c,\lambda'}|\hat{V}_1|A^{+}_{c,\lambda} > |^2};$$
$$\overline{T_2(\lambda', \lambda)} = \sum_{\lambda_1} \frac{\overline{< A^{-}_{c,\lambda'}|\hat{V}_1|A^{+}_{c,\lambda_1} >< A^{+}_{c,\lambda_1}|\hat{V}_1|A^{+}_{c,\lambda} >}}{k_0^2 - k_1^2 - i0}. \tag{5.12}$$

All the amplitudes in (5.12) depends on the choice of coherent potential in the Eq. (5.8). The coherent peak in the scattering cross-section is defined by the first term in Eq. (5.12), and the value of parameter λ'_0 for scattered wave corresponding

to this peak depends on the experimental setup and sample model. For instance, in X-ray reflectometry the coherent peak corresponds to the specular reflection under the condition of the conservation of the projection of wave vector to the sample surface $\boldsymbol{k}'_{0\|} = \boldsymbol{k}_{\|}$. In the case of two-wave diffraction, the coherent peak is determined by the vector with lateral component $\boldsymbol{k}'_{0\|} = \boldsymbol{k}_{\|} + \boldsymbol{H}_{\|}$, and the amplitude of this peak becomes essential if the vector $\boldsymbol{k}$ is located near the Bragg condition.

The basic idea of the self-consistent approach is in the choice of the potential $\hat{V}_c$ in such a way that it contains the contributions of further after the zeroth terms of DWBA into coherent peak. This fact permits to obtain the equation for coherent potential, the form of which changes in dependence on the accuracy, required for accounting of fluctuations. A similar approach has been developed for uniformly fitted solution of Schrödinger equation and several other quantum systems (see review [11]).

To satisfy all the above-mentioned requirements, the potential $\hat{V}_c$ and corresponding vectors $|A^{\pm}_{c,\lambda}>$ have to be selected in the form providing the sum of all corrections to the coherent peak to be zero in each order of approximation. For the terms with quadratic order of fluctuations, the condition has to be satisfied ($\xi = 1$):

$$\begin{aligned}&\Re\{< \lambda|\hat{V}_c^{+}|A^{+}_{c,\lambda'_0} >< A^{-}_{c,\lambda'_0}|\overline{\hat{V}_1}|A^{+}_{c,\lambda} >\}+\\&\{\overline{|T_1(\lambda'_0,\lambda)|^2} - 2\Re\{T_0^{*}(\lambda'_0,\lambda)\overline{T_2(\lambda'_0,\lambda)}\} = 0.\end{aligned} \tag{5.13}$$

The detailed form of Eq. (5.13) with substituted amplitudes:

$$\begin{aligned}&2\Re\{< \lambda|\hat{V}_c^{+}|A^{+}_{c,\lambda'_0} >< A^{-}_{c,\lambda'_0}|\overline{\hat{V}_1}|A^{+}_{c,\lambda} >\} + \overline{|< A^{-}_{c,\lambda'_0}|\overline{\hat{V}_1}|A^{+}_{c,\lambda} >|^2}\\&- 2\Re\{< \lambda|\hat{V}_c^{+}|A^{+}_{c,\lambda'_0} >< A^{-}_{c,\lambda'_0}|\overline{\hat{V}_1\hat{G}\hat{V}_1}|A^{+}_{c,\lambda} >\} = 0.\end{aligned} \tag{5.14}$$

By re-defining the coherent potential:

$$\hat{V}_c = \overline{\hat{V}} + \hat{X}, \tag{5.15}$$

and in the absence of correlations in fluctuation potential, the term $\overline{\hat{V}_1\hat{V}_1^{+}} = \overline{\hat{V}_1} \times \overline{\hat{V}_1} = 0$. Therefore, the only first term remains in Eq. (5.14), which leads to the following result: the coherent potential coincides with the averaged scattering potential of media ($\hat{X} = 0$) in this order of approximation:

$$\hat{V}_c = \overline{\hat{V}}. \tag{5.16}$$

However, the correlations exist in real samples and the coherent potential has to be re-normalized due to the re-scattering processes, which change also the coherent wave $|A^{+}_{c,\lambda}>$ in wave Eq. (5.9). To calculate the correlation contribution of $\hat{X}$ into coherent potential (5.14), the following non-linear equation in coordinate representation is used:

$$\hat{X}(\boldsymbol{r})A^{+}_{c,\lambda}(\boldsymbol{r})$$
$$= \frac{1}{2J}\int d\boldsymbol{r}' A^{-*}_{c,\lambda'_0}(\boldsymbol{r}')[\hat{K}(\boldsymbol{r},\boldsymbol{r}') - \hat{X}^{+}(\boldsymbol{r})\hat{X}(\boldsymbol{r}')]A^{+}_{c,\lambda}(\boldsymbol{r}')A^{+}_{c,\lambda}(\boldsymbol{r})$$
$$- \int d\boldsymbol{r}'[\hat{K}(\boldsymbol{r},\boldsymbol{r}') - X^{+}(\boldsymbol{r})X(\boldsymbol{r}')]\hat{G}(\boldsymbol{r},\boldsymbol{r}')A^{+}_{c,\lambda}(\boldsymbol{r}');$$
$$J = < \lambda|\overline{\hat{V}^{+}} + \hat{X}^{+}|A^{+}_{c,\lambda'_0} >. \tag{5.17}$$

Here $\hat{K}(\boldsymbol{r},\boldsymbol{r}')$ is a two-points correlation function of the fluctuations of scattering potential:

$$\hat{K}(\boldsymbol{r},\boldsymbol{r}') = \overline{\hat{V}^{+}(\boldsymbol{r}')\hat{V}(\boldsymbol{r})} - \overline{\hat{V}^{+}}(\boldsymbol{r}')\overline{\hat{V}}(\boldsymbol{r}). \tag{5.18}$$

Because of the pole existing in a spectral expansion of the Green function [12]:

$$\hat{G} = \int \frac{d\boldsymbol{k}_1}{2\pi)^3}\frac{A^{+*}_{c,\lambda_1}(\boldsymbol{r}')A^{+}_{c,\lambda_1}(\boldsymbol{r})}{k_0^2 - k_1^2 + i0}$$
$$= \int \frac{d\boldsymbol{k}_1}{(2\pi)^3}A^{+*}_{c,\lambda_1}(\boldsymbol{r}')A^{+}_{c,\lambda_1}(\boldsymbol{r})\left[P\frac{1}{k_0^2 - k_1^2} - i\pi\delta(k_0^2 - k_1^2)\right], \tag{5.19}$$

both the real and the imaginary parts of the coherent potential are re-normalized. The imaginary part of the potential takes into account the weakening of the coherent wave due to the scattering from the fluctuations the media.

The Eqs. (5.9) and (5.17) are the system of self-consistent equations for the coherent potential and corresponding coherent wave under the assumption of two-point correlations in the fluctuations of the scattering potential. Despite this expression is obtained within the framework of DWBA of the second order, the contribution of the correlations is not necessarily to be small, being summed up over all order of DWBA series. For the selected above form of the potential, the additional terms created in the further orders of the expansion (5.9) vanish for two-points correlations. The further correlations to the self-consistent coherent potential are related to the three-points correlations. Within the validity of the discussed here approach, the Eq. (5.17) is equivalent to the equation Bethe-Salpeter for effective scattering potential [13], which is used in [8] for propagation of radiation in fluctuating media.

The solution for the Eqs. (5.9) and (5.17) can be found by the iteration method. The convergence of the iteration solution (5.22) is defined by the contribution of the correlations into coherent potential, which can be estimated as follows. Assuming the size of fluctuations to be small comparing to the extinction length for used X-ray radiation, the scattering from each particular fluctuation is described by kinematical theory, which means [14]:

$$\frac{e^2}{mc}\frac{L_f}{k_0}n_f \ll 1;\ L_f \approx (\Omega_f)^{1/3}, \tag{5.20}$$

where n_f, L_f, Ω_f are the electron density, the average linear size and the volume of fluctuation, respectively. The correction for the coherent potential caused by incoherent scattering from fluctuations is then estimated as:

$$\hat{V}_c^+ \approx \overline{\hat{V}} + \hat{X}^{(1)} = \overline{\hat{V}}(1+\xi_f);$$
$$\xi_f \approx (\frac{n_f}{n_e})^2 \frac{L_f^4}{L^4} N_f \approx (\frac{n_f}{n_e})^2 \frac{L_f}{L} \frac{\Omega_f}{R_f^3}. \tag{5.21}$$

Here n_e and L are electron density and linear size of the whole sample, N_f is the average number of fluctuations, and R_f is an average distance between them. All these values depend strongly on the character of fluctuations. For example, for X-ray reflection from rough surface with root mean square of roughness amplitude σ and average distance between repeating roughness profiles (lateral correlation length) L_c:

$$\xi_f \to \xi_{rough} \approx \frac{\sigma^2}{L L_c}.$$

For the X-ray diffraction in crystal possessing dislocations [1], characterized by length L_d, cross-section S_d and volume density C_d, the corresponding parameter is:

$$\xi_f \to \xi_d \approx \frac{(S_d L_d)^{4/3}}{L} C_d.$$

Provided the condition $\xi_f \ll 1$ is satisfied, the first non-zero corrections for the potential and for the equation for coherent wave are written as:

$$\hat{X}^{(1)}(\boldsymbol{r}) A_{c,\lambda}^{+(1)}(\boldsymbol{r})$$
$$= \frac{1}{2J} \int d\boldsymbol{r}' A_{c,\lambda_0'}^{-*(0)}(\boldsymbol{r}') \hat{K}(\boldsymbol{r},\boldsymbol{r}') A_{c,\lambda}^{+(0)}(\boldsymbol{r}') A_{c,\lambda}^{+(0)}(\boldsymbol{r})$$
$$- \int d\boldsymbol{r}' \hat{K}(\boldsymbol{r},\boldsymbol{r}') \hat{G}(\boldsymbol{r},\boldsymbol{r}') A_{c,\lambda}^{+(0)}(\boldsymbol{r}'));$$
$$\{\hat{L}_0 + \overline{\hat{V}(r)}\} A_{c,\lambda}^{+(0)}(\boldsymbol{r}) = 0; \; J_0 = \int d\boldsymbol{r} \boldsymbol{e}_s e^{-i\boldsymbol{kr}} \overline{\hat{V}^+(\boldsymbol{r})} A_{c,\lambda}^{+(0)}(\boldsymbol{r});$$
$$\{\hat{L}_0 + \overline{\hat{V}(r)} + \hat{X}^{(1)}(\boldsymbol{r})\} A_{c,\lambda}^{+(1)}(\boldsymbol{r}) = 0. \tag{5.22}$$

The cross-section of coherent scattering is then calculated by formula:

$$\frac{d\sigma_c(\lambda_0', \lambda)}{d\lambda_0'} = \frac{1}{(4\pi)^2} \sin^2\theta_{1s} | < \lambda_0' | [\overline{\hat{V}(r)} + \hat{X}^{(1)}(\boldsymbol{r})] | A_{c,\lambda}^{+(1)} > |^2, \tag{5.23}$$

where the contribution of the re-scattered from fluctuations radiation into coherent peak is taken into account.

As was demonstrated in the work [10] for X-ray reflectivity from rough surfaces and interfaces, the self-consistent potential permits to avoid the terms in calculation of coherent peak, which tend to increase in magnitude with the increase of the scattering angle. To exclude such a non-physical behavior, the phenomenological procedure of "exponentiating" has been used in [15, 16], which is not applicable for large roughness or high scattering angles (see also Sect. 3.2).

The cross-section of incoherent (diffuse) scattering at $\lambda' \neq \lambda'_0$ is defined by two-point correlation functions of the potential:

$$\frac{d\sigma_{nc}(\lambda', \lambda)}{d\lambda'}|_{\lambda' \neq \lambda'_0} = \frac{\sin^2 \theta_{1s}}{(4\pi)^2}$$
$$\times \left\{ \int d\boldsymbol{r} \int d\boldsymbol{r}' A^{-(0)}_{c,\lambda'}(\boldsymbol{r}') A^{-*(0)}_{c,\lambda'}(\boldsymbol{r}) \hat{K}(\boldsymbol{r}, \boldsymbol{r}') A^{+(0)}_{c,\lambda}(\boldsymbol{r}) A^{+*(0)}_{c,\lambda}(\boldsymbol{r}') \right.$$
$$\left. -2\Re \left[J_0 \int d\boldsymbol{r} \int d\boldsymbol{r}' A^{-*(0)}_{c,\lambda'}(\boldsymbol{r}) \hat{K}(\boldsymbol{r}, \boldsymbol{r}') \hat{G}(\boldsymbol{r}, \boldsymbol{r}') A^{+(0)}_{c,\lambda}(\boldsymbol{r}') \right] \right\}. \quad (5.24)$$

Using for the functions $A^{+(0)}_{c,\lambda}(\boldsymbol{r}')$ the solutions of the wave equation corresponding to the ideal interface, the formula (5.24) becomes equivalent to the expression for the cross-section of incoherent scattering from rough interface obtained in [16] with the DWBA method.

5.2 Diffuse Scattering from Roughness in XRR Geometry

The theory presented in the previous section is applied below for the description of incoherent X-ray scattering from rough surfaces and interfaces in X-ray reflectivity technique. The real surfaces are not ideally flat and have non-uniformities, which result in the dependence of electron density and X-ray polarizability on both z- and lateral x- and y-coordinates. The most common imperfection in XRR technique is a roughness of the surfaces and interfaces [17]. The presence of the roughness redistributes the scattered X-ray radiation at grazing incident/exit angles.

To simulate the scattered X-ray intensity in this case, the certain model for the statistical distribution of roughness has to be selected. First of all, we consider here the scattering from single surface, for which the recognized fractal model of roughness is used [15]. This model is applicable for most of the surfaces investigated by XRR method, however, some samples reveal different from fractal behavior like stepped staircase one in some semiconductor structures [18].

To implement the fractal model of roughness, the general structure of the scattering potential is considered here. Assuming the axis z is perpendicular to the sample surface as shown in Fig. 5.2, the dependence of X-ray polarizability χ on coordinate is expressed as:

$$\chi(\boldsymbol{r}) = \chi_0 H[z - z_0(x, y)], \quad (5.25)$$

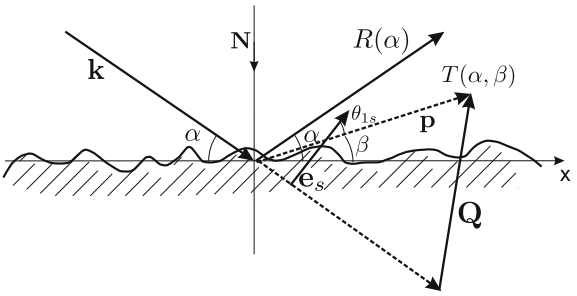

Fig. 5.2 X-ray scattering from rough surface, the angles α and β correspond to the incidence and exit beams, respectively. $R(\alpha)$ is the amplitude of specular reflected wave; $T(\alpha, \beta)$ is the amplitude of diffusely scattered waves; θ_{1s} is the angle between polarization vector of the incident wave and scattered wave vector

where χ_0 is a polarizability of the uniform media, $H(z)$ is a stepwise Heaviside function, and $z_0(x, y)$ is a function describing the real shape of the investigated surface.

The physical background of the model with sharp surface/interface as in expression (5.25) requires additional explanations. At the border of two real media there is a ultra-thin transition layer created by the atomic structure of surface and the characteristic dimension of this layer is comparable with the wavelength λ of X-ray. For the XRR technique, however, the essential information on the sample is localized in the X-ray intensity scattered at small angles comparable with critical angle of total external reflection $\alpha \sim \alpha_c \sim 10^{-2} \div 10^{-3}$. Thus, the non-uniformity with the dimension (mesoscopic scale) is only effective:

$$\Delta x \sim \Delta y \sim \lambda_z \sim \frac{\lambda}{\alpha_c} \sim 10 \div 10^3 \text{ nm}, \tag{5.26}$$

which is substantially larger than atomic non-uniformity (microscopic scale). Therefore, the transition layer composed of the electrons of the surface atoms in the potential (5.25) can be neglected.

Thus, the three-dimensional wave equation for each transversal component of vector potential of electromagnetic field with effective scattered potential $V(\boldsymbol{r})$ should be considered for the scattering from rough surfaces and interfaces:

$$\begin{aligned} [\Delta + k_0^2 + V(\boldsymbol{r})]A_s(\boldsymbol{r}) &= 0 \\ V(\boldsymbol{r}) = k_0^2 \chi_0 H[z - z_0(x, y)];\ k_0 &= \omega/c = 2\pi/\lambda. \end{aligned} \tag{5.27}$$

The resulting wave field $A_s(\boldsymbol{r})$ is a functional of $z_0(x, y)$. The wave is scattered at different angles to the sample surface, in opposite to the reflection from ideal plane surface. The intensity of specular reflection $|R(\alpha)|^2$ of the coherent scattering (5.23) is proportional to the sample surface area. Therefore the amplitude of specular peak is essentially higher than the amplitudes of the waves scattered at other than specular angles. This off-specular scattering constructs the profile of X-ray diffuse scattering $|T(\alpha, \beta)|^2$ shown in Fig. 5.2 and described by incoherent scattering in Eq. (5.24).

In the fractal model of roughness [15], the surface is assumed to be spatially uniform and the average value of the function $< z_0(x, y) >$ does not depend on x and y. Therefore, the plane of the surface can be selected to satisfy the condition $< z_0(x, y) >= 0$. The one-point distribution function of the roughness amplitudes $P(a)$ defines the probability density to find the roughness with amplitude $z_0 = a$, and it is also independent on the surface coordinates. For most of the applications, the Gaussian distribution is chosen for it:

$$P(z_0) = \frac{1}{\sigma\sqrt{2\pi}} e^{-a^2/2\sigma^2}, \tag{5.28}$$

where the parameter σ is the root mean square of the roughness amplitude.

In accordance to formulas (5.23) and (5.24), the intensity of the scattered radiation depends on the two-points correlations of scattered potential, and one parameter σ is not enough to describe correctly the scattering from rough surface. To average the intensity over the random function $z_0(x, y)$, the correlation between functions $z_0(x_1, y_1)$ and $z_0(x_2, y_2)$ in two different points of the surface has to be taken into account. Because of spatial uniformity, this correlation function $C(x, y)$ depends solely on the distance between these points:

$$\begin{aligned} &< z_0(x_1, y_1) z_0(x_2, y_2) >= C(x, y) \equiv C(R), \\ &R = x^2 + y^2, \quad x = x_1 - x_2, \ y = y_1 - y_2, \end{aligned} \tag{5.29}$$

where the correlation function is normalized as $C(0) = \sigma^2$.

In general case, the profile of X-ray diffuse scattering depends on the function $C(R)$, and the work [15] introduces this function in the form:

$$C(R) = \sigma^2 e^{-(R/L_c)^{2h}} \equiv \sigma^2 C_0 \left(\frac{R}{L_c} \right), \tag{5.30}$$

with physical background based on the fractal model of roughness. This model is most widely used up to date for the description of X-ray diffuse scattering from rough surfaces and interfaces [19].

Thus, the surface of real nanostructures is characterized by root mean square of roughness σ, correlation length L_c, and Hurst parameter h, related to the fractal dimension of roughness D as $D = 3 - h$. The evaluation of the samples possessing the rough surface and/or interfaces is reduced to the fitting at these parameters to minimize the difference between measured and simulated X-ray specular and diffuse intensities.

There are several useful characteristics of two-point random function $Z(R) \equiv [z_0(x_1, y_1) - z_0(x_2, y_2)]$, its average value and its dispersion are:

$$\overline{Z(R)} = 0; \ D_Z = 2[\sigma^2 - C(R)] = 2\sigma^2[1 - C_0]. \tag{5.31}$$

The two-point correlation function of the distribution of roughness amplitudes $W(a_1, a_2, R)$ corresponding to parameters (5.31) depends solely on the distance between surface and can be found by using general theory of Gaussian fluctuations [4]:

$$W(a_1, a_2, R) = P_{12}(a_1, a_2, R) - P(a_1)P(a_2)$$
$$= \frac{1}{2\pi\sigma^2}\left[\frac{1}{\sqrt{(1-C_0^2)}}e^{-\frac{a_1^2+a_2^2-2C_0a_1a_2}{2\sigma^2(1-C_0^2)}} - e^{-\frac{(a_1^2+a_2^2)}{2\sigma^2}}\right];$$
$$\int_{-\infty}^{\infty} da_{1,2}W(a_1, a_2, R) = 0. \tag{5.32}$$

Further we discuss the results obtained by different methods for calculation of X-ray diffuse scattering from single rough surface within the model (5.28)–(5.31), which permits to evaluate the accuracy of approximation in dependence on the parameters of the roughness.

The most simple approach is the Born (kinematic) approximation, when the scattering potential $V(\boldsymbol{r})$ in Eq. (5.27) is calculated using perturbation theory. In this case, the zeroth approximation for the initial and final states is described by plane waves, and according to the formula (5.12) the intensity cross-section is calculated for the surface $z_0(x, y)$ as integrals over the sample volume

$$\frac{d\sigma_B}{d\Omega_{\boldsymbol{p}}} = \frac{\sin^2\theta_{1s}}{16\pi^2}\left|\int d\boldsymbol{r}e^{-i\boldsymbol{Q}\boldsymbol{r}}V(\boldsymbol{r})\right|^2$$
$$= \frac{k_0^4|\chi_0|^2\sin^2\theta_{1s}}{16\pi^2}\int d\boldsymbol{r}e^{-i\boldsymbol{Q}\boldsymbol{r}}H[z - z_0(x, y)]\int d\boldsymbol{r}'e^{i\boldsymbol{Q}\boldsymbol{r}'}H[z' - z_0(x', y')], \tag{5.33}$$

where $\boldsymbol{Q} = \boldsymbol{p} - \boldsymbol{k}$ is the wave vector transfer of the scattering process (Fig. 5.2).

Using the fact of the fast X-ray wave field attenuation in the media, the integrals over coordinates z and z' in expression (5.33) can be calculated:

$$\frac{d\sigma_B}{d\Omega_{\boldsymbol{p}}} = \frac{k_0^4|\chi_0|^2\sin^2\theta_{1s}}{16\pi^2Q_z^2}\int_S d\boldsymbol{r}_\parallel\int_S d\boldsymbol{r}'_\parallel e^{-iQ_z[z_0(x,y)-z_0(x',y')]}e^{-i\boldsymbol{Q}\boldsymbol{R}}, \tag{5.34}$$

where Q_z is a normal component of the wave vector transfer, the integration area $S_\parallel$ is defined by the smaller of the quantities: the square of the interface $S_\parallel$ in the plane (x, y) or the incident beam footprint on the same plane S_b (3.5); $\boldsymbol{R} = \boldsymbol{r}_\parallel - \boldsymbol{r}'_\parallel$.

To obtain the value of the observed cross-section, the expressions (5.34) have to be averaged assuming the functions $z_0(x, y)$, $z_0(x', y')$ as random values a_1, a_2 with the distributions (5.28) and (5.32). As a result, the following expression is obtained:

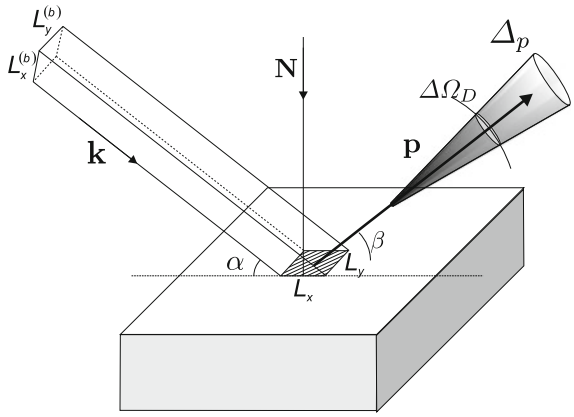

Fig. 5.3 The typical experimental geometry for measurement of X-ray diffuse scattering. The angles α and β are the incident and the exit angles, respectively; the cross-section of the incident beam $S_b = L_{b1}L_{b2}$; the angular aperture of the detector $\Delta\Omega_D = \Delta_{p1}\Delta_{p2}/k_0^2$; the polarization vectors of the scattered photons $\boldsymbol{e}_1 \equiv \boldsymbol{e}_\sigma$; $\boldsymbol{e}_2 \equiv \boldsymbol{e}_\pi$; the beam footprint on the sample $S = L_x L_y = S_b/\sin\alpha$

$$\frac{d\tilde{\sigma}_B}{d\Omega_{\boldsymbol{p}}} =< \frac{d\sigma_B}{d\Omega_{\boldsymbol{p}}} >= \frac{k_0^4|\chi_0|^2\sin^2\theta_{1s}}{16\pi^2 Q_z^2}\int da_1\int da_2\int_S d\boldsymbol{r}_\perp\int_S d\boldsymbol{r}'_\perp$$
$$e^{-iQ_z(a_1-a_2)}e^{-i\boldsymbol{QR}}[P(a_1)P(a_2)+W(a_1,a_2,R)]. \qquad (5.35)$$

In case of X-ray scattering, the size of the scattered surface is larger than wavelength, and the condition $SQ_\parallel^2 \gg 1$ is satisfied. Therefore, the integration in (5.35) can be extended to infinity and the substitutions $d\boldsymbol{r}_\parallel d\boldsymbol{r}'_\parallel = d\boldsymbol{R}d\boldsymbol{\rho}$; $\boldsymbol{\rho} = (\boldsymbol{r}_\parallel + \boldsymbol{r}'_\parallel)/2$ can be used.

To obtain the relationship between the cross-section and the intensity registered on detector normalized by incident flux, the kinematical relations between incident and scattered beams have to be used (Fig. 5.3). For typical for XRR incidence and exit angles $\alpha \sim \beta \sim \sqrt{|\chi_0|}$ and for both polarizations:

$$\sin^2\theta_s \approx 1;\ \ p_z = -\sqrt{k_0^2 - p_x^2} \approx -k_0\sin\beta.$$

Within the same accuracy, the integration over the detector surface perpendicular to the vector $\boldsymbol{p}$ can be replaced by the integration over the components of this vector in plane (x, y):

$$d\Omega_{\boldsymbol{p}} \approx \frac{dp_1dp_2}{k_0^2} \approx \frac{dp_ydp_z}{k_0^2} \approx \frac{dp_ydp_x}{k_0^2}\left|\frac{dp_z}{dp_x}\right| \approx \frac{dQ_ydQ_x}{k_0^2\sin\beta}. \qquad (5.36)$$

The differential cross-section is concentrated in a narrow diapason of Q_x, Q_y and therefore the number of photons registered by detector depends on the instrumental

function $\Phi(Q_x, Q_y)$ of the detector and on the angular aperture of the incident beam. The incident beam in high-resolution XRR technique is usually conditioned very precisely and can be considered as monochromatic. Then the observed X-ray intensity in the reciprocal space point Q_x, Q_y normalized by the incident X-ray flux is expressed as:

$$T_B(Q_x, Q_z) = \frac{1}{S_b} \int \frac{dQ'_y dQ'_x}{k_0^2 \sin\beta} \Phi(Q_x - Q'_x, Q_y - Q'_y) \frac{d\tilde{\sigma}}{d\Omega_{\boldsymbol{p}'}(Q'_x, Q'_y)}. \quad (5.37)$$

By substituting the expression (5.36) into (5.37) and integrating over variable $\boldsymbol{\rho}$, the following expression is obtained:

$$T_B(Q_x, Q_z) = \frac{k_0^2 |\chi_0|^2}{16\pi^2 Q_z^2 \sin\beta \sin\alpha} \int dQ'_y dQ'_x \Phi(Q_x - Q'_x, Q_y - Q'_y)$$
$$\int da_1 \int da_2 \int_S d\boldsymbol{R} e^{-iQ'_z(a_1-a_2)} e^{-i\boldsymbol{Q}'\boldsymbol{R}} [P(a_1)P(a_2) + W(a_1, a_2, R)]. \quad (5.38)$$

As has been discussed in the Sect. 3.2 for X-ray reflectivity, the non-physical behavior of (5.37) at $\alpha, \beta \to 0$ is caused by the incident or scattered beam footprints (Fig. 5.3) which may become larger than the sample size L_x. Therefore, for small angles $\alpha, \beta \ll \sqrt{|\chi_0|}$ in the expression (5.38) the multipliers $\bar{F}_b(\alpha)$, $\bar{F}_D(\beta)$ have to be used, which depend on the divergence of the incidence beam and the aperture of the detector. The analytical formula for instrumental function $\bar{F}(\theta)$ is given by Eq. (3.35), however, in the considered here situation it is obsolete because of failure of Born approximation at $\alpha, \beta \to 0$.

For the detectors with high resolution on both Q_x and Q_y (point detector), the instrumental function can be selected as Gaussian profile:

$$\Phi(Q_x, Q_y) = \frac{1}{2\pi} e^{-Q_x^2/2\Delta_x^2} e^{-Q_y^2/2\Delta_y^2}$$

with resolution elements $\Delta_{x,y}$ which are essentially smaller than the typical variations of $\Delta Q_{x,y}$ for X-ray diffuse scattering. Thus, integrating over a_1 and a_2 with Gaussian distributions (5.28) and (5.32) and over coordinates, the following analytical expression for intensity is derived:

$$T_{B1}(Q_x, Q_z) = \frac{k_0^2 |\chi_0|^2}{4Q_z^2 \sin\beta \sin\alpha} \int dQ'_y dQ'_x \Phi(Q_x - Q'_x, Q_y - Q'_y)$$
$$e^{-Q_z'^2\sigma^2} \{\delta(Q'_x)\delta(Q'_y) + \frac{1}{2\pi} \int_0^\infty R dR [e^{Q_z'^2 C(R)} - 1] J_0(Q'_\parallel R)\}$$
$$= \frac{k_0^2 |\chi_0|^2}{8\pi Q_z^2 \sin\beta \sin\alpha} \left\{ e^{-Q_x^2/2\Delta_x^2} + \Delta_x \Delta_y \int_0^\infty R dR [e^{Q_z^2 C(R)} - 1] J_0(|Q_x| R) \right\}. \quad (5.39)$$

where J_0 is Bessel function of zeroth order; the intensity is measured in the plane $Q_y = 0$; $Q_\parallel = \sqrt{Q_x^2 + Q_y^2} = |Q_x|$; the integral over R converges due to the asymptotic of the correlation function $C(R \to \infty) \to 0$, and

$$Q_x = k_0(\cos\beta - \cos\alpha);\ \ Q_z = k_0(\sin\beta + \sin\alpha). \tag{5.40}$$

The following approximations can be used for small incidence and scattering angles:

$$\alpha = \arcsin\frac{Q}{2k_0} + \arctan\frac{Q_x}{Q_z} \approx \frac{Q}{2k_0} + \frac{Q_x}{Q_z};$$
$$\beta = \arcsin\frac{Q}{2k_0} - \arctan\frac{Q_x}{Q_z} \approx \frac{Q}{2k_0} - \frac{Q_x}{Q_z};\ \ Q^2 = Q_x^2 + Q_z^2. \tag{5.41}$$

For kinematical scattering, the relation between Q_x and Q_z is [19]:

$$|Q_x| < \frac{Q_z^2}{2k_0}, \tag{5.42}$$

and introducing the dimensionless variable $u = R/L_c$, we finally obtain the formula:

$$T_{B1}(Q_x, Q_z) = \frac{|\chi_0|^2 k_0^4}{2\pi(Q_z^2 Q^2 - 4k_0^2 Q_x^2)} e^{-Q_z^2\sigma^2}$$
$$\times \left\{ e^{-Q_x^2/2\Delta_x^2} + \Delta_x \Delta_y L_c^2 \int_0^\infty u du [e^{Q_z^2\sigma^2 C_0(u)} - 1] J_0(|Q_x| L_c u) \right\};$$
$$C_0(u) = e^{-u^{2h}}. \tag{5.43}$$

The first term in (5.43) corresponds to the coherent peak and doesn't contain any additional information on the sample surface comparing to the specular peak in X-ray reflectivity. The second term is associated with the diffuse X-ray intensity, which is a subject of this section. The expression (5.43) describes the scattered X-ray intensity approximately due to used Born formula and the conditions $Q_z^2 > k_0^2|\chi_0|$, $QQ_z \pm 2k_0 Q_x > k_0^2|\chi_0|$, however, this expression defines the conditions at which the surface parameters L_c and h can be evaluated. For example, as follows from Eq. (5.43) the intensity of X-ray diffuse scattering increases when using detector with the slit registering the photons with all Q_y values:

$$\Phi(Q_x) = \frac{1}{\sqrt{2\pi}} e^{-Q_x^2/2\Delta_x^2}.$$

In this case, the integration over Q_y can be performed in (5.38), and as a result:

$$T_{B2}(Q_x, Q_z) = \frac{|\chi_0|^2 k_0^4}{4\pi^2(Q_z^2 Q^2 - 4k_0^2 Q_x^2)} e^{-Q_z^2\sigma^2}$$
$$\left\{\sqrt{2\pi} e^{-Q_x^2/2\Delta_x^2} + 2\Delta_x L_c \int_0^\infty du[e^{Q_z^2\sigma^2 C_0(u)} - 1]\cos(|Q_x|L_c u)\right\}. \quad (5.44)$$

As follows from the analytical estimate (5.44) and the kinematical estimate (5.42), the X-ray diffuse intensity may deliver the information on the structure of sample surface under the following conditions:

$$Q_z \le \sigma^{-1};\ |Q_x| \le \frac{Q_z^2}{2k_0} \approx \frac{1}{2k_0\sigma^2};\ L_c \ge \frac{1}{|Q_x|} \approx 2k_0\sigma^2. \quad (5.45)$$

Figure 5.4 shows the calculation of X-ray diffuse intensity using formula (5.44) from the $Si_{0.65}Ge_{0.35}$ sample with the parameters described in the figure capture. The intensity profile is a slowly decreasing function of the tangential component Q_x of the wave vector transfer in the kinematical approximation, which is applied for this simulation.

The intensity increase on the edges of available Q_x interval is due to mentioned above geometrical factor of the beam footprint enlargement. The Born approxima-

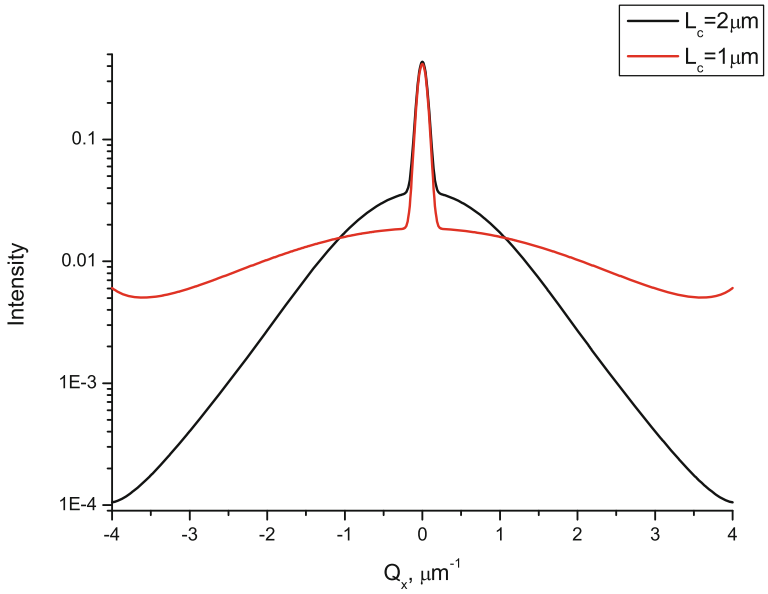

Fig. 5.4 X-ray diffuse scattering intensity calculated by using Born approximation (5.44) for $Si_{0.65}Ge_{0.35}$ sample with the rough surface described by the distribution function $\sigma = 1.5\,\text{nm}$, $h = 1$, $Q_z = 0.6\,\text{nm}$. The X-ray wavelength $\lambda = 0.154\,\text{nm}$; $k_0 = 2\pi/\lambda$; $\chi_0 = -1.99\ 10^{-5} + i5.27\ 10^{-7}$; $\Delta_x = 6\ 10^{-5}\,\text{nm}^{-1}$. The intensities $T_{1,2}(Q_x)$; $|Q_x| < Q_z^2/2k_0$ correspond to the values $L_{c1} = 1\,\mu\text{m}$ $L_{c2} = 2\,\mu\text{m}$

tion, however, doesn't allow to describe important physical effect observed in the experiment and called Yoneda wings [20]. The work [15] and further investigations (see citations in [19]) prove this and other specific effects [21] are caused by the refraction of incident and scattered waves inside media. All these dynamical processes can be explained by using DWBA. In most of the publications, dedicated to theoretical studies of diffuse X-ray scattering beyond the kinematical Born approximation, the only first order of DWBA is used. As a zeroth approximation for Eq. (5.27), the wave fields for the scattering at the plane border $z = 0$ are considered, which corresponds to the choice of the perturbation operator in the form:

$$V(\boldsymbol{r}) = V_0(z) + V_1(\boldsymbol{r}) \equiv k_0^2\chi_0 H(z) + k_0^2\chi_0\{H[z - z_0(x, y)] - H(z)\}. \quad (5.46)$$

The use of only first order DWBA for calculation of diffuse X-ray scattering has been shown [16, 22] to don't provide the conservation of whole radiation flux. Therefore, the formulas for diffusely scattered intensity involving second order DWBA have been derived. These equations take also into account the transition layer for the calculation of the specular reflection, which influences the diffuse scattering, too.

The non-perturbative solution of the wave equation for ideal interface corresponds to the potential $V_0(z)$ in (5.46) and is delivered by the waves (3.16) and (3.17) with Fresnel reflection and transmission coefficients:

$$\begin{aligned}
\boldsymbol{k} = (\boldsymbol{k}_\parallel; k_z = k_0 \sin\alpha);\ \ \boldsymbol{p} = (\boldsymbol{p}_\parallel; p_z = -k_0 \sin\beta);\\
\boldsymbol{A}_{\boldsymbol{k}}^{(+,0)}(\boldsymbol{r}) = \boldsymbol{e}^{(2)}(\boldsymbol{k}) e^{i\boldsymbol{k}_\parallel \boldsymbol{r}_\parallel} E_{k_z}^{(+,0)}(z);\\
E_{k_z}^{(+,0)}(z) = [e^{ik_z z} + r_F(k_z) e^{-ik_z z}]H(-z) + t_F(k_z) e^{ik_{zm} z} H(z);\\
\boldsymbol{A}_{\boldsymbol{p}}^{(-,0)*} = \boldsymbol{A}_{-\boldsymbol{p}}^{(+,0)} = \boldsymbol{e}^{(2)}(-\boldsymbol{p}) e^{-i\boldsymbol{p}_\parallel \boldsymbol{r}_\parallel} E_{-p_z}^{(+,0)}(z);\\
E_{-p_z}^{(+,0)}(z) = [e^{-ip_z z} + r_F(p_z) e^{ip_z z}]H(-z) + t_F(p_z) e^{-ip_{zm} z} H(z);\\
t_F(k_z) = \frac{2k_z}{k_z + k_{zm}},\ \ r_F(k_z) = \frac{k_z - k_{zm}}{k_z + k_{zm}},\\
k_{zm} = k_0\sqrt{\sin^2\alpha + \chi_0},\ \ p_{zm} = -k_0\sqrt{\sin^2\beta + \chi_0}.
\end{aligned} \quad (5.47)$$

The theory presented in previous section (see also [10]) proves that multiple scattering from the roughness results both in the diffusely scattered waves and modifies the form of coherent potential $V_c(z) \neq V_0(z)$ in (5.9). The transition layer modifies the corresponding solution of zeroth approximation, too.

In the Sect. 3.2 the influence of the dynamical effects (multiple scattering) on the profile of the specularly reflected beam has been discussed. In this section, the profile of the diffusely scattered intensity is calculated basing on the formula (5.24) for incoherent scattering. Several simplifications related to XRR geometry can be done, for example, at small scattering angles the polarization of waves doesn't influence the scattering cross-section and all wave fields in (5.24) can be considered as scalars, i.e. $\sin^2\theta_{1s} = 1$. Another simplification follows from the fact that the multiple

scattering changes the dependency of coherent potential on the coordinate z only, and the coherent wave fields in (5.24) can be selected as plane waves in transversal direction:

$$A_{\lambda}^{(+)} \to \boldsymbol{A}_{\boldsymbol{k}}^{(+)}(\boldsymbol{r}) = e^{i\boldsymbol{k}_{\parallel}\boldsymbol{r}_{\parallel}} E_{k}^{(+)}(z);$$
$$A_{\lambda'}^{(-)} \to \boldsymbol{A}_{\boldsymbol{p}}^{(-)}(\boldsymbol{r}) = e^{i\boldsymbol{p}_{\parallel}\boldsymbol{r}_{\parallel}} E_{p}^{(-)}(z). \tag{5.48}$$

The functions $E_{k}^{(\pm)}(z)$ satisfy to one-dimensional wave equation following from (5.9):

$$\left\{ \frac{d^2}{dz^2} + V_c(z) + k_0^2 - k_{\perp}^2 \right\} E_{k}^{(\pm)}(z) = 0, \tag{5.49}$$

with asymptotic behavior corresponding to divergent (+) and convergent (−) waves. To calculate the diffuse scattering cross-section for coherent potential $V_c(z)$, the approximation (5.16) can be engaged, which results in the following expression assuming model (5.28) for roughness distribution:

$$V_c(z) = k_0^2\chi_0 < H[z - z_0(x, y)] >= k_0^2\chi_0 \int_{-\infty}^{\infty} da\, P(a) H[z - a]$$
$$= \frac{k_0^2\chi_0}{\sigma\sqrt{2\pi}} \int_{-\infty}^{z} da e^{-a^2/2\sigma^2} = k_0^2\chi_0 \Phi(z/\sigma) \equiv k_0^2\chi_0\lambda(z);$$
$$\Phi(t) = \frac{1}{\sqrt{2\pi}} \int_{-\infty}^{t} dx e^{-x^2/2}. \tag{5.50}$$

In this potential, opposite to $V_0(z)$ in (5.46), the transition layer is taken into account for the formation of coherent wave. The Green function (5.19) is re-defined as:

$$G(\boldsymbol{R}, z, z') = \frac{1}{(2\pi)^3} \int d\boldsymbol{k}_1 \frac{e^{i\boldsymbol{k}_{1\parallel}\boldsymbol{R}} E_{k_{1z}}^{+*}(z') E_{k_{1z}}^{+}(z)}{k_0^2 - k_1^2 + i0};$$
$$\boldsymbol{R} = \boldsymbol{r}_{\parallel} - \boldsymbol{r}'_{\parallel}. \tag{5.51}$$

The expression for the cross-section of diffuse scattering can be derived from the general formula (5.24) for incoherent scattering by using new variables:

$$\boldsymbol{R} = \boldsymbol{r}_{\parallel} - \boldsymbol{r}'_{\parallel};\ \boldsymbol{\rho} = \frac{\boldsymbol{r}_{\parallel} + \boldsymbol{r}'_{\parallel}}{2},$$

$$\frac{d\sigma_D(\boldsymbol{p}, \boldsymbol{k})}{d\Omega_{\boldsymbol{p}}} = \frac{k_0^4 |\chi_0|^2 S}{(4\pi)^2} (M_1 - 2\Re[M_2]);$$

$$M_1 = \int d\boldsymbol{R} dz dz' e^{-i\boldsymbol{Q}_\parallel \boldsymbol{R}} E^-_{p_z}(z') E^{-*}_{p_z}(z) K(z, z', R) E^+_{k_z}(z) E^{+*}_{k_z}(z');$$

$$M_2 = \frac{J_0}{S} \int d\boldsymbol{R} d\boldsymbol{\rho} dz dz' e^{-i\boldsymbol{Q}_\parallel \boldsymbol{\rho}}$$

$$\times e^{i(\boldsymbol{p}_\parallel + \boldsymbol{k}_\parallel)\boldsymbol{R}/2} E^{-*}_{p_z}(z) K(z, z', R) G(\boldsymbol{R}, z, z') E^+_{k_z}(z');$$

$$K(z, z', R) = \int_{-\infty}^{\infty} da_1 \int_{-\infty}^{\infty} da_2 W(a_1, a_2 R)$$

$$\times [H(z - a_1) - \Phi(z/\sigma))][H(z' - a_2) - \Phi(z'/\sigma)], \tag{5.52}$$

where the distribution function $W(a_1, a_2 R)$ being defined in Eq. (5.32).

The integration over ρ in the second term of (5.52) results in the proportionality of this term to $\delta(\boldsymbol{Q}_\parallel)$ and its contribution solely into the peak corresponding to the specular reflection. The influence on the diffuse scattering cross-section is related to the re-normalization of specular reflectivity, which was considered in Sect. 3.2.

To calculate the X-ray scattering cross-section, the order of integration over the variables a and z has to be changed, which results in:

$$\frac{d\sigma_D(\boldsymbol{p}, \boldsymbol{k})}{d\Omega_{\boldsymbol{p}}} = \frac{k_0^4 |\chi_0|^2 S}{16\pi^2} \int d\boldsymbol{R} \int_{-\infty}^{\infty} da_1 \int_{-\infty}^{\infty} da_2 W(a_1, a_2, R)$$

$$\times F_{p_z, k_z}(a_1) F^* p_z, k_z(a_2) e^{-i\boldsymbol{Q}\boldsymbol{R}};$$

$$F_{p_z, k_z}(a) = \int_{-\infty}^{\infty} dz E^{-*}_{p_z}(z) [H(z - a) - \Phi(z/\sigma)] E^+_{k_z}(z). \tag{5.53}$$

The comparison of the expression (5.53) with the analogous kinematical one (5.39) demonstrates the fact, that dynamical effects in diffuse scattering are caused by the deviation of the incident and scattered coherent wave fields from the plane wave along the sample surface normal. In general case, the solution of the Eq. (5.43) with coherent potential $V_c(z)$ has a cumbersome form. Therefore, in most of applications the additional approximation is used, which is the ignorance of the transition layer in $V_c(z)$ caused by the coherent scattering from the roughness. Thus, the solution (5.40) is utilized corresponding to the ideal surface $V_c(z) = k_0^2 \chi_0 H(z)$, and the functions $F_{p_z, k_z}(a)$ are:

$$F_{p_z, k_z}(a) = -H(a) t_F(k_z) t_F(p_z) \int_0^a dz e^{ik_{zm} z} e^{-ip_{zm} z}$$

$$+ H(-a) \int_a^0 dz [e^{-ip_z z} + r_F(p_z) e^{ip_z z}][e^{ik_z z} + r_F(k_z) e^{-ik_z z}]$$

$$= H(a) t_F(k_z) t_F(p_z) K(k_{zm} - p_{zm}) + H(-a)[K(k_z - p_z)$$

$$+ r_F(p_z) r_F(k_z) K(-k_z + p_z) + r_F(p_z) K(k_z + p_z) + r_F(k_z) K(-k_z - p_z)];$$

$$K(q) = i \frac{e^{iqa} - 1}{q}. \tag{5.54}$$

Each term in the matrix element (5.54) has a physical meaning related to the additional reflection and transmission of the incidence and scattered waves from the distortions of the surface [21]. Because of this expression has still a complicated structure, the modified DWBA (MDWBA) is frequently used which makes it possible to analytically average over the roughness amplitudes:

$$F_{p_z,k_z}(a) \approx F^{(0)}_{p_z,k_z}(a) = t_F(k_z)t_F(p_z)K(k'_{zm} - p'_{zm}),$$
$$k'_{zm} = \Re\{k_{zm}\} = \frac{k_{zm} + k^*_{zm}}{2}, \tag{5.55}$$

and which corresponds to the following substitution for the wave field in a vacuum:

$$e^{ik_z z} + r_F(k_z)e^{-ik_z z} \approx t_F(k_z)e^{ik'_{zm}z}. \tag{5.56}$$

This approximation is valid for large values of k_z, when $r_F \to 0$; $t_F \to 1$; $k_{zm} \to k_z$. For the small values of k_z, the calculation of the matrix element (5.55) is performed in the vicinity $z \sim \sigma$, where the relationship (5.56) is satisfied due to conservation of the flux:

$$|r_F|^2 + \frac{k'_{zm}}{k_0}|t_F|^2 = 1. \tag{5.57}$$

The conservation of the flux doesn't depend on the approximation choice for the transmission and reflection coefficients, and remains valid also for transition layer if a self-consistent approach is used, as described in Sect. 3.2.

Assuming the validity of (5.56), the averaging over the roughness amplitudes with the distribution (5.32) is performed in a similar way as for kinematical model, and by accounting the geometrical factors the diffusely scattered intensity is calculated for one-dimensional detector by the following formula:

$$T_D(Q_x, Q_z) = \frac{k_0^2|\chi_0|^2\Delta_x}{8\pi^2 \sin\alpha \sin\beta |Q_{zm}|^2}|t_F(k_z)|^2|t_F(p_z)|^2 e^{-Q'^2_{zm}\sigma^2}$$
$$\times \int_0^\infty dx[e^{Q'^2_{zm}C(x)} - 1]\cos(|Q_x|x)\}$$
$$= \frac{2|\chi_0|^2\Delta_x L_c k_0^6 \sin\alpha \sin\beta}{\pi^2|(k_z + k_{zm})(p_z + p_{zm})|^2|Q_{zm}|^2} e^{-Q'^2_{zm}\sigma^2}$$
$$\times \int_0^\infty du[e^{Q'^2_{zm}\sigma^2 C_0(u)} - 1]\cos(|Q_x|L_c u);$$
$$Q_{zm} = p_{zm} - k_{zm} = -k_0(\sqrt{\sin^2\beta + \chi_0} + \sqrt{\sin^2\alpha + \chi_0}),$$
$$k_z = k_0 \sin\alpha;\ p_z = -k_0 \sin\beta, \tag{5.58}$$

which differs from the kinematical formula (5.37) by the transmission coefficients and re-defined normal component of the momentum transfer.

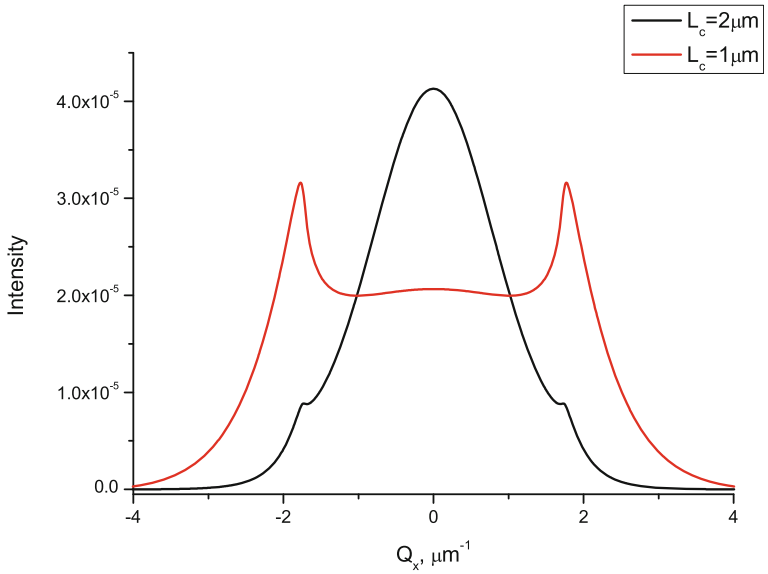

Fig. 5.5 The calculated Q_x profiles of X-ray diffuse scattering using MDWBA for the sample parameters from Fig. 5.4. The intensity $T_D(Q_x)$ is calculated at $Q_{z0} = 0.6\,\mathrm{nm}^{-1}$

Figures 5.5 and 5.6 shows that dynamical effects change the profiles of X-ray diffuse scattering essentially. For the incidence and scattering angles close to the critical angle of total external reflection, the transmission coefficient has a maximum (Sect. 3.3) and the scattered intensity has a peak called Yoneda wing [20]. Thus, the expression (5.57) describes well the qualitative dynamical effects in the scattered X-ray diffuse intensity.

For evaluation of a real experimental data, the important issue is how strong is the influence of used approximation on the accuracy of obtained quantitative values for roughness parameters. Another question is whether expression (5.55) remains valid for large amplitudes of the roughness. Figure 5.7 shows the relative corrections to the intensity of diffuse scattering for different roughness amplitudes:

$$\begin{aligned} \Delta F &= F_{p_z,k_z}(a) - F^{(0)}_{p_z,k_z}(a) \\ &= H(-a)[(K(k_z - p_z) - t_F(k_z)t_F(p_z)K(k'_{zm} - p'_{zm})) \\ &+ r_F(p_z)r_F(k_z)K(-k_z + p_z) + r_F(p_z)K(k_z + p_z) + r_F(k_z)K(-k_z - p_z)], \end{aligned} \tag{5.59}$$

that demonstrates the validity of MDWBA for entire diapason of root mean square roughness amplitude observed in the most of real samples. Thus, the main contribution into diffuse X-ray scattering from rough surface is delivered in the case when the incident and scattered beams have a maximal path in the media.

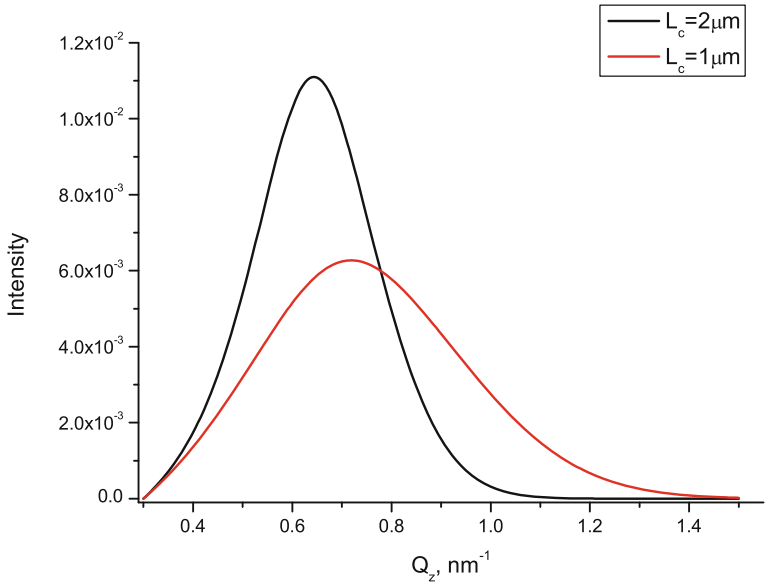

Fig. 5.6 The simulation of X-ray diffuse scattering Q_z profiles using MDWBA for the sample parameters from Fig. 5.4. The intensity $T_D(Q_z)$ corresponds $k_z = 0.3\,\mathrm{nm}^{-1}$; $Q_z \geq k_z$; $Q_x = k_x - \sqrt{k_0^2 - (Q_z - k_z)^2}$

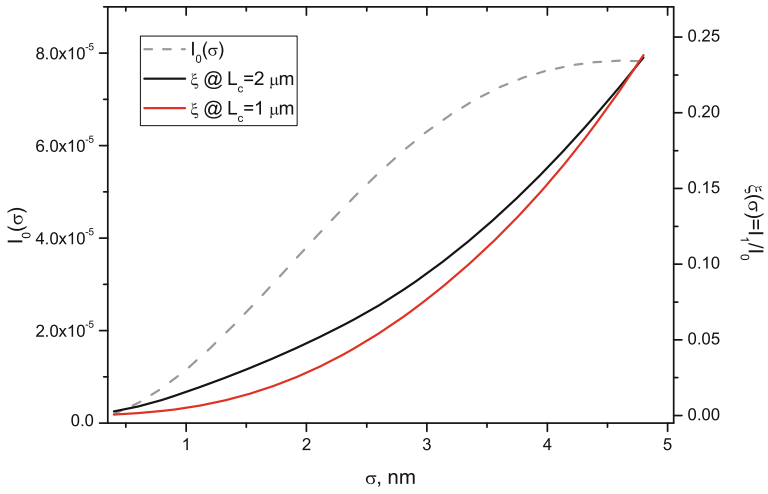

Fig. 5.7 The X-ray diffuse scattering $I_0(\sigma)$ calculated from formula (5.58), and the corrections $\xi(\sigma)$ coming out of MDWBA applicability area for different σ. The sample parameters from Fig. 5.4 are used at $Q_{z0} = 0.6\,\mathrm{nm}^{-1}$, $Q_{x0} = 2 \cdot 10^{-3}\,\mathrm{nm}^{-1}$

To take into account the coherent potential for the construction of zeroth approximation for wave field, we consider here the self-consistent DWBA. The potential is formed at the boundary transition layer with the thickness $\sim 2\sigma$ and the electron density profile (5.50). Then the wave fields in matrix element $F_{p_z,k_z}(a)$ in Eq. (5.53) are defined by analytical expressions (3.59) and (3.64):

$$E^{+}_{k_z}(z) = \lambda(z)T(k_z)e^{ik_{zm}z} + [1-\lambda(z)][R(k_z)e^{-ik_z z} + e^{ik_z z}];$$
$$E^{-*}_{p_z}(z) = \lambda(z)T(p_z)e^{-ip_{zm}z} + [1-\lambda(z)][R(p_z)e^{ip_z z} + e^{-ip_z z}], \qquad (5.60)$$

with the transmission $T(k_z)$ and reflection $R(k_z)$ coefficients following from the Eq. (3.66).

Figure 5.8 compares the simulated X-ray diffuse intensity by self-consistent DWBA and by approximation (5.58). The difference between them is due to the essential deviations of reflection and transmission coefficients from Fresnel coefficients r_F and t_F as well as due to the complicated dependency from the roughness amplitude comparing to the exponential factor in (5.58). The decrease of X-ray diffuse intensity in self-consistent approach is explained by the fact, that some waves scattered from roughness contribute to the coherent (specular) peak. The decrease of the intensity in this peak is slower with the increase of $|Q|$ than the decrease provided by Debye-Waller factor (see Sect. 3.4).

In practice, the modified DWBA explains the experimental data with satisfactory accuracy. The figures below demonstrate the evaluation results for thin SiO_2 layer on silicon substrate [23]. Three samples were made by thermal oxidation of Si(100)

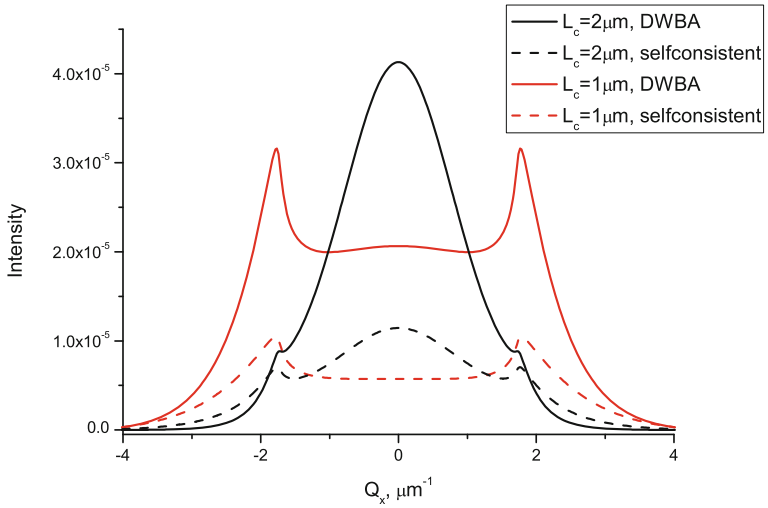

Fig. 5.8 X-ray diffuse intensity $I_S(\sigma)$ simulated by self-consistent DWBA and by formula (5.58). The sample parameters from Figure 5.4 are used, and $Q_{z0} = 0.6\,\mathrm{nm}^{-1}$, $Q_{x0} = 2 \cdot 10^{-3}\,\mathrm{nm}^{-1}$; $L_c = 2\,\mu\mathrm{m}$

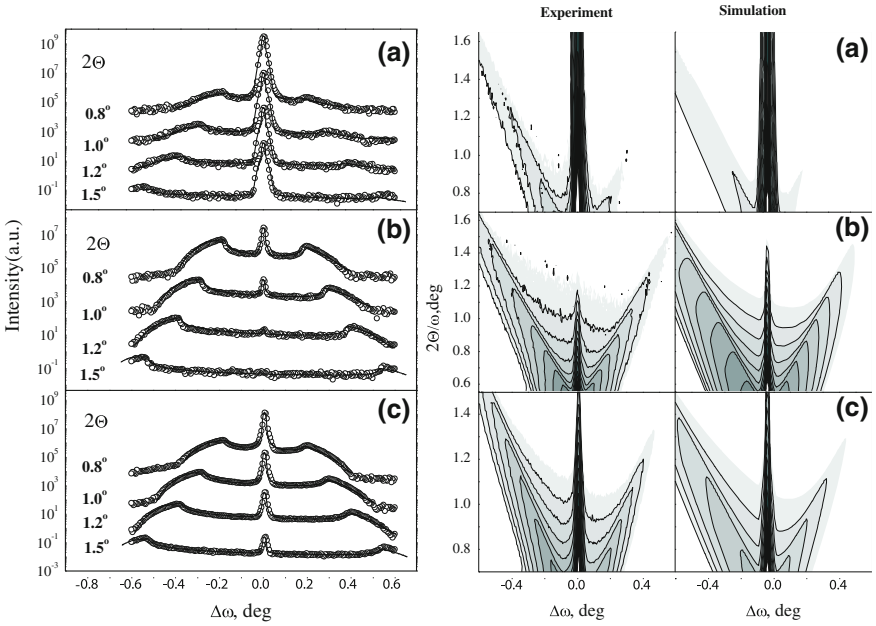

Fig. 5.9 In the *left panel*, the $\omega/2\Theta$ scans are presented from the samples 1, 2, and 3 (**a**, **b**, and **c**, respectively) for offsets $2\Theta = 1.5°$, $1.2°$, $1.0°$ and $0.8°$. The theory is given by *solid lines* and the experiment is shown by *open dots*. The *curves* are scaled by different factors for clarity. The *right panel* shows the measured (*left column*) and simulated (*right column*) reciprocal space maps around (000) reciprocal lattice point for samples 1, 2, and 3 (**a**, **b**, and **c**, respectively)

wafers. An thick oxide layer of nominal thickness 45 nm was grown on sample 1 by flowing O_2 over the sample. For sample 2, the Si wafer was first dipped in etching solution for two minutes and then thermally oxidized. Sample 3 was prepared in the same way as sample 2, and then the SiO_2 layer was striped off. All three samples are expected to have different character of surface roughness, which was a subject of X-ray investigations performed by XRR technique and diffuse scattering measurements. Figure 5.9 shows the $\omega/2\theta$ scans for samples 1, 2 and 3 (left panels), which were analyzed simultaneously with the reflectivity data, i.e. with respect to thickness, roughness and film density being optimal for the refine fits of both scan types. The experimental (open symbols) and simulated (solid lines) scans demonstrate acceptable coincidence for different values of offset $2\theta = 0.8°$, $1.0°$, $1.2°$ and $1.5°$. The right panel shows the simulated and experimental reciprocal space maps around (000) reciprocal lattice point for samples 1, 2 and 3 (maps a, b, and c, respectively). The agreement between the simulated maps and the experimental measurements is also rather good. The roughness root mean square and lateral correlation length values (σ, Λ) for the samples are found to be (0.4, 200), (4.1, 10), and (2, 11) nm for samples 1, 2, and 3, respectively.

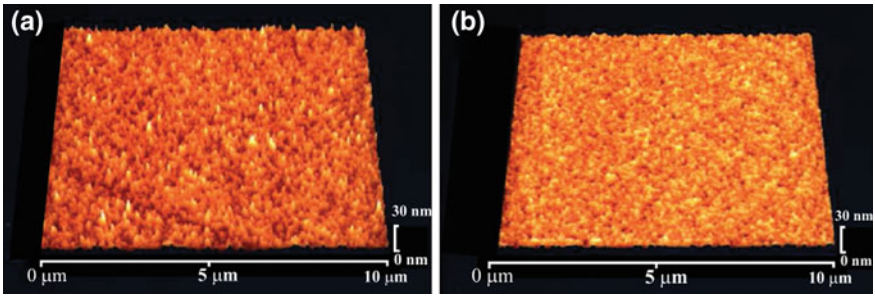

Fig. 5.10 Atomic force microscopy images of surface of samples 2 and 3 (panels (**a**) and (**b**), respectively). The sample 2 exhibits the large-scale roughness similar to island-like morphology. The roughness of sample 3 is approximately twice smaller as of the sample 2 one

Finally, the atomic force microscopy (AFM) studies confirmed the morphology of SiO_2/Si surfaces deduced from the X-ray experiments for the samples 2 and 3 (Fig. 5.10a, b, respectively). The scale of roughness and jaggedness is close to the values of lateral correlation length and rms roughness obtained from the simulation of specular reflectivity and diffuse scattering from investigated samples. We do not show the AFM image for sample 1 because of nearly smooth SiO_2 film surface in this case.

5.3 X-Ray Diffuse Scattering from Rough Interfaces in Multilayered Structures

X-ray diffuse scattering in XRR geometry is a sensitive instrument for characterization of interfaces between different media. Even more information is available from diffuse scattering intensity measured from multilayered systems possessing multiple interfaces as shown in Fig. 5.11. The application of these structures for modern technologies has been discussed in the Sect. 3.3.

The diffuse scattering from multiple interfaces is incoherent in general case, which results in blurring the features of X-ray scattering from single interfaces. The exception is a case of layer deposition in multilayered sample, which implements the correlation between amplitudes and position of the roughness in different interfaces. These correlations can be investigated by using X-ray diffuse scattering.

The theory of X-ray diffuse scattering from multiple interfaces is based on the DWBA with zeroth approximation for wave fields corresponding to Maxwell's equation for the structure with ideal boundaries (see, for example, [21–24] and citation therein). In this paragraph, the applicability of theory described in Sect. 5.1 and various approximations for calculation of X-ray intensity are discussed.

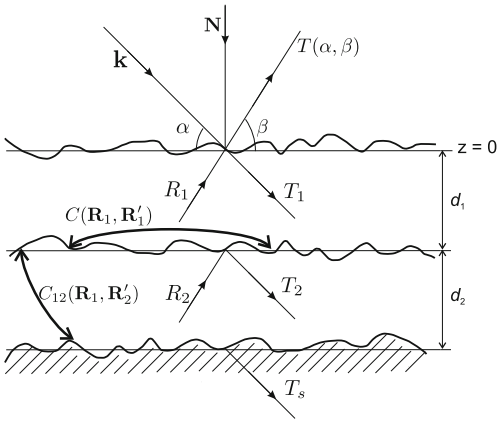

Fig. 5.11 Schematic representation of multilayered structures in XRR experiments and possible correlations between the parameters of interfaces. The function $C_i(\boldsymbol{R}_i, \boldsymbol{R}'_i)$ define the correlations between the roughness in one interface, $C_{ij}(\boldsymbol{R}_i, \boldsymbol{R}'_j)$ defines the correlations between the roughness in different interfaces

The Maxwell's Eq. (5.3) for arbitrary vector potential is written as follows (in XRR geometry, the polarization of the radiation can be neglected):

$$\{\Delta + k_0^2 + V(\boldsymbol{r})\}A(\boldsymbol{r}) = 0;$$
$$V(\boldsymbol{r}) = k_0^2 \sum_{i=1}^{N} [\chi_i - \chi_{i-1}] H[z - z_i(x, y)], \tag{5.61}$$

where the functions $z_i(x, y)$ describe the surface of i-interface between the layers with X-ray polarizabilities χ_i and χ_{i-1}, and $\chi_0 = 0$ corresponds to vacuum, and χ_N is an X-ray polarizability of the substrate (Fig. 5.11).

Assuming the roughness of different interfaces is not overlapping, the coherent scattering potential (5.16) can be distinguished for each interface and the Eq. (5.61) is then written as:

$$\{\Delta + k_0^2 + V_0(z) + \Delta V(\boldsymbol{r})\}A(\boldsymbol{r}) = 0;$$
$$V_0(z) = \sum_{i=1}^{N} V_i(z); \;\; \Delta V(\boldsymbol{r}) = k_0^2 \sum_{i=1}^{N} [\chi_i - \chi_{i-1}]\{H[z - z_i(x, y)] - \lambda_i(z)\};$$
$$V_i(z) = k_0^2 < H[z - z_i(x, y)] > \equiv k_0^2 \lambda_i(z - \bar{z}_i), \tag{5.62}$$

where the function $\lambda_i(z - \bar{z}_i)$ defines the shape of the transition layer for i-interface and, assuming the Gaussian distribution of roughness amplitude, is:

$$\lambda_i(z - \bar{z}_i) = \Phi(\frac{z - \bar{z}_i}{\sigma_i}); \quad \Phi(t) = \frac{1}{\sqrt{2\pi}} \int_{-\infty}^{t} dx e^{-x^2/2}. \tag{5.63}$$

Here the values $\bar{z}_i$ and σ_i characterize the average position and root mean square of roughness amplitude at i-interface, respectively, and thus the layer thickness is (Fig. 5.11):

$$d_i = \bar{z}_{i+1} - \bar{z}_i \gg \sigma_i + \sigma_{i-1};\ \bar{z}_1 \equiv 0.$$

In the first DWBA approximation for potential $\Delta V(\boldsymbol{r})$, X-ray diffuse intensity is calculated by Eq. (5.24) with wave fields following from the equations of zeroth approximation with transition layers at interfaces:

$$\boldsymbol{A}_{\boldsymbol{k}}^{(+)}(\boldsymbol{r}) = e^{i\boldsymbol{k}_\parallel \boldsymbol{r}_\parallel} E_k^{(+)}(z);\quad \boldsymbol{A}_{\boldsymbol{p}}^{(-)}(\boldsymbol{r}) = e^{i\boldsymbol{p}_\parallel \boldsymbol{r}_\parallel} E_p^{(-)}(z);$$
$$\{\Delta + k_0^2 - k_\perp^2 + V_0(z)\} E_k^{(\pm)}(z) = 0. \tag{5.64}$$

The wave fields $E_k^{(\pm)}(z)$ in (5.64) for multilayered structure with the potential $V_0(z)$ from (5.61) can be found using formulas (3.107)–(3.113) and are written as:

$$E_k^{(+)}(z) = \sum_{j=0}^{N} [T_j(k_{zj}) e^{ik_{zj}z} + R_j(k_{zj}) e^{-ik_{zj}z}];$$
$$E_p^{(-*)}(z) = E_{-p}^{(+)}(z) = \sum_{j=0}^{N} [T_j(p_{zj}) e^{-ip_{zj}z} + R_j(p_{zj}) e^{ip_{zj}z}];$$
$$k_{zj} = k_0 \sqrt{\sin^2\alpha + \chi_j};\ p_{zj} = -k_0 \sqrt{\sin^2\beta + \chi_j}, \tag{5.65}$$

with the coefficients defined by recurrent Parratt's Eq. (3.109) with the layer boundaries corresponding to the values $\bar{z}_j$:

$$T_0 = 1;\ X_0 = R_0;\ X_N = 0;$$
$$X_j = \frac{r_{j,j+1} + X_{j+1} e^{-2ik_{z(j+1)}d_{j+1}}}{1 + r_{j,j+1} X_{j+1} e^{2ik_{zj}d_j}};$$
$$T_{j+1} = \frac{1}{t_{j+1,j}} e^{i(k_{z(j+1)} - k_{zj})\bar{z}_j} T_j [1 + r_{j+1,j} X_j];$$
$$R_j = T_j X_j e^{-2ik_{zj}\bar{z}_j}; \tag{5.66}$$

The reflection $r_{j,j+1}$ and transmission $t_{j,j+1}$ coefficients at each interface are calculated by Fresnel's formulas (3.110) with Nevot-Croce factor in case of abrupt interfaces and by using formulas (3.111) for self-consistent model of the transition layer.

The calculation of the matrix element in Eq. (5.53) for non-overlapping interfaces is similar to the case of a single boundary. Based on the analysis of the approximations performed in previous section, the substitution $\lambda_j(z) = H(z - \bar{z}_j)$ in perturbation operator (5.61) can be done, which results in the following expression for matrix element through the functions of random values $\{a_j\}$:

$$F_{p_z,k_z}(\{a_j\}) = \sum_{j=0}^{N} F_j(a_j);\ F_j(a_j) = (\chi_{j+1} - \chi_j)[H(-a_j)M_j + H(a_j)M_{j+1}];$$
$$M_j = T_j(k_{zj})T_j(p_{zj})K(k_{zj} - p_{zj}) + T_j(k_{zj})R_j(p_{zj})K(k_{zj} + p_{zj}) +$$
$$+T_j(p_{zj})R_j(k_{zj})K(-k_{zj} - p_{zj}) + R_j(k_{zj})R_j(p_{zj})K(-k_{zj} + p_{zj});$$
$$K(q) = \frac{e^{iqa_j} - 1}{iq}. \tag{5.67}$$

The squared modulus of this matrix element is equal to:

$$|F_{p_z,k_z}(\{a_j\})|^2 = \sum_{j=0}^{N}\sum_{l=0}^{N} F_l^*(a_l')F_j(a_j), \tag{5.68}$$

and has to be averaged using two-point correlation functions for distribution of amplitudes $W_{lj}(a_l', a_j)$ containing the relation between the roughness at different interfaces. The general form of these functions follows from (5.32):

$$W_{lj} = \frac{1}{2\pi\sigma_i\sigma_l}\left[\frac{1}{\sqrt{(1-C_{lj}^2)}} e^{-\frac{a_l'^2 + a_j 2^2 - 2C_{lj}a_l'a_j}{2\sigma_i\sigma_l(1-C_{lj}^2)}} - e^{-\frac{a_l'^2}{2\sigma_l^2}} e^{-\frac{a_j^2}{2\sigma_j^2}}\right]. \tag{5.69}$$

There are several models of the correlation functions C_{lj} for the roughness amplitudes at different interfaces, which are applied in dependence on the interface types (see [21, 24, 25] and citation therein):

Uncorrelated (random) model is recommended for thick (>50 nm) layers, where the correlations between interfaces are eliminated during the growth process. Using the fractal correlation functions as (5.30) for each interface:

$$C_{lj} = \delta_{lj}C_j;\ C_j = \sigma_j^2 e^{-(\frac{R_j}{L_{c,j}})^{2h_j}};\ R_j = \sqrt{(x_j - x_j')^2 + (y_j - y_j')^2}. \tag{5.70}$$

Full correlation model assumes the full identity of the interface profiles, which may happen in the layers of superlattices (periodically repeating sequence of layers). Using the fractal model of roughness, the correlation function is selected as in Eq. (5.30) and is written:

$$C_{lj} = \sigma^2 e^{-(\frac{R_{lj}}{L_c})^{2h}};\ R_{lj} = \sqrt{(x_j - x_l')^2 + (y_j - y_l')^2}. \tag{5.71}$$

Ming correlation model provides the intermediate case between two above-mentioned, which is parametrized by vertical correlation length Λ and Hurst fractal parameter h:

$$C_{lj} = \sqrt{C_l(R_{lj})C_j(R_{lj})}e^{-(\frac{|\bar{z}_l - \bar{z}_j|}{\Lambda})^{2h}}. \tag{5.72}$$

Holy-Baumbach model implements the gradual increase of the roughness amplitude with increment μ from smaller values at the substrate to layer ones at the sample surface:

$$C_{lj} = \sigma_N^2[1 + \mu(N - \max(l, j))]e^{-(\frac{R_N}{L_{c,N}})^{2h_j}}. \tag{5.73}$$

The calculation of the average in Eq. (5.70) is a cumbersome task even for Gaussian model of the lateral and vertical correlations because of different functions appearing in the matrix element (5.67) and corresponding to the positive and the negative values a_j. Therefore, in practical calculations the assumption $M_j = M_{j+1}$ is used in (5.67) and the integration over the amplitudes with Gaussian distribution is performed analytically. The necessity to estimate the accuracy of this approximation was mentioned in [21], and the estimation for a single surface has been presented in Sect. 5.2. The equality $M_j = M_{j+1}$ corresponds to MDWBA, when the relationship (5.56) is used near the boundary:

$$T_j e^{ik_{zj}\bar{z}_j} + R_j e^{-ik_{zj}\bar{z}_j} = T_{j+1}e^{ik_{z(j+1)}\bar{z}_j} + R_{j+1}e^{-ik_{z(j+1)}\bar{z}_j}]. \tag{5.74}$$

Figure 5.7 demonstrates the validity of this approximation in a wide range of $k_z\sigma$ due to the conservation of flux (5.57). The condition (5.74) is valid when the values k_{zj} are substituted by real values $\Re k_{zj}$, which excludes the exponentially growing terms in the expression for X-ray intensity.

By averaging over the roughness amplitudes in MDWBA, the diffusely scattered X-ray intensity from the sample consisting of N layers is (one-dimensional detector with open aperture in Q_y direction assumed):

$$T_D(Q_x, Q_z) = \frac{k_0^2 \Delta_x}{8\pi^2 \sin\alpha \sin\beta} \sum_{l=0}^{N}\sum_{j=0}^{N}(\chi_{l+1} - \chi_l)^*(\chi_{j+1} - \chi_j)$$

$$\times \left\{ \sum_{m=0}^{3}\sum_{n=0}^{3} G_j^{(m)} G_l^{(n)*} \frac{\exp\{-1/2[(\sigma_j Q_{jz}^{(m)'})^2 + (\sigma_l Q_{lz}^{(n)'})^2]\}}{Q_{jz}^{(m)} Q_{lz}^{(n)*}} I_{jl}^{(mn)} \right\};$$

$$I_{jl}^{(mn)} = L_c^{jl} \int_0^\infty dx\{\exp[Q_{jz}^{(m)'} Q_{lz}^{(n)'} C_{jl}(x)] - 1\} \cos Q_x L_c^{jl} x. \tag{5.75}$$

Here, the indices (j, l) correspond to the summation over the layers, and the indices (m, n) enumerate the combinations of the reflection and transmission coefficients in matrix element (5.67); L_c^{jl} is a correlation length in correlation function C_{jl}. The function G and variable Q are defined as:

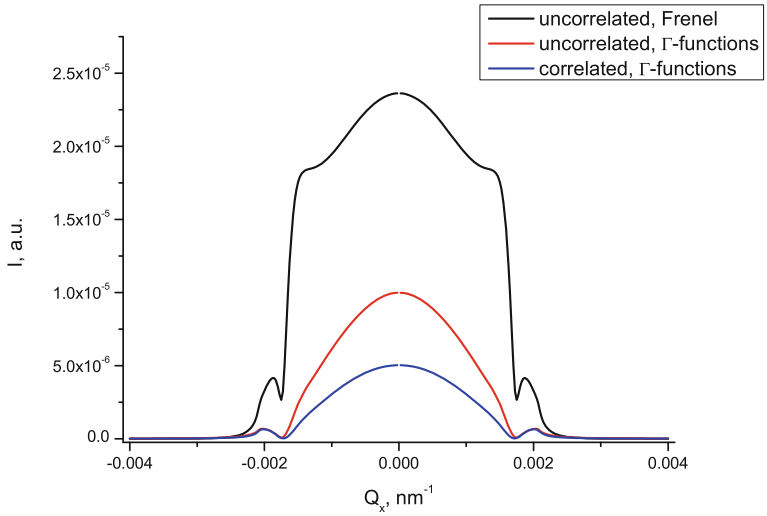

Fig. 5.12 Q_x scan of X-ray diffuse scattering for the sample consisting of 20 nm $Si_{0.65}$ $Ge_{0.35}$ layer on Si substrate with X-ray polarizability $\chi_1 = -1.99 \cdot 10^{-5} + i5.27 \cdot 10^{-7}$; $\chi_2 = -1.51 \cdot 10^{-5} + i3.50 \cdot 10^{-7}$; $\Delta_x = 6 \cdot 10^{-5}$ nm^{-1}. $Q_z = 0.6$ nm^{-1}, $\sigma_1 = 2$ nm, $\sigma_2 = 1.5$ nm; $L_{c1} = 1$ μm; $L_{c1} = 2$ μm; $h_1 = h_2 = 2$

$$G_j^{(0)} = T_j(k_{zj})T_j(p_{zj});\ G_j^{(1)} = T_j(k_{zj})R_j(p_{zj});$$
$$G_j^{(2)} = R_j(k_{zj})T_j(p_{zj});\ G_j^{(3)} = R_j(k_{zj})R_j(p_{zj});$$
$$Q_{jz}^{(0)} = k_{zj} - p_{zj};\ Q_{jz}^{(1)} = k_{zj} + p_{zj};\ Q_{jz}^{(2)} = -Q_{jz}^{(0)};\ Q_{jz}^{(3)} = -Q_{jz}^{(1)}. \quad (5.76)$$

The full X-ray intensity is then written as a sum of (5.75) and X-ray specular reflectivity from multilayered structure. Using the Gaussian instrumental function for detector as in (5.44):

$$T_S(Q_x, Q_z) = \frac{1}{\sqrt{2\pi}}|R_0(k_{z0})|^2 e^{-Q_x^2/2\Delta_x^2};\quad k_{z0} = k_0 \sin\alpha = Q_z/2, \quad (5.77)$$

the reflection coefficient $R_0(k_{z0})$ from the entire structure is delivered by the solution of Parratt's equations (5.66). Figure 5.12 demonstrates X-ray diffuse scattering profiles for different models of the vertical correlations of interface roughness and the shape of the transition layer for $Si_{0.65}Ge_{0.35}$ 20 nm layer on the Si substrate.

The analysis of diffuse X-ray scattering from periodic multilayered structure (superlattices) is a special case of XRR applications, which is widely used in modern technologies (Fig. 3.14). For these samples, the dynamical effects become apparent both in specular reflectivity (superlattice peaks in the reflection coefficients as in Fig. 3.15) and in diffuse scattering. As a result, X-ray scattering profile has a complex structure described in Ref. [21]. The widely used representation of the measured

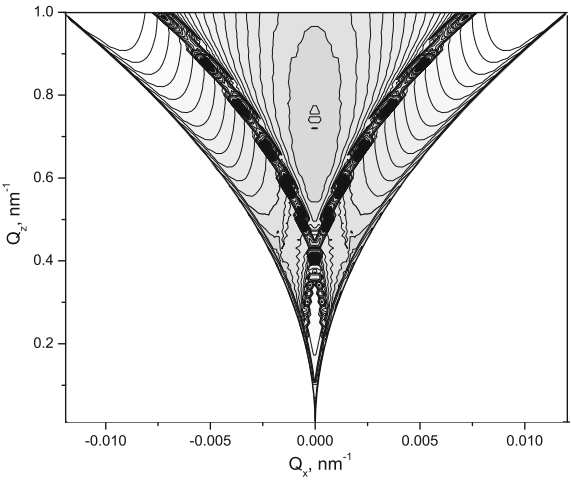

Fig. 5.13 Reciprocal space map (Q_x, Q_z) of diffuse X-ray scattering from 10 periods of bilayer Ge (5 nm)/$Si_{0.65}Ge_{0.35}$ (5 nm) on silicon substrate. The simulation parameters are: $\chi_1 = -1.99 \cdot 10^{-5} + i5.27 \cdot 10^{-7}$; $\chi_2 = -3.5 \cdot 10^{-5} + i8.3 \cdot 10^{-7}$; $\sigma_1 = 1$ nm, $\sigma_2 = 1$ nm; $L_{c1} = 1$ μm; $L_{c1} = 1$ μm; $h_1 = h_2 = 2$, uncorrelated interface roughness model

and simulated X-ray intensity is a reciprocal space map in coordinates (Q_x, Q_z) as shown in Fig. 5.13. The fitting of the whole map or multiple sections from such a map is a robust method to characterize the correlations of interfacial roughness within the multilayered samples .

The example below demonstrates the effectiveness of diffuse X-ray scattering studies in investigation of the morphology of Mo/Si superlattices [26]. Two Mo/Si multilayers consisting of 30 bi-layers with a total thickness of approximately 300 nm were prepared by ion beam sputtering on an Si wafer (sample 1) and a partially crystallized polished ceramic glass substrate (sample 2), each 2 inches in diameter. The X-ray reflectivity and diffuse scattering intensities were measured using a high-resolution X-ray diffractometer (Advanced Thin Film X-ray System ATX-G, Rigaku Corporation). X-rays with wavelength $\lambda = 0.15405$ nm (CuK_{α_1}) are generated from a Cu rotating anode (50 kV, 300 mA), collimated by a parabolic multilayer mirror and monochromated by a channel cut Ge(111) asymmetric monochromator. A divergent (0.1×10 mm) slit was used to control the exposure area on the sample surface, while a parallel pair of slits (0.2×15 mm) was used to limit the output signal. The diffuse X-ray scattering was measured via $\omega/2\theta$ scans with 2θ fixed in the interval $1.4° \div 7°$. Area mapping around the (000) reciprocal lattice point was used for qualitative analysis and separate ω-scans were used for precise fits. The recorded diffuse intensity can be used to determine the mesoscopic in-plane structure of surfaces and interfaces, lateral correlation of roughness, and the fractal dimension of jagged surfaces. Moreover, the distribution of diffuse intensity in reciprocal space may reflect the vertical correlation of interface roughness, if present. In this case, the incoherent wave fields may interfere constructively creating a halo around the specular beam.

The reciprocal space maps around the (000) reciprocal lattice point give a qualitative insight into the principal characteristics of interfacial roughness. The measured intensity maps shown in Fig. 5.14a, c for Samples 1 and 2, respectively, permit

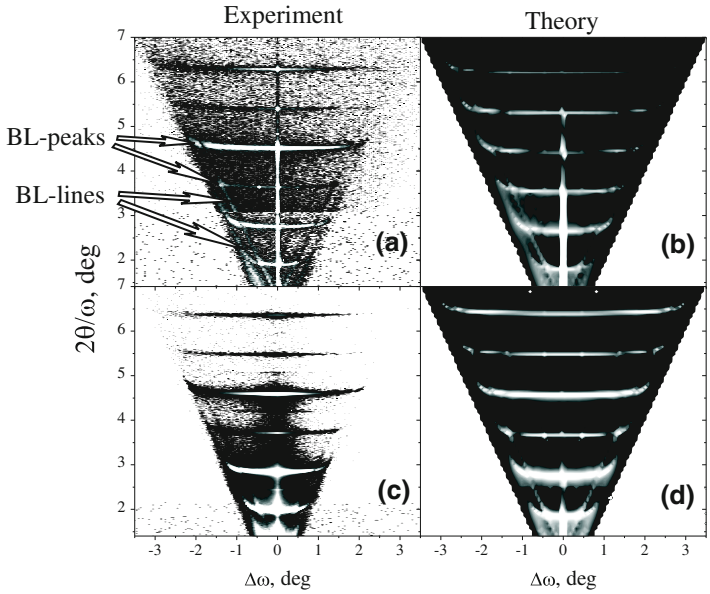

Fig. 5.14 Measured (*left column*) and simulated (*right column*) reciprocal space maps around (000) reciprocal lattice point for multilayers grown on Si wafer (**a**, **b**) and glass (**c**, **d**) substrates [26]. The resonant diffuse scattering sheets are clearly visible on both experimental maps. Bragg-like lines and peaks are denoted on the intensity map from the Sample 1

judgement about the common features of multilayers. First, a greater proportion of diffusely scattered intensity in the total reflectivity for Sample 2 indicates a larger value of roughness rms for this sample. Secondly, the interfacial roughness in both samples has a correlated nature indicated by the distribution of diffuse scattering as resonant diffuse (non-specular) scattering sheets. These banana-shaped stripes of concentrated diffuse intensity intersect the truncation rod, coinciding in Fig. 5.14 with the specular beam line, at equidistant points defined by the Bragg condition for the superlattice stack. The confinement of intensity to resonant diffuse scattering (RDS) sheets reflects the degree of the vertical replication of roughness, with the width of stripes in the horizontal direction being determined mainly by the lateral correlation of roughness. The slight upwards bending of the RDS at the edges is due to the refraction of X-rays in the stack. The large vertical width of the RDS in Fig. 5.14c gives evidence of poor (partial) roughness replication in Sample 2, whereas the high roughness conformity of Sample 1 results in strong confinement of RDS in Fig. 5.14a. In addition to the RDS stripes, the Bragg-like resonant lines can be observed in Fig. 5.14a. These lines are approximately parallel to the edges of the measurable area. They arise due to the dynamical effects of multiple specular reflection and extinction of the scattered radiation and can be explained on the basis of the concept of *Umweganregung* [19]. The location of these ridges is determined by double diffraction when the incident or exit wave occur in a Bragg-diffraction condition.

The maxima located on the Bragg-like lines appear when both the incident and exit angles satisfy the X-ray diffraction condition simultaneously. Bragg-like lines up to second order, and some Bragg-like peaks, are designated in Fig. 5.14a. Almost all of these dynamical effects are absent in the data from Sample 2, where the interface imperfections suppress multiple scattering. The panels (b) and (d) in Fig. 5.14 show the simulated maps for both samples after the final refinement.

The diffuse X-ray scattering from Sample 1, presented in Fig. 5.15a as a set of rocking curves recorded at different values of 2θ and drawn as open dots, contains the information about lateral character and vertical conformity of the interface roughness. For the simulated intensities (solid lines), only the diffuse X-ray scattering components are depicted, for the sake of clarity. The 2θ positions of the ω-scans are chosen to cross the resonant diffuse scattering sheets of Fig. 5.14. The sample parameters, refined from the fit procedure, show that the lateral correlation length of the interfacial roughness $\Lambda_1 = 70\,\text{nm}$ is shorter for Sample 1 than for Sample 2 grown on the glass substrate, $\Lambda_2 = 250\,\text{nm}$. The Hurst parameter is close to unity (i.e. the roughness of the interfaces has a Gaussian nature) and the vertical correlation of roughness reaches 50 nm, approximately 1/6 of the total multilayer thickness, consistent with strong confinement of diffuse intensity in RDS sheets. According to the theoretical model used, the lateral correlation length and the Hurst parameter were assumed to be the same for all interfaces.

The diffuse scattering data from Sample 2 are shown in Fig. 5.15b. The values of interfacial roughness obtained by data fitting in this case, $\sigma_{Si} \sim 0.9\,\text{nm}$ and $\sigma_{Mo} \sim 0.6\,\text{nm}$, are twice as large as those obtained for Sample 1. The thickness of basic and inter-diffusion layers are found to be nearly the same as for the sample on a crystalline substrate. The incoherent scattering, however, is comparable with the absolute magnitude of the specular beam, which smoothes the latter on the background of the diffuse intensity. The greater proportion of diffuse scattering in the detected intensity for this sample is again consistent with a large total roughness refined from simulations. A large value of lateral correlation length ($\Lambda \sim 250\,\text{nm}$) and a small value of Hurst parameter ($h \sim 0.6$) points to a jagged roughness profile with relatively long-distance repetition in the lateral direction. The difference in the fractal dimension of interfaces in Samples 1 and 2 can probably be attributed to the initial morphology of the respective substrate's surface. This fact along with the different primary substrate roughnesses, 0.4 and 1 nm for Samples 1 and 2, respectively, causes the discrepancy in the replication character of interface profiles in the vertical direction. Contrary to strongly conformal profiles within Sample 1 ($\xi_z \simeq 50\,\text{nm}$), vertical correlation of roughness in Sample 2 is found to be $\xi_z \simeq 5.5\,\text{nm}$, which only slightly exceeds the approximate distance between interfaces.

5.4 Grazing-Incidence Small Angle X-Ray Scattering

The general scattering theory presented in the Sect. 2.1 affirms that the comprehensive information on the investigated by X-rays sample is contained in the distribution of scattered X-ray intensity in three-dimensional reciprocal space defined by three

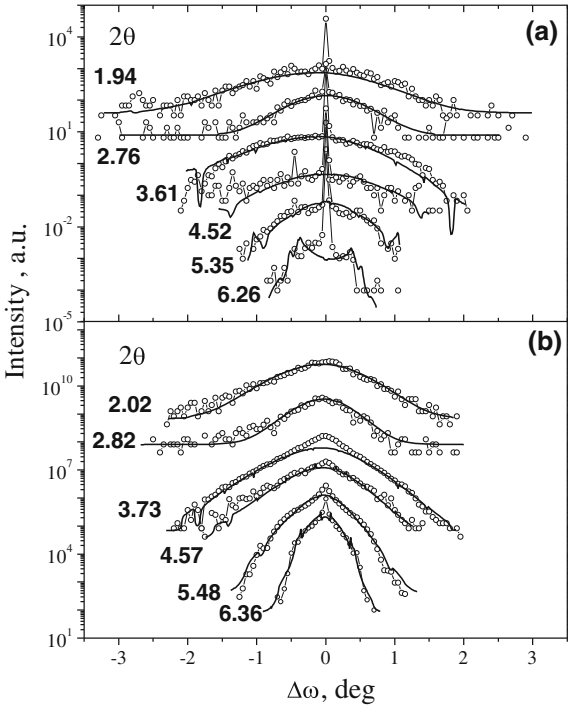

Fig. 5.15 $\omega/2\theta$-scans from Sample 1 (**a**) and 2 (**b**) for different fixed values of 2θ. The theoretical data are given by *solid lines* and experiment is represented by *open circles*. The numbers mean the 2θ values and the *curves* at different 2θ offsets are rescaled for clarity

components of wave vector transfer $\boldsymbol{Q}$. The specular reflectivity considered in the Sect. 2.1 corresponds to the one-dimensional projection of this space onto the axis Q_z. The resulting X-ray intensity profile contains the information on the distribution of electron density along z-axis. The diffuse X-ray scattering discussed in previous section is a two-dimensional Q_x, Q_z section of the reciprocal space which gives access to the sample characteristics in x, z plane. Finally, the analysis of the three-dimensional landscape of the scattered X-ray intensity delivers the information on the three-dimensional structure of nanoscale objects (size, shape, spatial ordering, etc) located onto or near the surface of the investigated samples.This X-ray technique called grazing-incidence small angle X-ray scattering is widely applied nowadays for investigation of samples with nanoscale patterns on the surface, such as wires, dots, pillars and others. There are many publications dedicated to the theoretical background and experimental results of GISAXS method (see, for example, [27] and citation therein). Therefore, in this section we make a short outline of some peculiarities of GISAXS analysis and simulation within the framework of general scattering theory as well as discuss the accuracy of approximations used for this analysis.

The kinematical variables describing experimental geometry of GISAXS are shown in Fig. 5.16, where $\boldsymbol{k}$ and $\boldsymbol{p}$ define the wave vectors of the incident and the scattered beams, respectively. For GISAXS, the use of two-dimensional detector is

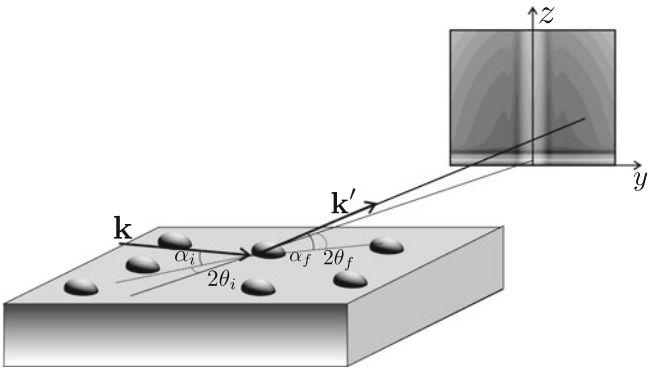

Fig. 5.16 The experimental geometry of GISAXS measurements using two-dimensional detector

very effective for recording of the scattered X-ray intensity. The variables α_i and α_f define the angles of vectors $\boldsymbol{k}$ and $\boldsymbol{p}$ to the sample surface, respectively, and the angles $2\theta_i$ and $2\theta_f$ are the in-plane angles with respect to the normal to the detector plane. The components of the wave vector transfer are then expressed as:

$$\begin{aligned} \boldsymbol{Q} &= \boldsymbol{p} - \boldsymbol{k}; \\ p_z = -k_0 \sin\alpha_f;\ p_y = k_0 \cos\alpha_f \sin 2\theta_f;\ p_x &= k_0 \cos\alpha_f \cos 2\theta_f; \\ k_z = k_0 \sin\alpha_i;\ k_y = k_0 \cos\alpha_i \sin 2\theta_i;\ k_x &= k_0 \cos\alpha_i \cos 2\theta_i. \end{aligned} \tag{5.78}$$

In many cases, the angles are defined with respect to the plane constructed by the incidence beam and the normal, which corresponds to $\theta_i = 0$ and the expression (5.78) is simplified to:

$$\begin{aligned} p_z = -k_0 \sin\alpha_f;\ p_y = k_0 \cos\alpha_f \sin 2\theta_f;\ p_x &= k_0 \cos\alpha_f \cos 2\theta_f; \\ k_z = k_0 \sin\alpha_i;\ k_y = 0;\ k_x &= k_0 \cos\alpha_i; \\ Q_z = k_0(\sin\alpha_i + \sin\alpha_f);\ Q_y &= k_0 \cos\alpha_f \sin 2\theta_f; \\ Q_x &= k_0(\cos\alpha_f \cos 2\theta_f - \cos\alpha_i). \end{aligned} \tag{5.79}$$

The specular reflection corresponds to the angles $\alpha_i = \alpha_f$, $2\theta_i = 2\theta_f$ and its intensity is essentially higher than the diffuse scattering into other directions, and therefore the GISAXS profile is analyzed with the cut out specular spot. In the processes of the scattering from the surfaces, the intensity of the scattered radiation decreases rapidly with the increase of the scattering angles. Thus, the typical observation angles in GISAXS technique are of the order $\sqrt{|\chi|} \sim 10^{-2}\ rad$. The scattering angles can be expressed directly through the detector coordinates (x_d, z_d) and detector-sample distance D:

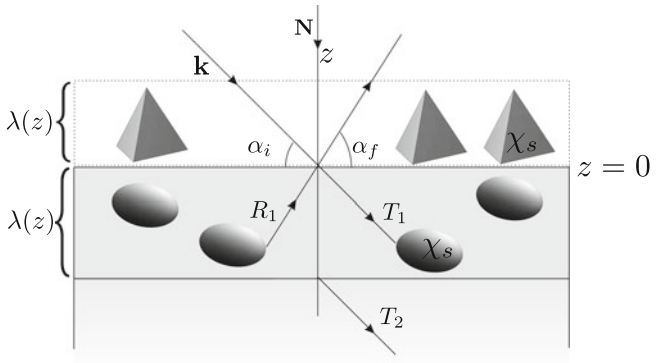

Fig. 5.17 Typical structure of the samples investigated by GISAXS technique. The transition layer may occur both at $z > 0$ (inclusions), and at $z < 0$ (supported islands)

$$\sin\alpha_f = \frac{z_d}{D}; \quad \sin 2\theta_f = \frac{y_d}{\sqrt{D^2 - z_d^2}}. \tag{5.80}$$

The main purpose of GISAXS technique is an investigation of the spatial correlations and the morphology of the compact nano-objects. These objects can be located both on the top of the sample surface and as inclusion in under-surface area (Fig. 5.17). Both these cases are considered on the basis of the same theory implementing the boundary layer with positive and negative coordinates z and with the scattered potential $V_S(\boldsymbol{r})$ different than the substrate potential $V(\boldsymbol{r})$.

For the simulation of X-ray intensity in GISAXS geometry, the statistic approach and DWBA with potential $V_S(\boldsymbol{r})$ are used, similarly to the diffuse X-ray scattering in XRR geometry. As described in the Sect. 2.1, firstly the solutions of the zeroth approximation (5.9) for coherent waves are found, which are defined by the Eqs. (5.48) and (5.49). For GISAXS intensity, the diffuse scattering from the surface roughness is neglected, and the coherent potential is constructed from the potential $V_0(z)$ of the ideally flat substrate with polarizability χ_0 and average potential $\bar{V}_S(z)$ of the transition layer:

$$V_c(z) = V_0(z) + \bar{V}_S(z) \equiv k_0^2\chi_0 H(z) + < V_S(\boldsymbol{r}) >, \tag{5.81}$$

where the scattering potential of objects is averaged both over their shapes and over the positions of their centers on the substrate S.

The majority of works reporting the simulation of GISAXS profiles don't consider the transition layer created by the potential of nano-objects when constructing the zeroth approximation of DWBA. However, the theory of X-ray diffuse scattering (Fig. 5.8) affirms that the re-normalization of the reflection and transmission coefficients in self-consistent approach is of the same order as incoherent part of potential and influences essentially the calculated scattered X-ray intensity. This fact of the importance of transition layer has been emphasized for GISAXS in [28].

To calculate $\bar{V}_S(z)$, the following expression for the scattering potential for N nano-objects is used:

$$V_S(\boldsymbol{r}) = k_0^2 \chi_1 \sum_{n=1}^{N} \Omega(\boldsymbol{r} - \boldsymbol{R}_n);$$
$$\chi_1 = \chi_S, if\ z < 0;\ \chi_1 = \chi_S - \chi_0, if\ z > 0, \tag{5.82}$$

where $\Omega(\boldsymbol{r} - \boldsymbol{R}_n)$ is a dimensionless function defining the size and the shape of the object, located in the position $\boldsymbol{R}_n$. All nano-objects are assumed to be composed of the same material with X-ray polarizability χ_S, and the condition $z < 0$ corresponds to the supported islands and $z > 0$ describes the inclusions within the substrate.

In opposite to diffuse X-ray scattering in XRR, where the integral characteristics of the roughness are modeled, the scattering potential in GISAXS implements the parameters of the function $\Omega(\boldsymbol{r})$ and the coordinates $\boldsymbol{R}_n$ as random values. The spatial shape of nano-objects is modeled by simple geometrical forms (truncated sphere, parallelepiped, tetrahedron, etc), which are selected basing on the results of supplemental studies or growth conditions. In the simulation of GISAXS intensity, the form-factor of the nano-object $F(\boldsymbol{Q})$ is more convenient parameter to fit than the function $\Omega(\boldsymbol{r})$; the former is expressed through the latter as:

$$\Omega(\boldsymbol{r}) = \frac{1}{(2\pi)^3} \int d\boldsymbol{Q} F(\boldsymbol{Q}) e^{i\boldsymbol{Q}\boldsymbol{r}};\ F(\boldsymbol{Q}) = \int d\boldsymbol{r}\, \Omega(\boldsymbol{r}) e^{-i\boldsymbol{Q}\boldsymbol{r}}, \tag{5.83}$$

being justified by the volume v_0 of a nano-object as $F(0) = v_0$. Below we explicitly write the form-factors of truncated pyramid and sphere frequently used as a model of nano-objects shape [27]:

Truncated pyramid with square basis of size $2R$, the height h and inclination angle α:

$$F(\boldsymbol{Q}) = 4 \int_0^h dz \frac{\sin Q_x R_z \sin Q_y R_z}{Q_x Q_y} e^{-iQ_z z};\ R_z = R - \frac{z}{\tan\alpha}. \tag{5.84}$$

Truncated sphere with radius R and height h (here J_1 is a Bessel function):

$$F(\boldsymbol{Q}) = \frac{2\pi e^{iQ_z(h-R)}}{Q_\perp} \int_0^h dz R_z \frac{J_1(Q_\parallel R_z)}{Q_\perp} e^{iQ_z z};$$
$$R_z = \sqrt{R^2 - z^2};\ Q_\parallel = \sqrt{Q_x^2 + Q_y^2}. \tag{5.85}$$

For more examples of nano-object shapes see the review [27]. The parameters of form-factor $\xi_i = (R, h, \alpha, ..)$ are the random values with independent distribution functions $p(\xi_i)$, characterized by the average values $\bar{\xi}$ and dispersions D_ξ. The statistic nature of the potential (5.82) is related to the random positions of the nano-objects. The selection of the distribution function for variable $\boldsymbol{R}_n$ parameterizes the

fitting of GISAXS data, too. For small concentration of nano-objects satisfying the condition for the surface density ρ_S:

$$\rho_S Q_\parallel^2 \approx \rho_S k_0^2 |\chi_0|^2 \ll 1, \tag{5.86}$$

the scattering from each object occurs independently, and therefore the one-particle distribution function $P(\boldsymbol{R}_\perp)$ is only essential.

However, for many of nano-size objects used in modern technology the condition (5.86) is not satisfied, and thus the two-particle distribution function $P_{12}(\boldsymbol{R}_{1\parallel}, \boldsymbol{R}_{2\parallel})$ has to be considered, which is related to the correlation function $g(\boldsymbol{R}_{1\parallel} - \boldsymbol{R}_{2\parallel})$. By the definition [4], the value $\rho_S g(\boldsymbol{R}_\parallel) d\boldsymbol{R}_{2\parallel}$ provides the probability to find the second nano-object near the position $d\boldsymbol{R}_{2\parallel}$ on the distance $\boldsymbol{R}_\parallel$ from the first nano-object. Here, we don't consider the special cases of ordered nano-objects [27] and assume the uniform distribution of objects:

$$P(\boldsymbol{R}_\parallel) d\boldsymbol{R}_\parallel = \frac{d\boldsymbol{R}_\parallel}{S} = const. \tag{5.87}$$

For the correlation function, the models are used which are parametrized by correlation length L_c and oscillation period D_c describing the partial far-distance ordering in the position of nano-objects. The frequently used functions $g(\boldsymbol{R}_\parallel)$ and interference function $S(\boldsymbol{Q}_\parallel)$ are given in [27] as:

1. **Debye hard core model (applied for small density ρ_S)**:

$$\begin{aligned} g(R_\parallel) = 0,\ 0 < R_\parallel < L_c; \quad g(R_\parallel) = 1,\ R_\parallel > L_c; \\ S(\boldsymbol{Q}_\parallel) = 1 + \rho_S \int_S d\boldsymbol{R}_\parallel [g(R_\parallel) - 1] e^{i \boldsymbol{Q}_\parallel R_\parallel} \\ = 1 - 2\pi\rho_S \frac{J_1(Q_\parallel L_c)}{Q_\parallel^2};\ 2\pi\rho_S L_c^2 < 1. \end{aligned} \tag{5.88}$$

2. **Oscillation Zhu model** [29] **(effective for large ρ_S)**:

$$\begin{aligned} g(R_\parallel) = 1 - e^{-R_\parallel / L_C} \cos \frac{2\pi R_\parallel}{D_c}; \\ S(\boldsymbol{Q}_\parallel) = 1 - \frac{\rho_S L_c^2 D_c^2}{2} \left[\frac{D_c - i2\pi L_c}{[(D_c - i2\pi L_c)^2 + L_c^2 D_c^2 Q_\parallel^2]^{3/2}} \right. \\ \left. + \frac{D_c + i2\pi L_c}{[(D_c + i2\pi L_c)^2 + L_c^2 D_c^2 Q_\parallel^2]^{3/2}} \right];\ \rho_S D_c^2 < 1;\ D_c \ll L_c. \end{aligned} \tag{5.89}$$

3. **Paracrystal model** [30] **(applicable for dense position of nano-objects with far-distance ordering)**:

$$S(\boldsymbol{Q}_{\parallel}) = \frac{1-\phi^2(Q_{\parallel})}{1+\phi^2(Q_{\parallel})-2\phi(Q_{\parallel})\cos Q_{\parallel} D_c}; \quad \phi(Q_{\parallel}) = \exp[-\pi Q_{\parallel}^2 L_c^2]. \tag{5.90}$$

In some practical cases, the good fitting results of GISAXS patterns are obtained using the weighted mixture of several models described by different $\Omega_l(\boldsymbol{r})$ and $p_l(\xi_i)$, [27]. The averaging of (5.82) with uniform function (5.87) results in the following scattering potential of the transition layer:

$$\bar{V}_S(z) = k_0^2\chi_1 \sum_{n=1}^{N} P(\boldsymbol{R}_{n\parallel}) \int d\boldsymbol{R}_{n\parallel} < \Omega(\boldsymbol{r}-\boldsymbol{R}_{n\parallel}) > = k_0^2\chi_1\rho_S \int d\boldsymbol{r}_{\parallel} < \Omega(\boldsymbol{r}) >= k_0^2\chi_1\bar{s}_{\parallel}\rho_S\lambda(z), \tag{5.91}$$

where $\bar{s}_{\parallel}$ is an average square of the nano-object's cross-section, and the profile $\lambda(z)$ of the transition layer depends on the type of the nano-object's localization:

$$\lambda(z) = \pm[H(z \pm \bar{h}) - H(z)], \tag{5.92}$$

where signs ($\pm$) refer to the supported islands and the inclusions (Fig. 5.17), and $\bar{h}$ is an average height of the nano-object.

Thus, the solution of the wave equation with potential (5.81) in zeroth DWBA approximation corresponds to the reflection problem from bi-layered structure and is delivered by formulas (5.64) and (5.65):

$$\{\Delta + k_0^2 + V_c(z)\}A(\boldsymbol{r}) = 0;$$
$$\boldsymbol{A}_{\boldsymbol{k}}^{(+)}(\boldsymbol{r}) = e^{i\boldsymbol{k}_{\perp}\boldsymbol{r}_{\perp}}E_k^{(+)}(z); \quad \boldsymbol{A}_{\boldsymbol{p}}^{(-)}(\boldsymbol{r}) = e^{i\boldsymbol{p}_{\perp}\boldsymbol{r}_{\perp}}E_p^{(-)}(z);$$
$$E_k^{(+)}(z) = \sum_{j=0}^{2}[T_j(k_{zj})e^{ik_{zj}z} + R_j(k_{zj})e^{-ik_{zj}z}];$$
$$E_p^{(-*)}(z) = E_{-p}^{(+)}(z) = \sum_{j=0}^{2}[T_j(p_{zj})e^{-ip_{zj}z} + R_j(p_{zj})e^{ip_{zj}z}];$$
$$V_c(z) = k_0^2[\chi_1\bar{s}_{\parallel}\rho_S\lambda(z) + \chi_0 H(z)]. \tag{5.93}$$

To calculate the X-ray scattering cross-section from nano-objects in the first order of DWBA and on the basis of formula (5.24), the only transmission $T_1(k_{z1})$ and reflection $R_1(k_{z1})$ coefficients for transition layer are required:

$$T_1(k_{z1}) = \frac{t_{01}}{B} e^{i(k_{0z}-k_{1z})z_0};\ R_1(k_{z1}) = -\frac{r_{21}t_{21}}{B} e^{i(k_{0z}+k_{1z})z_0} e^{2ik_{1z}\bar{h}};$$
$$B = 1 + r_{10}r_{21}e^{2ik_{1z}\bar{h}};\ t_{jl} = \frac{2k_{jz}}{k_{jz}+k_{lz}};\ r_{jl} = -\frac{k_{jz}-k_{lz}}{k_{jz}+k_{lz}};$$
$$k_{0z} = k_0 \sin\alpha_i;\ k_{1z} = k_0\sqrt{\sin^2\alpha_i + \tilde{\chi}_1};\ k_{2z} = k_0\sqrt{\sin^2\alpha_i + \chi_0},$$
$$p_{0z} = -k_0 \sin\alpha_f;\ p_{1z} = -k_0\sqrt{\sin^2\alpha_f + \tilde{\chi}_1};\ p_{2z} = -k_0\sqrt{\sin^2\alpha_f + \chi_0} \quad (5.94)$$

with $z_0 = -\bar{h}$; $\tilde{\chi}_1 = \chi_S \bar{s}_\parallel \rho_S$ corresponding to supported islands and $z_0 = 0$; $\tilde{\chi}_1 = (\chi_S - \chi_0)\bar{s}_\parallel \rho_S + \chi_0$ to the inclusions. The parameter $\bar{s}_\parallel \rho_S = \Pi_S$ defines the portion of the sample surface occupied by nano-objects, and thus Π_S is a "porosity" of the layer filling.

The specular rod at $\boldsymbol{Q}_\parallel = \boldsymbol{p}_\parallel - \boldsymbol{k}_\parallel \approx 0$ is determined by the squared modulus of the reflection coefficient $R_0(k_{0z})$:

$$R_0(k_{0z}) = \frac{[r_{10} + r_{21}e^{2ik_{1z}\bar{h}}]}{B} e^{2ik_{0z}z_0}. \quad (5.95)$$

In real GISAXS experiments, however, the detector is protected from intense specular beam by beam stopper [27] to avoid the distortion of X-ray pattern at non-specular angles.

The GISAXS pattern at $\boldsymbol{p}_\parallel \neq \boldsymbol{k}_\parallel$ is found from formula (5.24) for X-ray intensity cross-section resulted from the matrix element (5.93) and potential (5.82) ($p_{zj} < 0$):

$$\frac{d\sigma_G(\boldsymbol{p},\boldsymbol{k})}{d\Omega_{\boldsymbol{p}}} = \frac{k_0^4|\chi_1|^2}{(4\pi)^2}|\sum_j M_j(\boldsymbol{Q}_\parallel, k_z, p_z)e^{i\boldsymbol{Q}_\parallel \boldsymbol{R}_{j\parallel}}|^2;$$
$$M_j(\boldsymbol{Q}_\parallel, k_z, p_z) = T_1(k_{z1})T_1(p_{z1})F(\boldsymbol{Q}_\parallel, k_z - p_z)$$
$$+T_1(k_{z1})R_1(p_{z1})F(\boldsymbol{Q}_\parallel, k_z + p_z) + R_1(k_{z1})T_1(p_{z1})F(\boldsymbol{Q}_\parallel, -k_z - p_z)$$
$$+R_1(k_{z1})R_1(p_{z1})F(\boldsymbol{Q}_\parallel, -k_z + p_z), \quad (5.96)$$

where $F(\boldsymbol{Q}_\parallel, Q_z)$ is a form-factor as in (5.83) for the selected model of nano-object.

Using the statistical approach, this cross-section has to be averaged both over the shape parameters of nano-object with distribution $p(\xi_i)$ and over the position $\boldsymbol{R}_{j\parallel}$ with correlation function $g(\boldsymbol{R}_\parallel)$. By utilizing the relations for averaged values [4], the GISAXS intensity is written as [27]:

$$< \frac{d\sigma_G(\boldsymbol{p},\boldsymbol{k})}{d\Omega_{\boldsymbol{p}}} >= \frac{k_0^4|\chi_1|^2 N}{(4\pi)^2}[< |M(\boldsymbol{Q}_\parallel, k_z, p_z)|^2 >$$
$$-| < M(\boldsymbol{Q}_\parallel, k_z, p_z) > |^2 + | < M(\boldsymbol{Q}_\parallel, k_z, p_z) > |^2 S(\boldsymbol{Q}_\parallel)], \quad (5.97)$$

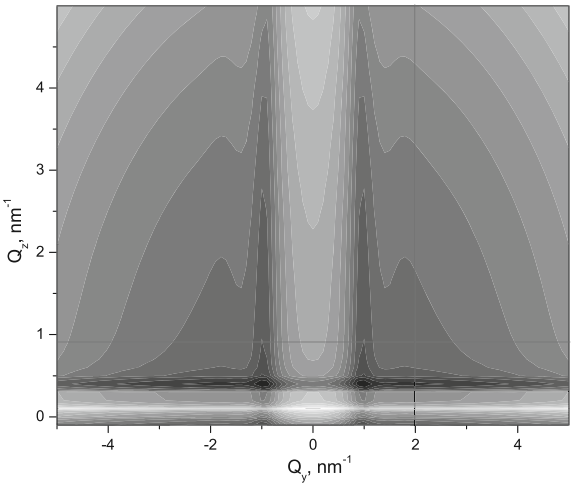

Fig. 5.18 GISAXS pattern in (Q_z, Q_y) coordinates for the sample consisting of Pt balls ($\chi_S = -1.04 \cdot 10^{-4} + i1.02 \cdot 10^{-5}$) located on MgO substrate ($\chi_0 = -2.3 \cdot 10^{-5} + i2.44 \cdot 10^{-7}$). The model parameters are: $\bar{R} = 0.5\,\text{nm}$; $\sigma_R = 0.03\,\text{nm}$; $D_c = 2\Pi\,\text{nm}$; $L_c = 0.1 \cdot D_c$; $\Pi = 0.5$; $\rho_S = 8\,\text{nm}^{-2}$

where the brackets $< .. >$ mean the averaging over the parameters of the shape; the interference function is defined by Eq. (5.89); the term proportional to $\delta(\boldsymbol{Q}_\parallel)$ is already included in specular reflection coefficient (5.95).

The expression (5.96) and (5.97) permit to simulate GISAXS intensity as two-dimensional pattern or one-dimensional profiles, corresponding to different scans in a real space. The statistical characteristics of all nano-objects are modeled by the same distribution function, i.e. the mono-disperse approximation is used. Figure 5.18 shows the typical GISAXS pattern from the sample described in the caption. The quantitative values of the sample parameters can be evaluated from the fitting of the selected sections of GISAXS pattern to the measured data. The examples of such sections are shown in Fig. 5.19.

Even without accurate data fitting, the estimate for the physical sample parameters can be obtained from the peak position on the presented profiles. The most intense peaks are the Yoneda wings described in previous sections. From these peaks the following parameters can be identified: (i) **the oscillation period of the correlation function** $\bar{D} \approx \frac{2\pi}{Q_y}$ is determined from the peaks at $Q_y \approx 1\,\text{nm}^{-1}$; (ii) **the correlation length** $\bar{L} \approx \frac{1}{\Delta_2}$, where Δ_2 is a half-width of the Yoneda peak. Finally, (iii) **the average geometrical size of the nano-object** $\bar{R} \approx \frac{1}{\Delta_1}$, where Δ_1 is a half width at full maximum of the highest peak on Q_z-scan, is determined, too. The review [27] describes the multiple models for GISAXS evaluation with high accuracy, and the reader is referred to this work for further details.

Here we provide two practical applications of GISAXS technique for investigation of nano-scale objects used in modern technologies [31]: Fe_2O_3 nano-particles and

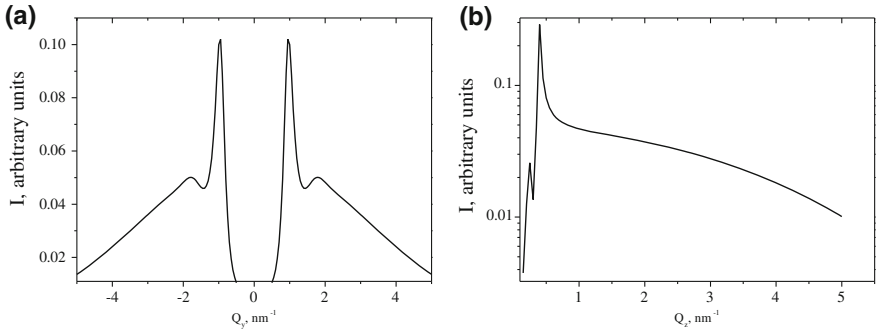

Fig. 5.19 **a** Q_y-scan at $Q_z = 0.8\,\mathrm{nm}^{-1}$ and **b** Q_z-scan at $Q_y = 2.0\,\mathrm{nm}^{-1}$ for the sample described in Fig. 5.18

Si nano-pattern (dots). The self-assembled iron oxide nano-particles synthesized by a high-temperature solution phase reaction and the silicon dots produced by an ion bombardment have been investigated by using atomic force microscopy and grazing-incidence small-angle scattering technique. Both methods delivered the consistent results on the estimate for the particle size and shape and primary knowledge on the ordering of the objects. A distorted-wave Born approximation approach has been used for X-ray data fitting. In the case of the silicon dots, the dense long-range particle distribution over the whole sample surface is found, whereas FeO nano-particles exhibit the short-range correlations. Both results are consistent with the local AFM investigations (see details in [31]).

The Fig. 5.20 shows the AFM phase image from FeO nano-particles. The images display relatively uniform distribution of the objects with the certain amount of gaps not filled by the particles. The X-ray measurements in grazing-incidence geometry (Fig. 5.21a) show the side wings revealing the characteristic lateral ordering presenting in the sample. Using the information obtained from the AFM studies, i.e. close

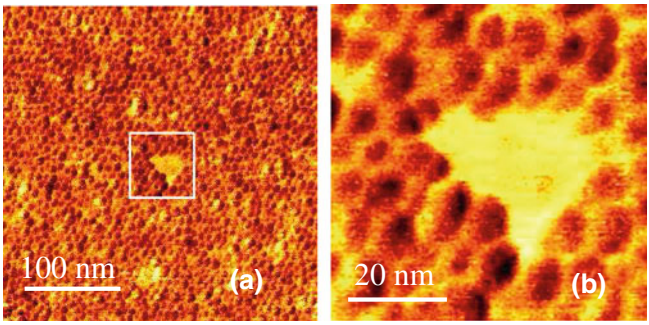

Fig. 5.20 AFM images of FeO nano-particles: **a** phase forward scan overlayed with the topography scale, **b** zoomed area around the gap on the *left panel*

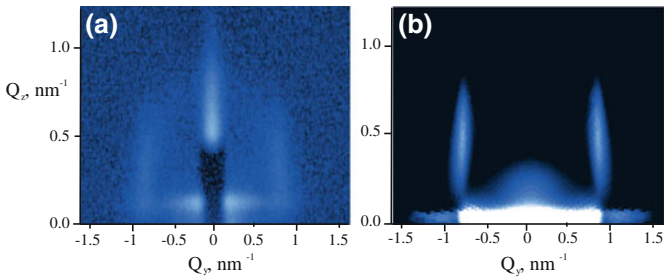

Fig. 5.21 GISAXS reciprocal space map from FeO nanoparticles on Si substrate (**a**) measured and (**b**) simulated by DWBA at incidence angle 0.36°

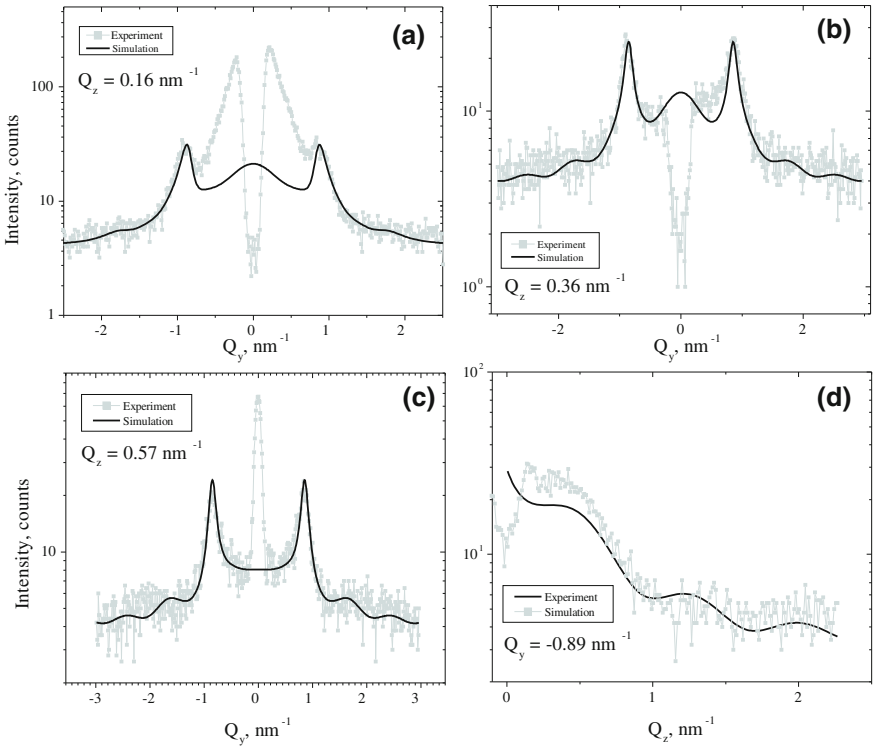

Fig. 5.22 Selected Q_z and Q_y sections of measured GISAXS reciprocal space map fitted by the sample model described in the text. In the typical fitting procedure, up to the 10 sections have been involved

packing structure of the particles and assuming the electron density of the particles and substrate are known, the Q_y-elongated peak below the side wings points to the value of the particle's diameter. For the measured at the incidence angle 0.36° X-ray data presented in Fig. 5.21a, several Q_z and Q_y sections (Fig. 5.22) have been fitted

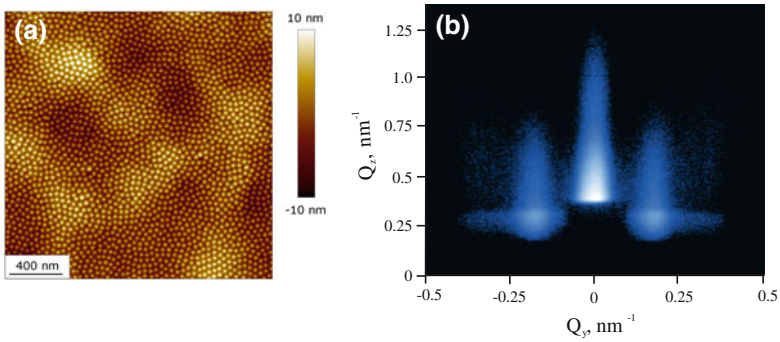

Fig. 5.23 **a** AFM image of silicon nano-dots; **b** GISAXS reciprocal space map from Si *nano-dots* measured at incidence angle 0.22°

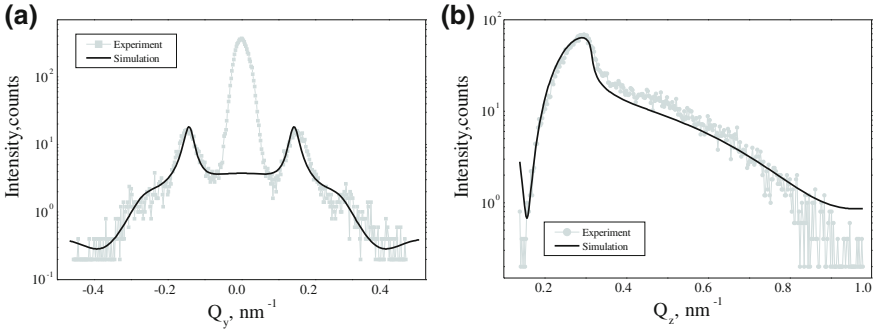

Fig. 5.24 Selected experimental (*dots*) and fitted (*solid lines*) sections extracted from the reciprocal space map on Fig. 5.23

on the basis of a single sample model and joint cost function by using a least-square minimizing algorithm and varying the following sample parameters: particle radius value r, its root mean square σ, and lateral correlation length Λ. The good fits were obtained when using the uniform parameter distribution and spherical shape of the objects. The radius of nano-particles $r = 3.0 \pm 3.1$ nm found from the data fitting correlates well with independently fitted value of the correlation period $\Lambda = 7.3$ nm and with the value estimated from AFM investigations. The model of the uniform (not gaussian) radius distribution ascribes the large dispersion of parameter, assuming the equal probability for all values in the limited interval. The full reciprocal space map simulation of GISAXS scattering from the sample with fitted parameters (Fig. 5.21b) replicates all the qualitative features presented on the experimental map.

The AFM studies of silicon nano-dots (Fig. 5.23a) demonstrate an evident paracrystalline structure, for which X-ray investigation methods fit best of all. The GISAXS reciprocal space map (Fig. 5.23b) measured at incidence angle 0.22° shows satellite maxima extended along Q_z direction. The best fit has been obtained using paracrystal model for cylindrically shaped nano-dots. The radius and the height of the cylinders

are found to be $r = 9.4 \pm 2.2\,\text{nm}$ and $h = 8.3 \pm 0.8\,\text{nm}$, respectively; the correlation length $\Lambda = 41.5\,\text{nm}$ estimates the size of the domain, where particles position correlates in the long-range order, and the correlation period $D = 10.2\,\text{nm}$ gives an average distance between the centers of the dots. As in the case of FeO nanoparticles, the set of the Q_z and Q_y sections (Fig. 5.24) of the reciprocal space map have been fitted simultaneously on the basis of the unique sample model and common cost function. The results obtained for the particles parameters confirm the values received from the AFM studies, however, deliver more detailed information on the particle's shape and correlation averaged over the large sample area.

References

1. M.A. Krivoglaz, *X-Ray and Neutron Diffraction in Nonideal Crystals* (Springer, Berlin, 1996)
2. A.M. Afanas'ev, P.A. Aleksandrov, R.M. Imamov, *X-ray Diagnostics of Sub-milimeter Layers* (Nauka, Moscow, 1989). (in russian)
3. P. Walters, *An Introduction to Ergodic Theory* (Springer, New York, 1982)
4. L.D. Landau, E.M. Lifshitz, *Statistical Physics*, 2nd edn. (Pergamon Press, Oxford, 1984)
5. M.L. Goldberger, K.M. Watson, *Collision Theory* (Wiley, New York, 1964)
6. V.G. Baryshevsky, *High-Energy Nuclear Optics of Polarized Particles* (World Scientific, Singapore, 2012)
7. R.J.Glauber, *Lectures in Theoretical Physics*, eds. by W. Brittin, L. Dunham (Interscience Publishers, New York, 1959)
8. N.Kato, Acta. Cryst. **A36**, 763 (1980); **A36**, 770 (1980)
9. K.M. Pavlov, V.I. Punegov, Acta. Cryst. **A56**, 227 (2000); YA.I. Nesterets, V.I. Punegov, Acta. Cryst. **A56**, 540 (2000)
10. I.D. Feranchuk, S.I. Feranchuk, A.P. Ulyanenkov, Phys. Rev. B **75**, 085414 (2007); F. Chukhovskii, Acta Cryst. **A67**, 200 (2011)
11. I.D. Feranchuk, L.I. Komarov, I.V. Nichipor, A.P. Ulyanenkov, Ann. Phy. NY **238**, 370 (1995)
12. A.I. Akhiezer, V.B. Berestetsky, *Quantum Electrodynamics* (Nauka, Moscow, 1969)
13. V. Holý, K.T. Gabrielyan, Phys. Stat. Sol. B **140**, 39 (1987)
14. L.D. Landau, E.M. Lifshitz, *Electrodynamics of Condensed Matter*, 2nd edn. (Nauka, Moscow, 1982). (in russian)
15. S.K. Sinha, E.B. Sirota, S. Garoff, H.B. Stanley, Phys. Rev. B **38**, 2297 (1988)
16. D.K.G. de Boer, Phys. Rev. B **49**, 5817 (1994)
17. M. Tolan, *X-ray Scattering from Soft-Matter Thin Films* (Springer, Berlin, 1999)
18. V. Holý, C. Gianini, L. Tapfer, T. Marschner, W. Stolz, Phys. Rev. B **55**, 9960 (1997)
19. U. Pietsch, V. Holy, T. Baumbach, *High-Resolution X-ray Scattering: From Thin Films to Lateral Nanostuctures*, 2nd edn. (Springer, Berlin, 2004)
20. Y. Yoneda, Phys. Rev. **131**, 2010 (1963)
21. V. Holý, T. Baumbach, Phys. Rev. B **49**, 10668 (1994)
22. D.K.G. de Boer, Phys. Rev. B **51**, 5297 (1995)
23. A. Ulyanenkov, K. Omote, R. Matsuo, J. Harada, S-Y. Matsuno. J. Phys. D Appl. Phys. **32**, 1313 (1999)
24. J.-P. Schlomka, M. Tolan, L. Schwalowsky, O.H. Seeck, J. Stettner, W. Press, Phys. Rev. B **51**, 2311 (1995)
25. M. Schmidbauer, *X-Ray Diffuse Scattering from Self-Organized Mesoscopic Semiconductor Structures* (Springer, Berlin, 2004)
26. A. Ulyanenkov, R. Matsuo, K. Omote, K. Inaba, J. Harada, M. Ishino, M. Nishii, O. Yoda, J. Appl. Phys. **87**, 7255 (2000)

27. G. Renaud, R. Lazzari, F. Leroy, Surf. Sci. Rep. **64**, 255 (2009)
28. G. Renaud, R. Lazzari, F. Leroy, Phys. Rev. B **76**, 125411 (2007)
29. P.W. Zhu, J.W. White, J. Chem. Phys. **22**, 9169 (1996)
30. R. Hosemann, S.N. Bagchi, *Direct Analysis of Diffraction by Matter* (North-Holland Publishing, Amsterdam, 1962)
31. A. Ulyanenkov, J. Chrost, P. Siffalovic, L. Chitu, E. Majkova, K. Erlacher, H. Guerault, G. Maier, M. Cornejo, B. Ziberi, F. Frost, Phys. Status Solidi A **208**, 2619 (2011)

Chapter 6
X-Ray Diffraction from Crystals with Defects

In the Chap. 4, the X-ray diffraction from perfect crystals has been considered in details, however, the real crystals always posses the defects. The distribution of the diffracted X-ray radiation depends on the type of the defects and their concentration, which is manifested as: (1) attenuation of coherent scattering potential $\chi_{\boldsymbol{H}}$ due to static Debye-Waller factor, and as a result, the diminution of the diffracted intensity calculated by formulas in Chap. 4. This intensity is called further coherent because of it is formed by the diffraction on the crystallographic lattice and is not sensitive to microstructure. Being formed by a whole volume of the diffracted sample, the coherent intensity shows up as sharp peaks similar to delta-functions (4.14); (2) additional broad component of X-ray intensity called diffuse scattering. In opposite to coherent component, the distribution of diffuse X-ray scattering is determined by the defects type, in particular by the displacement field created by defects.

The diffuse X-ray scattering from defects is proportional to Fourier transform of strain fields created by the defects. The strongly localized strain fields caused by point defects result in a broad distribution of diffuse scattering and diminish weakly the coherent intensity. In opposite, the extensive defects like dislocation lines, which have slowly decreasing strain fields and distort the crystallographic order in large area, result in diffuse intensity concentrated near reciprocal lattice point and diminish essentially the coherent peaks. The two-dimensional defects (stacking faults) substantially re-distribute the diffracted intensity and require a special consideration.

In this chapter, the incident X-ray beam is assumed to illuminate a large gauge volume, and the resulting X-ray diffraction intensity originates from the interaction of X-rays with a big statistical ensemble of atoms, which undergo the influence of defects. There is no need in intense X-ray sources for investigation of such systems, and laboratory equipment is used effectively for studies, however, the results obtained deliver the statistically averaged characteristics of the defect ensembles. By using highly intense X-ray beams in synchrotrons or XFELs, the strain field of particular objects without averaging can be investigated (coherent X-ray diffraction [1], high-resolution 3D X-ray diffraction [2]). There is also an alternative approach to the analytical one described in this chapter, which utilized the numerical modeling of

A. Benediktovitch et al., *Theoretical Concepts of X-Ray Nanoscale Analysis*,
Springer Series in Materials Science 183, DOI: 10.1007/978-3-642-38177-5_6,

the statistical systems on the basis of Monte-Carlo method [3, 4]. In the most cases, the results obtained by the analytical statistical methods are valid and confirmed experimentally on microscopic level.

6.1 X-Ray Polarizability of Crystal with Defects

The distortion of crystallographic structure caused by defects is described using the displacement fields created by these defects. Being periodic in the absence of defects, the origin of the crystallographic unit cell makes a shift from the initial state $\boldsymbol{n} = l_1\boldsymbol{a} + l_2\boldsymbol{b} + l_3\boldsymbol{c};\ l_i = 0, \pm 1, \pm 2, \ldots$, to the point $\boldsymbol{n} + \boldsymbol{u}(\boldsymbol{n})$ in the presence of defects, where $\boldsymbol{u}(\boldsymbol{n})$ is a total displacement field of all defects.

The displacement field of a defect is defined by the equations of microscopic elasticity theory [5]. The solutions of these equations are found either analytically [6] or by using a finite elements method. For the macroscopic approach, the displacement fields are supposed to be small and slowly changeable within the elasticity limits. In the case of large deformations of crystallographic lattice, the calculations based on the molecular potentials and quantum mechanics methods are necessary. The contribution of the domains with large deformations into X-ray diffraction is small indeed, because of the disordered area with weak correlations between atomic positions does not contribute to the diffraction signal. Thus, the macroscopic elastic theory is suitable for calculation of the displacement fields investigated by X-ray diffraction. Using this approximation, the wave function of electrons in the distorted crystal is assumed to be periodic with the correction for deformation, and deviates from the one for perfect crystal (1.49) by the vector $\boldsymbol{u}(\boldsymbol{n})$:

$$\psi_{\alpha,\boldsymbol{\kappa}}(\boldsymbol{r} + \boldsymbol{n} + \boldsymbol{u}(\boldsymbol{n})) = e^{i\boldsymbol{\kappa}\boldsymbol{n}}\psi_{\alpha,\boldsymbol{\kappa}}(\boldsymbol{r}), \tag{6.1}$$

and the expression for current (1.42) will be modified, too. The periodicity of wave function (1.49) leads to the expansion of X-ray polarizability $\chi_{\mu,\lambda}(\boldsymbol{k}, \omega)(\boldsymbol{r})$ into a sum over the vectors of reciprocal lattice $\sum_{\boldsymbol{H}} e^{i\boldsymbol{H}\boldsymbol{r}}\chi_{\mu,\lambda}(\boldsymbol{k}, \boldsymbol{H}, \omega)$ and makes possible a direct transition to Fourier representation (1.57). In the presence of displacement fields, the additional multiplier appears, which varies slowly with variation of coordinate $\boldsymbol{r}$. Here we return back to coordinate representation (1.36) and consider a first term in (1.36):

$$J_\mu(r, \omega)^{(e)} =$$

$$-r_0 c \sum_j^{N_e} \sum_l^{N_e} \int d\boldsymbol{r}' < \Psi_0 | \delta(\boldsymbol{r} - \boldsymbol{r}_j)\delta(\boldsymbol{r}' - \boldsymbol{r}_l)\delta_{jl}\delta_{\mu\lambda}A_\lambda(\boldsymbol{r}', \omega)|\Psi_0 > =$$

$$-r_0 c A_\mu(\boldsymbol{r}, \omega) \sum_{\boldsymbol{n}} \sum_{\alpha,\boldsymbol{\kappa}}^{occ} \frac{1}{N} g_{\alpha,\boldsymbol{\kappa}} |\tilde{\psi}_{\alpha,\boldsymbol{\kappa}}(\boldsymbol{r} - \boldsymbol{n} + \boldsymbol{u}(\boldsymbol{n}))|^2 \tag{6.2}$$

The value $\sum_{\boldsymbol{n}} \sum_{\alpha,\boldsymbol{\kappa}}^{occ} \frac{1}{N} g_{\alpha,\boldsymbol{\kappa}} |\tilde{\psi}_{\alpha,\boldsymbol{\kappa}}(\boldsymbol{r} - \boldsymbol{n} + \boldsymbol{u}(\boldsymbol{n}))|^2$ is an electron density of the crystal $\sum_{\boldsymbol{n}} \frac{1}{N} \tilde{\rho}(\boldsymbol{r} - \boldsymbol{n} + \boldsymbol{u}(\boldsymbol{n}))$, where $\tilde{\rho}(\boldsymbol{r})$ is an electron density distribution inside a crystallographic unit cell. To sum up over $\boldsymbol{n}$ in (6.2), the Poisson summation formula is used:

$$\begin{aligned} \sum_{\boldsymbol{n}} \tilde{\rho}(\boldsymbol{r} - \boldsymbol{n} - \boldsymbol{u}(\boldsymbol{n})) &= \sum_{\boldsymbol{n}} \int d^3 \boldsymbol{Q} e^{-i \boldsymbol{Q} \boldsymbol{r}} \int d^3 \boldsymbol{r}' \rho(\boldsymbol{r}' - \boldsymbol{n} - \boldsymbol{u}(\boldsymbol{n})) e^{i \boldsymbol{Q} \boldsymbol{r}'} \\ &= \sum_{\boldsymbol{n}} \int d^3 \boldsymbol{Q} e^{-i \boldsymbol{Q}(\boldsymbol{r} - \boldsymbol{n} - \boldsymbol{u}(\boldsymbol{n}))} F(\boldsymbol{Q}), \end{aligned} \tag{6.3}$$

and the definition (1.49) has been applied. Assuming a small variation of the displacement fields inside unit cell and small deformations $|\boldsymbol{n}| \gg |\boldsymbol{u}(\boldsymbol{n})|$, the approximate expression $\boldsymbol{u}(\boldsymbol{n}) \approx \boldsymbol{u}(\boldsymbol{r})$ is used in further calculations. By utilizing (1.47), the X-ray polarizability for the elastic scattering in deformed crystal $\chi_{\boldsymbol{H}}^{(e),\mathrm{def}}$ differs from the one for ideal crystal $\chi_{\boldsymbol{H}}^{(e),\mathrm{id}}$ by multiplier $e^{i \boldsymbol{H} \boldsymbol{u}(\boldsymbol{r})}$. For the part of X-ray polarizability related to the anomalous dispersion, the use of (1.55) and (6.1) results in:

$$\chi^{\mathrm{def}}(\boldsymbol{r}) = \sum_{\boldsymbol{H}} e^{i \boldsymbol{H} \boldsymbol{u}(\boldsymbol{r})} \chi_{\boldsymbol{H}}^{\mathrm{id}} e^{-i \boldsymbol{H} \boldsymbol{r}}. \tag{6.4}$$

To numerically calculate X-ray polarizability using (6.4), the distribution of the displacement fields $\boldsymbol{u}(\boldsymbol{r})$ created by all crystal defects has to be known. Within the framework of linear elasticity theory, the displacement field of a single defect doesn't depend on the presence of other defects, and total displacement is defined by the superposition of all displacements:

$$\boldsymbol{u}(\boldsymbol{r}) = \sum_{\alpha,t} u_{\alpha}(\boldsymbol{r}; \boldsymbol{n}_{t,\alpha}), \tag{6.5}$$

where the summation is performed over all defects types α, located in the nodes $\boldsymbol{n}_{t,\alpha}$. As introduced in [7] by Krivoglaz, we use the random values $c_{\boldsymbol{n}}$, describing the defects in atomic positions $\boldsymbol{n}$:

$$c_{\boldsymbol{n}} = \begin{matrix} 1 & \text{defect is at site } \boldsymbol{n} \\ 0 & \text{defect is not at site } \boldsymbol{n}. \end{matrix} \tag{6.6}$$

The knowledge of the distribution of these values defines the statistical properties of the defects and permits to calculate the average values of any physical parameter depending on defects. In general case, the values $c_{\boldsymbol{n}}$ and $c_{\boldsymbol{n}'}$ are inter-dependent, which happens when the positions of the defects are correlated. However, first of all we calculate the X-ray intensities in the assumption of non-correlated defects, viz. supposing all the defects are of the same type and distributed uniformly. The distribution function in this case is conditioned by the probabilities depending on a single parameter c, which has a meaning of the probability of the defect to be found in the atomic position:

$$P(c_{\boldsymbol{n}} = 1) = c, \tag{6.7}$$

$$P(c_{\boldsymbol{n}} = 0) = 1 - c. \tag{6.8}$$

The propagation of X-rays in a crystal with defects depends on the following parameters: (1) the average polarizability, which includes the Debye-Waller factor $\langle e^{i\boldsymbol{H}\boldsymbol{u}(\boldsymbol{r})}\rangle$, and (2) average correlation function $g(\boldsymbol{r}, \boldsymbol{r}')$, which is $g(\boldsymbol{r}, \boldsymbol{r}') = \langle e^{i\boldsymbol{H}(u(\boldsymbol{r})-u(\boldsymbol{r}'))}\rangle$.

The averaging procedure [7] by using (6.7) and (6.5) results in

$$\left\langle e^{i\sum_{\boldsymbol{n}} c_{\boldsymbol{n}} s(\boldsymbol{n})_{\boldsymbol{r}}}\right\rangle = \left\langle \prod_{\boldsymbol{n}} e^{ic_{\boldsymbol{n}} s(\boldsymbol{n})_{\boldsymbol{r}}}\right\rangle = \prod_{\boldsymbol{n}} \left\langle e^{ic_{\boldsymbol{n}} s(\boldsymbol{n})_{\boldsymbol{r}}}\right\rangle$$
$$= \prod_{\boldsymbol{n}} (ce^{is(\boldsymbol{n})_{\boldsymbol{r}}} + (1-c)\cdot 1) = e^{\sum_{\boldsymbol{n}} \ln[1+c(e^{is(\boldsymbol{n})_{\boldsymbol{r}}}-1)]} \tag{6.9}$$

where $s(\boldsymbol{n})_{\boldsymbol{r}}$ is equal to $\boldsymbol{H}\boldsymbol{u}(\boldsymbol{r}; \boldsymbol{n})$ for Debye-Waller factor and to $\boldsymbol{H}(\boldsymbol{u}(\boldsymbol{r}; \boldsymbol{n}) - \boldsymbol{u}(\boldsymbol{r}'; \boldsymbol{n}))$ for correlation function. In Eq. (6.9), the assumption of non-correlating defects has been used, which allows the averaging of each multiplier $e^{ic_{\boldsymbol{n}} s(\boldsymbol{n})_{\boldsymbol{r}}}$ in the product $\prod_{\boldsymbol{n}}$ separately. There is another assumption of the smallness of c, which is always valid because of the displacement fields created by defects are considered as a perturbation with respect to the perfect crystallographic structure. Using this fact, the approximate expression can be used:

$$\langle e^{is(\boldsymbol{n})}\rangle \approx e^{\sum_{\boldsymbol{n}} c(e^{is(\boldsymbol{n})}-1)}. \tag{6.10}$$

By changing to the continuous integration limits and using $\rho = c/\Omega$:

$$\langle e^{i\boldsymbol{H}\boldsymbol{u}(\boldsymbol{r})}\rangle = e^{\int d^3\boldsymbol{r}'\rho(e^{i\boldsymbol{H}\boldsymbol{u}(\boldsymbol{r};\boldsymbol{r}')}-1)}$$
$$\langle e^{i\boldsymbol{H}(\boldsymbol{u}(\boldsymbol{r}_1)-\boldsymbol{u}(\boldsymbol{r}_2))}\rangle = e^{\int d^3\boldsymbol{r}'\rho(e^{i\boldsymbol{H}(\boldsymbol{u}(\boldsymbol{r}_1;\boldsymbol{r}')-\boldsymbol{u}(\boldsymbol{r}_2;\boldsymbol{r}')}-1)}. \tag{6.11}$$

Because of the value $\boldsymbol{H}\boldsymbol{u}(\boldsymbol{r}; \boldsymbol{r}')$ is small, the integral in (6.11) can be expanded into series, which results for Debye-Waller factor:

$$\langle e^{i\boldsymbol{H}\boldsymbol{u}(\boldsymbol{r})}\rangle \approx e^{i\boldsymbol{H}\langle\boldsymbol{u}(\boldsymbol{r})\rangle} e^{-\frac{1}{2}\langle(\boldsymbol{H}\boldsymbol{u}(\boldsymbol{r}))^2\rangle}, \tag{6.12}$$
$$\langle\boldsymbol{u}(\boldsymbol{r})\rangle = \int d^3\boldsymbol{r}'\rho\boldsymbol{u}(\boldsymbol{r}; \boldsymbol{r}'), \quad \langle(\boldsymbol{H}\boldsymbol{u}(\boldsymbol{r}))^2\rangle = \int d^3\boldsymbol{r}'\rho(\boldsymbol{H}\boldsymbol{u}(\boldsymbol{r}; \boldsymbol{r}'))^2.$$

This expression can also be obtained assuming the random nature of the displacement field in the point $\boldsymbol{r}$ with Gaussian normal distribution, which is used in some works [8, 9]. The central limit theorem is used as a basis for this assumption, which states that the random value being a sum of a large number of independent and equally distributed random values has a normal distribution. For the crystal defects this is true if the density of defects is high and the displacement fields attenuate slowly. The displacement field $\boldsymbol{u}(\boldsymbol{r})$ is in reality a the sum of random values $\sum_{\boldsymbol{n}} c_{\boldsymbol{n}}\boldsymbol{u}(\boldsymbol{r}; \boldsymbol{n})$.

Provided the slow attenuation of the displacement fields, the number of terms in this sum contributing to certain position is large enough and the condition of central limit theorem is fulfilled. If the theorem is not applicable or there is a divergence in (6.12), the exact expressions (6.11) have to be used.

The existing correlations between the positions of defects change essentially the pattern of the diffracted X-ray intensity. To calculate the Debye-Waller factor and correlation function in this case, the averaging has to be done:

$$\left\langle \prod_{\boldsymbol{n}} e^{i\boldsymbol{c_n}\boldsymbol{s}(\boldsymbol{n})} \right\rangle \equiv \mathbf{M} \prod_{\boldsymbol{n}} e^{i\boldsymbol{H}\boldsymbol{c_n}\boldsymbol{s}(\boldsymbol{n})}, \tag{6.13}$$

where $\mathbf{M}$ means the mathematical expectation of a random value. Omitting the vector notations in indices and using:

$$e^{c_i s_i} = 1 + c_i \alpha_i, \;\; \alpha_i = (e^{s_i} - 1), \tag{6.14}$$

the expression (6.13) is calculated using the methods developed in [7, 10]:

$$\mathbf{M} e^{\sum_k c_k s_k} = \mathbf{M} \prod_i (1 + c_i \alpha_i). \tag{6.15}$$

To realize numerically the expression (6.15), the following values have to be calculated:

$$\mathbf{M} \sum_{i,j,\ldots k} c_i c_j c_k \ldots \alpha_i \alpha_j \alpha_k \ldots \tag{6.16}$$

which in turn depend on the average values $\mathbf{M} c_i c_j c_k \ldots$. For two-points correlations:

$$\mathbf{M} c_i c_j = \delta_{ij} + c^2 (1 + w_{ij}), \tag{6.17}$$

where the first term stands for coincident nodes i and j, $w_{ij} = w_{|i-j|}$ is a pair correlation function. The coincidence of nodes has to be taken into account in all expressions:

$$\mathbf{M} c_i c_j c_k = \delta_{ijk} \mathbf{M} c_i + \delta_{ij} \mathbf{M}' c_i c_k + \delta_{ik} \mathbf{M}' c_i c_j + \delta_{jk} \mathbf{M}' c_i c_j + \mathbf{M}' c_i c_j c_k, \tag{6.18}$$

where $\mathbf{M}'$ is applicable for random values from different nodes. For the random variable taking a value 0 and 1, the statement $c_i^n = c_i$ is valid. Below we express the multi-lateral correlations through the pair correlations using Kirkwood approximation:

$$M' c_i c_j c_k = c^3 (1 + w_{ij})(1 + w_{ik})(1 + w_{jk}), \tag{6.19}$$

and the expression (6.15) is modified to:

$$\mathbf{M}e^{\sum_k c_k s_k} = \mathbf{M}\prod_i (1 + c_i\alpha_i) = 1 + \sum_i \alpha_i \mathbf{M}c_i + \sum_{i<j} \alpha_i\alpha_j \mathbf{M}' c_i c_j + \sum_{i<j<k} \alpha_i\alpha_j\alpha_k \mathbf{M}' c_i c_j c_k + \ldots \tag{6.20}$$

This series can be represented as cumulant expansion:

$$\begin{aligned}
&\mathbf{M}\prod_i (1 + c_i\alpha_i) = e^{\sum_{n=1}^{\infty} \frac{T_n}{n!}} \\
&T_1 = \sum_i \mathbf{M}c_i\alpha_i \\
&T_2 = \sum_{i\neq j} \alpha_i\alpha_j(\mathbf{M}' c_i c_j - (\mathbf{M}c_i)^2) = \sum_{i\neq j} c^2\alpha_i\alpha_j w_{ij} \\
&T_3 = \sum_{i\neq j\neq k} \alpha_i\alpha_j\alpha_k \mathbf{M}' c_i c_j c_k - 3T_1T_2 - T_1^3 = \sum_{i\neq j\neq k} \alpha_i\alpha_j\alpha_k c^3(3w_{ij}w_{ik} + w_{ij}w_{ik}w_{jk}) \\
&\ldots
\end{aligned} \tag{6.21}$$

where the small magnitude of $\mathbf{M}c_k = c$ and the approximation $\sum_{i_1<i_2\ldots<i_n} \approx \frac{1}{n!}\sum_{i_1\neq i_2\ldots\neq i_n}$ are taken into account. As follows from (6.21), each term corresponds to the correlations between the groups (clusters) consisting of a single (no correlations), two (pair correlation), three and so on defects. Figure 6.1 shows schematically the term T_3, where three diagrams on the left side correspond to the terms $\sum_{i\neq j\neq k} \alpha_i\alpha_j\alpha_j c^3(w_{ij}w_{jk} + w_{jk}w_{ik} + w_{ij}w_{ik})$, and the connection between all three vertices corresponds to $\sum_{i\neq j\neq k} \alpha_i\alpha_j\alpha_j c^3 w_{ij}w_{ik}w_{jk}$.

The connections between two vertices only (three-particle cluster is split into one-particle and two-particle) or non-connected vertices (three-particle cluster is split into three one-particle ones) are taken into consideration in terms T_2 and T_1, i.e. T_3 accounts only non-reducible three-particles connections.

In the same way, the contribution of clusters of higher order into cumulant expansion is found, being represented by a n-times integral. By analogue with the group expansion for non-ideal gas [11] they have to be considered if the correlation function w_{ij} becomes not negligible. In this case the contribution of N-particle cluster (N is a full number of dislocations in a sample) becomes essential.

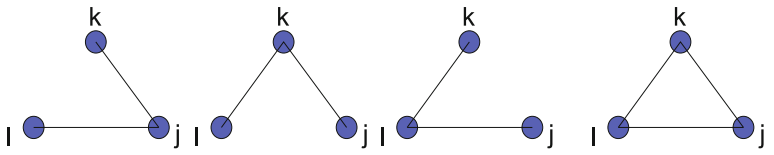

Fig. 6.1 Schematic representation of the connections between defects described by the term T_3 in Eq. (6.21)

6.2 Dynamical X-Ray Diffraction in a Crystal with Defects

The transmission of X-rays in a deformed crystal with defects is determined by the Eqs. (1.41, 1.53, 1.57) and (6.4):

$$\Delta \boldsymbol{A}(\boldsymbol{r}) + \frac{\omega^2}{c^2}(1 + \sum_{\boldsymbol{H}} e^{i\boldsymbol{H}\boldsymbol{u}(\boldsymbol{r})}\chi_{\boldsymbol{H}} e^{-i\boldsymbol{H}\boldsymbol{r}})\boldsymbol{A}(\boldsymbol{r}) = 0, \tag{6.22}$$

where the argument of function ω is omitted and σ-polarization is assumed for simplicity (X-rays are supposed to be monochromatic). Similarly to Chap. 5, the far distance approximation is considered, and two-wave diffraction concept is used, which implements the wave field:

$$\boldsymbol{A}(\boldsymbol{r}) = \boldsymbol{e}_\sigma(A_0(\boldsymbol{r}) + A_H(\boldsymbol{r})e^{i\boldsymbol{H}\boldsymbol{r}}), \tag{6.23}$$

and Eq. (6.22) is split into two differential equations:

$$\begin{aligned}(\Delta + k_0^2(1+\chi_0))A_0(\boldsymbol{r}) + k_0^2 e^{i\boldsymbol{H}\boldsymbol{u}(\boldsymbol{r})}\chi_{\boldsymbol{H}} A_H(\boldsymbol{r}) = 0\\ (\Delta + 2i\boldsymbol{H}\nabla - \boldsymbol{H}^2 + k_0^2(1+\chi_0))A_H(\boldsymbol{r}) + k_0^2 e^{-i\boldsymbol{H}\boldsymbol{u}(\boldsymbol{r})}\chi_{-\boldsymbol{H}} A_0(\boldsymbol{r}) = 0.\end{aligned} \tag{6.24}$$

Both amplitudes $A_0(\boldsymbol{r})$ and $A_H(\boldsymbol{r})$ contain the rapidly oscillating part $e^{i\tilde{\boldsymbol{k}}_{\boldsymbol{0}}\boldsymbol{r}}$, where $\tilde{\boldsymbol{k}}_{\boldsymbol{0}} = -\boldsymbol{N}\gamma_0 + \boldsymbol{k}_{0,||}$ is a wave vector of the incident wave, here we use the notations of Chap. 4 (4.31). Thus, for slowly varying functions $\tilde{A}_0(\boldsymbol{r})$ and $\tilde{A}_H(\boldsymbol{r})$ we obtain:

$$\begin{aligned}(\Delta + 2i\tilde{\boldsymbol{k}}_{\boldsymbol{0}}\nabla)A_0(\boldsymbol{r}) + k_0^2 e^{i\boldsymbol{H}\boldsymbol{u}(\boldsymbol{r})}\chi_{\boldsymbol{H}} A_H(\boldsymbol{r}) = 0\\ (\Delta + 2i\tilde{\boldsymbol{k}}_{\boldsymbol{H}}\nabla + \alpha)A_H(\boldsymbol{r}) + k_0^2 e^{-i\boldsymbol{H}\boldsymbol{u}(\boldsymbol{r})}\chi_{-\boldsymbol{H}} A_0(\boldsymbol{r}) = 0.\end{aligned} \tag{6.25}$$

The reduction of these formulas for the ideal crystal is straightforward: assuming $e^{i\boldsymbol{H}\boldsymbol{u}(\boldsymbol{r})} = 1$ and solutions as $A_0(\boldsymbol{r}) = A_0 e^{i\delta z}$, $A_H(\boldsymbol{r}) = A_H e^{i\delta z}$, we arrive back at (4.41). As discovered in the Chap. 4, for high incidence angles the value δ^2 is negligible in comparison with δ, which corresponds to the neglecting the second derivatives Δ with respect to $\tilde{\boldsymbol{k}}\nabla$. The Eq. (6.25) with omitted Δ are known as Takagi-Taupin [12] equations and widely used for description of X-ray scattering from bent and deformed crystals [13]. For grazing-incidence geometry, however, the second derivatives should be accounted and therefore they are remained in (6.24) to cover also GID case.

The function $e^{i\boldsymbol{H}\boldsymbol{u}(\boldsymbol{r})}$ in (6.24) is a random value, and thus the wave fields in crystal $A_0(\boldsymbol{r})$ and $A_H(\boldsymbol{r})$ are random values, too. The observed quantity is an X-ray intensity $I(\boldsymbol{k}_{in}, \boldsymbol{k}_{out})$ registered by detector in the direction $\boldsymbol{k}_{out}$ and averaged over all defects of a gauge volume. To calculate this intensity, the distribution of two-point correlation function $\langle A_H(\boldsymbol{r}_1)A_H(\boldsymbol{r}_2)^*\rangle$ on the crystal surface should be known [14]. The variable $\langle A_H(\boldsymbol{r}_1)A_H(\boldsymbol{r}_2)^*\rangle$ is called the second statistical moment of the field, and to calculate it at the sample surface, the following requisites have to be found:

(1) an equation describing its evolution inside the crystal, (2) the first moment of the field $\langle A_H(\boldsymbol{r})\rangle$, which is an average (coherent) wave field in crystal. To find both requirements, the method developed in the radiative transfer theory in random media [15] is used here, which represents the Eq. (6.24) in a operator form [14]:

$$\begin{gathered}(L_0 - V)A(\boldsymbol{r}) = 0,\\ L_0 = \begin{pmatrix} \Delta + k_0^2(1+\chi_0) & k_0^2 e^{-W}\chi_{\boldsymbol{H}} \\ k_0^2 e^{-W}\chi_{-\boldsymbol{H}} & \Delta + 2i\boldsymbol{H}\nabla - \boldsymbol{H}^2 + k_0^2(1+\chi_0) \end{pmatrix},\\ V = -\begin{pmatrix} 0 & k_0^2\chi_{\boldsymbol{H}} f(\boldsymbol{r}) \\ k_0^2\chi_{-\boldsymbol{H}} f^*(\boldsymbol{r}) & 0 \end{pmatrix}, \quad A = \begin{pmatrix} A_0(\boldsymbol{r}) \\ A_H(\boldsymbol{r}) \end{pmatrix}\\ e^{-W} = \langle e^{i\boldsymbol{H}\boldsymbol{u}(\boldsymbol{r})}\rangle, \quad f(\boldsymbol{r}) = e^{i\boldsymbol{H}\boldsymbol{u}(\boldsymbol{r})} - e^{-W}, \end{gathered} \tag{6.26}$$

here L_0 is an operator of diffraction from uniform crystal with static Debye-Waller factor e^{-W} in two-wave approximation, V describes the fluctuating scattering properties of the crystal with defects, and $\langle V\rangle = 0$. The expression for evaluation of coherent wave field [15] $\langle A(\boldsymbol{r})\rangle = 0$ is found from:

$$(L_0 - V_{\text{eff}})\langle A(\boldsymbol{r})\rangle = 0, \tag{6.27}$$

which reduces the problem to the finding of effective potential V_{eff}. By comparing the Eqs. (6.26) and (6.27), the effective potential is defined as:

$$\langle V A(\boldsymbol{r})\rangle = V_{\text{eff}}\langle A(\boldsymbol{r})\rangle. \tag{6.28}$$

To find V_{eff}, the field source Q is introduced in the right part of (6.26):

$$A = GQ,\ G = (L_0 - V)^{-1}, \tag{6.29}$$

where G is a Green function of operator $L_0 - V$: $(L_0 - V)_{\boldsymbol{r}} G(\boldsymbol{r}, \boldsymbol{r}') = \delta(\boldsymbol{r} - \boldsymbol{r}')$. By averaging (6.29) and assuming the source Q independent on defects distribution:

$$\langle A\rangle = \langle G\rangle Q. \tag{6.30}$$

In a similar way, from (6.27) follows:

$$\langle A\rangle = (L_0 - V_{\text{eff}})^{-1} Q, \tag{6.31}$$

and comparing (6.30) and (6.31), the operator expression for V_{eff} is finally obtained:

$$V_{\text{eff}} = L_0 - \langle G\rangle^{-1}. \tag{6.32}$$

The equation for coherent wave field (6.27) with effective potential (6.31) is called a Dyson equation, by analogue with the physics of elementary particles, and the effective potential V_{eff} is named a polarization [16] or mass [15] operator.

To make an averaging procedure in (6.32), this expression is expanded in a series over V. For this purpose the operator equalities are used $(AB)^{-1} = B^{-1}A^{-1}$ and $(1+A)^{-1} = \sum_{n=0}^{\infty}(-A)^n$:

$$V_{\text{eff}} = L_0 - \langle G\rangle^{-1} = L_0 - \langle (L_0(1 - G_0V)^{-1}\rangle^{-1} = \langle VG_0V\rangle + \ldots \tag{6.33}$$

here G_0 is a Green function for diffraction operator for averaged crystal and $\langle V\rangle = 0$. The next after $\langle VG_0V\rangle$ terms have an order of V^3 and higher. Generally, the terms with the order higher than two are neglected. If necessary, the diagram technique and cumulant expansion for higher orders can be used [14, 16].

For the correlation function $\Gamma(\boldsymbol{r}_1, \boldsymbol{r}_2) = \langle A(\boldsymbol{r}_1)A(\boldsymbol{r}_2)^*\rangle$, the equations are obtained in a similar manner, i.e. the analogue of (6.26) for non-averaged correlation function is a product of Eq. (6.26):

$$(L_0 - V)_1(L_0 - V)_2^* A(\boldsymbol{r}_1)A^*(\boldsymbol{r}_2) = 0, \tag{6.34}$$

where indices 1 and 2 mean the operator action on the coordinates $\boldsymbol{r}_1$ and $\boldsymbol{r}_2$, respectively. The equation for $\Gamma(\boldsymbol{r}_1, \boldsymbol{r}_2)$ is found in the form:

$$(L_1^{(eff)}L_2^{(eff)*} - K_{12})\Gamma_{1,2} = 0, \tag{6.35}$$

with intensity operator K_{12}, which describes the influence of random deformations on correlation function Γ_{12}, $L^{(eff)} = L_0 - V_{\text{eff}}$. Finally, we obtain for K_{12}:

$$K_{12} = L_1^{(eff)}L_2^{(eff)*} - \langle G_1G_2\rangle^{-1} = L_1^{(eff)}L_2^{(eff)*} - \langle (L_0 - V)_1^{-1}(L_0 - V)_2^{-1}\rangle^{-1} = \langle V_1V_2\rangle + \ldots \tag{6.36}$$

The equation for the correlation function of wave field (6.35) with intensity operator (6.36) is called Bethe-Salpeter equation, by analogue with relativistic quantum mechanics. Similarly to (6.36), the terms in (6.33) with higher than second order of V are neglected, otherwise they can be found by diagram method and cumulant expansion [14, 16].

To calculate the effective potential (6.32) and intensity operator K_{12} (6.36), the Green function $G_0(\boldsymbol{r}, \boldsymbol{r}')_{ij}$ of the operator L_0 has to be known. By the definition, the Green function must satisfy the condition:

$$L_{0ik}^{(\boldsymbol{r})}G_0(\boldsymbol{r}, \boldsymbol{r}')_{kj} = \delta(\boldsymbol{r} - \boldsymbol{r}')\delta_{ij}. \tag{6.37}$$

The definition of Green-function used in this section is slightly different than the one used in [13, 17], where the scalar Green function of the differential equation of the second order is used. This equation is obtained from (6.25) by using Takagi-Taupin

formalism and by excluding the amplitude of the diffracted wave. The wave fields in a crystal are then found based on the Green theorem, which is reduced to the contour integrals containing the magnitudes of the wave fields on the boundaries. In this section, we consider the matrix Green function for the operator L_0. The method proposed here is universal and not based on the Takagi-Taupin approximation.

Let us consider the crystal with the plane surface and introduce a coordinate system with axis z along the inward normal to the surface $z > 0$. The function $G_0(\boldsymbol{r}, \boldsymbol{r}')$ is expanded into in-plane waves:

$$G_0(\boldsymbol{r}, \boldsymbol{r}')_{ij} = \frac{1}{(2\pi)^2} \int_{-\infty}^{\infty} d^2\boldsymbol{k}_{||} e^{i\boldsymbol{k}_0(\boldsymbol{r}-\boldsymbol{r}')} G_{ij}^{(z)}(\boldsymbol{k}_{||})(z, z'), \tag{6.38}$$

where $\boldsymbol{k}_{||}$ lies in the plane XY, $\boldsymbol{k}_0 = \boldsymbol{k}_{||} + \boldsymbol{e}_z\gamma_0$, $\gamma_0 = \sqrt{k_0^2(1+\chi_0(z)) - k_{||}^2}$. Using the definition of δ-function:

$$\frac{1}{(2\pi)^2} \int_{-\infty}^{\infty} d^2\boldsymbol{k}_{||} e^{i\boldsymbol{k}_{||}(\boldsymbol{r}-\boldsymbol{r}')} = \delta(\boldsymbol{r}_{||} - \boldsymbol{r}'_{||}), \tag{6.39}$$

the condition (6.37) is fulfilled only if the equation is satisfied:

$$L_{0ik}^{(z)}(\boldsymbol{k}_{||}) G_{kj}^{(z)}(\boldsymbol{k}_{||})(z, z') = \delta(z - z')\delta_{ij}. \tag{6.40}$$

Here $L_{0ij}^{(z)}(\boldsymbol{k}_{||})$ is an operator resulted from the action of $L_{0ij}^{(\boldsymbol{r})}$ on vector $e^{i\boldsymbol{k}_0\boldsymbol{r}} f_j(z)$:

$$L_{0ij}^{(\boldsymbol{r})} f_j(z) e^{i\boldsymbol{k}_0\boldsymbol{r}} = e^{i\boldsymbol{k}_0\boldsymbol{r}} L_{0ij}^{(z)}(\boldsymbol{k}_{||}) f_j(z). \tag{6.41}$$

Thus, the problem is reduced to the one-dimensional Green function $G_{kj}^{(z)}(\boldsymbol{k}_{||})(z, z')$ and to the integration over $\boldsymbol{k}_{||}$. The mixed representation of the Green function, as a function of the Fourier component $\boldsymbol{k}_{||}$ for in-plane and (z, z') for out-of-plane, fits well for the problems, which have a translational symmetric nature within in-plane direction. For one-dimensional Green function, the operator $L_{0ij}^{(z)}(\boldsymbol{k}_{||})$ can be written as:

$$L_{0ij}^{(z)}(\boldsymbol{k}_{||}) = \begin{pmatrix} \frac{d^2}{dz^2} + 2i\gamma_0 \frac{d}{dz} & k_0^2 e^{-W} \chi_{\boldsymbol{H}} \\ k_0^2 e^{-W} \chi_{-\boldsymbol{H}} & \frac{d^2}{dz^2} + 2i\gamma_h \frac{d}{dz} + \alpha \end{pmatrix}. \tag{6.42}$$

There are several assumptions used below for derivation of Green function. We exclude here the case of grazing incidence/exit and thus neglect the second derivatives $\frac{d^2}{dz^2}$. The operator (6.42) is not self-adjoint in general case because of the imaginary parts in X-ray polarizability $\chi_{\boldsymbol{H}}, \chi_{-\boldsymbol{H}}$. For such operator, the complete system of eigenfunctions consists of the eigenfunctions of this operator and the ones of the adjoint to it operator (6.42) [18]. Neglecting the imaginary part of X-ray polarizability ($k_0^2 e^{-W} \chi_{\boldsymbol{H}} = k_0^2 e^{-W} \chi_{-\boldsymbol{H}} = \chi$) and the refraction effects ($\chi_0 = 0$), the boundary conditions (4.98) become exact. We assume also the crystal to be uniform and semi-infinite, which result in self-adjoint $L_{0ij}^{(z)}(\boldsymbol{k}_{||})$:

$$L_{0ij}^{(z)}(\boldsymbol{k}_{||}) = \begin{pmatrix} 2i\gamma_0 \frac{d}{dz} & \chi H(z) \\ \chi H(z) & 2i\gamma_h \frac{d}{dz} + \alpha \end{pmatrix}, \tag{6.43}$$

where $H(z)$ is a Heaviside function. The Green function can be expressed through the complete system of the eigenfunctions of the operator ${L_0}^{(z)}$, namely satisfying the condition:

$$L_{0ij}^{(z)} A_j^{(p)}(z) = pA_i^{(p)}(z), \tag{6.44}$$

and functional completeness:

$$\int dp A_i^{(p)}(z) A_j^{(p)}(z')^* = \delta(z - z')\delta_{ij}. \tag{6.45}$$

The Green function is expressed as:

$$G_{ij}^{(z)} = \int dp \frac{A_i^{(p)}(z) A^{(p)*}{}_j(z')}{p}, \tag{6.46}$$

which is derived from (6.40) by substitution of (6.44, 6.45).

The eigenfunctions (6.44) are found by a similar algorithm, described for the diffraction from multilayered structures in Chap. 4. For simplicity, we consider here the Laue geometry: $\gamma_0 > 0, \gamma_h > 0$. The boundary conditions comprise the presence of incident wave and the absence of diffracted wave on the infinite distance $z \to -\infty$. At the boundary $z = 0$ the incident and diffracted waves are continuous:

$$\begin{aligned} A_{(1)}^{(p)}(z) &= \nu_1 \begin{pmatrix} e^{\frac{p}{2i\gamma_0} z} \\ 0 \end{pmatrix} H(-z) + \nu_1 \begin{pmatrix} \frac{v_2 e^{iu_1 z} - v_1 e^{iu_2 z}}{v_2 - v_1} \\ \frac{v_1 v_2 \left(e^{iu_1 z} - e^{iu_2 z}\right)}{v_2 - v_1} \end{pmatrix} e^{iu_1(p)z} H(z) \\ u_1(p) &= \frac{\alpha\gamma_0 - p(\gamma_0 + \gamma_h) - \sqrt{4\gamma_0\gamma_h\chi^2 + (\alpha\gamma_0 + p\gamma_h - p\gamma_0)^2}}{4\gamma_0\gamma_h} \\ u_2(p) &= \frac{\alpha\gamma_0 - p(\gamma_0 + \gamma_h) + \sqrt{4\gamma_0\gamma_h\chi^2 + (\alpha\gamma_0 + p\gamma_h - p\gamma_0)^2}}{4\gamma_0\gamma_h} \\ v_{1,2} &= \frac{p + 2u_{1,2}\gamma_0}{\chi}. \end{aligned} \tag{6.47}$$

To fulfill the completeness of eigenfunctions, the solutions with the boundary conditions have to be also used, comprising the presence of the diffracted wave and the absence of the incidence wave at $z \to -\infty$:

$$A_{(2)}^{(p)}(z) = \nu_2 \begin{pmatrix} 0 \\ e^{\frac{p-\alpha}{2i\gamma_h} z} \end{pmatrix} H(-z) + \nu_2 \begin{pmatrix} \frac{e^{iu_2 z} - e^{iu_1 z}}{v_2 - v_1} \\ \frac{v_2 e^{iu_2 z} - v_1 e^{iu_1 z}}{v_2 - v_1} \end{pmatrix} e^{iu_1(p)z} H(z). \tag{6.48}$$

The coefficients $\nu_1(p)$ and $\nu_2(p)$ are determined from the normalization of function. The eigenfunctions of self-adjoint operator have to be orthogonal:

$$\int_{-\infty}^{\infty} dz A^{(p)}_{(1,2)_i}(z) A^{(p')}_{(1,2)_i}(z)^* = \delta(p - p'). \tag{6.49}$$

To prove this fact, the integration limit on z is substituted by a large number L tending to infinity, (6.47) is substituted into (6.49) and the expression is integrated. The terms containing $e^{i(u_1(p)-u_1(p'))L}$ and $e^{i(u_2(p)-u_2(p'))L}$ can be replaced by $e^{i\frac{du_1(p)}{dp}(p-p')L}$ and $e^{i\frac{du_2(p)}{dp}(p-p')L}$, respectively, due to the properties of δ-function. The expressions including $e^{i(u_1(p)-u_2(p'))L}$ and similar terms result in rapidly oscillating functions and don't contribute to the final result. Furthermore, we use the equalities:

$$\lim_{L\to\infty} \frac{1 - e^{-ikL}}{ik} = \pi\delta(k) - i\mathrm{P}\frac{1}{k},$$
$$\delta(ak) = \frac{\delta(k)}{|a|}, \tag{6.50}$$

where P means the integration in the sense of eigenvalue. As a result, the terms at $i\mathrm{P}\frac{1}{p-p'}$ give zero value, and at $\delta(p - p')$ the value $8\pi\gamma_0$ is obtained. In a similar way, for (6.48) the value $8\pi\gamma_h$ is calculated at δ-function and from (6.49) follows:

$$\nu_1 = \frac{1}{\sqrt{8\pi\gamma_0}}, \quad \nu_2 = \frac{1}{\sqrt{8\pi\gamma_h}}. \tag{6.51}$$

The system of functions derived is complete, that is proved by satisfying the condition:

$$\int_{-\infty}^{\infty} dp(A^{(p)}_{(1)\,i}(z) A^{(p)}_{(1)\,j}(z')^* + A^{(p)}_{(2)\,i}(z) A^{(p)}_{(2)\,j}(z')^*) = \delta(z - z')\delta_{ij}. \tag{6.52}$$

For the region $z, z' < 0$, the expressions (6.47) and (6.48) along with (6.51) lead directly to (6.52). For the region $z, z' > 0$, the integration is more cumbersome and performed in the following way. First of all, due to the validity of $v_1 v_2 = -\frac{\gamma_0}{\gamma_h}$, the terms containing $e^{i(u_1 z - u_2 z')}$ become zero in (6.52), and only the terms containing $e^{iu_1(z-z')}$ and $e^{iu_2(z-z')}$ remain. Then, we split the Eq. (6.52) into two integrals with $e^{iu_1(p)(z-z')}$ and $e^{iu_2(p)(z-z')}$ and introduce the substitutions $\xi = u_1(p)$ and $\xi = u_2(p)$, respectively. After the transformations involving Eqs. (6.47),(6.48) and (6.51), the coefficient $1/2\pi$ at $e^{i\xi(z-z')}$ is obtained for elements 11 and 22 in (6.52) and zero coefficient for elements 12 and 21, which proves the validity of (6.52).

As a next step, the Green function can be calculated from (6.46). The calculation of integral over p is ambiguous because of unclear way of integration in the vicinity $p = 0$. The method of integration is selected in dependence on the asymptotic of Green function, whether it is retarded or advanced. To derive the method of integration,

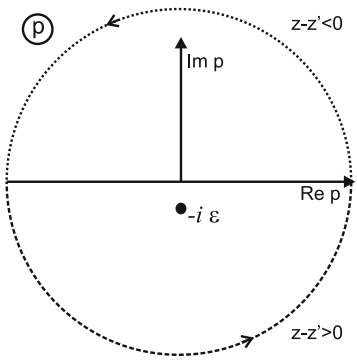

Fig. 6.2 The illustration of the integration procedure for Eq. (6.46)

the integration over real values p is transferred into complex plane (Fig. 6.2). We introduce the contour, which contains the real axis and is closed at the complex infinity. Provided the integrand tends to zero at complex infinity, the contour integral coincides with unknown integral on the real axis. The value of contour integral is determined by the residues in singularities, which are found from integrand (6.46). Using (6.47), (6.48) and (6.51), for the region $z, z' < 0$:

$$G_{ij}^{(z,z')} = \int \frac{dp}{p} \begin{pmatrix} \frac{1}{4\pi\gamma_0} e^{\frac{p}{2i\gamma_0}(z-z')} & 0 \\ 0 & \frac{1}{4\pi\gamma_h} e^{\frac{p-\alpha}{2i\gamma_h}(z-z')} \end{pmatrix}, \tag{6.53}$$

and for the region $z, z' > 0$:

$$G_{ij}^{(z,z')} = \int \frac{dp}{p} \frac{1}{4\pi(\gamma_0 + v_1^2\gamma_h)} \begin{pmatrix} \frac{v_1^2\gamma_h e^{iu_2(z-z')} + \gamma_0 e^{iu_1(z-z')}}{\gamma_0} & v_1\left(e^{iu_1(z-z')} - e^{iu_2(z-z')}\right) \\ v_1\left(e^{iu_1(z-z')} - e^{iu_2(z-z')}\right) & \frac{v_1^2\gamma_h e^{iu_1(z-z')} + \gamma_0 e^{iu_2(z-z')}}{\gamma_h} \end{pmatrix}. \tag{6.54}$$

In the expression (6.53), the only pole is $p = 0$, whereas in (6.54) additionally to $p = 0$ the denominator equals to zero at:

$$p_B = \frac{\alpha\gamma_0 \pm 2i\chi\sqrt{\gamma_0\gamma_h}}{\gamma_0 - \gamma_h}. \tag{6.55}$$

These values of p correspond to Bragg condition, and $u_1(p_B) = u_2(p_B)$, $v_1(p_B) = v_2(p_B)$. The matrix in (6.53) becomes zero and the singularity in (6.55) disappears.

The following procedure of integration around pole $p = 0$ is accepted depending on the behavior of (6.53). Because of G_{11} describes the Green function of plane wave and at $z - z' > 0$ the integrand of G_{11} tends to infinity in upper semi-plane and

to zero in a lower semi-plane, the contour of integration has to be closed in lower semi-plane and vice versa at $z - z' < 0$ (Fig. 6.2). For retarded Green function, the perturbation in position z' influences the wave fields in area $z > z'$, which happens when the pole is located in a lower semi-plane. Thus, to perform the integration in (6.53) and (6.54) the replacement has to be done:

$$\int \frac{dp}{p} \to \int \frac{dp}{p + i\epsilon'} \tag{6.56}$$

where ϵ is an infinitesimal value pointing the direction of the integration path. It has a meaning of the absorption leading to the wave decay at $+\infty$.

For the residue in the position $-i\epsilon$ and at $z - z' > 0$, the integration is executed in a negative direction of a real axis and thus the result is multiplied by -1, which calculates (6.53) as:

$$G_{ij}^{(z,z')} = \begin{pmatrix} \frac{1}{2i\gamma_0} & 0 \\ 0 & \frac{1}{2i\gamma_h} e^{\frac{-\alpha}{2i\gamma_h}(z-z')} \end{pmatrix} H(z - z'). \tag{6.57}$$

For expression (6.54) at large p, which corresponds to the essential deviation from Bragg condition, we have $v_1 \to 0$, $u_1 \to \frac{p}{2i\gamma_0}$, $u_2 \to \frac{p-\alpha}{2i\gamma_h}$, and as a result:

$$\begin{aligned} G_{ij}^{(z,z')} = & \frac{1}{2i(\gamma_0 + v_1^2\gamma_h)} \times \\ & \times \begin{pmatrix} \frac{v_1^2\gamma_h e^{iu_2(z-z')} + \gamma_0 e^{iu_1(z-z')}}{\gamma_0} v_1 \left(e^{iu_1(z-z')} - e^{iu_2(z-z')}\right) \\ v_1 \left(e^{iu_1(z-z')} - e^{iu_2(z-z')}\right) \end{pmatrix} \\ & \begin{pmatrix} \\ \frac{v_1^2\gamma_h e^{iu_1(z-z')} + \gamma_0 e^{iu_2(z-z')}}{\gamma_h} \end{pmatrix} \\ & \times H(z - z'), \end{aligned} \tag{6.58}$$

where all values are calculated at $p = 0$. At large deviations from the Bragg condition, the variable $v_1 \to 0$, and (6.58) is reduced to (6.57). The difference between (6.58) and (6.57) is essential in the domain where $v_1 \approx 1$, i.e. near the Bragg condition.

The validity of the statement (6.40) is proved by direct substitutions. At $z \neq z'$, the operator $L_{0ij}^{(z)}$ produces zero when Green function acts on (6.58) and (6.57) due to the structure of Green functions composed of eigenfunctions $L_{0ij}^{(z)}$ corresponding to eigenvalue $p = 0$. At $z = z'$, the Green functions are discontinued in a singular point, where operator $L_{0ij}^{(z)}$ results in δ-function. The final expression for three-dimensional Green function is delivered by (6.38).

6.3 Effective Potential and Applicability of Kinematical Theory

The solution of the Eqs. (6.33) and (6.36) is not straightforward, even considering only the first order terms in (6.27) and (6.35). The operator V_{eff} is an integral operator, if the approximation (6.33) is used:

$$V_{eff\,\alpha,\beta}\boldsymbol{A}(\boldsymbol{r})_\beta = Q\int d^3\boldsymbol{r}'\begin{pmatrix}\langle f(\boldsymbol{r})f(\boldsymbol{r}')^*\rangle G_0(\boldsymbol{r},\boldsymbol{r}')_{22} & \langle f(\boldsymbol{r})f(\boldsymbol{r}')\rangle G_0(\boldsymbol{r},\boldsymbol{r}')_{21}\\ \langle f(\boldsymbol{r})^* f(\boldsymbol{r}')^*\rangle G_0(\boldsymbol{r},\boldsymbol{r}')_{12} & \langle f(\boldsymbol{r})^* f(\boldsymbol{r}')\rangle G_0(\boldsymbol{r},\boldsymbol{r}')_{11}\end{pmatrix}\cdot\begin{pmatrix}A_0(\boldsymbol{r}')\\ A_H(\boldsymbol{r}')\end{pmatrix},$$
$$Q = k_0^4\chi_{\boldsymbol{H}}\chi_{-\boldsymbol{H}}. \tag{6.59}$$

There are two types of terms in the Eq. (6.59): (1) the average values $\langle f(\boldsymbol{r})f(\boldsymbol{r}')^*\rangle$, $\langle f(\boldsymbol{r})f(\boldsymbol{r}')\rangle$, ... describing the displacement fields of the defects and the properties of statistical ensemble of defects, and (2) Green functions $G_0(\boldsymbol{r},\boldsymbol{r}')_{ij}$, describing the X-ray dynamical diffraction process. The value

$$g(\boldsymbol{r},\boldsymbol{r}') = \langle f(\boldsymbol{r})f(\boldsymbol{r}')^*\rangle = \langle e^{i\boldsymbol{H}(\boldsymbol{u}(\boldsymbol{r})-\boldsymbol{u}(\boldsymbol{r}'))}\rangle - e^{-2W} \tag{6.60}$$

is called the correlation function of the crystallographic lattice [7]. The averaging over the ensemble of defects is performed in the way, similar to one used for Eq. (6.11). Assuming non-correlated defects, we obtain:

$$g(\boldsymbol{r},\boldsymbol{r}') = \exp\left(\int d^3\boldsymbol{r}_s\rho(\boldsymbol{r}_s)(e^{i\boldsymbol{H}(\boldsymbol{u}(\boldsymbol{r};\boldsymbol{r}_s)-\boldsymbol{u}(\boldsymbol{r}';\boldsymbol{r}_s))}-1)\right) - e^{-2W}. \tag{6.61}$$

For the points $\boldsymbol{r}$ and $\boldsymbol{r}'$ separated by a large distance, the displacement fields are determined by the defects groups located in the vicinity of these points. For large distance, the displacement fields can be assumed independent each of other, and the integral in (6.61) is represented by the sum of integrals around the points $\boldsymbol{r}$ and $\boldsymbol{r}'$, i. e. $\int d^3\boldsymbol{r}_s \approx \int_{\boldsymbol{r}_s\sim\boldsymbol{r}} d^3\boldsymbol{r}_s + \int_{\boldsymbol{r}_s\sim\boldsymbol{r}'} d^3\boldsymbol{r}_s$, each resulting in Debye-Waller factor W. Thus, the correlation function (6.61) demonstrates the feature typical for all correlation functions describing the near ordering: tends to zero at far distances. In opposite case, when $\boldsymbol{r}$ and $\boldsymbol{r}'$ are located close each to other, the correlation function is modeled by Gaussian. To prove this fact, the expansion $\boldsymbol{u}(\boldsymbol{r};\boldsymbol{r}_s) - \boldsymbol{u}(\boldsymbol{r}';\boldsymbol{r}_s) \approx \frac{\partial\boldsymbol{u}(\boldsymbol{r};\boldsymbol{r}_s)}{\partial\boldsymbol{r}_i}\Delta\boldsymbol{r}_i$ can be used assuming the $\Delta\boldsymbol{r} = \boldsymbol{r} - \boldsymbol{r}'$ is smaller than variation of the displacement fields. Expanding the exponent up to the second order:

$$g(\boldsymbol{r},\boldsymbol{r}') = e^{iH_i\langle\epsilon_{ij}\rangle\Delta r_j}e^{-\frac{1}{2}H_iH_j\langle\epsilon_{ik}\epsilon_{jl}\rangle\Delta r_k\Delta r_l} - e^{-2W}, \tag{6.62}$$

where tensor $\langle\epsilon_{ij}\rangle$ describes the average deformation of the crystal caused by the average displacement fields from the defects, the tensor $\langle\epsilon_{ik}\epsilon_{jl}\rangle$ characterizes the root mean square deformation of crystal due to the fluctuating displacement field:

$$\langle \epsilon_{ij} \rangle = \int d^3 \boldsymbol{r}_s \rho(\boldsymbol{r}_s) \frac{\partial \boldsymbol{u}(\boldsymbol{r}; \boldsymbol{r}_s)_i}{\partial \boldsymbol{r}_j} \tag{6.63}$$

$$\langle \epsilon_{ik} \epsilon_{jl} \rangle = \int d^3 \boldsymbol{r}_s \rho(\boldsymbol{r}_s) \frac{\partial \boldsymbol{u}(\boldsymbol{r}; \boldsymbol{r}_s)_i}{\partial \boldsymbol{r}_k} \frac{\partial \boldsymbol{u}(\boldsymbol{r}; \boldsymbol{r}_s)_j}{\partial \boldsymbol{r}_l}.$$

In opposite to correlation function (6.60), the non-diagonal elements of the matrix (6.59), containing the functions $\langle f(\boldsymbol{r}) f(\boldsymbol{r}') \rangle$, have to be averaged with respect to the sum of the displacement fields. As a result, the function becomes a fast oscillating and tends to zero for the points $\boldsymbol{r}$ and $\boldsymbol{r}'$ located both on far distances each from other and close each to other.

To calculate the effective potential (6.59), the correlation function of defects $g(\boldsymbol{r}, \boldsymbol{r}')$ and Green function have to be known, which are found by using the theory of differential equation [19]. The explicit form of Green function clearly displays the reason to abandon the non-diagonal elements of matrix (6.59). These elements contain the terms $G(\boldsymbol{r}, \boldsymbol{r}')_{21}$ and $G(\boldsymbol{r}, \boldsymbol{r}')_{12}$, which describe the creation of the diffracted wave from the direct one, and vice versa. The mentioned functions contribute essentially near the Bragg condition (see (6.58)), and tend to zero otherwise, whereas $G(\boldsymbol{r}, \boldsymbol{r}')_{11}$ and $G(\boldsymbol{r}, \boldsymbol{r}')_{22}$ are transformed into Green function of wave in a vacuum (6.57) when moving away from Bragg point.

How important is the accounting of dynamical effects in the effective potential? In general case, the Eq. (6.27) is a three-dimensional integro-differential one, however, assuming the correlation function (6.61) and Green function both depend on the $\boldsymbol{r} - \boldsymbol{r}'$ only:

$$g(\boldsymbol{r}, \boldsymbol{r}') = g(\boldsymbol{r} - \boldsymbol{r}'), \tag{6.64}$$

$$G_0(\boldsymbol{r}, \boldsymbol{r}')_{ij} = G_0(\boldsymbol{r} - \boldsymbol{r}')_{ij}, \tag{6.65}$$

the problem is simplified significantly. Whereas the assumption (6.64) means the uniformity of the displacement fields in a sample, the Eq. (6.65) is valid for Takagi-Taupin approximation, as follows from Sect. 6.2. The effective potential then becomes a diagonal integral operator with the kernel:

$$V_{eff\,\alpha,\beta} = \int d^3 \boldsymbol{r}' \begin{pmatrix} V_1(\boldsymbol{r} - \boldsymbol{r}') & 0 \\ 0 & V_2(\boldsymbol{r} - \boldsymbol{r}') \end{pmatrix} \tag{6.66}$$

$$V_1(\boldsymbol{r} - \boldsymbol{r}') = Q g(\boldsymbol{r} - \boldsymbol{r}') G_0(\boldsymbol{r} - \boldsymbol{r}')_{22}, \;\; V_2(\boldsymbol{r} - \boldsymbol{r}') = Q g(\boldsymbol{r} - \boldsymbol{r}')^* G_0(\boldsymbol{r} - \boldsymbol{r}')_{11}. \tag{6.67}$$

The action of this operator on the displacement field is a convolution of operator kernel with a field, and in the Fourier space the action boils down to simple multiplication:

$$V_1 A_0 e^{i\boldsymbol{kr}} = V_1(\boldsymbol{k}) A_0 e^{i\boldsymbol{kr}}, \tag{6.68}$$
$$V_2 A_h e^{i\boldsymbol{kr}} = V_2(\boldsymbol{k}) A_h e^{i\boldsymbol{kr}},$$
$$V_1(\boldsymbol{k}) = \frac{Q}{(2\pi)^3} \int d^3\boldsymbol{r} e^{-i\boldsymbol{kr}} g(\boldsymbol{r}) G_0(\boldsymbol{r})_{22},$$
$$V_2(\boldsymbol{k}) = \frac{Q}{(2\pi)^3} \int d^3\boldsymbol{r} e^{-i\boldsymbol{kr}} g(\boldsymbol{r})^* G_0(\boldsymbol{r})_{11}.$$

Thus, the effective potential leads to additional X-ray polarizability:

$$\chi_{0\text{eff}}(\boldsymbol{k})_{ii} = -V_i(\boldsymbol{k})/k_0^2. \tag{6.69}$$

This polarizability is different for direct and diffracted waves $\chi_{0\text{eff}}(\boldsymbol{k})_{11} \neq \chi_{0\text{eff}}(\boldsymbol{k})_{22}$ and possesses the dispersion $\chi_{0\text{eff}} = \chi_{0\text{eff}}(\boldsymbol{k})$.

Furthermore we use isotropic Gaussian distribution for the correlation function:

$$g_G(\boldsymbol{r}) = e^{-\frac{r^2}{2l_d^2}}. \tag{6.70}$$

As demonstrated in (6.62), the Gaussian distribution is parametrized by value l_d meaning the distance where correlation function drops down essentially and called correlation length. Using the Green function (6.38), we obtain:

$$V_2(\boldsymbol{k}_0) = \frac{Q}{(2\pi)^4} \int dz d^2\boldsymbol{k}_{||} e^{-\frac{1}{2}(\boldsymbol{k}_{||}-\boldsymbol{k}_{0||})^2 l_d^2} e^{i(k_z(\boldsymbol{k}_{||})-k_{0z})z} e^{-\frac{z^2}{2l_d^2}} G_{11}^{(z)}(\boldsymbol{k}_{||})(z). \tag{6.71}$$

There are two kinds of functions in this formula, which vary in different scales when integrating over $\boldsymbol{k}_{||}$. The first kind is a correlation function, which decreases at deviations $\boldsymbol{k}_{||} - \boldsymbol{k_0} \sim 1/l_d$, and the other is one-dimensional Green function $G_{11}^{(z)}(\boldsymbol{k}_{||})(z)$ tending to the asymptotic value in vacuum at deviations of the order of Bragg peak width. To emphasize these two scales in (6.71), the parametrization of $\boldsymbol{k}$ through the angle variables of deviation from Bragg condition is used:

$$\boldsymbol{k} = k_0(\cos(\omega_0 + \tilde{\omega})\cos(\tilde{\phi}), \cos(\omega_0 + \tilde{\omega})\sin(\tilde{\phi}), \sin(\omega_0 + \tilde{\omega})). \tag{6.72}$$

Let us assume that ω_0 corresponds to Bragg condition and to vector $\boldsymbol{k}_0$ in (6.71) simultaneously. If the deviations $\tilde{\omega}$ and $\tilde{\phi}$ are small, and the diffraction is coplanar, the following formula is obtained with the accuracy $o(\tilde{\omega}, \tilde{\phi})$:

$$V_2(\boldsymbol{k}_0) = \frac{Q l_d k_0 \sin\omega_0}{(2\pi)^{\frac{7}{2}}} \int d\tilde{\omega} e^{-\frac{1}{2}k_0^2 \sin^2\omega_0 \tilde{\omega}^2 l_d^2} \tag{6.73}$$
$$\times \int dz e^{ik_0 \cos\omega_0 \tilde{\omega} z} e^{-\frac{z^2}{2l_d^2}} G_{11}^{(z)}(\alpha)(z), \quad \alpha = 2k_0^2 \sin 2\theta_B \tilde{\omega},$$

where $d^2\boldsymbol{k}_{||}$ is expressed through the small angles $\tilde{\omega}$, $\tilde{\phi}$. The Green function is conveniently written through the parameter α in this case (see Chap. 4), which doesn't depend on $\tilde{\phi}$ at small $\tilde{\omega}$ and $\tilde{\phi}$ allowing the integration over the variable $\tilde{\phi}$ in (6.73). By integrating over z using (6.58), the final formula for effective potential is written as:

$$V_2(\boldsymbol{k}_0) = \frac{Ql_d^2 k_0 \sin\omega_0}{2(2\pi)^3} \int d\tilde{\omega} e^{-\frac{1}{2}k_0^2 \sin^2\omega_0 \tilde{\omega}^2 l_d^2} \times \frac{\gamma_0 f([k_0 \cos\omega_0\tilde{\omega} + u_1(\alpha)]l_d) + v_1(\alpha)^2\gamma_h f([k_0\cos\omega_0\tilde{\omega} + u_2(\alpha)]l_d)}{2i\gamma_0(\gamma_0 + v_1(\alpha)^2\gamma_h)}, \quad (6.74)$$

$$f(kl) = e^{-\frac{1}{2}k^2l^2}\left(1 - \mathrm{erf}\left(i\frac{kl}{\sqrt{2}}\right)\right).$$

In the integrand of (6.74), there are evidently two scales of variation over $\tilde{\omega}$. The exponents appeared due to Gaussian correlation function decrease at deviations:

$$\tilde{\omega} \sim \frac{1}{k_0 l_d}. \quad (6.75)$$

The expression appeared due to Green function tends to the asymptotic vacuum value $\frac{f(k_0\cos\omega_0\tilde{\omega})}{2i\gamma_0}$ at deviation (see Chap. 4):

$$\tilde{\omega} \sim |\chi_{\boldsymbol{H}}|. \quad (6.76)$$

Thus, the expectable criteria is obtained: the dynamical effects are important in the effective potential if the correlation function decreases at the scale of order of the extinction length:

$$l_d \sim \frac{1}{k_0|\chi_{\boldsymbol{H}}|} \sim L_e. \quad (6.77)$$

In the most of practical cases, the defects structure has a correlation function which decreases faster and the dynamical effects are negligible. To estimate the magnitude of the effective polarizability comparing to periodical X-ray polarizability, the Eq. (6.74) is used:

$$\chi_{0\mathrm{eff}}(\boldsymbol{k}_0)_{22} \sim i|\chi_H|k_0 l_d \sim i\frac{l_d}{L_e}, \quad (6.78)$$

notably a similar ratio of correlation length to the extinction length is obtained. The imaginary potential reflects the fact of transfer of coherent intensity into diffuse one, and the imaginary effective polarizability describes this decrease of the coherent intensity.

Thus, the effective potential, being a correction for coherent potential due to displacement fields of defects, is essential for the correlation length larger than the extinction length. The dynamical effects have to be also taken into account at this

condition. For the specific case of grazing-incidence diffraction, the geometrical factors have to be introduced, too. The extinction length can drop down many times in this case, which softens the conditions (6.77) and (6.78).

The presence of the displacement fields always originates the diffuse scattering, which contains a valuable information on the distribution of defects. To calculate the intensity of diffuse scattering $I(\boldsymbol{r})$, the correlation function $\Gamma(\boldsymbol{r}_1, \boldsymbol{r}_2)$ has to be determined from Bethe-Salpeter Eq. (6.35). We represent here this equation as:

$$\Gamma_{1,2} = \Gamma^c_{1,2} + G_1 G_2^* \langle V_1 V_2^* \rangle \Gamma^c_{1,2} + G_1 G_2^* \langle V_1 V_2^* \rangle G_1 G_2^* \langle V_1 V_2^* \rangle \Gamma^c_{1,2} + ..., \quad (6.79)$$

where $\Gamma^c_{1,2} = A_c(\boldsymbol{r}_1) A_c(\boldsymbol{r}_2)^*$ is a correlation function for the coherent amplitude found from (6.27) and the Eq. (6.36) has been utilized. Each subsequent term differs from the previous one by operator $G_1 G_2^* \langle V_1 V_2^* \rangle$, which influence is proportional to l_d / L_e, as follows from (6.33). Assuming this parameter small, the formula for intensity is obtained:

$$I(\boldsymbol{r}) = \Gamma(\boldsymbol{r}, \boldsymbol{r}) = \Gamma(\boldsymbol{r}, \boldsymbol{r})^c + \int d^3\boldsymbol{r}_1 d^3\boldsymbol{r}_2 G_0(\boldsymbol{r}, \boldsymbol{r}_1) G_0(\boldsymbol{r}, \boldsymbol{r}_2)^* \langle V(\boldsymbol{r}_1) V(\boldsymbol{r}_2)^* \rangle \Gamma(\boldsymbol{r}_1, \boldsymbol{r}_2)^c \quad (6.80)$$

By the analogue with X-ray reflectivity, the detector recording X-ray intensities is placed on a large distance from the sample.Then the asymptotic expression for Green function (5.11) can be used and for this reason we return back from matrix form (6.26) to (6.22). For example, in two-wave approximation the value $\langle V(\boldsymbol{r}_1) V(\boldsymbol{r}_2)^* \rangle$ becomes:

$$\langle V(\boldsymbol{r}_1) V(\boldsymbol{r}_2)^* \rangle = Q(g(\boldsymbol{r}_1, \boldsymbol{r}_2) e^{i\boldsymbol{H}(\boldsymbol{r}_1 - \boldsymbol{r}_2)} + c.c.). \quad (6.81)$$

Finally, the formula for intensity using (5.11) takes the form known as distorted-wave Born approximation DWBA:

$$I(\boldsymbol{r}) = \frac{Q}{16\pi^2 r^2} \int d^3\boldsymbol{r}_1 d^3\boldsymbol{r}_2 \boldsymbol{A}_{\boldsymbol{p}}^{(-)}(\boldsymbol{r}_1)^* \boldsymbol{A}_{\boldsymbol{p}}^{(-)}(\boldsymbol{r}_2) (g(\boldsymbol{r}_1, \boldsymbol{r}_2) e^{i\boldsymbol{H}(\boldsymbol{r}_1 - \boldsymbol{r}_2)} + c.c.) A_c(\boldsymbol{r}_1) A_c(\boldsymbol{r}_2)^*, \quad (6.82)$$

where each wave field has to be represented as a sum of incident and diffracted waves with corresponding exponents, and the rapidly oscillating exponents are omitted due to two-wave approximation. When the dynamical effects can be neglected in the wave fields of non-perturbed system, the kinematical expression is valid:

$$I(\boldsymbol{r}) \sim \int d^3\boldsymbol{r}_1 d^3\boldsymbol{r}_2 e^{i\boldsymbol{q}(\boldsymbol{r}_1 - \boldsymbol{r}_2)} g(\boldsymbol{r}_1, \boldsymbol{r}_2), \ \ \boldsymbol{q} = \boldsymbol{k}_{out} - \boldsymbol{k}_{in} - \boldsymbol{H}, \ \ \boldsymbol{r}/r = \boldsymbol{k}_{out}/k_0. \quad (6.83)$$

6.4 One-Dimensional Defects (Dislocations)

The intensity of diffuse X-ray scattering is calculated from the correlation function of the displacement fields of defects, which is conditioned by two properties: (1) type of defects, and (2) physical properties of the defects ensemble. The type of the defect defines the displacement fields $\boldsymbol{u}(\boldsymbol{r};\boldsymbol{r}_s)$ of a single defect, which is included in correlation functions (6.60) and (6.11). The properties of the ensemble are described through the density of defects $\rho(\boldsymbol{r})$ and correlation function of the defects positions $w(\boldsymbol{r},\boldsymbol{r}')$. The analysis of X-ray diffuse scattering measured near several Bragg reflections permits to determine the type of defects, their density and correlation properties. This procedure is very well established for dislocations [20–22].

The dislocations are the frequently occurring type of the defects in crystallographic materials. In the polycrystalline samples, the known distribution of dislocations allows to microscopically describe the plasticity properties [23]. In the semiconductor heteroepitaxial structures, the presence of dislocations influences the electronic properties of the devices. The evaluation of the distribution and the status of the dislocation is therefore an important part of material characterization in modern technology [24, 25].

We consider initially the ensemble of infinite line dislocations, which is used as a model for the line profile analysis in polycrystalline materials [20, 21] as well as for HRXRD analysis in heteroepitaxial structures [22]. The analysis of dislocation loops is similar to the case of point defects and described in details in [7, 26].

To solve the problem, the displacement field of a single dislocation has to be found, which is calculated using the continuous theory of elasticity [5]. The displacement field $\boldsymbol{u}(\boldsymbol{r})$ has to satisfy the condition of equilibrium:

$$c_{ijkl}\frac{\partial^2 u_k}{\partial x_j \partial x_l} = 0, \tag{6.84}$$

and to the boundary conditions: the disruption of the displacement fields by value of Burgers vector $\boldsymbol{b}$ in the path around dislocation line and the absence of forces at free surface:

$$\oint d\boldsymbol{u} = -\boldsymbol{b}, \sigma_{ij}n_j|_S = 0, \tag{6.85}$$

here c_{ijkl} is a stiffness tensor and σ_{ij} is a stress tensor. The solution of this problem for the case of infinite anisotropic media was proposed by Eshelby [27] and generalized by Stroh [23, 28, 29]. The solution for isotropic media with half-plane boundary is reported in [30], and the displacement fields in an explicit form are given in [22]. These fields are represented by a sum of the displacement field in infinite media, the displacement field of the image dislocation relatively to free surface, and additional surface term.

Thus, both the displacement fields and the integration method in (6.60) depends on the arrangement of dislocations, which can be:

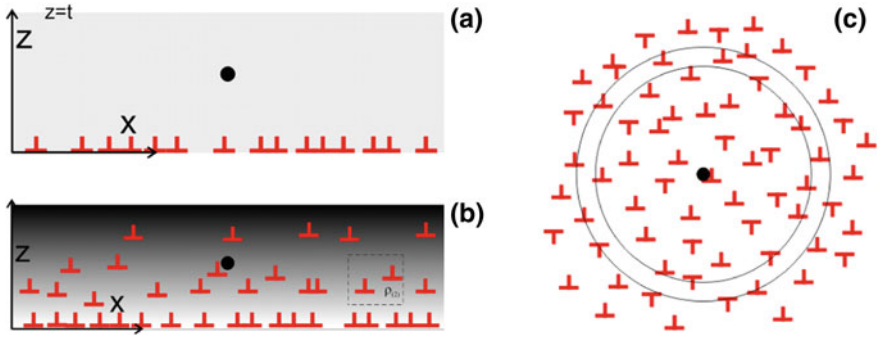

Fig. 6.3 The arrangement of dislocations considered in the section: **a** on the surface of the film-substrate interface, **b** in graded structures, **c** threading dislocations

- parallel dislocation lines in the plane parallel to the sample surface. The model describes the boundary between epitaxial film and substrate. The density of dislocations has a dimension m^{-1} (number of lines per length unit, which they intersect in the direction perpendicular to dislocation lines), Fig. 6.3a.
- parallel dislocation lines distributed within the layer. The density of dislocations has a dimension m^{-2}, Fig. 6.3b. This model describes partly relaxed layers with the gradient of the dopant concentration;
- parallel dislocation lines which are perpendicular to the crystal surface. The density of dislocations has a dimension m^{-2}, Fig. 6.3c. This model describes the threading dislocations and the influence of dislocations on the line profiles of X-ray diffraction from polycrystalline materials.

6.4.1 Parallel Edge Dislocations at Interfaces

In the epitaxial growth of the materials possessing a crystallographic lattice mismatch, the accommodation of the lattice strains may occur in different ways [31]. In the initial stage of growth, the lateral crystallographic structure of film replicates the structure of the substrate. The film accumulates an essential elastic energy and internal stress may achieve Gigapascals, which is close to the limit of plasticity. Further growth over the critical thickness results in misfit dislocations with Burgers vector with the lateral component, which releases the elastic strain in the film. The dislocation line of the misfit dislocation lies along the interface between the layers (substrate), which have different lattice constants in a bulk state. The direction of the dislocation line follows the crystallographic axes [23], and as a result, the array of parallel dislocation lines appears.

First of all, we discuss the importance of coherent scattering and dynamical effects in the presence of misfit dislocations. Assuming the non-correlated defects, the Debye-Waller factor (DWF) is expressed as in (6.11):

$$\langle e^{i\boldsymbol{H}\boldsymbol{u}(\boldsymbol{r})}\rangle = e^{W(z)} = e^{\rho\int dx(e^{i\boldsymbol{H}\boldsymbol{u}(x,z)}-1)}. \tag{6.86}$$

The spatial dependence of the displacement fields of a single dislocation $\boldsymbol{u}(x, z)$ is parametrized solely by the layer thickness d. Representing the displacement field as $b\boldsymbol{u}_b(\tilde{x} = x/d, \tilde{z} = z/d)$, where b is a Burgers vector, the Eq. (6.86) is written as:

$$e^{W(\tilde{z})} = e^{\rho d\phi(\tilde{z})}, \tag{6.87}$$

$$\phi(\tilde{z}) = \int d\tilde{x}(e^{ib\boldsymbol{H}\boldsymbol{u}(\tilde{x},\tilde{z})} - 1). \tag{6.88}$$

The dependence of DWF on the thickness is universal, and the type of dislocations and Bragg reflection influence the function $\phi(\tilde{z})$, which varies slowly within the layer. The DWF value decreases exponentially with increase of thickness and concentration of dopants. To prove this fact, the convergence of integrand in (6.88) is analyzed below.

Despite of discontinuity in the displacement fields by Burgers vector, the value $e^{ib\boldsymbol{H}\boldsymbol{u}(\tilde{x},\tilde{z})}$ is continuous because of in the singular points the phase of exponent changes its value by $2\pi n$. When integrating around zero, the integrand has a finite value, and at $x \to \infty$ the displacement fields are decreased as (the singularity is at $x = 0$):

$$\boldsymbol{u}_{b_x}(x, z) \xrightarrow{x\to\infty} \frac{b_x}{\pi}\left(\frac{2}{x}, 0, -\frac{1 + 2(1 - 2\alpha)z}{x^2}\right), \tag{6.89}$$

$$\boldsymbol{u}_{b_y}(x, z) \xrightarrow{x\to\infty} \frac{b_y}{\pi}\left(0, \frac{1}{x}, 0\right),$$

$$\boldsymbol{u}_{b_z}(x, z) \xrightarrow{x\to\infty} \frac{b_z}{\pi}\left(-\frac{1}{\pi x^2}, 0, -\frac{2(1 + 3(1 - 2\alpha)z)}{x^3}\right).$$

Here u_{b_i} is a displacement field due to i-component of the Burgers vector, the symbol˜ is omitted, $\alpha = \frac{1}{2(1-\nu)}$ and ν is a Poisson ratio. Expanding the exponent in (6.88) at large x, the terms with $1/x$ are canceled when integrating over symmetric limits and the value of integral is finite.

Figure 6.4a shows the dependence of $\phi(\tilde{z})$ for edge dislocations in fcc crystal with Burgers vector $\frac{1}{2}[110]$ and dislocation line $[\bar{1}10]$ for Bragg reflection (224). Debye-

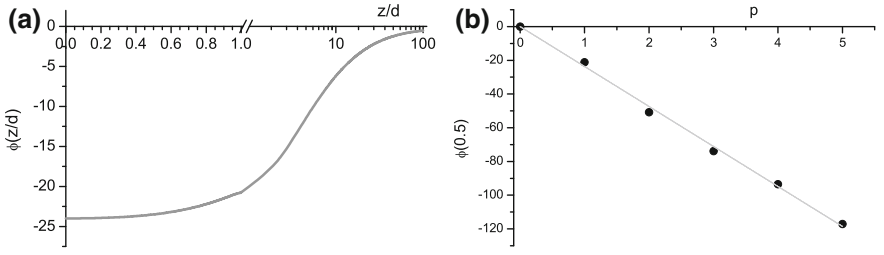

Fig. 6.4 The dependence of Debye-Waller factor from (**a**) thickness and (**b**) Bragg reflection

Waller factor remains almost constant inside film ($0 < \tilde{z} < 1$) and decreases deep into substrate. The same behavior is observed for other types of dislocations.

With the increase of the Bragg reflection order, DWF decreases. The contribution from the area of large x values in integral (6.88) is proportional to the reflection order. Figure 6.4b demonstrates the function $\phi(\tilde{z} = 0.5)$ for reflections multiple to (224) $\boldsymbol{H}_p = p\boldsymbol{H}$, and the function is very close to linear, which again confirms the largest contribution into integral from large x.

Using the known dependence of DWF on dislocation density and thickness, the coherent scattering can be estimated. To characterize the relaxation status of crystallographic lattice, the macroscopic relaxation degree is introduced:

$$R = \frac{a_l - a_s}{a_l^{(0)} - a_s}, \tag{6.90}$$

where a_l, a_s are the lattice constants of layer and substrate, respectively; $a_l^{(0)}$ is a lattice constant of layer in a bulk state. The value $R = 0$ corresponds to pseudomorphic layer and $R = 1$ to fully relaxed one. The difference between a_l and a_s supposed to be small. Assuming the difference between the length of N cells of substrate Na_s and N cells of layer is compensated by $\rho N a_s$ dislocations with misfit relieving Burgers vector b_x, the following relation is obtained:

$$R = \frac{\rho b_x}{\epsilon}, \quad \epsilon = \frac{a_l^{(0)} - a_s}{a_s}. \tag{6.91}$$

The relationship between the layer thickness and the density of dislocations is predetermined from the microscopic premises for creation of dislocations in strained crystallographic layers. There are different models [24, 25] of this process, for example, in the model of Mathews and Blakeslee the relaxation happens after the critical thickness d_{cr} and changes according to the law:

$$R(d) = H(d - d_{cr})\left(1 - \frac{d_{cr}}{d}\right). \tag{6.92}$$

The critical thickness is calculated from the pre-condition that the energy required for spread of dislocations is less than the energy released during development of dislocations. The equation for critical thickness estimation is:

$$\frac{b}{d_{cr}} \ln \frac{d_{cr}}{b} \sim \epsilon. \tag{6.93}$$

The real process of dislocation propagation is complex and includes the interaction and reproduction of dislocations and other effects. As a result, the critical thickness measured in the experiments is larger than one calculated from (6.93), see Fig. 6.5. The parameter ρd is higher than unity if the essential relaxation exists (Fig. 6.5)

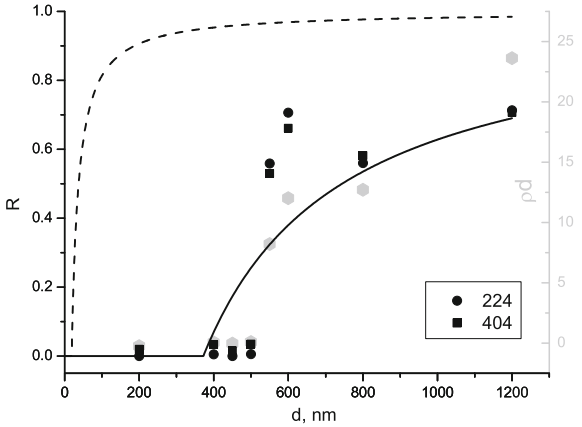

Fig. 6.5 Dependence of relaxation degree and ρd on the layer thickness for $In_{0.06}Ga_{0.94}As/GaAs$ evaluated from (224) and (004) Bragg reflections [32]. The dash line corresponds to (6.92) at critical thickness (6.93). The solid line represents the fitting of (6.92) with critical thickness as fittable parameter

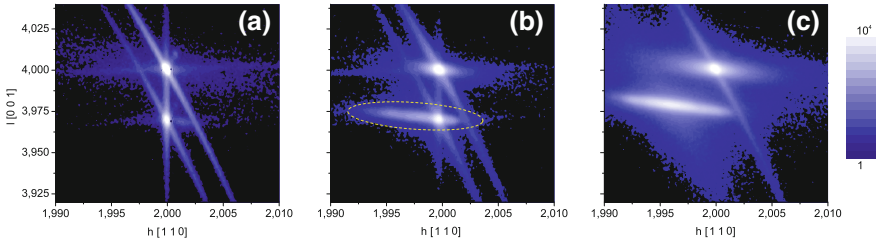

Fig. 6.6 Experimental reciprocal space maps for the $In_{0.06}Ga_{0.94}As/GaAs$ samples of thickness: 200 nm (**a**), 500 nm (**b**), 1200 nm (**c**). In the case (**b**), the onset of the diffuse scattering is marked with dashed line [32]

and according to (6.87) the Debye-Waller factor reduces drastically the coherent intensity. Thus, the distribution of the diffracted X-ray intensity is dominated by coherent component for the thickness below critical one and by diffuse component afterwards. The co-existence of both components in a similar proportion is only possible in a narrow diapason near critical thickness (Fig. 6.6).

Furthermore, the diffuse X-ray scattering is calculated by using (6.83). Using correlation function (6.83), we receive from (6.61):

$$I(\boldsymbol{q}) = \int_0^d \int_0^d dz_1 dz_2 \int_{-\infty}^{\infty} dx e^{i(q_x x + q_z(z_1 - z_2))} g(x, z_1, z_2), \;\; x = x_1 - x_2, \tag{6.94}$$

$$g(\tilde{x}, \tilde{z_1}, \tilde{z_2}) = \exp\left[\rho d\, \alpha(\tilde{x}, \tilde{z_1}, \tilde{z_2})\right] - e^{2W}, \;\; \alpha = \int d\tilde{x}' (e^{ib\boldsymbol{H}(\boldsymbol{u}(\tilde{x}-\tilde{x}', \tilde{z_2}) - \boldsymbol{u}(-\tilde{x}', \tilde{z_1}))} - 1), \tag{6.95}$$

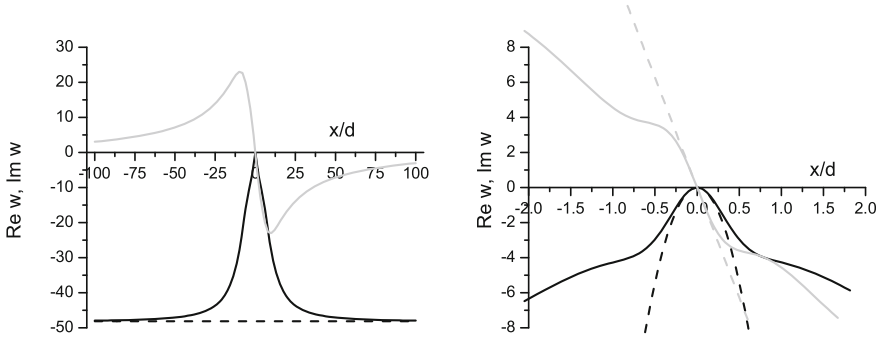

Fig. 6.7 The real and imaginary parts of $w(\tilde{x}, \tilde{z}_1 = 0.5, \tilde{z}_2 = 0.5)$ (6.95) in wide (*left panel*) and narrow (*right panel*) diapasons of x. The *dash line* in a *left panel* shows asymptotic $2\phi(0.5)$. The *dash lines* in a *right panel* show the limits (6.63) for real and imaginary parts

where the dimensionless distances $\tilde{x}, \tilde{z}$ (6.87) are used. The convergence of integral (6.89) follows from the asymptotic (6.95). Figure 6.7 shows the function $\alpha(\tilde{x}, \tilde{z_1}, \tilde{z_2})$ for edge dislocations in fcc crystal with Burgers vector $\frac{1}{2}[110]$, dislocation line $[\bar{1}10]$ and Bragg reflection (224). At large values of x, the function $\alpha(\tilde{x}, \tilde{z_1}, \tilde{z_2})$ tends to $\phi(\tilde{z_1}) + \phi(\tilde{z_2})$ and taking into account (6.61), the correlation function tends to zero. At small values of x, the real part is approximated by quadratic function, and the imaginary part by linear one (see Fig. 6.7), which follows from (6.62) and (6.63). For small deviations, the difference of the displacement fields is:

$$\boldsymbol{u}(\tilde{x}-\tilde{x}', \tilde{z_2})-\boldsymbol{u}(-\tilde{x}', \tilde{z_1}) \approx \frac{\partial \boldsymbol{u}(-\tilde{x}', \tilde{z})}{\partial \tilde{x}'}\tilde{x} + \frac{\partial \boldsymbol{u}(-\tilde{x}', \tilde{z})}{\partial \tilde{z}}\delta z, \;\; \Delta z = \tilde{z_2}-\tilde{z_1}. \quad (6.96)$$

The average deformation in (6.63) is calculated by analytical integration over $\tilde{x}'$:

$$\epsilon_{xx} = \rho b_x H(\tilde{z})H(1-\tilde{z}), \;\; \epsilon_{zz} = -\frac{\nu}{1-\nu}\rho b_x H(\tilde{z})H(1-\tilde{z}). \quad (6.97)$$

The deformation ϵ_{xx} is harmonized with (6.90) and (6.91) as well as the connection between ϵ_{xx} and ϵ_{zz} is given by Hook's law. In the real samples, the dislocation lines along $[\bar{1}10]$ providing the deformation ϵ_{xx} coexist with dislocation lines of the same density in perpendicular direction providing the deformation $\epsilon_{yy} = \epsilon_{xx}$. Assuming these two dislocation systems independent, the general correlation function and DWF are obtained as a product of correlation functions and DWF, respectively, for each system of defects (6.10), and finally for the component $\epsilon_{zz} = -\frac{2\nu}{1-\nu}\rho b_x$.

The formula for root mean square deformation $\langle \epsilon_{ik}\epsilon_{jl} \rangle$ is written:

$$\langle \epsilon_{ik}\epsilon_{jl} \rangle = \int \frac{d\tilde{x}'}{d^2}\frac{\partial u_i}{\partial \tilde{x}_k}\frac{\partial u_j}{\partial \tilde{x}_l}. \quad (6.98)$$

The analytical integration results in cumbersome expressions, for example, the term $\int d\tilde{x}' \left(\frac{\partial u_x(-\tilde{x}',\tilde{z})}{\partial \tilde{x}'}\right)^2$ for $\boldsymbol{u}$ related to Burgers vector with component b_x is:

$$\int d\tilde{x}' \left(\frac{\partial u_x(-\tilde{x}',\tilde{z})}{\partial \tilde{x}'}\right)^2 = b_x^2 \frac{\alpha^2(\tilde{z}(\tilde{z}(\tilde{z}+1)(2\tilde{z}+5)-9)-21)\tilde{z}^4 + 2\alpha(\tilde{z}+1)(\tilde{z}(\tilde{z}(\tilde{z}+3)+6)-2)\tilde{z}^2 - 2(\tilde{z}+1)^2\left(2\tilde{z}^2+\tilde{z}+1\right)}{8\pi(\tilde{z}-1)(\tilde{z}+1)^5}. \tag{6.99}$$

The correlation function $g(\boldsymbol{r}_1, \boldsymbol{r}_2) = g(x_1, z_1; x_2, z_2)$ for considered here defects depends on the difference of in-plane arguments $x = x_1 - x_2$ and doesn't depend on these arguments itself, which is a consequence of the in-plane uniformity. In the direction z, the sample is non-uniform, however, using approximation (6.96) the correlation function can also be written as $g(\boldsymbol{r}_1, \boldsymbol{r}_2) = g(x_1 - x_2, z_1 - z_2, \bar{z})$ in the direction z, where $\bar{z} = (z_1 + z_2)/2$ is an average depth at which the correlation function is investigated. The closer the points $\boldsymbol{r}_1$ and $\boldsymbol{r}_2$, the better the approximation is (see Fig. 6.8).

The applicability area for (6.96), (6.62) and (6.63) is determined by the parameter ρd. For X-ray intensity (6.94), the region makes the largest contribution, where the correlation function has a maximum. As follows from Figs. 6.7 and 6.8, the expansion (6.96) is valid up to values $w(\tilde{x}, \tilde{z_1}, \tilde{z_2}) \sim -1$, corresponding to correlation function $e^{-\rho d}$. Provided the parameter ρd is large enough, the contribution of this region is crucial. The integration limits on $x_1 - x_2$ and $z_1 - z_2$ can be extended to the infinity and the integration results in:

$$I(\boldsymbol{q}) = \int_0^d \frac{d\bar{z}}{\sqrt{\det \mathbf{w}_{ij}(\bar{z})}} e^{-\frac{(q-q^{(0)})_i \mathbf{w}_{ij}^{-1}(\bar{z})(q-q^{(0)})_j}{2}}, \tag{6.100}$$

$$q_i^{(0)} = \epsilon_{ij} H_j, \;\; \mathbf{w}_{ij} = H_k H_l \langle \epsilon_{ki} \epsilon_{lj} \rangle,$$

where the constant terms are omitted. The resulting distribution of X-ray intensity is close to Gaussian. For some estimates, the value $\mathbf{w}_{ij}(\bar{z})$ can be replaced by maximal value $\mathbf{w}_{ij}(0)$ at the sample surface, i.e. on the maximal distance from the defects [22].

As follows from (6.100) and (6.98), the typical width of the peak is $\sqrt{\rho/d}$. However, for the materials with large values ρd, the width of experimental peaks is much narrower than $\sqrt{\rho/d}$ [22, 33]. The reason for such behavior is the presence of correlations in the position of dislocations.

The correlations are formed due to different reasons related to the dynamics of dislocations, for instance, the periodic position of dislocations minimizes the elastic energy [5, 34]. The dislocations tend to glide to the periodic arrangement, however, the placement of the glide plane different from the interface plane or interaction with other defects prevents from this process. Because of the complexity of this dynamics, the correlation of the positions of dislocations is described empirically by pair distribution function.

The expression for correlation function is defined by cumulant series (6.21). The analytical summing of all terms in this series is complicated task and, therefore, the Monte-Carlo modeling of correlation function has been proposed [3, 33, 35, 36] to calculate the intensity distribution. The analytical methods, however, also play an important role is some special cases, for example, for the case of large parameter ρd. In the continuous limit of (6.21) with only T_1, T_2 remained, the correlation function $g(x, z_1, z_2)$ is:

$$g(x, z_1, z_2) = \\ e^{\rho d \int d\tilde{x}' \alpha(\tilde{x}-\tilde{x}', \tilde{z}_1, \tilde{z}_2) + \frac{1}{2}\rho^2 d^2 \int d\tilde{x}' d\tilde{x}'' w(x'-x'') \alpha(\tilde{x}-\tilde{x}', \tilde{z}_1, \tilde{z}_2) \alpha(\tilde{x}-\tilde{x}'', \tilde{z}_1, \tilde{z}_2)} \tag{6.101}$$

Using the approximation (6.96), the exponential function in (6.101) is expanded up to the second order of $\frac{\partial u}{\partial x_i}$. The omitted terms ($T_3$ and others) contain the functions of higher than second order of $\frac{\partial u}{\partial x_i}$. The resulting expression has a form of (6.62), and the average of deformation remains as in (6.97), but the root mean square of deformation changes from (6.98) to:

$$\langle \epsilon_{ik} \epsilon_{jl} \rangle = \int \frac{d\tilde{x}'}{d^2} \frac{\partial u_i(\tilde{x} - \tilde{x}', \tilde{\tilde{z}})}{\partial \tilde{x}_k} \frac{\partial u_j(\tilde{x} - \tilde{x}', \tilde{\tilde{z}})}{\partial \tilde{x}_l} \\ + \int \frac{d\tilde{x}' d\tilde{x}''}{d^2} \rho w(x' - x'') \frac{\partial u_i(\tilde{x} - \tilde{x}', \tilde{\tilde{z}})}{\partial \tilde{x}_k} \frac{\partial u_j(\tilde{x} - \tilde{x}'', \tilde{\tilde{z}})}{\partial \tilde{x}_l}. \tag{6.102}$$

In the integrand, the displacement fields drop down at the scale of d. The correlation function w is essential on the scale of several average distance between dislocations, i.e. $1/\rho d \ll 1$. Thus, the assumption about the faster decline of w than the decline of the displacement fields is valid:

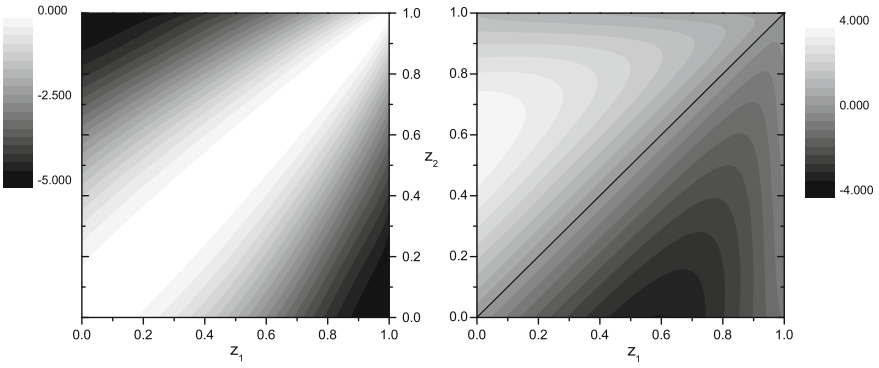

Fig. 6.8 The real (*left panel*) and imaginary (*right panel*) parts $w(0, \tilde{z}_1, \tilde{z}_2)$ (6.95). Near the line $z_1 = z_2$, the function depends on the difference of arguments (iso-lines are perpendicular to lines $z_1 - z_2$)

$$w(x' - x'') \approx \delta(x' - x'') \int w(x)dx. \tag{6.103}$$

The substitution of (6.103) into (6.102) shows that the root mean square deformation $\langle \epsilon_{ik}\epsilon_{jl}\rangle^{(\text{uncorr})}$ calculated in non-correlated approximation (6.98) is related to the one with correlations $\langle \epsilon_{ik}\epsilon_{jl}\rangle^{(\text{corr})}$ given by (6.102) as:

$$\langle \epsilon_{ik}\epsilon_{jl}\rangle^{(\text{corr})} = r\langle \epsilon_{ik}\epsilon_{jl}\rangle^{(\text{uncorr})}, \tag{6.104}$$

$$r = 1 + \rho \int w(x)dx. \tag{6.105}$$

The parameter r has a physical meaning when the dislocations on a large area are considered: r is a ratio of the dispersion of dislocations number to their average number [22, 33]:

$$r = \frac{\mathbf{M}(N - \mathbf{M}N)^2}{\mathbf{M}N}. \tag{6.106}$$

The pair density of distribution function $p(x_1, x_2)$ is derived from (6.17):

$$p(x_1, x_2) = \rho\delta(x_1 - x_2) + \rho^2(1 + w(x_1 - x_2)), \tag{6.107}$$

and for the average values on the interval L we obtain:

$$\mathbf{M}N = \rho L, \tag{6.108}$$

$$\mathbf{M}N^2 = \int_{-L/2}^{L/2} dx_1 \int_{-L/2}^{L/2} dx_2\, p(x_1, x_2) = \rho L + \rho^2 L^2 + \rho L \int w(x)dx.$$

Substituting (6.108) into (6.106), the expression (6.105) is obtained, and for non-correlating dislocations $r = 1$. Provided the probability to find a dislocation in a node doesn't depend on other dislocations, the number of dislocations on fixed interval is determined by Poisson distribution, for which dispersion equals to average value and according to (6.106) $r = 1$. In the presence of correlations, the dispersion of dislocations number decreases and $r < 1$, and the width of the X-ray diffuse peak $\sqrt{r\rho/d}$ becomes more narrow. Using the definition (6.105), the decrease of r can also be explained: the correlation function for small values of x is negative (two dislocations placed face to face are un-probable), and with the increase of x it tends to zero, which result in a negative value of integral. The detailed review of the influence of correlation function on the shape of X-ray peak is presented in [3, 35]. In the limiting case of periodical arrangement of dislocations typical for the heterostructures with large value of lattice misfit, the parameter r tends to zero. In this case, the approximation (6.103) is invalid and all terms in (6.21) have to be considered. The calculation of correlation function from the displacement field of the entire array of dislocations [5] is a proper method in this situation. The periodicity of the displacement fields causes the satellite peaks around Bragg peak and due to

finite value of Debye-Waller factor the coherent contribution should be taken into account. The detailed analysis and the experimental results for this case can be found in [3, 37].

6.4.2 Parallel Edge Dislocations in Graded Layers

One of the mechanism to reduce the density of parasitic threading dislocations in the growth of heterostructures possessing essential misfits, is a creation of intermediate layer called a virtual substrate. This layer is composed of the solid solution with graded concentration of dopant through the layer depth. As a result, the dislocations appear within the entire thickness of the layer and glide less interacting each with other [31, 38].

The relaxation of graded epitaxial films occurs in the same way as in the case of abrupt boundary between the materials with large misfit by creation of misfit dislocations parallel to the interface. In this growth mode, the dislocations are characterized by areal dislocation density, in opposite to linear dislocation density used in previous section. The areal dislocation density is the number of dislocation lines per unit area in the plane perpendicular to the dislocation lines. For a (001) oriented cubic crystal, there are two orthogonal sets of parallel dislocation lines, whose directions we take as x and y axes. For each set of dislocations, the density is,

$$\rho(z) = \frac{1}{b_x a_x(z)} \frac{da_x(z)}{dz}, \tag{6.109}$$

where $a_x(z)$ is the lattice spacing in the plane of interface in the direction perpendicular to the dislocation line, and b_x is the Burgers vector component that provides the relaxation. Here the z axis is along the normal to the plane of the interface. For typical gradient layers, e.g. virtual substrates, the dimensionless parameter ρd^2, where d is the layer thickness, varies between 10^1 and 10^3. The static Debye-Waller factor $e^{-\rho d^2}$ is negligibly small and the dynamical X-ray scattering effects can be neglected. Thus, we can restrict ourselves by kinematical theory. The relaxation of the graded epitaxial films can also be characterized by the relaxation parameter $R(z)$ defined with respect to the substrate and the analogue of (6.90) is:

$$R(z) = \frac{a_x(z) - a_x^{(s)}}{a_x^{(0)}(z) - a_x^{(s)}}, \tag{6.110}$$

where $a_x^{(s)}$ is the substrate lateral lattice parameter, $a_x^{(0)}(z)$ is the lateral lattice parameter which the film would have if at depth z it were completely relaxed. The value $a_x^{(0)}(z)$ for a two-component solid solution alloy $A_x B_{1-x}$ can be found from concentration $c(z)$ at depth z, e.g. using Vegard's law: $a_x^{(0)}(z) = c(z)a_A + [1 - c(z)]a_B$. In this case it follows from (6.109) that dislocation density, relaxation and concentration

profiles are connected analogously to (6.91) by

$$R(z) = \frac{b_x \int_0^z \rho(z')dz'}{\epsilon\, c(z)}, \tag{6.111}$$

where $\epsilon = (a_A - a_B)/a_B$ is the crystal lattice mismatch between materials A and B and. The difference of the lattice parameters a_A and a_B is assumed here to be small, $\epsilon \ll 1$.

The displacement of atoms from their positions in ideal periodic lattice taken as a reference consists of two contributions. One is the displacement with respect to the substrate in a fully pseudomorphic layer. For the two-component solid solution alloy $A_x B_{1-x}$, the displacement gradient is proportional to the concentration $c(z)$ of the component A and can be written, using Vegard's law and assuming isotropic elasticity, as [39]

$$du_z^{\mathrm{p}}(z)/dz = \frac{1+\nu}{1-\nu}\epsilon\, c(z), \tag{6.112}$$

where ν is the Poisson ratio. The z-component (6.112) is the only non-zero component of the displacement $\mathbf{u}^{\mathrm{p}}$.

The other contribution to the displacement is due to displacement fields of the misfit dislocations. The correlation function g in the approximation of non-correlated dislocations (6.61) is then written as:

$$g(x, z_1, z_2) = \exp[T(x, z_1, z_2)], \tag{6.113}$$

where

$$T(x, z_1, z_2) = \int_0^d dz' \rho(z') \tau(x, z_1, z_2, z') \tag{6.114}$$

and

$$\tau(x, z_1, z_2, z') = \int_{-\infty}^{\infty} dx' (e^{i\boldsymbol{H}\cdot[\boldsymbol{u}(x'+x, z_2; z') - \mathbf{u}(x', z_1; z')]} - 1). \tag{6.115}$$

Despite of the large value of the parameter ρd^2, the direct usage of approximation (6.96) leads to the divergent expressions. In the framework of formula (6.96), the imaginary part of the function $\tau(x, z_1, z_2, z')$ is linear over x and ζ and describes the deformation (6.63):

$$\begin{aligned} &\operatorname{Im} \tau(x, z_1, z_2, z') \\ &= \int_{-\infty}^{\infty} dx' \boldsymbol{H} \cdot \left[\frac{\partial \boldsymbol{u}(x', z_1; z')}{\partial x'} x + \frac{\partial \boldsymbol{u}(x', z_1; z')}{\partial z_1} \zeta \right], \end{aligned} \tag{6.116}$$

and leads to shift of the peak center according to the average strain of the layer lattice, while the real part describing the root mean square deformation (6.63) is quadratic over these distances:

$$\begin{aligned}&\operatorname{Re}\tau^{(2)}(x, z_1, z_2, z')\\&= -\left[w_{11}x^2 + 2w_{12}x\zeta + w_{22}\zeta^2\right].\end{aligned} \tag{6.117}$$

Here it is denoted

$$w_{11}(z, z') = \frac{1}{2}\int_{-\infty}^{\infty} dx' \left(\boldsymbol{H}\cdot\frac{\partial \mathbf{u}(x', z; z')}{\partial x'}\right)^2, \tag{6.118}$$

the functions $w_{12}(z, z')$ and $w_{22}(z, z')$ are defined similarly by making derivatives over z instead of the derivatives over x'. The quadratic form of the real part of T in the case of uniform relaxed layers leads to anisotropic Gaussian shape (6.100) of diffracted peak with the minor axis parallel to the diffraction vector $\boldsymbol{H}$. The real part Re τ is denoted in (6.117) as Re $\tau^{(2)}$ to indicate the expansion quadratic over x and ζ.

The expansions (6.116) and (6.117) are accurate enough to calculate the X-ray diffraction peaks from uniform relaxed films with misfit dislocations located at the interface. However, for dislocations distributed in the film we find that the coefficients $w_{ij}(z, z')$ (here $i, j = 1, 2$) diverge at $z' \to z$ as $w_{ij}(z, z') \propto \left|z - z'\right|^{-1}$, see (6.99). As a result, this approximation leads to an erroneous divergence of the integral (6.114), while in an accurate calculation the integral converges. The same problem arose for uniformly distributed dislocations in Ref. [40]. In this latter case the contribution to the correlation function from small separations was estimated and used to re-normalize the contribution from the upper limit of the integral. Since this upper limit was an ill-defined crystallite size, its change was not important, see below. In the present case, however, the contribution from the lower limit is essential and the upper limit is a well-defined film thickness.

The singularity of the function $w_{ij}(z, z')$ at $z' \to z$ appears since the expansion (6.117) becomes invalid. In the limit $z' \to z$, numerical calculations show that the real part Re $\tau(x, z_1, z_2, z')$ is well approximated by the expression

$$\begin{aligned}&\operatorname{Re}\tau^{(1)}(x, z_1, z_2, z')\\&\approx \sqrt{x^2 + \zeta^2}[a_0 + a_1\cos(2\phi) + a_2\sin(2\phi)],\end{aligned} \tag{6.119}$$

where $\phi = \arctan(\zeta/x)$ and the coefficients $a_i(z, z')$ $(i = 1, 2, 3)$ remain finite at $z' \to z$ and decrease as the distance $\left|z - z'\right|$ increases. Re τ is denoted in this approximation as Re $\tau^{(1)}$, to indicate that it is linear over $\sqrt{x^2 + \zeta^2}$.

One of the methods to determine the values $a_i(z, z')$, $w_{ij}(z, z')$ is to numerically calculate the function of four arguments $\tau(x, z_1, z_2, z')$ and to fit its real part to the sum Re $(\tau^{(1)} + \tau^{(2)})$ given by Eqs. (6.119) and (6.117) [41]. The result of the fit is three functions $w_{ij}(z, z')(i, j = 1, 2)$ and three functions $a_i(z, z')(i = 1, 2, 3)$. w_{ij} decrease to zero at $z' \to z$, while a_i are maximal in this limit and decrease when the distance $\left|z - z'\right|$ increases.

The imaginary part $\mathrm{Im}\,\tau(x, z_1, z_2, z')$ is well approximated by Eq. (6.116), and the integrals can be calculated analytically, analogously to (6.96):

$$\mathrm{Im}\,\tau(x, z_1, z_2, z') \approx -i\left[\delta\widetilde{q}_x(z, z')x + \delta\widetilde{q}_z(z, z')\zeta\right], \tag{6.120}$$

where

$$\begin{aligned}\delta\widetilde{q}_x(z, z') &= H_x b_x H(z - z'),\\ \delta\widetilde{q}_z(z, z') &= -\frac{2\nu}{1-\nu} H_z b_x H(z - z').\end{aligned} \tag{6.121}$$

The accuracy of this approximation increases with the decreasing x and ζ.

We now substitute (6.120) and (6.121) into (6.114), and combine the result with (6.112), to obtain the wave vectors defining the local peak position,

$$\begin{aligned}\widetilde{q}_x(z) &= Q_x b_x \int_0^z dz'\rho(z'),\\ \widetilde{q}_z(z) &= -\frac{2\nu}{1-\nu} Q_z b_x \int_0^z dz'\rho(z') - Q_z \frac{1+\nu}{1-\nu}\epsilon\, c(z).\end{aligned} \tag{6.122}$$

Finally, collecting the equations above, we can represent the X-ray scattering intensity as

$$\begin{aligned}I(q_x, q_z) = \int_0^d dz \iint_{-\infty}^{\infty} dx\, d\zeta e^{i\{[q_x - \widetilde{q}_x(z)]x + [q_z - \widetilde{q}_z(z)]\zeta\}}\\ \times \exp\left[\int_0^d dz'\rho(z')\,\mathrm{Re}\,\tau(x, z, \zeta, z')\right],\end{aligned} \tag{6.123}$$

where, in the approximation that we described above, $\mathrm{Re}\,\tau = \mathrm{Re}\,(\tau^{(1)} + \tau^{(2)})$, the two contributions are given by Eqs. (6.119) and (6.117), and we write their arguments as z, ζ instead of $z_1 = z$ and $z_2 = z + \zeta$.

High-resolution X-ray diffraction is a standard tool to measure the relaxation in epitaxial films. For uniform layers, a comparison of the diffraction peak positions on the reciprocal space maps (RSMs) taken in a symmetric and in an asymmetric reflection provides the lattice parameter of the film and the degree of relaxation [41–43]. The problem becomes more complicated for layers containing the lattice parameter gradients due to concentration variations. Instead of separate peaks from uniform layers on the RSMs, one observes in the graded layers a continuous intensity distribution. The work [41] demonstrates the determination of the concentration and the dislocation density profiles from RSMs of graded epitaxial films without assuming any relations between these profiles and using the RSM intensity distributions only.

The scans of constant q_x of the intensity distribution $I(q_x, q_z)$ on a RSM usually have well defined maxima (see Fig. 6.10), whose positions we denote as $q_{z\,\max}(q_x)$. Equation (6.122) approximately give, in the parametric form, the line $q_{z\,\max}(q_x)$. The

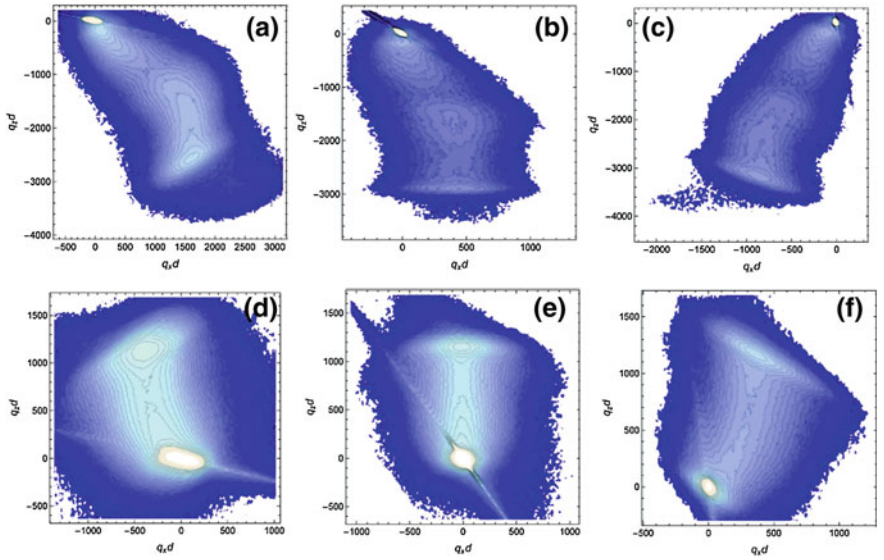

Fig. 6.9 Experimental reciprocal space maps from the sample containing graded $In_xGa_{1-x}As$ layer for 224^- (**a**), 004 (**b**), 224^+ (**c**) Bragg reflections and from the sample containing graded $GaAs_{1-x}P_x$ layer for 224^- (**d**), 004 (**e**), 224^+ (**f**) Bragg reflections

fitting of the experimental RSMs can be simplified by defining this line on the experimental map and substituting corresponding values $q_{z\,\max}$, $q_{x\,\max}$ instead of $\widetilde{q}_z$, $\widetilde{q}_x$ into (6.122). Then, combining the two equations (6.122), one can directly express $c(z)$ through $q_{z\,\max}$, $q_{x\,\max}$. The value of z is obtained, in the current approximation for the dislocation density $\rho(z)$, by numerically solving the first Eq. (6.122). We denote by z^* this value of z. That allows us to reduce the search from two unknown functions, $c(z)$ and $\rho(z)$, to the search of just one unknown function.

We can also make a rough estimate of the intensity $I\,(q_{z\,\max},\ q_{x\,\max})$. Let us assume that the most essential contribution into diffraction intensity when integrating (6.123) over dz is given by a small vicinity of the point z^*. This assumption works better as the dislocation density increases and the integrand, as a function of z, becomes a sharp peaked function. Then, we can write

$$\begin{aligned}
&\int_0^d dz\, e^{i\{[q_x-\widetilde{q}_x(z)]x+[q_z-\widetilde{q}_z(z)]\zeta\}} \\
&\approx \int_0^\infty dz\, \exp\left\{ i\left(\frac{d\widetilde{q}_x(z)}{dz}x+\frac{d\widetilde{q}_z(z)}{dz}\zeta\right)(z-z^*)\right\} \\
&\approx 2\pi\delta\left(\frac{d\widetilde{q}_x(z)}{dz}x+\frac{d\widetilde{q}_z(z)}{dz}\zeta\right).
\end{aligned} \tag{6.124}$$

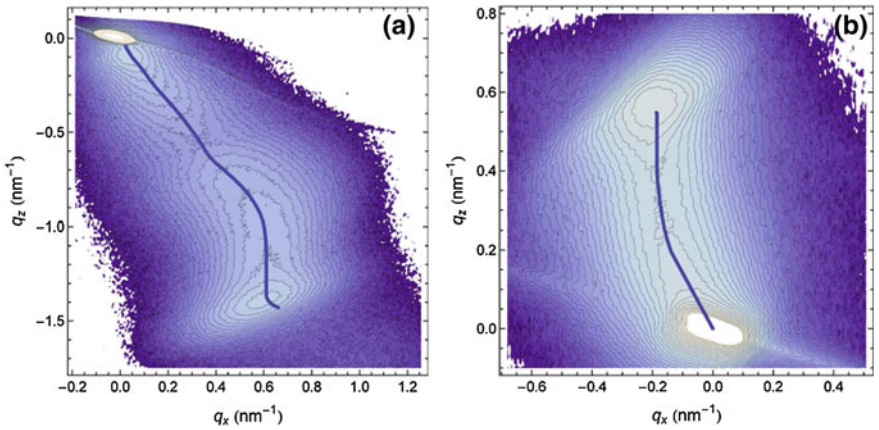

Fig. 6.10 Example of reciprocal space maps from graded samples, **a** $In_xGa_{1-x}As/GaAs$ and **b** $GaAs_{1-x}P_x/GaAs$, (224) reflection [41]. The blue line shows the positions of local maxima $q_{x\,\max}(q_{z\,\max})$ used for linking profiles $c(z)$ and $\rho(z)$ during data fitting procedure [see Eq. (6.122) and subsequent discussion]

In this approximation, the integration over $dx\,d\zeta$ is reduced to the one-dimensional integration in the direction normal to the line $q_{x\max}(q_{z\max})$. If we make further severe approximation, assuming that w_{ij} and a_i are constants, we arrive at a notably simple relation

$$I(q_{x\max}, q_{z\max}) \propto 1 \Big/ \frac{d\widetilde{q}_z(z^*)}{dz} \propto 1/\rho(z^*). \tag{6.125}$$

Qualitatively, Eq. (6.125) states that, the smaller is the dislocation density, the larger is the thickness of a sublayer contributing to diffraction intensity. However, Eq. (6.125) only qualitatively describes the experimental data, and can be used to obtain the first approximation for further fit of the dislocation density profile. By performing the comprehensive fitting of reciprocal space maps based on (6.123), the depth profile of the dislocation density can be obtained (Fig. 6.11).

Another example of the application of experimental HRXRD method and successful theoretical interpretation of measured reciprocal space maps (Fig. 6.12) is reported in [42] for three samples grown on different substrates and therefore possessing different relaxation status and dislocation structure. Three reverse-graded $Si_{0.2}Ge_{0.8}$ relaxed buffers were grown on (001), (011) and (111) silicon substrates (see detailed design of the samples in [42]). The measured and simulated on the basis of the presented in this section theory maps demonstrate a good agreement and prove the validity of the evaluation approach.

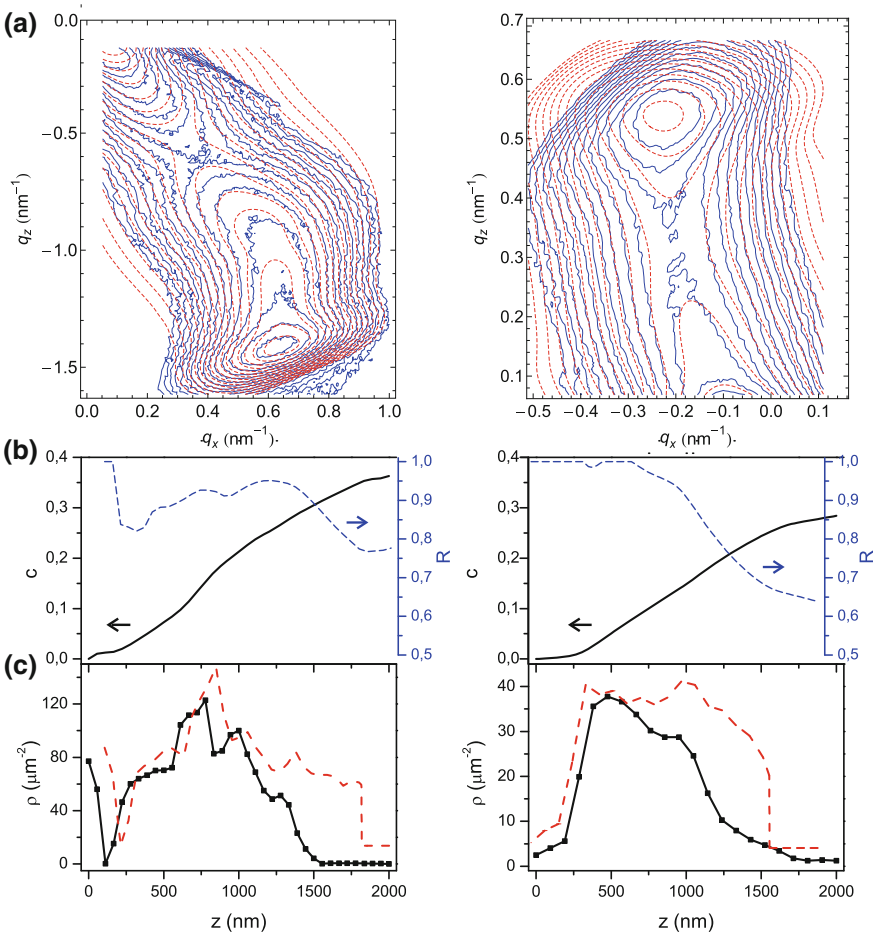

Fig. 6.11 Results of fitting of reciprocal space maps for sample $In_xGa_{1-x}As/GaAs$ (*left*) and sample $GaAs_{1-x}P_x/GaAs$ (*right*) [41]. **a** Contour plots of experimentally recorded (*blue solid lines*) and fitted (*red dashed lines*) intensity distribution from reflection 224^-. The step of iso-intensity contours is $10^{0.1}$. **b** Concentration and relaxation depth profiles. **c** The fitted misfit dislocation density (*full line*), black squares denote points $\rho(z_i)$ which were used for fitting. The *dashed line* corresponds to dislocation distribution according to model [44, 45]

6.4.3 Parallel Dislocations Lines Perpendicular to Sample Surface

The model of parallel dislocations lines, which lie perpendicular to the surface describes the threading dislocations penetrating heteroepitaxial structure and have the dislocation lines perpendicular to the interfaces of heteroepitaxial layers and sample surface. The density of threading dislocations influences essentially the functional properties of electronic devices built of semiconductor heterostructures. The typical

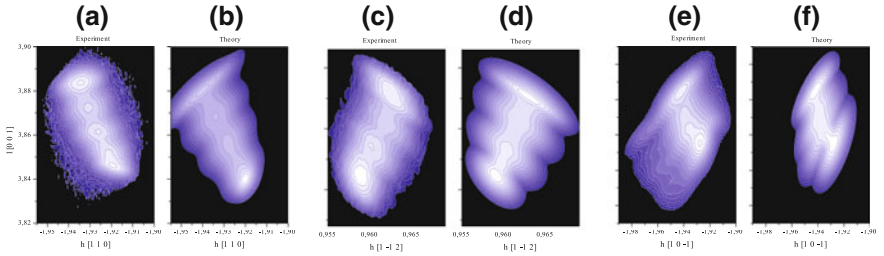

Fig. 6.12 Experimental and simulated reciprocal space maps (**a**, **b**) $(224)^-$ in grazing-incidence angle geometry for the (001) sample; (**c**, **d**) $(224)^+$ in grazing-exit angle geometry for the (011) sample; (**e**, **f**) $(135)^-$ in grazing-incidence angle geometry for the (111) sample

example is III-nitrides (AlN, GaN and InN), for study of which the X-ray diffraction is widely used [46, 47].

This model is also applicable to the description of dislocations inside the crystallites of polycrystalline materials. The real distribution of dislocations in polycrystals is sophisticated: the dislocation lines are distorted, collected into groups near the crystal walls, the size of crystallites fluctuates, etc. The analysis of the diffraction line profile based on the above model is nevertheless very effective [20, 21]. The accurate analysis of used approximations and the comparison with numerical Monte-Carlo simulations has been presented in [36], and below we use the results of this work.

The essential feature of all the above-mentioned systems is a correlation of the dislocation positions formed during the movement of the dislocations, which tend to reduce a full elastic energy [48]. To determine the correlation function, the terms T_1 and T_2 in (6.21) have to be taken into consideration. The polycrystalline samples differ from semiconductor epitaxial structures with defined thicknesses by existing distribution of crystallites over the shape and size. Due to this fact, the displacement fields in infinite media are utilized in further theoretical calculations. In the correlation function, the dislocations with various directions of Burgers vector have to be taken into account. For example, for screw dislocations there are two Burgers vectors $\pm b_z$, which result in the displacement fields of the opposite signs. The modeling of the dynamics of dislocations [48] demonstrates the tendency to correlation for the dislocations of opposite signs to reduce the elastic energy and thus to create so-called dipoles. The fact of the compensation of the displacement fields by the dislocations of opposite signs is used in a restrictedly random distribution proposed by Wilkens and widely used in a line profile analysis [49]. As a result, we obtain using (6.21):

$$
\begin{aligned}
&g(\boldsymbol{r}) = e^{T_1(\boldsymbol{r})+T_2(\boldsymbol{r})} \\
&T_1(\boldsymbol{r}) = -\frac{1}{2}\sum_{\alpha}\rho_\alpha H_k H_l \int d^2\boldsymbol{r}' \frac{\partial u_k(\boldsymbol{r}')^{(\alpha)}}{\partial x_i}\frac{\partial u_l(\boldsymbol{r}')^{(\alpha)}}{\partial x_j} x_i x_j \\
&T_2(\boldsymbol{r}) = -\frac{1}{2}\sum_{\alpha,\beta}\rho_\alpha\rho_\beta H_k H_l \int\int d^2\boldsymbol{r}' d^2\boldsymbol{r}'' \frac{\partial u_k(\boldsymbol{r}')^{(\alpha)}}{\partial x_i}\frac{\partial u_l(\boldsymbol{r}'')^{(\beta)}}{\partial x_j} w_{\alpha\beta}(\boldsymbol{r}'-\boldsymbol{r}'') x_i x_j, \\
&i, j = 1, 2 \; k, l = 1, 2, 3
\end{aligned}
\tag{6.126}
$$

where α and β means the type of dislocation (Burgers vector) and integration is performed in XY plane. We assume here that the system is uniform and correlation function depends solely on difference $\boldsymbol{r}$. The imaginary part of T_1 is eliminated due to compensation of average deformations caused by the dislocations of the opposite signs. The density of dislocations is supposed to be high enough and thus the expansions (6.96) and (6.63) have been utilized. To complete the integration in T_1, the polar coordinates are used, where the derivatives of the displacement fields are written as in (6.3):

$$\frac{\partial u_k(\boldsymbol{r}')^{(\alpha)}}{\partial x_i} = \frac{v(\phi)_{ki}^{(\alpha)}}{r'}, \tag{6.127}$$

where the tensor $v(\phi)_{ki}^{(\alpha)}$ depends on the dislocation type, and finally:

$$T_1(\boldsymbol{r}) = -\frac{1}{2}\sum_{\alpha}\rho_\alpha H_k H_l n_i n_j r^2 \int_0^{2\pi} d\phi v(\phi)_{ki}^{(\alpha)} v(\phi)_{lj}^{(\alpha)} \int_0^{\infty} \frac{dr'}{r'}. \tag{6.128}$$

Here $\boldsymbol{n}$ is a unit vector in direction $\boldsymbol{r}$, and in the expression (6.128), the integral over r' diverges both on upper and lower limits. The divergence on the upper limit is conditioned by the size of crystallite L, which varies for different crystals and depends on the shape of crystallite. The divergence on the lower limit is related to the approximation (6.96) and to the expansion of exponent. Because of the upper limit L is badly defined, we can use for the lower limit the distance r_m, below which the expansion of the exponent is invalid:

$$\boldsymbol{H}(\boldsymbol{u}(\boldsymbol{r}_1 - \boldsymbol{r}_m) - \boldsymbol{u}(\boldsymbol{r}_2; \boldsymbol{r}_m)) \sim Hvr/r_m \sim Hbr/r_m \sim 1,$$

and for T_1:

$$T_1(\boldsymbol{r}) = -\frac{1}{2}\sum_{\alpha}\rho_\alpha G_{klij} E_{klij}^{(\alpha)} r^2 \ln\frac{L}{Hbr}, \quad G_{klij} = H_k H_l n_i n_j,$$
$$E_{klij}^{(\alpha)} = \int_0^{2\pi} d\phi v(\phi)_{ki}^{(\alpha)} v(\phi)_{lj}^{(\alpha)}, \tag{6.129}$$

where in accordance with line profile analysis, the geometrical G and elastic E terms are distinguished.

To calculate T_2 in (6.126) with the same accuracy, the approximation (6.103) is used, which leads to the integral similar to (6.128). As a lower integration limit, the distance can be used where the approximation (6.103) fails: the characteristic radius R_c of the correlation function $w_{\alpha\beta}$. For correlation function, the following expression is obtained:

$$T_1(\boldsymbol{r}) + T_2(\boldsymbol{r}) =$$
$$-\frac{1}{2}G_{klij}r^2\left(\ln\frac{L}{Hbr}\sum_{\alpha}E^{\alpha}_{klij}\rho_{\alpha} + \ln\frac{L}{R_c}\sum_{\alpha,\beta}\rho_{\alpha}\rho_{\beta}E^{\alpha\beta}_{klij}\int d\boldsymbol{r}' w_{\alpha\beta}(\boldsymbol{r}')\right),$$
$$E^{(\alpha\beta)}_{klij} = \int_0^{2\pi} d\phi v(\phi)^{(\alpha)}_{ki} v(\phi)^{(\beta)}_{lj}. \tag{6.130}$$

This formula doesn't depend on the size L if the multipliers at logarithms in (6.130) are compensated, which is equivalent to the existance of dislocations with opposite Burgers vectors in pairs [36]. Let us consider the screw dislocations $\alpha, \beta = +b, -b$ assuming the equal densities of dislocations of opposite sign $\rho_{+b} = \rho_{-b} = \rho/2$, where ρ is a full density, and the absence of correlations between dislocations of the same sign $w_{+b+b} = w_{-b-b} = 0$. To satisfy the compensation condition, the following equation has to be fulfilled:

$$\frac{\rho}{2}\int d\boldsymbol{r}' w_{+b-b}(\boldsymbol{r}') = 1, \tag{6.131}$$

here the equalities $E^{+b-b}_{klij} = -E^{+b+b}_{klij} = -E^{-b-b}_{klij} = -E_{klij}$ are used. By the definition of correlation function, the formula (6.131) means the probability to find a dislocation of the opposite sign at arbitrary distance from the original dislocation equals unity, or alternatively, the dislocations with the opposite signs create the pairs. In this assumption, the equation is obtained:

$$g(\boldsymbol{r}) = e^{-\frac{1}{2}\rho G_{klij}E_{klij}r^2\ln\frac{R_c}{Hbr}}. \tag{6.132}$$

To apply this expression for correlation function to line profile analysis, the experimental conditions have to be accurately considered. In X-ray diffraction experiments, the crystallites of various spatial orientations are irradiated and contribute to the detected intensity $I_m(\boldsymbol{q})$:

$$I_m(\boldsymbol{q}) = \int d^3\boldsymbol{g}\, f(\boldsymbol{g}) I_{\mathrm{cr}}(\hat{T}(\boldsymbol{g})\cdot\boldsymbol{q}_{\mathrm{cr}}), \tag{6.133}$$

where $\boldsymbol{g}$ means formally the orientation of crystallites (for example, three Euler's angles), $f(\boldsymbol{g})$ is the orientational distribution function (the portion of crystallites with orientation $\boldsymbol{g}$), $\hat{T}(\boldsymbol{g})$ is a rotation matrix corresponding to orientation $\boldsymbol{g}$, $I_{\mathrm{cr}}(\boldsymbol{q})$ is an X-ray intensity diffracted by a single crystallite (all crystallites are assumed to be identical), and $\boldsymbol{q}_{\mathrm{cr}}$ is defined in a coordinate system of a crystallite, details see in Chap. 7. The distribution of X-ray intensity $I_{\mathrm{cr}}(\hat{T}(\boldsymbol{g})\cdot\boldsymbol{q}_{\mathrm{cr}})$ decays rapidly with change of orientation and the value $f(\boldsymbol{g})$ can be fixed to constant within the diffraction peak area. Thus, the integration of (6.133) is equivalent to integration of $I_{\mathrm{cr}}(\boldsymbol{q})$ over the sphere in reciprocal space with the radius equal to the module of wave vector transfer (Fig. 6.13a).

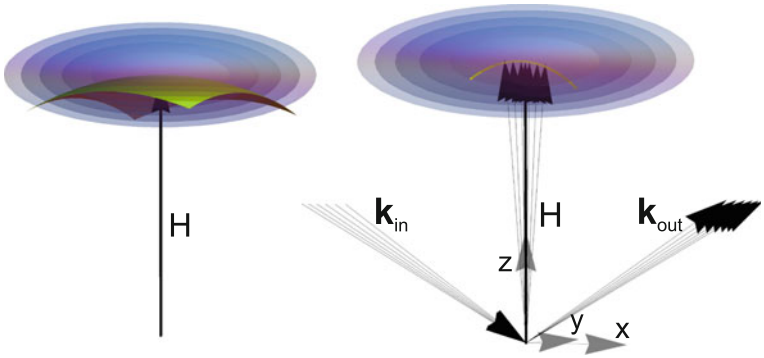

Fig. 6.13 The physical principles of X-ray diffraction measurements from polycrystalline materials (**a**) and coherent epitaxial structures (**b**)

If the peak width is small, the sphere can be replaced by plane (tangential plane approximation, [50]) and for X-ray intensity we obtain:

$$I(\boldsymbol{Q}) = I(|\boldsymbol{Q}|) = \int d^3\boldsymbol{r} \int dq_x dq_y e^{i\boldsymbol{qr}} g(\boldsymbol{r}) = \\ = \int dz e^{iq_z z} g(x=0, y=0, z);\ \boldsymbol{Q} = \boldsymbol{H} + \boldsymbol{q}, \tag{6.134}$$

here z-direction is along $\boldsymbol{H}$. Thus, for line profile analysis, the one-dimensional correlation function is required:

$$g(z) = e^{-\frac{1}{2}\rho H^2 G^{(p)}_{klij} E_{klij} z^2 \ln \frac{R_c}{Hbz}},\ G^{(p)}_{klij} = \frac{H_k H_l H_i H_j}{H^4}. \tag{6.135}$$

To calculate the integral (6.134), the integration area $z > R_c/Hb$ has to be included where the logarithm is negative and the integral diverges. This area doesn't fulfill the assumption $r \ll L$, R_c made for derivation of (6.132) and the correlation function drops down rapidly at these conditions. Therefore, for large values of r the modification of logarithmic term is necessary. The function $f(z)$ has to tend to $\ln \frac{R_c}{Hbz}$ for small z, to be positive and to tend to zero at large z. For restrictedly random distribution, the proper expression has been proposed by Wilkens [51], which is bulky and unclear, however, is frequently used in literature. The works [36, 46] introduced a simple function satisfying all above mentioned requirements:

$$f(z) = \ln \frac{R_c + Hbz}{Hbz}. \tag{6.136}$$

The correlation radius R_c can be represented as $M/\sqrt{\rho}$, where M is called a correlation radius measured in the units of average distance between dislocations. The

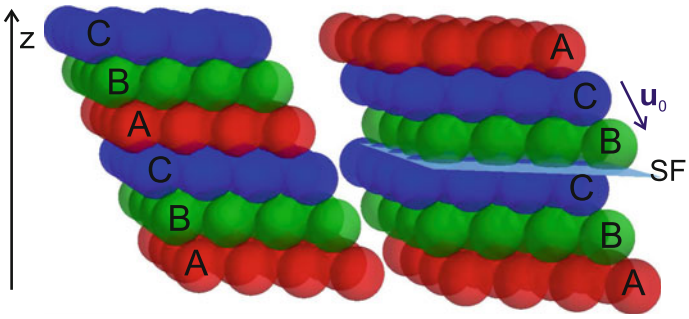

Fig. 6.14 Deformation stacking faults in fcc materials. The axis z is along $< 111 >$

parameter $C \sim G^{(p)}_{klij} E_{klij}$ is called a dislocation contrast factor and it depends both on the dislocation type and Bragg reflection. This dependence permits to identify the dislocations type and density [20] and correlation radius M using several Bragg reflections data [52].

6.5 Two-Dimensional Defects (Stacking Faults)

Stacking faults are the two-dimensional defects observed in crystalline [47] and polycrystalline [53] materials and influencing their mechanical and electrical properties. The X-ray diffraction methods are sensitive to this type of defects and characterize them comprehensively [54, 55].

X-ray diffraction from crystalline structures containing stacking faults has been studied by Landau [56], Henricks and Teller [57], and further in the work [50, 58–61] and other. For the numerical data evaluation, several programs have been developed including DIFFaX [62], which is used in other line profile analysis software [54, 63].

The example of deformation stacking faults in fcc material is shown in Fig. 6.14. To calculate the correlation function and Debye-Waller factor, the displacement fields created by a single defect have to be determined. In opposite to the defects considered in the previous sections, the displacement fields of the stacking faults are found from the geometrical consideration and not from the equations of the elasticity theory (6.84). Particularly, the presence of the defect in the point z leads to the shift of all upper layers by vector $\boldsymbol{u}_0$. The displacement field is then presented as:

$$\boldsymbol{u}(z, z') = \boldsymbol{u}_0 H(z - z'). \tag{6.137}$$

Assuming the positions of stacking faults non-correlated, the Debye-Waller factor is determined from (6.11):

$$e^W = e^{\int_{-\infty}^{\infty} dz\rho(e^{i\boldsymbol{H}\boldsymbol{u}_0 H(z-z')}-1)} \sim e^{L_z\rho(e^{i\boldsymbol{H}\boldsymbol{u}_0}-1)} \sim e^{N_d(e^{i\boldsymbol{H}\boldsymbol{u}_0}-1)}, \quad (6.138)$$

here L_z is a characteristic size of the sample in stacking direction, ρ is a density of stacking faults and N_d is an average number of defects in the sample. The number of defects is assumed to be large enough to satisfy a statistical approximation on the defects ensemble. Therefore, the coherent scattering is absent unless the condition $\boldsymbol{H}\boldsymbol{u}_0 = 0$ is fulfilled. The expression for correlation function follows from (6.61):

$$g(z_1, z_2) = e^{\rho(e^{i\boldsymbol{H}\boldsymbol{u}_0 \frac{z_1-z_2}{|z_1-z_2|}}-1)|z_1-z_2|}. \quad (6.139)$$

Using (6.83) and geometrical consideration of defects, the scattered X-ray intensity is calculated as:

$$I(\boldsymbol{q}) = \delta(\boldsymbol{q}_{||}) \int_{-\infty}^{\infty} dz e^{iq_z z} g(z). \quad (6.140)$$

The factor $\delta(\boldsymbol{q}_{||})$ shows that the broadening of the diffraction peak occurs in the direction of stacking, and in perpendicular to this direction the presence of stacking faults is not evident from the diffraction data. In the case of fcc materials, see Fig. 6.14, the translation by vector $3\boldsymbol{u}_0$ is equal to the lattice period and $e^{3i\boldsymbol{H}\boldsymbol{u}_0} = 1$. This fact initiates three possibilities $e^{i\boldsymbol{H}\boldsymbol{u}_0} = 1, e^{2\pi i/3}, e^{-2\pi i/3}$, the realization of which depends on the Bragg reflection $\boldsymbol{H}$, see [53, 64] for details. For $e^{i\boldsymbol{H}\boldsymbol{u}_0} = 1$, the stacking faults don't influence the scattering process, which remains coherent. For $e^{i\boldsymbol{H}\boldsymbol{u}_0} = e^{\pm 2\pi i/3}$, using (6.140) and integrating with infinite limits, we obtain:

$$I(\boldsymbol{q}) = \delta(\boldsymbol{q}_{||}) \frac{w}{(q_z - q_0)^2 + w^2}, \quad q_0 = \pm\frac{\sqrt{3}}{2}\rho, \quad w = \frac{3}{2}\rho, \quad (6.141)$$

where the peak has a Lorentzian shape, q_0 is a peak shift and w is a peak width.

The approach presented above is based on the fact that stacking faults are described by the displacement field derived from the geometrical consideration. However, in many cases the appearance of stacking faults leads to the sequence of layers, which is not described by the displacement fields (6.137). Moreover, the expressions (6.11) and (6.61) are based on the assumption of low concentration of defects c, see Eq. (6.7). For some materials, the sequence of the layers is variable [65], which means the high concentration of stacking faults. In such a case, the stacking faults are described by the probability to observe a particular sequence of layers [57, 58, 60, 62].

The estimate for Debye-Waller factor (6.138) remains valid. For fluctuating potential V in (6.26), the scattering operator at each atomic layer $k_0^2\rho_i(\boldsymbol{r} - \boldsymbol{r}_i)\boldsymbol{A}(\boldsymbol{r}, t)$ is chosen and L_0 is a operator of propagation of X-rays in vacuum. The formula (6.61) in kinematic approximation is then transformed to:

$$I(Q_z) = \sum_{n=1}^{N} \sum_{n'=1}^{N} \left\langle f_n f_{n'}^* e^{i\,\boldsymbol{Q}(\boldsymbol{r}_n - \boldsymbol{r}'_n)} \right\rangle, \quad f_n = \int d^2\boldsymbol{r}_{||} \rho_n(\boldsymbol{r}_{||}) e^{i\,\boldsymbol{Q}\boldsymbol{r}_{||}}, \tag{6.142}$$

here f_n is a form factor of n-th layer, $\boldsymbol{r}_n$ is a location of n-th layer and N is a full number of layers.

The averaging in (6.142) is performed over all possible sequences of layers. This averaging is conveniently realized using Markov chains [65]. Let us assume that there are m types of layers, and the rule of stacking is determined by probabilities π_{ij} of the layer of type i to be followed by the layer of type j [62]. In the deformation faults in fcc shown in Fig. 6.14, there are three types of layers: A, B and C. Denoting by α the probability of stacking fault, the probability for layer A to be followed by layer A is zero, by layer B is $1-\alpha$, and by layer C is α. The matrix π_{ij} has a form:

$$\pi_{ij} = \begin{pmatrix} 0 & 1-\alpha & \alpha \\ \alpha & 0 & 1-\alpha \\ 1-\alpha & \alpha & 0 \end{pmatrix}. \tag{6.143}$$

In the absence of the correlation between the defects positions, the sequence of layers forms a Markov chain with probability matrix π_{ij}. The matrix π_{ij} has a property $\sum_j \pi_{ij} = 1$ (a stochastic matrix) which leads to the fact that one of the eigenvalues equals 1 and corresponding eigenvector σ_i obeys $\sum_i \sigma_i \pi_{ij} = \sigma_j$. This vector corresponds to the stationary state of Markov chain, the state which is obtained after a large enough number of steps. The probability $P_{s_1 s_2 \ldots s_n}$ to have a sequence of n layers where the first layer is in a given state s_1, the second is in state s_2,..., the n-th is in state s_n in a stationary chain is given by:

$$P_{s_1 s_2 \ldots s_n} = \sigma_{s_1} \pi_{s_1 s_2} \pi_{s_2 s_3} \ldots \pi_{s_{n-1} s_n}. \tag{6.144}$$

The averaging in (6.142) can be performed with help of (6.144):

$$\langle f_1 f_n^* e^{i\,\boldsymbol{Q}(\boldsymbol{r}_1 - \boldsymbol{r}_n)} \rangle \tag{6.145}$$

$$= \sum_{s_1=1\ldots m, \ldots, s_n=1\ldots m} P_{s_1 s_2 \ldots s_n} f_{s_1} e^{i\phi(n)} f_{s_n}^*$$

$$= \sum_{s_1, \ldots, s_n} P_{s_1 s_2 \ldots s_n} f_{s_1} e^{i(\phi_{s_1 s_2} + \phi_{s_2 s_3} + \ldots + \phi_{s_{n-1} s_n})} f_{s_n}^*$$

$$= \sum_{s_1, \ldots, s_n} \sigma_{s_1} f_{s_1} \pi_{s_1 s_2} e^{i\phi_{s_1 s_2}} \pi_{s_2 s_3} e^{i\phi_{s_2 s_3}} \ldots \pi_{s_{n-1} s_n} e^{i\phi_{s_{n-1} s_n}} f_{s_n}^*, \tag{6.146}$$

here $\phi(k) = i\,\boldsymbol{Q}\boldsymbol{r}_k$, $\phi_{ij} = i\,\boldsymbol{Q}_0 \boldsymbol{r}_{ij}$ is a phase gained by the scattered wave due to the sequence of layers $i-j$, $\boldsymbol{r}_{ij}$ is a stacking vector between layers of type i and j. Introducing the matrix $T_{ij} = \pi_{i\,j} e^{i\phi_{ij}}$ [62] the summation in (6.145) can be converted to matrix multiplication:

$$\langle f_1 f_n^* e^{i\boldsymbol{Q}(\boldsymbol{r}_1-\boldsymbol{r}_n)}\rangle = \sum_{i,j} \sigma_i f_i T_{ij}^{(n-1)} f_j. \tag{6.147}$$

The substitution of (6.147) into (6.142) and summing over n, n' in infinite limits results in:

$$I = g_i (1-T)_{ij}^{-1} f_j^* + c.c. - f_i^* f_i, \;\; g_i = \sigma_i F_i. \tag{6.148}$$

For simplicity, we consider the case when all $\boldsymbol{r}_{ij}$ have the same value in the stacking direction, thus T_{ij} is represented as:

$$T_{ij} = e^{2\pi i\, l} T_{ij}^{||}, \quad T_{ij}^{||} = \pi_{ij} e^{i\boldsymbol{Q}_{||}\cdot\boldsymbol{r}_{ij}}. \tag{6.149}$$

Here the variable Q_z is represented as $\frac{2\pi l}{d_\perp}$, where l means the Miller index in the direction z, the parameter $d_\perp$ is a crystallographic interplane distance along z. For the case of deformation fcc stacking T_{ij} has the form:

$$T_{ij} = \begin{pmatrix} 0 & e^{\frac{2i\pi}{3}}(1-\alpha) & e^{-\frac{2i\pi}{3}}\alpha \\ e^{-\frac{2i\pi}{3}}\alpha & 0 & e^{\frac{2i\pi}{3}}(1-\alpha) \\ e^{\frac{2i\pi}{3}}(1-\alpha) & e^{-\frac{2i\pi}{3}}\alpha & 0 \end{pmatrix}. \tag{6.150}$$

The intensity (6.148) can be expressed in an explicit way if eigensystem of (6.149) is introduced [60, 61]. The matrix (6.149) is in general not symmetric, hence it has different left and right eigenvectors and eigenvalues are the complex quantities:

$$\begin{aligned} T_{ij}^{||} e_j^{(R,\alpha)} &= v^{(\alpha)} e_j^{(R,\alpha)}, \\ e_i^{(L,\alpha)} T_{ij}^{||} &= v^{(\alpha)} e_i^{(L,\alpha)}, \\ v^{(\alpha)} &= |v^{(\alpha)}| e^{2\pi i \phi^{(\alpha)}}. \end{aligned} \tag{6.151}$$

Thus, the vectors $T_{ij}^{||}$ can be represented as:

$$T_{ij}^{||} = \sum_{\alpha=1}^{M} v^{(\alpha)} e_i^{(R,\alpha)} e_j^{(L,\alpha)}. \tag{6.152}$$

Taking into account the properties of eigenvectors, the inverse matrix $(1-T)_{ij}^{-1}$ is:

$$(1-T)_{ij}^{-1} = \sum_{\alpha=1}^{M} \frac{e_i^{(R,\alpha)} e_j^{(L,\alpha)}}{1 - |v^{(\alpha)}| e^{-2\pi i\,(l-\phi^{(\alpha)})}}, \tag{6.153}$$

and the substitution of (6.153) in (6.148) after some algebra results in:

$$I(l) = \sum_{\alpha=1}^{M} \left(w_{\text{sym}}^{(\alpha)} + w_{\text{asym}}^{(\alpha)} \frac{\sin(2\pi(l - \phi^{(\alpha)}))}{2\pi} \right) \times \text{Lor}\left(\frac{\sin(\pi(l - \phi^{(\alpha)}))}{\pi}, \gamma^{(\alpha)} \right), \tag{6.154}$$

here δ-function like dependence on $\boldsymbol{q}_{||}$ is hidden in form factors of layers and Lor (x, γ) is a Lorentz function:

$$\text{Lor}(x, \gamma) = \frac{\gamma}{\pi \left(\gamma^2 + x^2\right)}. \tag{6.155}$$

The weights for symmetric and asymmetric parts $w_{\text{sym}}^{(\alpha)}$, $w_{\text{asym}}^{(\alpha)}$ and Lorentzian width $\gamma^{(\alpha)}$ are:

$$w_{\text{sym}}^{(\alpha)} = \text{Re}(G_i^* e_i^{(R,\alpha)} e_j^{(L,\alpha)} F_j) \frac{|v^{(\alpha)}| + 1}{2\sqrt{|v^{(\alpha)}|}}, \tag{6.156}$$

$$w_{\text{asym}}^{(\alpha)} = \text{Im}(G_i^* e_i^{(R,\alpha)} e_j^{(L,\alpha)} F_j) \frac{2\pi\sqrt{|v^{(\alpha)}|}}{1 - |v^{(\alpha)}|},$$

$$\gamma^{(\alpha)} = \frac{1 - |v^{(\alpha)}|}{2\pi\sqrt{|v^{(\alpha)}|}}.$$

The sine functions in the Lorentzians can be expanded near integer l values:

$$I(l) = \sum_{\alpha=1}^{M} \sum_{l_0=-l_{max}}^{l_{max}} \left(w_{\text{sym}}^{(\alpha)} + w_{\text{asym}}^{(\alpha)} (l - l_0 - \phi^{(\alpha)}) \right) \text{Lor}(l - l_0 - \phi^{(\alpha)}, \gamma^{(\alpha)}). \tag{6.157}$$

Thus, using the physical approach described in this section, the shape of the diffraction peak in Bragg reflection l is a sum of the symmetric and asymmetric Lorentz functions, which is in agreement with experimental data [54].

References

1. I. Robinson, R. Harder, Coherent x-ray diffraction imaging of strain at the nanoscale. Nat. Mater. **8**, 291–298 (2009)
2. B. Jakobsen, H.F. Poulsen, U. Lienert, J. Almer, S.D. Shastri, H.O. Sorensen, C. Gundlach, W. Pantleon, Formation and subdivision of deformation structures during plastic deformation. Sci. **312**(5775), 889–892 (2006)

3. Vladimir M. Kaganer, Karl K. Sabelfeld, X-ray diffraction peaks from partially ordered misfit dislocations. Phys. Rev. B **80**, 184105 (Nov 2009)
4. V. Holy, T. Baumbach, D. Lubbert, L. Helfen, M. Ellyan, P. Mikulik, S. Keller, S.P. DenBaars, J. Speck, Diffuse x-ray scattering from statistically inhomogeneous distributions of threading dislocations beyond the ergodic hypothesis. Phys. Rev. B **77**, 094102 (2008)
5. L.D. Landau, E.M. Lifshitz, *Theory of Elasticity*, vol 7, 3-rd edn, (Butterworth-Heinemann, Oxford, UK, 1986)
6. S. Timoshenko, J.N. Goodier, *Theory of elasticity*, 3-rd edn. (McGraw-Hill, New York, 1951)
7. M.A. Krivoglaz. *X-ray and neutron diffraction in nonideal crystals*, (Springer, Berlin, 1996)
8. V. Holy, J.H. Li, G. Bauer, F. Schaffler, H.-J. Herzog, Diffuse X-ray scattering from misfit dislocations in SiGe epitaxial layers with graded Ge content. J. Appl. Phys. **78**(8), 5013–5021 (1995)
9. B.E. Warren, X-ray studies of deformed metals. Prog. Met. Phys. **8**, 147–202 (1959)
10. Ryogo Kubo, *Statistical mechanics: an advanced course with problems and solutions* (Elsevier, Amsterdam, 1965)
11. R.P. Feynman, *Statistical Mechanics: A Set Of Lectures*, (Westview Press, 1998)
12. S. Takagi, J. Phys. Soc. Japan **26**, 1239 (1969)
13. A. Authier, *Dynamical Theory of X-ray Diffraction* (Oxford University Press, New York, 2001)
14. V. Holy, K.T. Gabrielyan, Dyson and Bethe-Salpeter equations for dynamical X-ray diffraction in crystals with randomly placed defects. Phys. Stat Solidi. **140**(1), 39–50 (1987)
15. L.A. Apresjan, J.A. Kravcov, Teorija perenosa izlučenija: Statističeskie i volnovye aspekty. Nauka, 1983.
16. A.N. Polyakov, F.N. Chukhovskii, D.I. Piskunov, Dynamic scattering of X-rays in disordered crystals: statistical theory. Zh. Eksp. Theor. Phys. **99**, 589–609 (1991)
17. Z.G. Pinsker *Dynamical Scattering of X-Rays in Crystals* (Springer, New York,1978)
18. M.A. Naimark, *Linear Differential Operators* (F. Ungar Pub. Co, New York, 1968)
19. H. Feshbach, P.M. Morse, *Methods of Theoretical Physics* (McGraw-Hill, New York, 1953)
20. T. Ungár, J. Gubicza, G. Ribárik, A. Borbély, Crystallite size distribution and dislocation structure determined by diffraction profile analysis: principles and practical application to cubic and hexagonal crystals. J. Appl. Crystallogr. **34**(3), 298–310 (2001)
21. M. Leoni, J. Martinez-Garcia, Paolo Scardi, Dislocation effects in powder diffraction. J. Appl. Crystallogr. **40**(4), 719–724 (Aug 2007)
22. V.M. Kaganer, R. Köhler, M. Schmidbauer, R. Opitz, B. Jenichen, X-ray diffraction peaks due to misfit dislocations in heteroepitaxial structures. Phys. Rev. B **55**, 1793–1810 (1997)
23. Jens Lothe, John Price Hirth, *Theory of Dislocations* (Krieger Pub. Co., New York, 1982)
24. S. Suresh L.B. Freund, *Thin Film Materials: Stress Defect Formation and Surface Evolution* (Cambridge University Press, Cambridge, 2004)
25. John E. Ayers, *Heteroepitaxy of Semiconductors: Theory, Growth, and Characterization* (Taylor and Francis, Boca Raton, FL, 2007)
26. K.P. Ryaboshapka, *Physics of X-ray Scattering from Deformed Crystals* (Navukova Dumka, Kiev, 1993)
27. J.D. Eshelby, W.T. Read, W. Shockley, Anisotropic elasticity with applications to dislocation theory. Acta Metall. **1**(3), 251–259 (1953)
28. A.N. Stroh, Dislocations and cracks in anisotropic elasticity. Phil. Mag. **3**(30), 625–646 (1958)
29. J. Martinez-Garcia, M. Leoni, P. Scardi, A general approach for determining the diffraction contrast factor of straight-line dislocations. Acta Crystallogr. A **65**(2), 109–119 (2009)
30. A.K. Head, Edge dislocations in inhomogeneous media. Proc. Phys. Soc. London, Sect. B **66**(9), 793 (1953)
31. B. Yu, Bolkhovityanov, L.V Sokolov, Ge-on-Si films obtained by epitaxial growing: edge dislocations and their participation in plastic relaxation. Semicond. Sci. Technol. **27**(4), 043001 (2012)
32. A. Benediktovitch, F. Rinaldi, S. Menzel, K. Saito, T. Ulyanenkova, T. Baumbach, I.D. Feranchuk, A. Ulyanenkov, Lattice tilt, concentration, and relaxation degree of partly relaxed InGaAs/GaAs structures. Phys. Status Solidi (a). **208**(11), 2539–2543 (2011)

33. Vladimir M. Kaganer, Karl K. Sabelfeld, Short range correlations of misfit dislocations in the X-ray diffraction peaks. Phys. Status Solidi (a). **208**(11), 2563–2566 (2011)
34. Péter Dusán Ispánovity, István Groma, Géza Györgyi, Evolution of the correlation functions in two-dimensional dislocation systems. Phys. Rev. B, **78**, 024119 (Jul 2008)
35. V.M. Kaganer, O. Brandt, H. Riechert, K.K. Sabelfeld, X-ray diffraction of epitaxial films with arbitrarily correlated dislocations: Monte Carlo calculation and experiment. Phys. Rev. B **80**, 033306 (2009)
36. V.M. Kaganer, K.K. Sabelfeld, X-ray diffraction peaks from correlated dislocations: Monte Carlo study of dislocation screening. Acta Crystallogr. A **66**(6), 703–716 (2010)
37. D.K. Satapathy, V.M. Kaganer, B. Jenichen, W. Braun, L. Daweritz, K.H. Ploog, Periodic array of misfit dislocations at the MnAsGaAs interface studied by synchrotron X-ray diffraction. Phys. Rev. B **72**, 155303 (Oct 2005)
38. B. Yu. Bolkhovityanov, O.P. Pchelyakov, S.I. Chikichev, Silicon germanium epilayers: physical fundamentals of growing strained and fully relaxed heterostructures. Phys. Usp. **44**(7), 655–680 (2001)
39. S. Danis, V. Holy, J. Stangl, G. Bauer, Diffuse X-ray scattering from graded sige/si layers. Europhys. Lett. **82**(6), 66004 (2008)
40. V.M. Kaganer, K.K. Sabelfeld, X-ray diffraction peaks from correlated dislocations: Monte Carlo study of dislocation screening. Acta Crystallogr. A **66**, 703–716 (2010)
41. A. Benediktovich, A. Ulyanenkov, F. Rinaldi, K. Saito, V. Kaganer, Concentration and relaxation depth profiles of $In_xGa_{1-x}As$/GaAs and $GaAs_{1-x}P_x$/GaAs graded epitaxial films studied by x-ray diffraction. Phys. Rev. B **84**, 035302 (2011)
42. A. Zhylik, A. Benediktovich, A. Ulyanenkov, H. Guerault, M. Myronov, A. Dobbie, D.R. Leadley, T. Ulyanenkova, High-resolution X-ray diffraction investigation of relaxation and dislocations in SiGe layers grown on (001), (011) and (111) Si substrates. J. Appl. Phys. **109**, 123714 (2011)
43. A. Zhylik, F. Rinaldi, M. Myronov, K. Saito, S. Menzel, A. Dobbie, D.R. Leadley, T. Ulyanenkova, I.D. Feranchuk, A. Ulyanenkov, High-resolution reciprocal space mapping of distributed bragg reflectors and virtual substrates. Phys. Status Solidi a. **208**, 2582–2586 (2011)
44. J. Tersoff, Dislocations and strain relief in compositionally graded layers. Appl. Phys. Lett. **62**(7), 693–695 (1993)
45. J. Tersoff, Erratum: Dislocations and strain relief in compositionally graded layers [appl. phys. lett. 62, 693 (1993)]. Appl. Phys. Lett. **64**(20), 2748–2748 (1994)
46. V.M. Kaganer, O. Brandt, A. Trampert, K.H. Ploog, X-ray diffraction peak profiles from threading dislocations in GaN epitaxial films. Phys. Rev. B **72**, 045423 (Jul 2005)
47. M.A. Moram, M.E. Vickers, X-ray diffraction of iii-nitrides. Rep. Prog. Phys. **72**(3), 036502 (2009)
48. Ferenc F. Csikor, István Groma, Probability distribution of internal stress in relaxed dislocation systems. Phys. Rev. B **70**, 064106 (Aug 2004)
49. M. Wilkens, The determination of density and distribution of dislocations in deformed single crystals from broadened X-ray diffraction profiles. Phys. Status Solidi (a), **2**(2), 359–370 (1970)
50. A.J.C. Wilson, X-ray diffraction by random layers: ideal line profiles and determination of structure amplitudes from observed line profiles. Acta Crystallogr. **2**(4), 245–251 (Aug 1949)
51. M. Wilkens. In Fundamental aspects of dislocation theory, pages 1195–1221. National Bureau of Standards, Institute for Materials Research, U.S. Govt. Print, April 1969.
52. Gabor Ribarik and Tamas Ungar. Characterization of the microstructure in random and textured polycrystals and single crystals by diffraction line profile analysis. Materials Science and Engineering: A, 528(1):112–121, 2010. Special Topic Section: Local and Near Surface Structure from Diffraction.
53. B.E. Warren, *X-Ray Diffraction* (Courier Dover Publications, New York, 1990)
54. Levente Balogh, Géza Tichy, Tamás Ungár, Twinning on pyramidal planes in hexagonal close packed crystals determined along with other defects by X-ray line profile analysis. J. Appl. Crystallogr. **42**(4), 580–591 (Aug 2009)

55. M. Barchuk, V. Holý, D. Kriegner, J. Stangl, S. Schwaiger, F. Scholz, Diffuse X-ray scattering from stacking faults in a-plane GaN epitaxial layers. Phys. Rev. B **84**, 094113 (Sep 2011)
56. L.D. Landau, Phys. Z. Soviet. **12**, 579 (1937)
57. Sterling Hendricks, Edward Teller, X-ray interference in partially ordered layer lattices. J. Chem. Phys. **10**(3), 147–167 (1942)
58. H. Jagodzinski, Eindimensionale Fehlordnung in Kristallen und ihr Einfluss auf die Röntgeninterferenzen. I. Berechnung des Fehlordnungsgrades aus den Röntgenintensitäten. Acta Crystallogr. **2**(4), 201–207 (Aug 1949)
59. H. Jagodzinski, Eindimensionale Fehlordnung in Kristallen und ihr Einfluss auf die Röntgeninterferenzen. II. Berechnung der Fehlgeordnetendichtesten Kugelpackungen mit Wechselwirkungen der Reichweite 3. Acta Crystallogr. **2**(4), 208–214 (Aug 1949)
60. J. Kakinoki, Y. Komura, Diffraction by a one-dimensionally disordered crystal. I. The intensity equation. Acta Crystallogr. **19**(1), 137–147 (Jul 1965)
61. J. Kakinoki, Diffraction by a one-dimensionally disordered crystal. II. Close-packed structures. Acta Crystallogr. **23**(6), 875–885 (Dec 1967)
62. M.M.J. Treacy, J.M. Newsam, M.W. Deem, A general recursion method for calculating diffracted intensities from crystals containing planar faults. Proc. R. Soc. Lond. A **433**(1889), 499–520 (1991)
63. Matteo Leoni, Alessandro F. Gualtieri, Norberto Roveri, Simultaneous refinement of structure and microstructure of layered materials. J. Appl. Crystallogr. **37**(1), 166–173 (Feb 2004)
64. L. Velterop, R. Delhez, H. de Th, E.J. Keijser, Mittemeijer, D. Reefman, X-ray diffraction analysis of stacking and twin faults in f.c.c. metals: a revision and allowance for texture and non-uniform fault probabilities. J. Appl. Crystallogr. **33**(2), 296–306 (2000)
65. V.S. Kopp, V.M. Kaganer, J. Schwarzkopf, F. Waidick, T. Remmele, A. Kwasniewski, M. Schmidbauer, X-ray diffraction from nonperiodic layered structures with correlations: analytical calculation and experiment on mixed Aurivillius films. Acta Crystallogr. A **68**(1), 148–155 (2012)

Chapter 7
X-Ray Diffraction Residual Stress Analysis in Polycrystals

In the previous chapters, the X-ray analysis has been applied to the samples with the electron density distributed uniformly in a macroscopic volume: the constant value for XRR analysis and three-dimensional periodic function in case of HRXRD analysis. These samples are usually grown with a predicted design to realize certain physical or mechanical properties of a final structure. The natural materials, however, possess in most cases the mixed structure, consisting of a large number of crystallites of various shape and size with random distribution over the sample volume. This kind of physical structure is called a polycrystalline form and it occurs in the majority of existing samples.

The non-destructive X-ray studies explore the properties of polycrystals, which influence the macroscopic characteristics of the products made of polycrystalline materials. There are different methods of X-ray analysis described in numerous monographs: the powder diffractometry performs the chemical and structural analysis of the material [1] and determines the grain size [2] and microstructural imperfections, the texture X-ray analysis studies the preferable orientations of the crystallites [3], X-ray stress analysis evaluates the residual stresses and strains in the samples [4, 5].

The chapter deals with the residual stress analysis, and the theoretical concepts described in previous chapters are used here to interpret the X-ray residual stress measurements. The first section introduces the basic physical definitions used further in X-ray stress analysis. The most difficult part of the theoretical interpretation is a description of the elastic interaction between crystalline grains which influences the microscopic properties of the crystallites. The second section presents the approximations and models used for solution of this problem. The third section considers the powder X-ray diffractometry in a connection with X-ray stress analysis. The forth section deals with the macroscopically isotropic samples, and the expressions for X-ray elastic constants are derived. The covariant methods and vector parametrization of the rotation space group are utilized to simplify the operations with tensors. Finally, the macroscopically anisotropic material are discussed in the fifth section of this chapter.

A. Benediktovitch et al., *Theoretical Concepts of X-Ray Nanoscale Analysis*,
Springer Series in Materials Science 183, DOI: 10.1007/978-3-642-38177-5_7,

7.1 X-Ray Stress Measurements

The residual stresses are defined by the distribution of the forces and the moments of forces, which exist in an equilibrium state in the polycrystals. The stresses influence the mechanical properties and the fatigue life of a material under external exposure. The residual stresses are the result of the elastic or plastic deformation of crystallites, and the distribution of the stress in a volume is distinguished by the several scales, $\sigma = \sigma_I + \sigma_{II} + \sigma_{III}$ [4]: (i) macroscopic, where the stress σ_I is averaged over the large number of grains, (ii) mesoscopic, where σ_{II} is an average stress inside grain, and (iii) microscopic, where σ_{III} describes the fluctuation of local stress inside a crystallite around value σ_{II}. The mechanical properties of the sample are defined mostly by macro-residual stress σ_I, the evaluation of which by X-ray stress measurements involve the calculation of σ_{II} and σ_{III} as well (Sect. 7.2).

The real microstructure of polycrystals is very complex. For the description of areas with coherent crystallographic structure, there are different spatial scales and naming conventions for micro-objects exist: crystallite, subgrain, dislocation cell, cell-block, grain and others [6]. Depending on the material, these objects have various relationships. In this chapter, we are not focusing on any particular material and therefore use the words crystallite and grain as synonyms.

In according to elastic theory [7], the stress tensor $\sigma_{ij}(\boldsymbol{r})$ in the position $\boldsymbol{r}$ is a symmetric tensor of a second rank which defines the force density F_i acting on the square $dS_j = n_j dS$ as follows:

$$F_i(\boldsymbol{r}) = \sigma_{ij}(\boldsymbol{r}) n_j dS, \;\; i, j = 1, 2, 3, \tag{7.1}$$

where n_j are the components of a normal vector to the square dS and the repeating indices are summed up accordingly.

In general case, the components $\sigma_{ij}(\boldsymbol{r})$ have different values in different crystallites, however, the averaging over all grains results in a macro-residual stress:

$$\sigma_{ij} \equiv \langle \sigma_{ij}(\boldsymbol{r}) \rangle, \tag{7.2}$$

which has to be evaluated in the most of the practical applications and is a target of the residual stress analysis.

Thereafter, we consider the basic principles of X-ray diffraction stress analysis for polycrystals with uniform and isotropic distribution of the crystallites [4, 5, 8]. The stresses σ_{ij} in the sample lead to the variation of the interplane distances inside the crystallites, and the value d_{hkl} for the plane $\{hkl\}$ depends on the orientation of grain in a polycrystal (Fig. 7.1).

The linear dimension of the grains in polycrystalline materials is essentially less than the extinction length of X-rays, and according to (6.77) the X-ray scattering from a single grain is described by a kinematical diffraction theory. The position of the diffraction peak for the radiation with the wavelength λ is determined by Bragg law:

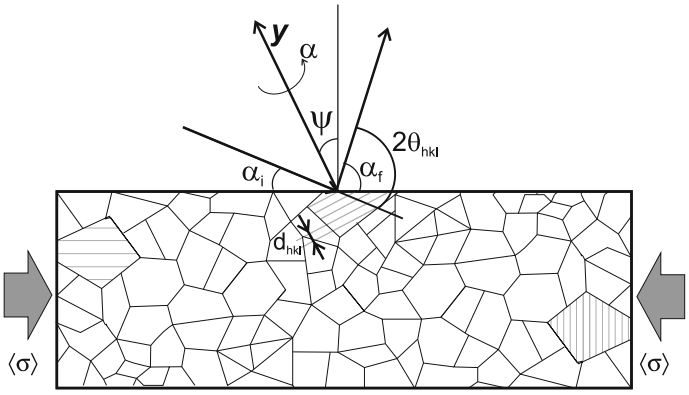

Fig. 7.1 X-ray diffraction from polycrystalline sample to measure residual stress inside the sample

$$2d_{hkl}\sin\theta_{hkl} = \lambda, \tag{7.3}$$

where angle θ_{hkl} is a Bragg angle for reflection hkl. Assuming the value $d^{(0)}_{hkl}$ and Bragg angle $\theta^{(0)}_{hkl}$ are known for the investigated crystal under the non-stressed condition, the measurement of the position of the diffraction peak θ_{hkl} delivers the elastic deformation of corresponding crystallographic planes:

$$\epsilon^{hkl} = \frac{d_{hkl} - d^{(0)}_{hkl}}{d^{(0)}_{hkl}} \approx -(\theta_{hkl} - \theta^{(0)}_{hkl})\cot\theta^{(0)}_{hkl}. \tag{7.4}$$

This value is a component of the strain tensor $\epsilon_{ij}(\boldsymbol{r})$, which depends on the coordinate and is connected to the stress tensor by Hooke's law [7]:

$$\epsilon_{ij}(\boldsymbol{r}) = s_{ijkl}(\boldsymbol{r})\sigma_{kl}(\boldsymbol{r}), \tag{7.5}$$

where $s_{ijkl}(\boldsymbol{r})$ is a local compliance tensor, which may vary both inside grain and at the grain boundary (Sect. 7.2). In a primitive model of uniform and isotropic polycrystal consisting of the isotropic grains [5], the averaging over the coordinates in (7.5) establishes the relationship between the measured average strain tensor $\epsilon_{ij} = \langle\epsilon_{ij}(\boldsymbol{r})\rangle$ in sample, the evaluated macroscopic stress tensor σ_{ij} and the compliance tensor S_{ijkl}, which is referred to the whole polycrystal but for uniform sample contains two parameters S_1, $1/2S_2$ [7] only:

$$\epsilon_{ij} = \langle s_{ijkl}(\boldsymbol{r})\sigma_{kl}(\boldsymbol{r})\rangle = S_{ijkl}\sigma_{kl} = \left[S_1\delta_{ij}\delta_{kl} + \frac{1}{2}S_2\frac{\delta_{ik}\delta_{jl} + \delta_{il}\delta_{jk}}{2}\right]\sigma_{kl}, \tag{7.6}$$

These parameters are expressed through the Young modulus E and Poisson ratio ν as:

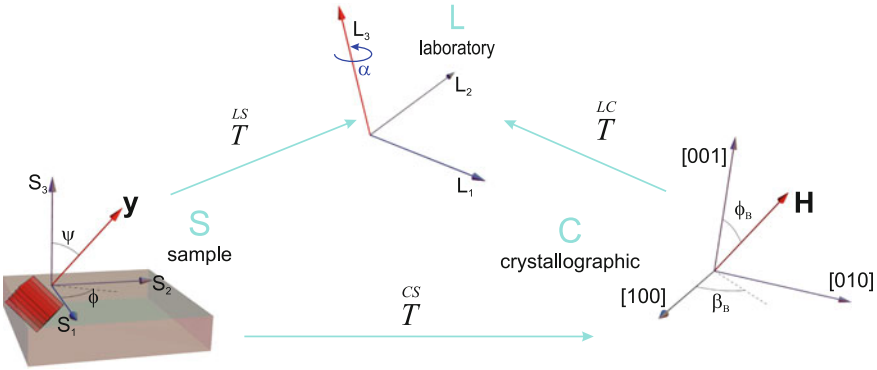

Fig. 7.2 The coordinate systems used in X-ray diffraction residual stress analysis in polycrystals

$$S_1 = -\frac{\nu}{E}; \quad \frac{1}{2}S_2 = \frac{1+\nu}{E}. \tag{7.7}$$

Each of three tensors in (7.6) has a simplified form in various coordinate systems used for residual stress analysis (Fig. 7.2).

The coordinate system S is related to the sample as a whole, and the axis $z(i = 3)$ coincides with the normal to the sample surface. In the coordinates S, the components of the macroscopic stress tensor σ_{ij} are initially defined. The laboratory coordinate system L is set to merge the direction of the axis z' and reciprocal lattice vector $\boldsymbol{H}$ of crystallites, corresponding to the Bragg angle $2\theta_{hkl}$. This direction in a system S is defined by the unit vector $\boldsymbol{y}(\psi, \phi)$; $\boldsymbol{Q} = Q\boldsymbol{y} \approx 2\pi \boldsymbol{y}/d^{(0)}_{hkl}$ with angles ψ and ϕ (Fig. 7.2). The definition of the vector $\boldsymbol{y}$ is possible by other parameters, which can be more convenient for interpretation of the measurements from the samples with preferred orientations, see Sect. 7.3. The experimentally measured strain (7.4) defines the component of strain tensor $\epsilon^{hkl}_{\psi\phi} = \epsilon^{L}_{33}$ in a coordinate system L.

Finally, the crystallographic coordinate system C is defined by the crystallographic axes of crystallites, and the stiffness tensor is set in this coordinate system. Assuming the uniform and isotropic sample model (Sect. 7.2), the parameters S^C_1 and S^C_2 are equal for all grains and calculated from the crystallographic parameters of a crystal composing a crystallite. They also coincide with the macroscopic parameter S_1 and S_2 of polycrystal in Eq. (7.6).

In isotropic polycrystal, the components of the strain tensor (7.6) in system S are expressed through the value ϵ^{L}_{33} by three components of the rotation operator $\hat{T}(\boldsymbol{y})$ (Fig. 7.2):

$$\epsilon^{hkl}_{\psi\phi} = \epsilon^{L}_{33} = T_{3i}(\boldsymbol{y})\epsilon_{ij}T_{j3}(\boldsymbol{y}), \tag{7.8}$$

which is the same as vector $(\boldsymbol{y})$ is the system S:

$$T_{3i}(\boldsymbol{y}) = T_{i3}(\boldsymbol{y}) = (\sin\psi\cos\phi, \sin\psi\sin\phi, \cos\psi). \tag{7.9}$$

Using the Eqs. (7.6)–(7.9), the relationship between the measured by X-ray diffraction strains and components of the residual stress tensor is:

$$\epsilon_{\psi\phi}^{hkl} = \frac{1}{2}S_2 \sin^2\psi[\sigma_{11}\cos^2\phi + \sigma_{12}\sin 2\phi + \sigma_{22}\sin^2\phi - \sigma_{33}] + \frac{1}{2}S_2 \sin 2\psi[\sigma_{13}\cos\phi + \sigma_{23}\sin\phi] + S_1(\sigma_{11} + \sigma_{22}) + \sigma_{33}(\frac{1}{2}S_2 + S_1). \tag{7.10}$$

The Eq. (7.10), named often as fundamental equation of X-ray stress analysis, contains 6 unknown components of the stress tensor. They can be found as a solution of the system of linear equations obtained from the measurement of strain at 6 different angles ψ and ϕ. The values of the diagonal and non-diagonal components of the strain tensor may differ essentially, and thus even small errors in the measured positions of the diffraction peaks make the analysis unstable. Therefore, another analytical methods utilizing the specific features of Eq. (7.10) are used for the treatment of X-ray data. The most commonly used technique is a $\sin^2\psi$ method, introduced for the first time in [9].

The method is based on the fact, that the boundary conditions of the sample shape are not essential for uniform and isotropic macroscopic polycrystal. Therefore, the coordinate system S is approaching the system P of the stress tensor [7], where $\sigma_{ij} = \sigma_i\delta_{ij}$; $\sigma_i \equiv \sigma_{ii}$ and thus tensor contains the diagonal elements only. In this case, the dependence of the function $\epsilon_{\psi\phi}^{hkl}$ on $\sin^2\psi$ at fixed ϕ is defined by a straight line (Fig. 7.3a). Thus, the interpolation of several measurements carried out at different $\sin^2\psi$ and $\phi = 0$ and $\phi = \pi/2$ by a straight line makes it possible to calculate values σ_{11} and σ_{22} from the inclination angles of the line. The intersection of the line with the ordinate delivers the value σ_{33}.

As follows from (7.10), the presence of non-diagonal components in σ_{ij}, i.e. the deviation in the directions of the axes of S and P systems, leads to the dependence of $\epsilon_{\psi\phi}^{hkl}$ on the sign of the calculation angle ψ. This fact results in elliptical form of the curves $\epsilon_{\psi\phi}^{hkl}(sin^2\psi)$, which allows to calculate the values σ_{13} and σ_{23}, too (Fig. 7.3b).

For anisotropic and non-uniform polycrystals, the method described above does not permit to calculate the components of the stress tensor, however, the curves $\epsilon_{\psi\phi}^{hkl}(sin^2\psi)$ are helpful to investigate qualitatively the distribution of the stresses in the sample, for example, presence of stress gradient or texture (Fig. 7.3c, d).

The quantitative residual stress analysis in case of essential deviations from $\sin^2\psi$ law assumes the averaging of (7.6) by using microscopic models (microstress) for separate grains and their elastic interaction (7.2) as well as the consideration of texture of polycrystalline sample (7.3). In general case, the resulting equations contain a complicated relationship between the microscopic compliance tensor of separate grains and components of macroscopic tensor S_{ijkl} referred to the whole sample. In the framework of macroscopically isotropic model and in the presence of anisotropy inside grains, the Eq. (7.10) can be used to interpret the experimental data:

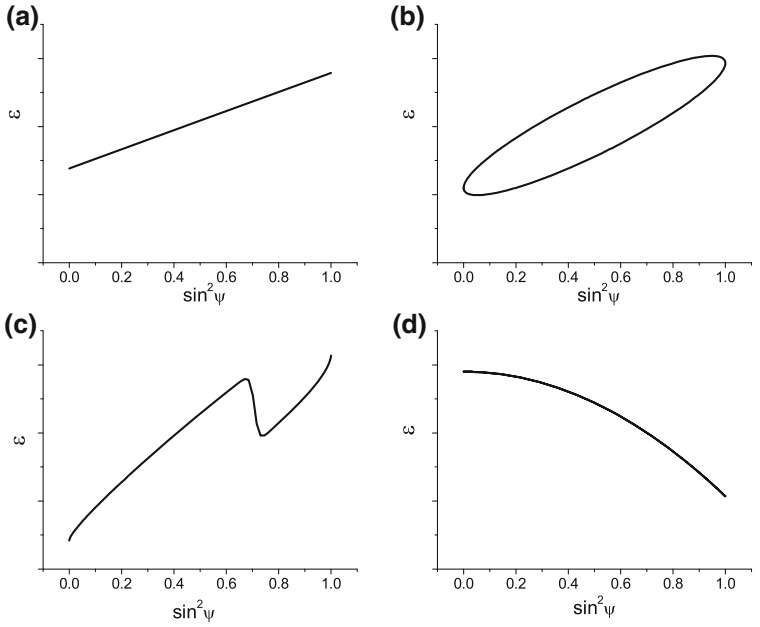

Fig. 7.3 Typical shapes of the function $\epsilon_{\psi\phi}^{hkl}(sin^2\psi)$ for the measurement of strain by point detector: **a** linear function in case of diagonal stress tensor, **b** elliptical function in case of non-zero σ_{13} and σ_{23}, **c** oscillating function in the presence of texture, **d** parabolic function in case of strong gradient of $\sigma_{ij}(z)$ toward the normal to the sample surface

$$\epsilon_{\psi\phi}^{hkl} = \frac{1}{2}S_2^{hkl}\sin^2\psi[\sigma_{11}\cos^2\phi + \sigma_{12}\sin 2\phi + \sigma_{22}\sin^2\phi - \sigma_{33}] + \frac{1}{2}S_2^{hkl}\sin 2\psi[\sigma_{13}\cos\phi + \sigma_{23}\sin\phi] + S_1^{hkl}(\sigma_{11}+\sigma_{22}) + \sigma_{33}\left(\frac{1}{2}S_2^{hkl} + S_1^{hkl}\right). \tag{7.11}$$

Here the coefficients S_2^{hkl} and S_1^{hkl} depend on the diffraction vector and can be considered as phenomenological X-ray elastic constants [2] (see Sect. 7.4 for more details).

There are several improved techniques of X-ray measurements, which optimize the study of residual stresses in polycrystals. The grazing-incidence X-ray diffraction (GIXRD) is used for the investigation of stress gradients in surface layers and coatings [8]. At small incidence angles α near the critical angle of total external reflection α_c, the diffraction peak is formed in the grains located in the depth, which depends on the incidence angle (Fig. 7.4).

The depth, where 63 % of the full intensity of diffraction peak is formed, is called informational depth τ and for thick layer it is expressed as [2]:

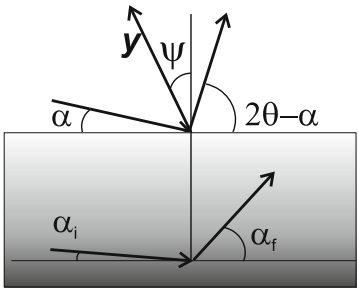

Fig. 7.4 In GIXRD geometry, the incidence α_i and exit α_f angles for the reflection hkl differ from the impinging angle α and leaving angle $(2\theta - \alpha)$ due to the refraction effect

$$\tau(\alpha) = \frac{\sin\alpha \sin(2\theta - \alpha)}{\mu[\sin\alpha + \sin(2\theta - \alpha)]};\ \mu = \frac{4\pi}{\lambda}\beta, \tag{7.12}$$

where β is an imaginary part of the refraction index $n = 1 - \delta - i\beta$ (see Chap. 1). By varying the incidence angle of X-rays, the stress can be measured from different distances in-depth from the surface. At the angles comparable with α_c, where $\sin^2\alpha_c = 2\delta$, the refraction of both incident and exit beams becomes essential (Fig. 7.4), which results in the angular shift of the diffraction peak at 2θ with respect to the Bragg angle $2\theta^{hkl}$ in formula (7.4). The corrections for refraction change also the informational depth and have to be accounted for the reconstruction of stress gradients [10]. The formulas for the corrections are:

$$\begin{aligned} &2\theta^{hkl} = \alpha_i(\alpha) + \alpha_f(\alpha);\ \tan\alpha_i = \frac{B_+(\alpha)}{\cos\alpha};\ \tan\alpha_f = \frac{B_+(2\theta - \alpha)}{\cos(2\theta - \alpha)};\\ &\tau'(\alpha) = \tau(\alpha)\frac{1}{\sin\alpha B_-(\alpha)};\\ &B_\pm(\alpha) = \frac{1}{\sqrt{2}}[\sqrt{(\sin^2\alpha - 2\delta)^2 + 4\beta^2} \pm (\sin^2\alpha - 2\delta)]^{1/2}. \end{aligned} \tag{7.13}$$

The transition layer at the surface sample caused by roughness (Chap. 3) also distorts the informational depth and the corresponding corrections have to be applied for calculation of stress gradients [11].

The Eqs. (7.10) and (7.11) are used above for the experimental geometry, which measures the shift of diffraction peak at fixed indices (hkl), i.e. by varying the direction $\boldsymbol{y}(\psi)$ of the diffraction vector $\boldsymbol{Q}$ at fixed length Q. However, these equations are valid for the case of different indices, when the angle ψ^{hkl} is connected to the Bragg and the incidence angles as:

$$\psi^{hkl} = \theta^{hkl} - \alpha, \tag{7.14}$$

and varies from one diffraction peak to another without rotation of sample. This approach is called multiple hkl stress evaluation and is used in GIXRD geometry to evaluate stress gradients [10, 12]. The Eq. (7.11) is applied in this case in the form

[12]:

$$\epsilon_{\phi}^{hkl} = \frac{1}{2} S_2^{hkl} [\sigma_{\phi} \sin^2 \psi^{hkl} + \tau_{\phi} \sin 2\psi^{hkl}] + S_1^{hkl} (\sigma_{11} + \sigma_{22});$$
$$\sigma_{\phi} = \sigma_{11} \cos^2 \phi + \sigma_{12} \sin 2\phi + \sigma_{22} \sin^2 \phi; \ \tau_{\phi} = \sigma_{13} \cos \phi + \sigma_{23} \sin \phi. \quad (7.15)$$

For determination of the values σ_{ϕ}, τ_{ϕ} and $(\sigma_{11} + \sigma_{22})$ at fixed ϕ, it is enough to measure the strain for 3 reflections. However, the equation system obtained can be badly defined or has no any exact solution due to big difference between σ_{ϕ} and τ_{ϕ}. Therefore, in practice the multiple measurements are performed and the stress is calculated by fitting the strain for all reflections on the basis of formula (7.15) [10].

The presented above technique of X-ray diffraction stress measurements is commonly used and utilizes a point or linear X-ray detectors, which record the scattered X-ray signal in the diffraction plane corresponding to the angle ψ (Fig. 7.2). Recently the two-dimensional detectors became popular for residual stress measurements [13]. In that case, the diffraction signal from the uniform polycrystal is exposed as Debye rings with the radius defined by the reflection (hkl) and with variation of the angle along the Debye ring between 0 and 2π. The detection of X-ray signal out of the diffraction plane introduces another degree of freedom in the relative arrangement of the coordinate systems and this fact requires the modification of the Eq. (7.11) for residual stress analysis. The derivation of a new equation for two-dimensional data is done in [13]. This technique offers an extended opportunities for stress analysis in the samples with large size of grains and highly textured materials.

Independently on the X-ray measurement technique used for stress analysis, the results are strongly influenced by the selected model of grain interaction and the distribution of grains in a sample, as reflected in the Hooke's law (7.5). This important issue is discussed in the following sections.

7.2 Grain-Interaction Models

The stress and strain inside the single crystallite (grain) are connected by the Hooke's law. The Bragg peak, however, is formed by the signals coming from the number of grains with different rotation angle α (Fig. 7.2). Within this set of grains, there are different magnitudes of microscopic strain and stress observed, which differ from the macroscopic values to be evaluated. Therefore, the relation between the strain $\epsilon_{ij}(\boldsymbol{g})^{(S)}$ in a single grain (coordinate system (S)) having orientation $\boldsymbol{g}$ and the macroscopically averaged stress tensor $\langle \sigma_{ij} \rangle^{(S)}$ has to be established. This relationship will help to find the dependence between macroscopic stress in a sample and measured experimentally by X-ray diffraction strain. Within the framework of linear elasticity theory, this relationship is expressed as:

$$\epsilon_{ij}^{(S)}(\boldsymbol{g}) = A_{ijkl}(\boldsymbol{g}) \langle \sigma_{kl} \rangle^{(S)}. \quad (7.16)$$

The coefficients $A_{ijkl}(\boldsymbol{g})$ depend non-linearly on the orientation of grain $\boldsymbol{g}$ and on the stiffness tensor of grain $c^{(C)}_{ijkl}$.

The problem of calculation of macroscopic parameters of the sample consisting of non-uniform areas has a long history [14]. The determination of averaged elastic, dielectric, electroconductive and thermoconductive properties have a similar mathematical formulations in linear theory. The elastic properties of polycrystal are found from the equations of the elastic equilibrium with the boundary conditions:

$$\frac{\partial}{\partial x_k} c_{ikjl}(\boldsymbol{r}) \frac{\partial u_j}{\partial x_l} = 0, \;\; u_i^{(1)}|_\Gamma = u_i^{(2)}|_\Gamma, \sigma_{ij}^{(1)} n_j|_\Gamma = \sigma_{ij}^{(2)} n_j|_\Gamma, \tag{7.17}$$

where $c_{ikjl}(\boldsymbol{r})$ is a stiffness tensor, which varies from one crystallite to another when $\boldsymbol{r}$ varies, Γ is a boundary between regions (1) and (2) with the normal $\boldsymbol{n}$. The boundary conditions for electrostatics in media have similar form:

$$\frac{\partial}{\partial x_i} \epsilon_{ij}(\boldsymbol{r}) \frac{\partial \phi}{\partial x_j} = 0, \;\; \phi^{(1)}|_\Gamma = \phi^{(2)}|_\Gamma, D_j^{(1)} n_j|_\Gamma = D_j^{(2)} n_j|_\Gamma, \tag{7.18}$$

where ϵ_{ij} is a permittivity, ϕ is a potential and D_i is an electric displacement field. By substituting ϵ_{ij} for the tensor of electroconductivity and D_i for the current density, we obtain the equations for electroconductive properties of material. By substituting ϕ for the temperature and ϵ_{ij} for the tensor of thermal conduction, and D_i for the heat flux, we obtain the equations for thermoconductive properties, and so on. Thus, the methods developed for one branch of physics can be transformed to another. With regard to the elastic properties, however, the mathematical background is more complex due to the involvement of tensors of higher rank and vectors u_i instead of the scalar ϕ.

There are following approaches to the solution of above-mentioned problem:

- Exact solutions for certain models, for example, the exact solution of the Eq. (7.17) for adjoined isotropic spheres with similar properties in isotropic surrounding, so called composite sphere assemblage [15, 14]. The number of these models, which allow an exact solution is relatively small.
- The methods based on the expansion into series over small parameter. The small parameter can be concentration of particles in composite material [14, 16], the anisotropy degree of the crystallites in a sample [17], and so on. In case if the parameter is not small, the series can be used for qualitative analysis [18]. An equivalent formulation of this approach is a chain of the equations Born-Bogolubov-Green-Kirkwood-Ivone [19].
- The methods for determination of lower and upper boundaries of the macroscopic parameters [14, 18]. These methods are based on the variation principle: the exact solution of the Eqs. (7.17) and (7.18) minimizes the energy.
- Self-consistent methods, where the ansatz for (7.17) and (7.18) is constructed as follows: the interaction between particles is substituted for the interaction of separate particle with effective media, the properties of which have to be found.

The effective permittivity has been found by Bruggeman [20] using this method. For the elastic properties of polycrystalline materials, the self-consistent methods are based on eigenstrain approach [21], where the Eshelby problem is solved for the stress initiated by the inclusions [22]. Based on this approach, Kröner proposed a self-consistent method for calculation of elastic properties of polycrystals known as Eshelby-Kröner model [23].

- The method based on the simplified models of grain interaction. Instead of solution of (7.17), the ad hoc assumptions are used for distribution of stresses and strains in grains [24]. As a result, the boundary conditions (7.17) are broken, however, the proper selection of model allows to obtain a good fit between experimental data and theory.
- A numerical solution of (7.17) and (7.18) and further averaging of the prior found fields. This approach is frequently used for optical properties of metamaterials [25]. In opposite to the artificial metamaterials, where the fragments are designed initially, the polycrystalline samples obey many random parameters. For the numerical solution of (7.17), the shape and crystallographic orientation of each crystallite have to be known. The method of finite elements is proved [26, 27] to show a good agreement with analytical methods.

Hereafter, we consider the frequently used models and methods for solution of Eq. (7.16).

7.2.1 Voigt Model

The first grain-interaction model has been proposed by Voigt in 1910 [28]. This model assumes that all crystallites have the same strain ϵ_{ij} independently on their orientations. As a result, the microscopic strain equals to the averaged macroscopic one:

$$\epsilon_{ij}^{(S)}(\boldsymbol{g}) = \langle \epsilon_{ij}^{(S)} \rangle. \tag{7.19}$$

Thus, the stress tensor in crystallite with orientation $\boldsymbol{g}$ is calculated by formula:

$$\sigma_{ij}^{(S)}(\boldsymbol{g}) = c_{ijkl}^{(S)}(\boldsymbol{g}) \langle \epsilon_{kl}^{(S)} \rangle, \tag{7.20}$$

where $c_{ijkl}^{(S)}(\boldsymbol{g}) = T_{ii'jj'kk'll'}^{(SC)}(\boldsymbol{g}) c_{i'j'k'l'}^{(C)}$ is a stiffness tensor of crystallite with orientation $\boldsymbol{g}$ in coordinate system (S). To derive the relationship (7.16), the macroscopic stress tensor $\langle \sigma_{ij} \rangle^{(S)}$ has to be determined. For determination, the Eq. (7.20) has to be averaged over crystallite orientations $\boldsymbol{g}$ with respect to the orientation distribution function (ODF) $f(\boldsymbol{g})$, (see more detailed discussion on ODF and transformation $T^{(SC)}$ in the Sect. 7.4):

$$\langle \sigma_{ij}^{(S)} \rangle = C_{ijkl}^{(S)} \langle \epsilon_{kl}^{(S)} \rangle, \tag{7.21}$$
$$C_{ijkl}^{(S)} = \int d^3 g f(\boldsymbol{g}) T_{ii'jj'kk'll'}^{(SC)}(\boldsymbol{g}) c_{i'j'k'l'}^{(C)}.$$

Using (7.19), (7.21) and (7.16), the following statement is obtained for Voigt model:

$$A_{ijkl}^{V} = (C_{ijkl}^{(S)})^{-1}. \tag{7.22}$$

In this model, the tensor A_{ijkl}^{V} is independent on the crystallite orientation $\boldsymbol{g}$, which results in a linear character of $\sin^2 \psi$ even in the presence of texture.

The Voigt model is a pretty rough approximation for grain interaction, where the boundary conditions of the elasticity theory (7.17) are deliberately not satisfied. The strains are continuous at the boundaries of crystallites, however, the stresses suffer the discontinuity (7.20). The totally opposite situation occurs in a Reuss model.

7.2.2 Reuss Model

The Reuss model [29] assumes all the crystallites have the same stress σ_{ij} independently on the orientation. As a result, the microscopic stress of a single crystallite equals to the macroscopic one averaged over the whole sample:

$$\sigma_{ij}^{(S)}(\boldsymbol{g}) = \langle \sigma_{ij}^{(S)} \rangle. \tag{7.23}$$

The strain tensor of a crystallite with the orientation $\boldsymbol{g}$ is:

$$\epsilon_{ij}^{(S)}(\boldsymbol{g}) = s_{ijkl}^{(S)}(\boldsymbol{g}) \langle \sigma_{ij}^{(S)} \rangle, \tag{7.24}$$

where $s_{ijkl}^{(S)}(\boldsymbol{g}) = T_{ii'jj'kk'll'}^{(SC)}(\boldsymbol{g}) s_{i'j'k'l'}^{(C)}$ is a compliance tensor of crystallite with orientation $\boldsymbol{g}$ in a coordinate system S. By comparing (7.24) and (7.16), we conclude:

$$A_{ijkl}^{R}(\boldsymbol{g}) = s_{ijkl}^{(S)}(\boldsymbol{g}), \tag{7.25}$$

where tensor A_{ijkl}^{R} depends on the crystallite orientation $\boldsymbol{g}$, which leads to the nonlinearity of $\sin^2 \psi$ in the presence of texture.

The Reuss model is similarly rough as the Voigt one: the boundary conditions of the elasticity theory are not fulfilled. In opposite to the Voigt model, the stresses are continuous at the crystallite boundaries and the strains (7.24) are discontinuous.

7.2.3 Hashin-Shtrikman Boundaries for Rigidity Modulus

The models of Voigt and Reuss describe the limiting cases of grain interaction. The microscopic mechanical elastic constants binding $\langle\sigma_{ij}\rangle$ and $\langle\epsilon_{ij}\rangle$ are shown in [30] to satisfy the inequality:

$$K^R \leq K \leq K^V, \;\; G^R \leq G \leq G^V. \tag{7.26}$$

Here K and G are real values of macroscopic bulk and rigidity moduli, and $K^{V,R}$, $G^{V,R}$ are the values found by Voigt and Reuss models.

The result (7.26) can be illustrated by analogue with the electrical conductivity [16]. In the Reuss model, all grains have equal stress value, which by analogue with (7.17) and (7.18) corresponds to equal current in all conductors. Thus, the Reuss model is analogous to the sequential connection of the conductors, which results in the highest resistance value. The Voigt model corresponds to the equal voltage on all conductors, and thus is analogous to parallel connection, which gives the minimal resistance. For any other types of connection, the resulting resistance will have an intermediate value between the ones mentioned above.

Despite both Voigt and Reuss models are very approximate, the expressions (7.25) and (7.22) do not depend neither from the grain shape nor from their mutual locations. Is it possible to obtain more accurate limits and to identify which information about the crystallites is required for this purpose, we analyze below the Eq. (7.17) following the work [18].

Let us split stiffness tensor $c_{ikjl}(\boldsymbol{r})$ into sum of constant tensor C_{ikjl} which we define later and tensor $\delta c_{ikjl}(\boldsymbol{r})$ which varies from crystallite to crystallite:

$$c_{ikjl}(\boldsymbol{r}) = C_{ikjl} + \delta c_{ikjl}(\boldsymbol{r}). \tag{7.27}$$

The Eq. (7.17) is then expressed as:

$$C_{ikjl}\frac{\partial^2}{\partial x_k \partial x_l}u_j + f_i(\boldsymbol{r}) = 0,\; f_i(\boldsymbol{r}) = \frac{\partial}{\partial x_k}\delta c_{ikjl}(\boldsymbol{r})\frac{\partial u_j}{\partial x_l}. \tag{7.28}$$

The structure of this equation is similar to one of (6.26): there is a constant differential operator $C_{ikjl}\frac{\partial^2}{\partial x_k \partial x_l}$ analogous to L_0 in (6.26) and a fluctuating term. Based on the Eq. (7.28), we have to find the averaged effective parameters of the physical system, and therefore use the methods similar to the ones described in the Sect. 6.2, namely represent (7.28) in an integral form:

$$u_i(\boldsymbol{r}) = u_i(\boldsymbol{r})^{(0)} + \int d^3\boldsymbol{r}' G_{ij}(\boldsymbol{r},\boldsymbol{r}') f_j(\boldsymbol{r}'), \tag{7.29}$$

$$C_{ikjl}\frac{\partial^2}{\partial x_k \partial x_l}G_{jm}(\boldsymbol{r},\boldsymbol{r}') + \delta_{im}\delta(\boldsymbol{r}-\boldsymbol{r}') = 0,$$

where $G_{ij}(\boldsymbol{r}, \boldsymbol{r}')$ is a Green function of the elasticity theory [7, 21]; and the arbitrary solution of the uniform equation $u_i(\boldsymbol{r})^{(0)}$ is chosen to satisfy the boundary conditions at the border of polycrystal. Then the Green function has to satisfy the condition:

$$G_{jm}(\boldsymbol{r}, \boldsymbol{r}')|_{\boldsymbol{r}\in\Gamma} = 0 \tag{7.30}$$

at the boundary of the polycrystal. By integrating and using (7.29) and (7.30), we arrive at:

$$u_i(\boldsymbol{r}) = u_i(\boldsymbol{r})^{(0)} - \int d^3\boldsymbol{r}' \frac{\partial G_{ij}(\boldsymbol{r}, \boldsymbol{r}')}{\partial x'_k} \delta c_{jknl}(\boldsymbol{r}') \frac{\partial u_n(\boldsymbol{r}')}{\partial x'_l}. \tag{7.31}$$

To calculate the strains, the Eq. (7.31) has to be differentiated:

$$\epsilon_{ip}(\boldsymbol{r}) = \epsilon_{ip}(\boldsymbol{r})^{(0)} - \int d^3\boldsymbol{r}' \frac{\partial G_{(\underline{i}j}(\boldsymbol{r}, \boldsymbol{r}')}{\partial x_{\underline{p})} \partial x'_k} \delta c_{jknl}(\boldsymbol{r}') \epsilon_{nl}(\boldsymbol{r}'), \tag{7.32}$$

where due to the symmetry of the stiffness tensor with respect to the transposition of indices [1] $\delta c_{jknl}(\boldsymbol{r}') \frac{\partial u_n}{\partial x'_l} = \delta c_{jknl}(\boldsymbol{r}') \epsilon_{nl}$:

$$a_{(\underline{i}\underline{j})} b_{ij} = a_{(\underline{i}\underline{j})} b_{(\underline{i}\underline{j})}. \tag{7.33}$$

The expression (7.32) can be written as:

$$\boldsymbol{\epsilon} = \boldsymbol{\epsilon}^{(0)} - \boldsymbol{\Gamma} : \delta\boldsymbol{c} : \boldsymbol{\epsilon}, \tag{7.34}$$

where symbol : means the convolution over two indices, and $\boldsymbol{\Gamma}$ is an integral operator [18]:

$$(\Gamma_{ipjk} f)(\boldsymbol{r}) = \int d^3\boldsymbol{r}' \frac{\partial G_{(\underline{i}j}(\boldsymbol{r}, \boldsymbol{r}')}{\partial x_{\underline{p})} \partial x'_k} f(\boldsymbol{r}'). \tag{7.35}$$

Using this equation, the expression (7.16) can be re-written in an operator form. By reversing (7.34):

$$\boldsymbol{\epsilon} = (\mathbf{1} + \boldsymbol{\Gamma} : \delta\boldsymbol{c})^{-1} : \boldsymbol{\epsilon}^{(0)}, \tag{7.36}$$

where $\mathbf{1}$ is a unity tensor of 4th rank. We assume that the strain $\boldsymbol{\epsilon}^{(0)}$ at the boundary of polycrystal is uniform (the general case is discussed in [18]), then the macroscopic strain $\langle\boldsymbol{\epsilon}\rangle$ is equal to $\boldsymbol{\epsilon}^{(0)}$:

$$\langle\boldsymbol{\epsilon}\rangle = \boldsymbol{\epsilon}^{(0)}. \tag{7.37}$$

[1] The parenthesis near underlined indices mean the symmetrization operation, $a_{(\underline{i}\underline{j})kl} \equiv \frac{1}{2}(a_{ijkl} + a_{jikl})$. In these notations, the symmetry of stiffness tensor relatively the transposition of indices has a form $c_{ijkl} = c_{(\underline{i}\underline{j})kl} = c_{ij(\underline{k}\underline{l})} = c_{(\underline{ijkl})}$, where the latter equality means the symmetry with respect to the transposition of index pair.

Applying the Hooke's law, we obtain for macroscopic values:

$$\langle \boldsymbol{\sigma} \rangle = \boldsymbol{C}_M : \boldsymbol{\epsilon}^{(0)}, \tag{7.38}$$

and for microscopic values:

$$\boldsymbol{\sigma} = (\boldsymbol{C} + \delta \boldsymbol{c}) : \boldsymbol{\epsilon}. \tag{7.39}$$

After averaging (7.39) and using (7.36), the expression for macroscopic stiffness tensor is:

$$\boldsymbol{C}_M = \boldsymbol{C} + \langle \delta \boldsymbol{c} : (\mathbf{1} + \boldsymbol{\Gamma} : \delta \boldsymbol{c})^{-1} \rangle, \tag{7.40}$$

and the relationship (7.16) is found to be:

$$\boldsymbol{A} = (\mathbf{1} + \boldsymbol{\Gamma} : \delta \boldsymbol{c})^{-1} : \boldsymbol{C}_M^{-1}. \tag{7.41}$$

Within the accuracy of approximation (7.17), these expressions are exact. However, similarly to the case of (6.33), for the calculation of (7.40) and (7.41) the operators have to be found, which are inverse to the non-local integral operators. This is a challenging problem, and the models of Voigt, Reuss and Eshelby-Kröner are the approximate methods to calculate (7.40) and (7.41).

In the same way as in (6.33), the inverse operators can be represented as an expansion into series, and thus (7.40) is written as:

$$\boldsymbol{C}_M = \boldsymbol{C} + \langle \delta \boldsymbol{c} \rangle - \langle \delta \boldsymbol{c} : \boldsymbol{\Gamma} : \delta \boldsymbol{c} \rangle + \ldots \tag{7.42}$$

The first two terms in (7.42) correspond to the Voigt model, whereas the same formula, being constructed not from stiffness tensor C but from compliance tensor S, will correspond to Reuss model. In both approximations, there is no need to know the shape and mutual arrangement of the crystallites, however, for the calculation of the subsequent term in the series this information is necessary. Indeed, the operator $\boldsymbol{\Gamma}$ is non-local, and therefore for calculation of the third term in (7.42) the value $\langle \delta \boldsymbol{c}(\boldsymbol{r}_1) \delta \boldsymbol{c}(\boldsymbol{r}_2) \rangle$ must be known, which is a correlation function of the second order for the elastic properties of polycrystal. To calculate further terms in the series, the correlation functions of higher order must be simulated. In general case, the series (7.42) is divergent, and the special summation techniques have to be applied for the final calculation [18].

Using the derived above equations, the expressions for upper and lower limits of the macroscopic stiffness tensor $\boldsymbol{C}_M$ can be obtained. To isolate the operator $\boldsymbol{\Gamma}$, the equation (7.34) is re-formulated as [18]:

$$(\delta \boldsymbol{c}^{-1} + \boldsymbol{\Gamma}) : \widetilde{\boldsymbol{\sigma}} = \boldsymbol{\epsilon}^{(0)}, \qquad \widetilde{\boldsymbol{\sigma}} = \delta \boldsymbol{c} : \boldsymbol{\epsilon}. \tag{7.43}$$

This equation for fluctuating stress parameter $\widetilde{\boldsymbol{\sigma}}$ can be considered as a consequence of the minimization of the functional:

$$\frac{\delta F[\widetilde{\boldsymbol{\sigma}}]}{\delta \widetilde{\boldsymbol{\sigma}}} = 0, \quad F[\widetilde{\boldsymbol{\sigma}}] = \int d^3\boldsymbol{r} \left(\frac{\widetilde{\boldsymbol{\sigma}} : \delta \boldsymbol{c}^{-1} : \widetilde{\boldsymbol{\sigma}}}{2} + \frac{\widetilde{\boldsymbol{\sigma}} : \boldsymbol{\Gamma} : \widetilde{\boldsymbol{\sigma}}}{2} - \widetilde{\boldsymbol{\sigma}} : \boldsymbol{\epsilon}^{(0)} \right). \quad (7.44)$$

Alternatively, using (7.43) the functional $F[\widetilde{\boldsymbol{\sigma}}]$ is:

$$F[\widetilde{\boldsymbol{\sigma}}] = -\int d^3\boldsymbol{r} \frac{\widetilde{\boldsymbol{\sigma}} : \boldsymbol{\epsilon}^{(0)}}{2} = \int d^3\boldsymbol{r} \left(\frac{\boldsymbol{\epsilon}^{(0)} : \boldsymbol{C} : \boldsymbol{\epsilon}}{2} - \frac{\boldsymbol{\sigma} : \boldsymbol{\epsilon}^{(0)}}{2} \right) \quad (7.45)$$

$$= V \boldsymbol{\epsilon}^{(0)} : \frac{\boldsymbol{C} - \boldsymbol{C}_M}{2} : \epsilon^{(0)},$$

where Eq. (7.38) is used and V is a volume of the polycrystal.

As follows from (7.44), the exact solution of (7.43) delivers the extremum of the functional $F[\widetilde{\boldsymbol{\sigma}}]$. If the value $\delta \boldsymbol{c}^{-1}$ is positive definite, [2] the extremum will be a minimum [18]. For any probe field $\widetilde{\boldsymbol{\sigma}}_{\text{probe}}$, the following inequality is satisfied:

$$F[\widetilde{\boldsymbol{\sigma}}_{\text{probe}}] \geq V \boldsymbol{\epsilon}^{(0)} : \frac{\boldsymbol{C} - \boldsymbol{C}_M}{2} : \epsilon^{(0)}. \quad (7.46)$$

By reduction of $F[\widetilde{\boldsymbol{\sigma}}_{\text{probe}}]$ to the form $V \boldsymbol{\epsilon}^{(0)} : \frac{\boldsymbol{C}_v}{2} : \epsilon^{(0)}$, the Eq. (7.46) delivers the upper limit for $\boldsymbol{C}_M$. Using a similar algorithm for the compliance tensor S, in case of negative definite value $\delta \boldsymbol{c}^{-1}$, we obtain [18]:

$$F[\widetilde{\boldsymbol{\sigma}}_{\text{probe}}] \leq V \boldsymbol{\epsilon}^{(0)} : \frac{\boldsymbol{C} - \boldsymbol{C}_M}{2} : \epsilon^{(0)}, \quad (7.47)$$

from where the lower limit for $\boldsymbol{C}_M$ is received. To explicitly calculate both limits, the following probe field is used:

$$\widetilde{\boldsymbol{\sigma}}_{\text{probe}} = \sum_n \widetilde{\boldsymbol{\sigma}}_n \Theta_n(\boldsymbol{r}), \quad (7.48)$$

where the sum is performed over all grains of polycrystal, and the field inside each grain is assumed to be constant. The function $\Theta_n(\boldsymbol{r})$ describes the shape of n-th grain: $\Theta_n(\boldsymbol{r})$ equals to 1 inside grain and to 0 outside. The coefficients $\widetilde{\boldsymbol{\sigma}}_n$ are determined by the minimization of the functional F, which for the field (7.48) is:

[2] To clarify whether the tensor is positive definite, the special representation (7.121) is used (see Sect. 7.4). In this representation, the positive definition corresponds to $\boldsymbol{C} = (3\kappa_c, 2\min(\mu_c, \mu'_c), 2\min(\mu_c, \mu'_c))$, and negative definition to $\boldsymbol{C} = (3\kappa_c, 2\max(\mu_c, \mu'_c), 2\max(\mu_c, \mu'_c))$, respectively.

$$F[\widetilde{\boldsymbol{\sigma}}_n] = \sum_n V_n \frac{\widetilde{\boldsymbol{\sigma}}_n : \delta \boldsymbol{c}_n^{-1} : \widetilde{\boldsymbol{\sigma}}_n}{2} \tag{7.49}$$
$$+ \sum_{n,m} \frac{\widetilde{\boldsymbol{\sigma}_n} : \int d^3\boldsymbol{r}_1 d^3\boldsymbol{r}_2 \Theta_n(\boldsymbol{r}_1)\Theta_m(\boldsymbol{r}_2)\boldsymbol{\Gamma}(\boldsymbol{r}_1,\boldsymbol{r}_2) : \widetilde{\boldsymbol{\sigma}_m}}{2} - \sum_n V_n \widetilde{\boldsymbol{\sigma}_n} : \boldsymbol{\epsilon}^{(0)}.$$

With respect to the coefficients $\widetilde{\boldsymbol{\sigma}}_n$, the expression (7.49) is a quadratic form of type $\frac{1}{2}\sum_{n,m} a_{nm}\widetilde{\sigma_n}\widetilde{\sigma_m} + \sum_n b_n \widetilde{\sigma_n}$. It can be easily found that the extremum is $\frac{1}{2}\sum_n b_n \widetilde{\sigma_n}^*$, where $\widetilde{\sigma_n}^*$ is a solution of the equation $\sum_m a_{nm}\widetilde{\sigma_m}^* + b_n = 0$. Applying these expressions to (7.49), the extremum of the functional is found to be:

$$F = -\frac{1}{2}\sum\nolimits_n V_n \widetilde{\boldsymbol{\sigma}_n}^* : \boldsymbol{\epsilon}^{(0)}, \tag{7.50}$$
$$V_n \delta \boldsymbol{c}_n^{-1} : \widetilde{\boldsymbol{\sigma}}_n^* + \sum\nolimits_m \int d^3\boldsymbol{r}_1 d^3\boldsymbol{r}_2 \Theta_n(\boldsymbol{r}_1)\Theta_m(\boldsymbol{r}_2)\boldsymbol{\Gamma}(\boldsymbol{r}_1,\boldsymbol{r}_2) : \widetilde{\boldsymbol{\sigma}_m}^* = V_n \boldsymbol{\epsilon}^{(0)}.$$

As follows from (7.50), due to the operator Γ the expression for $\widetilde{\boldsymbol{\sigma}_n}^*$ is non-local and requires the correlation function for the grain shape. The function Γ is calculated on the basis of Green function with the boundary conditions (7.30). The functions Γ and Γ^∞ calculated for infinite crystal can be connected for fluctuating $\widetilde{\boldsymbol{\sigma}}$. By neglecting the condition (7.30), the additional term appears in (7.31), which includes the integral over the surface:

$$u_i(\boldsymbol{r}) = u_i(\boldsymbol{r})^{(0)} \tag{7.51}$$
$$- \int d^3\boldsymbol{r}' \frac{\partial G_{ij}^\infty(\boldsymbol{r},\boldsymbol{r}')}{\partial x_k'} \widetilde{\sigma_{jk}}(\boldsymbol{r}') + \int d^2 S n_k G_{ij}^\infty(\boldsymbol{r},\boldsymbol{r}')\widetilde{\sigma_{jk}}(\boldsymbol{r}').$$

In case of uniform boundary conditions, the averaged values $\langle\boldsymbol{\sigma}\rangle$ and $\langle\boldsymbol{\epsilon}\rangle$ are also uniform, and we can assume the value $\langle\widetilde{\boldsymbol{\sigma}}\rangle$ uniform, too. In the integration of (7.51) over the surface, the contribution from $\langle\widetilde{\boldsymbol{\sigma}}\rangle$ is compensated [18]. By using the Gauss theorem and replacing the displacements by strain, the expression analogous to (7.34) is obtained:

$$\boldsymbol{\epsilon} = \boldsymbol{\epsilon}^{(0)} - \boldsymbol{\Gamma}^\infty : (\widetilde{\boldsymbol{\sigma}} - \langle\widetilde{\boldsymbol{\sigma}}\rangle). \tag{7.52}$$

Substituting this expression in (7.50) and applying the translational invariance, we arrive at:

$$V_n \delta \boldsymbol{c}_n^{-1} : \widetilde{\boldsymbol{\sigma}}_n + V \sum_m \int d^3\boldsymbol{\rho} f_{nm}(\boldsymbol{\rho})\boldsymbol{\Gamma}^\infty(\boldsymbol{\rho}) : \widetilde{\boldsymbol{\sigma}_m}^* = \tag{7.53}$$
$$V_n \boldsymbol{\epsilon}^{(0)} + V_n \int d^3\boldsymbol{\rho}\Gamma^\infty(\boldsymbol{\rho}) : \langle\widetilde{\boldsymbol{\sigma}}^*\rangle,$$
$$f_{nm}(\boldsymbol{\rho}) = \frac{1}{V}\int d^3\boldsymbol{r}\Theta_n(\boldsymbol{r})\Theta_m(\boldsymbol{r}+\boldsymbol{\rho}),$$

where f_{nm} is a correlation function of the grain shape.

In the case of spherically symmetric correlation function $f_{nm}(\boldsymbol{\rho}) = f_{nm}(\rho)$, the expression (7.53) can be essentially simplified, and the explicit solution is obtained on the basis of Eshelby tensor. To derive this formula, the Green function of the infinite media is represented as an expansion through the plane waves, and from (7.29) follows:

$$G_{ij}^{\infty}(\boldsymbol{\rho}) = \int d^3\boldsymbol{k} \frac{M_{ij}(\boldsymbol{n})}{(2\pi)^3 k^2} e^{i\boldsymbol{k}\boldsymbol{\rho}}, \quad M_{ij}(\boldsymbol{n}) = (C_{ikjl} n_k n_l)^{-1}, \quad \boldsymbol{k} = k\boldsymbol{n}, \tag{7.54}$$

where $M_{ij}(\boldsymbol{n})$ is a Chirstoffel tensor (acoustic tensor). Using formula (7.35), the integral in (7.53) is expressed as:

$$\int d^3\boldsymbol{\rho} f_{nm}(\rho)\Gamma_{ipjk}^{\infty}(\boldsymbol{\rho}) = \int d^2\boldsymbol{n} \frac{M_{(\underline{i}\underline{j}}(\boldsymbol{n})}{(2\pi)^3} n_{\underline{p})} n_k \int \rho^2 d\rho k^2 dk \int d^2\boldsymbol{n}_\rho f_{nm}(\rho) e^{ik\rho\boldsymbol{n}\boldsymbol{n}_\rho}. \tag{7.55}$$

The integral over the directions $\boldsymbol{n}_\rho$ is conveniently calculated in spherical coordinates with the axis z along $\boldsymbol{n}$, and further integration over k by using

$$\delta'(x) = \frac{1}{\pi} \lim_{L\to\infty} \left(\frac{L\cos Lx}{x} - \frac{\sin Lx}{x} \right)$$

and integrating over ρ by using

$$x\delta'(x) = -\delta(x), \quad \int_0^a \delta(x)dx = \frac{1}{2}\mathrm{Sign}(a)$$

modifies (7.55) to the expression:

$$\int d^3\boldsymbol{\rho} f_{nm}(\rho)\Gamma_{ipjk}^{\infty}(\boldsymbol{\rho}) = E_{ipjk} f_{nm}(0), \tag{7.56}$$

where

$$E_{ipjk} = \frac{1}{4\pi} \int d^2\boldsymbol{n} M_{(\underline{i}\underline{j}}(\boldsymbol{n}) n_{\underline{p})} n_k. \tag{7.57}$$

This simple formula is a consequence of the spherical symmetry $f_{nm}(\boldsymbol{\rho})$ of the grains. The similar results is obtained [18, 31] for the grains of elliptical shape, where the tensor $\boldsymbol{E}$ is:

$$E_{ipjk} = \frac{a_1 a_2 a_3}{4\pi} \int d^2\boldsymbol{n} \frac{M_{(\underline{i}\underline{j}}(\boldsymbol{n}) n_{\underline{p})} n_k}{(n_1^2 a_1^2 + n_2^2 a_2^2 + n_3^2 a_3^2)^{3/2}}, \tag{7.58}$$

where the coordinate system coincides with the ellipse axes, and a_1, a_2, a_3 are the lengths of the semi-axes. The dimensionless tensor $\boldsymbol{E} : \boldsymbol{C}$ is called an Eshelby tensor

[21] which is used for calculation of strain fields for the inclusions inside the sample [22]. Substituting (7.58) into (7.53) and utilizing the equality $f_{nm}(0) = \delta_{nm} V_n / V$, the following expression is found:

$$(\delta \boldsymbol{c}_n^{-1} + \boldsymbol{E}) : \widetilde{\boldsymbol{\sigma}}_n^* - \boldsymbol{E} : \langle \widetilde{\boldsymbol{\sigma}}^* \rangle = \boldsymbol{\epsilon}^{(0)}, \tag{7.59}$$

from where the relation between the fluctuating stress $\widetilde{\boldsymbol{\sigma}}_n^*$ and the average value $\langle \widetilde{\boldsymbol{\sigma}}^* \rangle$ follows:

$$\widetilde{\boldsymbol{\sigma}}_n^* = \boldsymbol{B}_n : (\boldsymbol{\epsilon}^{(0)} + \boldsymbol{E} : \langle \widetilde{\boldsymbol{\sigma}}^* \rangle), \quad \boldsymbol{B}_n = (\delta \boldsymbol{c}_n^{-1} + \boldsymbol{E})^{-1}. \tag{7.60}$$

By averaging this formula, the connection between $\langle \widetilde{\boldsymbol{\sigma}}^* \rangle$ and average strain is obtained:

$$\langle \widetilde{\boldsymbol{\sigma}}^* \rangle = (\mathbf{1} - \langle \boldsymbol{B} \rangle : \boldsymbol{E})^{-1} : \langle \boldsymbol{B} \rangle : \boldsymbol{\epsilon}^{(0)}, \quad \langle \boldsymbol{B} \rangle = \sum_n \frac{V_n}{V} \boldsymbol{B}_n. \tag{7.61}$$

The expressions (7.60) and (7.61) connect the fluctuating stresses $\widetilde{\boldsymbol{\sigma}}_n^*$ with the average strain $\epsilon^{(0)}$. Thus, the functional (7.49) minimized on the class of the functions (7.48) can be expressed through the quadratic form of $\epsilon^{(0)}$ according to (7.50). Comparing this result with the equation (7.46), the upper boundary for macroscopic stiffness tensor in case of positively defined $\delta \boldsymbol{c}_n^{-1}$ (or lower boundary in case of negatively defined $\delta \boldsymbol{c}_n^{-1}$) is:

$$\boldsymbol{C}_{HS} = \boldsymbol{C} + (\mathbf{1} - \langle \boldsymbol{B} \rangle : \boldsymbol{E})^{-1} : \langle \boldsymbol{B} \rangle. \tag{7.62}$$

These estimates for the boundaries of the macroscopic rigidity modulus have been proposed by Hashin and Shtrikman [32]. Due to taking into account the correlation properties of the grains by Eshelby tensor, the boundaries are found to be more narrow than the ones provided by Voigt and Reuss.

Using the Eq. (7.48) as a model solution of the Eq. (7.17), the relation (7.16) between the strain in the grain with the orientation $\boldsymbol{g}$ and the macroscopic stress on the basis of (7.52), (7.62), (7.60), and (7.61), we obtain:

$$\boldsymbol{A}_{HS}(\boldsymbol{g}) = [\mathbf{1} - \boldsymbol{E} : (\boldsymbol{B}(\boldsymbol{g}) : \{\mathbf{1} + \boldsymbol{E} : (\boldsymbol{C}_{HS} - \boldsymbol{C})\} - \{\boldsymbol{C}_{HS} - \boldsymbol{C}\})] : \boldsymbol{C}_{HS}^{-1}. \tag{7.63}$$

7.2.4 Self-Consistent Model of Eshelby-Kröner

The tensor $\boldsymbol{C}$ in the expressions (7.27)–(7.52) can be chosen in an arbitrary way, except of the case when using (7.46) and (7.47) the boundaries for macroscopic stiffness tensor $\boldsymbol{C}_M$ have to be determined. In this case, the positive (negative) definite difference $\delta \boldsymbol{c}_n$ is required for each grain n. To find the model solution of (7.17) or to minimize the functional (7.44), the tensor $\boldsymbol{C}$ has to be defined. The easiest way

is to set tensor $\boldsymbol{C}$ equal to the macroscopic stiffness tensor $\boldsymbol{C}_M$, and then (7.37) and (7.38) are written as:

$$\boldsymbol{C} = \boldsymbol{C}_M, \quad \langle \boldsymbol{\sigma} \rangle = \boldsymbol{C} : \langle \boldsymbol{\epsilon} \rangle = \boldsymbol{C} : \boldsymbol{\epsilon}^{(0)} \tag{7.64}$$

This assumption sets the value of $\langle \widetilde{\boldsymbol{\sigma}}^* \rangle$ to zero because of:

$$\langle \boldsymbol{\sigma} \rangle = \langle (\boldsymbol{C} + \delta \boldsymbol{c}) : \boldsymbol{\epsilon} \rangle = \boldsymbol{C} : \boldsymbol{\epsilon}^{(0)} + \langle \widetilde{\boldsymbol{\sigma}} \rangle = \boldsymbol{C} : \boldsymbol{\epsilon}^{(0)}. \tag{7.65}$$

As a next step, we minimize the functional (7.44) on the class of probe functions (7.48), and again obtain the formulas (7.59)–(7.61). Using (7.60) and (7.43), the strain of the n-grain is equal to:

$$\boldsymbol{\epsilon}_n = \delta \boldsymbol{c}_n^{-1} : \boldsymbol{B}_n : \boldsymbol{\epsilon}^{(0)} = (\boldsymbol{1} + \boldsymbol{E} : \delta \boldsymbol{c}_n)^{-1} : \boldsymbol{\epsilon}^{(0)}. \tag{7.66}$$

The requirement of the average strain from (7.66) to be equal $\boldsymbol{\epsilon}^{(0)}$ leads to the equation:

$$\langle (\boldsymbol{1} + \boldsymbol{E} : \delta \boldsymbol{c}_n)^{-1} \rangle = \boldsymbol{1}. \tag{7.67}$$

This tensor expression is a system of equations for the determination of the components of the tensor $\boldsymbol{C}$. Indeed, the tensor $\boldsymbol{C}$ defines the tensor $\boldsymbol{E}$ through the Eqs. (7.54) and (7.58), and this relationship is non-linear in general case. The number of independent parameters in averaged tensors (the left part of (7.67) and macroscopic tensors $\boldsymbol{E}$ and $\boldsymbol{C}$) is equal. For example, the tensors are described by two parameters in case of macroscopic isotropy (absence of texture), see details in Sect. 7.4. As a result, the expression (7.67) contains as many independent equations as the number of independent components in tensor $\boldsymbol{C}$. Due to the procedures of convolution in (7.54) and of integration in (7.58), the relationship between $\boldsymbol{E}$ and $\boldsymbol{C}$ is non-linear and cumbersome. As a consequence, the system of equations (7.67) is also non-linear. In a simple case of microscopic isotropy and cubic symmetry of the crystallites, the formula (7.67) leads to the cubic equation (7.147), see [23, 21].

The equations analogous to (7.67) can be obtained in another ways, for example, the macroscopic Hooke's law (7.65) satisfying to $\langle \widetilde{\boldsymbol{\sigma}}^* \rangle = 0$ results in the following equation, according to (7.61):

$$\langle \boldsymbol{B} \rangle = \langle (\delta \boldsymbol{c}_n^{-1} + \boldsymbol{E})^{-1} \rangle = \boldsymbol{0}. \tag{7.68}$$

For the crystallites of the same shape having equal Eshelby tensors, the equation (7.68) is equivalent to (7.162). However, if the tensor $\boldsymbol{E}$ varies from one crystallite to another $\boldsymbol{E} = \boldsymbol{E}_n$, the formulas (7.68) and (7.67) give different results. This situation occurs in case of morphological texture [33, 34] with the grains of anisotropic elliptical shape in different orientations.

The relationship (7.16) for the considered model follows directly from (7.66) and (7.64):

$$\boldsymbol{A}_{EK}(\boldsymbol{g}) = (\boldsymbol{1} + \boldsymbol{E} : \delta \boldsymbol{c}(\boldsymbol{g}))^{-1} : \boldsymbol{S}. \tag{7.69}$$

The frequently used method of the derivation of equation (7.67) is based on the model of the inclusions inside the infinite matrix [22, 23]. This approach substitutes the problem of grain interaction by the model of the grain of spherical (elliptical) shape included into infinite effective media, called matrix. The stiffness tensor of matrix is assumed to be equal to the stiffness tensor of polycrystal, which has to be found. To solve this problem, the strain inside n-th grain has to be determined. The parameter $\delta \boldsymbol{c}(\boldsymbol{r})$ in the equation (7.28) has the following form:

$$\delta \boldsymbol{c}(\boldsymbol{r}) = \delta \boldsymbol{c}_n \Theta_n(\boldsymbol{r}). \tag{7.70}$$

To determine the strain in n-th grain, the equation (7.28) has to be solved, which also can be reduced to the formula (7.32). The sample is supposed to be infinite and, therefore, the Green function of infinite media is admitted. By analogue with (7.54) and (7.55), the integral is modified to:

$$\begin{aligned}(\Gamma^{\infty}_{ipjk}\delta c_{jklm}\epsilon_{lm})(\boldsymbol{r}) = \int d^2\boldsymbol{n}\frac{M_{(\underline{i}\underline{j})}(\boldsymbol{n})}{(2\pi)^3}n_{\underline{p})}n_k \\ \times \int d^3\boldsymbol{r}'\delta c_{jklm}\epsilon_{lm}(\boldsymbol{r}')\int k^2 dk e^{ik\boldsymbol{n}(\boldsymbol{r}-\boldsymbol{r}')}.\end{aligned} \tag{7.71}$$

We assume here that the strain inside n-th grain is uniform and the grain has a spherical shape, and the integral over k is presented in the form of [31]:

$$\int k^2 dk e^{ik\boldsymbol{n}(\boldsymbol{r}-\boldsymbol{r}')} = -\nabla^2_{\boldsymbol{r}}\int dk e^{ik\boldsymbol{n}(\boldsymbol{r}-\boldsymbol{r}')} = -\nabla^2_{\boldsymbol{r}}\pi\delta(\boldsymbol{n}(\boldsymbol{r}-\boldsymbol{r}')). \tag{7.72}$$

The integral over $\boldsymbol{r}'$ is easy to calculate in spherical coordinates with the axis z along the vector $\boldsymbol{n}$:

$$\int d^3\boldsymbol{r}'\nabla^2_{\boldsymbol{r}}\delta(\boldsymbol{n}(\boldsymbol{r}-\boldsymbol{r}')) = \pi(R^2-(\boldsymbol{n}\boldsymbol{r})^2), \tag{7.73}$$

here R is a radius of grain. The expression obtained has a physical meaning of the square of disc formed in the space of $\boldsymbol{r}'$ by the intersection of the sphere with the radius R and the plane defined by the equation $\boldsymbol{n}(\boldsymbol{r}-\boldsymbol{r}') = 0$. Finally, for the function (7.71) we obtain:

$$\begin{aligned}(\Gamma_{ipjk}\delta c_{jklm}\epsilon_{lm})(\boldsymbol{r}) = \int d^2\boldsymbol{n}\frac{M_{(\underline{i}\underline{j})}(\boldsymbol{n})}{(2\pi)^3}n_{\underline{p})}n_k\delta c_{jklm}\epsilon_{lm} \\ \times(-\pi^2)\nabla^2_{\boldsymbol{r}}(R^2-(\boldsymbol{n}\boldsymbol{r})^2) = \boldsymbol{E}:\delta\boldsymbol{c}:\epsilon_n.\end{aligned} \tag{7.74}$$

This formula shows that for the spherical grains the strain inside the grain is uniform. The dependence on the radius $\boldsymbol{r}$ disappears when the section of the grain by the plane is a curve of the second order, i.e. sphere and ellipse. By substituting (7.74) into (7.32):

$$\boldsymbol{\epsilon}_n = \boldsymbol{\epsilon}^{(0)} - \boldsymbol{E}:\delta\boldsymbol{c}_n:\epsilon_n. \tag{7.75}$$

The formula (7.66) follows immediately from the expression above, that confirms the equivalence of the approaches based on the variational principle and effective media.

The expressions similar to (7.75) and (7.66) exist also in the electrostatics, for example, the external field causes the uniform field in sphere or ellipsoid [35]. The calculations based on (7.57) result for the sphere with the permittivity ϵ_0 in the tensor $\boldsymbol{E}$:

$$E_{ij} = \frac{1}{3\epsilon_0}\delta_{ij}. \tag{7.76}$$

The tensor analogous to the tensor Eshelby $\boldsymbol{E} : \boldsymbol{C}$ in this case is equal to $\frac{1}{3}\delta_{ij}$ and it is called the tensor of depolarization or demagnitization in electrostatics and magnetostatics, respectively [36]. As follows from (7.66), the electric field $\boldsymbol{E}_1$ inside sphere with permittivity ϵ_1 and the electric field $\boldsymbol{E}_0$ in the media with permittivity ϵ_0 are connected as [35]:

$$\boldsymbol{E}_1 = \frac{3\epsilon_0}{2\epsilon_0 + \epsilon_1}\boldsymbol{E}_0. \tag{7.77}$$

The algorithm of the calculation of the properties of composite random media using the method of effective media and the expressions (7.77) and (7.67) has been proposed by Bruggeman [20]. This technique is successfully applied for calculation of optical properties of the composite and nanostructured materials [16].

7.2.5 Grain Interaction in Thin Film. Vook-Witt and Inverse Vook-Witt Models

The considered in the previous sections grain interaction was assumed to take a place in a sample with a large number of grain in all spatial directions. The statistical methods used for calculation of physical parameters are based on this assumption. The important class of the investigated by X-ray stress method samples are thin films and coatings. The number of grains in a lateral direction of film is statistically large enough, however, in the direction of a surface normal it can be small. The entire thickness of the film often contains a single grain [5, 37, 38], and thus the system is rather two-dimensional than three-dimensional. The methods described above are therefore not applicable for coatings in general case.

The averaging over all directions is no longer possible because of the evident anisotropy, which complicates the calculation of the Eq. (7.16). For these samples, the simple phenomenological models of grain interaction are used, which take into account the difference of physical properties in lateral and normal directions.

The frequently used model of such type is a Vook-Witt model [39, 40], which adopts the Voigt model in lateral direction (equal strains), and the Reuss model (equal stresses) in the normal direction. Introducing z axis along the normal to the film, the strain and stress tensors in n-th grain are expressed as:

$$\boldsymbol{\epsilon}_n = \begin{pmatrix} \langle\epsilon_{11}\rangle & \langle\epsilon_{12}\rangle & \cdot \\ \langle\epsilon_{12}\rangle & \langle\epsilon_{22}\rangle & \cdot \\ \cdot & \cdot & \cdot \end{pmatrix}, \quad \boldsymbol{\sigma}_n = \begin{pmatrix} \cdot & \cdot & \langle\sigma_{13}\rangle \\ \cdot & \cdot & \langle\sigma_{23}\rangle \\ \langle\sigma_{13}\rangle & \langle\sigma_{23}\rangle & \langle\sigma_{33}\rangle \end{pmatrix}, \tag{7.78}$$

where the symbol $\cdot$ means the component is being not fixed by the model but found from the elasticity theory.

The strain and stress fields (7.78) can be found from the exact solutions of the elastic equations (7.17) in a certain geometry of the polycrystal. By considering the polycrystalline film as a stack of the parallel infinite plates, the Eq. (7.78) satisfies the boundary conditions (7.17), and the uniform inside the plates strain fields are the solutions of the differential equation (7.17). To find the relation (7.16) based on the assumption (7.78), we formulate the Hooke's law for n-th grain:

$$\boldsymbol{\sigma}_n = \boldsymbol{c}_n : \boldsymbol{\epsilon}_n, \tag{7.79}$$

which expresses the strain $\boldsymbol{\epsilon}_n$ and the stress $\boldsymbol{\sigma}_n$ in the grain through the average values $\langle\boldsymbol{\epsilon}\rangle$ and $\langle\boldsymbol{\sigma}\rangle$. Keeping in mind the symmetry of the tensors, the formula (7.78) contains six undefined variables:

$$\epsilon_{n13}, \epsilon_{n23}, \epsilon_{n33}, \sigma_{n11}, \sigma_{n12}, \sigma_{n22},$$

and the relationship (7.79) gives six equations, accordingly.

To present the following expressions in a simple form, the coordinate free covariant notations [38, 41] are introduced instead of the indices. The assumptions (7.78) can be re-written as [38]:

$$\boldsymbol{\Pi}_{||} : \boldsymbol{\epsilon} = \boldsymbol{\Pi}_{||} : \langle\boldsymbol{\epsilon}\rangle, \quad \boldsymbol{\Pi}_{\perp} : \boldsymbol{\sigma} = \boldsymbol{\Pi}_{\perp} : \langle\boldsymbol{\sigma}\rangle, \quad \boldsymbol{\Pi}_{||} + \boldsymbol{\Pi}_{\perp} = \mathbf{1}, \tag{7.80}$$

where the tensor of 4th rank $\boldsymbol{\Pi}_{||}$ means the projection of the 2nd rank tensor on the plane with the normal $\boldsymbol{n}$. The projection of the vector onto the plane with the normal $\boldsymbol{n}$ is performed by the projector $\boldsymbol{t}$, see (4.20). The projection of the 2nd rank tensor is then written as:

$$\boldsymbol{\Pi}_{||} : \boldsymbol{\epsilon} = \boldsymbol{t} \cdot \boldsymbol{\epsilon} \cdot \boldsymbol{t}, \quad \boldsymbol{t} = \mathbf{1} - \boldsymbol{n} \otimes \boldsymbol{n}, \tag{7.81}$$

or in the index form [38]:

$$\begin{aligned} \Pi_{||ijkl} =& t_{i(\underline{k}}t_{\underline{jl})} \\ =& \frac{1}{2}(\delta_{ik}\delta_{jl} + \delta_{il}\delta_{jk}) - \frac{1}{2}(\delta_{ik}n_jn_l + \delta_{il}n_jn_k + \delta_{jk}n_in_l + \delta_{jl}n_in_k) \\ & + n_in_jn_kn_l, \\ \Pi_{\perp ijkl} =& \frac{1}{2}(\delta_{ik}\delta_{jl} + \delta_{il}\delta_{jk}) - \Pi_{||ijkl}. \end{aligned} \tag{7.82}$$

Here we took into account the fact of the symmetry of the projected tensors over the indices k and l, which leads to the symmetrization of the projector, see (7.33). To explicitly find the tensor (7.16), the Eq. (7.79) is written in the following form:

$$\boldsymbol{\Pi}_{||} : \boldsymbol{\sigma}_n + \boldsymbol{\Pi}_{\perp} : \boldsymbol{\sigma}_n = \boldsymbol{c}_n : \boldsymbol{\Pi}_{||} : \boldsymbol{\epsilon}_n + \boldsymbol{c}_n : \boldsymbol{\Pi}_{\perp} : \boldsymbol{\epsilon}_n. \tag{7.83}$$

Using the model (7.78) and Hooke's law for the averaged values (7.38), the tensor (7.16) for the n-th grain is:

$$\boldsymbol{A}_n = \boldsymbol{c}_n : (\boldsymbol{\Pi}_{||} : \boldsymbol{c}_n - \boldsymbol{c}_n : \boldsymbol{\Pi}_{\perp})^{-1} : (\boldsymbol{c}_n : \boldsymbol{\Pi}_{||} - \boldsymbol{\Pi}_{\perp} : \boldsymbol{C}_M). \tag{7.84}$$

To use (7.84), the macroscopic stiffness tensor C_M has to be determined, which follows from the averaging of (7.84):

$$\begin{aligned} (\mathbf{1} + \boldsymbol{\beta} : \boldsymbol{\Pi}_{\perp}) : \boldsymbol{C}_M =& \boldsymbol{\alpha} : \boldsymbol{\Pi}_{||}, \\ \boldsymbol{\alpha} =& \langle \boldsymbol{c}_n : (\boldsymbol{\Pi}_{||} : \boldsymbol{c}_n - \boldsymbol{c}_n : \boldsymbol{\Pi}_{\perp})^{-1} : \boldsymbol{c}_n \rangle, \\ \boldsymbol{\beta} =& \langle \boldsymbol{c}_n : (\boldsymbol{\Pi}_{||} : \boldsymbol{c}_n - \boldsymbol{c}_n : \boldsymbol{\Pi}_{\perp})^{-1} \rangle. \end{aligned} \tag{7.85}$$

In general, there no operator exists, which is inverse to the projectional one, and in (7.85) the operator $\mathbf{1} + \boldsymbol{\beta} : \boldsymbol{\Pi}_{\perp}$ also has no inverse one. Thus, the operator C_M cannot be determined from (7.85), and we use for this purpose the expression analogous to (7.83) with the compliance tensor $\boldsymbol{s}_n$. After some transformations, we obtain formula analogous to (7.85) but with S_M, and using $\boldsymbol{C}_M = \boldsymbol{S}_M^{-1}$ obtain:

$$\begin{aligned} \boldsymbol{\gamma} : \boldsymbol{\Pi}_{\perp} : \boldsymbol{C}_M =& (\mathbf{1} + \boldsymbol{\delta} : \boldsymbol{\Pi}_{||}), \\ \boldsymbol{\gamma} =& \langle \boldsymbol{s}_n : (\boldsymbol{\Pi}_{\perp} : \boldsymbol{s}_n - \boldsymbol{s}_n : \boldsymbol{\Pi}_{||})^{-1} : \boldsymbol{s}_n \rangle, \\ \boldsymbol{\delta} =& \langle \boldsymbol{s}_n : (\boldsymbol{\Pi}_{\perp} : \boldsymbol{s}_n - \boldsymbol{s}_n : \boldsymbol{\Pi}_{||})^{-1} \rangle. \end{aligned} \tag{7.86}$$

This equation does not define C_M unambiguously similarly to (7.85). However, the operators $\mathbf{1} + \boldsymbol{\beta} : \boldsymbol{\Pi}_{\perp}$ in (7.85) and $\boldsymbol{\gamma} : \boldsymbol{\Pi}_{\perp}$ in (7.86) are the projectors onto different subspaces, which complement each other. Therefore, the sum of (7.85) and (7.86) with arbitrary coefficient k defines the function C_M unambiguously:

$$\boldsymbol{C}_M = (\mathbf{1} + \boldsymbol{\beta} : \boldsymbol{\Pi}_{\perp} + k\boldsymbol{\gamma} : \boldsymbol{\Pi}_{\perp})^{-1} : (\boldsymbol{\alpha} : \boldsymbol{\Pi}_{||} + k[\mathbf{1} + \boldsymbol{\delta} : \boldsymbol{\Pi}_{||}]). \tag{7.87}$$

The expressions (7.84) and (7.87) comprehensively determine the relationship (7.16). These formulas do not contain the parameters, which describe the correlation properties of the grain locations, as the tensor $\boldsymbol{E}$ in equations (7.69) and (7.63) does. In this sense, the Vook-Witt model is similar to the models of Voigt and Reuss: the mutual influence of grains is not considered, and the resulting expressions depend only on the fraction of grains with certain orientations and do not depend on the morphology of the polycrystal. The strain inside the grain is uniform.

Both Voigt and Reuss models are the limiting cases of grain interaction. The Vook-Witt model with Voigt approach in a lateral direction and Reuss approach in a normal one, is also a limiting case of the grain interaction. The reversed case of Vook-Witt model with Voigt model in a normal and Reuss model in a lateral directions has been proposed in [37] and is called inverse Vook-Witt model:

$$\boldsymbol{\Pi}_{||} : \boldsymbol{\sigma} = \boldsymbol{\Pi}_{||} : \langle \boldsymbol{\sigma} \rangle, \quad \boldsymbol{\Pi}_{\perp} : \boldsymbol{\epsilon} = \boldsymbol{\Pi}_{\perp} : \langle \boldsymbol{\epsilon} \rangle. \tag{7.88}$$

By comparing (7.88) and (7.80), the expressions (7.84)–(7.87) in the models of Vook-Witt and inverse Vook-Witt differ by the substitution of $\boldsymbol{\Pi}_{\perp}$ for $\boldsymbol{\Pi}_{||}$ and vice versa. In opposite to Vook-Witt model, there is no system exists for which the strain and stress fields found by the inverse Vook-Witt model are the exact solutions [38].

The intermediate cases between Vook-Witt and inverse Vook-Witt models are proposed in [37] to describe the grain interaction by a linear combination of former ones. The alternative approach for the intermediate cases is Eshelby-Kröner model for the elliptical grains [5, 38]. The variable parameter, which makes a balance between both limiting cases is a ratio of semi-axes of the ellipsoid. Generally speaking, the model designed for the bulk polycrystal is not applicable to the thin polycrystalline film. However, in the limiting cases, the Eshelby-Kröner model becomes effectively two-dimensional. For the oblate ellipsoid ($a_1 = a_2 >> a_3$, axis z along normal to the surface), the Eshelby-Kröner model transforms into Vook-Witt model [5] and is an exact solution. The opposite limiting case of the stretched ellipsoid $a_1 = a_2 << a_3$ in the Eshelby-Kröner approach coincides with the infinite cylinder model, which being a two-dimensional model gives different results than the inverse Vook-Witt one [5].

7.3 Residual Stress Analysis as a Particular Case of Powder Diffractometry

The real microstructure of the polycrystals is very complex [42]. X-ray diffraction provides the results of X-ray scattering from a large volume of the sample, and this fact leads to a contribution of numerous factors into the detected X-ray profile. The practical data treatment of the recorded X-ray intensities assumes the use of a simplified sample model parametrized by the effective physical variables [2].

The typical model assumes the polycrystal as consisting of a large number of the crystalline blocks (grains). Each grain has a certain shape, size and orientation of the crystallographic lattice, and may contain the defects of a crystallographic lattice, for instance, dislocations. Due to different reasons (plastic deformation, thermal expansion, etc.), the polycrystal may have the macroscopic residual stresses.

Using the results of previous chapter, the intensity of the diffracted X-ray radiation from the polycrystal can be calculated. The dynamical effects are neglected here, because of due to the disorientation of the grains, the typical scale of the cor-

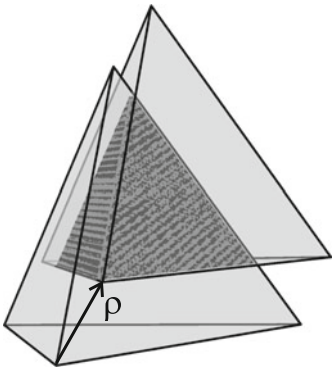

Fig. 7.5 The sketch for calculation of the auto-correlation function of the grain shape (7.92)

relation function (6.60) given by the correlation length l_d is less than the size of the grain. This estimate is taken with a certain reserve, because of the presence of the defects diminishes the parameter l_d. The size of the grains is essentially less than the extinction length, and thus the diffraction can be treated as kinematical, according to (6.77). The general expression for the intensity in this case is (6.83):

$$I(\boldsymbol{Q}) = \int d^3\boldsymbol{r}_1 d^3\boldsymbol{r}_2 e^{i(\boldsymbol{Q}-\boldsymbol{H})(\boldsymbol{r}_1-\boldsymbol{r}_2)} g(\boldsymbol{r}_1, \boldsymbol{r}_2), \tag{7.89}$$

here $\boldsymbol{Q} = \boldsymbol{k}_{out} - \boldsymbol{k}_{in}$ is a momentum transfer, $g(\boldsymbol{r}_1, \boldsymbol{r}_2)$ is a correlation function of polycrystal, $\boldsymbol{H}$ is a reciprocal lattice vector of the excited reflection. We omitted the constant coefficients in the expression because of in the most of the cases the relative intensities are evaluated within a single diffraction profile. The effects of the instrumental and resolution functions are also neglected, which can be accounted by the special functions [2]. Assuming the disoriented grains, the correlation function of the whole system consists of the sum of the correlation functions of the grains:

$$I(\boldsymbol{Q}) = \sum_n \int d^3\boldsymbol{r}_1 d^3\boldsymbol{r}_2 e^{i(\boldsymbol{Q}-\boldsymbol{H}_n)(\boldsymbol{r}_1-\boldsymbol{r}_2)} g_n(\boldsymbol{r}_1, \boldsymbol{r}_2)\Theta_n(\boldsymbol{r}_1)\Theta_n(\boldsymbol{r}_2). \tag{7.90}$$

Here the sum is taken over all grains of polycrystal, $\boldsymbol{H}_n$ is a reciprocal lattice vector corresponding to the average lattice of n-th grain, g_n is a correlation function inside n-th grain, $\Theta_n(\boldsymbol{r})$ is a function describing the shape of n-th grain, which is equal to unity inside the grain and to zero outside. The defects are supposed to be distributed uniformly inside the grain, and the influence of the grain shape on the strain field is neglected. Under these conditions, the correlation function depends on the relative distance $\boldsymbol{\rho} = \boldsymbol{r}_1 - \boldsymbol{r}_2$, and using the integration over the variables $\boldsymbol{r}_1$ and $\boldsymbol{\rho}$, we obtain:

$$I(\boldsymbol{Q}) = \sum_n \int d^3\boldsymbol{\rho} e^{i(\boldsymbol{Q}-\boldsymbol{H}_n)\boldsymbol{\rho}} g_n(\boldsymbol{\rho}) \int d^3\boldsymbol{r}_1 \Theta_n(\boldsymbol{r}_1)\Theta_n(\boldsymbol{r}_1 - \boldsymbol{\rho}). \tag{7.91}$$

The integral over $\boldsymbol{r}_1$ as a function of the distance $\boldsymbol{\rho}$ is an auto-correlation function of the grain shape: it is a volume of the intersectional area, which is created by the original and the shifted by vector $\boldsymbol{\rho}$ grains (Fig. 7.3). According to (6.60), the correlation function in the presence of several independent types of defects is a product of correlation functions for each defect type. As follows from (7.91), the influence of the grain shape can also be represented by a correlation function:

$$g_V(\boldsymbol{\rho})_n = \frac{1}{V_n}\int d^3\boldsymbol{r}_1 \Theta_n(\boldsymbol{r}_1)\Theta_n(\boldsymbol{r}_1 - \boldsymbol{\rho}), \tag{7.92}$$

where V_n is a volume of n-th grain.

The values $g_n(\boldsymbol{\rho})$, $g_V(\boldsymbol{\rho})_n$ and $\boldsymbol{H}_n$ vary from grain to grain. However, the grain shape and volume, the defects inside the grain and the orientation of grain are statistically independent, and these parameters can be averaged separately:

$$I(\boldsymbol{Q}) = \sum_n V_n \int d^3\boldsymbol{\rho}\langle e^{i(\boldsymbol{Q}-\boldsymbol{H}_n)\rho}\rangle\langle g_n(\boldsymbol{\rho})\rangle\langle g_V(\boldsymbol{\rho})_n\rangle. \tag{7.93}$$

The number of the grains in the sample is usually large and, therefore, the distribution functions can be introduced for the parameters. For the sake of simplicity, the distributions of grain shapes [43] and defects [44] are omitted here. The distribution of the grain orientations (texture) is described by the orientational distribution function [45] $f(\boldsymbol{g})$:

$$f(\boldsymbol{g})d^3\boldsymbol{g} = \frac{dV_g}{V}, \tag{7.94}$$

where $\boldsymbol{g}$ is a set of three parameters describing the orientation of crystallographic lattice of grain with respect to the sample, dV_g is a total volume of grains, which have an orientation within the interval $\boldsymbol{g}, \boldsymbol{g} + d\boldsymbol{g}$ and V is a volume of polycrystal. The isotropic distribution of grains corresponds to $f(\boldsymbol{g}) = 1$. Taking into account (7.94) the Eq. (7.92) becomes:

$$I(\boldsymbol{Q}) = V\int d^3\boldsymbol{\rho}d^3\boldsymbol{g}\, f(\boldsymbol{g})e^{i(\boldsymbol{Q}-\boldsymbol{H}(g))\rho}g(\boldsymbol{\rho}), \tag{7.95}$$

where $g(\boldsymbol{\rho})$ is a product of the averaged correlation functions $\langle g_n(\boldsymbol{\rho})\rangle\langle g_V(\boldsymbol{\rho})_n\rangle$, the constant multiplier V is omitted in further calculations.

For the orientation of the grain $\boldsymbol{g}$ (parametrization of the rotation group [46]), the Euler angles are frequently chosen. In this parametrization, the law of the parameters composition is quite complex. Therefore we use further the vector parametrization of the rotation group known as Gibbs vector [41, 46]. In this parametrization, the rotation is parametrized by the vector $\boldsymbol{c}$ with the direction defined by the axis of rotation and with the length equals to $\tan\phi/2$, where ϕ is a rotation angle. The rotation matrix is expressed through $\boldsymbol{c}$ as [41, 46]:

$$T_{ij}(\boldsymbol{c}) = \frac{(1-\boldsymbol{c}^2)\delta_{ij} + 2\boldsymbol{c}_i\boldsymbol{c}_j + 2\varepsilon_{ikj}\boldsymbol{c}_k}{1+\boldsymbol{c}^2}, \tag{7.96}$$

where ε_{ikj} is the antisymmetric Levi-Cevita pseudo-tensor. The vector parametrization is outstanding among other parameterizations because of its elegant composition law, which enables to express two successive rotations with parameters $\boldsymbol{c}^{(1)}$ and $\boldsymbol{c}^{(2)}$ as a single rotation with the parameter $\boldsymbol{c}^{(12)}$ [41, 46]:

$$T_{ij}(\boldsymbol{c}^{(2)})T_{jk}(\boldsymbol{c}^{(1)}) = T_{ik}(\left\langle \boldsymbol{c}^{(2)}, \boldsymbol{c}^{(1)} \right\rangle) = T_{ik}(\boldsymbol{c}^{(12)}), \tag{7.97}$$

$$\left\langle \boldsymbol{c}^{(2)}, \boldsymbol{c}^{(1)} \right\rangle = \frac{\boldsymbol{c}^{(1)} + \boldsymbol{c}^{(2)} + \boldsymbol{c}^{(2)} \times \boldsymbol{c}^{(1)}}{1-\boldsymbol{c}^{(1)}\boldsymbol{c}^{(2)}}.$$

Additionally, the vector parametrization has the following convenient properties:

$$T_{ij}(\{0,0,0\}) = \delta_{ij};\ \boldsymbol{T}(\boldsymbol{c})^{-1} = \boldsymbol{T}(-\boldsymbol{c}). \tag{7.98}$$

Using this parametrization, the formula (7.95) is written as:

$$I(\boldsymbol{Q}) = \int d^3\boldsymbol{\rho} \frac{d^3\boldsymbol{c}}{\pi^2(1+\boldsymbol{c}^2)^2} f(\boldsymbol{c}) e^{i(\boldsymbol{Q}-\boldsymbol{H}(\boldsymbol{c}))\boldsymbol{\rho}} g(\boldsymbol{\rho}). \tag{7.99}$$

Here $1/\pi^2(1+\boldsymbol{c}^2)^2$ is a weight function for invariant integration over the rotation group [41], the corresponding weight function for parametrization through the Euler angles is $\sin\theta/8\pi^2$ [47].

The dependence of the reciprocal lattice vector $\boldsymbol{H}(\boldsymbol{c})$ from the grain orientation $\boldsymbol{c}$ is conditioned in the following way. The vector $\boldsymbol{H}$ is defined by Miller indices in the coordinate system $\boldsymbol{C}$, and due to the stresses of II type it varies both for direction and module from grain to grain. Assuming the small magnitude of strains, the components of vector $\boldsymbol{H}^{(L)}$ corresponding to the average crystallographic lattice of grain with the orientation $\boldsymbol{c}$ can be represented as:

$$\boldsymbol{H}^{(L)} = \boldsymbol{T}(\boldsymbol{c}^{(LC)})\boldsymbol{H}^{(C)}(\boldsymbol{c}), \quad \boldsymbol{H}^{(C)}(\boldsymbol{c}) = \boldsymbol{H}^{(0)}(1-\epsilon_H(\boldsymbol{c})) + \delta\boldsymbol{H}_\perp(\boldsymbol{c}), \tag{7.100}$$

$$\epsilon_H(\boldsymbol{c}) = \frac{\boldsymbol{H}^{(0)} \cdot \boldsymbol{\epsilon}(\boldsymbol{c}) \cdot \boldsymbol{H}^{(0)}}{\boldsymbol{H}^{(0)^2}}, \quad \delta\boldsymbol{H}_\perp(\boldsymbol{c}) = \boldsymbol{\epsilon}(\boldsymbol{c}) \cdot \boldsymbol{H}^{(0)} - \boldsymbol{H}^{(0)}\epsilon_H,$$

here $\boldsymbol{H}^{(0)}$ corresponds to a non-deformed lattice, and vector $\delta\boldsymbol{H}_\perp(\boldsymbol{c})$ is perpendicular to $\boldsymbol{H}^{(0)}$.

To calculate (7.99), the vectors $\boldsymbol{Q}, \boldsymbol{H}$ and $\boldsymbol{\rho}$ have to be defined in the same coordinate system, say in the system L. The parameter $\boldsymbol{c}$ in (7.99) then characterizes the transition from the coordinate system C to the system L, and it is denoted here $\boldsymbol{c}^{(LC)}$. The grains, which satisfy the Bragg condition $\boldsymbol{H}^{(C)}(\boldsymbol{c}) = \boldsymbol{Q}$, are characterized by the parameter $\boldsymbol{c}^{(LC)}$ equals to:

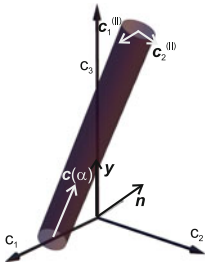

Fig. 7.6 The sketch for the coordinate system $\alpha, c_1^{(||)}, c_2^{(||)}$ defined by (7.102) in the space of the parameters of the rotation group

$$\boldsymbol{c}(\alpha) = \left\langle \tan\frac{\alpha}{2}\boldsymbol{e}_z, \frac{\boldsymbol{n}\times\boldsymbol{e}_z}{1+\boldsymbol{n}\boldsymbol{e}_z}\right\rangle = \frac{\tan\frac{\alpha}{2}(\boldsymbol{n}+\boldsymbol{e}_z)+\boldsymbol{n}\times\boldsymbol{e}_z}{1+\boldsymbol{n}\boldsymbol{e}_z}, \tag{7.101}$$

where unit vector $\boldsymbol{n}$ is chosen along $\boldsymbol{H}^{(C)}$, the vector $\boldsymbol{y}$ is replaced by the vector $\boldsymbol{e}_z$ from the coordinate system L (Fig. 7.6). The transformation (7.101) has an evident meaning of the sequences: (i) the rotation around axis $\boldsymbol{n}\times\boldsymbol{e}_z$ perpendicular to vectors $\boldsymbol{n}$ and $\boldsymbol{e}_z$ is applied, which transfers $\boldsymbol{n}$ into $\boldsymbol{e}_z$, (ii) the rotation at arbitrary angle α around $\boldsymbol{e}_z$ is executed.

To integrate over $d^3\boldsymbol{c}$ in (7.99), the new coordinate system with the axis z along $\boldsymbol{c}(\alpha)$ is introduced in the parameter space $\boldsymbol{c}$ (Fig. 7.6):

$$\boldsymbol{c}(\alpha, c_1^{(||)}, c_2^{(||)}) = \boldsymbol{c}(\alpha) + c_1^{(||)}\boldsymbol{n}\times\boldsymbol{e}_z + c_2^{(||)}(\boldsymbol{n}+\boldsymbol{e}_z)\times(\boldsymbol{n}\times\boldsymbol{e}_z), \tag{7.102}$$

where variation of the parameter α corresponds to the grains in the Bragg condition, which differ by various α angles around $\boldsymbol{H}||\boldsymbol{Q}$; the crystallites with the parameters $c_1^{(||)}$ and $c_2^{(||)}$ are deviated from the Bragg condition. Using the Eqs. (7.100) and (7.96) and assuming small strains and deviations from the Bragg angle, the expression (7.99) in the chosen coordinate system is written as:

$$I(\boldsymbol{y}\boldsymbol{Q}) = \int \frac{d\alpha dc_1^{(||)}dc_2^{(||)}}{\pi^2(1+\boldsymbol{c}^2)^2} J_{\boldsymbol{c}}(\alpha, c_1^{(||)}, c_2^{(||)}) f(\boldsymbol{c}) \tag{7.103}$$
$$\times \int dxdydz e^{i(Q-H_0(1-\epsilon_H(\boldsymbol{c})))z} e^{iH_0K[(x,y),(c_1^{(||)},c_2^{(||)})]} g(x,y,z).$$

Here J is a Jacobian of the transformation, $K[(x,y),(c_1^{(||)}, c_2^{(||)})]$ is a bilinear form on (x,y) and $(c_1^{(||)}, c_2^{(||)})$, and its coefficients depend on $\boldsymbol{n}$ and are of the order of unity.

When integrating (7.103) over x and y, the fact of a large width of the texture ODF, which is broader than the diffraction peak, results in the estimate:

$$\delta c_{1,2}^{(||)} \gg 1/Hl_d. \tag{7.104}$$

The largest contribution in (7.103) is made by the values $(c_1^{(||)}, c_2^{(||)})$ which are less than $1/Hl_d$ and, therefore, all the terms containing $(c_1^{(||)}, c_2^{(||)})$ can be assumed to be constant except of the exponent $e^{iH_0K[(x,y),(c_1^{(||)},c_2^{(||)})]}$. This turns the integral over $(c_1^{(||)}, c_2^{(||)})$ into delta-function of x, y, and the intensity is proportional to Fourier image $g(0, 0, z)$, that corresponds to (6.134), see Fig. 6.4.3. Alternatively, to integrate over $(c_1^{(||)}, c_2^{(||)})$, the integral over x, y can be replaced by a delta-function, according to criteria (7.104). In other words, the Bragg condition is re-written as $\delta(\boldsymbol{Q} - \boldsymbol{H}(\boldsymbol{c}))$. The Jacobian, the weight function and other terms cancel each other, and the expression can be obtained:

$$I(\boldsymbol{y}Q) = \int d\alpha f(\boldsymbol{c}(\alpha)) \int dz e^{i(Q - H_0(1-\epsilon_H(\boldsymbol{c}(\alpha))))z} g(0, 0, z). \tag{7.105}$$

Thus, the measured X-ray intensity is a sum of intensities from all grains with the orientations different by the angle α from the vector $\boldsymbol{H}$.

The residual stress analysis requires the measurement of the intensity maximum in the direction $\boldsymbol{y}$. The position of the maximum of (7.105) is calculated by using a cumulant expansion:

$$I(\boldsymbol{y}Q) = \int d\alpha f(\boldsymbol{c}(\alpha)) \int dz g(0, 0, z) e^{i(Q-H_0)z} e^{iH_0\langle\epsilon_H\rangle z} e^{-\frac{1}{2}H_0^2K_2z^2} e^{-i\frac{1}{6}H_0^3K_3z^3} \ldots \tag{7.106}$$

$$K_2 = \langle\epsilon_H^2\rangle - \langle\epsilon_H\rangle^2, K_3 = \langle\epsilon_H^3\rangle - 3\langle\epsilon_H^2\rangle\langle\epsilon_H\rangle + 2\langle\epsilon_H\rangle^3,$$

$$\langle\epsilon_H^n\rangle = \frac{\int d\alpha f(\boldsymbol{c}(\alpha))\epsilon_H(\boldsymbol{c}(\alpha))^n}{\int d\alpha f(\boldsymbol{c}(\alpha))}.$$

The correlation function $g(0, 0, z)$ is usually symmetric, and therefore the second term in the cumulative expansion does not influence the diffraction peak position. Provided the third and further odd cumulative terms decrease slower than correlation function, the position of the maximum Q_m is defined by the first cumulative term:

$$Q_m = H_0(1 - \langle\epsilon_H\rangle). \tag{7.107}$$

This equation is equivalent of (7.4).

With the known relationship between the strain and the macroscopic residual stress in the grain, the residual stresses in the sample can be determined on the basis of (7.107). This basic expression for the X-ray stress analysis has been derived using several physical assumptions. For the traditional metallic samples these assumptions are valid in the majority of the cases, however, when analyzing the modern materials possessing the strong texture or intentionally designed nanoscale structure, the above described approximations have to be carefully validated.

7.4 Residual Stress in Macroscopically Isotropic Materials. X-Ray Elastic Constants

The polycrystal is macroscopically isotropic when all crystallite orientations are equiprobable (absence of texture) and all directions inside macroscopical polycrystal are equivalent. The mechanical elastic properties are then defined by two parameters, for example, by bulk and rigidity moduli. The macroscopically isotropic case is realized in the absence of texture in the models of Voigt, Reuss and Eshelby-Kröner for spherical grains[3]. In the models of Vook-Witt and inverse Vook-Witt, even in the absence of texture there is an anisotropy due to the operators $\boldsymbol{\Pi}_{\perp}$ and $\boldsymbol{\Pi}_{||}$, which distinguish the normal direction to the surface.

To determine the stresses by X-ray method, the position of the diffraction peak in the direction $\boldsymbol{y}$ has to be related to the macroscopic stress $\langle\sigma_{ij}\rangle^{(S)}$. As follows from (7.107), the peak shift defines the value:

$$\{\epsilon_H(\boldsymbol{y})\} = \frac{1}{2\pi}\int d\alpha\epsilon_H(\boldsymbol{c}(\alpha))) = \frac{\boldsymbol{H}^{(0)}\cdot\int d\alpha\boldsymbol{\epsilon}(\boldsymbol{c}(\alpha))\cdot\boldsymbol{H}^{(0)}}{2\pi\boldsymbol{H}^{(0)2}}, \tag{7.108}$$

where the braces mean the averaging over the grains contributing to diffraction. The connection between the stress and the strain in coordinate system S is given by the Eq. (7.16). To write the expression (7.108) in the coordinate system S, the fact of the coincidence of the direction of vector $\boldsymbol{H}^{(0)}$ and $\boldsymbol{y}$ due to the Bragg condition is used (see also the logic of the derivations from (7.105) to (7.107)). Using (7.16), we obtain:

$$\{\epsilon_H(\boldsymbol{y})\} = y_i y_j \frac{\int d\alpha A_{ijkl}(\boldsymbol{c}(\alpha))}{2\pi}\langle\sigma_{kl}\rangle^{(S)}, \tag{7.109}$$

or in indexless form:

$$\{\epsilon_H(\boldsymbol{y})\} = \boldsymbol{y}\otimes\boldsymbol{y} : \frac{\int d\alpha\boldsymbol{A}(\boldsymbol{c}(\alpha))}{2\pi} : \langle\boldsymbol{\sigma}\rangle^{(S)}. \tag{7.110}$$

To perform the integration over the angle α, the components of the 4-th rank tensor $\boldsymbol{A}$ have to be transformed from the coordinate system C into the system S, which is done by four times convolution:

$$A^{(S)}_{ijkl} = T^{(SC)}_{ii'}T^{(SC)}_{jj'}T^{(SC)}_{kk'}T^{(SC)}_{ll'}A^{(C)}_{i'j'k'l'}. \tag{7.111}$$

The operation requires the transformation of 81 components resulting in the cumbersome expressions. To make the results compact, the Voigt notations are used [4], which take into account the symmetry property $c_{ijkl} = c_{\underline{(ij)}kl} = c_{ij\underline{(kl)}} = c_{\underline{(ijkl)}}$. In the result, the 4-th rank tensor is represented as symmetric 6×6 matrix, which has 21 component. This number is equal to the number of parameters, required to

[3] The statements for Eshelby-Kröner model (7.69) are also valid for Hashin-Strickman model (7.63).

describe the elastic properties of crystal with a lowest monoclinic symmetry. The cubic crystal has 3 independent components, and the transformation (7.111) contains the exceeding number of operations in this case. Below the transformation of (7.111) is described, which takes into account the high symmetry of the tensor [48]. We separate the isotropic part of the tensor, which is not undergoing to the transformations, and the averaging over the orientations is thus reduced to the truncation of the anisotropic components.

From the point of view of the group theory, the 4-th rank tensors form the representation space of the rotation group, and it can be decomposed into irreducible representation (IR) spaces [49]. In the case of a lowest triclinic symmetry, the stiffness (compliance) tensor is decomposed in:

$$\begin{aligned} &2 \text{ IR with weight } l = 0 \text{ (scalars):} \quad \boldsymbol{\sigma}_s, \ s = 1, 2 \\ &4 \text{ IR with weight } l = 2 \text{ (deviators):} \quad \boldsymbol{\delta}_{d,m}, \ d = 1..4, m = -2, .., 2 \\ &1 \text{ IR with weight } l = 4 \text{ (nonor):} \quad \boldsymbol{\eta}_m, \ m = -4, .., 4. \end{aligned} \tag{7.112}$$

The basis tensors $\boldsymbol{\sigma}_s$, $\boldsymbol{\delta}_{d,m}$, $\boldsymbol{\eta}_m$ can be calculated with the help of the Clebsch-Gordan coefficients $C^{j,m}_{j_1,m_1;j_2,m_2}$ starting from the circular vectors:

$$\boldsymbol{e}^{(-1)} = \frac{1}{\sqrt{2}}(-1, i, 0), \ \boldsymbol{e}^{(0)} = (0, 0, -1), \ \boldsymbol{e}^{(1)} = \frac{1}{\sqrt{2}}(1, i, 0), \tag{7.113}$$

which are the IR of weight $l = 1$:

$$\begin{aligned} \sigma_{1\,pqrs} =& C^{0,0}_{1,i'';1,m'} C^{1,m'}_{1,i';0,0} C^{0,0}_{1,i;1,j} e^{(i)}_p e^{(j)}_q e^{(i')}_r e^{(i'')}_s = \delta_{pq}\delta_{rs}, \\ i, j, i', i'', m =& -1, 0, 1, \ \ p, q, r, s = 1, 2, 3. \end{aligned} \tag{7.114}$$

The basic tensors (7.112) possess a completeness property (any stiffness or compliance tensor can be expanded using them) and are mutually orthogonal:

$$\begin{aligned} \boldsymbol{\sigma}_s :: \boldsymbol{\sigma}^*_{s'} =& \delta_{ss'}, \ \ \boldsymbol{\delta}_{d,m} :: \boldsymbol{\delta}^*_{d',m'} = \delta_{dd'}\delta_{mm'}, \ \ \boldsymbol{\eta}_m :: \boldsymbol{\eta}^*_{m'} = \delta_{mm'}, \\ \boldsymbol{\sigma}_s :: \boldsymbol{\delta}^*_{d',m'} =& 0, \ \ \boldsymbol{\sigma}_s :: \boldsymbol{\eta}^*_{m'} = 0, \ \ \boldsymbol{\delta}_{d,m} :: \boldsymbol{\eta}^*_{m'} = 0, \end{aligned} \tag{7.115}$$

where the symbol :: means the convolution over 4 indices: $\boldsymbol{a} :: \boldsymbol{b}^* = a_{ijkl} b^*_{ijkl}$.

The IR decomposition highlights the symmetry properties of the compliance tensor and separates its isotropic and anisotropic parts, e.g. the stiffness tensor for cubic system has the form:

$$\begin{aligned} \boldsymbol{C}^{\text{cub}} =& (C_{11} + 2C_{12})\boldsymbol{\sigma}_1 + \frac{2}{\sqrt{5}}(3 + 2A)C_{44}\boldsymbol{\sigma}_2 + 4(A - 1)C_{44}\boldsymbol{\eta}_c, \\ \boldsymbol{\eta}_c =& \frac{1}{4}\left(\boldsymbol{\eta}_{-4} + \sqrt{\frac{14}{5}}\boldsymbol{\eta}_0 + \boldsymbol{\eta}_4\right), \end{aligned} \tag{7.116}$$

where the Voigt notations are used, $A = \frac{C_{11}-C_{12}}{2C_{44}}$ is the Zener's anisotropy factor. In isotropic case $A = 1$, the anisotropic part $\boldsymbol{\eta}_c$ disappears.

The rotation transformation in the subspace of IR of weight l is performed by using the angular momentum matrices. For the rotation described by the vector parameter $\boldsymbol{c}$, the expression is [41]:

$$T^{(l)}_{nn'} = e^{2\boldsymbol{c}\boldsymbol{J}\arctan c} = \sum_{m=-l}^{l} \frac{P^l_m(-i\boldsymbol{c}\boldsymbol{J}^{(l)}_{nn'}/c)}{P^l_m(-im)} e^{-2im\arctan c}, \quad P^l_m(x) = \prod_{m'=-l, m'\neq m}^{l} (x + im'), \tag{7.117}$$

where $\boldsymbol{J}$ is the vector (J_x, J_y, J_z) composed of the matrices of angular momentum.

Besides the transformation of tensors from one coordinate system into another, the multiplication of tensors and the inversion are the important operations for calculation of the tensor $\boldsymbol{A}$ on the basis of Eqs. (7.22), (7.63) and (7.69). Using the Voigt notations, these operations are reduced to the multiplication and inversion of 6×6 matrices. This approach, however, does not take into account the symmetry of the tensor. Using the expansion (7.112), the tensors $\boldsymbol{\sigma}_1, \boldsymbol{\sigma}_2, \boldsymbol{\eta}_c$ are shown below to create a closed group with respect to the operation of multiplication (convolution over two indices), which is written as:

	$\boldsymbol{\sigma}_1$	$\boldsymbol{\sigma}_2$	$\boldsymbol{\eta}_c$
$\boldsymbol{\sigma}_1$	$\boldsymbol{\sigma}_1$	0	0
$\boldsymbol{\sigma}_2$	0	$\frac{\boldsymbol{\sigma}_2}{\sqrt{5}}$	$\frac{\boldsymbol{\eta}_c}{\sqrt{5}}$
$\boldsymbol{\eta}_c$	0	$\frac{\boldsymbol{\eta}_c}{\sqrt{5}}$	$\frac{3\boldsymbol{\sigma}_2}{10\sqrt{5}} + \frac{\boldsymbol{\eta}_c}{10}$.

(7.118)

Thus, for the macroscopically isotropic media consisting of the grains with a cubic symmetry, the 4-th rank tensor is expanded into tensors $\boldsymbol{\sigma}_1$, $\boldsymbol{\sigma}_2$ and $\boldsymbol{\eta}_c$:

$$\boldsymbol{a} = \{a_1, a_2, a_\eta\} = a_1\boldsymbol{\sigma}_1 + a_2\boldsymbol{\sigma}_2 + a_\eta\boldsymbol{\eta}_c. \tag{7.119}$$

The averaging over the orientations is then reduced to the truncation of anisotropic part:

$$\langle \boldsymbol{a} \rangle = \{a_1, a_2, 0\}. \tag{7.120}$$

The necessity to use the special representation of tensors occurs also for the energy functionals (7.44) and (7.45). The inequalities (7.47) and (7.46) make the restrictions to the tensor characteristics determining the system energy and not to the components of the stiffness tensor. The elastic energy of the unity volume of sample $\boldsymbol{\epsilon} : \boldsymbol{C} : \boldsymbol{\epsilon}/2$ is a quadratic form with respect to the strain $\boldsymbol{\epsilon}$. Because of the elastic energy can not be negative, this quadratic form is always positively defined. To understand which values are restricted by the inequalities for elastic energy, the Voigt notations are used and the 6×6 stiffness matrix is presented on the basis of eigenvectors:

$$\langle \boldsymbol{C} \rangle = \sum_{\nu} \lambda_\nu \boldsymbol{\zeta}_\nu, \;\; \boldsymbol{\zeta}_\nu = \sum_{i} \boldsymbol{e}_{\nu,i} \otimes \boldsymbol{e}_{\nu,i}, \tag{7.121}$$

here λ_ν are the eigenvalues, $\boldsymbol{e}_{\nu,i}$ are the eigenvectors, and the summation over i corresponds to the degenerated eigenvectors. The positive definition means $\lambda_\nu > 0$, and the inequality (7.46) is equivalent to the inequalities for eigenvalues $\lambda_\nu^C \le \lambda_\nu^{C_M}$. Thus, the inequalities (7.47) and (7.46) constrain the eigenvalues of the tensors.

The representation (7.121) is also convenient due to the simplification of the multiplication table (7.118). For example, using the expansion for the crystals with a cubic system [18]:

$$\begin{gathered} \boldsymbol{a} = (3\kappa, 2\mu, 2\mu') = 3\kappa\boldsymbol{\zeta}_1 + 2\mu\boldsymbol{\zeta}_2 + 2\mu'\boldsymbol{\zeta}_3, \\ \boldsymbol{\zeta}_1 = \boldsymbol{\sigma}_1, \;\; \boldsymbol{\zeta}_2 = \frac{2}{\sqrt{5}}\boldsymbol{\sigma}_2 + 2\boldsymbol{\eta}_c, \;\; \boldsymbol{\zeta}_3 = \frac{3}{\sqrt{5}}\boldsymbol{\sigma}_2 - 2\boldsymbol{\eta}_c, \end{gathered} \tag{7.122}$$

which coincides with the expression (7.121), the analogue of the above table is written as:

$$\begin{array}{c|ccc} & \boldsymbol{\zeta}_1 & \boldsymbol{\zeta}_2 & \boldsymbol{\zeta}_3 \\ \hline \boldsymbol{\zeta}_1 & \boldsymbol{\zeta}_1 & 0 & 0 \\ \boldsymbol{\zeta}_2 & 0 & \boldsymbol{\zeta}_2 & 0 \\ \boldsymbol{\zeta}_3 & 0 & 0 & \boldsymbol{\zeta}_3 \end{array}. \tag{7.123}$$

The relation between the expressions (7.122) and (7.119) is simple:

$$\boldsymbol{a} = \{a_1, a_2, a_\eta\} = (3\kappa, 2\mu, 2\mu') = \left(a_1, \frac{a_2}{\sqrt{5}} + \frac{3a_\eta}{10}, \frac{a_2}{\sqrt{5}} - \frac{a_\eta}{5}\right), \tag{7.124}$$

and the product of the tensors and the inverse tensor are:

$$\begin{gathered} \boldsymbol{a} : \boldsymbol{b} = (9\kappa_a\kappa_b, 4\mu_a\mu_b, 4\mu'_a\mu'_b), \\ \boldsymbol{a}^{-1} = (1/3\kappa, 1/2\mu, 1/2\mu'). \end{gathered} \tag{7.125}$$

The inverse relation between representations is found to be:

$$\boldsymbol{a} = (3\kappa, 2\mu, 2\mu') = \{a_1, a_2, a_\eta\} = \left\{3\kappa, \frac{4\mu + 6\mu'}{\sqrt{5}}, 4\mu - 4\mu'\right\}. \tag{7.126}$$

Thus, the products of the tensors and the inverse tensor are calculated conveniently using the expression (7.122), and the averaging and the transformation between different coordinate systems using the expression (7.119) are simplified. The similar expressions can be constructed for low symmetry tensors, too [50].

As follows from (7.22), (7.25), (7.63) and (7.69), the formula for tensor $\boldsymbol{A}_n$ for n-th grain contains the isotropic tensors only ($\boldsymbol{C}_M$ and $\boldsymbol{E}$) and the stiffness tensor of n-th grain $\boldsymbol{c}_n$. Applying the tensor operations of summation, multiplication and

inversion for isotropic tensors and tensor $\boldsymbol{c}_n$, the resulting tensor can be presented in the form of (7.119). The tensor $\boldsymbol{A}_n$ in the coordinate system C is then written as:

$$\boldsymbol{A}_n^{(C)} = \{A_1, A_2, A_\eta\}, \tag{7.127}$$

and for the grains composed of the same material, the formula (7.127) does not depend on the orientation of the grain. Because of the isotropic tensors $\boldsymbol{\sigma}_1$ and $\boldsymbol{\sigma}_2$ are not modified with the transformations between the coordinate systems, the integral in (7.110) is calculated as:

$$\frac{\int d\alpha \boldsymbol{A}(\boldsymbol{c}(\alpha))}{2\pi} = A_1\boldsymbol{\sigma}_1 + A_2\boldsymbol{\sigma}_2 + A_\eta\overline{\boldsymbol{\eta}_c}, \quad \overline{\boldsymbol{\eta}_c} = \frac{1}{2\pi}\int d\alpha \hat{\boldsymbol{T}}^{(SC)}(\alpha)\boldsymbol{\eta}_c, \tag{7.128}$$

where $\hat{\boldsymbol{T}}^{(SC)}$ is the symbol meaning the transformation of the tensor components either by (7.111) or (7.117).

To calculate the tensor $\overline{\boldsymbol{\eta}_c}$, we use the basis IR with the weight $l = 4$, where the transformation is performed by the matrices (7.117). For calculation of (7.117), the parametric vector $\boldsymbol{c}^{(SC)}$ has to be defined as a function of angle α. The expression (7.101) presents the transformation from the coordinate system C to the system L, and in a way similar to (7.101), the parametric vector $\boldsymbol{c}^{(SL)}$ can be found, which corresponds to the transition from L to S:

$$\boldsymbol{c}^{(SL)} = \frac{\boldsymbol{e}_z \times \boldsymbol{y}}{1 + \boldsymbol{e}_z\boldsymbol{y}}. \tag{7.129}$$

As a result, the parametric vector $\boldsymbol{c}^{(SC)}(\alpha)$ is obtained as a combination of the sequential transformations from the system C to the system L, and then from L to S:

$$\boldsymbol{c}^{(SC)}(\alpha) = \langle \boldsymbol{c}^{(SL)}, \boldsymbol{c}^{(LC)}(\alpha)\rangle = \left\langle \frac{\boldsymbol{e}_z \times \boldsymbol{y}}{1 + \boldsymbol{e}_z\boldsymbol{y}}, \tan\frac{\alpha}{2}\boldsymbol{e}_z, \frac{\boldsymbol{n} \times \boldsymbol{e}_z}{1 + \boldsymbol{n}\boldsymbol{e}_z}\right\rangle. \tag{7.130}$$

In this expression, the only transformation depending on the angle α is the one corresponding to the parametric vector $\tan\frac{\alpha}{2}\boldsymbol{e}_z$. This fact helps to calculate the integral over α, using the diagonal form of the matrix J_z and the formula (7.117):

$$T_{nn'}^{(l)}(\tan\frac{\alpha}{2}\boldsymbol{e}_z) = \delta_{n,n'}e^{-in\alpha}. \tag{7.131}$$

From this equation, for the matrix of transformation in the space IR with the weight $l = 4$, we obtain:

$$\frac{1}{2\pi}\int d\alpha \hat{\boldsymbol{T}}^{(SC)}(\alpha) = T_{n0}^{(4)}\left(\frac{\boldsymbol{e}_z \times \boldsymbol{y}}{1 + \boldsymbol{e}_z\boldsymbol{y}}\right) T_{0n'}^{(4)}\left(\frac{\boldsymbol{n} \times \boldsymbol{e}_z}{1 + \boldsymbol{n}\boldsymbol{e}_z}\right), \quad n, n' = -4, .., 4, \tag{7.132}$$

and for $\boldsymbol{\eta}_c$ the following formula is found:

$$\overline{\boldsymbol{\eta}_c} = \boldsymbol{\eta}_n T^{(4)}_{n0} \left(\frac{\boldsymbol{e}_z \times \boldsymbol{y}}{1 + \boldsymbol{e}_z \boldsymbol{y}} \right) T^{(4)}_{0n'} \left(\frac{\boldsymbol{n} \times \boldsymbol{e}_z}{1 + \boldsymbol{n} \boldsymbol{e}_z} \right) \eta_{cn'}, \tag{7.133}$$

where the coefficients $\eta_{cn'}$, defining the value $\boldsymbol{\eta}_c$ in the expansion over the basis $\boldsymbol{\eta}_{n'}$ in (7.112) are taken from the equation (7.116). To calculate the function (7.110) with the values (7.128) and (7.133), the direction of vector $\boldsymbol{y}$ in coordinate system S and the orientation of the reciprocal lattice vector in the system C have to be fixed:

$$\begin{aligned} \boldsymbol{y} &= (\sin(\psi)\cos(\phi), \sin(\psi)\sin(\phi), \cos(\psi)), \\ \boldsymbol{n} &= \frac{1}{(h^2 + k^2 + l^2)^{1/2}} (h, k, l). \end{aligned} \tag{7.134}$$

The matrices $\boldsymbol{y} \otimes \boldsymbol{y} : \boldsymbol{\sigma}_2$ and $\boldsymbol{y} \otimes \boldsymbol{y} : \overline{\boldsymbol{\eta}_c}$ are found to be proportional each to other. The Eq. (7.110) can then be presented in a universal form by using X-ray elastic constants (XEC), which leads to the Eq. (7.11) with:

$$\begin{aligned} S_1^{(hkl)} &= \frac{1}{30} \left(10A_1 - 2\sqrt{5}A_2 + 3A_\eta (5\Gamma - 1) \right), \\ \frac{1}{2} S_2^{(hkl)} &= \frac{1}{10} \left(2\sqrt{5}A_2 - 3A_\eta (5\Gamma - 1) \right), \end{aligned} \tag{7.135}$$

where the dependence on the Miller indices hkl of the reciprocal lattice vector is given by the invariant Γ:

$$\Gamma = \frac{h^2k^2 + h^2l^2 + k^2l^2}{\left(h^2 + k^2 + l^2\right)^2}. \tag{7.136}$$

Below we consider XEC for polycrystals of a cubic symmetry for various models of grain interaction.

7.4.1 Voigt Model

According to (7.21) and (7.22), the tensor (7.116) has to be averaged and then inversed. Using formula (7.119), the averaging is carried out by (7.120):

$$\langle \boldsymbol{C}^{\text{cub}} \rangle = \left\{ C_{11} + 2C_{12}, \frac{2(C_{11} - C_{12}) + 6C_{44}}{\sqrt{5}}, 0 \right\}. \tag{7.137}$$

By using the relationship (7.122) and the representation (7.124), the inverse tensor is found with the help of (7.125):

$$\langle \boldsymbol{C}^{\text{cub}} \rangle^{-1} = \left(\frac{1}{C_{11} + 2C_{12}}, \frac{5}{2(C_{11} - C_{12} + 3C_{44})}, \frac{5}{2(C_{11} - C_{12} + 3C_{44})} \right). \tag{7.138}$$

In the formula (7.135) for XEC, using the Eqs. (7.119) and (7.126), we obtain the expression (7.138) in the form of (7.119), and from (7.135):

$$S_1 = \frac{2C_{44} - C_{11} - 4C_{12}}{2(C_{11} + 2C_{12})(C_{11} - C_{12} + 3C_{44})}, \qquad (7.139)$$
$$\frac{1}{2}S_2 = \frac{5}{2(C_{11} - C_{12} + 3C_{44})}.$$

These expressions are independent on the Bragg reflection hkl.

7.4.2 Reuss Model

The X-ray elastic constants have a simple form if using the components of the compliance tensor $\boldsymbol{S}$. The tensor $\boldsymbol{A}$ coincides with the compliance tensor, and in the form of (7.119) is written as:

$$\boldsymbol{A} = \boldsymbol{S}^{\text{cub}} = \left\{ S_{11} + 2S_{12}, \frac{4(S_{11} - S_{12}) + 3S_{44}}{2\sqrt{5}}, 2(S_{11} - S_{12}) - S_{44} \right\}. \qquad (7.140)$$

Substituting this equation into (7.135), we obtain:

$$S_1^{(hkl)} = S_{12} + S_0\Gamma, \qquad (7.141)$$
$$\frac{1}{2}S_2^{(hkl)} = S_{11} - S_{12} - 3S_0\Gamma, \quad S_0 = S_{11} - S_{12} - S_{44}/2.$$

7.4.3 Eshelby-Kröner Model

The Voigt and Reuss models are the limiting cases of the grain interaction. The previous section considered the narrower than those two bounds for the bulk elastic modules. The transfer of the results obtained in this section to the XEC bounding has to be done with a caution. The values of XEC are determined by the averaging over the angle α and not by the averaging over the orientations. As a result, the equation (7.135) contains the dependence on the anisotropic part and on the Miller indices.

Nevertheless, several general conclusions can be made on the basis of the estimates for the boundaries of the macroscopic elastic modules. For simple case of rotationally symmetric biaxial stress state, and from the expression (7.135) for (7.11) we obtain:

$$\{\epsilon_H(\psi)\} = \left(\frac{2}{3}A_1 + (3\sin^2\psi - 2)\frac{2\sqrt{5}A_2 + 3A_\eta(1 - 5\Gamma)}{30} \right)\sigma_{||}. \qquad (7.142)$$

As follows from the expressions (7.118) and (7.120), the component $a_1 = 3\kappa$ is not mixed with other components in tensor operations, and for all the models the equality $A_1 = \frac{1}{C_{11}+2C_{12}}$ is satisfied. Thus, according to (7.142), the $\sin^2\psi$ plots for all models in case of rotationally symmetric biaxial stress cross the same point at $\sin^2\psi = 2/3$.

The inclination angle of $\sin^2\psi$ plot is defined by the parameters A_2 and A_η. Using the representation (7.122), the following relationship is received:

$$\{\epsilon_H(\psi)\} = \left(2\kappa_A + \frac{2}{3}(3\sin^2\psi - 2)(\mu_A(1-3\Gamma) + 3\Gamma\mu'_A)\right)\sigma_{||}. \qquad (7.143)$$

The definition (7.136) shows that the inequality is satisfied: $0 \le \Gamma \le 1/3$, which means the values $1-3\Gamma$ and 3Γ are always positive. To determine the limits of the function $\sin^2\psi$, the variation limits of μ_A and μ'_A have to be found. Assuming the strain fields are uniform inside the grain (7.48), the macroscopic compliance tensor depends on the tensor $\boldsymbol{A}$ as:

$$\boldsymbol{S} = (3\kappa_s, 2\mu_s, 2\mu_s) = \langle \boldsymbol{A} \rangle = (3\kappa_A, \frac{2}{5}(2\mu_A + 3\mu'_A), \frac{2}{5}(2\mu_A + 3\mu'_A)). \qquad (7.144)$$

The boundaries for macroscopic elastic moduli are defined by the boundaries of parameters κ_s and μ_s. As follows from (7.144), the limits for μ_s determine the limits of the linear combination $2\mu_A + 3\mu'_A$, and thus constrain the limits of the function $\sin^2\psi$ only at $\Gamma = 1/5$. However, the models defining the boundaries of the macroscopic moduli are frequently considered to constrain the $\sin^2\psi$ plot, too (Fig. 7.7).

Within the approximation of strain uniformity inside the grain (7.48) and spherical symmetry of the correlation function of grains (7.53), the Eshelby-Kröner model

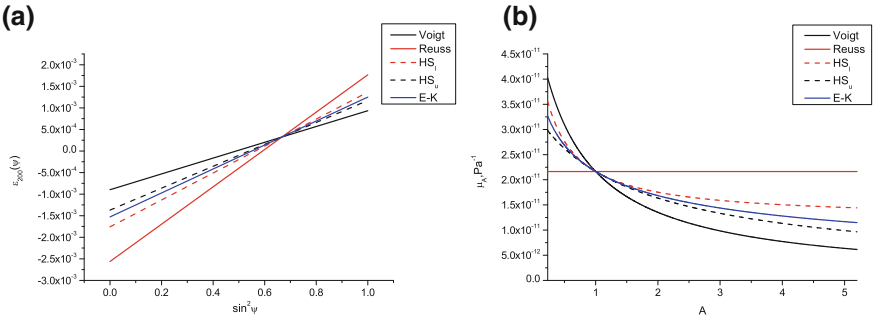

Fig. 7.7 **a** $\sin^2\psi$ plot for Cu sample possessing the residual stress of 200 MPa, the Bragg (200) reflection, for the models of Voigt (V) and Reuss (R), and for the boundary models of Hashin-Strickman (HS) and Eshelby-Kröner (E-K). **b** The dependence μ_A at fixed C_{11} and C_{12} for the same models. The models determining the boundaries for macroscopic moduli constrain the parameters μ_A and μ'_A; for HS model, the tensor $\boldsymbol{A}$ from (7.63) has been used

satisfies the equation (7.43), which is due to the self-consistency of the tensor $\boldsymbol{C}$ in the Eq. (7.67). In the case of macroscopically isotropic media, spherically symmetric correlation function of grain shape and the cubic symmetry of the crystallites, this equation can be essentially simplified [21, 23]. In that case, the tensor $\boldsymbol{E}$ is found by the analytical integration of (7.57), and for the representation (7.122) we obtain:

$$\begin{aligned}\boldsymbol{E} &= \left(\frac{1}{3C_{11}}, \frac{2\left(4C_{11}-C_{12}\right)}{15C_{11}\left(C_{11}-C_{12}\right)}, \frac{2\left(4C_{11}-C_{12}\right)}{15C_{11}\left(C_{11}-C_{12}\right)}\right) \\ &= \left(\frac{1}{3\kappa_C+4\mu_C}, \frac{3\kappa_C+6\mu_C}{15\kappa_C\mu_C+20\mu_C^2}, \frac{3\kappa_C+6\mu_C}{15\kappa_C\mu_C+20\mu_C^2}\right).\end{aligned} \tag{7.145}$$

To calculate the expression (7.67), the representation (7.122) is used again for multiplication and inversion of tensors and the representation (7.118) for the averaging. As a result, the following equation is derived:

$$\begin{aligned}&\Bigg(-\frac{3\left(\kappa-\kappa_C\right)}{-6\kappa_C-4\mu_C+3\kappa}, \\ &-\frac{6\left(\kappa_C+2\mu_C\right)\left(3\mu'\left(\kappa_C\left(\mu_C+2\mu\right)+4\mu\mu_C\right)-\mu_C^2\left(9\kappa_C+8\mu_C+4\mu\right)\right)}{\left(9\kappa_C\mu_C+6\mu\kappa_C+8\mu_C^2+12\mu\mu_C\right)\left(6\kappa_C\mu'+9\kappa_C\mu_C+12\mu_C\mu'+8\mu_C^2\right)}, \\ &-\frac{6\left(\kappa_C+2\mu_C\right)\left(3\mu'\left(\kappa_C\left(\mu_C+2\mu\right)+4\mu\mu_C\right)-\mu_C^2\left(9\kappa_C+8\mu_C+4\mu\right)\right)}{\left(9\kappa_C\mu_C+6\mu\kappa_C+8\mu_C^2+12\mu\mu_C\right)\left(6\kappa_C\mu'+9\kappa_C\mu_C+12\mu_C\mu'+8\mu_C^2\right)}\Bigg) = (0,0,0),\end{aligned} \tag{7.146}$$

where the parameters κ_C and μ_C characterize the macroscopic tensor $\boldsymbol{C}$, the parameters κ, μ and μ' describe the stiffness tensor of the crystallite with a cubic symmetry. The system (7.146) contains 2 independent equations, and taking into account the positiveness of values κ_C, μ_C, κ, μ and μ', we have:

$$\begin{aligned}\kappa_C &= \kappa, \\ \mu_C^3+\frac{1}{8}(9\kappa+4\mu)\mu_C^2-\frac{3}{8}(\kappa+4\mu)\mu'\mu_C-\frac{3}{4}\kappa\mu\mu' &= 0.\end{aligned} \tag{7.147}$$

The parameter κ_C, which has a physical meaning of a bulk modulus, has the same value for both Voigt and Reuss models, and thus $\kappa_C = \kappa$ is an exact solution. The cubic equation for μ_C has a single positive root, and the expression (7.147) defines comprehensively the tensor $\boldsymbol{C}$. When tensor $\boldsymbol{C}$ is known, the XEC are found by substituting (7.69) into (7.135):

$$\begin{aligned}S_1^{(hkl)} &= \frac{1}{9\kappa}-a+b\Gamma, \quad \frac{1}{2}S_2^{(hkl)} = 3a-3b\Gamma, \\ a &= \frac{5\left(3\kappa_C+4\mu_C\right)}{6\left(9\kappa_C\mu_C+6\mu\kappa_C+8\mu_C^2+12\mu\mu_C\right)}, \\ b &= -\frac{15\left(\mu-\mu'\right)\left(\kappa_C+2\mu_C\right)\left(3\kappa_C+4\mu_C\right)}{\left(9\kappa_C\mu_C+6\mu\kappa_C+8\mu_C^2+12\mu\mu_C\right)\left(6\mu'\left(\kappa_C+2\mu_C\right)+\mu_C\left(9\kappa_C+8\mu_C\right)\right)}.\end{aligned} \tag{7.148}$$

7.5 Residual Stress in Macroscopically Anisotropic Materials. X-Ray Stress Factors

In the presence of texture or direction-dependent grain interaction, the relation between strain $\{\epsilon_H(\boldsymbol{y})\}$ and macroscopic stress in polycrystal can not be presented by Eq. (7.11). To confirm this fact, the changes implemented by a macroscopic anisotropy in the equations (7.108) - (7.136) are considered below. The relationship between the strain $\{\epsilon_H(\boldsymbol{y})\}$ and the macroscopic stress in polycrystal (7.110) becomes:

$$\{\epsilon_H(\boldsymbol{y})\} = \boldsymbol{y} \otimes \boldsymbol{y} : \frac{\int d\alpha f(\boldsymbol{c}(\alpha))\boldsymbol{A}(\boldsymbol{c}(\alpha))}{\int d\alpha f(\boldsymbol{c}(\alpha))} : \langle \boldsymbol{\sigma} \rangle^{(S)}. \tag{7.149}$$

The ODF function $f(\boldsymbol{c})$ is a function of the orientation of the system C relatively to the system S. The parametric vector (7.130) depending on the vector $\boldsymbol{y}$ and angles ψ, ϕ is an argument of ODF, and the right part of (7.149) may have different kinds of dependency from the angles ψ and ϕ. This means the non-linearity of $\sin^2\psi$ plot, and the XEC provided by (7.11) and (7.136) are not sufficient for proper data interpretation. In this situation, the expression (7.149) is written in the form:

$$\{\epsilon_H(\boldsymbol{y})\} = \boldsymbol{F}(\boldsymbol{y}) : \langle \boldsymbol{\sigma} \rangle^{(S)}, \tag{7.150}$$

$$\boldsymbol{F}(\boldsymbol{y}) = \boldsymbol{y} \otimes \boldsymbol{y} : \frac{\int d\alpha f(\boldsymbol{c}^{(SC)}(\alpha))\boldsymbol{A}(\boldsymbol{c}(\alpha))}{\int d\alpha f(\boldsymbol{c}^{(SC)}(\alpha))},$$

and the functions $\boldsymbol{F}(\boldsymbol{y})$ defined in the coordinate system S are called X-ray stress factors (XSF).

As follows from (7.150), to calculate XSF, the tensor $\boldsymbol{A}$, which characterizes the grain with the orientation $\boldsymbol{c}(\alpha)$, has to be found in the coordinate system S. For macroscopically isotropic models, the tensor $\boldsymbol{A}$ in the coordinate system C is equal for all crystallites independently on their orientations. Mathematically it is a consequence of the fact that the macroscopic tensors $\boldsymbol{C}$ and $\boldsymbol{E}$ are the isotropic tensors, which are independent on the coordinate system. In the case of macroscopically anisotropic polycrystal, the macroscopic tensors are generally anisotropic. As a result, to calculate the tensor $\boldsymbol{A}$, the operations with the anisotropic tensors have to be carried out in different coordinate systems. The final product of these tensors is not expressed through the tensors themselves, and the analogue of (7.118) can not be constructed using a small number of basic elements. Below we discuss the XSF calculation algorithms for different grain interaction models.

7.5.1 Voigt Model

In accordance with (7.21) and (7.22), the tensor (7.116) has to be averaged and then inverted. The averaging is carried out with an accounting of ODF as described in

the Eq. (7.21). After these procedures, the tensor $\boldsymbol{A}$ being equal for all crystallites is derived in the coordinate system S, and by the reduction of the integral over α the XSF are:

$$\boldsymbol{F}(\boldsymbol{y}) = \boldsymbol{y} \otimes \boldsymbol{y} : \langle \boldsymbol{c} \rangle^{-1}. \tag{7.151}$$

Here the value $\langle \boldsymbol{c} \rangle^{-1}$ is constant and XSF are independent on hkl. The dependence on the angles ψ and ϕ is contained in the term $\boldsymbol{y} \otimes \boldsymbol{y}$. As a consequence, the plot of residual stress versus angles ψ and ϕ depends quadratically on the trigonometric functions, but in general case differs from (7.11).

7.5.2 Reuss Model

In the Reuss model, the tensor $\boldsymbol{A}$ is equal to the compliance tensor of a crystallite (7.25). Because of the expression for the tensor $\boldsymbol{A}$ does not contain the operations with macroscopic tensors, the expansion (7.119) can be used, which results similarly to (7.128) in:

$$\boldsymbol{F}(\boldsymbol{y}) = \boldsymbol{y} \otimes \boldsymbol{y} : \left(S_1 \boldsymbol{\sigma}_1 + S_2 \boldsymbol{\sigma}_2 + S_\eta \frac{\int d\alpha f(\boldsymbol{c}^{(SC)}(\alpha)) \int d\alpha \hat{\boldsymbol{T}}^{(SC)}(\alpha) \boldsymbol{\eta}_c}{\int d\alpha f(\boldsymbol{c}^{(SC)}(\alpha))} \right), \tag{7.152}$$

$$S_1 = \boldsymbol{S} :: \boldsymbol{\sigma}_1 = S_{11} + 2S_{12},$$
$$S_2 = \boldsymbol{S} :: \boldsymbol{\sigma}_2 = \frac{4(S_{11} - S_{12}) + 3S_{44}}{2\sqrt{5}}, \quad S_\eta = (A-1)S_{44}.$$

This formula can be applied in an analytical form in the important case of the textured materials described by axial or spherical components [51, 52]. The ODF in this case is modeled by simple functions describing the grain groups, which have allocated orientation and the distribution of the directions, for example, ODF in a form of:

$$f(\boldsymbol{c}_p, \boldsymbol{c}) = N e^{S \cos \omega}, \cos \omega = \frac{\mathrm{Tr}(\boldsymbol{T}(\boldsymbol{c}_p)^{-1}.\boldsymbol{T}(\boldsymbol{c})) - 1}{2}, \tag{7.153}$$

here $\boldsymbol{c}_p$ is a vector-parameter specifying the primary orientation, N is a normalization constant, $1/S$ describes the spread of the directions, Tr is a trace of the matrix. Using the explicit form of the matrix (7.96), we obtain:

$$\cos \omega/2 = \frac{1 + \boldsymbol{c}\boldsymbol{c}_p}{\sqrt{(1 + c^2)(1 + c_p^2)}}, \tag{7.154}$$

and utilizing the expressions for $\boldsymbol{c}^{(SC)}(\alpha)$ in (7.130), the ODF dependence on the angle α is:

$$\cos\omega = \cos^2(\theta^*/2)\cos(\alpha+\delta+2\arctan b/a) - \sin^2(\theta^*/2), \tag{7.155}$$

$$a = \frac{1+\boldsymbol{n}\boldsymbol{y}-\boldsymbol{c}_p\boldsymbol{n}\boldsymbol{y}}{\sqrt{(1+c_p^2)(\boldsymbol{n}+\boldsymbol{y})^2}},\quad b = \frac{\boldsymbol{c}_p(\boldsymbol{n}+\boldsymbol{y})}{\sqrt{(1+c_p^2)(\boldsymbol{n}+\boldsymbol{y})^2}},\quad \cos^2(\theta^*) = \boldsymbol{n}\boldsymbol{T}(\boldsymbol{c}_p)\boldsymbol{y},$$

$$\tan\delta/2 = \frac{\sin(\beta_B-\phi)\sin(\phi_B/2)\sin(\psi/2)}{\cos(\phi_B/2)\cos(\psi/2)+\cos(\beta_B-\phi)\sin(\phi_B/2)\sin(\psi/2)},$$

where β_B and ϕ_B are the angles defining the unity vector in the coordinate system C along the reciprocal lattice vector (Fig. 7.2).

The analogous relationships can be found for axial components, with ODF:

$$f(\boldsymbol{c}_p,\boldsymbol{c}) = Ne^{S\cos\omega},\ \cos\omega = \boldsymbol{f}_p\boldsymbol{T}^{(SC)}\boldsymbol{n}_p, \tag{7.156}$$

where $\boldsymbol{f}_p$ is a vector of primary fiber direction in the coordinate system S, $\boldsymbol{n}_p$ is a primary fiber vector in the coordinate system C, N is a normalization coefficient, and $1/S$ defines the characteristic distribution of the directions. By utilizing the explicit form of the transformation matrix (7.96) and using the expressions for $\boldsymbol{c}^{(SC)}(\alpha)$ in (7.130), the following formulas are derived:

$$\cos\omega = \cos\theta_y\cos\theta_n + \sin\theta_y\sin\theta_n\cos(\alpha+\delta_f), \tag{7.157}$$

$$\cos\theta_n = \boldsymbol{n}\boldsymbol{n}_p,\ \cos\theta_y = \boldsymbol{f}_p\boldsymbol{y},\ \tan\delta_f = \frac{\boldsymbol{f}_\perp\boldsymbol{n}_\perp}{\boldsymbol{f}_\perp\boldsymbol{n}_\perp\boldsymbol{e}_z},$$

$$\boldsymbol{n}_\perp = (\mathbf{1}-\boldsymbol{e}_z\otimes\boldsymbol{e}_z)\cdot\boldsymbol{T}\left(\frac{\boldsymbol{n}\times\boldsymbol{e}_z}{1+\boldsymbol{n}\boldsymbol{e}_z}\right)\cdot\boldsymbol{n}_p,$$

$$\boldsymbol{f}_\perp = (\mathbf{1}-\boldsymbol{e}_z\otimes\boldsymbol{e}_z)\cdot\boldsymbol{T}\left(\frac{\boldsymbol{y}\times\boldsymbol{e}_z}{1+\boldsymbol{e}_z\boldsymbol{y}}\right)\cdot\boldsymbol{f}_p.$$

In both axial and spherical component cases, the dependence of ODF on the angle α is expressed as $e^{k_1\cos(\alpha+k_2)}$. Similar to the Eqs. (7.130)–(7.131), the transformation matrix $\hat{\boldsymbol{T}}^{(SC)}(\alpha)$ in (7.152) has a form $e^{in\alpha}$. By using the equation:

$$\int_0^{2\pi} d\alpha e^{k_1\cos(\alpha+k_2)-im\alpha} = 2\pi e^{imk_2}I_m(k_1), \tag{7.158}$$

with I_m being a modified Bessel function of m-th order and applying (7.158), (7.157) and (7.155), we obtain for (7.152):

$$\boldsymbol{F}(\boldsymbol{y}) = \boldsymbol{y} \otimes \boldsymbol{y} : \Big(S_1 \boldsymbol{\sigma}_1 + S_2 \boldsymbol{\sigma}_2 + S_\eta \boldsymbol{\eta}_n T^{(4)}_{nl} \left(\frac{\boldsymbol{e}_z \times \boldsymbol{y}}{1 + \boldsymbol{e}_z \boldsymbol{y}} \right) \delta_{ll'} \frac{I_l(S\omega) e^{il\phi}}{I_0(S\omega)} T^{(4)}_{l'n'} \left(\frac{\boldsymbol{n} \times \boldsymbol{e}_z}{1 + \boldsymbol{n}\boldsymbol{e}_z} \right) \eta_{cn'} \Big). \tag{7.159}$$

Here the notations of (7.133) have been used, and the angles ω, ϕ for the spherical components are:

$$\omega = \cos^2(\theta^*/2), \;\; \phi = \delta + 2 \arctan b/a,$$

and for the case of axial components:

$$\omega = \sin\theta_y \sin\theta_n, \;\; \phi = \delta_f.$$

This formula can be generalized for $\boldsymbol{S}$ tensor of arbitrary symmetry [53].

The expression (7.159) demonstrates the transition from XSF to XEC. From one hand, the relation between the measured strain and the stress (7.11) takes a place in a case of the isotropic material. As follows from (7.159) and (7.152), in isotropic case $A = 1$, the anisotropic part $S_\eta = 0$ disappears along with the term of texture. From the other hand, in the limit of the isotropic ODF, the value S tends to zero, the functions $I_l(S\omega)$ tend to zero, except of $I_0(S\omega)$, and we obtain the expression (7.133), which results in (7.11).

7.5.3 Eshelby-Kröner Model

In the presence of texture, the Eq. (7.67) becomes very cumbersome. In opposite to the isotropic case, where the simple analytical expression (7.145) exists, the relation between $\boldsymbol{E}$ and $\boldsymbol{C}$ in anisotropic polycrystals is given by cumbersome integrals (7.57) and (7.58). The averaging procedure involves ODF, which again complicates the calculations comparing to the isotropic sample, where the equation (7.120) is valid. As a result, the expressions (7.67) become a system of non-linear equations, where the analytical solution similar to (7.147) is not possible.

The appropriate solution for the textured polycrystals is a construction of the iterative procedure based on (7.67) for calculation of the tensor $\boldsymbol{C}$ [33, 34]. For example, the Eq. (7.66) is re-written as:

$$\boldsymbol{\epsilon}^{(0)} = \boldsymbol{\epsilon}^{(0)} + [\langle (\mathbf{1} + \boldsymbol{E} : \delta \boldsymbol{c}_n)^{-1} \rangle - \mathbf{1}] : \boldsymbol{\epsilon}^{(0)}, \tag{7.160}$$

where the second term in the right side equals to zero for the exact solution of (7.67). By expressing the strain $\epsilon^{(0)}$ through the stress $\langle \boldsymbol{\sigma} \rangle$ using the macroscopic compliance tensor $\boldsymbol{S} = \boldsymbol{C}^{-1}$, the following equation is obtained:

$$\boldsymbol{S} = \boldsymbol{S} + [\langle (\mathbf{1} + \boldsymbol{E} : \delta \boldsymbol{c}_n)^{-1} \rangle - \mathbf{1}] : \boldsymbol{S}. \tag{7.161}$$

Based on this equation, the iterative scheme can be constructed as follows:

$$\boldsymbol{S}^{(n+1)} = \boldsymbol{S}^{(n)} + f[\langle(\mathbf{1} + \boldsymbol{E}^{(n)} : \delta\boldsymbol{c}_n)^{-1}\rangle - \mathbf{1}] : \boldsymbol{S}^{(n)}, \tag{7.162}$$

where $\boldsymbol{E}^{(n)}$ is calculated using $\boldsymbol{C}^{(n)} = \boldsymbol{S}^{(n)^{-1}}$. The coefficient f is determined empirically: the small values of f provide the convergence, however, require longer iterations, whereas the large values of f make the iterations unstable. Using (7.69) and (7.150), the expression for XSF is:

$$\boldsymbol{F}(\boldsymbol{y}) = \boldsymbol{y} \otimes \boldsymbol{y} : \frac{\int d\alpha f(\boldsymbol{c}^{(SC)}(\alpha))(\mathbf{1} + \boldsymbol{E} : (\hat{\boldsymbol{T}}^{(SC)}(\alpha)\boldsymbol{c} - \boldsymbol{C}))^{-1}}{\int d\alpha f(\boldsymbol{c}^{(SC)}(\alpha))} : \boldsymbol{S}, \tag{7.163}$$

with macroscopic tensors $\boldsymbol{E}, \boldsymbol{C}, \boldsymbol{S} = \boldsymbol{C}^{-1}$ being defined in the coordinate system S and stiffness tensor of a separate crystallite $\boldsymbol{c}$ being defined in the coordinate system C.

7.5.4 Vook-Witt and Inverse Vook-Witt Models

Unlike the above discussed models, the Vook-Witt and inverse Vook-Witt models implement the macroscopic anisotropy in the absence of texture.[4] The basic expressions (7.84)–(7.87) contain the anisotropic tensors $\boldsymbol{\Pi}_{\perp}$ and $\boldsymbol{\Pi}_{||}$, which distinguish the direction of a surface normal among others (Fig. 7.8 and 7.9).

The presence of texture incorporates another source of a macroscopic anisotropy. Basing on the formulas (7.150) and (7.84), the following expression is obtained for XSF:

$$\begin{aligned} &\boldsymbol{F}(\boldsymbol{y}) = \boldsymbol{y} \otimes \boldsymbol{y} : \\ &\quad \frac{\int d\alpha f(\boldsymbol{c}^{(SC)}(\alpha))\boldsymbol{c}(\alpha) : (\boldsymbol{\Pi}_{||} : \boldsymbol{c}(\alpha) - \boldsymbol{c}(\alpha) : \boldsymbol{\Pi}_{\perp})^{-1} : (\boldsymbol{c}(\alpha) : \boldsymbol{\Pi}_{||} - \boldsymbol{\Pi}_{\perp} : \boldsymbol{C}_M)}{\int d\alpha f(\boldsymbol{c}^{(SC)}(\alpha))}, \\ &c(\alpha) = \hat{\boldsymbol{T}}^{(SC)}(\alpha)\boldsymbol{c}. \end{aligned} \tag{7.164}$$

Here the macroscopic tensors are defined in the coordinate system S, and the stiffness tensor of a separate crystallite $\boldsymbol{c}$ in a coordinate system C.

[4] A similar situation occurs in Eshelby-Kröner model with the elliptical grains possessing a certain orientation [5].

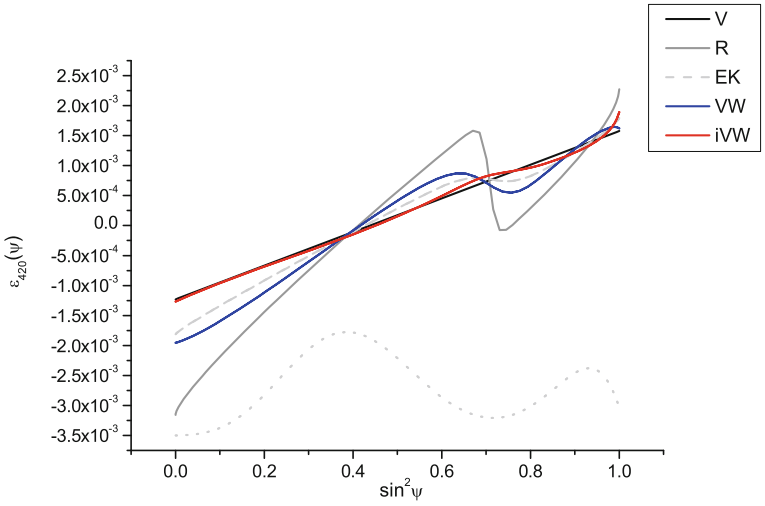

Fig. 7.8 $\sin^2\psi$ plot for Cu sample with symmetric biaxial stress 200 MPa, for (420) Bragg reflection for Voigt (V), Reuss (R), Eshelby-Kröner (E-K), Vook-Witt (VW), and inverse Vook-Witt (iVW) models. The axial texture with half-width $1/S = 20$ degree is included in the simulations, and $\boldsymbol{f}_p$ coincides with the normal $\boldsymbol{n}_p$ in the direction (111). The dashed line shows the value $\int d\alpha f(\boldsymbol{c}^{(SC)}(\alpha))$, which is proportional to the intensity of reflection at fixed ψ and ϕ

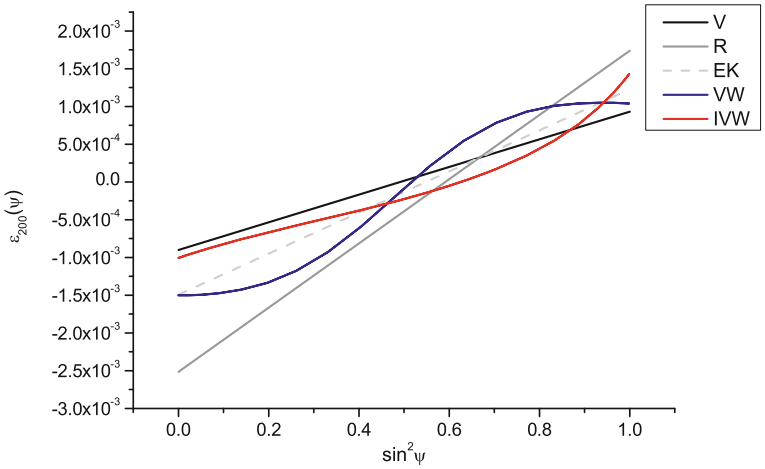

Fig. 7.9 $\sin^2\psi$ plot for Cu sample with symmetric biaxial stress 200 MPa and for Bragg reflection (200) in the absence of texture for Voigt (V), Reuss (R), Eshelby-Kröner (E-K), Vook-Witt (VW) and inverse Vook-Witt (iVW) models. The morphologic texture inherent in Vook-Witt and inverse Vook-Witt models leads to the non-linearity even in the absence of the orientational texture

References

1. V.K. Pecharsky, P.Y. Zavalij, *Fundamentals of Powder Diffraction and Structural Characterization of Materials* (Springer, New York, 2005)
2. E.J. Mittemeijer, P. Scardi (eds), *Diffraction Analysis of the Microstructure of Materials* (Springer, Berlin, 2004)
3. U.F. Kocks, C.N. Tomé, H.-R. Wenk, *Texture and Anisotropy: Preferred Orientations in Polycrystals and Their Effects on Material Properties* (Cambridge University Press, Cambridge, 1998)
4. I.C. Noyan, J.B. Cohen, *Residual Stress: Mesurements by Diffraction and Interpretation* (Springer, Berlin, 1987)
5. U. Welzel, S. Freour, E.J. Mittemeijer, Direction-dependent elastic grain-interaction models a comparative study. Phil. Mag. **85**(21), 2391–2414 (2005)
6. T. Ungár, Dislocation densities, arrangements and character from X-ray diffraction experiments. Mater. Sci. Eng. A **309**, 14–22 (2001)
7. L.D. Landau, E.M. Lifshitz, *Theory of Elasticity*, vol. 7, 3rd edn (Butterworth-Heinemann, Oxford, 1986)
8. Mario Birkholz, *Thin Film Analysis by X-Ray Scattering* (Wiley, Weinheim, 2006)
9. E. Macherauch, P. Müller, Das $\sin^2\psi$ - Verfahren der röntgenographischen Spannugsmessung. Zeitschrift angewandte Physik **13**, 305–312 (1961)
10. V. Uglov, V. Anischik, S. Zlotski, I. Feranchuk, T. Alexeeva, A. Ulyanenkov, J. Brechbuehl, A. Lazar. Surf. Coat. Technol. **202**, 2389 (2009)
11. A. Benediktovich, H.H. Guerault, I. Feranchuk, V. Uglov, A. Ulyanenkov, Influence of surface roughness on evaluation of stress gradients in coatings. Mater. Sci. Forum **681**, 121–126 (2011)
12. V. Hauk, *Structural and Residual Stress Analysis by Nondestructive Methods: Evaluation-Application-Assessment* (Elsevier Science, Amsterdam, 1997)
13. B.B He, *Two-dimensional X-ray Diffraction* (Wiley, New Jersey, 2009)
14. Z. Hashin, Analysis of composite materials. J. Appl. Mech. **50**(2), 481–505 (1983)
15. G.W. Milton, The coherent potential approximation is a realizable effective medium scheme. Commun. Math. Phys. **99**(4), 463–500 (1985)
16. R.J. Gehr, R.W. Boyd, Optical properties of nanostructured optical materials. Chem. Mater. **8**(8), 1807–1819 (1996)
17. I.M. Lifshitz, L.N. Rosenzweig, To the theory of elastic properties of the polycrystals. Russ. J. Exp. Theoret. Phys. **16**(11), 967–980 (1946)
18. J.R. Willis, Variational and related methods for the overall properties of composites. Adv. Appl. Mech. **21**, 1–78 (1981)
19. Jr. W.F. Brown, Solid mixture permittivities. J. Chem. Phys. **23**(8), 1514–1517 (1955)
20. D.A.G Bruggeman, The calculation of various physical constants of heterogeneous substances. I. The dielectric constants and conductivities of mixtures composed of isotropic substances. Ann. Phys. **24**(132), 636–679 (1935)
21. T. Mura, *Micromechanics of Defects in Solids* (Springer, New York, 1987)
22. J.D. Eshelby, The determination of the elastic field of an ellipsoidal inclusion, and related problems. Proc. R. Soc. Lond. A. Math. Phys. Sci. **241**(1226), 376–396 (1957)
23. E. Kröner, Berechnung der elastischen Konstanten des Vielkristallsaus den Konstanten des Einkristalls. Zeitschrift für Physik A Hadrons and Nuclei **151**(4), 504–518 (1958)
24. U. Welzel, J. Ligot, P. Lamparter, A.C. Vermeulen, E.J. Mittemeijer. Stress analysis of polycrystalline thin films and surface regions by x-ray diffraction. J. Appl. Crystallogr. **38**(1), 1–29 (2005)
25. A. Andryieuski, S. Ha, A.A. Sukhorukov, Y.S. Kivshar, A.V. Lavrinenko, Bloch-mode analysis for retrieving effective parameters of metamaterials. Phys. Rev. B **86**(3), 035127 (2012)
26. T. Maas Harald Wern, N. Koch, Self-consistent calculation of the X-ray elastic constants of polycrystalline materials for arbitrary crystal symmetry. Mater. Sci. Forum. **404–407**, 127–132 (2002)

27. R.A. Lebensohn, O. Castelnau, R. Brenner, P. Gilormini, Study of the antiplane deformation of linear 2-d polycrystals with different microstructures. Int. J. Solids Struct. **42**(20), 5441–5459 (2005)
28. W. Voigt, Lehrbuch der Kristallphysik (Leipzig Teubner, 1910)
29. A. Reuss, Berechnung der Fliessgrenze von Mischkristallen auf Grund der Plastizitatsbedingung fuer Einkristalle. ZAMM J. Appl. Math. Mech. / Zeitschrift fur Angewandte Mathematik und Mechanik **9**(1), 49–58 (1929)
30. R Hill, The elastic behaviour of a crystalline aggregate. Proc. Phys. Soc. A. **65**(5), 349 (1952)
31. R.J. Asaro, D.M. Barnett, The non-uniform transformation strain problem for an anisotropic ellipsoidal inclusion. J. Mech. Phys. Solids. **23**(1), 77–83 (1975)
32. Z. Hashin, S. Shtrikman, A variational approach to the theory of the elastic behaviour of polycrystals. J. Mech. Phys. Solids. **10**(4), 343–352 (1962)
33. G. Kneer, Uber die Berechnung der Elastitatsmoduln vielkristallner Aggregate mit Textur. physica status solidi (b). **9**(3), 825–838 (1965)
34. N. Koch, U. Welzel, H. Wern, E.J. Mittemeijer, Mechanical elastic constants and diffraction stress factors of macroscopically elastically anisotropic polycrystals: the effect of grain-shape (morphological) texture. Phil. Mag. **84**(33), 3547–3570 (2004)
35. L.D. Landau, E.M. Lifshitz, J.B. Sykes, J.S. Bell, M.J. Kearsley, L.P. Pitaevskii, *Electrodynamics of Continuous Media*, vol. 364 (Pergamon Press, Oxford, 1960)
36. J.A. Osborn, Demagnetizing factors of the general ellipsoid. Phys. Rev. **67**(11–12), 351–357 (1945)
37. U. Welzel, M. Leoni, E.J. Mittemeijer, The determination of stresses in thin films; modelling elastic grain interaction. Phil. Mag. **83**(5), 603–630 (2003)
38. D. Faurie, O. Castelnau, R. Brenner, P.O. Renault, E. Le Bourhis, P. Goudeau, In situ diffraction strain analysis of elastically deformed polycrystalline thin films, and micromechanical interpretation. J. Appl. Crystallogr. **42**(6), 1073–1084 (2009)
39. R.W. Vook, F. Witt, Thermally induced strains in evaporated films. J. Appl. Phys. **36**(7), 2169–2171 (1965)
40. M. Leoni, U. Welzel, P. Lamparter, EJ Mittemeijer, J.D. Kamminga, Diffraction analysis of internal strain-stress fields in textured, transversely isotropic thin films: theoretical basis and simulation. Phil. Mag. A. **81**(3), 597–623 (2001)
41. F.I. Fedorov, *The Lorentz Group* (Nauka, Moscow, 1979)
42. E.J. Mittemeijer, *Fundamentals of Materials Science: The Microstructure-Property Relationship Using Metals as Model Systems* (Springer, Heidelberg, 2011)
43. T. Ungár, J. Gubicza, G. Ribárik, A. Borbély, Crystallite size distribution and dislocation structure determined by diffraction profile analysis: principles and practical application to cubic and hexagonal crystals. J. Appl. Crystallogr. **34**(3), 298–310 (2001)
44. G. Ribarik, T. Ungar, Characterization of the microstructure in random and textured polycrystals and single crystals by diffraction line profile analysis. Special topic section: local and near surface structure from diffraction. Mater. Sci. Eng. A, **528**(1), 112–121 (2010)
45. H.J. Bunge, P.R. Morris, *Texture Analysis in Materials Science: Mathematical Methods* (Butterworths, London, 1982)
46. G.A. Korn, T.M. Korn, *Mathematical Handbook for Scientists and Engineers: Definitions, Theorems, and Formulas for Reference and Review* (Dover Publications, Mineola, 2000)
47. I.M. Gelfand, R.A. Minlos, Z.Y. Shapiro, H.K. Farahat, *Representations of the Rotation and Lorentz Groups and Their Applications*, vol. 35 (Pergamon Press, New York, 1963)
48. A. Benediktovitch, F. Rinaldi, S. Menzel, K. Saito, T. Ulyanenkova, T. Baumbach, I.D. Feranchuk, A. Ulyanenkov, Lattice tilt, concentration, and relaxation degree of partly relaxed InGaAs/GaAs structures. Phys. Status Solidi (a). **208**(11), 2539–2543 (2011)
49. Y.I. Sirotin, M.P. Shaskolskaya, *The Basics of Crystallophysics* (Nauka, Moscow, 1975)
50. L.J. Walpole, On the overall elastic moduli of composite materials. J. Mech. Phys. Solids. **17**(4), 235–251 (1969)
51. S. Matthies, K. Helming, T. Steinkopff, K. Kunze, Standard distributions for the case of fibre textures. Phys. Status Solidi (b). **150**(1), K1–K5 (1988)

52. T. Eschner et al., Texture analysis by means of model functions. Textures Microstruct. **21**, 139–139 (1993)
53. A. Benediktovich, I. Feranchuk, A. Ulyanenkov, Calculation of X-ray stress factors using vector parameterization and irreducible representations for SO(3) group. Mater. Sci. Forum. **681**, 387–392 (2011)

Index

A. Benediktovitch et al., *Theoretical Concepts of X-Ray Nanoscale Analysis*, Springer Series in Materials Science, DOI: 10.1007/978-3-642-38177-5,